Non-Newtonian Fluid Selection for Achieving Flow Similarity in Stirred Vessels

Andrew Russell

A thesis submitted for the degree of Doctor of Philosophy

Department of Chemical Engineering

Imperial College London

September 2019

Abstract

Many key engineering applications in the chemical sector incorporate the "duty of agitation" through the use of mixing-based unit operations to achieve the desired transport phenomena governing the particular system. These industrial processes often occur in stirred vessels equipped with centrally-mounted impellers, with the material commonly associated with high levels of toxicity, expense, handling difficulty and complex rheological behaviour. The industrial fluids of interest to this project display viscoplastic behaviour, where the fluid deforms with shear-thinning characteristics, once a yield stress has been exceeded. The mixing of viscoplastic fluids in stirred vessels can lead to the formation of caverns, where regions of flow surround the central impeller, outside of which the material is stagnant. The optimisation of industrial processes often involves the implementation of appropriately scaled-down systems and the utilisation of suitable replacement model fluids.

After an extensive literature review of typical viscoplastic materials and the agitation of these fluid types in stirred vessels, a vast number of viscoplastic model fluids were formulated, rheologically characterised and fitted with mathematical rheology models. A computational platform (the '*Model Fluid Selection Tool*') was developed and acted as a rheological database, which was used as part of an operational function of the tool for suggesting suitable model fluids that most closely match the rheological properties of the 'real', industrial formulations. Highly transparent Carbopol model fluids were mixed in stirred vessels equipped with small, centrally-mounted impellers (Rushton turbines and pitched-blade turbines) over multiple scales, ranging in volume from 2-20 L, with key geometrical length scale ratios being maintained. A method for achieving cavern size similarity was determined, by scaling the dimensionless cavern diameter, D_c/D, against a combination of dimensionless parameters: $Re_m^{-0.3}Re_y^{0.6}n^{-0.1}k_s^{-1}$, where Re_m, Re_y, n and k_s are the modified power-law Reynolds number, yield stress Reynolds number, flow behaviour index and impeller geometry constant, respectively. The functional relationship between D_c/D and $Re_m^{-0.3}Re_y^{0.6}n^{-0.1}k_s^{-1}$ was utilised in a second computational platform (the '*Matching and Predictive Mixing Tool*') for predicting cavern sizes in systems of known scale and rheology, and matching dimensionless cavern sizes in a second system when the scale and/or rheology was changed. Finally, the mixing effectiveness in dual-impeller systems for agitation of viscoplastic fluids was assessed. This research project presents novel methods for matching fluids in terms of rheological properties, whilst presenting a protocol for scaling the mixing of these fluids in stirred vessel systems.

Publications

Collini, H., Mohr, M., Luckham, P.F., Shan, J., Russell, A.W., 2018. The effects of polymer concentration, shear rate and temperature on the gelation time of aqueous silica-poly(ethylene oxide) 'Shake Gels'. J. Colloid Interface Sci. 517, 1–8.

Russell, A.W., Kahouadji, L., Mirpuri, K., Quarmby, A., Piccione, P.M., Matar, O.K., Luckham, P.F., Markides, C.N., 2019. Mixing viscoplastic fluids in stirred vessels over multiple scales: A combined experimental and CFD approach. Chem. Eng. Sci. 208, 115129-1–16.

Liyanage, R., Russell, A.W., Crevor, S., Crawshaw, J.P., 2019. Experimental insights into the impact of an inverse Saffman-Taylor phenonmenon on convective mixing. Phys. Rev. Fluids, Submitted

Russell, A.W., Kahouadji, L., Shin, S., Chergui, J., Juric, D., Matar, O.K., Luckham, P.F., Markides, C.N., 2019. Assessing the mixing effectiveness of dual-impeller systems in the agitation of viscoplastic fluids. Chem. Eng. Sci., In Preparation

Russell, A.W., Piccione, P.M., Luckham, P.F., Markides, C.N., 2019. Development of a computational platform for matching rheology and predicting the mixing of viscoplastic fluids. Chem. Eng. Sci., In Preparation

Declaration of Originality

I declare that the work presented in this thesis is my own and that all other work was appropriately referenced.

Copyright Declaration

Acknowledgements

I would first like to thank my supervisors, Professor Paul Luckham and Professor Christos Markides. I think it is safe to say that this project fell between your areas of respective interest, however I am hugely appreciative of the considerable amount of time you spent helping and supporting me throughout the last four years. It has been both a massive learning curve and a thoroughly enjoyable experience, and I have you both to thank for getting me to this stage.

I am very grateful to my industrial sponsor, Syngenta, and in particular my industrial supervisor for the first three and a half years, Patrick Piccione. Your passion and interest for this work was very evident from the first day onwards, and I am lucky to have had your support and help throughout this project. Thank you also to Andrew Quarmby for all your help with the Syngenta-based experimental mixing work, you made my time spent at Syngenta very fun. Many thanks also to Anita Rea, Neil Gibson and John Hone for their technical expertise and assistance throughout the project.

Many thanks also to the Clean Energy Processes group and the Luckham group, in particular Iuliia Elizarova and Rui Yan Lee. When I look back on my time at Imperial, the time spent with you both in the lab, the office and at conferences will form some of my fondest memories. Although I was not an official member of the Matar Fluids Group, I am hugely appreciative to Professor Omar Matar and Lyes Kahouadji for including me into the MFG as if I were. It was great collaborating with you both and I am proud of the work we produced together. Many thanks also to Princen Princen for your assistance with the model fluid formulation and rheological characterisation.

I would not have got through this project without the support of my friends and family. I would like to thank my school friends, and in particular the Los Blancos football team, my Bristol friends and all my friends from Imperial, including the Moon group and the 4 B's. Massive thanks to all my family, in particular Mum, Dad, Lindsey and Callum for your constant love and support. You helped me keep the perspective I needed throughout this process, for which I am deeply grateful.

And finally, Lucy. Words cannot describe how appreciative I am of everything you have done for me, not only throughout this PhD, but over the last few years. Thank you.

Abbreviations

Nomenclature

A_b	Blade angle [°]
C	Impeller clearance [m]
C_1	Upper impeller clearance [m]
C_2	Lower impeller clearance
D	Impeller diameter [m]
D_c	Cavern diameter [m]
D_d	Disc diameter [m]
D_h	Hub diameter [m]
F_a	Axial force component [-]
F_{fsi}	Solid-body force [N]
Fr	Froude number [-]
G	Impeller separation [m]
g	Gravitational acceleration [m s^{-2}]
h	Distance between parallel plates [m]
H	Liquid fill height [m]
H_b	Blade height [m]
H_c	Cavern height [m]
H_h	Hub height [m]
K	Flow consistency index [Pa s^n]
k_s	Impeller geometry constant [-]
L_b	Blade length [m]
M	Impeller torque [N m]
N	Impeller rotational speed [s^{-1}, rpm]
N_b	Blade number [-]
N_f	Axial force number [-]
N_H	Highest impeller rotational speed [s^{-1}, rpm]
N_L	Lowest impeller rotational speed [s^{-1}, rpm]
n	Flow behaviour index [-]
p	Pressure [Pa]
P	Power input [W]
Po	Power number [-]
R	Tank radius [m]
Re	Reynolds number [-]
Re_{HB}	Herschel-Bulkley Reynolds number [-]

Re_m	Modified power-law Reynolds number [-]
Re_y	Yield stress Reynolds number [-]
s	Number of analysed shear stress data points [-]
S	Shaft diameter [m]
S_a	Cavern-air surface area [m^2]
S_p	Cavern-suspension surface area [m^2]
S_w	Cavern-wall surface area [m^2]
T	Tank diameter [m]
T_b	Blade thickness [m]
T_d	Disc diameter [m]
t	Time [s]
u	Velocity [m s^{-1}]
$\mathbf{u}$	Velocity field [m s^{-1}]
u_z	Axial velocity component [m s^{-1}]
u_θ	Azimuthal velocity component [m s^{-1}]
V	Tank volume [L]
W_b	Blade width [m]

Greek Letters

α	Ellipse parameter [-]
β	Elliptical torus aspect ratio [-]
$\dot{\gamma}$	Shear rate [s^{-1}]
$\bar{\dot{\gamma}}$	Mean shear rate [s^{-1}]
$\dot{\gamma}_c$	Critical shear rate [s^{-1}]
∇	Del operator [m^{-1}]
η_{pl}	Constant plastic viscosity [Pa s]
μ	Fluid dynamic viscosity [Pa s]
ρ	Fluid density [kg m^{-3}]
σ	Normal stress [Pa]
$\bar{\sigma}$	Bulk stress [Pa]
σ_{ij}	Cauchy stress tensor [Pa]
τ	Shear stress [Pa]
$\boldsymbol{\tau}$	Stress tensor [Pa]
τ_{a}	Friction force per unit area at air-suspension interface [Pa]
τ_F	Fitted shear stress value [Pa]
τ_R	Raw shear stress value [Pa]
τ_{w}	Friction force per unit area at vessel wall [Pa]

τ_y	Fluid yield stress [Pa]
v	Kinematic viscosity [m s^{-1}]
Ψ	Static distance function [-]

Abbreviations

AAD	Average absolute deviation
C934	Carbopol 934
C940	Carbopol 940
C980	Carbopol 980
C981	Carbopol 981
CU10	Carbopol Ultrez 10
CU21	Carbopol Ultrez 21
CU30	Carbopol Ultrez 30
CFD	Computational fluid dynamics
CMC	Carboxymethyl cellulose
DHR	Double helical ribbon
EDL	Electric double layer
ERT	Electrical resistance tomography
GG	Guar gum
GG-2HPE	Guar gum 2-hydroxypropyl ether
HEC	Hydroxyethyl cellulose
HFA	Hot-film anemometry
HPC	Hydroxypropyl cellulose
LDA	Laser Doppler anemometry
MFST	Model Fluid Selection Tool
MPMT	Matching and Predictive Mixing Tool
PBT	Pitched-blade turbine impeller
PEG	Polyethylene glycol
PEO	Polyethylene oxide
PLIF	Planar laser-induced fluorescence
PIV	Particle image velocimetry
RT	Rushton turbine impeller
UDV	Ultrasound Doppler velocimetry
XG	Xanthan gum

Table of Contents

List of Figures

List of Tables

Thesis Motivation and Outline

Thesis Motivation

In numerous chemical industries, mixing-based unit operations are often used to achieve the desired transport phenomena defining a given system. Many industrial processing materials exhibit complex rheological characteristics and are often associated with high levels of reactivity, expense and handling difficulty. To better understand and overcome any potential issues that may arise whilst performing industry-scaled mixing operations, it is often desirable to implement scaled-down, physically-similar laboratory experiments, utilising replacement 'model' fluids. These model fluids must accurately simulate the rheological characteristics of the industrial formulations, whilst also being safe, inexpensive and easy to handle. The rheological properties of the industrial formulations are often viscoplastic in nature: displaying shear-thinning behaviour once the yield stress has been exceeded, and solid-like behaviour otherwise. These fluids can be described by mathematical rheology models, such as the Herschel-Bulkley model or the Casson model. Although numerous viscoplastic model fluid systems have been studied in the literature, limited effort has been placed into the development of a methodology that not only acts as a database for these types of fluids, but that is also capable of suggesting model fluids systems that most closely match the rheological properties of the 'to-be-matched' or 'real' fluids of interest, which could then be used to simulate a particular mixing-based unit operation at a given scale. Development of such a methodology is an important focus for this study.

Carbopol fluids have been shown to be a typical viscoplastic fluid and have therefore been used in the literature as model fluids when characterising viscoplastic flows in stirred vessels equipped with a centrally-mounted impeller. When these materials are agitated by the central impeller in a vessel system, a 'cavern' can form, whereby material surrounding the impeller is flowing as the impeller-induced stresses are great enough to exceed fluid's yield stress. Outside of this region, the material is stagnant. Although the mixing of Carbopol fluids in stirred vessels has been widely studied in the literature, few studies have investigated the mixing of these fluids over multiple scales, in an attempt to match flows and achieve dynamic similarity. As a result, both experimental and computational investigations are required to examine the flow of these fluids over scales and for the development of a scaling method to achieve flow similarity of these fluid types over scales of varying size.

Thesis Outline

This thesis is constructed of seven main chapters. The first chapter starts with an in-depth review on the fundamental theory behind fluid rheology, before discussing the classification of fluids and the mathematical models used to describe the various fluid types. A literature review of typical viscoplastic fluids is also presented, followed by a discussion of the mixing of viscoplastic fluids in stirred vessels equipped with single and multi-impellers. Details relating to the formulation and rheological characterisation of viscoplastic fluids are then presented in Chapter 2, with the raw rheological flow curves being fitted with various mathematical models. Chapter 3 is a presentation of a computational platform, known as the '*Model Fluid Selection Tool*', that has been developed as a viscoplastic model fluid database, as well as being a method for matching the rheological profiles of 'real', industrial fluids with potential replacement model fluids. The mixing of viscoplastic Carbopol fluids in stirred vessels over multiple scales is then discussed in Chapter 4, with a scaling method for achieving cavern size similarity for the fluids and systems investigated being presented. Details of this scaling method are then utilised in a computational platform, known as the '*Matching and Predictive Mixing Tool*', discussed in Chapter 5. This methodology enables the cavern size in known mixing systems and fluids to be predicted, whilst also allowing cavern sizes in a second system to be matched, if the scale of the mixing system and/or fluid rheology has been changed. Chapter 6 assesses the mixing effectiveness of various dual-impeller mixing systems in the agitation of viscoplastic materials, with the aim of achieving full-vessel homogeneity. Finally, Chapter 7 is an overall conclusion of the findings of this research project, and with suggestions for future work being presented.

Chapter 1: Theoretical Background and Literature Review

1.1 Fluid rheology

1.1.1 Theoretical background

The concept of rheology was first coined by Bingham (1922) and is the study of the deformation and flow of matter (Barnes *et al.* (1989)). To understand the basic concepts and definitions associated with the rheology of fluids, a simple flow situation must first be considered. In this situation, a substance is contained between two parallel plates, separated by distance, h, as seen in Figure 1.1. If the substance is a fluid, it will flow with a steady velocity, u in the x-direction, when a force is applied to the top plate, whilst the bottom plate remains stationary. The force acts on the surface area over which it is applied, resulting in a shear stress, τ_{xy} (force per unit area) being exerted on the fluid. A fluid can be defined as a substance that has the capability to deform continuously, or flow, when a stress is applied to it. In Figure 1.1, if the fluid were to be replaced by a solid, the solid would be unable to flow under the influence of an applied stress and hence elastic deformation would ensue (Barnes *et al.* (1989); Streeter *et al.* (1998); Mewis and Wagner (2012)).

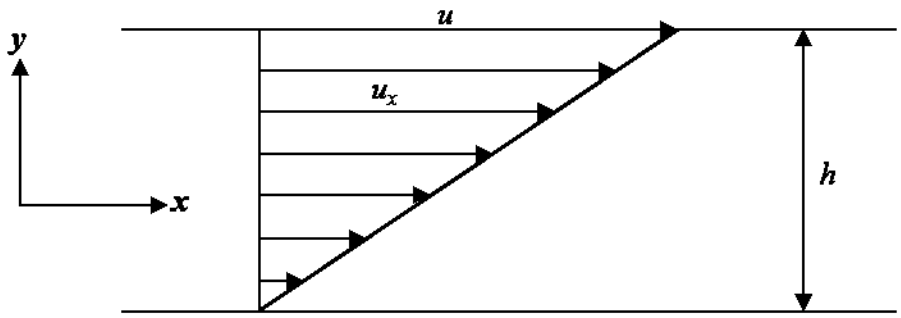

Figure 1.1. Deformation of a fluid between two parallel plates, illustrating simple shear flow.

The fluid layers near the solid boundaries will have the same velocity as the solid boundary in question. In this example, the fluid in immediate contact with the top plate will have the same velocity as the top plate, whilst the fluid in contact with the lower plate will be stationary, fulfilling the 'no-slip' boundary conditions. As seen in Figure 1.1, the parallel flow of the fluid layer will result in a linear and uniform variation of velocity between the plates, from u at the top plate, to zero at the bottom plate, as the shear stress applied to the top plate acts on each fluid layer, until it is transmitted to the bottom plate. This velocity gradient, known as the shear rate, $\dot{\gamma}$, or the rate of deformation, is defined in Eq. 1.1, where u_x are the local velocities in the x-direction, within the fluid (Streeter *et al.* (1998); Goodwin and Hughes (2008); Björn *et al.* (2012); Mewis and Wagner (2012)).

$$\frac{du_x}{dy} = \frac{u}{h} = \dot{\gamma} = \text{constant} \tag{1.1}$$

In simple, one-dimensional fluid flow, the magnitude of applied shear stress, τ_{xy} can be related to the shear rate, $\dot{\gamma}$ via Newton's constitutive equation of viscosity (Eq. 1.2). The proportionality constant is known as the dynamic viscosity, μ and is defined as the fluid's resistance to deformation. Newtonian fluids display ideal fluid behaviour, with a linear relationship being exhibited by the shear stress and shear rate, leading to a constant dynamic viscosity. The dynamic viscosity can be related to the kinematic viscosity, ν using the fluid density, ρ, as seen in Eq. 1.3. Newton's constitutive equation of viscosity describes the relationship between the kinematics and stresses for a given fluid. It can be used in conjunction with the governing conservation laws of mass (Eq. 1.4) and linear momentum (Eq. 1.5) to solve relevant flow problems (Richardson (1989); Schramm (2000); Streeter *et al.* (1998); Björn *et al.* (2012); Mewis and Wagner (2012)).

$$\tau_{xy} = \mu \frac{du_x}{dy} = \mu\dot{\gamma} \tag{1.2}$$

$$\nu = \frac{\mu}{\rho} \tag{1.3}$$

$$\frac{\partial \rho}{\partial t} + \rho \nabla \cdot \mathbf{u} = 0 \tag{1.4}$$

$$\rho \frac{\partial \mathbf{u}}{\partial t} + \rho \mathbf{u} \cdot \nabla \mathbf{u} = \rho \mathbf{g} - \nabla p + \nabla \cdot \boldsymbol{\tau} \tag{1.5}$$

From Eq. 1.2-1.5, $\mathbf{u}$ is the velocity field, ∇ is the Del operator (or vector differential operator), p is the pressure, $\boldsymbol{\tau}$ is the stress tensor and $\mathbf{g}$ is the gravitational acceleration. Eq. 1.4 is the 'continuity equation' and describes the conservation of mass on a fluid, whilst Eq. 1.5 highlights that various forces are balanced on a fluid element to enable linear momentum to be conserved (Richardson (1989)). Thus far, the theory behind unidirectional flow has been discussed, which can be generalised to accurately portray the three-dimensional flow of fluids. Two types of forces can be exerted on a three-dimensional fluid parcel (of arbitrary shape and size): body forces and surface forces. Body forces (e.g. gravitational or electromagnetic forces) act on the fluid parcel from a distance. They are long-range forces, with gravitational forces providing the weight of the parcel. Surface forces (e.g. viscous or elastic forces) are exerted onto the fluid parcel through direct contact with other fluid parcels. Each fluid particle surrounding the parcel in question has a certain velocity, with each particle varying in magnitude and direction compared to neighbouring particles. Therefore, all velocities associated with the neighbouring particles act on the central parcel with a net resultant force that is exerted over the specific contact surface area. An example of a typical surface force is pressure. These stress components acting on a generalised three-dimensional fluid flow can be visualised by considering a box (or parallelepiped) with finite dimensions and infinitesimal volume, surrounding an arbitrary point in the fluid, with the surface stresses acting on the fluid volume being the

result of the surrounding medium (Figure 1.2) (Barnes *et al.* (1989); Richardson (1989); Streeter *et al.* (1998); Brown *et al.* (2004); Goodwin and Hughes (2008); Mewis and Wagner (2012)).

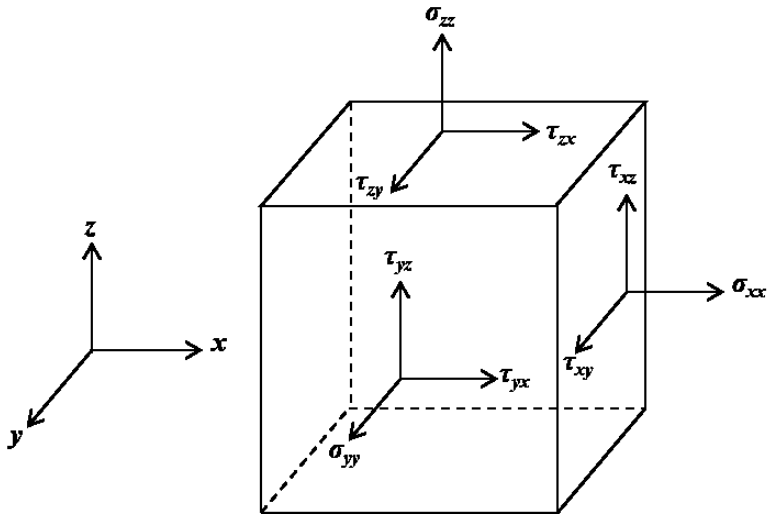

Figure 1.2. Parallelepiped of infinitesimal volume, surrounding a point in a fluid, used to describe the stress state of a generalised, three-dimensional fluid.

Having defined each plane using the Cartesian coordinate in the normal direction, the three planes can be further decomposed into three orthogonal stress components per plane, resulting in a total of nine stress components required for a full description of this generalised stress state. The three stress components (one per plane) that act in the perpendicular direction to planes are known as the normal stresses: σ_{xx}, σ_{yy} and σ_{zz}. Normal stresses act outwardly from the surface of the fluid volume, changing the volume of the fluid box, which is resisted by the fluid's bulk modulus of elasticity. This outward direction is defined as being 'positive', and the average of the three normal stresses is known as the bulk stress, $\bar{\sigma}$. The pressure, p, acts inwardly towards the centre of the box and is defined as the negative of the bulk stress (Eq. 1.6) (Streeter *et al.* (1998); Mewis and Wagner (2012)).

$$p = -\bar{\sigma} = -\frac{1}{3}\left(\sigma_{xx} + \sigma_{yy} + \sigma_{zz}\right) \tag{1.6}$$

The two remaining stresses per plane act on the fluid box in a tangential direction, parallel to the plane. These are shear stresses, τ and are responsible for the deformation of the fluid (Figure 1.1). The shear stress components that act across the diagonal to one another are symmetric (or equivalent), e.g. $\tau_{xy} = \tau_{yx}$, hence explaining why there is a total of nine stress components, and not more. These stress components can be represented by the 3 × 3 Cauchy stress tensor (Eq. 1.7), that completely describes the three-dimensional flow of fluids. It should be noted that the first of the two subscript values describes the normal to the plane in which the stress acts, and the second defines the direction in which

the stress is acting. For example, τ_{xy} describes the shear stress acting in the *y*-direction on a surface perpendicular to the *x*-direction (Streeter *et al.* (1998); Mewis and Wagner (2012)).

$$\sigma_{ij} = \begin{pmatrix} \sigma_{xx} & \tau_{xy} & \tau_{xz} \\ \tau_{yx} & \sigma_{yy} & \tau_{yz} \\ \tau_{zx} & \tau_{zy} & \sigma_{zz} \end{pmatrix} \tag{1.7}$$

1.1.2 Fluid classification

The rheological properties of fluids can be obtained through characterisation using an instrument known as a 'rheometer'. Rheometers can either be shear stress-controlled or shear rate-controlled, with the test fluid being contained within the measurement geometry, consisting of a stationary device (often a cup or a plate) and a rotating probe attached to a motor. In shear stress-controlled rheometers, a torque (rotational force) is pre-set, with the angular deflection of the probe being measured by an optical encoder, and the resulting angular velocity of the probe being calculated. The torque and velocity can then be translated into shear stress and shear rate values, respectively, using conversion factors, allowing the flow curve of the material to be obtained (Walters (1975); Nguyen and Boger (1992); Tornberg (2016); Fernanda (2018)). Fluids can be rheologically described as either displaying Newtonian or non-Newtonian behaviour. Fluids exhibiting ideal, Newtonian behaviour display direct proportionality between the magnitude of applied shear stress and the resulting shear rate that ensues, and hence the dynamic viscosity is constant (Eq. 1.2) and defines the gradient of the fluid's linear flow curve. Common examples of Newtonian fluids include water, glycerol, olive oil and bitumen (Streeter *et al.* (1998); Schramm (2000); Björn *et al.* (2012)). In contrast, non-Newtonian fluids exhibit a non-linear relationship between the shear stress and the shear rate, and hence the dynamic viscosity is no longer a constant and is dependent on the value of shear stress applied to the material. Typical examples of non-Newtonian fluids include shear-thinning (pseudoplastic), Bingham plastic, viscoplastic and shear-thickening (dilatant) fluids, with discussion of these fluid types presented in the subsequent sections (Sections 1.1.2.1-1.1.2.4). These types of fluids can be time-dependent or time-independent, whereby if the fluid has time-dependent properties, the dynamic viscosity of the fluid will vary with time at a constant applied shear stress and temperature. Fluids with time-dependent properties can either be thixotropic or rheopectic in nature, with discussion of these types of fluids presented in Sections 1.1.2.5 and 1.1.2.6, respectively. Finally, viscoelastic fluid properties will briefly be discussed in Section 1.1.2.7. A graphical depiction of the rheological flow curves, presented in a linear-linear shear stress-shear rate plot, of the various (time-independent) fluid types can be seen in Figure 1.3, where *Flow Curve A* is typical of a Newtonian fluid, *Flow Curve B* is a shear-thinning fluid, *Flow Curve C* is a Bingham plastic, *Flow Curve D* is a viscoplastic material and *Flow Curve E* is a shear-thickening fluid (Wilkinson (1960); Skelland (1967); Streeter *et al.* (1998); Schramm (2000); Björn *et al.* (2012); Mewis and Wagner (2012).

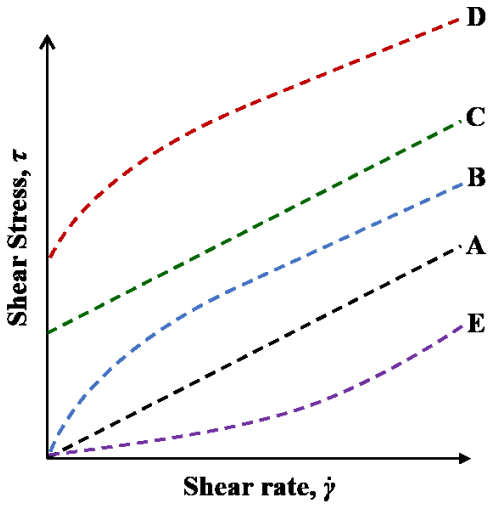

Figure 1.3. Graphical representation of the rheological flow curves of common time-independent fluid types, where: *A* = a Newtonian fluid, *B* = a shear-thinning (pseudoplastic) fluid, *C* = a Bingham plastic, *D* = a viscoplastic fluid and *E* = a shear-thickening (dilatant) fluid (adapted from Mewis and Wagner (2012)).

A number of different geometries can be used for measuring the rheological properties of fluids in a rheometer, including a concentric cylinder system, a cone-and-plate, a plate-and-plate and a vane-and-cup. In this work, a focus was placed on using the vane-and-cup geometry, due to the gel-like nature of the fluids of interest. Also, vane-based geometry have traditionally been used to avoid the phenomenon of wall slip in low shear rate regime, allowing for an accurate description of a fluid's yield stress (defined in Section 1.1.2.2) to be obtained (Nguyen and Boger (1983, 1985, 1992); Yoshimura *et al.* (1987); Buscall *et al.* (1993); Barnes and Nguyen (2001)). Further discussion relating to the requirement of vane geometry for rheological characterisation of fluids in this work, along with a schematic depiction of a 6-bladed vane-and-cup system, can be found in Section 2.4.

1.1.2.1 Shear-thinning fluids

Shear-thinning fluids, also known as pseudoplastic fluids, exhibit a decrease in dynamic viscosity, with increasing shear stress (or shear rate) being applied to the material, as seen in *Flow Curve B* in Figure 1.3. At rest, the particles or molecules in shear-thinning suspensions form an irregular internal order, leading to the material having a high viscosity (or resistance to flow). As a shear stress is applied to the material and is steadily increased, the molecules align themselves within the direction of flow, leading to the deformation of the fluid structures and the breaking down of aggregates. The result is the decrease in the fluid's viscosity, until a limiting viscosity (μ_{lim}) is reached at particularly high shear stresses and shear rates, when the molecules are at a maximum dispersion for the given suspension, resulting in the rheological flow curve becoming linear and plateauing. In time-independent fluids, when the applied shear stress is ceased, the structures within the fluid rebuild instantaneously and the fluid returns to its

resting state viscosity, whilst in time-dependent (thixotropic) fluids, this restructuring takes far longer (Schramm (2000); Goodwin and Hughes (2008); Björn *et al.* (2012); Mewis and Wagner (2012)). Common examples of shear-thinning fluids include blood (Baskurt and Meiselman (2003)) and polymer-based fluids, such as carboxymethyl cellulose solutions (Benchabane and Bekkour (2008)).

1.1.2.2 Bingham plastics

Bingham plastics, or ideal plastics, are fluids that exhibit a yield stress, which once exceeded, deform in a pseudo-Newtonian fashion, as depicted by *Flow Curve C* in Figure 1.3. The yield stress is defined as the shear stress value that must be applied to the material to induce flow or deformation within the material. If shear stress values are applied to the material that are smaller than the yield stress, the material will behave like an elastic solid, as the three-dimensional internal structure is capable of preventing motion within the material. When the yield stress is overcome, there is direct proportionality in Bingham plastics between the magnitude of applied shear stress and rate of shear, leading to a constant dynamic viscosity with increasing applied shear stress (Wilkinson (1960); Skelland (1967); Papanastasiou (1987); Schramm (2000); Goodwin and Hughes (2008); Björn *et al.* (2012)). The term 'yield stress' is often seen in the literature as being a contentious topic (Barnes and Walters (1985); Barnes (1999); Møller *et al.* (2006)), however, it can often be interpreted in two ways, depending on the conditions of the system in question, and whether or not the fluid in question has associated time-dependent flow properties. The 'static' yield stress is the yield stress value measured in an undisturbed material, whilst the 'dynamic' yield stress is the yield stress measured in a material which has been broken down and can be obtained from the material's equilibrium flow curve. In fluids which have time-independent rheological properties, these two definitions represent the same yield stress value, however in time-dependent fluids, such as thixotropic fluids (Section 1.1.2.5), the value of the 'static' yield stress is often greater than that of the 'dynamic' yield stress (Cheng (1986); Sun and Gunasekaran (2009); Björn *et al.* (2012)).

1.1.2.3 Viscoplastic fluids

Viscoplastic fluids are also materials that exhibit a yield stress, however unlike Bingham plastics, there is a non-linearity of the flow once the yield stress has been exceeded, as depicted by *Flow Curve D* in Figure 1.3. More specifically, once the yield stress has been overcome, the fluids display shear-thinning behaviour, with the dynamic viscosity decreasing as the shear stress being applied to the material increases, until a limiting viscosity (μ_{lim}) at particularly high shear stress and shear rate values is reached. Increasing applied shear stress values beyond the values associated with the limiting viscosity plateau will have no effect on the viscosity of the system. As with Bingham plastics, if the shear stress values applied to the material do not exceed the yield stress, the material will displayed elastic, solid-like behaviour (Streeter *et al.* (1998); Goodwin and Hughes (2008); Björn *et al.* (2012); Balmforth *et al.*

(2014); Dinkgreve *et al.* (2016); Malkin *et al.* (2017)). Common examples of viscoplastic materials include tomato ketchup (Bottiglieri *et al.* (1991)) and mayonnaise (Liu *et al.* (2007)). The formulation and characterisation of fluids that exhibit viscoplastic rheological properties will be the focus of this project, with the aim of finding model fluid systems that exhibit the desired rheological properties, whilst also being safe, inexpensive, easy-to-handle and, ideally, transparent, to ease the visualisation of these fluids in stirred vessel systems, although this last feature is not a necessity. Further discussion of potential model fluids can be found in Chapter 2, whilst the agitation of these fluids in stirred vessel systems is presented in Chapters 4 and 6. The reader is directed to the works of Mitsoulis (2007) and Coussot (2014)) for a comprehensive review of the flows of viscoplastic materials and yield stress fluids.

1.1.2.4 Shear-thickening fluids

Shear-thickening fluids, also known as dilatant fluids, have the opposite properties to shear-thinning fluids, whereby an increase in dynamic viscosity is displayed when the shear stress applied to the material increases, as seen in *Flow Curve E* in Figure 1.3, with this behaviour often associated with suspensions with very high particle volume fractions (Schramm (2000); Goodwin and Hughes (2008); Björn *et al.* (2012); Mewis and Wagner (2012)). The microstructural mechanisms behind the shear-thickening behaviour exhibited by colloidal suspensions, such a silica-based systems (Bender and Wagner (1995)), are not fully known, however two opposing theories have been proposed and are widely accepted as being the most likely explanations for this type of rheological behaviour, and they are: (1) the order-to-disorder theory (ODT), first suggested by Hoffman (1972), and (2) the hydrocluster theory (Boersma *et al.* (1995); Raghavan and Khan (1997); Hoffman (1998)). The ODT suggests that the flow transitions from an ordered state of layered particles into a disordered, shear-thickened state at a critical shear rate, with instability driven by hydrodynamic forces causing the particles to be 'jostled', breaking up the layered flow (Raghavan and Khan (1997); Hoffman (1998)). The hydrocluster theory, via the use of Stokesian dynamics simulations, suggests that the shear-thickening observed in concentrated dispersions corresponds to the formation of larger clusters of particles, rather than the destruction of ordered layers. Hydrodynamic shear forces overcome Brownian and repulsive steric forces, inducing the formation of these clusters, and consequently an increase in viscosity (Hunter (1987); Boersma *et al.* (1995); Raghavan and Khan (1997)). Everyday examples of shear-thickening systems include corn starch-water suspensions (Crawford *et al.* (2013)) and cement pastes (Cyr *et al.* (2000)). Silica-polyethylene oxide aqueous mixtures, known as 'shake-gels', display reversible, discontinuous shear-thickening behaviour, differing from the shear-thickening behaviour previously described. 'Shake-gels' are associated with an abrupt and distinct increase in viscosity under a constant applied shear rate caused by significant microstructural changes within the particle-polymer system (Ramos-Tejada and Luckham (2015); Collini *et al.* (2018)).

1.1.2.5 Thixotropic fluids

Thixotropic fluids are an example of time-dependent non-Newtonian fluids, that exhibit a reversible decrease in dynamic viscosity with time, at a constant applied shear stress (or shear rate) and temperature. The phenomenon of thixotropy is caused by the breaking and reforming of intermolecular forces (commonly ionic and hydrogen bonds) within the fluid. When a thixotropic material is in a state of rest, it has an internal three-dimensional gel network of intermolecular bonds, giving the system solid-like properties. When a steady shear stress is applied to the gel, the three-dimensional network of intermolecular bonds is disrupted, with the material losing its solid-like properties and resulting in decrease in dynamic viscosity, allowing the material to become more liquid-like and therefore flow. If the applied shear stress is then halted and the fluid is left to rest, the gel structure will gradually re-build with the intermolecular bonds reforming through Brownian motion, leading to an increase in viscosity, until the three-dimensional gel network reforms and the material returns to its resting state viscosity. This recovery of the resting state structure and viscosity is a much slower process than the processes described in Section 1.1.2.1 relating to time-independent shear-thinning fluids, which is seen as being instantaneous by comparison. As seen in Figure 1.4, when plotting shear stress against shear rate for a thixotropic fluid (with a yield stress), a thixotropic hysteresis loop (denoted by the '*1*' in the figure) forms, with the shear stress values being greater at a given shear rate, as the shear stress is increased up to a given shear rate value ('*up*'-curve), compared to the shear stress values when the shear rate is decreased back down to zero ('*down*'-curve) (Skelland (1967); Hunter (1987); Barnes *et al.* (1989); Braun and Rosen (1999); Schramm (2000); Björn *et al.* (2012)). Typical examples of thixotropic fluids include toothpastes (Ardakani *et al.* (2011)) and clay suspensions (Pignon *et al.* (1998); Osipov *et al.* (1984)), with both of these examples also exhibiting a yield stress value. For a comprehensive review of thixotropy, the reader is directed to the works of Mewis (1979) and Barnes (1997). In the current work, a number of thixotropic fluids were formulated, namely clay suspensions. However, for all fluids studied in this project, only the shear stress '*downward*' (or '*down*') sweeps curves were used for rheological characterisation, with a focus on gaining information relating to the '*dynamic*' yield stress and to negate any potential time-dependent rheological properties of the model fluid systems.

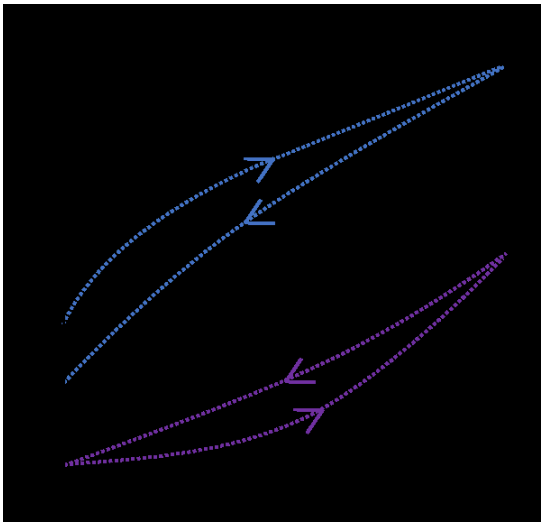

Figure 1.4. Shear stress-shear rate plot illustrating (1) thixotropic and (2) rheopectic hysteresis loops, with the directions of the arrows indicating the '*up*'- and '*down*'-curves, respectively, for the two systems.

1.1.2.6 Rheopectic fluids

Like thixotropic fluids, rheopectic fluids, also known as anti-thixotropic fluids, are time-independent non-Newtonian fluids. They display a reversible increase in dynamic viscosity with time at a constant applied shear stress and temperature, and hence display the opposite rheological properties to thixotropic fluids. When the fluid is left to rest, the viscosity of the system slowly decreases back to its resting state viscosity and again, this recovery process is far slower than the recovery displayed by shear-thickening fluids at rest. The resulting hysteresis loop displayed by rheopectic fluids can be seen in the shear stress-shear rate plot in Figure 1.4, denoted by the '*2*' in the figure. As would be expected, the shear stress values associated with the '*up*'-curve at a given shear rate are lower than the shear stress values at the same shear rate values in the '*down*'-curve. Rheopexy is rarely observed, but it can be induced in some fluids via gentle agitation, allowing the particles in the fluid to form expansive structures, which resist the action of shearing (Skelland (1967); Hunter (1987); Schramm (2000)).

1.1.2.7 Viscoelastic fluids

Viscoelastic materials exhibit the properties of both a viscous liquid and an elastic solid. If a constant shear stress was to be applied to an elastic solid, the material will deform indefinitely, until the stress is halted, with the material returning immediately to its non-deformed state. The energy required for this deformation would be stored as potential energy, and can be recovered on release of the applied shear stress. However, when a stress is applied to an ideal liquid, the material flows and when the stress is halted, the liquid does not regain its original structure and remains in the deformed state, with all energy lost through heat dissipation. Viscoelastic material have intermediate behaviour between these two

extremes. When non-particulate viscoelastic fluids (such as polymer solutions) are mixed in stirred vessels systems, the Weissenberg effect is commonly observed, whereby the material tracks up the shaft of the mixer system upon agitation. For all the fluids mixed in Chapters 4 and 6, the viscoelastic properties of the fluids were not of interest to the systems in question and hence were not measured, and the Weissenberg effect was not observed (Dealy and Vu (1977); Mewis and Wagner (2012)).

1.1.3 Mathematical models for fluid rheology

Many different empirical mathematical rheology models have been developed to accurate describe and model the various fluids mentioned in Section 1.1.2. In this section, a number of commonly used rheology models will be discussed, including the Power Law (or Ostwald-De Waele) model (Ostwald (1926)), the Bingham model (Bingham (1922)), the Herschel-Bulkley model (Herschel and Bulkley (1926)) and the Casson model (Casson (1959)). In particular, the Herschel-Bulkley model and the Casson model will be used throughout this work to describe the flows of viscoplastic materials.

1.1.3.1 Power Law model

The Power Law model (Eq. 1.8) was developed by Ostwald (1926) to characterise the rheological behaviour of the fluids with a non-linear relationship between applied shear stress and shear rate, namely shear-thinning and shear-thickening materials. The log-log plot of shear stress against shear rate leads to a linear curve, with the gradient equal to the value of the flow behaviour index, n. When $n > 1$, shear-thickening fluids are being described, whilst shear-thinning fluids are being portrayed when $0 < n < 1$. When $n = 1$, Newtonian behaviour is being modelled. From Eq. 1.8, K is the flow consistency index. This model is a simple, two-parameter system, however it lacks a description of the yield stress. From this model, an equation for the dynamic viscosity can be derived using Newton's law of viscosity (Eq. 1.2), as seen in Eq. 1.9 (Ostwald (1926); Wilkinson (1960); Pevere *et al.* (2007); Goodwin and Hughes (2008); Björn *et al.* (2012); Mewis and Wagner (2012)).

$$\tau = K\dot{\gamma}^n \tag{1.8}$$

$$\mu = K\dot{\gamma}^{n-1} \tag{1.9}$$

1.1.3.2 Bingham model

The Bingham model (Eq. 1.10) was developed by Bingham (1922) to describe the rheological behaviour of Bingham plastics, which exhibit a yield stress, which once exceeded, flow with ideal, Newtonian behaviour. From Eq. 1.10, τ_y is the fluid yield stress and η_{pl} is the constant plastic viscosity, which defines the gradient of the flow curve. The Bingham model is a simple two-parameter system, however it will not

be used for the fitting the rheological flow curves of potential model fluid systems in this work (Chapter 2 and 3), as it does not describe materials which flow with shear-thinning characteristics once the yield stress has been exceeded. When τ_y = 0, the Bingham model is reduced to describing Newtonian systems (Wilkinson (1960); Skelland (1967); Mitsoulis (2007); Pevere *et al.* (2007); Björn *et al.* (2012)).

$$\tau = \tau_y + \eta_{\mathrm{pl}}\dot{\gamma} \tag{1.10}$$

1.1.3.3 Herschel-Bulkley model

The Herschel-Bulkley model (Eq 1.11) was first developed by Herschel and Bulkley (1926) to describe the rheological behaviour of viscoplastic materials, which display power law behaviour once a yield stress has been exceeded, as outlined in Section 1.1.2.3. From Eq 1.11, τ_y is the fluid yield stress, and as with the Power Law model, K is the flow consistency index and n is the flow behaviour index. If τ_y = 0, then the Herschel-Bulkley model can be reduced to the Power Law model, and if $\tau_y > 0$ and $n = 1$, then a Bingham fluid is being described. Although the Herschel-Bulkley model has the disadvantage of being a slightly more complex, three-parameter model, it provides a better description of viscoplastic flows than the two previously discussed models and will be used throughout this work in the fitting of the raw rheological flow curves of model fluid systems (Chapter 2 and 3). When fitting raw rheological data with this model, and any other model involving a yield stress term, it is imperative to fit over the widest range of shear rates possible, with a particular focus on going to the lowest shear rate values possible for a given system, to maximise the accuracy of the yield stress value that is obtained. As with the Power Law model, the dynamic viscosity can be derived using this equation in conjunction with Newton's law of viscosity (Eq. 1.2), as seen in Eq. 1.12 (Wilkinson (1960); Skelland (1967); Barnes (1999); Pevere *et al.* (2007); Björn *et al.* (2012); Mewis and Wagner (2012)).

$$\tau = \tau_y + K\dot{\gamma}^n \tag{1.11}$$

$$\mu = \frac{\tau_y}{\dot{\gamma}} + K\dot{\gamma}^{n-1} \tag{1.12}$$

1.1.3.4 Casson model

The Casson model (Eq. 1.13) was developed by Casson (1959) with the aim of also being used to describe the rheological behaviour of viscoplastic materials. From Eq. 1.13, as with the Bingham model, τ_y is the fluid yield stress and η_{pl} is the constant plastic viscosity. The Casson model has the advantage of being a simpler two-parameter system, compared to the Herschel-Bulkley model, and will also be used throughout this work to model the raw viscoplastic flow curves of potential model fluid systems (Chapter 2 and 3) (Mitsoulis (2007); Pevere *et al.* (2007); Goodwin and Hughes (2008)).

$$\sqrt{\tau} = \sqrt{\tau_y} + \sqrt{\eta_{\mathrm{pl}}\dot{\gamma}} \tag{1.13}$$

1.2 Typical viscoplastic fluids

In the literature, numerous different viscoplastic materials have been rheologically investigated. In this section, a number of these fluids will be discussed, as they display the desired shear-thinning and yield stress properties, representative of the 'to-be-matched' industrial formulations, whilst also being safe, being inexpensive, having low levels of reactivity and facile handling, and therefore having the potential to be model fluid systems. In particular, a select number of clay suspensions, polymer solutions and microgels will be reviewed and discussed.

1.2.1 Clay suspensions

Grim (1968) stated that "the term clay implies a natural, earthy, fine-grained material which develops plasticity when mixed with limited amounts of water", where plasticity is "the property of the moistened material to be deformed under application of pressure, with the deformed shape being retained when the deforming pressure is removed" (Grim (1968)). Clays are naturally-occurring minerals and exist as the colloidally-active components in soils, rocks and sediments. Clays typically have a particle size of < 2 μm, although the specific morphology depends on the clay in question. Clay minerals are part of the phyllosilicates group, and have a structural framework composed of tetrahedral and octahedral sheets, stacked upon one another in a parallel fashion. The tetrahedral sheets are formed of silica-based tetrahedra, which form a hexagonal network to produce sheets with a $Si_4O_6(OH)_4$ configuration. The octahedral sheet consists of a central metal cation, surrounded by oxygen atoms and hydroxyl groups. These octahedra are connected to neighbouring ones to form an octahedral sheet. The octahedral sheets associate with one or two tetrahedral sheets through connecting oxygen atoms, to form a unit layer, with unit layers stacking upon one another to form the crystal lattice, with bonding between unit layers occurring through electrostatic, van der Waals type interactions. Clay minerals have use in a wide range of industrial applications, including in drilling fluids, cements, paints, cosmetic, pesticide and pharmaceutical products (Grim (1968); Newman and Brown (1987); Galan (1996); Rossi (1997); Balci (1999); Benna-Zayani *et al.* (1999); Luckham and Rossi (1999); Liu and Zhang (2007); Bilotti (2009)).

Clay particles have the capability to undergo isomorphic substitutions of cations in their structure with cations of similar size but different valence. These replacement cations are often associated with a lower charge than the ions present in the clay's structure. As a result, these exchange reactions lead to the clays having a net negative surface charge, allowing these negatively charged adsorption sites to be occupied by exchangeable cations from aqueous solutions. This results in the electrical charge being compensated for, with the extent of negative charge on the clay being quantified by the '*cation*

exchange capacity' which defines the total amount of adsorbed cations on the clay (Grim (1968); Laudelout (1987); Rossi (1997); Luckham and Rossi (1999); Goodwin (2004); Lemić *et al.* (2005); Bilotti (2009)). Cation exchange reactions are not limited to individual cations, as larger cationic compounds can also adsorb to clay surfaces. Lemić *et al.* (2005) investigated the adsorption mechanism and surface modification of sepiolite clay with various quaternary ammonium cationic surfactants (QACS), whilst Li and Bowman (1998) studied the adsorption mechanism onto zeolites, and kaolinite, illinite and smectite clay minerals. Clay particles also contain neutral adsorption sites, through Si-OH groups at the external surface of tetrahedral sheets, which can be accessed by small organic moieties and polymers such as polyethylene oxide (Brownawell *et al.* (1990); Li and Bowman (1998); Casal *et al.* (2001); Lemić *et al.* (2005); Liu and Zhang (2007); Ruiz-Hitzky *et al.* (2011)).

Due to their small particle size, clay suspensions can be classified as colloidal suspensions. The interactions between clay particles govern various properties, such as rheology, stability and phase behaviour of the colloidal system. Stability within a clay suspension can be predicted through the summation of the repulsive and attractive forces between clay particles. Attractions between clay particles arise from van der Waals forces, the most important being London dispersion forces, which are the attractive forces between non-polar molecules. A molecule's motion of electrons in one particle causes the formation of an instantaneous dipole moment, which in turn produces a dipole in a molecule of a neighbouring particle. The summation of these pairwise interactions between molecules produces a strong attraction between two particles. In clay suspensions, mutual repulsion of particles is often introduced through charge stabilisation. As previously discussed, clay particle faces have a negative surface charge, and therefore form an electric double layer (EDL) in polar solvents (for example water). The cations present in the clay structure dissolve into the water, forming a slightly basic medium. The negatively charged particles attract these counter-ions, which stick to the clay surface to form the 'Stern' layer. A diffuse layer of electrolytic ions surrounds the Stern layer, which has a thickness known as the Debye length. The concentration of counter-ions (for example metal cations) and co-ions (OH^- ions from water) exponentially decreases and increases, respectively, with increasing distance from the particle surface. The combination of these two layers form the EDL, and when the EDL of two particles overlap, a concentration gradient between this overlapping volume and the bulk solution is created, leading to the osmotic repulsion of particles. The summation of these repulsions and attractions gives the total interaction potential and forms the basis of the '*Derjaguin-Laudau-Verwey-Overbeek*' (DLVO) theory. The system's stability can be determined by plotting the total interaction energy against the distance of surface separation between two particles (Derjaguin (1940); Derjaguin and Landau (1941); Verwey and Overbeek (1948); Hogg *et al.* (1966); Wiese and Healy (1970); Overbeek (1977); Luckham and Rossi (1999); Hamley (2000); van Duijneveldt (2001); Eastman (2005); Araki (2013); Russell (2015)).

If the clay mass fraction is great enough in a given suspension, the particles will flocculate together and orientate themselves through Brownian motion into positions that minimises free energy, resulting in

the formation of a continuous, three-dimensional gel network throughout the structure. Brownian motion in clay suspensions is the random step-wise movement of particles caused by the thermal energy of molecules in the aqueous phase. Clay suspensions with platelet-like particles are able to associate through the following three mechanisms: face-to-face, edge-to-face and edge-to-edge (Figure 1.5). Edge-to-edge and edge-to-face flocculation results in the formation of voluminous, '*house-of-cards*' type structures, whilst face-to-face aggregation produces thicker, larger flakes. The strength of gels is governed by the pH, salt concentration and clay mass fractions, within the systems and defines the rheological properties of the suspension. In particulate suspensions of differing morphologies, different particle association mechanisms have been suggested. Suspensions of spherical particles associate to form chains of particles, similar to a '*string of beads*' structure, which can associate with one another through intermolecular bonding. Rod-like particle suspensions flocculate to form gels with a '*brush-heap*' structure, again with intermolecular bonding resulting in the strengthening of the gel network (Olphen (1964); Chen *et al.* (1990); Benna-Zayani *et al.* (1999); Everett (1999); Luckham and Rossi (1999); Viseras *et al.* (1999); Shalkevich *et al.* (2007)).

Figure 1.5. Particle association mechanisms, from a side-view perspective, in suspensions of platelet-like clay suspensions: (a) dispersed suspension, (b) face-to-face association, (c) edge-to-face association, and (d) edge-to-edge association (adapted from Luckham and Rossi (1999)).

1.2.1.1 Montmorillonite

Montmorillonite is a naturally-occurring di-octahedral smectite clay, meaning that 2/3 of lattice sites in the octahedral layer are occupied with trivalent cations, with the third site vacant, leading to an idealised structural formula of $M_y^+ nH_2O(Al_{2-y}Mg_y)Si_4O_{10}(OH)_2$ (Figure 1.6). Montmorillonite has platelet-like particle morphology and as previously described, each individual platelet has a constant negative surface charge due to isomorphic substitution within the tetrahedral and octahedral layers. To compensate for the negative surface charge, exchangeable ions can fill the negatively charged adsorption sites. When these cations are exclusively Na^+, then Na^+-montmorillonite is formed, which is also known as Bentonite, and from the idealised structural formula above, M = Na and y = 0.33. In this work, a pharmaceutical grade of Bentonite, known as Bentopharm, will be used for fluid formulation and rheological characterisation. Bentonite has the capacity for lattice expansion through the mechanism of swelling, due to the presence of polar molecules in the interlayer region of the clay

structure. In the crystalline state, the negatively-charged sheets are held together by bridging cations (for example, Na^+ and K^+). In the presence of water, these ions can dissociate into the aqueous solution, resulting in EDL repulsion between layers and swelling (Mooney *et al.* (1952); Norrish (1954); MacEwan (1961); Grim (1968); Swartzen-Allen and Matijević (1974); Hunter (1987); Rossi (1997); Luckham and Rossi (1999); Leach *et al.* (2005); Amorim *et al.* (2007); Bilotti (2009); Cui *et al.* (2013)).

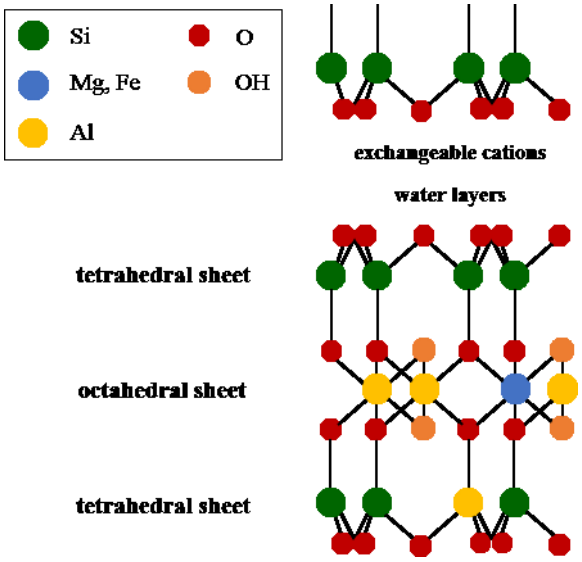

Figure 1.6. Schematic structure of montmorillonite, adapted from the work of Luckham and Rossi (1999).

The rheological properties of Bentonite suspensions have been widely researched in the literature. In an early study, Rand *et al.* (1980) looked at the effects of pH and salt concentration on the rheological properties of Bentonite suspensions, with the aim of determining which particle association mechanism was responsible for the observed behaviour. In dilute suspensions (< 1 wt% bentonite), Newtonian behaviour was observed over the pH range 4-11 and at NaCl concentrations < 5×10^{-3} mol dm^{-3}. In Bentonite suspensions > 1 wt%, with the addition of NaCl concentrations > 5×10^{-3} mol dm^{-3}, edge-to-edge association resulted in the suspensions having a yield stress, shear-thinning behaviour and thixotropic character. Brandenburg and Lagaly (1988) looked at the effect of pH, salt concentration and temperature on the rheological properties of a 4 wt% bentonite solution. It was suggested, at $\dot{\gamma} = 94.5\ s^{-1}$, there was a maximum shear stress at pH 4, before a sharp decrease to a minimum at pH 6-7.5, before a strong increase up to pH 9. It is hypothesised that the decrease to the minimum is due to the breakdown of the '*house-of-cards*' structure. In the presence of Ca^{2+} ions, face-to-face contacts preferentially formed in alkaline media. Lower shear stress values were attributed with an increase in temperature, at a given shear rate. Benna-Zayani *et al.* (1999) also studied the effect of pH on the rheological behaviour of three Bentonite samples, at mass fractions of 5.5, 8.5 and 12.5 wt%. HCl and NaOH solutions were used to

alter the pH (2-12) and found there was a maximum in yield stress in the weakly acidic pH range, attributed to the strong '*house-of-cards*' structure, which broke down at higher pH values (8.5-10), before a sharp increase in very alkaline media, due strong mutual repulsions between particles. Heller and Keren (2001) investigated particle-particle associations in 2 wt% Bentonite suspensions at various electrolyte concentrations, using rheological measurements. In the presence of small quantities of NaCl, the particle EDLs were compressed, resulting in reduced shear-thinning characteristics. At greater NaCl concentrations, shear-thinning behaviour increased and a yield stress was observed, likely to be attributed to face-to-face particle associations. Rossi *et al.* (2002, 2003) showed that increasing clay concentration in aqueous Bentonite suspensions at constant pH led to more pronounced shear-thinning behaviour and increased yield stress values, due to the increased quantity of clay particles in the suspension, enhancing the strength of the gel network. The authors also investigated the addition of non-ionic polyether-type polymers on the rheological properties of bentonite suspensions. For all clay mass fractions, there was an initial increase in yield stress with increased surfactant (polymer) concentration, before then declining and reaching a plateau at higher concentrations. This suggested optimum flocculation occurred below full surface coverage of particles. Kelessidis *et al.* (2011) looked at the effect of polymer addition, namely Carbopol 980 (C980) and carboxymethyl cellulose (CMC), on the rheological properties of 3 and 4 wt% Bentonite suspensions. Addition of ≤ 1.5 wt% CMC to 3 wt% Bentonite resulted in a decrease τ_y and K values. At > 1.5 wt%, τ_y plateaued, whilst K continued to increase. Addition of ≤ 0.15 wt% C980 to 3 and 4 wt% Bentonite suspensions led to a decrease τ_y and K value, before addition of higher mass fractions of C980 resulted in an increase τ_y and K values, as C980 solutions display viscoplastic properties when a given mass fraction is reached. Numerous other authors have also investigated how various conditions, including clay mass fraction, pH, temperature, salt content, the presence of polymers, influence the rheological properties of Bentonite suspensions (Kelessidis and Maglione (2008); Benyounes *et al.* (2010); Abu-Jdayil (2011); Ben Azouz *et al.* (2016)).

1.2.1.2 Laponite suspensions

Laponite is a synthetic, hectorite-type clay, with platelet-like particle morphology and high longitudinal monodispersity compared to natural clays, with a particle diameter of 25-30 nm and a thickness of 1-2 nm. It has a three-layered particle structure commonly associated with smectite clays, and a negative surface charge due to isomorphic substitutions of Mg^{2+} ions with Li^{+} ions, which can be compensated for by the adsorption of exchangeable cations. Laponite has the general chemical formula of $Na_{0.7}Si_8(Mg_{5.5}Li_{0.4})O_{20}(OH)_4$ (Figure 1.7) and in the dry state, has the appearance of a white, free-flowing powder. When dispersed into the aqueous phase (at pH > 10), a transparent suspension results, due to Laponite having a very small crystallite size compared to naturally-occurring clays, and high purity due to being synthetic and therefore having a low level of contaminants, such as iron, resulting in a decrease in light scattering intensity and colour. Laponite has a high sensitivity towards changes in pH and is

unstable at neutral and acidic pH values. When pH < 8.5, H^+ ions attack the mineral structure, resulting in dissolution of cations in the lattice and lattice degradation (Neumann and Sansom (1970); Perkins *et al.* (1974); Avery and Ramsay (1986); Ramsay (1986); Thompson and Butterworth (1992); Morvan *et al.* (1994); Mourchid *et al.* (1995); Mongondry *et al.* (2005); Stefanescu *et al.* (2006); Huang and Berg (2006); Cummins (2007); Shalkevich *et al.* (2007); Jatav and Joshi (2014)).

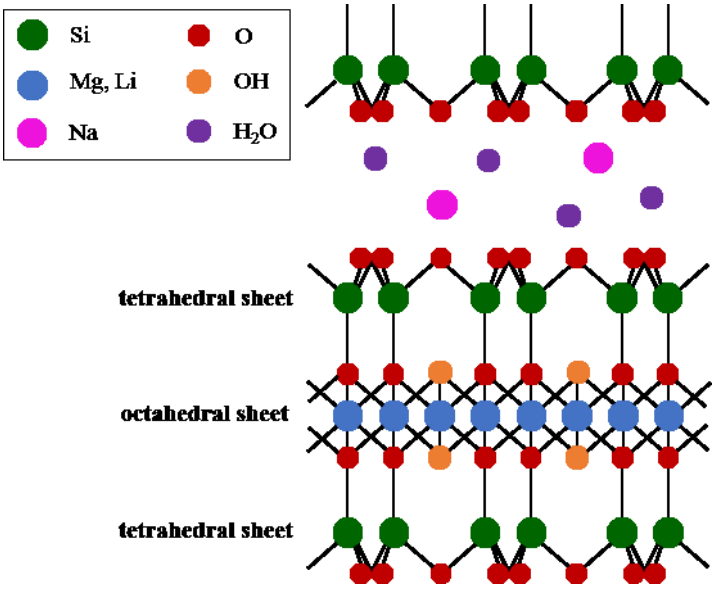

Figure 1.7. Schematic structure of Laponite, adapted from the work of Cummins (2007).

Pignon *et al.* (1996) looked at the thixotropic properties of Laponite suspensions using combined rheology and visualisation techniques. They determined that the Laponite gels have four flow regimes, associated with four shear rate ranges. Below a critical shear rate value, the material behaves elastically. At low shear rates, shear is restricted to a fine layer of the sample, stick slip is observed and shear stress decreases with increasing shear rate. At intermediate shear rates, the thickness of the layer increases, and the associated shear stress is constant and at a minimum. At high shear rates, the sample is homogeneously sheared and shear stress increases with increasing shear rate. Over a series of studies, Bonn *et al.* (1998, 1999, 2002) looked at the aging of Laponite suspensions through the use of rheological measurements and light-scattering techniques, and showed that at a low, constant applied shear stress, the viscosity of the system will increase with time until the flow is halted, however above a critical shear stress, the viscosity of the system will decrease with increasing time. Laponite is seen as a colloidal glass, and at low applied shear stress values, the particles are jammed in the 'cage'-like manner by neighbouring particles, resulting in aging (an increase in viscosity with time). As aging increases, the system's dynamics slow, as does the rates of particle diffusion. However under larger applied shear stresses, the fluids become unjammed and flow with shear-thinning characteristics.

In a similar study, Coussot *et al.* (2002) looked at the rheological properties of three typical yield stress fluids, including a 3 wt% Laponite suspension (again termed a colloidal glass), which displayed both a yield stress and notable thixotropic behaviour, with an increase in viscosity at low applied shear stresses with time. Martin *et al.* (2002) used a number of techniques, including the rheological experiments, to focus on the mechanisms of gel-fluid and fluid-gel transitions in Laponite suspensions. The gel network was seen to form due to particles flocculating through edge-to-face interactions, which were disrupted in the presence of an applied shear stress, and hence the thixotropic behaviour of Laponite suspensions stems from the changes to the continuous gel network. Over two studies, Labanda *et al.* (2005, 2007) investigated the presence of sodium polyacrylate (at varying molecular weights) on the rheological properties of dilute Laponite suspensions. The addition of sodium polyacrylates affects the interactions between Laponite particles, with the sodium polyacrylate adsorbing onto the particle surface. At high sodium polyacrylate molecular weights and mass fractions, the sodium polyacrlate promoted aggregations through the interparticle bridging of Laponite particles. Thixotropy was observed in both the presence and absence of polymer.

1.2.1.3 Sepiolite suspensions

Sepiolite is a naturally-occurring hydrated magnesium silicate clay, with elongated needle-like particle morphology, with length and widths of 0.2-2 μm and 0.01 μm, respectively. Sepiolite has an ideal structural formula of $Si_{12}O_{30}Mg_8(OH)_4(OH_2)_4 \cdot 8H_2O$ and is formed of an alternating block-and-tunnel structure (Figure 1.8), extending in the fibre direction (*c*-direction), hence unlike smectite clays, it is unable to swell in aqueous media due to covalent bonding between the blocks. The blocks have a 2:1 description and are comprised of a central octahedral magnesium-based sheet, enclosed by two central tetrahedral silica sheets, with each block linked to the next through apical oxygens in the silica sheets. As with montmorillonite and Laponite, sepiolite has a net negative surface charge due to isomorphic substitutions of cations within the lattice, which can be compensated for through exchangeable cations adsorbing into these negatively-charged sites. Si-OH groups present on the edges of the particles can be used as neutral adsorption sites for organic moieties and small compounds. Water fills the tunnels between the blocks, which can be evacuated through heat treatment (Preisinger (1957); Caillère and Hénin (1961); Velde (1992); Galan (1996); Kuang *et al.* (2003); Lemić *et al.* (2005); Zhang and Van Duijneveldt (2006); García-Romero and Suárez (2010); Alvarez *et al.* (2011); López-Galindo *et al.* (2011); Shuali *et al.* (2011); Suárez and García-Romero (2011); Araki (2013)).

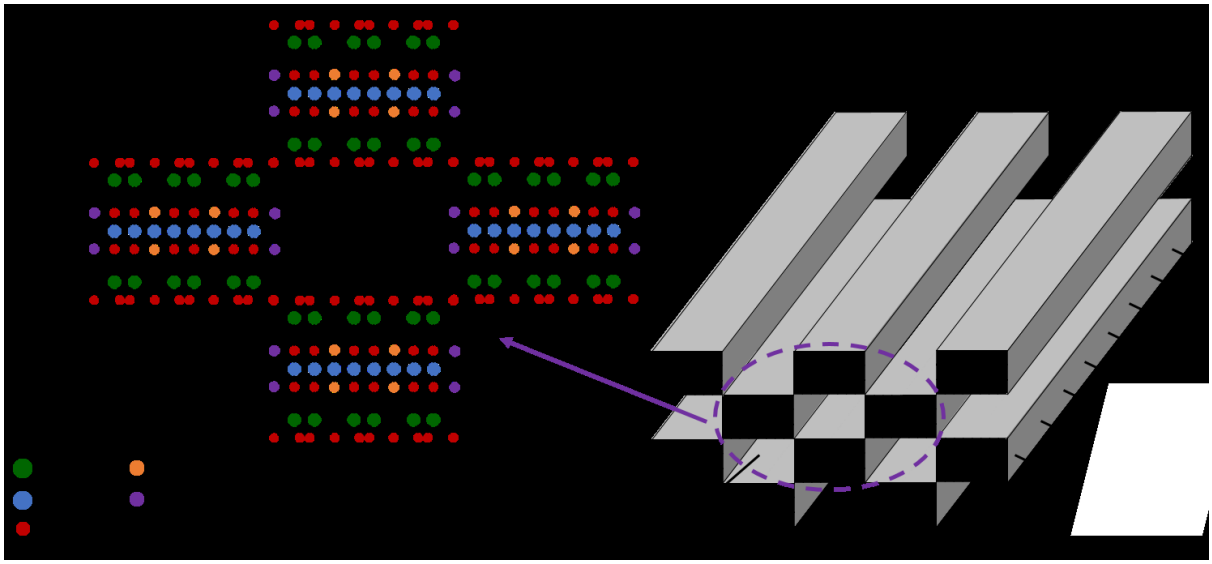

Figure 1.8. Schematic structure of sepiolite clay, adapted from Ruiz-Hitzky (2001) and Yu *et al.* (2011).

A number of authors have studied the rheological properties of sepiolite-based suspensions. Viseras *et al.* (1999) looked at the mixing conditions on the flow curves of sepiolite and Bentonite suspensions. Both the Bentonite and sepiolite suspensions at a volume fractions of 10 vol% displayed yield stress values and shear-thinning characteristics, whilst thixotropy was also exhibited. Sample preparation methods and mixing conditions were found to have a distinct effect on the flow curves of both the Bentonite and sepiolite suspensions. pH had a particular effect on the sepiolite suspensions, with neutral pH systems producing greater shear stresses at a given shear rate. Çinar *et al.* (2009) also investigated the effects of pH on rheological properties of sepiolite suspensions, through the addition of different acids to the suspensions. The rheological properties of the suspensions were measured in a viscometer at constant speed, and it was determined there was a maximum in viscosity (at a given shear rate) at pH~8. Pignon *et al.* (2009) used sepiolite as a rheology modifier in aqueous PEO (4 wt%, $M_w = 1 \times 10^5$ g mol^{-1}) solutions, which were Newtonian in the absence of particles. Sepiolite volume fractions of 0.05-2.00 vol% were added to the PEO solutions, leading to a transition from Newtonian to shear-thinning behaviour, which became more pronounced with increasing clay content, attributed to increased electrostatic interactions between the clay fibres, and between the particles and the polymer chains. However, the sepiolite content was too low to induce a yield stress within the suspensions. Franchini *et al.* (2009) investigated the effects of clay mass fraction on the rheological properties of sepiolite-epoxy nanocomposites. Pure epoxy monomer displayed Newtonian behaviour. On addition of up to 8.4 wt% sepiolite, the suspensions exhibited notable shear-thinning character. 8.4 wt% unmodified sepiolite, aminosilane-modified sepiolite and glycidysilane-modified sepiolite were added to the epoxy suspensions, with the glycidylsilane-modified sepiolite-epoxy suspensions exhibiting the most distinctive shear-thinning properties, and unmodified-epoxy suspensions exhibiting the least distinctive shear-thinning character. The sepiolite-

epoxy suspensions also exhibited notable yield stress values and thixotropy, with the magnitude of yield stress depending on clay content and the type of surface functionalisation. Sabzi *et al.* (2013) performed oscillatory and steady shear rheological measurements on polylactic acid-sepiolite nanocomposites. Clay mass fraction was varied from 1-10 wt% in the polylactic acid dispersions, and the degree of shear-thinning behaviour became more pronounced with increased clay content. Carmona *et al.* (2018) investigated the effects of the addition of ionic surfactants on the rheological properties of 3 wt% sepiolite gels, using an anionic and cationic surfactant. The suspensions displayed viscoplastic behaviour, with the yield stress of the suspensions increasing with increasing cationic surfactant concentration. Upon addition of anionic surfactant, there was an initial increase in yield stress, before further addition of anionic surfactant resulted in a noticeable decrease in the yield stress of the suspensions, caused by electrostatic interactions between the clay and surfactant changing the microstructure of the clay.

1.2.1.4 Other clay suspensions

A number of other clay suspensions have been known to exhibit viscoplastic properties. Kaolinite is a naturally-occurring di-octahedral clay in the kaolinite mineral group, which has platelet-like morphology and is constructed of approximately 50 twin-layered sheets stacked upon one another and held together by hydrogen bonds. These hydrogen bonds are strong and therefore kaolinite is unable to undergo complete swelling in aqueous media (Grim (1968); Velde (1992); Luckham and Rossi (1999); Sjöberg *et al.* (1999); Liu and Zhang (2007); King (2009); Gupta and Miller (2010); Gupta *et al.* (2011)). Numerous authors have investigated the effect of clay content, pH, temperature, electrolyte concentration, and the presence of surfactant and polymer concentration on the rheological properties of kaolinite suspensions and showed that under the correct conditions, these suspensions will display viscoplastic behaviour. These suspensions often require very high clay mass fractions (of order 25 wt%) to exhibit these rheological properties (Coussot and Piau (1994); Coussot *et al.* (1996); Sjöberg *et al.* (1999); Mpofu *et al.* (2003); Rabideau *et al.* (2012); Sakthivelu *et al.* (2012)). Attapulgite is a naturally-occurring fibrous, magnesium silicate clay, formed of needle-like particles. As with sepiolite, it has an alternating block-and-tunnel structure and is therefore unable to swell. In the literature, attapulgite has often been used as a rheology modifier in composite systems (Luckham and Rossi (1999); Shen *et al.* (2005); Liu and Chen (2008); Yin *et al.* (2009); Kawashima *et al.* (2013)).

1.2.2 Polymer solutions

The rheological properties of various polymer solutions have widely studied and characterised in the literature. Many polymers of interest to the current work are naturally-occurring polysaccharides, derived from cellulose (Figure 1.9), which is formed of single repeating units of D-glucose, which are linked through the carbons 1 and 4 through β-linkages. From Figure 1.9, the R groups in cellulose are hydrogen

atoms. Derivatives such hydroxyethyl cellulose (HEC) and hydroxypropyl cellulose (HPC) are examples of cellulose ethers, with ether groups at carbon 2, 3 and 6, depending on the degree of substitution, with R = H or CH_2CH_2OH for HEC, and R = H or $CH_2CH(CH_3)OH$ for HPC. Carboxymethyl cellulose sodium salt (CMC) is another example of a salt-based cellulose derivative, where ester groups can form at carbons 2, 3 and 6, depending on the degree of substitution, with R = H or $CH_2COO^-Na^+$. Other commonly investigated polysaccharides, include Xanthan gum (XG), Guar gum (GG) and Guar gum derivatives, which are slightly more complex carbohydrate-based polymers. Finally, also of interest to this work is Actigum, a commercial grade of an extracellular polysaccharide called scleruglucan, secreted by a filamentous fungus *Sclerotium*. All of these polymers, when dispersed in aqueous medium, have the capability to display shear-thinning behaviour, with some polymer solutions also exhibiting a yield stress value under the correct conditions (Stevens (1990); Walton and Lorimer (2000); Park and Khan (2009); Sheskey *et al.* (2017); Jindal and Khattar (2018)).

Figure 1.9. Chemical structure of cellulose, where R = H and n is the number of repeating units.

Ghannam and Esmail (1997) used steady shear rheometry to investigate the rheological properties of CMC solutions, at mass fractions ranging from 1-5 wt%. The 1 wt% solution exhibited near Newtonian behaviour, whilst solutions >1 wt% displayed shear-thinning characteristics, which became more pronounced with increasing CMC mass fraction. Thixotropic properties were exhibited by the 4 wt% and 5 wt% solutions, whilst all the solutions lacked a yield stress. Benchabane and Bekkour (2008) performed a similar study, investigating the rheological properties of CMC (M_w = 700000 g mol^{-1}) solutions, ranging in mass fraction from 0.2-7.0 wt%, using steady shear measurements. All fluids displayed shear-thinning properties, with increased viscosities (at given shear rates) in suspensions with greater mass fractions of CMC. The solutions displayed thixotropy, which became more pronounced with increased CMC mass fraction. The solutions did not exhibit yield stresses. Ramachandran *et al.* (1999) investigated the rheological properties of HPC gels (1-3 wt%, $M_w = 3.7\times10^5$-1.15×10^6 g mol^{-1}) in propylene glycol, water, ethanol and mixtures of these compounds. The gels were shear-thinning and did not display yield stresses or thixotropy. The apparent viscosity of the solutions increased at a given shear rate ($\dot{\gamma}$ = 500 s^{-1}) with increased HPC content and molecular weight of HPC, whilst at a given HPC mass fractions, the gels

dispersed in propylene glycol produced dispersions with increased apparent viscosities at this shear rate. For each solvent system, the degree of shear-thinning behaviour was enhanced with increased HPC mass fraction. A number of authors have investigated the rheological behaviour of hydrophobically-modified (HM)-HEC in the presence and absence of surfactants (Patruyo *et al.* (2002); Zhao and Chen (2007)). Maestro *et al.* (2002) showed that HEC solutions (M_w = 9×10^5 and 1.3×10^6 g mol^{-1}) and HM-HEC displayed shear thinning behaviour, with thixotropy only being observed in the HM-HEC solutions. The viscosity at a given shear rate increased with increased HM-HEC content, whilst the low shear viscosities decreased with increasing temperature. Torres *et al.* (2014) investigated the effect of polymer content on the extensional and shear rheology of GG solutions ($M_w = 2.9\times10^6$ g mol^{-1}). All solutions displayed shear-thinning behaviour, which became more enhanced with increased polymer content, but lacked a yield stress. Choppe *et al.* (2010) studied the effects of various parameters on the rheological properties of XG solutions using oscillatory and shear measurements. The solutions showed distinct shear-thinning, with the low shear viscosities dramatically decreasing with increased temperatures. It was stated that all solutions lacked a yield stress however, a number of authors have used XG solutions as a model yield stress fluid for mixing studies in stirred vessel systems (Elson *et al.* (1986); Amanullah *et al.* (1998a); Pakzad *et al.* (2008a)). Grassi *et al.* (1996) investigated the rheological behaviour of scleroglucan gels ranging in mass fraction from 0.13-2.00 wt%. All solutions displayed weakly shear-thinning behaviour, with the samples from 0.38-2.00 wt% exhibiting a marked yield stress, which increased with increased scleroglucan mass fraction. All scleroglucan samples displayed thixotropic properties.

1.2.3 Microgels

Microgels are cross-linked polymers, formed of particle-like 'sponges' that have the capacity to swell and de-swell in aqueous (and non-aqueous) media, in response to external stimuli, such as temperature or pH (Piau (2007); Bonham *et al.* (2014)). Carbopol™ dispersions are typical examples of microgels.

1.2.3.1 Carbopol dispersions

Carbopol dispersions are non-thixotropic, cross-linked microgels (commonly allyl-pentaerythritol or allyl-sucrose is used for cross-linking), with the capacity to swell in aqueous media (Figure 1.10). They are based on the polyacrylic acid structure, and are commonly used for modelling viscoplastic fluids. In an extensive review on the properties of Carbopol gels, Piau (2007) described the structure of Carbopol dispersions as being "polydisperse glasses made of individual swollen hydrophilic elastic sponges". Swelling of these individual sponges results in the formation of disordered suspensions with glass-like structures, with competition between each of the elastic microgels (or sponges) to absorb as much water as possible for maximum swelling. Each strongly cross-linked sponge interacts with neighbouring sponges through covalent linkages to form a network. When a critical concentration of Carbopol is reached, the sponges are

jammed together to form a disordered glassy structure, giving rise to strong repulsive forces between individual microgel structures. When a critical stress value is applied to the system, it will start to flow through global structural rearrangement, leading to homogeneous macroscopic deformation of the material. When Carbopol is dispersed in an aqueous medium, such as water, the resulting dispersion has an acidic pH (pH ~3). This acidic pH can be neutralised using a base (for example, NaOH (aq), KOH (aq) or a solution of triethanolamine, TEA), which aids the formation of cross-linking between polymer chains and enhances microgel swelling. Increasing the pH acts to ionise carboxylic acid (COOH) groups to carboxylate (COO^-) groups, leading to mutual ionic repulsions between the polymer chains in the microgel and expanded particles (see Figure 1.10). Polyanionic polymer microgel structures, similar to Carbopol, have been utilised in drug delivery applications due to their capacity for swelling and shrinking under the influence of external stimuli in the aqueous media (Kiser *et al.* (1998); Kim *et al.* (2003); Oppong *et al.* (2006); Piau (2007); Coussot *et al.* (2009); Møller *et al.* (2009b); Todica *et al.* (2010); Coussot (2014)).

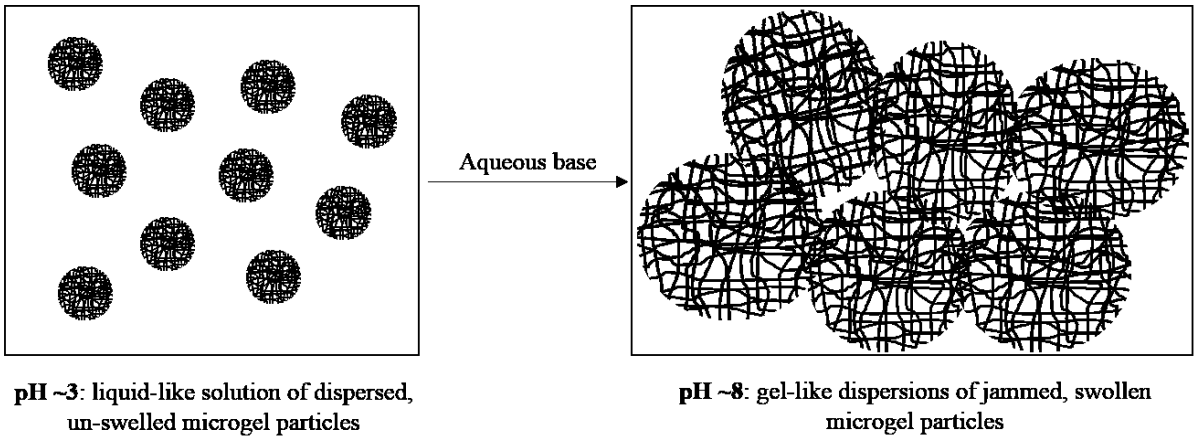

Figure 1.10. Schematic representation of the swelling of a microgel through the addition of a basic medium, adapted from Bonham *et al.* (2014).

Islam *et al.* (2004) examined the rheological properties of Carbopol 980 dispersions in a solvent system comprising of water, glycerol, propylene glycol and TEA. The Carbopol systems demonstrated temperature stability over the range of 5-65°C, with each sample exhibiting viscoplastic behaviour, which was well described by the Herschel-Bulkley model. The rheological behaviour of the Carbopol systems were relatively constant over the pH range 5.0-8.0. Compared to standard Carbopol-water dispersions, the Carbopol dispersions in this study displayed greater shear-thinning characteristics, likely to be caused by the enhanced hydrogen bonding capability due to the glycerol and propylene glycol components. In his extensive study, Piau (2007) investigated the physical and rheological effects of Carbopol 940 dispersions. As part of the investigation, a number of different techniques were used for characterisation, including steady shear measurements on dispersions of Carbopol 940 ranging from

0.04-0.10 wt%, with these dispersions being described as exhibiting elastoviscoplastic behaviour, which could be described by the Herschel-Bulkley model, with all samples lacking thixotropic properties. It was also shown that sonication of the samples had a dramatic effect on the rheological properties, leading to vastly reduced and near constant viscosities over the investigated shear rate range, caused by the destruction of large agglomerates within the samples. Møller *et al.* (2009a, 2009b) looked at the characterisation of yield stress fluids, by investigating the non-thixotropic nature of Carbopol suspensions. It was shown that when applying shear stresses above the yield stress, the material flowed with a time-independent viscosity (no marked aging), however, when shear stresses applied to the system were below the yield stress (but non-zero), the viscosity did not display a Newtonian viscosity plateau, instead rising infinitely, showing that yield stress is indeed the transition between the solid and flowing state. Coussot *et al.* (2009) used MRI velocimetry, in conjunction with conventional rheometrical techniques, to assess the local and macroscopic rheological properties of Carbopol suspensions. As briefly discussed regarding Laponite suspensions in Section 1.2.1.2, at low applied shear stress values, only part of a thixotropic material is sheared whilst the rest of the material remains stagnant, a phenomenon known as shear banding. However, over the investigated shear rate range, the Carbopol systems did not exhibit this property, with global homogeneous deformation occurring, leading to the dispersions being accurately represented by the Herschel-Bulkley model. Over two studies, Ovarlez *et al.* (2012, 2013) also showed that flows of non-thixotropic Carbopol gels did not exhibit the property of shear-banding. The shear-induced sedimentation of yield stress fluids, including Carbopol gels, in the low shear rate regime were also investigated. Dinkgreve *et al.* (2018) suggested that Carbopol samples can exhibit slight thixotropy, depending on the preparation procedure of the dispersion, with intense stirring over a long time period inducing thixotropic properties as the microgel is broken into smaller fragments, generating depletion interactions between the remaining larger microgels.

1.3 Database of rheological fluids and platform for model fluid selection

In this work, based on the findings from the literature, a number of viscoplastic fluids will be formulated and rheologically characterised (Chapter 2), with the aim of finding suitable model fluid systems that represent the flow properties of real, industrial formulations at Syngenta. Due to a large volume of fluids being characterised, a computational tool will be developed (Chapter 3), known as the '*Model Fluid Selection Tool*', which will act as a rheological database, whilst also being capable of suggesting appropriate model fluids that most closely match the rheological properties of the 'to-be-matched' industrial fluid. Having searched the literature, the prospect of constructing a computational tool as the one described is a novel concept. Lee et al. (2009) developed a rheological database for polymer systems used in enhanced oil recovery (mainly hydrolysed polyacrylamide). The effects of salinity, temperature, shear rate, polymer content and molecular weight on the rheological properties of the polymer solutions were investigated, with these data aiding the formation of the polymer database. However, these fluids

did not have the yield stress component, which is a highly important feature to the fluids of interest to this work, and as far as it can be deduced, Lee et al. (2009) simply developed a database for relevant systems to enhanced oil recovery. It was a rheology storage platform, which lacked the ability suggest fluid systems that most closely match the rheological properties of the fluid of interest, as is being proposed in the current work. The '*Model Fluid Selection Tool*' will also have the capability to mathematically fit the raw rheological flow curves with multiple empirical models, whilst also allowing the user to enter in rheological parameters of fluids obtained from the literature. Finally, in certain scenarios, the '*Model Fluid Selection Tool*' will have the capability not only suggest the best matched model fluid system, but to also perform an interpolation process within a given family of model fluids, to suggest a hypothetical model fluid system that may more accurately match the rheological properties of the fluid of interest. An in-depth discussion on the '*Model Fluid Selection Tool*' can be found in Chapter 3.

1.4 Mixing viscoplastic fluids in stirred vessels

When viscoplastic fluids are agitated by a central impeller within a vessel, a '*cavern*' can form. The term was first coined by Wichterle and Wein (1975,1981) and can be described as a well-mixed zone surrounding the rotating impeller. Outside of this region, the material is stagnant because the stresses being imparted on the material are not sufficiently large to exceed the fluid's yield stress (Solomon *et al.* (1981); Wichterle and Wein (1981); Elson *et al.* (1986); Arratia *et al.* (2006)). From an industrial perspective, it is desirable to minimise stagnant zones and to achieve '*complete*' mixing: a state where fluid motion is invoked throughout the entire vessel volume, resulting in product formation, transport phenomena rates and economic gains all being maximised, and product degradation and precursor losses being minimised. As a result, the choice of impeller system is of importance when mixing these types of fluids. A number of different impeller systems have been investigated for these fluids (and fluids with less complex rheological properties), including multiple, centrally-mounted small impellers, close-clearance impellers (Bertrand *et al.* (1996); Aubin *et al.* (2000); Curran *et al.* (2000); Shekhar and Jayanti (2003); Iranshahi *et al.* (2006); Ihejirika and Ein-Mozaffari (2007); Prajapati and Ein-Mozaffari (2009); Patel *et al.* (2012); Ameur (2015)), coaxial impellers (Pakzad *et al.* (2013a, 2013b, 2013c); Kazemzadeh *et al.* (2016, 2016b, 2017)) and side-entering small impellers (Saeed *et al.* (2007); Hui *et al.* (2009); Sossa-Echeverria and Taghipour (2014, 2015)).

1.4.1 Mixing viscoplastic fluids with single-impeller systems

Extensive experimental and numerical studies have investigated how various operating conditions, including the geometry and design of the impeller and tank, as well as the impeller rotational speeds (N) and fluid rheology, have affected the fluid flow dynamics and cavern properties of viscoplastic fluids in agitated vessel systems. Various experimental techniques have been developed and utilised to determine

the fluid flow characteristics of viscoplastic fluids in stirred vessels (Mavros, 2001), including simple dye visualisation (Galindo and Nienow (1992, 1993); Galindo *et al*. (1996); Amanullah *et al.* (1997, 1998a, 1998b)) and tracer techniques (Jaworski *et al.* (1994); Elson *et al.* (1986); Elson (1988)), dynamic conductivity tests (Saeed *et al.* (2008); Saeed and Ein-Mozaffari (2008); Patel *et al.* (2012)), hot-film anemometry (HFA) (Solomon *et al.* (1981)), laser Doppler anemometry (LDA) (Hirata *et al.* (1994)), ultrasound Doppler velocimetry (UDV) (Ihejirika and Ein-Mozaffari (2007); Saeed *et al.* (2007); Pakzad *et al.* (2008a); Ein-Mozaffari and Upreti (2009); Hui *et al.* (2009)), planar laser-induced fluorescence (PLIF) (Arratia *et al.* (2006); Adams and Barigou, (2007)), particle image velocimetry (PIV) (Sossa-Echeverria and Taghipour (2014, 2015); Cortada-Garcia *et al.* (2017, 2018)) and electrical resistance tomography (ERT) techniques (Pakzad *et al.* (2008b, 2008c, 2013b, 2013c)). Computational fluid dynamics (CFD) have been an increasingly employed in recent years to characterise viscoplastic flows in stirred vessels. CFD allows for various operating parameters to be readily altered and studied, which is often more cost-effective and time-efficient than experiments, and in turn allows for processes to be optimised and mixing performance in stirred vessels to be easily assessed (Cortada-Garcia *et al.* (2018)). As a result, numerous studies have utilised both experimental and numerical methods for the investigation of viscoplastic flows in stirred vessels.

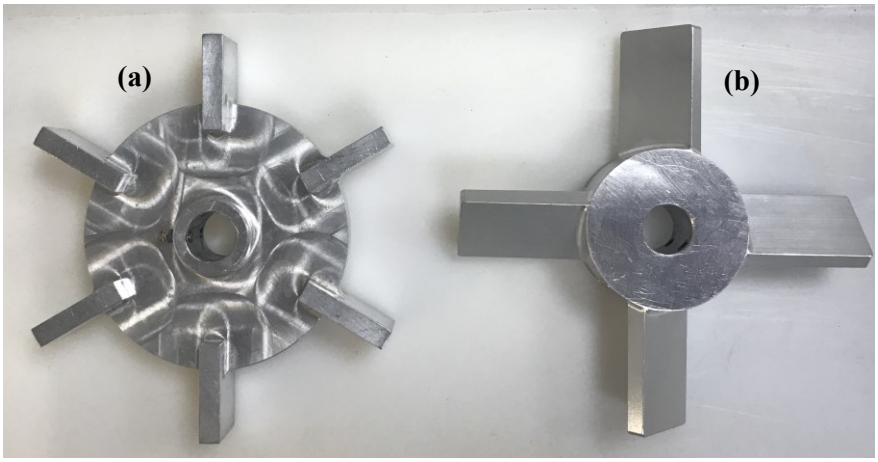

Figure 1.11. Generic depiction of two types of small, central impellers: (a) a 6-bladed Rushton turbine (RT) impeller, and (b) a 4-bladed 45° pitched-blade turbine (PBT) impeller.

In an early study, Wichterle and Wein (1981) studied the agitation of viscoplastic suspensions of particulate solids with Rushton turbine (RT) impellers and propellers. They utilised dye visualisation techniques to look at the effects of impeller geometry (impeller type and blade angle), impeller diameter, D and impeller rotational speed, N on cavern size. It was determined that the threshold of mixing was achieved, and mixing was deemed successful, when the stagnant zones in the vessel formed an insignificant part of the total volume of the liquid. Solomon *et al.* (1981) investigated the agitation of viscoplastic Xanthan gum (XG) and Carbopol fluids, and shear-thinning carboxymethyl cellulose (CMC)

solutions, using RT impellers (with impeller diameter-to-tank diameter ratios, $D/T = 0.33$ and 0.50) alone, and in conjunction with 6-bladed 45° pitched-blade turbine (PBT) impellers ($D/T = 0.33$ and 0.50), under aerated and unaerated conditions. A generic depiction of a Rushton turbine (6-bladed) and a pitched-blade turbine (4-bladed, 45° pitch) can be seen in the image in Figure 1.11. The resulting flow patterns were highlighted via flow visualisation techniques and HFA, with the viscoplastic fluids producing spherical caverns which grew in size with increasing N values. The larger impellers required lower power inputs to produce well-mixed systems, compared to the smaller impellers. A theoretical model for cavern size prediction, known as the spherical cavern model (Eq. 1.14) was developed by Solomon *et al.* (1981) based on a torque and momentum balance. It was assumed that the power from the impeller dissipated through the fluid to the cavern wall, where the shear stress was equal to the fluid's yield stress. The predicted cavern sizes were in good agreement with experimental data, under both aerated and unaerated conditions.

$$\left(\frac{D_c}{D}\right)^3 = \left(\frac{4Po}{\pi^3}\right)\left(\frac{\rho N^2 D^2}{\tau_y}\right) \tag{1.14}$$

where D_c, ρ, and Po are the dimensionless cavern diameter, fluid density and Power number (ratio of the resistance force to the inertial force), respectively, with all other terms having been previously defined. Nienow *et al.* (1983) studied the agitation of numerous Newtonian, shear-thinning viscoelastic (CMC solutions) and viscoplastic (Carbopol 940 (C940) and XG solutions) fluids by a 6-bladed RT impeller. They looked at the effects of rheological properties on the impeller power consumption and under both aerated and unaerated conditions, determined that the presence of a yield stress and greater levels of elasticity led to the lowest Po values. In a series of studies, Elson *et al.* (1986, 1988, 1990a, 1990b)) used x-ray heavy metal tracers and visualisation techniques to study the effects of impeller geometry, impeller size, fluid rheology and N on the flow of viscoplastic XG fluids. They determined that larger impellers (where D/T varied from 0.25 to 0.6) were better at inducing fluid flow in the XG solutions, with increased N values producing larger caverns. They showed that axial impellers (e.g. marine propellers) were more efficient mixers than radial impellers (e.g. RT impellers), in terms of cavern volume per unit power input. In accordance with experimental observations, Elson *et al.* (1986) developed the right circular cylindrical model (Eq. 1.15), used to predict cavern sizes in viscoplastic fluids. It was adapted from the spherical model (Solomon et al., 1981), and described the cavern shape as being a right circular cylinder capped by flat ends, giving a better description of the cavern height, H_c.

$$\left(\frac{D_c}{D}\right)^3 = \left(\frac{P_o}{\left[\left(\frac{H_c}{D_c}\right) + \frac{1}{3}\right]\pi^2}\right)\left(\frac{\rho N^2 D^2}{\tau_y}\right) \tag{1.15}$$

where all terms are the same as those previously defined. Over two studies, Galindo and Nienow (1992, 1993) evaluated the power consumption of an axial flow Lightnin A-315 impeller ($D/T = 0.49$) and a radial flow SCABA 6SRGT impeller ($D/T = 0.44$), used for the agitation of solutions of XG and C940.

Dye visualisation techniques were used to highlight cavern formation in the C940 solutions. For the axial impeller, upward pumping mode resulted in cavern volumes up to 60% larger than the downing pumping modes at the same given power drawn. Cavern sizes resulting from agitation by the A-315 and SCABA impellers were compared to the theoretical values from the cylindrical model (Elson *et al.* (1986)) and it was found that the model gave a better prediction for the SCABA geometry. Power consumptions of the SCABA impeller were compared to previously obtained RT data and for a given Reynolds number, less power was required for the SCABA impeller resulting in more efficient mixing of viscoplastic fluids. In a later study, Galindo *et al.* (1996) used dye visualisation to characterise the formation, size and morphology of caverns in a C940 solution, agitated by single- and dual-RT impellers and upward-pumping one- and two-stage Intermig impellers (both radial, $D/T = 0.53$). They determined that a single-RT produced larger caverns than a one-stage Intermig impeller at low power drawn, but at higher power drawn both impellers behaved comparably.

Hirata *et al.* (1994) and Jaworski *et al.* (1994) focused on the fluid flow close to the cavern boundary in Carbopol solutions, defining the cavern boundary with respect to fluid velocities. Hirata *et al.* (1994) used LDA to highlight the flow dynamics within the fluid upon agitation with an RT impeller, of impeller diameter-to-tank diameter ratio, $D/T = 0.5$. They defined the tangential velocity at the cavern boundary as being 1% of the impeller tip velocity. However, they also determined that the cylindrical model (Elson *et al*. (1986)) gave a good prediction of cavern sizes and an acceptable description of cavern morphology. Jaworski *et al.* (1994) used a 45° pitched-blade turbine (PBT) for agitation and small (SiC) and large (alumina) tracer particles, in conjunction with a laser light sheet and a video technique, to measure velocities at the cavern wall, stating that the velocity at the cavern boundary was ~8 μm s^{-1}. Moore *et al.* (1995) performed LDA measurements of the tangential velocity distributions around both a 6-bladed RT impeller and a 6-bladed 45° PBT impeller (both $D/T = 0.34$) in a 0.17% C940 solution. Both impellers generated predominantly tangential flow, with vortices present above and below the impeller blades. The absolute velocities around the RT were approximately twice that of those around the PBT, although this has a limited effect on cavern size. Comparisons were made between the cavern boundary definitions proposed by Elson *et al.* (1986) (fluid velocity fell to zero at the boundary) and Hirata *et al*. (1994) (the boundary is equal to 1% of the velocity tip speed). Both definitions gave good predictions of the measured tangential velocity distributions on the centreline of both impellers. Over two studies, Amanullah *et al.* (1997, 1998a) used dye visualisation techniques to investigate the cavern properties and flow patterns in various C940 solutions, assessing the mixing performance of various axial flow SCABA 3SHP1 impellers ($D/T = 0.33$, 0.44 and 0.49) at different clearances from the vessel base. Larger impellers and higher clearance produced greater cavern sizes for a given power input. A mathematical model for predicting the size and shape of caverns in viscoplastic fluids agitated with an axial flow impeller was developed. The axial force model (Eq. 1.16)

assumed the cavern had a torus morphology and it incorporated the sum of both the axial and tangential force components into the total momentum imparted on the fluid:

$$\left(\frac{D_c}{D}\right)^2 = \frac{1}{\pi}\left(\frac{\rho N^2 D^2}{\tau_y}\right)\sqrt{N_f^2 + \left(\frac{4Po}{3\pi}\right)^2} \tag{1.16}$$

where all terms have previously been defined except $N_f = F_a/\rho N^2 D^2$, which is the dimensionless axial force number and F_a is the axial force component imparted by the impeller. Good agreement between the experimental results and predictions were obtained, particularly at higher Reynolds numbers. The axial force model was better at predicting cavern diameters in the selected viscoplastic fluids with axial flow impellers than the previously suggested cavern models (Solomon *et al.* (1981); Elson *et al.* (1986)), and can be extended to radial flow impellers by assuming $N_f = 0$. Wilkens *et al.* (2005) looked to build upon the axial force model (Amanullah *et al.* (1998a)) and developed a model that predicted caverns in Bingham plastic fluids as having an elliptical torus shape. They used Heinz ketchup as the test fluid and discerned cavern shape and sizes through injection of glitter as a tracer into the impeller region. The ketchup was then frozen before a section of the frozen solid was dissected and analysed. Three different impellers were used for agitation: two flat 6-bladed radial impellers (two different D values) and an axial 45° pitched-blade impeller. They determined that the cavern shape and size was dependent the torque of the impeller and the fluid's yield stress, with the impeller type defining the aspect ratio of the ellipse. From this basis, a simplified constant torque model was developed (Eq. 1.17 and Eq. 1.18) for predicting cavern diameters and heights for these types of fluids, with predicted cavern sizes in relatively good agreement with the experimental results.

$$D_c = \left(\frac{32M}{\pi^2 \alpha \tau_y}\right)^{1/3} \tag{1.17}$$

$$H_c = \frac{\beta D_c}{2} \tag{1.18}$$

where M is the impeller torque, β is the ratio of ellipse major axis to minor axis (the aspect ratio of the elliptical torus) and α is the ellipse parameter, with all other terms having previously been defined. Hui *et al.* (2009) used ERT and LDV to characterise the agitation of hardwood and softwood pulp suspensions (1-5 wt%) with a side-entering Maxflo impeller ($D/T = 0.43$), with the effects of impeller position from the tank wall, N, pulp type and pulp τ_y values on cavern formation being studied. Increased N produced increased cavern volumes, whilst higher N values were required to generate caverns of a given size as τ_y of the suspensions increased. At a constant mass fraction, the softwood suspensions had a greater τ_y than the hardwood suspensions, and as a result, higher N values were required to generate caverns of a given volume in the softwood suspensions. At a given N, cavern volumes were smaller when the impeller off-wall clearance was smaller. The caverns were described as being truncated right-

circular cylinders, and a cavern size prediction model was developed for these side-entering systems, using similar force balance methods as Amanullah *et al.* (1998a), but including interactions between the cavern and vessel boundaries (Eq. 1.19), resulting in more accurate predictions of cavern volumes than the aforementioned cavern models.

$$\tau_y S_p + \tau_w S_w + \tau_a S_a = \rho N^2 D^4 \sqrt{N_f^2 + \left(\frac{4Po}{3\pi}\right)^2} \tag{1.19}$$

where τ_y τ_w and τ_a is the fluid yield stress, the friction force per unit area at the vessel wall and the friction force per unit area at the air-suspension interface, respectively, and S_p, S_w and S_a is cavern-suspension surface, cavern-wall surface and the cavern-air surface, respectively. Over two studies, Sossa-Echeverria and Taghipour (2014, 2015) used PIV and CFD techniques to study the mixing of viscoplastic fluids in vessels equipped with side-entry impellers, investigating the impact of vessel shape, impeller type and impeller clearance from the rear tank wall, on the flow patterns and velocity fields in C940 solutions. Three axial flow, 3-bladed impellers (all $D/T = 0.29$ relative to the cylindrical tank) were used in the study: a Maxflo Mark II impeller, an A310 impeller and an A312 impeller, and two vessel shapes: cylindrical and rectangular. The pitch ratio (the ratio of pitch to impeller diameter) for the Maxflo Mark II, A312 and A310 impellers were 0.44, 0.90 and 1.50, respectively, whilst four different impeller clearances were investigated. Larger impeller pitch ratios increased fluid discharge from the impeller, resulting in a larger extent of axial flow and greater mixing volumes. The CFD model was able to predict three-dimensional nature of the flow, however, it was unable to capture the flow symmetry shown via experiment.

Arratia *et al.* (2006) used PLIF, PIV and CFD to investigate the mixing of a C940 solution with an RT impeller and a 3-RT impeller configuration (all $D/T = 0.31$). Flow visualisation within the caverns highlighted key characteristics and structures of chaotic flow within the caverns, and moving the shaft off-centre increased mixing efficiency within the vessel through breaking spatial symmetry, with the CFD model capturing the main elements of the flow. Adams and Barigou (2007) used PLIF and CFD to characterise the caverns and pseudo-caverns that form in viscoplastic fluids (a C940 fluid) and power-law fluids, respectively. The fluids were agitated with a 6-bladed 45° PBT ($D/T = 0.33$) impeller, with numerical and experimental cavern sizes in good agreement at low Reynolds number. Predictions from theoretical cavern models were compared to the results from this work, with the axial force model proposed by Amanullah *et al.* (1998a) most accurately predicting cavern shapes and sizes. Xiao *et al.* (2014) used CFD to investigate the agitation of a viscoplastic fluid by 6-bladed 45° pitch single- and dual-PBT ($D/T = 0.33$) systems in a baffled vessel system. For the single impeller system, they replicated the tank and impeller setup used by Adams and Barigou (2007), along with the rheological properties of the 0.1 wt% C940 fluid. They developed a new torus model (Eq. 1.20), based on the model proposed by Amanullah *et al.* (1998a), which took into account cavern-vessel interactions and assumed that the circular centre of the torus should not be outside the impeller swept region, as the

Reynolds number increases. The new model was validated by both CFD and experimental results, and more accurately described the cavern as having an 'apple' torus morphology, rather than a 'horn' torus morphology as Reynolds number increased. As a result, the new model gave a better prediction of cavern shape and size than the previous models, as the cavern approached the tank wall.

$$\tau_y\left(S_p + kS_w\right) = \rho N^2 D^4 \sqrt{N_f^2 + \left(\frac{4Po}{3\pi}\right)^2} \tag{1.20}$$

where S_p is the cavern-stagnant material interface area and S_w is the surface area of the cavern-vessel contact, which are both dependent on r_c, which is the circular radius of the torus. k is the ratio of wall friction force to yield stress, whilst all other terms have previously been defined.

Saeed *et al.* (2008a, 2008b) used dynamic conductivity studies and CFD to characterise the extent of non-ideal flow (channelling and dead zones) in continuous-flow mixer systems, containing XG solutions, equipped with four different axial flow impellers (D/T = 0.45): a 3-blade A100 propeller, a 4-blade A200 PBT, a 3-blade A310 hydrofoil and a 3-blade A320 impeller. The dynamic conductivity studies showed the A200 impeller was the most efficient impeller. The calculated *Po* agreed well with experimental values and the extent of non-ideal flow decreased with increased N, and decreased feed flow rate, τ_y values and XG concentration. Over three studies, Patel *et al.* (2011, 2012a, 2012b) also used dynamic conductivity methods to investigate various operating conditions on the dynamic performance and mixing quality in continuous-flow mixing vessels containing XG solutions. Various impeller types were used in these studies, including small, central impellers: seven axial impellers and four radial impellers, and close-clearance impellers: an anchor, a Maxblend impeller and a double helical ribbon (DHR). Of the various small, central impellers, the most effective impellers for enhancing mixing quality (channelling minimised and fully mixed volume maximised) were the axial-flow Lightnin A320 impeller and the radial-flow Scaba 6SRGT impeller. As mixing quality was maximised, the power drawn by the A320 and the Scaba impellers were far greater than the Maxblend, whilst the DHR was also far more efficient at maximising mixing quality than the A320 and Scaba impellers. Increased N, increased D, decreased liquid fill heights, increased jet velocities, increased residence times (and therefore decreased flow rates), decreased fluid mass fractions and τ_y values, the upward pumping mode of axial-flow impellers and using a top inlet-bottom outlet configuration all had the effect of maximising mixing quality within the mixed vessel systems. In a similar study, Patel *et al.* (2015) used CFD to study the effect of rheological properties on the extent of non-ideal flow in viscoplastic fluids agitated with a 6-bladed RT impeller (D/T = 0.47) in a continuous flow reactor, and determined the mixing effectiveness increased with decreased K, decreased n, and decreased τ_y values. In further studies, Patel *et al.* (2013a, 2013b, 2014a, 2014b) employed ERT techniques to characterise the flows of opaque XG solutions. As before, the effects numerous operating conditions on the mixing quality in these solutions were investigated, with similar results being obtained to those previously

discussed. In a series of studies, Pakzad *et al.* (2008a, 2008b, 2008c) used UDV, ERT and CFD techniques to evaluate the flow fields in XG solutions that result through agitation with a 6-bladed Scaba 6SRGT radial flow impeller ($D/T = 0.45$). Velocity predictions from CFD simulations agreed well with the measured UDV results, as did the computed power values. ERT was employed to examine the flow patterns and to monitor cavern growth with increasing Reynolds number, with the computed and measured cavern sizes in good agreement. ERT was also used to show that decreased mixing times were achieved with increased N, Reynolds number, and specific power consumptions, whilst increased τ_y values led to increased mixing times, at a given N.

1.4.2 Mixing fluids with single impeller systems over scales

The mixing of viscoplastic fluids in stirred vessels has been extensively studied, however, limited studies have investigated the mixing of such fluids over multiple scales, in an attempt to match flows and achieve dynamic similarity. In a recent study, Piccione *et al.* (2017) scaled-up a Newtonian system known as the "blue bottle" reaction, which is the oxidation of leucomethylene blue to methylene blue (Campbell (1963); Cook *et al.* (1994); Adamčíková *et al.* (1999); Anderson *et al.* (2012)). The reaction was performed in geometrically-similar vessels (1 L and 10 L) and mass transfer rates were matched over both scales. For this to be achieved, at a constant volumetric gas flow per liquid volume, greater N speeds were required on the smaller scale. Lundén (1995) used CFD to study the mixing of a Newtonian fluid over two geometrically-similar scales with a 6-bladed RT ($D/T = 0.33$) impeller, where $T = 0.2$ m for the small scale and $T = 2$ m for the large scale. Scaling was performed with respect to (a) constant Reynolds number, (b) constant tip speed and (c) constant power input per volume. The predicted flow patterns and turbulence fields were mainly independent of scale, but minor changes were found when the Reynolds number was changed. Letellier *et al.* (2002) used CFD to analyse flows in Newtonian and shear-thinning fluids over three geometrically-similar scales (0.03, 3.8 and 11.5 m^3). Agitation occurred with an industrial dual-impeller system comprised of a MIG double-flux impeller ($D/T = 0.9$), situated above a 4-bladed PBT impeller ($D/T = 0.6$). The numerical results showed there was huge variations in the flow dynamics and patterns when scaling at constant energy per volume, and breaking geometrical similarity or modifications to the stirring system was suggested as a method to reduce the variations in flow patterns over scales. Zhang *et al.* (2014) used a helical ribbon for agitation of a corn stover-water mixture. A power-law model was introduced and measured torque values of the the mixing system in a small reactor were then applied to two larger reactors. Calculated power consumption and mixing efficiency by CFD modelling agreed with experimental results. Arratia *et al.* (2006) used solely numerical techniques for the prediction of mixing performance in viscoplastic fluids when scaling with respect to vessel size, by measuring cavern sizes directly from the velocity fields created through RT agitation in four tanks of varying size (15-500 L).

As a result of the limited findings from the literature on the characterisation of viscoplastic flows in stirred vessels over different scales, Chapter 4 will focus on the mixing of viscoplastic fluids over three different scales in vessel systems, equipped with different types of small, centrally-mounted impellers, with the aim of matching dimensionless cavern sizes over scales.

1.4.3 Mixing viscoplastic fluids with multi-impeller systems

Mixing of viscoplastic fluids in vessels equipped with multi-impeller systems, including coaxial mixers, in an attempt to maximise mixing performance, has been investigated by numerous authors. Coaxial impellers incorporate both small-central impellers (e.g. RT impellers, Scaba impellers, PBT impellers and propellers) and close-clearance impellers (e.g. anchors, helical ribbons and Maxblend impellers), with both impeller types being fitted on either the same or separate shafts. In a series of studies, Pakzad *et al.* (2013a, 2013b, 2013c) looked at the agitation of Xanthan gum (XG) solutions with various coaxial systems, using electrical resistance tomographic (ERT) techniques in conjunction with computational fluid dynamics (CFD) simulations. In the first two studies, Pakzad *et al.* (2013a, 2013b) used a Scaba-anchor impeller system for agitation, and the effects of fluid rheology and speed ratios between the two impellers on mixing time, flow patterns and power consumptions were considered. In the third study, Pakzad *et al.* (2013c) compared the mixing efficiency of a novel impeller type, the ASI impeller (a combination of a PBT and a Scaba impeller) to that of a RT impeller, an axial-radial impeller (ARI) and an axial PBT impeller for the mixing of XG solutions. The ASI impeller proved to be the most efficient mixer, with mixing efficiency being enhanced when combining with an anchor in a coaxial system. In a subsequent study, Kazemzadeh *et al.* (2016a) used ERT and CFD to study the impact of fluid rheology and defined impeller ratios on the mixing performance (in terms of mixing time and power consumption) of a Scaba-anchor coaxial mixer on the agitation of XG solutions. In two further studies, Kazemzadeh *et al.* (2016b, 2017) looked at the mixing performance (in terms of mixing times and mixing efficiency) of coaxial mixers comprising of a wall-scraping anchor and different dual, central impellers (RT impellers, Scaba impellers and PBT impellers) in the agitation of XG solutions.

As previously stated, from an industrial perspective, it is desirable to attain a state of '*complete*' mixing, whereby the fluid is in motion throughout the vessel and no stagnant zones exist, in order to maximise production formation and economic gains, and minimise precursor loses and product degradation. Coaxial mixers would be the preferred method for invoking this state on smaller scales, however on larger scales, combinations of central impellers are often used instead, due to the high costs and unfeasibly high power consumptions associated with the construction and use, respectively, of close-clearance impellers. Several authors have investigated the mixing performance of impeller systems comprising of multiple small, central impellers in the agitation of materials ranging from simple Newtonian to more complex, non-Newtonian (shear-thinning and viscoplastic) fluids.

Baudou *et al.* (1997) performed LDV visualisation experiments and LDA velocity measurements in a non-standard tall vessel containing water and equipped with different combinations of TT MIXEL propellers ($D/T = 0.5$). Four 2-impeller and one 3-impeller configurations were investigated, with the aim of optimising impeller position, clearance, separations (distance between impellers) and number to achieve best mixing and homogenisation. Smaller impeller separations generated one large circulation loop in the vessel, leading to flow being maximised and the avoidance of dead zones. The 3-propeller system resulted in better mixing than the 2-propeller configurations. Multiple authors have used tracer conductivity measurements in conjunction with CFD simulations to assess the mixing performance of various multiple impeller systems (including RT impellers, Scaba radial turbines and Scaba hydrofoils) in the agitation of Newtonian solutions (Vrabel *et al.* (2000), Montante and Magelli (2004)). Over two studies, Jaworski *et al.* (2000) and Bujalski *et al*. (2002) used CFD techniques and dynamic conductivity measurements to evaluate the mixing of a Newtonian system (water with aqueous NaCl tracer) in a vessel equipped with dual-RT impellers ($D/T = 0.5$). Jaworski *et al.* (2000) showed their simulations predicted radial and axial velocities well, but wrongly predicted tangential circulation in the opposite direction to the impeller rotation. Computed θ_{95} (time required for the solution to reach 95% homogenisation) was 2-3 times longer than measured values. Bujalski *et al*. (2002) employed a multiple reference frame (MRF) method to eliminate the wrongly predicted tangential circulation and simulated more accurate transient tracer concentration distributions. Despite these improvements, θ_{95} was still 2 times longer than measured values. Aubin and Xuereb (2006) numerically studied the mixing of Newtonian fluids with varying viscosity values and Reynolds numbers, in a vessel fitted with 4 axial Intermig impellers ($D/T = 0.9$).The starting impeller rotational position (with respect to neighbouring impellers) and separations were varied, with mixing performances being evaluated and operational limitations being determined. Rotating impellers from the typical 90° to 45° position, and reducing impeller separations led to improved fluid exchange between impeller stages for each fluid.

Kelly and Humphrey (1998) used CFD simulations to study the impact of N, fluid rheology and the distance between a cooling coil bank and fermentor wall, on the flow of viscous shear-thinning fluids (representative of fermentation broths) in a 75 m^3 fermenter equipped with three axial Lightnin A315 impellers ($D/T = 0.45$). Greater N values were required to minimise stagnant zones when n increased from 0.2 to 0.6, at constant $K = 25$ Pa s^n. Alvarez *et al.* (2002) used PLIF, UV visualisation and numerical simulations to study the mechanisms of the development and evolution of mixing structures, and the flow patterns in laminar Newtonian and non-Newtonian flows, agitated by single and 3-stage discs, standard 6-blade RTs and modified 3-blade RTs (all $D/T = 0.32$). The presence of blades in the RT impellers produced choatic flow in the Newtonian fluids, compared to the regular 2D flows resulting from agitation by the discs. In the non-Newtonian flows, spontaneous chaos occurred when mixing with all impeller types and configurations due to the non-linearity of the fluid rheology. Letellier *et al.* (2002) used CFD to analyse flows in Newtonian and shear-thinning fluids over three geometrically-similar scales (0.03, 3.8 and 11.5 m^3) with an industrial

dual-impeller system comprised of a MIG double-flux impeller (D/T = 0.9), situated above a 4-blade pitched blade turbine (PBT) (D/T = 0.6). Discussion of the findings can be seen in Section 1.4.2.

The mixing of viscoplastic fluids in vessels equipped with multiple, central impellers has also been investigated. Solomon *et al.* (1981) used HFA and flow visualisation techniques to investigate the flow patterns in XG, Carbopol and CMC solutions, agitated with RT impellers (D/T = 0.33 and 0.50) alone and in conjunction with 6-bladed PBT impellers (D/T = 0.33 and 0.50), in a dual impeller system. The power and specific power input required to achieve complete mixing was dramatically reduced using the dual PBT-RT impellers, compared to the single RT systems. For both the single and dual-impeller systems, the larger impellers required lower power inputs to achieve well-mixed systems. Galindo *et al.* (1996) evaluated mixing performance of single and dual-RT and 1- and 2-stage Intermig (all D/T = 0.53) impellers using dye visualisation methods. In a C940 solution, the dual-RT system produced caverns that reached the cavern wall at lower power drawn (0.92 kW m^{-3}) than the two-stage Intermig system (1.35 kW m^{-3}). Comparing at the same power drawn (at < 5 kW m^{-3}), the dual-RT system gave larger cavern volumes than the two-stage Intermig system. Above 5 kW m^{-3}, both impellers were able to mix almost all of the liquid volume (~90%). Before the caverns reached the tank wall, the cavern aspect ratio, H_c/D_c for both caverns was ~0.4 in the dual-RT system, over the range of investigated N. However, for the two-stage Intermig system, before the caverns reached the tank wall, H_c/D_c initially increased from 0.3 to 0.4, before remaining constant at ~0.4. Amanullah *et al.* (1998b) compared the mixing performance of four pairs of impellers: standard 6-blade RT impellers (D/T = 0.33), large 6-blade RT impellers (D/T = 0.42), SCABA 6SRGT impellers (D/T = 0.54) (all radial flow) and axial Prochem Maxflo T impellers (D/T = 0.44), in a 150 L fermenter containing a Xanthan fermentation. The dual-standard RT impellers configuration was inferior to the other three impeller types, with large diameter, low power number impellers, such as the Prochem Maxflo T and SCABA 6SRGT impellers being favoured for enhanced Xanthan productivity and reduced costs. Arratia *et al.* (2006) investigated the mixing of Newtonian (glycerin) and viscoplastic (0.1 wt% C940) fluids via experimental and numerical methods. Tracer visualisation techniques (PLIF and UV fluorescence) were employed, with PIV used to obtain 2-D velocity fields. When agitation occurred with a 3-RT configurations (all D/T = 0.31, impeller separation and clearance = 0.375T) in the C940 solution, key mixing mechanisms and flow features were captured, including cavern formation and distinct cavern-cavern segregation, with as many separate mixing zones being highlighted as impellers used for agitation. It was found that viscoplastic flows in multi-RT systems possessed separatrices that forbid flow of material from one cavern to another. Breaking spatial symmetry weakened the segregation, resulting in better mixing between caverns. Xiao *et al.* (2014) used CFD to evaluate the mixing of low yield stress viscoplastic fluids by single and dual 6-blade PBT systems (D/T = 0.33), with the resulting caverns found to be toroidal in nature. In the dual-PBT system, CFD simulations at different impeller spacings, G (G = 0.6D up to G = 1.4D) were conducted at constant Reynolds number. With increased G, more fluid in the

upper region of the vessel was agitated by the upper PBT, leading to increased total cavern volumes. At high Reynolds number, the caverns developed from having 'horn' torus to 'apple' torus morphologies. A new torus model was developed and extended to the dual-impeller systems, resulting in better predictions of cavern development than the original torus model proposed by Amanullah *et al.* (1998a). Ameur *et al.* (2015) numerically studied the effect of multiple operating conditions on the mixing of various Xanthan gum solutions by 1-, 2- and 3-Scaba 6SRGT (D/T = 0.5) impeller systems. It was determined that mixing performance was maximised (stagnant zones minimised) in 3-impeller system.

Reviewing the existing literature has shown that using multi-impeller systems for mixing a range of fluids (from Newtonian to viscoplastic) has been partially investigated. Limited studies have looked at using a combination of different impeller types for the agitation of viscoplastic fluids, with the aim of optimising the system to enhance mixing effectiveness and achieve homogeneity throughout the vessel. Chapter 6 will focus on the mixing of viscoplastic Carbopol 980 solutions with dual-impeller systems comprised of PBT impellers and RT impellers, at different impeller separations (or spacings) with the intention of highlighting the tank and impeller geometrical setup that most effectively arrives at a state of full-tank homogeneity, by minimising the required impeller rotational speeds (and associated dimensionless parameters) and mixing times.

1.5 Research aims and objectives

The overall aim of this project is to achieve flow similarity in stirred vessel systems containing viscoplastic (yield stress, shear-thinning) fluids over multiple scales, by achieving cavern size similarity on each scale. Three different scales will be investigated, with quoted vessel volumes of 2 L, 5 L and 20 L, and two different impeller types will be used for mixing: 6-bladed Rushton turbines (RT) and 4-bladed 45° pitched-blade turbines (PBT). On each scale, the relevant length scale ratios will be maintained, as a means of achieving geometric similarity. To succeed in the overall aim of the project, several objectives have been defined:

Objective 1: The formulation and characterisation, using steady shear rheological measurements, of potential model fluid systems, that accurately simulate the viscoplastic properties of Syngenta's real, industrial formulations, whilst being safe, low in reactivity, inexpensive and easy to handle. Although it is not a necessity, ideally these model fluids would be transparent, to aid the visualisation of these fluid flows when, for example, mixing these fluids in transparent stirred vessel systems (Chapter 2).

Objective 2: The development of a computational platform, known as the '*Model Fluid Selection Tool*', that is capable of suggesting suitable model fluid systems (both real and hypothetical) that most closely match the rheological properties of the real, industrial fluid in question. This computational platform will also be able to mathematically fit the raw rheological flow curves of the model fluids with multiple

different empirical rheology models, before storing the physical and fitted rheological properties of the fluids in a database. This tool could be used when, for example, looking to assess the mixing on a given scale in a stirred vessel, but using a replacement model fluid that has the same rheological properties as the 'real' industrial fluid, but is safe and inexpensive to formulate (Chapter 3).

Objective 3: The mixing of selected transparent viscoplastic model fluids, with varying rheological properties, in stirred vessel systems, over multiple scales. The fluids will be mixed with geometrically-similar Rushton turbines over three scales, and geometrically-similar pitched blade turbines over two scales, and through the use of a dimensionless scaling method, the aim will be to achieve cavern size similarity for all selected fluids and flows. When investigating the flows that result from mixing with the same impeller type, flow similarity has the potential to be achieved, however when comparing different impeller types, only cavern size similarity can be achieved as the resulting flow patterns will differ (Chapter 4).

Objective 4: Incorporation of the dimensionless scaling method into a computational platform, known as the '*Matching and Predictive Mixing Tool*', that allows the cavern sizes of a viscoplastic fluid with known rheology in a pre-defined stirred vessel system, to be predicted. Another feature of this computational tool will be its capability to suggest the operating conditions required for matching dimensionless cavern sizes in a second system, to that of a known first system, when the scale of the geometry and/or the fluid rheology has been changed (Chapter 5).

Although not directly linked to the overall aim of the project, in Chapter 6, the mixing effectiveness of dual-impeller systems for the agitation of viscoplastic fluids will be assessed. The dual-impeller systems will consist of either dual-RT systems, dual-PBT systems, or systems consisting of combinations of both impeller types. Different impeller separations and impeller rotational speeds will be investigated, with the most effective impeller configuration being deemed as the system that achieves full tank homogeneity at the lowest mixing times, impeller rotational speeds, modified power-law Reynolds number and yield stress Reynolds number. Finally, in Chapter 7 the overall conclusions will be presented, along with suggestions for future work.

Chapter 2: Rheology of Potential Model Fluid Systems

2.1 Introduction

The focus of this chapter is to formulate and rheologically characterise a large number of potential model fluids, with the aim of finding fluid systems that display the desired viscoplastic rheological properties attributed with 'real' or 'industrial' fluids. All fluids investigated are relatively inexpensive, safe and easy-to-handle, whilst the property of transparency, although not being essential, is sought after, to aid particular applications, such as mixing the fluids in transparent stirred vessel systems. The aim of this chapter is to investigate and characterise model fluid systems, in an attempt to cover as wide a range of 'rheology space' as possible. The fluids that will be examined can be categorised into the following classes: particulate suspensions (with a focus on clay suspensions), polymer solutions, microgels (in particular Carbopol solutions), a myriad of mixtures and a small number of commercial products, such as tomato ketchup and mayonnaise. The clay systems include: Bentopharm, Laponite RD, sepiolite, hectorite and Acti-gel 208 suspensions, whilst the polymer solutions of interest include carboxymethyl cellulose, hydroxypropyl cellulose and Actigum. Various grades of Carbopol, an example of a typical microgel, are examined, including Carbopol 980, Carbopol 981, Carbopol Ultrez 10, Carbopol Ultrez 21 and Carbopol Ultrez 30. The mixtures investigated involve many of the particulate systems and the Carbopol grades, and either glycerol or carboxymethyl cellulose. For all of these fluids, the effects of mass fraction on the rheological properties of the fluids are determined, whilst for the Carbopol grades, the effects of pH and salt concentration are also explored. The rheological characterisation of all the fluids involves the use of a shear-stress controlled Anton Paar Modular Compact Rheometer 302 rheometer, fitted with a 6-bladed vane (Anton Paar ST20-6V-20/112.5 stirrer) and cup geometry (vane diameter = 20.00 mm, blade height = 20.00 mm, cup diameter = 28.92 mm). '*Downward*' (or '*down*') shear stress sweep measurements are used to attain the steady shear rheological properties of the fluids, with all measurements occurring at a temperature of 25°C. Many of the particulate suspensions display thixotropic properties, and therefore the downward shear stress sweeps were used for rheological characterisation, to gain information relating to the '*dynamic*' yield stress values of the fluids and to negate the potential time-dependent rheological properties of the fluids. Thixotropy and hysteresis loops will not be discussed in this work. Each of the resulting flow curves acquired from the downward shear stress sweeps are then fitted with various mathematical models, including the Power Law model (Eq. 1.8), Herschel-Bulkley model (Eq. 1.11) and Casson model (Eq. 1.13), with the fitted parameters from the model that produced the best description of the raw data being presented. A summary of the fitted data will then be discussed, highlighting the 'rheology space' that has been explored.

2.2 'Good' vs 'bad' rheological data

For the mathematical fitting procedures to be carried out correctly, it is imperative that only rheological data that can be classed 'appropriate' or 'good' is used. Figure 2.1 is a shear stress-shear rate plot of the rheological data of two fluids (*Fluids A* and *B*), acquired from downward shear stress sweep measurements. From the figure, various sections of the flow curves have been highlighted, as they do not represent the 'true' rheology of the fluid. The red circled regions highlight the characteristic feature displayed on a flow curve when 'slip' of material at the wall of the geometry has occurred. Wall slip, also known as wall depletion effects, occurs in disperse systems when the multi-phase fluid is brought in contact with a smooth, solid boundary (including in viscometers and rheometers), resulting in the formation of a very thin, lower-viscosity layer at the boundary consisting only of continuous phase, with the bulk flow remaining at its original concentration. Slip can be caused through electrostatic, hydrodynamic, viscoelastic and steric effects, and gravitational forces (Buscall *et al.* (1993); Barnes (1995); Walls *et al.* (2003); Buscall (2010)). This phenomenon is displayed in a wide range of fluid systems, including microgels (Piau (2007); Seth *et al.* (2008)), particulate systems (Buscall *et al.* (1993); Russel and Grant (2000); Walls *et al.* (2003)), and emulsions and foams (Denkov *et al.* (2005)). Slip is prominent in dispersed systems where low stresses are being exerted on the material, resulting in inhomogeneous flow, with the bulk flow deforming less than the lower-viscosity layer close to the wall. In rheometers, the resulting flow curves may show lower Newtonian plateaus than expected and pseudo-yield stress values at lower stresses than is representative of the given fluid. Various methods have been suggested for minimising or eliminating slip in viscometers and rheometers, including the use of roughened or serrated geometries, the use of vane geometry (Nguyen and Boger (1983, 1985, 1992); Yoshimura *et al.* (1987); Buscall *et al.* (1993); Barnes and Nguyen (2001)) or the increase in gap size in, for example, cone-and-plate geometry (Yoshimura and Prud'homme (1988); Buscall *et al.* (1993); Barnes (1995); Walls *et al.* (2003); Buscall (2010)). In this work, a 6-bladed vane geometry was used, however as seen from the flow curves in Figure 2.1, slip is still able to occur due to the smooth nature of the associated cup geometry. In terms of analysing flow curves exhibiting slip effects to obtain meaningful data, wall slip is often associated with low shear rate regions, therefore mathematically fitting data from high shear rates down to this low shear rate region, or extrapolating the 'true' flow curve in regions of low shear rate may be methods for overcoming the effects of slip. In *Fluid A*, slip is seen at $\dot{\gamma} \approx 0.1$ a.u., however in *Fluid B*, this occurs at a higher value, $\dot{\gamma} \approx 20$ a.u., with this difference likely caused by the fact *Fluid B* is a polymeric solution, hence viscoelastic effects cause the macromolecules to move towards the rotating geometry, promoting the formation of liquid-like layer at the wall (Barnes (1995)), whilst *Fluid A* is a heavily crosslinked, viscoplastic solution and hence the entanglement of polymer chains around the shaft does not occur in these pseudo-particulate suspensions (Dealy and Vu (1977)). Both fluids displayed inertial effects from the rheometer (purple regions), caused by the downward nature of the shear stress sweep measurements, associated with the instantaneous jump at the start of the measurement from no shear stresses being applied to the material

to shear stress values equating to approximately $\dot{\gamma} \approx 1000$ a.u. being applied. *Fluid B* also displayed turbulence-related effects at high shear stress values (yellow region), due to the relatively 'thin' nature of the fluid. The result was a misleading 'shear-thickening' type regime, which was not a true representation of the rheological properties of the fluid in this region. The region between the red and purple highlighted regimes in *Fluid A* ($\dot{\gamma} \approx 0.1$-1000 a.u.) and the red and yellow highlighted regimes in *Fluid B* ($\dot{\gamma} \approx 20$-450 a.u.) constitute as 'good' data. This band of 'good' data is too narrow in *Fluid B* for the accurate acquisition of fitted rheological parameters. However, the region of 'good' data is broad enough in *Fluid A* for a true representation of parameters, such as the yield stress, τ_y to be attained. As a result, in this chapter only fluids that produced a wide range of 'good' or 'appropriate' rheological data were examined and described using mathematical models, with all 'bad' data being neglected.

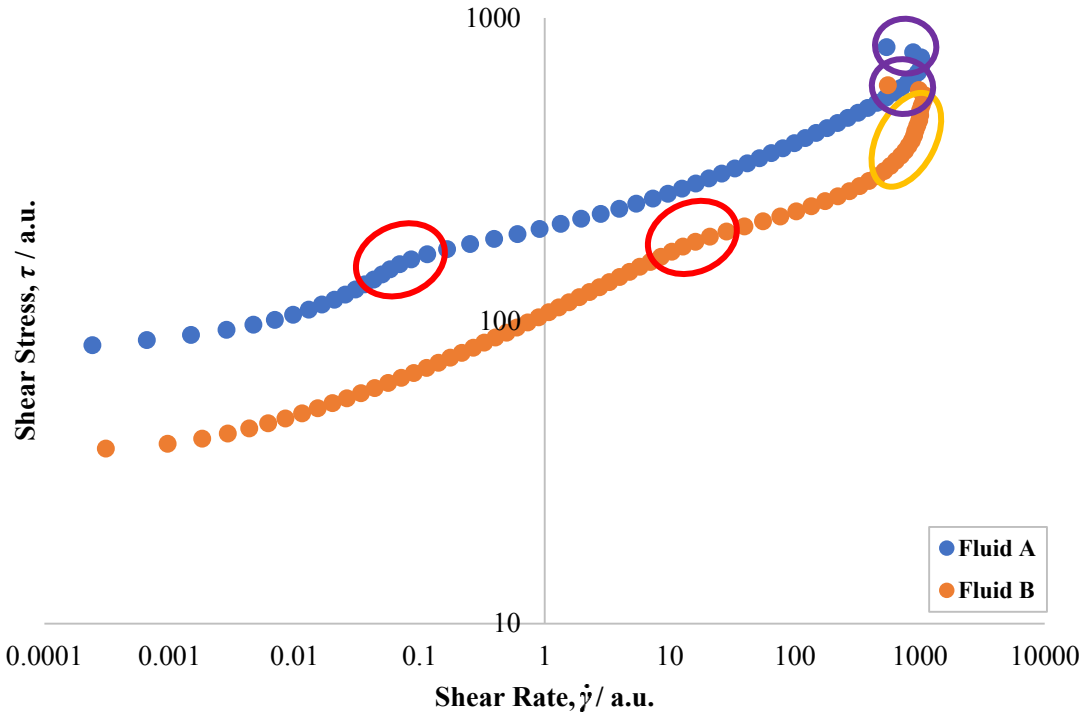

Figure 2.1. Raw rheological flow curves for two example fluids: *Fluid A* and *Fluid B*, used to highlight what constitutes as 'good' and 'bad' rheological data, with all the 'bad' regions being highlighted. For *Fluid A*: the 'good' data is the band between the red and purple regions, whilst for *Fluid B*: the 'good' data is between the red and yellow regions.

2.3 Rheological measurement procedure

Unless otherwise stated, the steady shear rheological properties of all fluids characterised in this chapter underwent the following rheological measurement procedure. Each fluid was manually agitated for ~10 s to ensure homogeneity throughout the sample, before 40-50 g of the fluid was loaded into a rheometrical cup geometry (cup diameter = 28.92 mm) and appropriately positioned in an Anton Paar Modular Compact Rheometer 302 rheometer, fitted with a 6-bladed vane (Anton Paar ST20-6V-20/112.5 stirrer, vane diameter = 20.00 mm, blade height = 20.00 mm). The vane was lowered into the

fluid, and the temperature of the fluid was set to 25°C. The fluid then underwent an initial pre-shear test (1200 a.u., 15 pt, 1 s pt^{-1}), before undergoing a downward shear stress sweep (60 points per stress decade (pt dec^{-1}), ramp logarithmic profile, 5 s pt^{-1}). The raw rheological flow curve acquired from the downward shear stress sweep was fitted with the Power Law model (Eq. 1.8), the Herschel-Bulkley model (Eq. 1.11) and the Casson model (Eq. 1.13). The model that produced the most accurate fit of the raw data, in terms of minimising the average absolute deviation per datum (AAD) values and maximising R^2 values, was used to describe the fluid in question. This procedure was used for the fitting of all fluids in this chapter and further discussion of the mathematical fitting processes and error quantification between raw and fitted data can be found in Section 3.4.

2.4 Impact of rheometrical geometry on rheological measurements

All of the rheological data presented in this chapter were acquired using the vane geometry. It was established relatively early on in the measurement series that the acquisition of data using the vane resulted in a number of issues, namely discrepancies between the flow curves obtained for a given fluid when using the vane geometry compared to other geometries, such as cone-and-plate and concentric cylinder systems. However, there was continued use of the vane geometry for these measurements, as a means of complying with the methods used at Syngenta and to therefore match the geometry previously used in the rheological characterisation of their industrial fluid formulations. As well as this, the default geometry conversion factor (used for converting the rotational rate to a shear rate) value of '1' was used, despite not being appropriate for the viscoplastic fluids being characterised in this work, as this value was also used throughout the Syngenta protocol. Further discussion of this can be found in later paragraphs in this section.

Typically, particle-based industrial slurries have a tendency to sediment and therefore using geometries, such as the vane, that provide uplift and reduce sedimentation whilst the measurement procedure is being performed is of the utmost importance. In addition to this, geometry including cone-and-plate or plate-and-plate, are not appropriate instrumentation for the measurement of slurries, because it is common practice for the gap size between the cone and the plate, or the plate and the plate to be at least ten times larger than the particle size within the slurries. In this case, the gap size of the cone-and-plate system at Imperial College was 0.101 mm, which is less than ten times larger than the particle sizes within the industrial slurries. Hence, use of these geometries can potentially result in damage to the particle-based systems, or particles can become 'jammed' within the gap between the geometry, which in turn could impact the acquisition of the true rheological properties of the fluid in question. However, despite the benefits of using vane geometry, there are also some noticeable disadvantages. Figure 2.2 is shear rate-shear stress plot of a Carbopol 980 (C980, 0.20 wt%, pH 6.26) solution, in which a number of different geometries were used to acquire the various flow curves (see Figure 2.3 for images of each

of the different geometries used). As seen in Figure 2.2, very similar flow curves were obtained when using the roughened cone-and-plate and sandblasted concentric cylinder geometry, however, the vane produced a vastly different curve, with every shear stress value at a given shear rate value being much larger when characterisation occurred with the vane than the other geometries. With the exception of the roughed cone-and-plate, all curves displayed wall slip effects. A discussion on wall slip can be found in Section 2.2 and therefore will not be presented here. The author carried out a similar study using a Newtonian, silicone oil of known viscosity, with the resulting flow curves from all of the various geometries being comparable, including the vane-based data.

The vane method has commonly been used as a direct means of measuring the yield stress in viscoplastic fluids. The vane is immersed within a sample and set to a low, constant rotational rate, with the yield stress of the fluid associated with a maximum value of torque being exerted on the vane shaft, whereby the dimensions of the vane and the shear stress distribution are known. The vane geometry is treated as a pseudo-cylinder (Figure 2.4) with fluid trapped between the vane blades, and the circular cylinder diameter defined by the vane tips, with an even distribution of shear stresses over the cylinder surface (Nguyen and Boger (1985); Yan and Adams (1997); Barnes and Nguyen (2001)). When the vane is fitted to the rheometer, the rheometer reads the attachment as being a solid cylinder, however when the rheological measurement occurs, the viscoplastic material between the blades deforms and flows, hence the assumption that the geometry can be treated as a solid cylinder and that there is an even distribution of shear stresses over the cylinder is not valid. When Anton Paar manufacture the vane geometry, they perform calibration testing on the vanes using a rheometer and Newtonian silicone oils of known viscosity. During the testing, the geometry conversion factor used to convert the rotational speed of the vane to a shear rate in the rheometer is set to a value of '1', and based on this, Anton Paar then determine a value for the shear stress factor that results in the correct viscosity value of the Newtonian calibration fluid (the silicone oil). Therefore, in this work, when the rheological characterisation of a silicone oil of known viscosity was performed with the various types of geometry, all of the flow curves were comparable, including the data acquired using the vane. This was because the conversion factors were valid for the Newtonian system in question, as deformation of the material between the vane's blades could not occur, and hence the viscosity of the material was able to be correctly measured. However, when the Newtonian silicone oil was replaced with a viscoplastic Carbopol fluid, the default shear rate conversion factor value of '1', and the resulting default shear stress conversion factor, were no longer appropriate for the system in question, as the material was now able to deform between the vane's blades and hence the vane could not be treated as a solid cylinder. This led to incorrect viscosity values of the viscoplastic fluid being measured throughout the rheological measurement, explaining the observed discrepancies in the flow curves being seen when the measurement geometry was varied (Figure 2.2).

Due to the issues associated with the default conversion factors discussed above, the units for shear rate (s^{-1}) and shear stress (Pa) in all vane-derived flow curves (except Figure 2.2) and the text presented in this

chapter will be replaced with 'arbitrary units' (a.u), along with the SI units associated with each of the parameters in the Herschel-Bulkley model, the Power law model and the Casson model presented in the tables, to highlight the inaccuracies of the vane measurements and to avoid confusion for the readers.

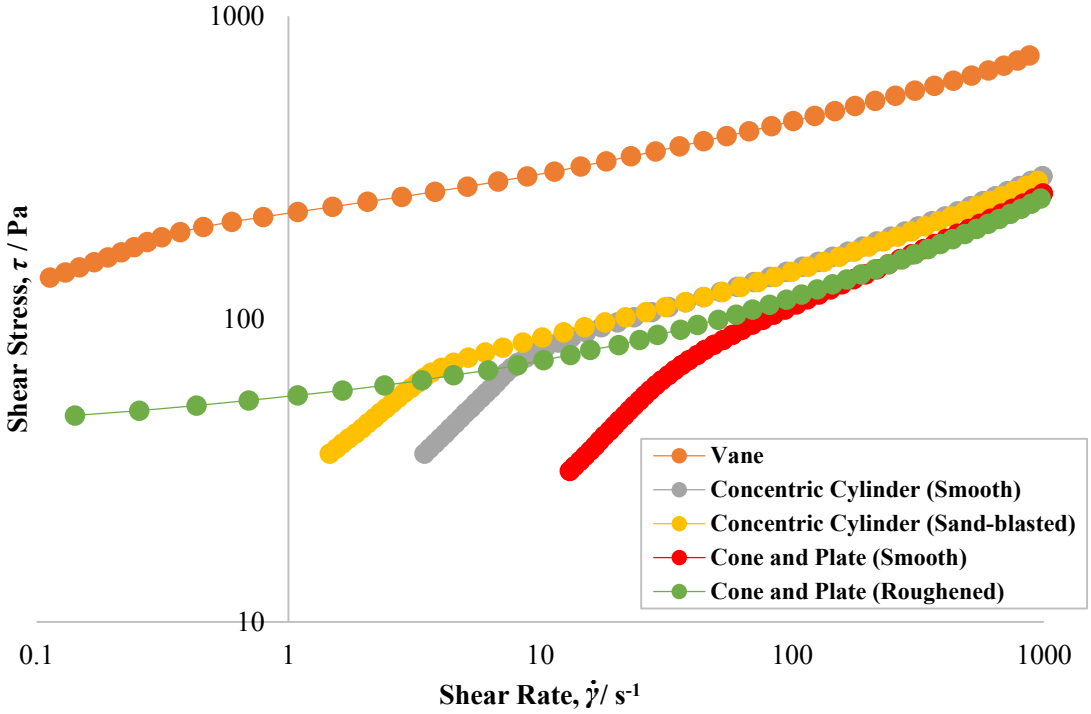

Figure 2.2. Raw rheological flow curves of a Carbopol 980 (C980, 0.20 wt%, pH 6.26) solution, acquired using different rheometrical geometries, including: a 6-bladed vane, a sandblasted concentric cylinder, a smooth concentric cylinder, a roughened cone-and-plate and a smooth cone-and-plate.

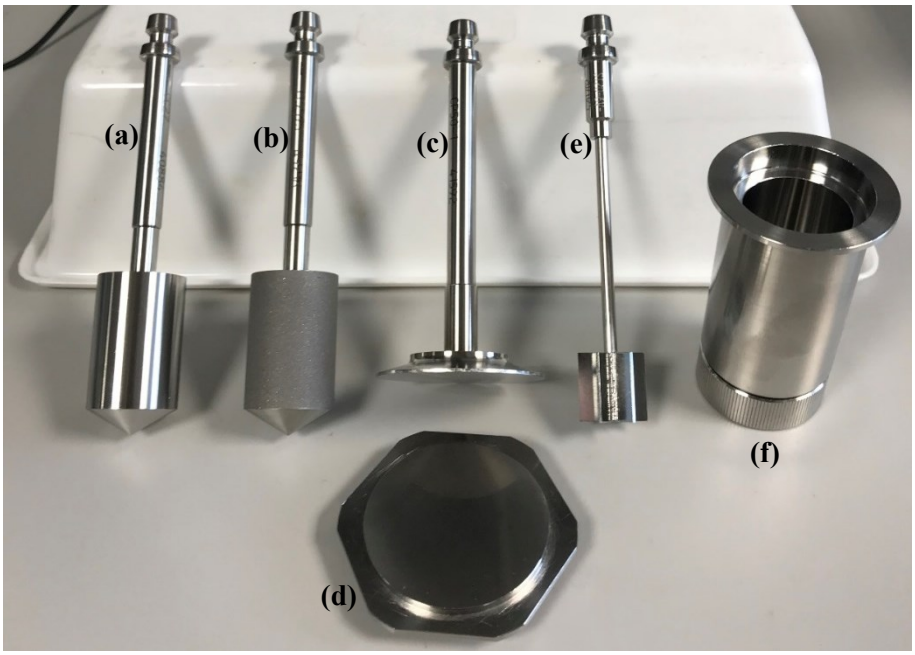

Figure 2.3. Image highlighting some of the commonly used rheometrical geometries, including: (a) a smooth concentric, (b) a sandblasted concentric cylinder, (c) a cone, (d) the associated plate, (e) a 6-bladed vane and (f) the cup used in association with the concentric cylinders and the 6-bladed vane.

However, for the sake of this work, the potential vane-based 'discrepancy' when characterising viscoplastic fluids is not an issue because all measurements were purposely carried out using the same instrumentation as the instrumentation used at Syngenta, including the same make of rheometer (Anton Paar), the same 6-bladed vane geometry specifications and the same Anton Paar vane default conversion factors. As a result, when characterising the same fluid using the instrumentation at Imperial College London and Syngenta, very similar results were acquired. This can be seen in Figure 2.5, where 6-bladed vane and cup geometries (both: vane diameter = 20.00 mm, blade height = 20.00 mm, cup diameter = 28.92 mm) were used for the rheological characterisation of a Carbopol 934 (C934, 0.50 wt%, pH 5.50) dispersion via an upward shear rate sweep (ramp logarithmic, $\dot{\gamma} = 0.1\text{-}600$ a.u., 10 pt dec^{-1}, 10 s pt^{-1}, 38 pt). From Figure 2.5, one curve was acquired using the Syngenta Anton Paar Modular Compact Rheometer 501 rheometer and the Syngenta 6-bladed vane and cup (dimensions above), whilst the other curve was generated using the Imperial Anton Paar Modular Compact Rheometer 302 rheometer and the Imperial 6-bladed vane and cup (dimensions above). As seen in Figure 2.5, the resulting curves were very similar, with an AAD = 1.71% and an $R^2 = 0.999$, highlighting that although varying geometry type will result in different flow curves, similarity in apparent flow curves can be attained when using the same type of geometry and the same vane default conversion factors. Therefore, when looking to find the 'best-matched' model fluids, in terms of rheological properties, to that of the 'real' fluid, it is imperative that there is consistency with fluid formulation and rheological measurement protocol. Further discussion of this can be found in Section 3.10.

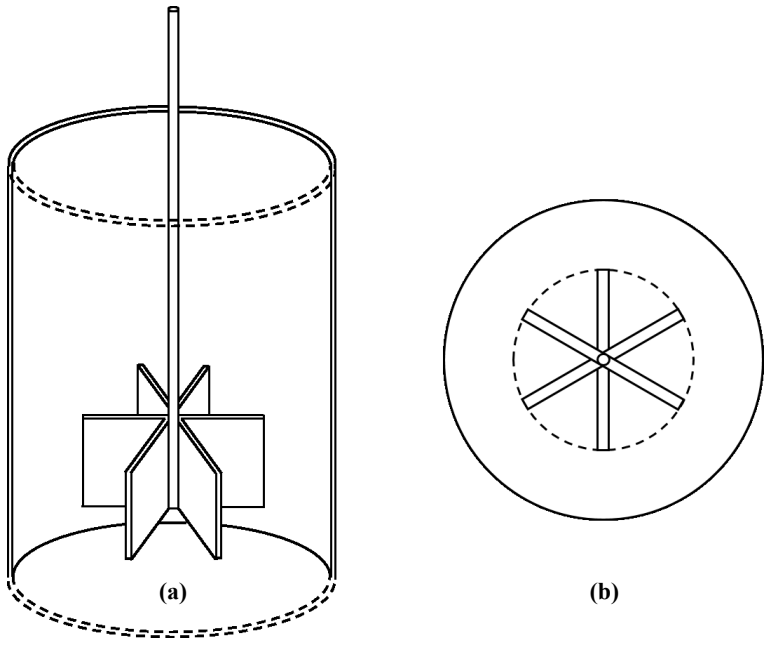

Figure 2.4. Schematic of a 6-bladed vane in a cup geometry from: (a) a side-view perspective and (b) a top-view perspective. The figure was adapted from the works of Nguyen and Boger (1985) and Yan and Adams (1997).

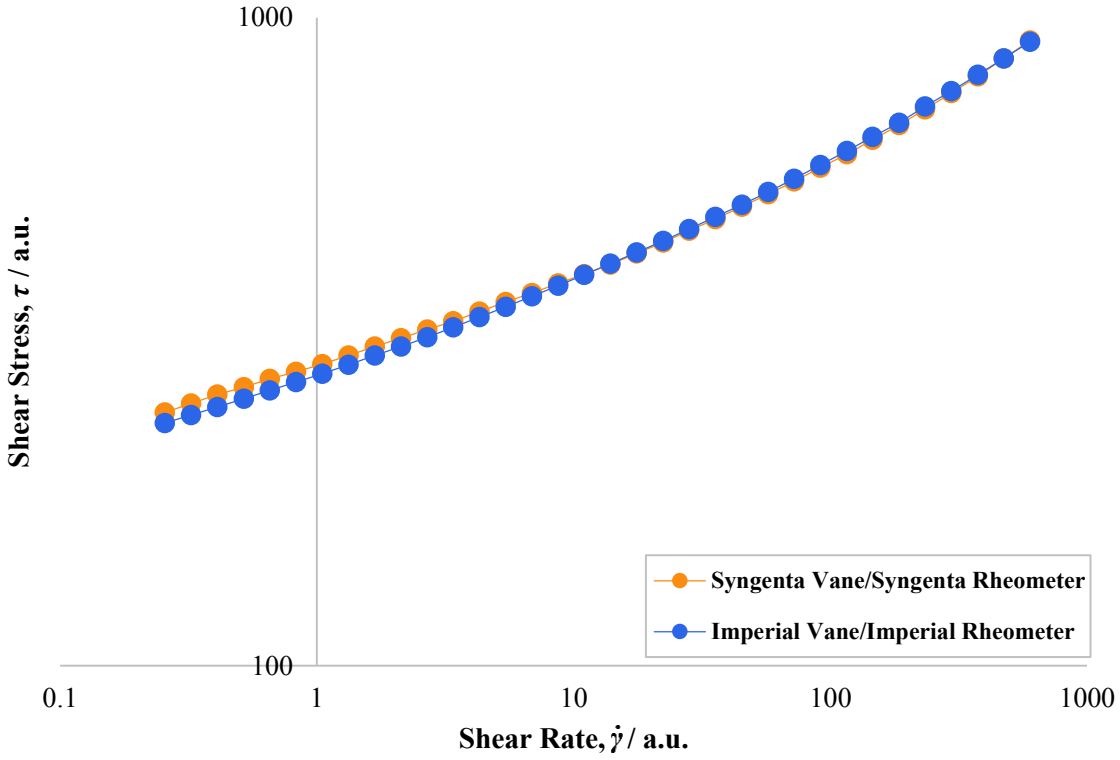

Figure 2.5. Raw rheological flow curves of a Carbopol 934 solution (0.50 wt%, pH 5.50), acquired using different a 6-bladed vane and cup geometries (vane diameter = 20.00 mm, blade height = 20.00 mm, cup diameter = 28.92 mm) and two different Anton Paar rheometers: Anton Paar Modular Compact Rheometer 501 (Syngenta) and Anton Paar Modular Compact Rheometer 302 (Imperial).

2.5 Particulate suspensions

A number of particle-based systems were formulated and rheologically characterised, with the aim of finding suitable model fluid systems which have the desired viscoplastic properties. The focus in this section were clay-based suspensions, and as seen from the literature review in Section 1.2.1, they commonly display a yield stress and exhibit shear-thinning behaviour once the yield stress has been exceeded, if the mass fraction (or solid loading) of the clay in water is high enough. The clay-water suspensions being investigated in the following sections are: Bentopharm suspensions: a pharmaceutical grade of Bentonite with platelet-like particle morphology; Laponite RD suspensions: a synthetic clay with platelet-like particle morphology; sepiolite: a naturally-occurring clay with needle-like particle shape; and hectorite: a naturally-occurring clay with platelet-like particle shape. Other particle-based systems, including kaolinite, Acti-Gel 208 and fumed silica suspensions will also be discussed.

2.5.1 Bentopharm suspensions

A 7.50 wt% Bentopharm (Wilfrid Smith Ltd) stock suspension was formulated (75 g Bentopharm, 925 g deionised water). The Bentopharm was added to the deionised water and the stock suspension

was stirred with an overhead stirrer (IKA EUROSTAR 60 motor) at 1700 rpm during addition of the Bentopharm (approximately 10 min), before being stirred for 90 min at 1200 rpm. The suspension was then high-shear mixed (Silverson high shear mixer, maximum speed) for 5 min. The 7.00 wt% and 7.50 wt% samples were generated from this suspension. A further 40 g of Bentopharm and 122 g of deionised water was added to 843 g of the stock Bentopharm suspension, to generate a suspension at 10.50 wt%. The suspension was again stirred at 1200 rpm for 90 min using the overhead stirrer, before being high-shear mixed for 5 min. A number of 80 g Bentopharm samples, ranging from 7.00-10.50 wt%, were generated through the addition of deionised water to different quantities of the 10.50 wt% Bentopharm stock solution, with each sample being left to rest for ~16 h, after which rheological characterisation then occurred. A summary of the physical properties of the Bentopharm fluids can be found in Table 2.1, whilst the samples themselves can be visualised in the image in Figure 2.6. As seen in Figure 2.6, the samples were opaque, and therefore simple dye techniques could not be used to visualise the flow of these fluids in stirred vessel systems.

Table 2.1. Physical properties of the Bentopharm samples, and the quantities of the 10.50 wt% Bentopharm stock suspension and additional deionised water used to generate each sample. *Bentopharm sample generated using the original 7.50 wt% Bentopharm stock solution, hence the quantities presented relate to the amount of 7.50 wt% Bentopharm stock solution used for fluid formulation.

Mass of 10.50 wt% Bentopharm stock solution / g	Mass of additional deionised water / g	Mass fraction of Bentopharm / wt%	pH
80.00	0.00	10.50	9.10
78.10	1.90	10.25	9.10
76.19	3.81	10.00	9.15
74.29	5.71	9.75	9.17
72.38	7.62	9.50	9.15
68.57	11.43	9.00	9.28
64.76	15.24	8.50	9.20
60.95	19.05	8.00	9.20
80.00*	0.00*	7.50	9.20
77.33*	2.67*	7.00	9.20

Figure 2.6. Images of the Bentopharm samples, ranging in mass fraction from 7.00-10.50 wt%.

The rheological properties of the samples were obtained as described in Section 2.3. In addition to this, the fluids underwent an upward shear stress sweep (60 pt dec^{-1}, ramp logarithmic profile, 5 s pt^{-1}) and downward ($\dot{\gamma} = 1000$-0.01 a.u.) and upward ($\dot{\gamma} = 0.01$-1000 a.u.) shear rate sweeps (5 pt dec^{-1}, 26 pt, ramp logarithmic duration, 4-60 s, total time = 549.5 s). The raw rheological flow curves acquired from the downward shear stress sweeps for each Bentopharm sample can be seen in Figure 2.7, and the resulting Herschel-Bulkley fitted data, along with the associated error quantification, the shear rate ranges over which the fits occurred, and the physical properties of the fluids can be seen in Table 2.2. As the mass fraction of Bentopharm in the fluids increased, the yield stress, τ_y and flow consistency index, K values of the samples increased. The increase in clay mass fraction results in a greater extent of electrostatic interactions between in the particles (discussion of clay particle interaction can be found in Section 1.2.1), leading to the strengthening of the three-dimensional gel network throughout the clay structure. The flow behaviour index, n values of the samples remained approximately constant over the investigated range of Bentopharm mass fractions.

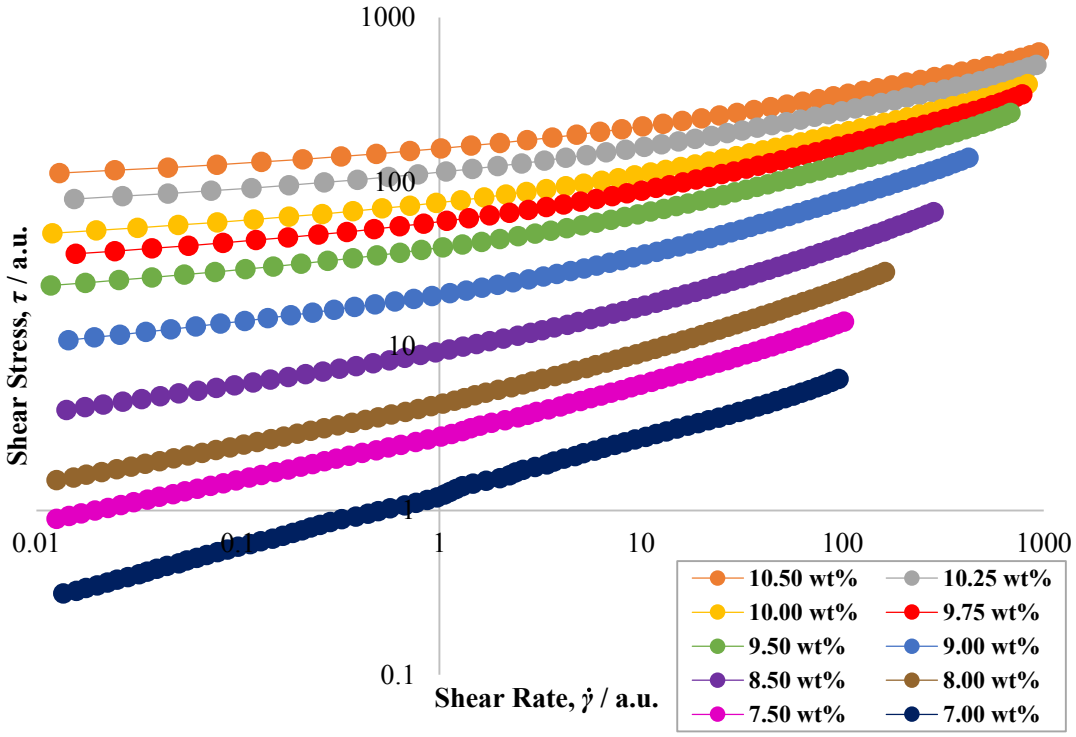

Figure 2.7. Raw rheological flow curves, acquired from shear stress down sweeps using 6-bladed vane geometry, of Bentopharm suspensions at various mass fractions, ranging from 7.00-10.50 wt%, with all suspensions at an approximately constant pH: 9.10-9.28.

Table 2.2. Herschel-Bulkley fitted data and the physical properties of the Bentopharm fluids, along with the associated error quantification of the mathematical fits and the shear rate range over which the fits occurred.

Physical properties		**Herschel-Bulkley rheological properties**			**Error quantification and analysis**		
Bentopharm mass fraction / wt%	**pH**	**Yield stress, τ_y / a.u.**	**Flow consistency index, *K* / a.u.**	**Flow behaviour index, *n***	**Optimised fit AAD / %**	**Optimised fit R^2 value**	**Shear rate range of optimised fit / a.u.**
10.50	9.10	102.7	54.3	0.32	0.79	0.999	0.0130-947
10.25	9.10	71.2	41.4	0.34	0.88	0.999	0.0154-919
10.00	9.15	45.2	28.3	0.37	1.05	0.999	0.0120-971
9.75	9.17	33.7	22.4	0.39	1.17	0.998	0.0157-897
9.50	9.15	22.2	16.5	0.40	1.66	0.998	0.0118-827
9.00	9.28	10.2	9.7	0.42	2.03	0.998	0.0144-558
8.50	9.20	3.7	5.2	0.43	3.25	0.996	0.0141-421
8.00	9.20	1.1	3.2	0.41	3.31	0.995	0.0126-262
7.50	9.20	0.45	2.4	0.36	2.02	0.998	0.0126-102
7.00	9.20	0.04	1.2	0.35	1.32	0.999	0.0136-96

2.5.2 Laponite RD suspensions

A 5.50 wt% Laponite RD (Laponite, Rockwood) stock suspension was formulated (72 g Laponite, 1128 g deionised water). The Laponite was added to the deionised water and the solution was stirred magnetically and using an overheard stirrer (IKA EUROSTAR 60 motor) for ~90 min at 1600-1800 rpm. The stock suspension was then high-shear mixed (Silverson high-shear mixer, full speed) for 5 min, before being left to rest for ~16 h. After the time elapsed, various 80 g Laponite samples, ranging from 3.50-5.25 wt% were formulated through the addition of deionised water to different quantities of the 5.50 wt% Laponite stock suspension. As seen in the image in Figure 2.8, the resulting Laponite fluids were highly transparent, hence simple dye techniques could be used to visualise the flow of these fluids in stirred vessel systems.

The rheological properties of the samples were obtained using the methods described in Section 2.3, however the downward shear stress sweep measurements occurred using 90 pt dec^{-1}, rather than 60 pt dec^{-1}. The 5.00 wt% Laponite sample ('*2*') underwent the additional upward shear stress sweep and the shear rate sweeps outlined in Section 2.5.1. The raw rheological flow curves acquired from the downward shear stress sweeps for each Laponite sample can be seen in Figure 2.9, and the resulting Herschel-Bulkley fitted data, along with the shear rate ranges of the fits, the errors associated with the fits, and the physical properties of the fluids can be found in Table 2.3. Due to the lack of a yield stress in the 3.75 wt% sample ('*7*'), the 3.50 wt% sample ('*8*') was not rheologically characterised. As before, as the mass fraction of Laponite in each sample increased, τ_y and K increase, whilst, after an initial decrease in n going from 5.25 wt% down to 4.75 wt%, n remained fairly constant over Laponite mass fraction range of 4.75 wt% down to 3.75 wt%. The Laponite suspensions displayed the desired viscoplastic properties at mass fractions of > 3.75 wt%, whilst also being associated with high levels of transparency. As a result, Laponite suspensions are ideal candidates as replacement model fluid systems.

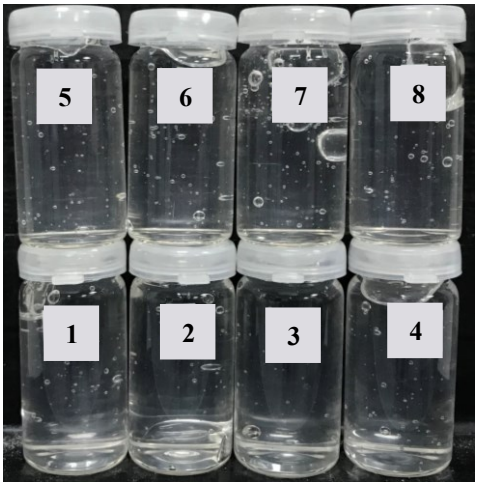

Figure 2.8. Images of the Laponite samples, ranging in mass fraction from 3.50-5.25 wt%. More specifically: '*1*' = 5.25 wt%, '*2*' = 5.00 wt%, '*3*' = 4.75 wt%, '*4*' = 4.50 wt%, '*5*' = 4.25 wt%, '*6*' = 4.00 wt%, '*7*' = 3.75 wt% and '*8*' = 3.50 wt%.

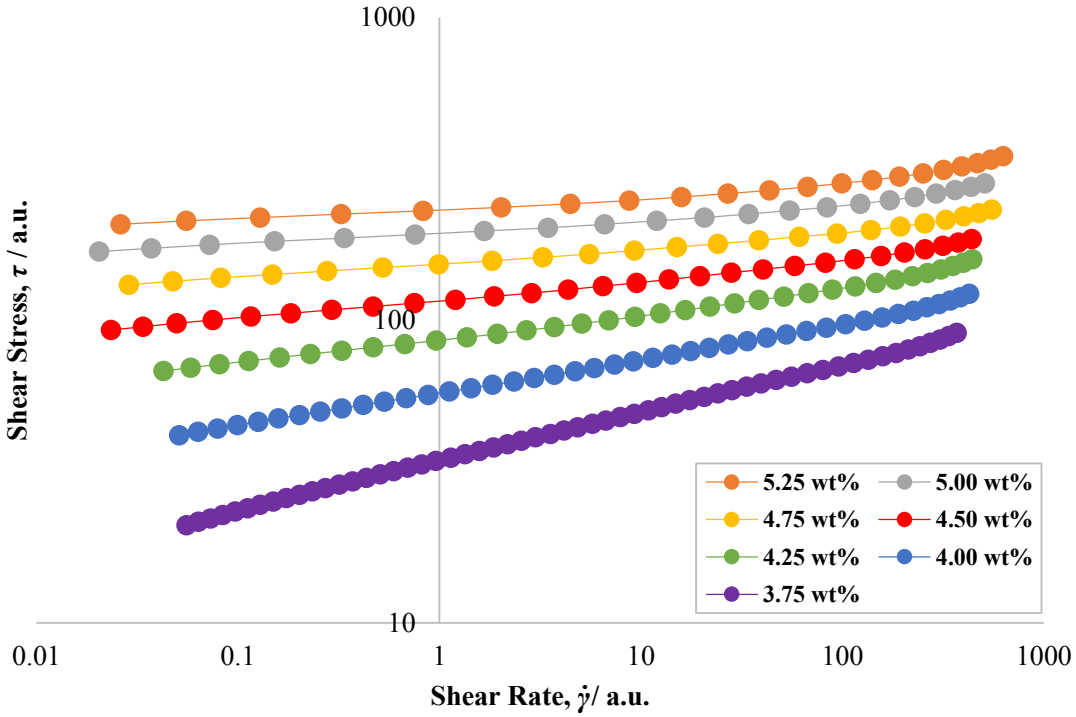

Figure 2.9. Raw rheological flow curves, acquired from shear stress down sweeps using 6-bladed vane geometry, of Laponite suspensions at various mass fractions, ranging from 3.75-5.25 wt%, with all suspensions at an approximately constant pH: 9.81-9.87.

Table 2.3. Herschel-Bulkley fitted data and the physical properties of the Laponite fluids, along with the associated error quantification of the mathematical fits and the shear rate range over which the fits occurred.

Physical properties		**Herschel-Bulkley rheological properties**			**Error quantification and analysis**		
Laponite mass fraction / wt%	**pH**	**Yield stress, τ_y / a.u.**	**Flow consistency index, *K* / a.u.**	**Flow behaviour index, *n***	**Optimised fit AAD / %**	**Optimised fit R^2 value**	**Shear rate range of optimised fit / a.u.**
5.25	9.81	203.7	23.9	0.27	1.07	0.993	0.0262-628
5.00	9.81	157.0	33.8	0.20	1.08	0.993	0.0205-511
4.75	9.82	90.0	63.4	0.11	1.17	0.989	0.0288-554
4.50	9.82	61.8	53.2	0.13	0.76	0.997	0.0234-440
4.25	9.87	42.6	42.8	0.15	0.62	0.998	0.0427-354
4.00	9.87	13.5	43.7	0.14	0.45	0.999	0.0511-344
3.75	9.87	0.00	34.2	0.16	0.68	1.000	0.0555-306

2.5.3 Sepiolite suspensions

A 10.00 wt% Sepiolite (Aldrich) stock suspension was formulated (100 g Sepiolite, 900 g deionised water). The sepiolite was added to the deionised water and the stock solution was stirred via magnetic agitation and then with an overhead stirrer (IKA EUROSTAR 60 motor) for 10 min, before being high-shear mixed (Silverson high shear mixer, maximum speed) for 5 min. A number of 80 g sepiolite

samples, ranging from 4.50-10.00 wt% were then formulated, through the addition of deionised water to different quantities of the 10.00 wt% sepiolite stock suspension. Each sample was then left to rest for ~20-30 h before rheological characterisation occurred. As seen in Figure 2.10, the resulting sepiolite fluids were opaque and as a result, complex tomographic techniques would be required to visualise the flow of these fluids in stirred vessel systems.

The rheological properties of the samples were obtained using the methods described in Section 2.3. In addition to this, each sample also underwent an upward shear stress sweep, and upward and downward shear rate sweeps, as outlined in Section 2.5.1. The downward shear stress sweeps were used for analysis and the raw rheological flow curves for each sepiolite sample can be seen in Figure 2.11. The Herschel-Bulkley model provided the most accurate mathematical fit of the raw data curves, with the resulting fitted parameters, along with the shear rate ranges of the fits, the errors associated with the fits and the physical properties of the fluids being seen in Table 2.4. As with the Bentopharm and Laponite fluids, as the mass fraction of sepiolite in the solutions increased, the τ_y and K values increased. At higher mass fractions, n was relatively constant, however as mass fractions decreased, the degree of shear-thinning behaviour in the samples became more enhanced.

Figure 2.10. Images of the sepiolite samples, ranging in mass fraction from 4.50-10.00 wt%.

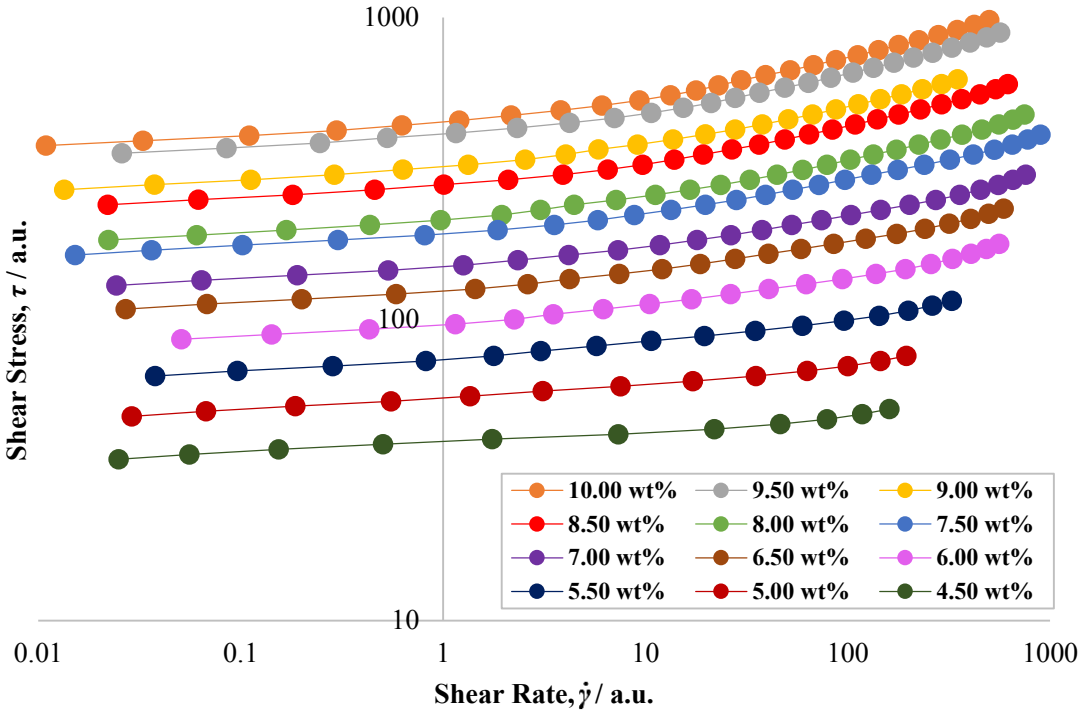

Figure 2.11. Raw rheological flow curves, acquired from shear stress down sweeps using 6-bladed vane geometry, of sepiolite suspensions at various mass fractions, ranging from 4.50-10.00 wt%, with all suspensions at an approximately constant pH: 8.75-9.03.

Table 2.4. Herschel-Bulkley fitted data and the physical properties of the sepiolite fluids, along with the associated error quantification of the mathematical fits and the shear rate range over which the fits occurred.

Physical properties		**Herschel-Bulkley rheological properties**			**Error quantification and analysis**		
Sepiolite mass fraction / wt%	**pH**	**Yield stress, τ_y / a.u.**	**Flow consistency index, *K* / a.u.**	**Flow behaviour index, *n***	**Optimised fit AAD / %**	**Optimised fit R^2 value**	**Shear rate range of optimised fit / a.u.**
10.00	8.75	359.3	87.6	0.32	0.57	0.999	0.0109-563
9.50	8.86	338.8	67.5	0.33	0.43	1.000	0.0258-568
9.00	8.80	254.0	64.5	0.30	0.34	1.000	0.0134-350
8.50	8.87	227.4	48.9	0.31	0.46	1.000	0.0220-620
8.00	8.89	170.2	43.2	0.29	0.40	0.999	0.0222-747
7.50	8.93	153.2	38.0	0.28	0.62	0.999	0.0152-776
7.00	8.84	119.9	29.1	0.27	0.44	0.999	0.0243-657
6.50	8.89	100.0	23.7	0.27	0.71	0.998	0.0270-680
6.00	8.89	78.3	17.6	0.26	0.88	0.996	0.0508-561
5.50	8.92	58.2	15.0	0.23	0.93	0.995	0.0377-394
5.00	9.03	31.5	23.4	0.11	1.09	0.985	0.0674-195
4.50	9.01	23.0	16.0	0.09	1.38	0.976	0.0249-161

2.5.4 Hectorite suspensions

A 12.90 wt% hectorite (Parchem) stock suspension was formulated (169 g hectorite, 1140 g deionised water). The hectorite was added to the deionised water and the bulk solution was stirred using an overheard stirrer (IKA EUROSTAR 60 motor) for ~60 min at 700-1000 rpm before being high-shear mixed (Silverson high shear mixer, maximum speed) for 5 min. The 12.90 wt% hectorite stock suspension was then left to rest for ~16 h. After the time elapsed, additional deionised water was then added to different quantities of the 12.90 wt% hectorite stock suspension, to formulate 80 g hectorite samples with mass fractions ranging from 8.50-12.50 wt%. As seen in Figure 2.12, the resulting hectorite fluids were white/brown in colour and are opaque, therefore again complex tomographic techniques would be required to visualise the flow of these fluids in stirred vessel systems.

The rheological properties of the samples were obtained using the methods described in Section 2.3, however the downward shear stress sweep measurements occurred using 120 pt dec^{-1}, rather than 60 pt dec^{-1}. The resulting raw rheological flow curves for the hectorite samples can be seen in Figure 2.13. For mass fraction values of hectorite ranging from 9.00-12.50 wt% (Samples '*3*'-'*9*'), the model that most accurately fit the raw data was the Casson model, whilst the Herschel-Bulkley model proved to be a better description of the raw data for mass fractions of 8.50 wt% (Sample '*1*') and 9.00 wt% (Sample '*2*'). Both the relevant Herschel-Bulkley and Casson fitted data, along with the shear rate ranges of the fits, the associated error analysis and the physical properties of the fluids can be seen in Table 2.5. As with the other systems, increased hectorite particle mass fractions led to increased τ_y values. For the 9.00-12.50 wt% samples ('*3*'-'*9*'), there was an overall decrease in the constant plastic viscosity, η_{pl}, whilst there was a decrease in K and an increase in n, when increasing the mass fraction from 8.50 wt% (Sample '*1*') to 9.00 wt% (Sample '*2*').

Figure 2.12. Images of the hectorite samples, ranging in mass fraction from 8.50-12.50 wt%. More specifically: '*1*' = 8.50 wt%, '*2*' = 9.00 wt%, '*3*' = 9.50 wt%, '*4*' = 10.00 wt%, '*5*' = 10.50 wt%, '*6'* = 11.00 wt%, '*7'* = 11.50 wt%, '*8*' = 12.00 wt% and '9' = 12.50 wt%.

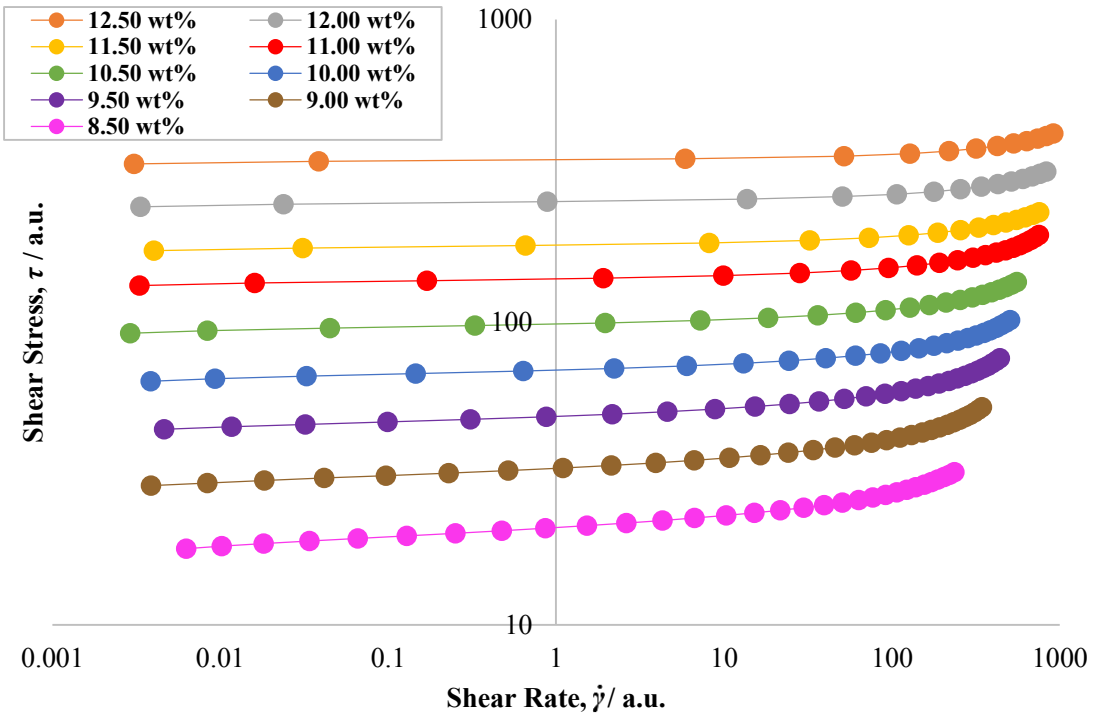

Figure 2.13. Raw rheological flow curves, acquired from shear stress down sweeps using 6-bladed vane geometry, of hectorite suspensions at various mass fractions, ranging from 8.50-12.50 wt%, with all suspensions at an approximately constant pH: 9.50-9.81.

Table 2.5. Herschel-Bulkley and Casson fitted data, and the physical properties of the hectorite fluids, along with the associated error quantification of the mathematical fits and the shear rate range over which the fits occurred.

Physical properties		**Herschel-Bulkley rheological properties**			**Casson rheological properties**		**Error quantification and analysis**		
Hectorite mass fraction / wt%	**pH**	**Yield stress, τ_y / a.u.**	**Flow consistency index, K / a.u.**	**Flow behaviour index, n**	**Yield stress, τ_y / a.u.**	**Constant plastic viscosity, η_{pl} / a.u.**	**Optimised fit AAD / %**	**Optimised fit R^2 value**	**Shear rate range of optimised fit / a.u.**
12.50	9.54	-	-	-	335.5	0.0042	0.98	0.975	0.00306-917
12.00	9.50	-	-	-	243.6	0.0045	1.00	0.981	0.00334-833
11.50	9.59	-	-	-	174.8	0.0043	0.97	0.984	0.00402-756
11.00	9.65	-	-	-	134.9	0.0052	1.19	0.983	0.00330-672
10.50	9.57	-	-	-	95.2	0.0056	1.23	0.986	0.00291-557
10.00	9.77	-	-	-	66.6	0.0063	1.54	0.985	0.00354-507
9.50	9.75	-	-	-	46.7	0.0070	1.77	0.985	0.00462-441
9.00	9.78	30.1	1.91	0.40	-	-	2.04	0.981	0.00387-345
8.50	9.81	17.9	2.52	0.30	-	-	2.06	0.982	0.00625-236

2.5.5 Other particulate suspensions

A number of other particle-based suspensions were formulated, and in some cases rheologically characterised, however they were deemed as being unsuitable model fluid systems. Both kaolinite, a naturally-occurring clay with disc-like morphology (Ma and Eggleton (1999)), and Acti-gel 208, a commercial attapulgite clay with lath-like particle morphology (Xue et *al.* (2006)) required very large solid loadings (or mass fractions) to induce fluids with yield stress values. Practically, it was difficult to formulate fluids at such high mass fractions, even with the use of an overhead stirrer equipped with a multi-impeller system. Also, a characteristic of model fluids is that they should be inexpensive, however when the mass fractions are particularly high, the cost of formulating these fluids on larger scales may be unfeasibly high. In the case of kaolinite (Kaolin, Sigma Aldrich) suspensions were formulated at mass fractions of 20-30 wt%, and although these suspensions appeared to have yield stress values, the characteristic slip, as seen in Figure 2.1, occurred at relatively high shear rates ($\dot{\gamma} > 10$ s^{-1}) for the suspensions with greater mass fractions. As a result, fitting this data with mathematical models would lead to inaccurate values of the yield stress. An Acti-gel 208 (Active Minerals International, LLC) suspension was formulated in deionised water at 21.7 wt% and appeared to displayed water-like Newtonian behvaiour. Therefore, although it may be possible to achieve the desired viscoplastic behaviour with this material at high mass fractions, this was not seen to be practical in the laboratory setting.

Suspensions of fumed silica (Aerosil 200, Evonik Industries AG) were also formulated and rheologically investigated. Fumed silica consists of branched, chain-like aggregates of spherical silicon dioxide (SiO_2) particles, with these aggregates interacting through hydrogen bonding between surface silanol (SiOH) groups, to form three-dimensional gel networks if the silica mass fractions are high enough (Schaefer and Hurd (1990); Abramoff and Covino, 1992; Raghavan *et al.* (1995, 1997, 1998, 2000)). An attractive property of fumed silica for this work is that, dispersed in an appropriate medium, the suspensions have the capacity to be refractive index matched (RI = 1.46) to produce transparent solutions (Sun *et al.* (2005)). In Figure 2.14, an image of fumed silica dispersed in: (a) deionised water (RI = 1.33) and (b) polyethylene glycol (PEG200, M_w = 200 g mol^{-1}, RI = 1.46), can be seen. It is clear from the image that a dispersion of fumed silica in PEG200 resulted in a greater degree of optical transparency compared to dispersions in deionised water. However, a number of authors have investigated the rheological properties of fumed silica-PEG and fumed silica-polyethylene oxide (PEO) solutions and have shown that these fluids do not exhibit the desired viscoplastic properties, with shear-thinning behaviour being shown at low and high shear rates, with transitional shear-thickening behaviour being displayed between these two regimes (Wu *et al.* (2006); Khandavalli and Rothstein (2014); Hasanzadeh *et al.* (2015)) .

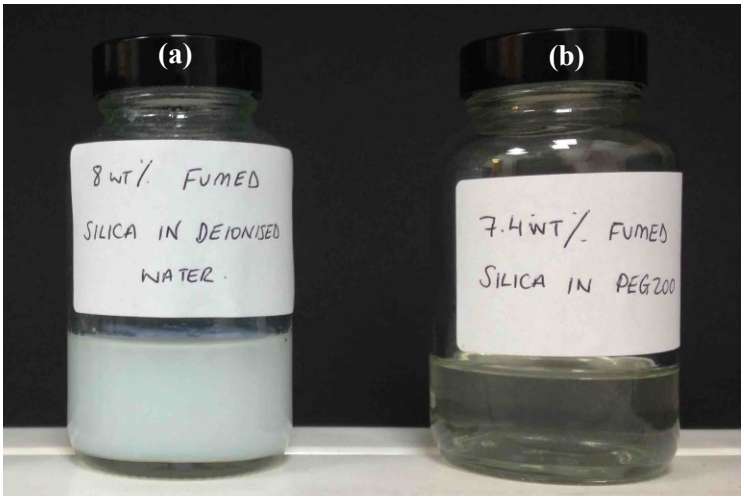

Figure 2.14. Fumed silica dispersed in: (a) deionised water and (b) PEG200. The fumed silica-deionised water suspension appears white and opaque, due to the difference in refractive index of fumed silica (RI = 1.46) and deionsied water (RI = 1.33), whilst the fumed silica-PEG 200 suspension has been appropriately refractive index matched and appears transparent.

2.6 Polymer solutions

Various polymer solutions were formulated and rheologically characterised in this section. Many naturally-occurring polymers are often associated with low levels of reactivity and expense, and have facile handling in the laboratory environment, however, as discussed in Section 1.2.2, they may not have the desired viscoplastic rheological properties: lacking the yield stress component, despite being shear-thinning in nature. In particular, three different types of polymer solutions have been studied, namely carboxymethyl cellulose (CMC) and hydroxypropyl cellulose (HPC), naturally-occurring polysaccharides with chemical structures similar to that of cellulose, and Actigum, a commercial grade of Scleroglucan, which is a naturally-occurring extracellular polysaccharide secreted by the fungus *Sclerotium* (Park and Khan (2009); Jindal and Khattar (2018)). Other polymer systems, including Xanthan gum (XG), Guar gum (GG), Guar gum 2-hydroxypropyl ether (GG-2HPE) and hydroxyethyl cellulose will also briefly be discussed.

2.6.1 Carboxymethyl cellulose solutions

A 10.00 wt% carboxymethyl cellulose sodium salt (CMC, M_w = 90000 g mol^{-1}, D.S. 0.70, Sigma Aldrich) stock solution was formulated (100 g CMC, 900 g deionised water). The CMC was added to the deionised water and the stock solution was stirrer with an overhead stirrer (IKA EUROSTAR 90 motor) at 2000 rpm for ~3 h. After the time elapsed, additional deionised water was then added to different quantities of the bulk 10.00 wt% CMC solution, to formulate 80 g CMC samples with mass fractions ranging from 5.50-10.00 wt%. The resulting CMC solutions can be visualised in Figure 2.15, with each of the samples displayed high levels of transparency.

The CMC fluids ranging in mass fraction from 6.50-10.00 wt%, then underwent rheological characterisation. The rheological properties of the samples were obtained using the methods described in Section 2.3, however the downward shear stress sweep measurements occurred using 15 pt dec^{-1}, rather than 60 pt dec^{-1}. In addition to this, each sample also underwent an upward shear stress sweep, and upward and downward shear rate sweeps, as outlined in Section 2.5.1. The downward shear stress sweeps were used for analysis and the raw rheological flow curves for each sample (CMC mass fractions of 6.50-10.00 wt% only) can be seen in Figure 2.16, whilst the resulting Power Law fitted data, along with the shear rate ranges of the fits, the associated errors of the fits and the physical properties of the fluids are summarised in Table 2.6. As expected, due to the lack of particles, the samples did not display a τ_y (the flow curves tended to shear stress values of 0 at low shear rates), however as the CMC mass fraction increased, K increased, whilst there is a slight decrease in n. As a result, these fluids displayed weakly shear-thinning behaviour.

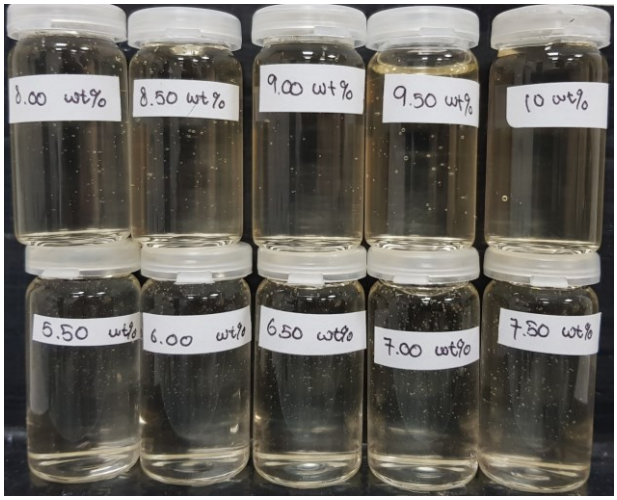

Figure 2.15. Images of the CMC samples, ranging in mass fraction from 5.50-10.00 wt%.

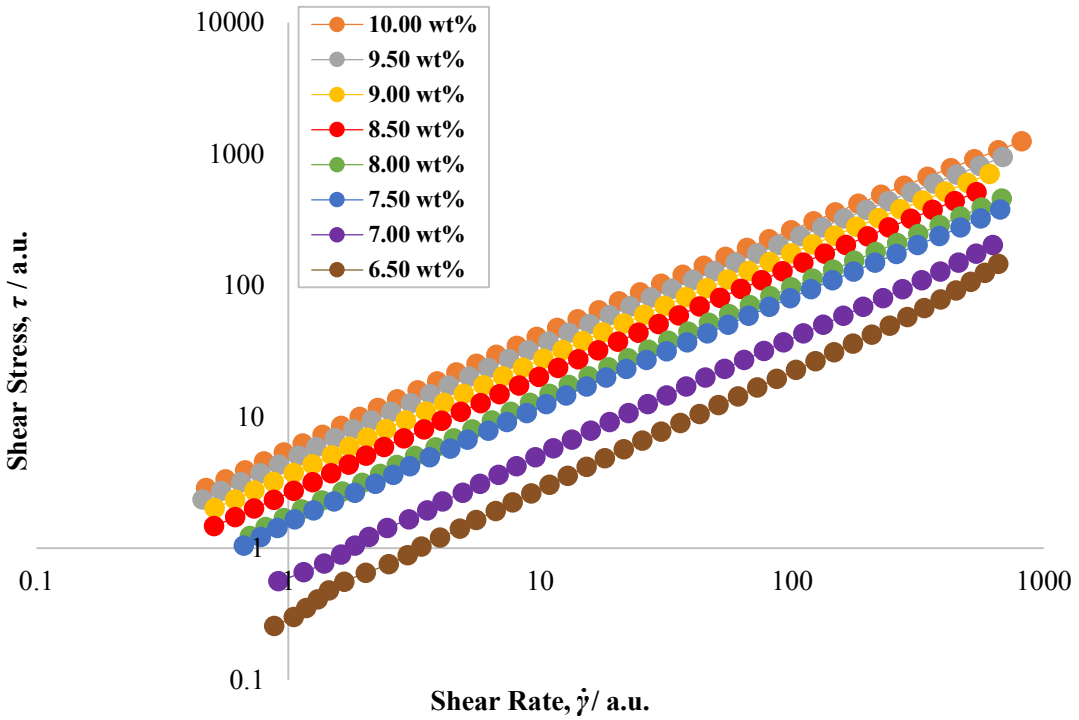

Figure 2.16. Raw rheological flow curves, acquired from shear stress down sweeps using 6-bladed vane geometry, of CMC solutions at various mass fractions, ranging from 6.50-10.00 wt%, with all suspensions at an approximately constant pH: 6.90-7.50.

Table 2.6. Power Law fitted data and the physical properties of the CMC fluids, along with the associated error quantification of the mathematical fits and the shear rate range over which the fits occurred.

Physical properties		**Power Law rheological properties**			**Error quantification and analysis**		
CMC mass fraction / wt%	**pH**	**Yield stress, τ_y / a.u.**	**Flow consistency index, K / a.u.**	**Flow behaviour index, n**	**Optimised fit AAD / %**	**Optimised fit R^2 value**	**Shear rate range of optimised fit / a.u.**
10.00	6.91	0.00	5.9	0.82	5.64	0.997	0.471-817
9.50	6.90	0.00	4.9	0.82	5.16	0.998	0.456-688
9.00	7.40	0.00	3.8	0.83	4.66	0.998	0.511-745
8.50	7.47	0.00	2.8	0.84	4.13	0.999	0.507-541
8.00	7.42	0.00	1.8	0.86	3.91	0.999	0.705-683
7.50	7.50	0.00	1.6	0.85	3.48	0.999	0.667-673
7.00	7.49	0.00	0.62	0.90	3.10	1.000	0.915-628
6.50	7.32	0.00	0.32	0.92	3.93	0.995	0.880-660

2.6.2 Hydroxypropyl cellulose solutions

A 14.00 wt% bulk hydroxypropyl cellulose (HPC, M_w = 100000 g mol^{-1}, Acros Organics) solution was formulated (143.25 g HPC, 880 g deionised water). The HPC was added to the deionised water and the bulk solution was stirred using an overheard stirrer (IKA EUROSTAR 60 motor) for ~2.5 h at 2000 rpm. After the time elapsed, additional deionised water was then added to different quantities of the bulk 14.00 wt% HPC solution, to formulate 80 g HPC samples with mass fractions ranging from 9.50-14.00 wt%, after which rheological characterisation occurred. The resulting HPC solutions can be visualised in the image in Figure 2.17, and as seen in the figure, each of the samples displayed high levels of transparency.

The rheological properties of the samples were obtained using the methods described in Section 2.3, however the downward shear stress sweep measurements occurred using 15 pt dec^{-1}, rather than 60 pt dec^{-1}. In addition to this, each sample also underwent an upward shear stress sweep, and upward and downward shear rate sweeps, as outlined in Section 2.5.1. The downward shear stress sweeps were used for analysis and the raw rheological flow curves for each of the HPC fluids can be seen in Figure 2.18, whilst the resulting Power Law fitted data, along with the errors associated with the fits, the shear rate ranges of the fits and the physical properties of the fluids are summarised in Table 2.7. Similar to the CMC rheological data, the samples do not display a τ_y due to the lack of particles, however as the HPC mass fraction increased, K increased, whilst there is a slight decrease in n. These fluids displayed near Newtonian behaviour, in particular the 9.50 wt% ('*1*'), 11.00 wt% ('*2*') and 12.50 wt% ('3') samples. The 14.00 wt% ('*4*') sample displayed weakly shear-thinning behaviour.

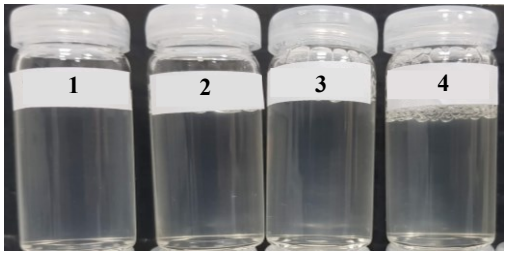

Figure 2.17. Images of the HPC samples, ranging in mass fraction from 9.50-14.00 wt%. More specifically: '*1*' = 9.50 wt%, '*2*' = 11.00 wt%, '*3*' = 12.50 wt% and '*4*' = 14.00 wt%.

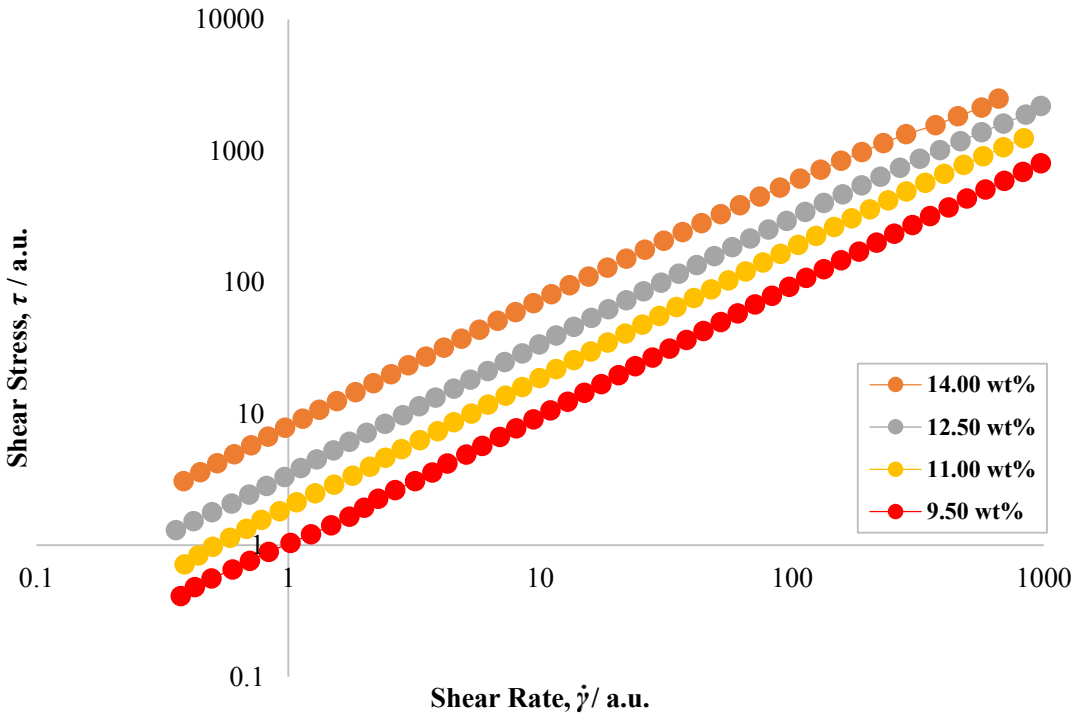

Figure 2.18. Raw rheological flow curves, acquired from shear stress down sweeps using 6-bladed vane geometry, of HPC solutions at various mass fractions, ranging from 9.50-14.00 wt%, with all suspensions at an approximately constant pH: 6.08-6.60.

Table 2.7. Power Law fitted data and the physical properties of the HPC fluids, along with the associated error quantification of the mathematical fits and the shear rate range over which the fits occurred.

Physical properties		**Power Law rheological properties**			**Error quantification and analysis**		
HPC mass fraction / wt%	**pH**	**Yield stress, τ_y / a.u.**	**Flow consistency index, *K* / a.u.**	**Flow behaviour index, *n***	**Optimised fit AAD / %**	**Optimised fit R^2 value**	**Shear rate range of optimised fit / a.u.**
14.00	6.08	0.00	8.39	0.90	7.36	0.992	0.384-663
12.50	6.21	0.00	3.63	0.95	5.04	0.996	0.358-976
11.00	6.60	0.00	1.94	0.98	2.77	0.998	0.338-835
9.50	6.38	0.00	1.03	0.98	2.62	0.999	0.374-976

2.6.3 Actigum CS 6 solutions

A bulk 4.00 wt% Actigum CS 6 (Actigum, Cargill) solution was formulated (40 g Actigum, 960 g deionised water). The Actigum added to the deionised water and the bulk solution was stirred using an overheard stirrer (IKA EUROSTAR 60 motor) for 20 min at 500 rpm, 90 min at 800 rpm, and then ~3.5 h at 1200 rpm. The stock solution was then left to rest for ~16 h. After the time elapsed, additional deionised water was then added to different quantities of the 4.00 wt% Actigum bulk solution, to formulate 80 g Actigum samples, ranging in mass fraction from 2.00-4.00 wt%. As seen

in Figure 2.19, the resulting Actigum fluids are yellow/white in colour and relatively opaque, with a degree of translucency at the lower mass fraction values (2.00-2.50 wt%).

The rheological properties of the samples were obtained using the methods described in Section 2.3, and the resulting raw rheological flow curves for each of the Actigum fluids, acquired from the downward shear stress sweeps, can be seen in Figure 2.20. For mass fraction values of Actigum ranging from 3.25-4.00 wt% (Samples '*6*'-'*9*'), the model that most accurately fit the raw data was the Casson model, whilst the Herschel-Bulkley model proved to be a better description of the raw data for mass fractions of 2.00-3.00 wt% (Samples '*1*'-'*5*'). Both the relevant Herschel-Bulkley and Casson fitted data, along with the shear rate ranges of the fits, the associated error analysis and the physical properties of the fluids can be seen in Table 2.8. The lowest shear rate values for each sample were > 1 a.u. and hence relatively high, because at lower values, slip was observed (as discussed Section 2.2). As with the particulate systems, increased Actigum mass fractions led to increased τ_y values. As discussed in Section 1.2.2, CMC and HPC are cellulose ethers with ethers groups at carbon 2, 3 and 6 on the cellulose structure (Figure 1.9), depending on the degree of substitution. Scleroglucan (or Actigum) also has side ether groups, however unlike CMC and HPC where these are side groups are small carboxylic acid compounds joined through the ether linkages, the side group is a cellulose group. As a result, it is hypothesised that, despite the lack of particles within the system, the Actigum samples display a yield stress due to the vastly increased degree of intermolecular bonding (electrostatic and hydrogen bonds) within the structure. For the 3.25-4.00 wt% samples ('*6*'-'*9*'), there was an overall increase in the constant plastic viscosity, η_{pl} with increasing Actigum mass fraction, whilst there was an overall increase in K and decrease in n, when increasing the mass fraction from 2.00 wt% (Sample '*1*') to 3.00 wt% (Sample '*5*').

Figure 2.19. Images of the Actigum samples, ranging in mass fraction from 2.00-4.00 wt%. More specifically: '*1*' = 2.00 wt%, '*2*' = 2.25 wt%, '*3*' = 2.50 wt%, '*4*' = 2.75 wt%, '*5*' = 3.00 wt%, '*6'* = 3.25 wt%, '*7'* = 3.50 wt%, '*8*' = 3.75 wt% and '9' = 4.00 wt%.

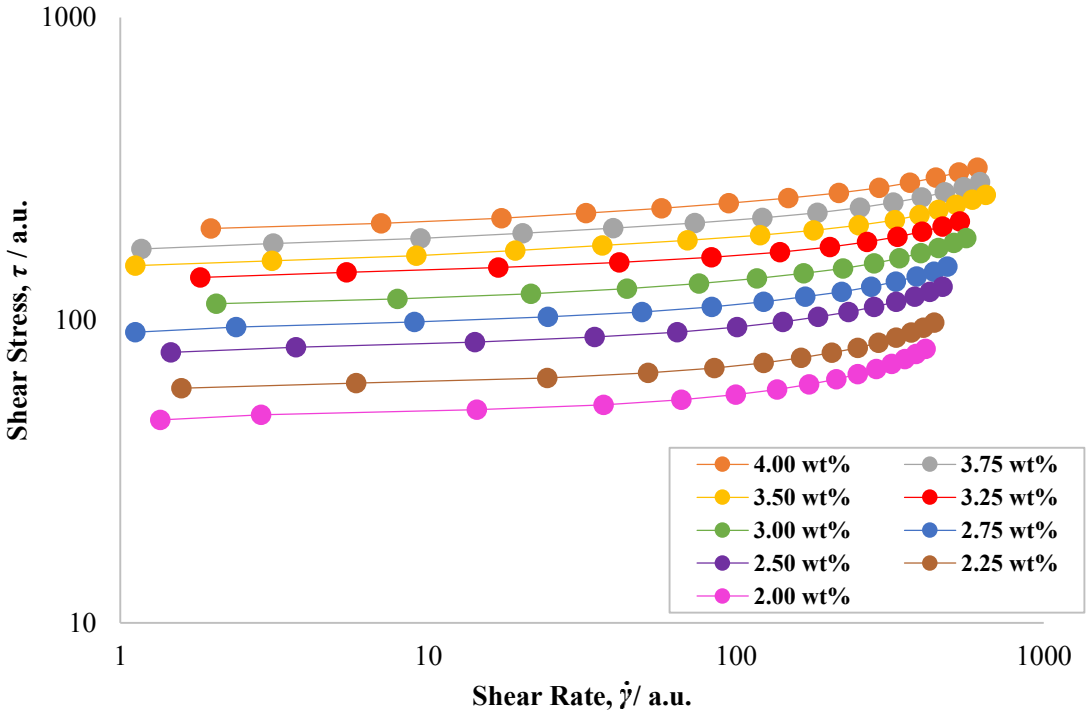

Figure 2.20. Raw rheological flow curves, acquired from shear stress down sweeps using 6-bladed vane geometry, of Actigum solutions at various mass fractions, ranging from 2.00-4.00 wt%, with all suspensions at an approximately constant pH: 6.10-6.26.

Table 2.8. Herschel-Bulkley and Casson fitted data, and the physical properties of the Actigum fluids, along with the associated error quantification of the mathematical fits and the shear rate range over which the fits occurred.

Physical properties		**Herschel-Bulkley rheological properties**			**Casson rheological properties**		**Error quantification and analysis**		
Actigum mass fraction / wt%	**pH**	**Yield stress, τ_y / a.u.**	**Flow consistency index, K / a.u.**	**Flow behaviour index, n**	**Yield stress, τ_y / a.u.**	**Constant plastic viscosity, η_{pl} / a.u.**	**Optimised fit AAD / %**	**Optimised fit R^2 value**	**Shear rate range of optimised fit / a.u.**
4.00	6.14	-	-	-	198.2	0.0223	0.81	0.996	1.97-610
3.75	6.20	-	-	-	172.6	0.0210	1.17	0.993	1.17-622
3.50	6.10	-	-	-	151.3	0.0194	1.54	0.987	1.12-649
3.25	6.22	-	-	-	135.8	0.0138	1.15	0.989	1.82-534
3.00	6.19	112.3	1.1	0.66	-	-	1.08	0.992	2.05-560
2.75	6.21	92.2	1.2	0.61	-	-	1.09	0.993	1.12-487
2.50	6.17	78.7	0.77	0.67	-	-	1.14	0.992	1.46-469
2.25	6.26	60.1	0.23	0.83	-	-	1.12	0.992	1.58-441
2.00	6.21	47.7	0.20	0.83	-	-	1.41	0.990	1.35-414

2.6.4 Other polymer solutions

Various other polymer solutions were formulated and rheologically examined, including: Xanthan gum (XG, Sigma Aldrich), Guar gum (GG, Sigma Aldrich) and Guar gum 2-hydroxypropyl ether (GG-2HPE, Aldrich) solutions. The XG, GG and GG-2HPE solutions produced similar flow curves to Figure 2.1, with a drop off in shear stress at relatively high shear rate values ($\dot{\gamma} > 10$ s^{-1}), resulting in inaccurate descriptions of the yield stress when these fluids were fitted with mathematical models. The reason for this drop off is likely to be cause by slip at the wall of the geometrical cup, enhanced by the viscoelastic properties of the fluids and the Weissenberg effect (where material tracks up the shaft of the mixer system), as discussed in Section 2.2. XG has been used as model viscoplastic fluids in stirred vessel systems, however, for these systems, the rheological properties were acquired using different rheometrical geometry, such as cone-and-plate geometry (Amanullah *et al.* (1998); Elson *et al.* (1986); Pakzad *et al.* (2008)). Hydroxyethyl cellulose (HEC, Natrosol) solutions were also investigated, with solutions displaying shear-thinning characteristics, whilst lacking a yield stress. The empirical, mathematical fits were relatively poor and therefore the data have not been presented here and were not included in the *Model Fluid Selection Tool* (Chapter 3).

2.7 Microgels

Microgels are cross-linked polymers, as discussed in Section 1.2.3. Carbopol is a heavily cross-linked microgel, based on the polyacrylic acid structure that swells in aqueous media, with swelling further enhanced in basic media. The reason for this enhanced swelling is caused by the ionisation of COOH groups to COO^- groups, leading to strong mutual repulsions between neighbouring polymer chains within the microgel sponges (Islam *et al.* (2004); Piau (2007)). To determine the degree of ionisation and how this relates to pH in a Carbopol system, an experiment was performed whereby increased masses of an aqueous 1.00 wt% NaOH (Sigma Aldrich) solution were added to an aqueous 0.50 wt% Carbopol Ultrez 10 (CU10, Lubrizol, temperature = 30°C) solution, and the pH of the CU10 solution was monitored with respect to NaOH concentration ([NaOH]), with the resulting plot seen in Figure 2.21. The figure shows there was a steady increase in pH with [NaOH] from pH 4-8. At pH > 8, there was a sudden jump in pH up until pH ~12.5, after which there was again a steady increase of pH with [NaOH]. Eq. 2.1 can be used to explain this behaviour with respect to the degree of ionisation of COOH to COO^- within the solution. At pH ~ 4, the degree of ionisation of COOH groups to COO^- groups is < 1%. As the [NaOH] increases, increased ionisation of COOH groups to COO^- groups occurs, up until pH 8, whereby the degree of ionisation ~100%. The pK_a is the pH value when the degree of ionisation is at 50%, which in this case is at pH 6. Up until pH ~8, the solution is acting as a buffer, with OH^- ions extracting H^+ ions from the COOH groups, hence resulting in the observed slow increase in pH of the system. However, at pH > 8, the solution is no longer acting as a buffer as the COOH groups have been fully ionised to COO^- groups

and the addition of further NaOH results in a sharp increase in pH, as further ionisation is unable to occur. The apparent plateau in pH values at [NaOH] > 0.05 mol dm^{-3} is merely due to the fact that pH is a logarithmic scale. In terms of rheological properties, the increased degree of ionisation between pH 4-8 will lead to expanded configurations as the electric double layers (EDL) surrounding polymer chains within the microgel sponges increases in size, leading to greater overlap of EDLs between neighbouring polymer chains and stronger osmotic repulsions (see Section 1.2.1 for a more in-depth explanation). The result is increased τ_y and K values. However, at a particular point, further increases in [NaOH] results in the extent of ions in the solution outweighing the effects of the degree of ionisation, resulting in shrinkage of the EDLs and hence less overlap between neighbouring EDLs, leading to weaker electrostatic repulsions and a decrease in τ_y and K values (Piau (2007)).

$$\mathrm{pH} = \mathrm{pK_a} + \log_{10}\left(\frac{[\mathrm{COO^-}]}{[\mathrm{COOH}]}\right) \tag{2.1}$$

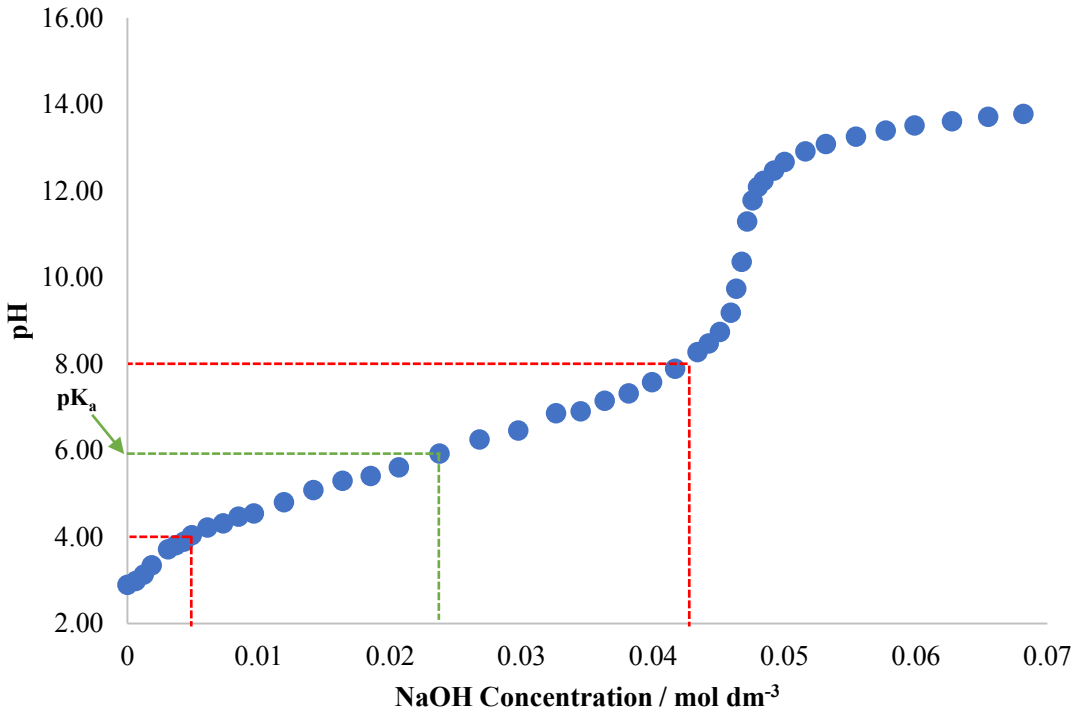

Figure 2.21. Looking at the effects of pH against concentration of NaOH in a Carbopol solution, taking a 0.50 wt% Carbopol Ultrez 10 as an example, to determine the how the degree of ionisation of COOH groups will vary with pH. The red line at pH ~4 indicates the NaOH concentration resulting in a degree of ionisation of < 1%, whilst the red line at pH ~8 highlights the NaOH concentration inducing a degree of ionisation of ~100%. The pK_a of the system is the pH value associated with the degree of ionisation = 50%, which in this case is at pH ~6.

2.7.1 Carbopol Ultrez 30 solutions

2.7.1.1 Constant pH

A bulk 4.00 wt% Carbopol Ultrez 30 (CU30, Lubrizol) solution was formulated (36 g CU30, 864 g deionised water). The CU30 was added to the deionised water and the bulk solution was stirred with an overhead stirrer (IKA EUROSTAR 60 motor) initially at 2000 rpm for ~1 h, 800 rpm for 20 min, then 600 rpm for ~18 h. After the time elapsed, additional deionised water was then added to different quantities of the 4.00 wt% CU30 bulk solution, to formulate 80g CU30 samples ranging in mass fraction from 1.25-4.00 wt%. As seen in Figure 2.22, the CU30 samples were slightly white in colour and had a mildly translucent nature. As a result, visualising these flows in stirred vessels with simple dye techniques may be difficult, and more complex techniques could be required.

The rheological properties of the samples were obtained using the methods described in Section 2.3. The resulting raw rheological flow curves, obtained through the downward shear stress sweeps, for all CU30 samples can be seen in Figure 2.23, and the resulting Herschel-Bulkley fitted data can be found in Table 2.9, along with the shear rate ranges of the fits, the associated errors of the fits and physical properties of the fluids. As would be expected, with increasing CU30 mass fraction, both τ_y and K increased, however n remained relatively constant over the range of investigated CU30 mass fractions. Although Carbopol is not a particulate system, the Carbopol systems are comprised of microgel sponges which can be treated as particles, therefore as the mass fraction increases, the quantity of microgel sponges increases, resulting in more densely packed, jammed structures and an increased number of intermolecular interactions, leading to increases in τ_y and K.

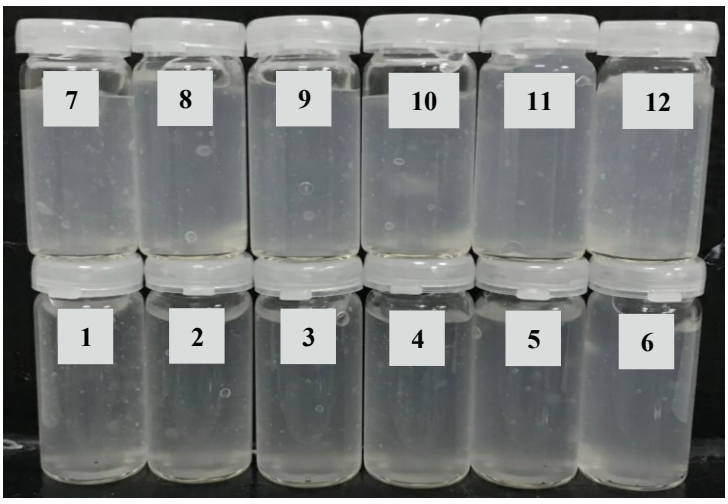

Figure 2.22. Images of the CU30 samples, ranging in mass fraction from 1.25-4.00 wt%. More specifically: '*1*' = 1.25 wt%, '*2*' = 1.50 wt%, '*3*' = 1.75 wt%, '*4*' = 2.00 wt%, '*5*' = 2.25 wt%, '*6'* = 2.50 wt%, '*7'* = 2.75 wt%, '*8*' = 3.00 wt%, '9' = 3.25 wt%, '*10'* = 3.50 wt%, '*11*' = 3.75 wt%, '*12*' = 4.00 wt%.

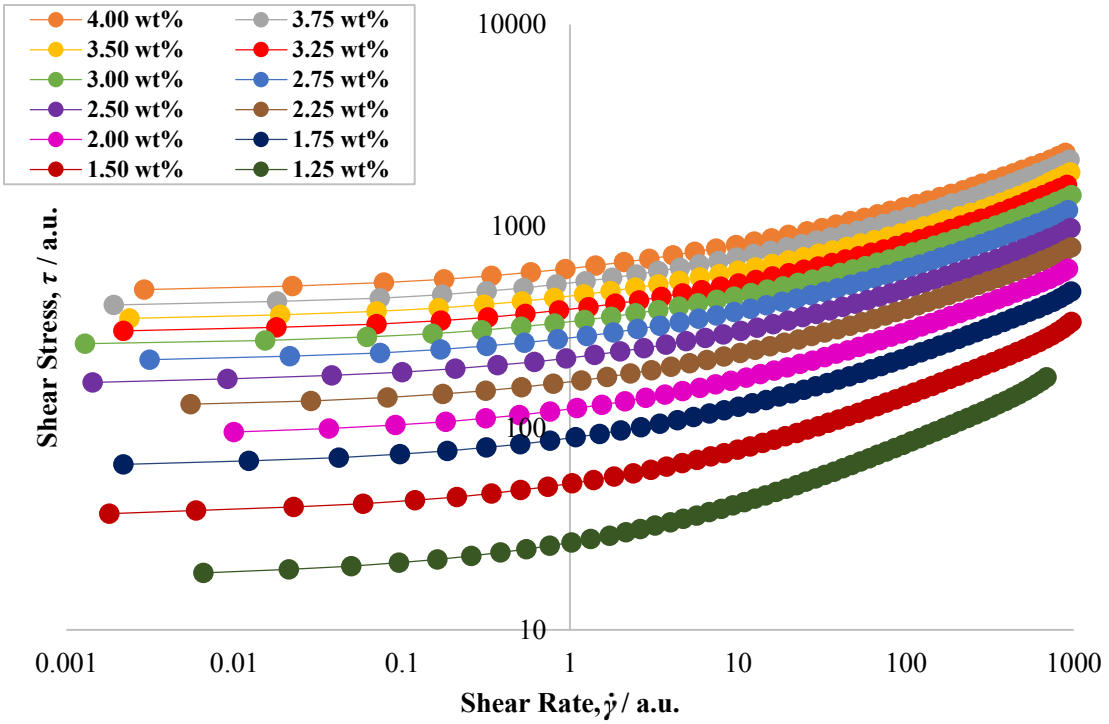

Figure 2.23. Raw rheological flow curves, acquired from shear stress down sweeps using 6-bladed vane geometry, of CU30 solutions at various mass fractions, ranging from 1.25-4.00 wt%, with all solutions at an approximately constant pH: 2.76-3.09.

Table 2.9. Herschel-Bulkley fitted data and the physical properties of the CU30 fluids, along with the associated error quantification of the mathematical fits and the shear rate range over which the fits occurred.

Physical properties		**Herschel-Bulkley rheological properties**			**Error quantification and analysis**		
CU30 mass fraction / wt%	**pH**	**Yield stress, τ_y / a.u.**	**Flow consistency index, K / a.u.**	**Flow behaviour index, n**	**Optimised fit AAD / %**	**Optimised fit R^2 value**	**Shear rate range of optimised fit / a.u.**
4.00	2.76	475.9	138.7	0.38	0.66	0.999	0.00291-895
3.75	2.77	399.5	122.8	0.38	0.81	0.999	0.00191-945
3.50	2.77	343.5	105.5	0.38	1.20	0.998	0.00237-954
3.25	2.79	298.4	88.6	0.39	0.73	0.999	0.00218-912
3.00	2.81	257.3	78.7	0.39	0.51	1.000	0.00129-972
2.75	2.87	212.7	67.0	0.39	0.36	1.000	0.00313-927
2.50	2.89	167.6	54.0	0.39	0.53	0.999	0.00143-957
2.25	2.91	125.9	43.7	0.39	0.39	0.9996	0.00549-967
2.00	2.91	90.7	33.4	0.40	0.26	0.9996	0.000926-927
1.75	2.95	64.6	24.7	0.40	0.26	0.9996	0.00218-968
1.50	3.04	37.6	15.3	0.42	0.67	0.9985	0.0018-972
1.25	3.09	18.5	8.6	0.44	0.46	0.9993	0.00655-688

2.7.1.2 Varying pH

A bulk 0.5 wt% Carbopol Ultrez 30 (CU30, Lubrizol) solution was formulated (2 g CU30, 398 g deionised water). The CU30 was added to the deionised water and the bulk solution was magnetically stirred for ~16 h. After the time elapsed, different quantities of a 2 wt% NaOH (aq) solution (5.92 g NaOH (Sigma Aldrich), 294.01 g deionised water) and additional deionised water were then added to 32 g samples of the CU30 bulk solution, to formulate 80 g, 0.20 wt% CU30 samples of varying pH, ranging from pH 4.65-11.26. As seen in Figure 2.24, the resulting 0.20 wt% CU30 fluids are associated with high levels of transparency and optical clarity.

The fluids, excluding the pH ~3.30 ('*1*') sample, then underwent rheological characterisation, with the rheological properties of the samples being obtained using the methods described in Section 2.3. The resulting raw rheological flow curves, obtained through the downward shear stress sweeps, can be seen in Figure 2.25, and the resulting Herschel-Bulkley fitted data can be found in Table 2.10, along with the shear rate ranges of the fits, the associated errors of the fits and the physical properties of the fluids. As previously discussed, when Carbopol is dissolved in water, the resulting solution is weakly acidic. However, when dilute base is introduced to the system, the carboxylic acid (COOH) groups on the polymer chains are ionised to carboxylate (COO^-) groups, leading to strong mutual repulsions between the chains in the microgel sponges and expanded configurations, hence leading to increased in τ_y and K when going from pH ~ 3.30 (Sample '*1*'), which displayed Newtonian behaviour, to pH 7.27 (Sample '*5*'), which displayed distinct viscoplastic behaviour. Although the pH 7.27 sample ('*5*') had the largest τ_y and K values, over the range of pH ~5-10, the τ_y can be treated as being approximately constant, whilst K increased up to a maximum at pH 7-8. As the pH is further increased (pH > 10), the quantity of ions in solution increased to the extent that it resulted in shrinkage of the electric double layers, as previously discussed, leading to weaker interactions between the chains in the microgel and hence reduced τ_y and K values, explaining why the pH 11.26 sample ('*6*') has significantly lower τ_y and K values than the samples in the pH range 5.31-9.31 (Samples '*3*'-'*5*'). For all 0.20 wt% CU30 samples rheologically characterised, n was seen to be relatively constant. Combining the observed viscoplastic behaviour of these CU30 fluids with their transparent nature, these fluids can be seen as being very suitable model fluid systems.

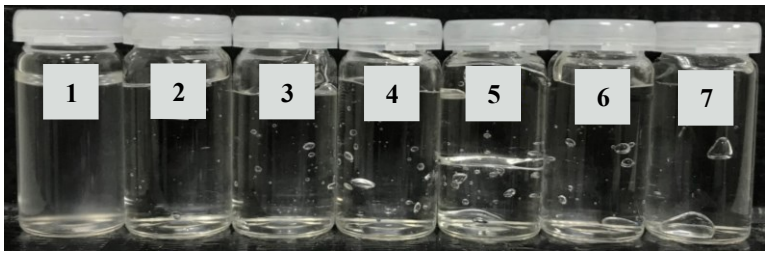

Figure 2.24. Images of the 0.20 wt% CU30 samples, ranging in pH from ~3.30-11.26. More specifically: '*1*' = pH ~3.30, '*2*' = pH 4.65, '*3*' = pH 5.31, '*4*' = pH 6.22, '*5*' = pH 7.27, '*6'* = pH 9.31 and '*7'* = pH 11.26.

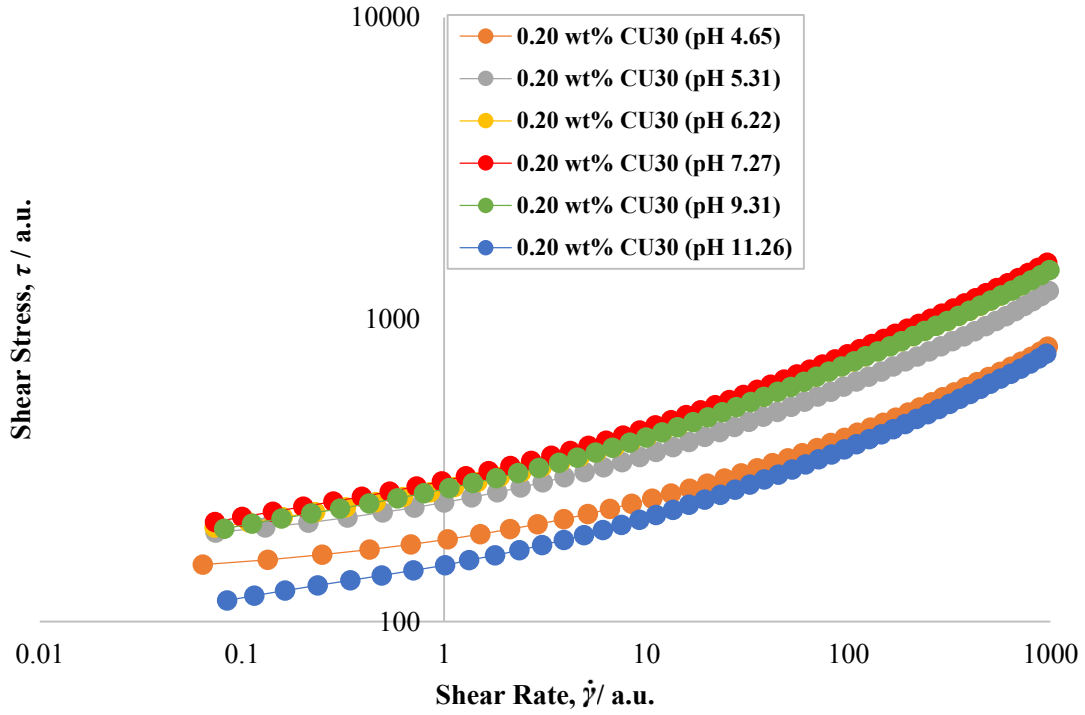

Figure 2.25. Raw rheological flow curves, acquired from shear stress down sweeps using 6-bladed vane geometry, of CU30 solutions at a constant mass fraction of 0.20 wt%, but varying pH values through additions of different quantities of a 2 wt% NaOH (aq) solution, ranging from pH 4.65-11.26.

Table 2.10. Herschel-Bulkley fitted data and the physical properties of the 0.20 wt% CU30 fluids, along with the associated error quantification of the mathematical fits and the shear rate range over which the fits occurred.

Physical properties			**Herschel-Bulkley rheological properties**			**Error quantification and analysis**		
CU30 mass fraction / wt%	**NaOH mass fraction / wt%**	**pH**	**Yield stress, τ_y / a.u.**	**Flow consistency index, K / a.u.**	**Flow behaviour index, n**	**Optimised fit AAD / %**	**Optimised fit R^2 value**	**Shear rate range of optimised fit / a.u.**
0.20	0.010	4.65	140.7	45.3	0.39	0.35	1.000	0.0639-973
0.20	0.020	5.31	169.4	78.2	0.37	0.48	0.999	0.0739-984
0.20	0.040	6.22	169.6	103.2	0.36	0.53	1.000	0.0733-939
0.20	0.060	7.27	174.5	115.2	0.36	0.45	1.000	0.0734-966
0.20	0.080	9.31	167.2	104.4	0.36	0.57	1.000	0.0817-991
0.20	0.090	11.26	102.7	49.3	0.37	0.86	0.999	0.0845-957

In this section, the rheological properties of CU30 samples at a constant mass fraction of 0.20 wt%, but varying pH values were assessed. Similar investigations were carried out at CU30 mass fractions of 0.075 wt%, 0.10 wt% and 0.125 wt%, whereby in each case, the rheological properties of samples over a range of pH values were determined. The results from these studies can be found in the Appendix, in

Section A.1. As would be expected similar trends were seen, with the fluids overall having decreased τ_y and K values as Carbopol mass fraction decreased.

2.7.1.3 Varying salt concentration

A bulk 0.30 wt% Carbopol Ultrez 30 (CU30, Lubrizol) solution was formulated (1.2 g CU30, 318.8 g deionised water). The CU30 was added to the deionised water and the bulk solution was magnetically stirred for ~24 h. After the time elapsed, 23 g of a 2 wt% NaOH (aq) solution (3.935 g NaOH (Sigma Aldrich), 196 g deionised water) solution and 57 g of deionised water were added to the bulk CU30 solution to form a solution at pH 7.23. Different quantities of additional deionised water and 1 wt% NaCl (aq) (3 g NaCl, (Sigma Aldrich), 297 g deionised water) were then added to 40 g of the 0.30 wt% CU30 bulk solution (pH 7.23), to formulate 80 g, 0.15 wt% CU30 samples, of varying salt content, ranging in NaCl mass fraction from 0.00-3.13×10^{-3} wt%. As seen in Figure 2.26, the resulting 0.15 wt% CU30 samples are associated with high levels of transparency and optical clarity.

The rheological properties of the samples were then obtained using the methods described in Section 2.3. The resulting raw rheological flow curves for the 0.15 wt% CU30 samples can be seen in Figure 2.27. The resulting Herschel-Bulkley fitted data can be seen in Table 2.11, along with the associated shear rate ranges of the fits, the error analysis for each of the fits and the physical properties of the fluids. As seen in Table 2.11, with increasing NaCl mass fraction in the sample, there is a decrease in τ_y and K values, whilst n remains constant. As was the case at high pH values in Section 2.7.1.2, the increase in NaCl mass fraction results in the concentration of ions surrounding the polymer chains in the microgel increasing, resulting in shrinkage of the electric double layers around the chains. This leads to contracted, less 'jammed' configurations, through a reduction in strength of the repulsions between polymer chains and hence a weakened three dimensional gel network, leading to reduced τ_y and K values.

Figure 2.26. Images of the 0.15 wt% CU30 samples, containing mass fractions of NaCl ranging from 0.00-3.13×10^{-3} wt%. More specifically, the mass fraction of NaCl in the samples were: '*1*' = 0.00 wt%, '*2*' = 0.63×10^{-3} wt%, '*3*' = 1.25×10^{-3} wt%, '*4*' = 1.63×10^{-3} wt%, '*5*' = 2.13×10^{-3} wt%, '*6*' = 2.50×10^{-3} wt% and '*7*' = 3.13×10^{-3} wt%. The pH values of each fluid were approximately constant, with pH values ranging from 7.23-7.54.

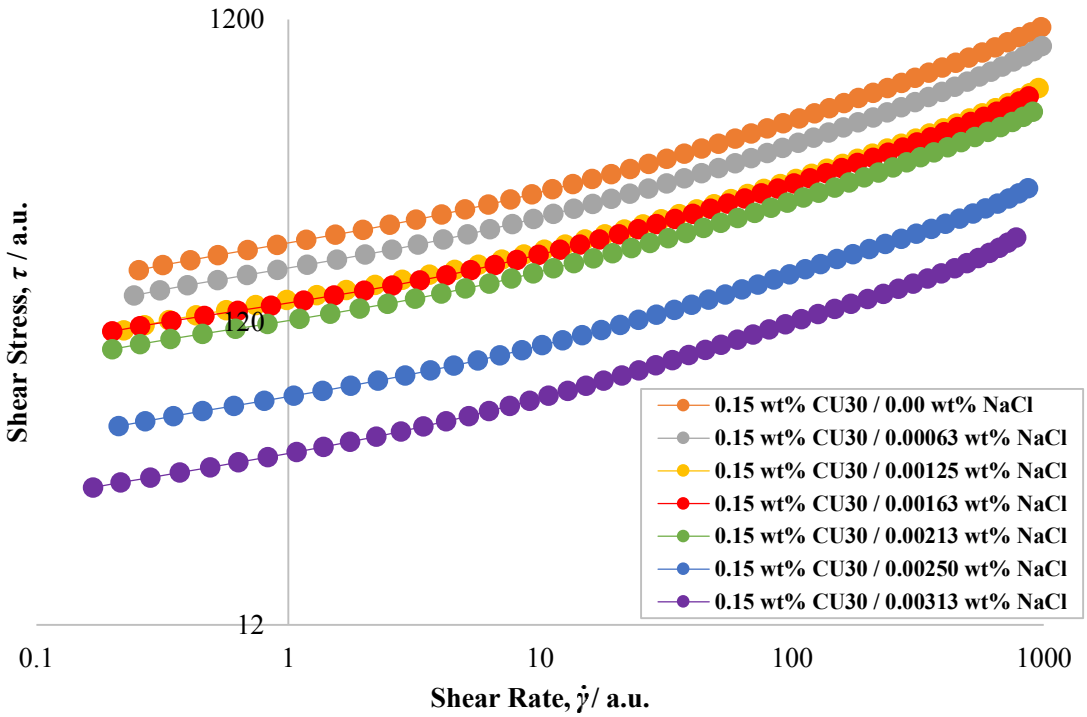

Figure 2.27. Raw rheological flow curves, acquired from shear stress down sweeps using 6-bladed vane geometry, of CU30 solutions at a constant mass fraction of 0.30 wt%, but containing varying quantities of NaCl, ranging from 0.00-3.13×10^{-3} wt%, with all solutions at an approximately constant pH 7.23-7.54.

Table 2.11. Herschel-Bulkley fitted data and the physical properties of the 0.15 wt% CU30 fluids, along with the associated error quantification of the mathematical fits and the shear rate range over which the fits occurred.

Physical properties			**Herschel-Bulkley rheological properties**			**Error quantification and analysis**		
CU30 mass fraction / wt%	**NaCl mass fraction (×10^{-3}) / wt%**	**pH**	**Yield stress, τ_y / a.u.**	**Flow consistency index, K / a.u.**	**Flow behaviour index, n**	**Optimised fit AAD / %**	**Optimised fit R^2 value**	**Shear rate range of optimised fit / a.u.**
0.15	0.00	7.54	135.6	80.8	0.36	0.81	1.000	0.255-978
0.15	0.63	7.47	115.7	63.2	0.37	1.08	0.999	0.244-982
0.15	1.25	7.37	86.8	53.0	0.35	0.89	0.999	0.222-882
0.15	1.63	7.36	87.8	49.4	0.36	0.70	0.999	0.200-871
0.15	2.13	7.23	76.8	43.2	0.36	0.70	0.999	0.200-905
0.15	2.50	7.24	39.9	27.4	0.34	0.63	0.999	0.212-866
0.15	3.13	7.24	24.3	19.5	0.34	0.78	0.998	0.168-777

2.7.2 Carbopol 981 solutions

There were practical difficulties when attempting to disperse the Carbopol 981 (C981) powder in water at C981 mass fractions of greater than approximately 1.20 wt%, even with the use of an overhead stirrer equipped with a multi-impeller system. As a result, C981 solutions were formulated

at three different mass fractions: 0.4 wt%, 0.6 wt% and 0.8 wt%, with the pH of the solutions being varied through the additions of dilute NaOH (aq) solution. In Section 2.7.2.1, the 0.8 wt% systems are discussed, however similar trends were obtained when varying pH values in the 0.40 wt% and 0.60 wt% systems. As would be expected, with decreasing Carbopol mass fraction, the fluids in the 0.40 wt% and 0.60 wt% systems overall had decreased τ_y and K values, compared to the 0.80 wt% systems. These results can be found in the Appendix in Section A.1.

2.7.2.1 Varying pH

Using similar methods to Section 2.6.1.2, a bulk 1.00 wt% Carbopol 981 (C981, Lubrizol) solution was formulated (10 g C981, 990 g deionised water). The C981 was slowly added to the deionised water and the bulk solution was stirred with an overhead stirrer (IKA EUROSTAR 60 motor) at 750 rpm for ~15 h. After the time elapsed, different quantities of a 2 wt% NaOH (aq) solution (8.061 g NaOH (Sigma Aldrich), 394 g deionised water) or 3 wt% NaOH (aq) solution (8.982 g NaOH (Sigma Aldrich), 294 g deionised water), and additional deionised water were then added to 64 g of the 1.00 wt% C981 bulk solution, to formulate 80 g, 0.80 wt% C981 solutions of varying pH ranging from 2.72-13.44. The resulting C981 fluids were highly transparent, as can be seen in Figure 2.28.

The fluids then underwent rheological characterisation (excluding the pH 3.52 sample ('*2*')), with the rheological properties of the samples being obtained using the methods described in Section 2.3. The raw rheological flow curves can be seen in Figure 2.29, and the resulting Herschel-Bulkley fitted data can be found in Table 2.12, along with the shear rate ranges of the fits, the associated errors of the fits and the physical properties of the fluids. As with the CU30 samples, C981 dispersed in water produces weakly acidic solutions, and through the addition of dilute base, the microgel configurations become expanded. As a result, the pH 2.72 sample ('*1*') had the lowest τ_y and K values of all the samples investigated. It was seen in the CU30 samples (from Section 2.7.1.2) that over the pH range of ~5-10, the τ_y values of the samples remained constant, whilst K increased up to a maximum at pH 7-8. In the case of these 0.80 wt% C981 fluids, an approximately constant τ_y value (36.5 ± 1.6 a.u.) was obtained over the pH range of 4.07-12.83, whilst K increased up to a maximum of 35.4 a.u. at pH 8.78 (Sample '*11*'), before decreasing at higher pH values. When the pH value of 13.44 (Sample '*14*') was reached, there was a slight reduction in both τ_y and K. Excluding Sample '*1*' (pH 2.72), the n values of the fluids remained approximately constant over the investigated range of pH values. These results show that, when attempting to formulate C981 fluids as a potential replacement model fluid to a 'real' fluid system, precision in formulating the fluid with a specific pH to acquire the desired rheological properties would not be necessary, especially when attempting to match yield stress values. Therefore, this model fluid family provides a certain flexibility when it comes to fluid formulation protocol that other model fluids may not provide, and therefore combined with the C981 fluids having the desired viscoplastic properties and a highly transparent nature, it can be deemed as being a useful model fluid system.

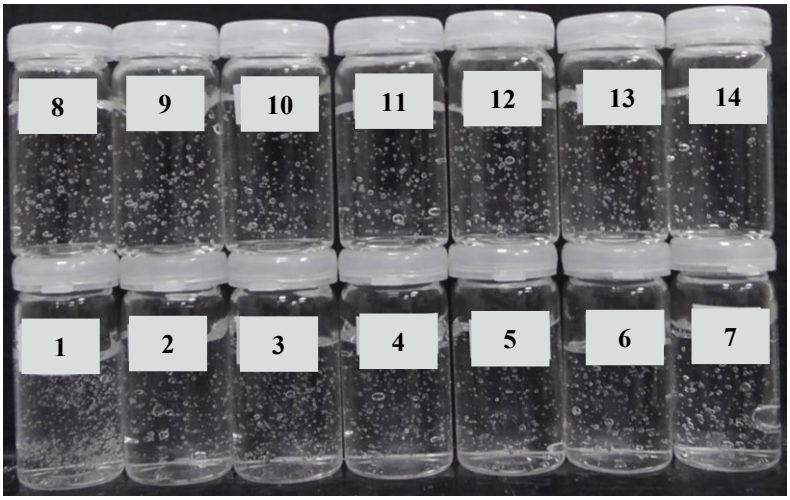

Figure 2.28. Images of the 0.80 wt% C981 samples, ranging in pH from 2.72-13.44. More specifically: '*1*' = pH 2.72, '*2*' = pH 3.52, '*3*' = pH 4.07, '*4*' = pH 4.76, '*5*' = pH 5.23, '*6'* = pH 5.74, '*7'* = pH 6.22, '*8*' = pH 6.64, '*9*' = pH 7.30, '*10*' = pH 8.49, '*11*' = pH 8.78, '*12*' = pH 11.66, '*13'* = pH 12.83 and '*14'* = pH 13.44.

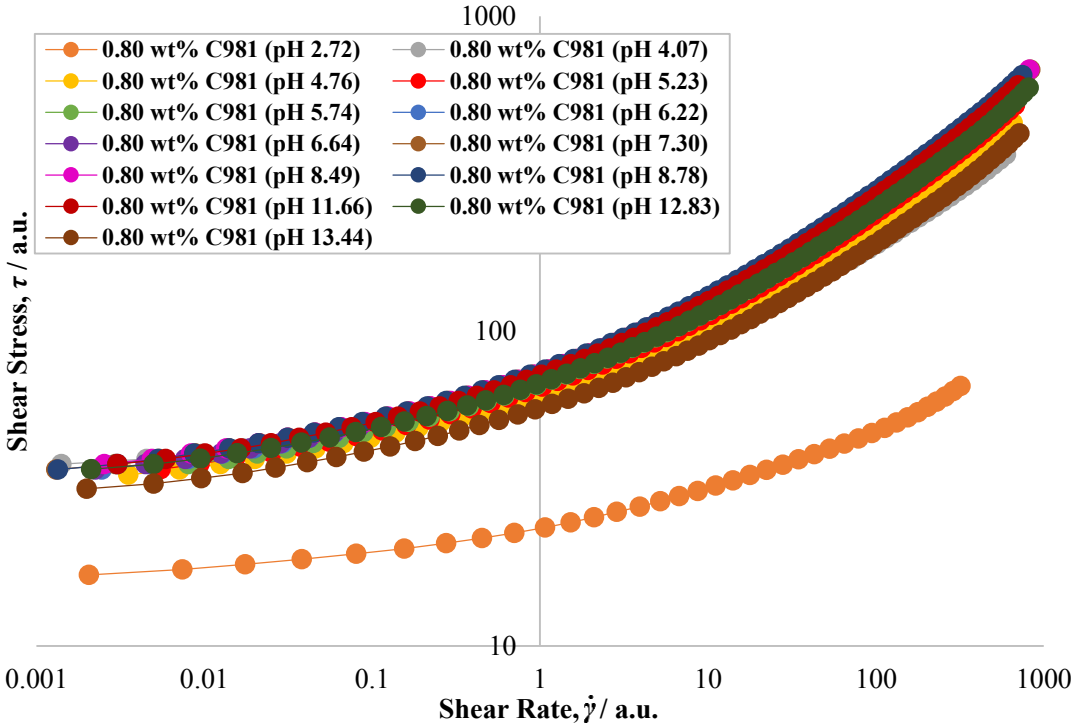

Figure 2.29. Raw rheological flow curves, acquired from shear stress down sweeps using 6-bladed vane geometry, of C981 solutions at a constant mass fraction of 0.8 wt%, but varying pH values through additions of different quantities of a 2 wt% and 3 wt% NaOH (aq) solution, ranging from pH 2.72-13.44.

Table 2.12. Herschel-Bulkley fitted data and the physical properties of the 0.80 wt% C981 fluids, along with the associated error quantification of the mathematical fits and the shear rate range over which the fits occurred.

Physical properties			Herschel-Bulkley rheological properties			Error quantification and analysis		
C981 mass fraction / wt%	**NaOH mass fraction / wt%**	**pH**	**Yield stress, τ_y / a.u.**	**Flow consistency index, K / a.u.**	**Flow behaviour index, n**	**Optimised fit AAD / %**	**Optimised fit R^2 value**	**Shear rate range of optimised fit / a.u.**
0.80	0.000	2.72	16.3	7.3	0.33	1.03	0.998	0.00205-320
0.80	0.040	4.07	38.1	24.2	0.40	1.46	0.999	0.00141-596
0.80	0.080	4.76	35.0	26.1	0.42	1.83	0.999	0.00352-654
0.80	0.118	5.23	35.9	28.7	0.43	1.74	0.999	0.0055-674
0.80	0.160	5.74	36.7	29.5	0.43	1.83	0.999	0.00804-702
0.80	0.200	6.22	36.7	32.9	0.42	2.05	0.999	0.00245-721
0.80	0.240	6.64	36.8	32.9	0.43	2.04	0.998	0.00224-759
0.80	0.280	7.30	37.4	34.4	0.42	2.22	0.998	0.00131-834
0.80	0.320	8.49	38.1	33.7	0.43	1.93	0.998	0.00254-820
0.80	0.330	8.78	37.1	35.4	0.42	2.07	0.999	0.00134-747
0.80	0.345	11.66	37.6	33.0	0.43	1.73	0.999	0.00304-704
0.80	0.360	12.83	36.8	29.7	0.43	1.89	0.998	0.00212-816
0.80	0.420	13.44	31.9	23.6	0.42	1.88	0.998	0.00199-716

2.7.3 Other Carbopol Solutions

A number of other Carbopol grades have been investigated, namely Carbopol 980 (C980), Carbopol Ultrez 10 (CU10) and Carbopol Ultrez 21 (CU21), with a large volume of fluids being formulated and rheologically characterised. Due to these fluids displaying similar rheological trends to the CU30 fluids, the resulting flow curves, mathematically-fitted data and physical properties of these fluids can be found in Section A.1 of the Appendix. For C980: fluids of constant pH and varying mass fraction (1.60-3.60 wt%) were rheologically investigated, as were fluids at constant mass fraction (0.125 wt% and 0.20 wt%) but varying pH, and fluids at 0.20 wt% C980 mass fraction and approximately constant pH but varying salt (NaCl) mass fraction. For CU10: fluids of constant pH and varying mass fraction (3.00-6.00 wt%) were rheologically investigated, as were fluids at constant mass fraction (0.10 wt%, 0.15 wt%, 0.20 wt% and 0.30 wt%) but varying pH. For CU21: fluids of constant pH and varying mass fraction (4.00-5.50 wt%) were rheologically investigated, as were fluids at constant mass fraction (0.10 wt%, 0.125 wt%, and 0.15 wt%) but varying pH. As was the case with the CU30 and C981 fluids, combining the highly transparent nature with the viscoplastic behaviour of these fluids results in all investigated Carbopol solutions being ideal candidates as replacement model fluid systems.

2.8 Mixtures with CMC

Numerous mixtures with carboxymethyl cellulose (CMC) were formulated and rheologically characterised in this section, with a focus on clay-based mixtures. Namely, Bentopharm/CMC, Laponite/CMC, hectorite/CMC and Acti-gel 208/CMC mixtures were all examined, as was the commercial polymer-based system, Actigum/CMC mixtures. Discussion on the possible reasons behind the resulting viscoplastic nature of the mixtures was explored, as were reasons behind why Carbopol Ultrez 30/CMC and sepiolite/CMC mixtures did not result in fluids with viscoplastic behaviour.

2.8.1 Bentopharm/CMC mixtures

In the preparation of Bentopharm/CMC mixtures, two Bentopharm stock suspensions were formulated: a 10.00 wt% suspension and an 11.50 wt% suspension. The 10.00 wt% Bentopharm (Wilfrid Smith Ltd) stock suspension was formulated (110 g Bentopharm, 990 g deionised water) by adding the Bentopharm to the deionised water and stirring suspension using an overheard stirrer (IKA EUROSTAR 60 motor) for 100 min at 850 rpm. The 10.00 wt% stock suspension was then high-shear mixed (Silverson high-shear mixer, maximum speed) for 5 min, before being left to rest for ~16 h. The 11.50 wt% Bentopharm (Wilfrid Smith Ltd) stock suspension was formulated (144 g Bentopharm, 1108 g deionised water), by adding the Bentopharm to the deionised water and stirring the suspension using the overheard stirrer for 70-90 min at 1300-2000 rpm. The 11.50 wt% stock suspension was then high-shear mixed (Silverson high-shear mixer, maximum speed) for 5 min, before being left to rest for ~16 h. Two separate bulk 7.00 wt% CMC (aq) solutions were created. For 7.00 wt% CMC *Solution 1*: 28 g CMC (M_w = 90000 g mol^{-1}, D.S. 0.70, Sigma Aldrich) was added to 372 g of deionised water and the solution was magnetically stirred for ~16 h, and then left to rest for 5 days before use. For 7.00 wt% CMC *Solution 2*: 14 g CMC (M_w = 90000 g mol^{-1}, D.S. 0.70, Sigma Aldrich) was added to 186 g of deionised water and the solution was magnetically stirred for ~16 h. Different quantities of the CMC solutions and additional deionised water were then added to varying amounts of the Bentopharm stock suspensions, to generate 80 g fluids at 8.50 wt% Bentopharm and varying mass fractions of CMC, ranging from 0.175-1.83 wt%. As seen in Figure 2.30, the resulting 8.50 wt% Bentopharm/CMC mixtures were brown in colour and were opaque, therefore simple dye techniques for the visualisation of the flows of these fluids in stirred vessels would not be possible.

The rheological properties of the samples were then obtained using the methods described in Section 2.3. The raw rheological flow curves can be seen in Figure 2.31, and the resulting Herschel-Bulkley fitted data can be found in Table 2.13, along with the shear rate ranges of the fits, the associated errors of the fits and the physical properties of the fits. In this case, the Herschel-Bulkley model was the best description of the mixtures, however, as seen in Section A.1 in the Appendix, through changing the mass fraction of Bentopharm in the suspensions, in some cases the Casson model resulted in a more accurate description of the raw rheological data. As seen in Table 2.13, as the mass fraction of CMC increased, the τ_y, K and n values of the samples increased. As discussed in Section 1.2.1.1, Bentopharm

is a pharmaceutical grade of Bentonite, and its particles have platelet-like morphology. The faces of the particles are negatively-charged, whilst the edges are positively-charged, depending on pH. CMC is a negatively-charged polymer, and one suggestion is that upon addition of CMC into the Bentopharm suspensions, the negatively-charged CMC is able to electrostatically interact with the positively-charged edges of the Bentopharm particles, to form a three-dimensional gel network. However, due to the fluids' pH values being above the isoeletric point, it is suggested that gelation instead occurs through a depletion flocculation mechanism (Jenkins and Snowden (1996)). Therefore, as CMC mass fraction increases within the suspensions, the strength of these depletion interactions increases, resulting in the formation of stronger gel networks and an increase in τ_y and K values. As seen in Section 2.6.1, CMC-water solutions are very weakly shear-thinning, hence explaining why increasing the mass fraction of CMC into the Bentopharm suspensions would lead to the observed increase in n values of the mixtures.

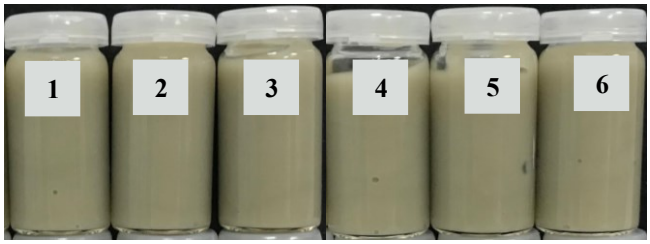

Figure 2.30. Images of the 8.50 wt% Bentopharm/CMC mixtures, ranging in CMC mass fraction from 0.175-1.83 wt%. More specifically, the mass fraction of CMC in the samples were: '*1*' = 0.175 wt%, '*2*' = 0.438 wt%, '*3*' = 0.875 wt%, '*4*' = 0.613 wt%, '*5*' = 1.23 wt% and '*6*' = 1.83 wt%.

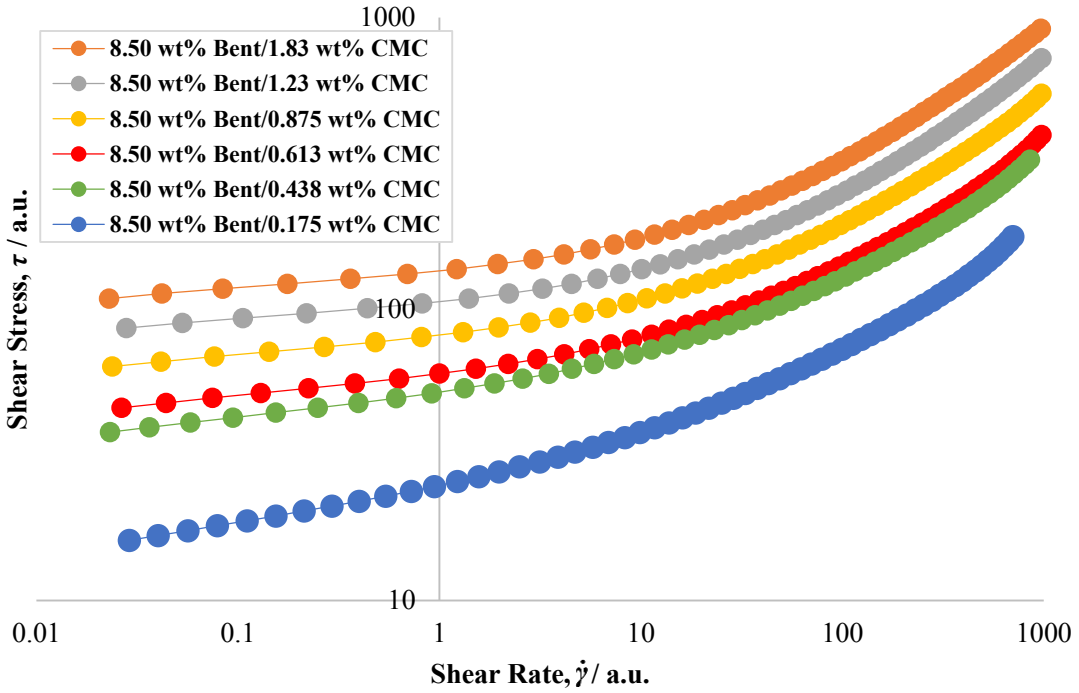

Figure 2.31. Raw rheological flow curves, acquired from shear stress down sweeps using 6-bladed vane geometry, of Bentopharm/CMC mixtures at a Bentopharm mass fraction of 8.50 wt%, and varying CMC mass fractions: 0.175-1.83 wt%, with all solutions at an approximately constant pH: 8.62-9.00. In the legend, Bentopharm has been abbreviated to 'Bent'.

Table 2.13. Herschel-Bulkley fitted data and the physical properties of the 8.50 wt% Bentopharm/CMC mixtures, along with the associated error quantification of the mathematical fits and the shear rate range over which the fits occurred.

Physical properties			Herschel-Bulkley rheological properties			Error quantification and analysis		
Bentopharm mass fraction/ wt%	**CMC mass fraction / wt%**	**pH**	**Yield stress, τ_y / a.u.**	**Flow consistency index, K / a.u.**	**Flow behaviour index, n**	**Optimised fit AAD / %**	**Optimised fit R^2 value**	**Shear rate range of optimised fit / a.u.**
8.50	0.175	8.96	16.1	7.5	0.45	3.18	0.993	0.0289-703
8.50	0.438	9.00	40.1	9.5	0.49	2.62	0.996	0.0232-855
8.50	0.613	8.72	49.2	8.5	0.53	2.58	0.996	0.0264-977
8.50	0.875	8.88	67.9	10.7	0.54	1.85	0.998	0.0238-975
8.50	1.23	8.76	91.8	11.0	0.58	1.47	0.999	0.0279-976
8.50	1.83	8.62	115.8	14.9	0.57	1.31	1.000	0.0229-970

In this section, Bentopharm/CMC mixtures were investigated at constant Bentopharm mass fractions of 8.50 wt%. Other Bentopharm/CMC mixtures were also examined, again by varying the mass fraction of the CMC in the mixtures, but now at constant Bentopharm mass fractions of 5.00 wt%, 6.00 wt%, 7.00 wt% and 7.75 wt%. Similar trends were displayed by these mixtures, but, as would be expected, the overall τ_y values were lower as there was less Bentopharm in the mixtures. As previously discussed, both the Herschel-Bulkley and Casson models were used to describe these fluids, depending on the fluid in question. These results can be found in the Appendix in Section A.1.

2.8.2 Laponite/CMC mixtures

A 5.00 wt% Laponite RD (Laponite, Rockwood) stock suspension was formulated (50 g Laponite, 950 g deionised water). The Laponite was added to the deionised water and the stock solution was stirred using an overheard stirrer (IKA EUROSTAR 60 motor) for 45 min at 600 rpm. The stock suspension was then high-shear mixed (Silverson high-shear mixer, maximum speed) for 5 min, before being left to rest for ~16 h. A 7.00 wt% carboxymethyl cellulose (CMC, M_w = 90000 g mol^{-1}, D.S 0.70, Sigma Aldrich) was formulated (28 g CMC, 372 g deionised water). The CMC was added to the deionised water and the bulk solution was stirred with the overhead stirrer for ~16 h at 500 rpm. After the time elapsed different quantities of additional deionised water and 7.00 wt% CMC (aq) were then added to 48 g of the 5.00 wt% Laponite stock suspension, to formulate 80 g, 3.00 wt% Laponite fluids of varying CMC mass fraction, ranging from 0.175-2.80 wt%. As can be seen from Figure 2.32, the 3.00 wt% Laponite/CMC mixtures are relatively transparent, and therefore simple dye techniques could be used for the visualisation of the flows of these fluids in stirred vessels.

The rheological properties of the samples (excluding the 3.00 wt% Laponite/0.438 wt% CMC sample (‘*4*’)) were then obtained using the methods described in Section 2.3, however the downward shear stress sweep measurements occurred using 90 pt dec^{-1}, rather than 60 pt dec^{-1}. The raw rheological flow curves can be

seen in Figure 2.33, and the resulting mathematically-fitted data can be found in Table 2.14, along with the shear rate ranges of the fits, the associated errors of the fits and the physical properties of the fluids. The Herschel-Bulkley model provided the best description of the majority of the mixtures, excluding the samples containing 1.40 wt% ('*8*') and 2.80 wt% ('*10*') of CMC, where the Casson model provided a better description. As with the Bentopharm/CMC mixtures, as the mass fraction of CMC increased within the samples, there was an increase in τ_y values. It is suggested that this is the result of the increased strength of the interactions resulting from depletion flocculation, to produce stronger three-dimensional gel networks.

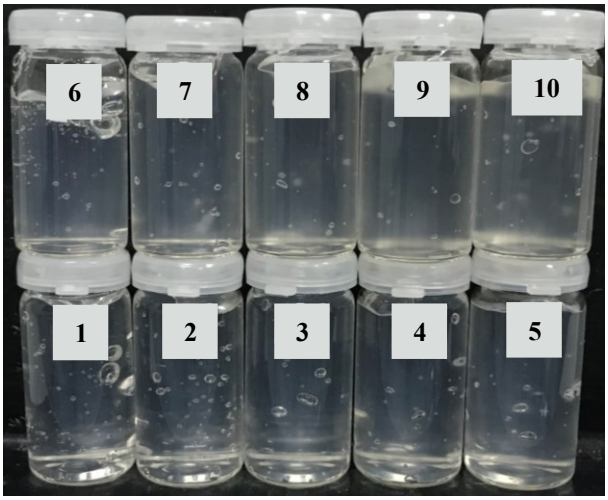

Figure 2.32. Images of the 3.00 wt% Laponite/CMC mixtures, ranging in CMC mass fraction from 0.175-2.80 wt%. More specifically, the mass fraction of CMC in the samples were: '*1*' = 0.175 wt%, '*2*' = 0.263 wt%, '*3*' = 0.350 wt%, '*4*' = 0.438 wt%, '*5*' = 0.525 wt%, '*6*' = 0.700 wt%, '*7*' = 1.05 wt%, '*8*' = 1.40 wt%, '*9*' = 2.10 wt% and '*10*' = 2.80 wt%.

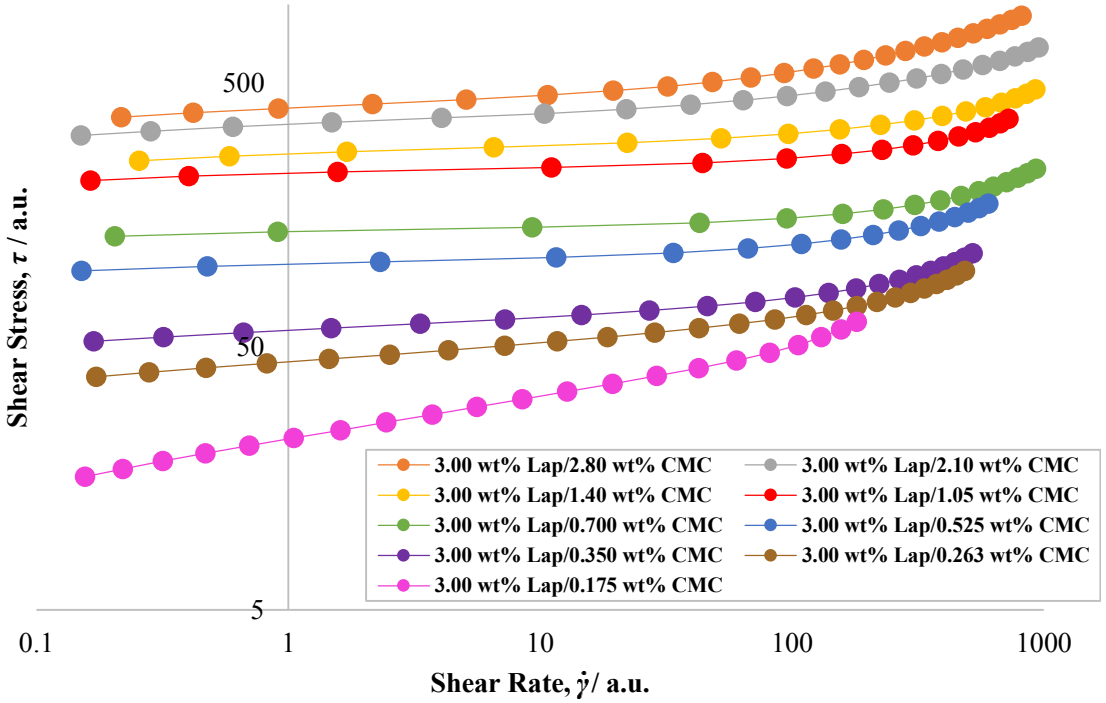

Figure 2.33. Raw rheological flow curves, acquired from shear stress down sweeps using 6-bladed vane geometry, of Laponite/CMC mixtures at a constant Laponite mass fraction of 3.00 wt%, and varying CMC mass fractions: 0.175-2.80 wt%, with all solutions at an approximately constant pH: 10.00-10.23. In the legend, Laponite has been abbreviated to 'Lap'.

Table 2.14. Herschel-Bulkley and Casson fitted data, and the physical properties of the 3.00 wt% Laponite/CMC mixtures, along with the associated error quantification of the mathematical fits and the shear rate range over which the fits occurred.

Physical properties			**Herschel-Bulkley rheological properties**			**Casson rheological properties**		**Error quantification and analysis**		
Laponite mass fraction / wt%	**CMC mass fraction / wt%**	**pH**	**Yield stress, τ_y / a.u.**	**Flow consistency index, *K* / a.u.**	**Flow behaviour index, *n***	**Yield stress, τ_y / a.u.**	**Constant plastic viscosity, η_{pl} / a.u.**	**Optimised fit AAD / %**	**Optimised fit R^2 value**	**Shear rate range of optimised fit / a.u.**
3.00	0.175	10.17	7.3	14.5	0.24	-	-	2.22	0.991	0.156-181
3.00	0.263	10.16	38.1	5.0	0.38	-	-	2.74	0.984	0.173-487
3.00	0.350	10.23	53.7	3.1	0.45	-	-	2.34	0.984	0.169-484
3.00	0.525	10.15	100.9	1.0	0.65	-	-	1.66	0.988	0.151-603
3.00	0.700	10.19	136.1	0.4	0.78	-	-	1.51	0.990	0.205-934
3.00	1.05	10.15	222.7	2.0	0.63	-	-	1.92	0.982	0.164-726
3.00	1.40	10.18	-	-	-	263.3	0.029	1.84	0.988	0.256-928
3.00	2.10	10.07	324.6	18.6	0.42	-	-	1.77	0.992	0.150-955
3.00	2.80	10.00	-	-	-	392.2	0.128	1.49	0.997	0.217-817

In this section, Laponite/CMC mixtures were investigated at constant Laponite mass fractions of 3.00 wt%. Laponite/CMC mixtures at 2.00 wt% Laponite mass fraction were also examined, again by varying the

mass fraction of CMC the in the mixtures (0.700-2.80 wt%). Similar trends were displayed but, as would be expected, the overall τ_y values were lower as there was less Laponite in the mixtures. The Herschel-Bulkley model were used to describe these fluids and these results can be found in the Appendix in Section A.1. Due to the viscoplastic characteristics of these Laponite/CMC mixtures, combined with their relatively transparent nature, these would be deemed as being very suitable model fluid systems.

2.8.3 Hectorite/CMC mixtures

A 16.90 wt% hectorite (Parchem) stock suspension was formulated, with details of this formulation process outlined in Section 2.5.4. A 7.00 wt% carboxymethyl cellulose (CMC, M_w = 90000 g mol^{-1}, D.S 0.70, Sigma Aldrich) was formulated (28 g CMC, 372 g deionised water). The CMC was added to the deionised water and the bulk solution was stirred with an overhead stirrer (IKA EUROSTAR 60 motor) for ~16 h at 500 rpm. After the time elapsed different quantities of additional deionised water and 7.00 wt% CMC (aq) were then added to 37.21 g of the 16.90 wt% hectorite stock suspension, to formulate 80 g fluids at 6.00 wt% hectorite and varying mass fractions of CMC, ranging from 0.525-3.75 wt%. As can be seen in Figure 2.34, the 6.00 wt% hectorite/CMC mixtures were brown/white in colour and were opaque, therefore simple dye techniques could not be used for the visualisation of the flows of these fluids in stirred vessels.

The rheological properties of the samples were then obtained using the methods described in Section 2.3, however the downward shear stress sweep measurements occurred using 120 pt dec^{-1}, rather than 60 pt dec^{-1}. The raw rheological flow curves can be seen in Figure 2.35, and the resulting Casson fitted data can be found in Table 2.15, along with the shear rate ranges of the fits, the associated errors of the fits and the physical properties of the fluids. As with both the Bentopharm/CMC and Laponite/CMC mixtures, as the mass fraction of CMC increased within the samples, there was an increase in τ_y values, and in this case the η_{pl} values. As before, it is suggested this is the result of the increased strength of the interactions resulting from depletion flocculation, strengthening the three-dimensional gel networks.

Figure 2.34. Images of the 6.00 wt% hectorite/CMC mixtures, ranging in CMC mass fraction from 0.525-3.75 wt%. More specifically, the mass fraction of CMC in the samples were: '*1*' = 0.525 wt%, '*2*' = 0.875 wt%, '*3*' = 1.30 wt%, '*4*' = 1.75 wt%, '*5*' = 2.63 wt% and '*6*' = 3.75 wt%.

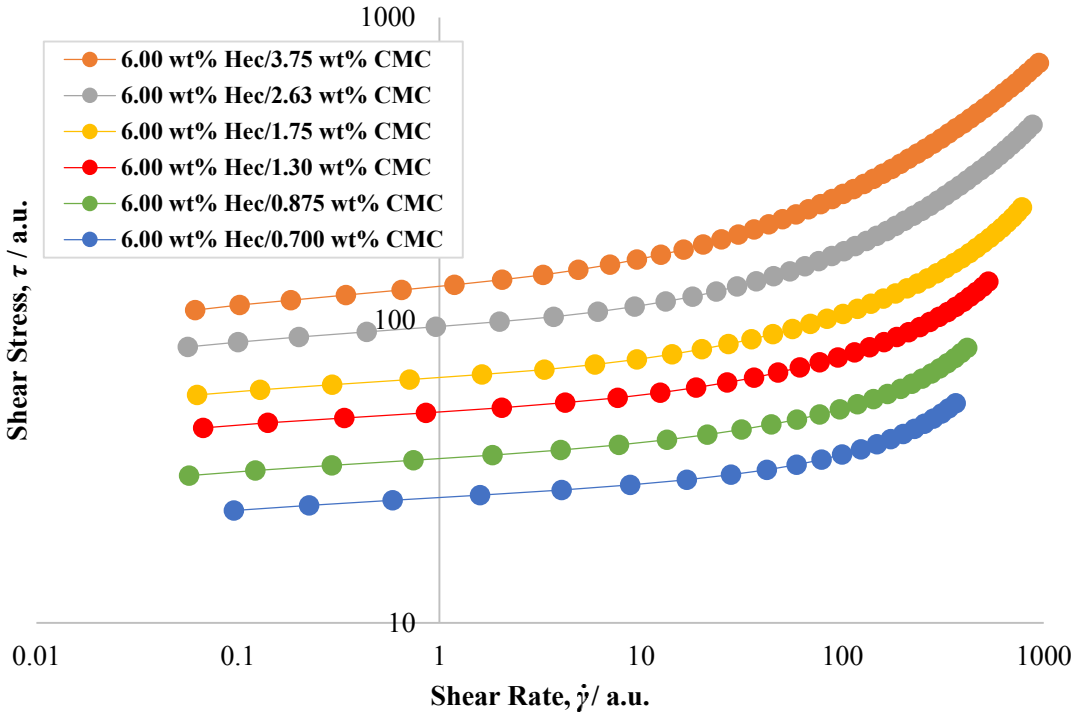

Figure 2.35. Raw rheological flow curves, acquired from shear stress down sweeps using 6-bladed vane geometry, of hectorite/CMC mixtures at a constant hectorite mass fraction of 6.00 wt%, and varying CMC mass fractions: 0.525-3.75 wt%, with all solutions at an approximately constant pH: 9.75-9.34. In the legend, hectorite has been abbreviated to 'Hec'.

Table 2.15. Casson fitted data and the physical properties of the 6.00 wt% hectorite/CMC mixtures, along with the associated error quantification of the mathematical fits and the shear rate range over which the fits occurred.

Physical properties			Casson rheological properties		Error quantification and analysis		
Hectorite mass fraction / wt%	CMC mass fraction / wt%	pH	Yield stress, τ_y / a.u.	Constant plastic viscosity, η_{pl} / a.u.	Optimised fit AAD / %	Optimised fit R^2 value	Shear rate range of optimised fit / a.u.
6.00	0.525	9.75	24.2	0.013	2.09	0.990	0.0954-366
6.00	0.875	9.51	32.3	0.023	2.28	0.992	0.0573-418
6.00	1.30	9.48	46.2	0.039	1.94	0.995	0.0673-532
6.00	1.75	9.44	59.3	0.066	2.15	0.995	0.0627-781
6.00	2.63	9.36	85.1	0.148	1.61	0.999	0.0564-880
6.00	3.75	9.34	117.2	0.269	1.82	0.999	0.0613-946

2.8.4 Acti-Gel 208/CMC mixtures

A 14.81 wt% Acti-Gel 208 (Actigel, Active Minerals International, LLC) stock solution was formulated (240 g Actigel, 1380 g deionised water). The Actigel was added to the deionised water and the stock solution was stirred using an overheard stirrer (IKA EUROSTAR 60 motor) for ~1.5 h at 400-500 rpm. 800g of the 14.81 wt% stock solution was taken and a further 70 g Actigel was added to it. The new bulk Actigel solution

(21.67 wt%) stirred with the overheard stirrer at 400 rpm for ~1 h and then high-shear mixed (Silverson high shear mixer, maximum speed) for 5 min. The stock solution was then left to rest for ~16 h. A 7.00 wt% carboxymethyl cellulose (CMC, M_w = 90000 g / mol, D.S 0.70, Sigma Aldrich) was formulated (28 g, CMC, 372 g deionised water). The CMC was added to the deionised water and the bulk solution was magnetically stirred for ~16 h. After the time elapsed different quantities of additional deionised water and 7.00 wt% CMC (aq) were added to 55.04 g of the 21.67 wt% Actigel stock solution, to formulate 80g fluids at 14.91 wt% Actigel and varying mass fractions of CMC, ranging from 0.700-2.18 wt%. As can be seen in Figure 2.36, the 14.91 wt% Actigel/CMC mixtures were brown/white in colour and were opaque, therefore simple dye techniques could not be used for the visualisation of the flows of these fluids in stirred vessels.

The rheological properties of the samples were then obtained using the methods described in Section 2.3. The raw rheological flow curves can be seen in Figure 2.37, and the resulting Herschel-Bulkley fitted data can be found in Table 2.16, along with the shear rate ranges of the fits, the associated errors of the fits and the physical properties of the fluids. As the mass fraction of CMC increased within the samples, there was an increase in τ_y values, a slight increase in K values and overall slight decrease in n values. Similar to what has been previously discussed, this is hypothesised to be the result of the increased strength of the interactions between particles resulting from depletion flocculation as the CMC mass fraction increased in the samples, strengthening the three-dimensional gel networks. Unlike Bentopharm, Laponite and hectorite, Actigel has lath-like particles rather than platelet-like particles, however it is still suggested that the gelation network caused by depletion flocculation can still form, due to the ends of the Actigel particles having a large enough surface area to produce a polymer concentration gradient between the bulk solution and the volume between the particles, leading to an osmotic pressure difference and the particles being drawn together (Jenkins and Snowden (1996)).

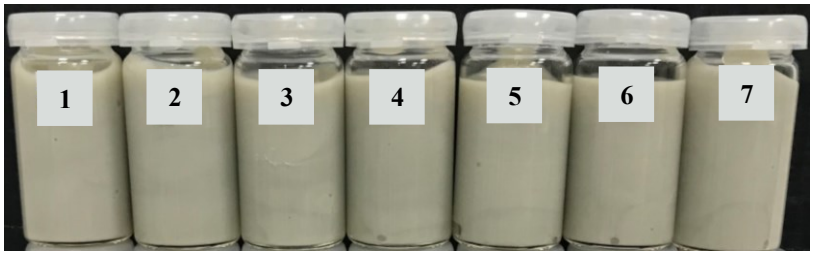

Figure 2.36. Images of the 14.91 wt% Actigel/CMC mixtures, ranging in CMC mass fraction from 0.700-2.18 wt%. More specifically, the mass fraction of CMC in the samples were: '*1*' = 0.700 wt%, '*2*' = 0.875 wt%, '*3*' = 1.05 wt%, '*4*' = 1.31 wt%, '*5*' = 1.54 wt%, '*6*' = 1.75 wt% and '*7*' = 2.18 wt%.

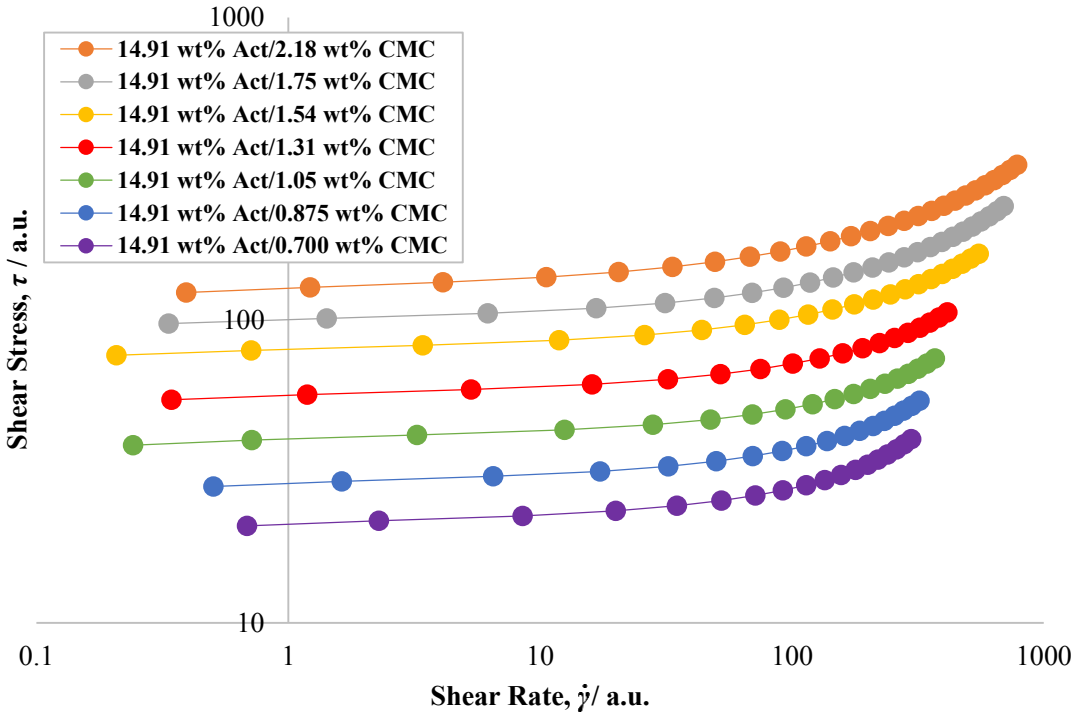

Figure 2.37. Raw rheological flow curves, acquired from shear stress down sweeps using 6-bladed vane geometry, of Actigel/CMC mixtures at a constant Actigel mass fraction of 14.91 wt%, and varying CMC mass fractions: 0.700-2.18 wt%, with all solutions at an approximately constant pH: 8.75-9.01. In the legend, Actigel has been abbreviated to 'Act'.

Table 2.16. Herschel-Bulkley fitted data and the physical properties of the 14.91 wt% Actigel/CMC mixtures, along with the associated error quantification of the mathematical fits and the shear rate range over which the fits occurred.

Physical Properties			**Herschel-Bulkley rheological properties**			**Error quantification and analysis**		
Actigel mass fraction / wt%	**CMC mass fraction / wt%**	**pH**	**Yield stress, τ_y / a.u.**	**Flow consistency index, *K* / a.u.**	**Flow behaviour index, *n***	**Optimised fit AAD / %**	**Optimised fit R^2 value**	**Shear rate range of optimised fit / a.u.**
14.91	0.700	8.83	21.4	0.10	0.90	1.45	0.993	0.686-298
14.91	0.875	8.75	29.0	0.19	0.83	1.43	0.992	0.504-321
14.91	1.05	8.77	40.3	0.26	0.82	1.52	0.993	0.242-370
14.91	1.31	8.94	56.3	0.45	0.77	1.33	0.994	0.344-415
14.91	1.54	8.97	79.3	0.68	0.76	1.37	0.995	0.208-552
14.91	1.75	8.88	101.3	0.65	0.81	1.21	0.997	0.393-695
14.91	2.18	9.01	128.3	1.41	0.73	1.42	0.997	0.393-785

In this section, Actigel/CMC mixtures were investigated at a constant Actigel mass fraction of 14.91 wt%. Actigel/CMC mixtures at an 11.45 wt% Actigel mass fraction were also examined, again by varying the mass fractions of the CMC added to the mixtures (1.23-3.30 wt%). Similar trends were

displayed and the Herschel-Bulkley model were used to describe these fluids, with these data being found in the Appendix in Section A.1.

2.8.5 Actigum/CMC mixtures

A 4.00 wt% Actigum CS 6 (Actigum, Cargill) stock solution was formulated, with details of this formulation process outlined in Section 2.6.3. A 7.00 wt% carboxymethyl cellulose (CMC, M_w = 90000 g / mol, D.S. 0.70, Sigma Aldrich) solution was formulated (28 g CMC, 372 g deionised water). The CMC was added to the deionised water and the stock solution was stirred with an overheard stirrer (IKA EUROSTAR 60 motor) at 500 rpm for ~16 h and was then left to rest for ~24 h. After the time elapsed different quantities of additional deionised water and the 7.00 wt% CMC (aq) solution were added to the 4.00 wt% Actigum bulk solution, to formulate 80 g fluids at 2.25 wt% Actigum and CMC mass fractions ranging from 0.00-3.06 wt%. As can be seen in Figure 2.38, the 2.25 wt% Actigum/CMC mixtures were yellow/white in colour and opaque, and therefore simple dye techniques could not be used for the visualisation of the flows of these fluids in stirred vessels.

The rheological properties of the samples were then obtained using the methods described in Section 2.3. The resulting raw rheological flow curves, acquired from the downward shear stress sweeps, can be seen in Figure 2.39, and the resulting mathematically-fitted data can be found in Table 2.17, along with the shear rate ranges of the fits, the associated errors for the fits, and the physical properties of the fluids. In both Figure 2.39 and Table 2.17, the data for the sample that did not contain CMC ('*1*') is not shown, with this data being found in Section 2.6.3. The lowest shear rate values for each sample were > 1 a.u. and hence relatively high, because at lower values, slip was observed (as discussed Section 2.2). The Herschel-Bulkley model was the best description of the samples containing 0.525 wt% and 1.05 wt% CMC (Samples '*2*' and '*3*', respectively), whilst the 2.10 wt% ('*4*') and 3.06 wt% ('*5*') CMC samples were more accurately fitted with the Casson model. As seen in both Figure 2.35 and Table 2.17, the fluids all have similar τ_y values, with an increase in K going from the 0.525 wt% sample ('*2*') to the 1.05 wt% sample ('*3*'), and an increase in η_{pl} going from the 2.10 wt% sample ('*4*') to the 3.06 wt% sample ('*5*'). This shows that as the mass fraction of CMC increases in the mixtures, the viscosity at a given shear rate (when $\dot{\gamma}$ > 20 a.u.) will also increase, without having a large effect on the τ_y value of the mixtures, and hence CMC could be used as a viscosity modifier for these types of mixtures.

Figure 2.38. Images of the 2.25 wt% Actigum/CMC mixtures, ranging in CMC mass fraction from 0.00-3.06 wt%. More specifically, the mass fraction of CMC in the samples were: '*1*' = 0.00 wt%, '*2*' = 0.525 wt%, '*3*' = 1.05 wt%, '*4*' = 2.10 wt% and '*5*' = 3.06.

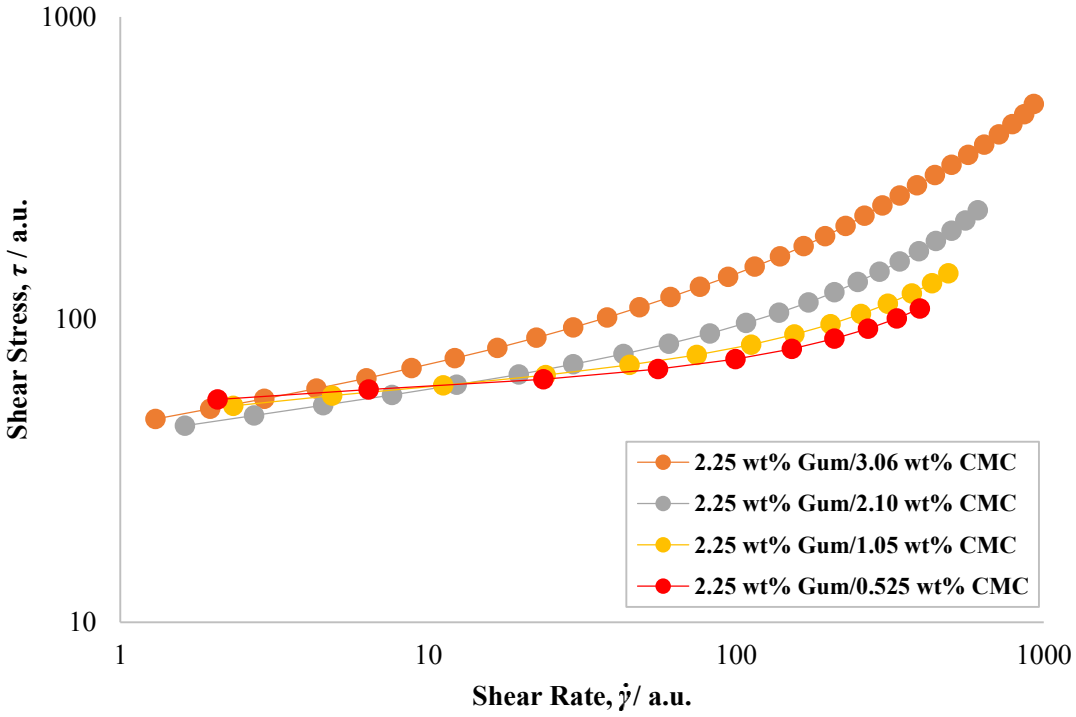

Figure 2.39. Raw rheological flow curves, acquired from shear stress down sweeps using 6-bladed vane geometry, of Actigum/CMC mixtures at a constant Actigum mass fraction of 2.25 wt%, and varying CMC mass fractions: 0.525-3.06 wt%, with all solutions at an approximately constant pH: 6.38-6.47. In the legend, Actigum has been abbreviated to 'Gum'.

Table 2.17. Herschel-Bulkley and Casson fitted data, and the physical properties of the 2.25 wt% Actigum/CMC mixtures, along with the associated error quantification of the mathematical fits and the shear rate range over which the fits occurred.

Physical Properties			**Herschel-Bulkley rheological properties**			**Casson rheological properties**		**Error quantification and analysis**		
Actigum mass fraction / wt%	**CMC mass fraction / wt%**	**pH**	**Yield stress, τ_y / a.u.**	**Flow consistency index, *K* / a.u.**	**Flow behaviour index, *n***	**Yield stress, τ_y / a.u.**	**Constant plastic viscosity, η_{pl} / a.u.**	**Optimised fit AAD / %**	**Optimised fit R^2 value**	**Shear rate range of optimised fit / a.u.**
2.25	0.525	6.41	54.2	0.90	0.68	-	-	1.60	0.994	2.07-396
2.25	1.05	6.47	51.9	1.36	0.67	-	-	2.12	0.994	2.33-490
2.25	2.10	6.44	-	-	-	42.0	0.110	2.73	0.995	1.62-611
2.25	3.06	6.38	-	-	-	44.2	0.265	2.88	0.999	1.3-929

2.8.6 Other CMC-based mixtures

Two other types of CMC-based mixtures were investigated, namely: 0.10 wt% CU30/CMC (0.044-0.175 wt%) fluids and 5.00-9.00 wt% sepiolite/CMC (0.525-3.50 wt%) fluids. The inclusion of CMC into the CU30 suspensions seemed to have a similar affect to the inclusion of large quantities of NaCl into CU30 suspensions, resulting in shrinkage of electric double layers of the polymer chains in CU30 microgel sponges, resulting in the solutions going from viscoplastic to Newtonian in nature. The inclusion of CMC into sepiolite samples did not have the same effect as the addition of CMC into the other clay suspensions, with the suspensions displaying shear-thinning behaviour but lacking a yield stress. Similar to Actigel, sepiolite has a needle-like particle morphology, however it is suggested that the lesser degree of depletion flocculation in the sepiolite/CMC systems is due to the smaller size of the particle ends. Sepiolite particles having an average width and thickness of approximately 20 nm and 7.5 nm, respectively (Bilotti *et al.* (2008)), compared to the slightly bigger particle ends of attapulgite (Actigel), which have an average width and thickness of 31 nm and 8.4 nm, respectively (Cao *et al.* (1996)). Also, there were lower mass fractions of sepiolite in the suspensions investigated, compared to the Actigel/CMC mixtures, which could also explain the lack of a yield stress.

2.9 Mixtures with glycerol

Numerous mixtures with glycerol were formulated and rheologically characterised in this section, with a focus on clay-based mixtures, namely Bentopharm/glycerol, Laponite/glycerol and sepiolite/glycerol mixtures. Other systems, including Actigum/glycerol and Carbopol/glycerol mixtures were also examined. Discussion of the effects of glycerol on the viscoplastic nature of the mixtures was explored.

2.9.1 Bentopharm/glycerol mixtures

An 11.50 wt% Bentopharm (Wilfrid Smith Ltd) stock suspension was formulated (in deionised water), with details of this formulation process outlined in Section 2.8.1. After the 11.50 wt% Bentopharm stock suspension was generated, different quantities of glycerol (glycerol bidistilled 99.5 %, VWR Chemicals) were added to varying amounts of the suspension, to formulate Bentopharm/glycerol mixtures, ranging in Bentopharm mass fraction from 8.50-10.00 wt%, and glycerol mass fraction from 13.04-26.09 wt%. As seen in Figure 2.40, the Bentopharm/glycerol mixtures were brown in colour and were opaque, therefore simple dye techniques for the visualisation of the flows of these fluids in stirred vessels would not be possible.

The rheological properties of the samples were then obtained using the methods described in Section 2.3. The raw rheological flow curves can be seen in Figure 2.41, and the resulting Herschel-Bulkley fitted data can be found in Table 2.18, along with the shear rate ranges of the fits, the associated errors of the fits and the physical properties of the fluids. As previously discussed, with increasing

Bentopharm mass fraction, there was an expected increase in τ_y and K values. As the glycerol mass fraction increased in the samples, there was a noticeable increase in n, likely to be caused by the fact that glycerol is a viscous, Newtonian fluid (see Section 2.10) and therefore $n = 1$. Hence increasing the mass fraction of glycerol will decrease the degree of shear-thinning behaviour in the systems.

Figure 2.40. Images of the Bentopharm/glycerol mixtures, ranging in Bentopharm mass fraction from 8.50-10.00 wt% and glycerol mass fraction from 13.04-26.09 wt%. More specifically, the samples had the following mass fractions of (a) Bentopharm and (b) glycerol: '*1*': (a) 8.50 wt%, (b) 26.09 wt%, '*2*': (a) 9.00 wt%, (b) 21.74 wt%, '*3*': (a) 9.50 wt%, (b) 17.39 wt%, '*4*': (a) 9.75 wt%, (b) 15.23 wt% and '*5*': (a) 10.00 wt%, (b) 13.04 wt%.

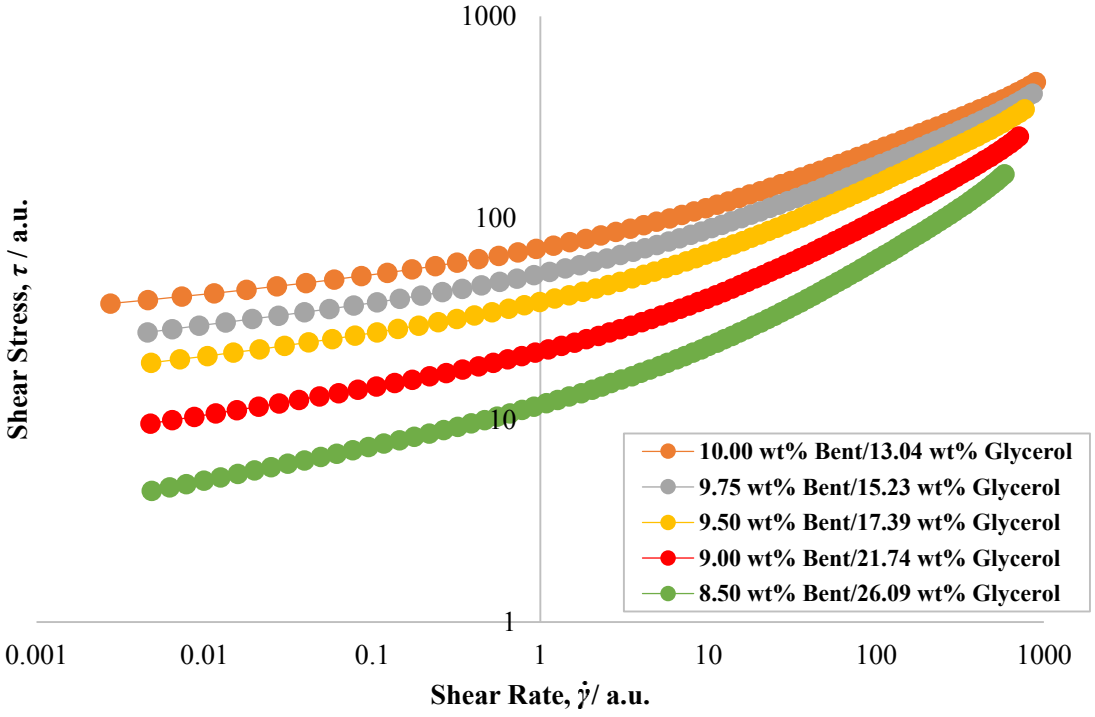

Figure 2.41. Raw rheological flow curves, acquired from shear stress down sweeps using 6-bladed vane geometry, of Bentopharm/glycerol mixtures at Bentopharm mass fractions: 8.50-10.00 wt%, and glycerol mass fractions: 13.04-26.09 wt%, with all solutions at an approximately constant pH: 8.79-9.08. In the legend, Bentopharm has been abbreviated to 'Bent'.

Table 2.18. Herschel-Bulkley fitted data and the physical properties of the Bentopharm/glycerol mixtures, along with the associated error quantification of the mathematical fits and the shear rate range over which the fits occurred.

Physical properties			Herschel-Bulkley rheological properties			Error quantification and analysis		
Bentopharm mass fraction / wt%	**Glycerol mass fraction / wt%**	**pH**	**Yield stress, τ_y / a.u.**	**Flow consistency index, *K* / a.u.**	**Flow behaviour index, *n***	**Optimised fit AAD / %**	**Optimised fit R^2 value**	**Shear rate range of optimised fit / a.u.**
8.50	26.09	9.07	4.8	6.3	0.49	5.09	0.994	0.00485-584
9.00	21.74	9.08	10.0	10.8	0.46	3.35	0.997	0.00476-712
9.50	17.39	9.06	19.2	18.2	0.43	2.01	0.999	0.00481-770
9.75	15.23	8.98	26.6	25.2	0.40	1.78	0.999	0.00458-857
10.00	13.04	8.79	36.9	33.0	0.37	1.50	0.999	0.00275-897

2.9.2 Laponite/glycerol mixtures

A 5.50 wt% Laponite RD (Laponite, Rockwood) stock suspension was formulated, with details of this formulation process outlined in Section 2.5.2. After the 5.50 wt% Laponite stock suspension was generated, different quantities of glycerol (glycerol bidistilled 99.5 %, VWR Chemicals) were added to varying amounts of the suspension, to formulate Laponite/glycerol mixtures, ranging in Laponite mass fraction from 3.75-4.75 wt%, and glycerol mass fraction from 0.00-31.81 wt%. As can be seen in Figure 2.42, the resulting Laponite/glycerol mixtures were transparent, therefore simple dye techniques could be used to visualise the flow of these fluids in stirred vessels.

The rheological properties of the samples were then obtained using the methods described in Section 2.3, however the downward shear stress sweep measurements occurred using 90 pt dec^{-1}, rather than 60 pt dec^{-1}. The raw rheological flow curves can be seen in Figure 2.43 and the resulting Herschel-Bulkley fitted data can be found in Table 2.19, along with the shear rate ranges of the fits, the associated errors of the fits and the physical properties of the fluids (excluding the samples that did not contain glycerol: Samples '*1*', '*5*' and '*8*', with this data found in Section 2.5.2). As previously discussed, with increasing Laponite mass fraction, there was an increase in τ_y and *K* values. However, for a given mass fraction of Laponite, as the glycerol mass fraction increased, *K* remained relatively constant. In the 3.75 wt% Laponite samples, as the glycerol mass fraction increased in the samples, there was a slight increase in *n*, however, for the 4.25 wt% Laponite samples and 4.75 wt% Laponite samples, *n* remained constant at each given mass fraction, regardless of glycerol mass fraction. As before with the other Laponite samples/mixtures, the Laponite/glycerol mixtures are deemed as being very good candidates as model fluid systems, due to these fluids having both the desired viscoplastic behaviour and transparent nature.

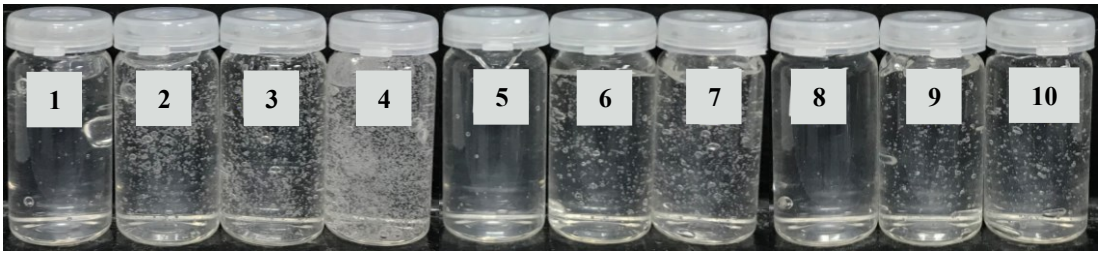

Figure 2.42. Images of the Laponite/glycerol mixtures, ranging in Laponite mass fraction from 3.75-4.75 wt% and glycerol mass fraction from 0.00-31.81 wt%. More specifically, the samples had the following mass fractions of (a) Laponite and (b) glycerol: '*1*': (a) 3.75 wt%, (b) 0.00 wt%, '*2*': (a) 3.75 wt%, (b) 10.61 wt%, '*3*': (a) 3.75 wt%, (b) 21.20 wt%, '*4*': (a) 4.25 wt%, (b) 31.81 wt%, '*5*': (a) 4.25 wt%, (b) 0.00 wt%, '*6*' (a) 4.25 wt%, (b) 11.36 wt%, '*7*': (a) 4.25 wt%, (b) 22.73 wt%, '*8*': (a) 4.75 wt%, (b) 0.00 wt%, '*9*': (a) 4.75 wt%, (b) 7.08 wt%, and '*10*': (a) 4.75 wt%, (b) 13.64 wt%.

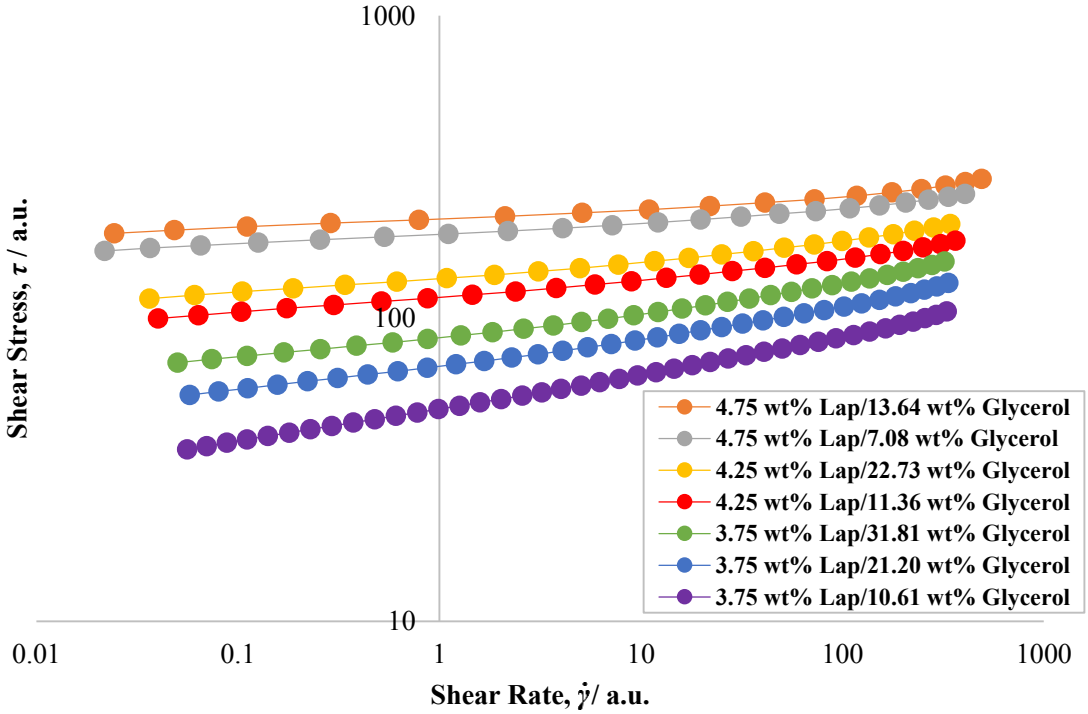

Figure 2.43. Raw rheological flow curves, acquired from shear stress down sweeps using 6-bladed vane geometry, of Laponite/glycerol mixtures at Laponite mass fractions: 3.75-4.75 wt%, and glycerol mass fractions: 7.08-31.81 wt%, with all solutions at an approximately constant pH: 9.70-9.84. In the legend, Laponite has been abbreviated to 'Lap'.

Table 2.19. Herschel-Bulkley fitted data and the physical properties of the Laponite/glycerol mixtures, along with the associated error quantification of the mathematical fits and the shear rate range over which the fits occurred.

Physical Properties			Herschel-Bulkley rheological properties			Error quantification and analysis		
Laponite mass fraction / wt%	**Glycerol mass fraction / wt%**	**pH**	**Yield stress, τ_y / a.u.**	**Flow consistency index, K / a.u.**	**Flow behaviour index, n**	**Optimised fit AAD / %**	**Optimised fit R^2 value**	**Shear rate range of optimised fit / a.u.**
3.75	10.61	9.79	16.7	33.3	0.16	0.52	0.999	0.0560-330
3.75	21.20	9.72	38.8	30.4	0.18	0.47	0.999	0.0576-336
3.75	31.81	9.70	57.3	28.6	0.21	0.47	0.999	0.0501-322
4.25	11.36	9.78	67.1	50.4	0.13	0.77	0.995	0.0401-365
4.25	22.73	9.70	81.5	54.2	0.13	0.85	0.995	0.0363-344
4.75	7.08	9.84	95.8	94.8	0.08	1.29	0.984	0.0218-407
4.75	13.64	9.74	123.7	89.7	0.08	1.64	0.971	0.0243-492

2.9.3 Sepiolite/glycerol mixtures

A 10.00 wt% Sepiolite (Aldrich) stock suspension was formulated (100 g Sepiolite, 900 g deionised water). The sepiolite was added to the deionised water and the stock suspension was stirred using a dual-impeller overheard stirrer (IKA EUROSTAR 60 motor) for 90 min at 700 rpm. The stock suspension was then high-shear mixed (Silverson high-shear mixer, maximum speed) for 5 min, before being left to rest for ~16 h. After time elapsed different quantities of additional deionised water and glycerol (glycerol bidistilled 99.5%, VWR Chemicals) were then added to the 10.00 wt% sepiolite stock suspension, to formulate 80 g fluids with sepiolite mass fractions at 5.00 wt% and 7.00 wt%, and glycerol mass fractions ranging from 12.50-50.00 wt%. As can be seen in Figure 2.44, the resulting sepiolite/glycerol mixtures were white/brown in colour and were opaque, therefore simple dye techniques for the visualisation of the flows of these fluids in stirred vessels would not be possible.

The rheological properties of the samples were then obtained using the methods described in Section 2.3. The raw rheological flow curves can be seen in Figure 2.45 and the resulting Herschel-Bulkley fitted data can be found in Table 2.20, along with the shear rate ranges of the fits, the associated errors of the fits and the physical properties of the fluids. As would be expected, increasing the mass fraction of sepiolite from 5.00 wt% to 7.00 wt% resulted in an increase in both τ_y and K values, and a slight increase in n. For a given sepiolite mass fraction, as the mass fraction of glycerol increased, there were very slight increase in all three Herschel-Bulkley parameters, suggesting increased mass fractions of glycerol resulted in a greater extent of hydrogen bonding and electrostatic interactions within the suspensions.

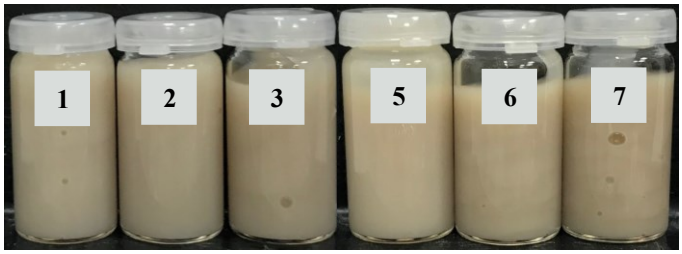

Figure 2.44. Images of the sepiolite/glycerol mixtures, with sepiolite mass fractions of 5.00 wt% and 7.00 wt%, and glycerol mass fraction ranging from 12.50-50.00 wt%. More specifically, the samples had the following mass fractions of (a) sepiolite and (b) glycerol: '*1*': (a) 5.00 wt%, (b) 12.50 wt%, '*2*': (a) 5.00 wt%, (b) 25.00 wt%, '*3*': (a) 5.00 wt%, (b) 37.50 wt%, '*5*': (a) 7.00 wt%, (b) 0.00 wt%, '*6*': (a) 7.00 wt%, (b) 15.00 wt% and '*7*': (a) 7.00 wt%, (b) 30.00 wt%. From the image, Sample '*4*': (a) 5.00 wt%, (b) 50.00 wt%, was missing.

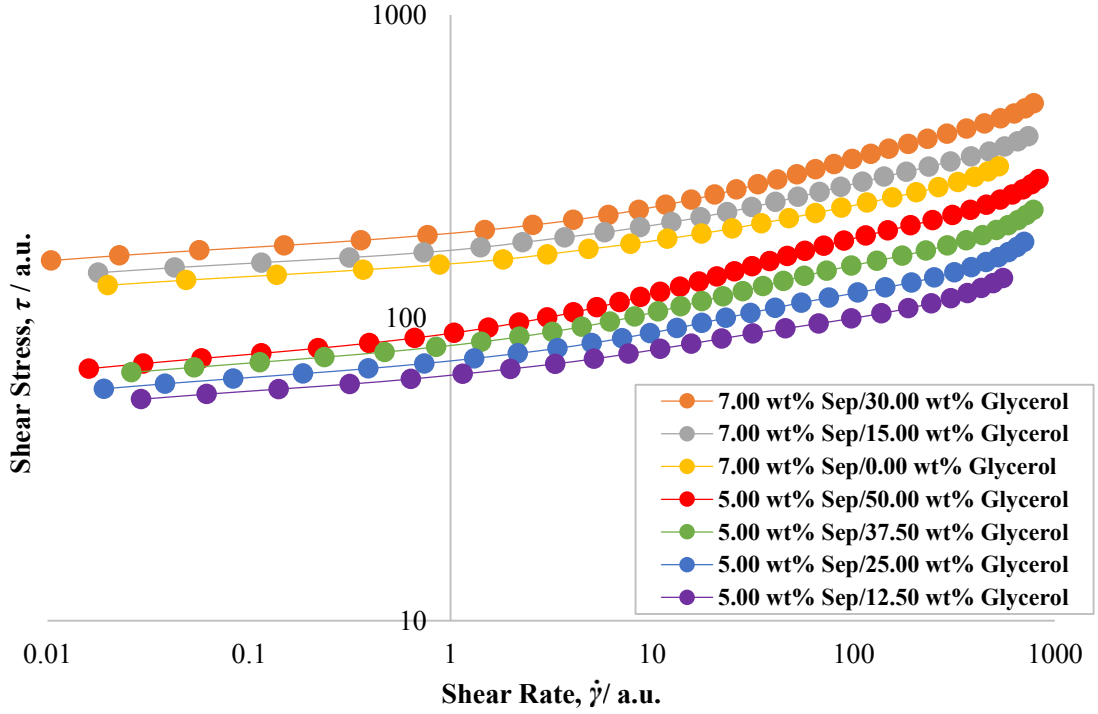

Figure 2.45. Raw rheological flow curves, acquired from shear stress down sweeps using 6-bladed vane geometry, of sepiolite/glycerol mixtures at sepiolite mass fractions: 5.00 wt% and 7.00 wt%, and glycerol mass fractions: 0.00-50.00 wt%, with all solutions at an approximately constant pH: 8.10-8.64. In the legend, sepiolite has been abbreviated to 'Sep'.

Table 2.20. Herschel-Bulkley fitted data and the physical properties of the sepiolite/glycerol mixtures, along with the associated error quantification of the mathematical fits and the shear rate range over which the fits occurred.

Physical properties			Herschel-Bulkley rheological properties			Error quantification and analysis		
Sepiolite mass fraction / wt%	**Glycerol mass fraction / wt%**	**pH**	**Yield stress, τ_y / a.u.**	**Flow consistency index, *K* / a.u.**	**Flow behaviour index, *n***	**Optimised fit AAD / %**	**Optimised fit R^2 value**	**Shear rate range of optimised fit / a.u.**
5.00	12.50	8.61	47.3	17.3	0.25	1.02	0.995	0.0291-553
5.00	25.00	8.34	52.4	19.8	0.27	1.32	0.994	0.0190-705
5.00	37.50	8.51	56.9	25.0	0.28	1.54	0.996	0.0261-782
5.00	50.00	8.10	57.3	33.1	0.28	1.72	0.997	0.0160-832
7.00	0.00	8.62	120.9	29.7	0.29	0.55	0.999	0.0199-528
7.00	15.00	8.39	131.8	35.83	0.30	0.61	0.999	0.0178-739
7.00	30.00	8.39	148.6	40.68	0.33	0.99	0.999	0.0104-786

2.9.4 Actigum/glycerol mixtures

A 4.00 wt% Actigum CS 6 (Cargill) stock solution was formulated, with details of this formulation process outlined in Section 2.6.3. After the 4.00 wt% Actigum stock solution was generated, different quantities of additional deionised water and glycerol (glycerol bidistilled 99.5 %, VWR Chemicals) were added to 65 g of the stock solution, to formulate 80 g, 3.25 wt% Actigum/glycerol mixtures, at glycerol mass fractions from 0.00-18.75 wt%. As seen in Figure 2.46, the resulting Actigum/glycerol mixtures were yellow/white in colour and were opaque, and therefore simple dye techniques could not be used for the visualisation of the flows of these fluids in stirred vessels.

The rheological properties of the samples were then obtained using the methods described in Section 2.3. The resulting raw rheological flow curves, acquired from the downward shear stress sweeps, can be seen in Figure 2.47, and the resulting mathematically-fitted data can be found in Table 2.21, along with the shear rate ranges of the fits, the errors associated with the fits and the physical properties of the fluids. The lowest shear rate values for each sample were > 1 a.u. and hence relatively high, because at lower values, slip was observed (as discussed Section 2.2). The samples containing 0.00 wt% (‘*1*’) and 12.50 wt% (‘*2*’) glycerol were best described by the Casson model, whilst the Herschel-Bulkley model more accurately described the sample containing 18.75 wt% (‘*3*’) glycerol. Increasing the glycerol content resulted in slightly increased τ_y values and increased viscosity values at a given shear rate.

Figure 2.46. Images of 3.25 wt% Actigum/glycerol mixtures, with glycerol mass fraction ranging from 0.00-18.75 wt%. More specifically, the samples had the following mass fractions glycerol: '*1*' = 0.00 wt%, '*2*' = 12.50 wt% and '*3*' = 18.75 wt%.

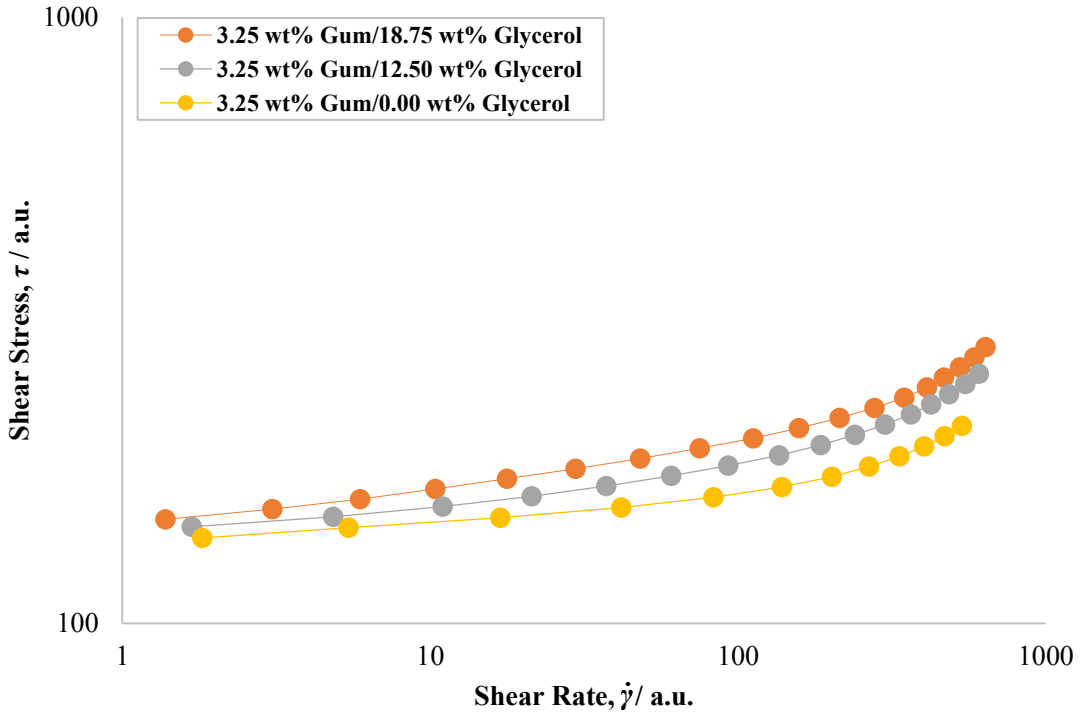

Figure 2.47. Raw rheological flow curves, acquired from shear stress down sweeps using 6-bladed vane geometry, of Actigum/glycerol mixtures at a constant Actigum mass fractions of 3.25 wt%, and glycerol mass fractions, ranging from 0.00-18.75 wt%, with all solutions at an approximately constant pH: 6.17-6.23. In the figure's legend, Actigum has been abbreviated to 'Gum'.

Table 2.21. Herschel-Bulkley and Casson fitted data, and the physical properties of the Actigum/glycerol mixtures, along with the associated error quantification of the mathematical fits and the shear rate range over which the fits occurred.

Physical properties			**Herschel-Bulkley rheological properties**			**Casson rheological properties**		**Error quantification and analysis**		
Actigum mass fraction / wt%	**Glycerol mass fraction / wt%**	**pH**	**Yield stress, τ_y / a.u.**	**Flow consistency index, K / a.u.**	**Flow behaviour index, n**	**Yield stress, τ_y / a.u.**	**Constant plastic viscosity, η_{pl} / a.u.**	**Optimised fit AAD / %**	**Optimised fit R^2 value**	**Shear rate range of optimised fit / a.u.**
3.25	0.00	6.17	-	-	-	135.8	0.014	1.15	0.989	1.82-534
3.25	12.50	6.23	-	-	-	141.8	0.026	1.08	0.994	1.68-606
3.25	18.75	6.23	142.5	7.9	0.43	-	-	1.70	0.987	1.38-638

2.9.5 C981/glycerol mixtures

A bulk Carbopol 981 (C981, Lubrizol) solution was formulated (20.4 g C981, 1679.6 g deionised water). The C981 was added to the deionised water and the bulk solution was stirred with an overhead stirrer (IKA EUROSTAR 60 motor) at 600-700 rpm for ~24 h. After the time elapsed, 116.50 g of a 3 wt% NaOH (aq) solution (8.997 g NaOH, 291 g deionised water) solution and 51.16 g of deionised water were added to 838.30 g of the bulk C981 solution to form a 1.00 wt% bulk C981 solution at pH 6.20. Different quantities of additional deionised water and glycerol (glycerol bidistilled 99.5%, VWR Chemicals) were added to 32 g of the 1.00 wt% C981 bulk solution (pH 6.20), to formulate 80 g, 0.40 wt% C981/glycerol mixtures, with the mass fraction of glycerol ranging from 0.00-60.00 wt%. As seen in Figure 2.48, the resulting C981/glycerol mixtures were transparent, and therefore simple dye techniques could be used for the visualisation of the flows of these fluids in stirred vessels.

The rheological properties of the samples were obtained using the methods described in Section 2.3.The raw rheological flow curves can be seen in Figure 2.45 and the resulting Herschel-Bulkley fitted data can be found in Table 2.22, along with the shear rate ranges of the fits, the errors associated with the fits and the physical properties of the fluids. As seen from both Figure 2.49 and Table 2.22, when the mass fraction of glycerol increased in the samples, τ_y remained relatively constant, however, there was a noticeable increase in K and a slight increase in n. As discussed in Section 2.9.1, glycerol is a viscous, Newtonian fluid and therefore, increasing the glycerol content within the samples has the effect of slightly reducing the shear-thinning behaviour of the fluids and increasing the viscosity of the fluids, at a given shear rate. Due to the highly transparent nature, in conjunction with the evidently viscoplastic behaviour of these fluids, C981/glycerol mixtures can be treated as an ideal candidate as a model replacement fluid system. Other C981/glycerol mixtures were also investigated, but at C981 mass fraction values of 0.60 wt% and 0.80 wt%. Again, the mass fraction of glycerol in these samples were varied and very similar trends were displayed, with the results for the 0.60 wt% C981/glycerol and the 0.80 wt% C981/glycerol mixtures being seen in Section A.1 of the Appendix.

Figure 2.48. Images of 0.40 wt% C981/glycerol mixtures, with glycerol mass fraction ranging from 0.00-60.00 wt%. More specifically, the samples had the following mass fractions glycerol: '*1*' = 0.00 wt%, '*2*' = 15.00 wt%, '*3*' = 30.00 wt%, '*4*' = 45.00 wt% and '*5*' = 60.00 wt%.

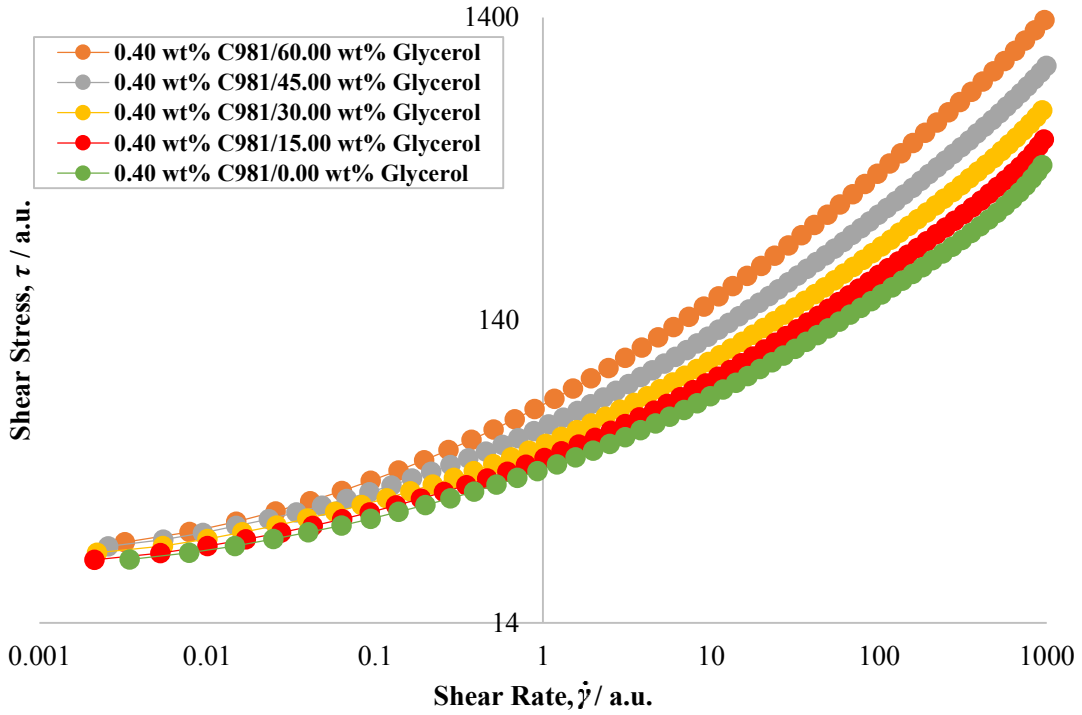

Figure 2.49. Raw rheological flow curves, acquired from shear stress down sweeps using 6-bladed vane geometry, of C981/glycerol mixtures at a constant C981 mass fractions of 0.40 wt%, and glycerol mass fractions, ranging from 0-60 wt%, with all solutions at an approximately constant pH: 6.57-6.89.

Table 2.22. Herschel-Bulkley fitted data and the physical properties of the C981/glycerol mixtures, along with the associated error quantification of the mathematical fits and the shear rate range over which the fits occurred.

Physical properties			**Herschel-Bulkley rheological properties**			**Error quantification and analysis**		
C981 mass fraction / wt%	**Glycerol mass fraction / wt%**	**pH**	**Yield stress, τ_y / a.u.**	**Flow consistency index, *K* / a.u.**	**Flow behaviour index, *n***	**Optimised fit AAD / %**	**Optimised fit R^2 value**	**Shear rate range of optimised fit / a.u.**
0.40	0.00	6.57	22.3	21.4	0.42	2.33	0.995	0.00345-943
0.40	15.00	6.61	22.7	24.7	0.43	2.46	0.996	0.00213-961
0.40	30.00	6.64	23.9	28.7	0.45	2.46	0.997	0.0022-942
0.40	45.00	6.75	25.0	35.1	0.46	2.62	0.998	0.00257-999
0.40	60.00	6.89	24.9	46.3	0.48	2.75	0.998	0.00322-969

2.9.6 Other Carbopol/glycerol mixtures

A large number of different Carbopol/glycerol mixtures were formulated and rheologically characterised, with very similar rheological trends being exhibited by these Carbopol/glycerol, as those displayed by the C981/glycerol mixtures from Section 2.9.5. As a result, these rheological data are presented in the Appendix. More specifically, 0.075-0.125 wt% CU30/glycerol mixtures, 0.125-0.20 wt% C980/glycerol, 0.10-0.20 wt% CU10/glycerol and 0.10-0.125 wt% CU21/glycerol were investigated and the resulting raw and fitted rheological data can be found in Section A.1. By combining

the highly transparent nature of these Carbopol/glycerol mixtures, with the exhibited viscoplastic behaviour, these mixtures are ideal candidates as model replacement fluid systems.

2.10 Commercial products

In this section the rheological properties of a small number of commercial products were investigated, namely: mayonnaise (Brake Bros Ltd), tomato ketchup (Sainsbury's Supermarkets Ltd), honey (Sainsbury's Basics Clear Honey, Sainsbury's Supermarkets Ltd) and glycerol (glycerol bidistilled 99.5, VWR Chemicals). In each case, the samples were loaded directly into the rheometrical geometry, before undergoing rheological characterisation. The mayonnaise and tomato ketchup samples underwent the same pre-shear and downward shear stress sweeps as previously described, whilst the honey and glycerol underwent the pre-shear test followed by a downward shear rate sweep (1000-0.01 a.u. (honey), 1000-0.1 a.u. (glycerol), 5 pt dec^{-1}, ramp logarithmic duration, 4-60 s). Due to the Newtonian, non-thixotropic nature of both honey and glycerol, the utilisation of a shear rate sweep, rather than a shear stress sweep will have a negligible effect on the rheological properties obtained. The raw rheological flow curves can be seen in Figure 2.50 and the associated mathematically-fitted data can be found in Table 2.23, along with the shear rate ranges and associated errors of the fits. The mayonnaise and tomato ketchup samples were best described by the Herschel-Bulkley model, whilst the Power Law model was used to describe the honey and glycerol samples, although as seen, $n \approx 1$ and hence the fluids are Newtonian.

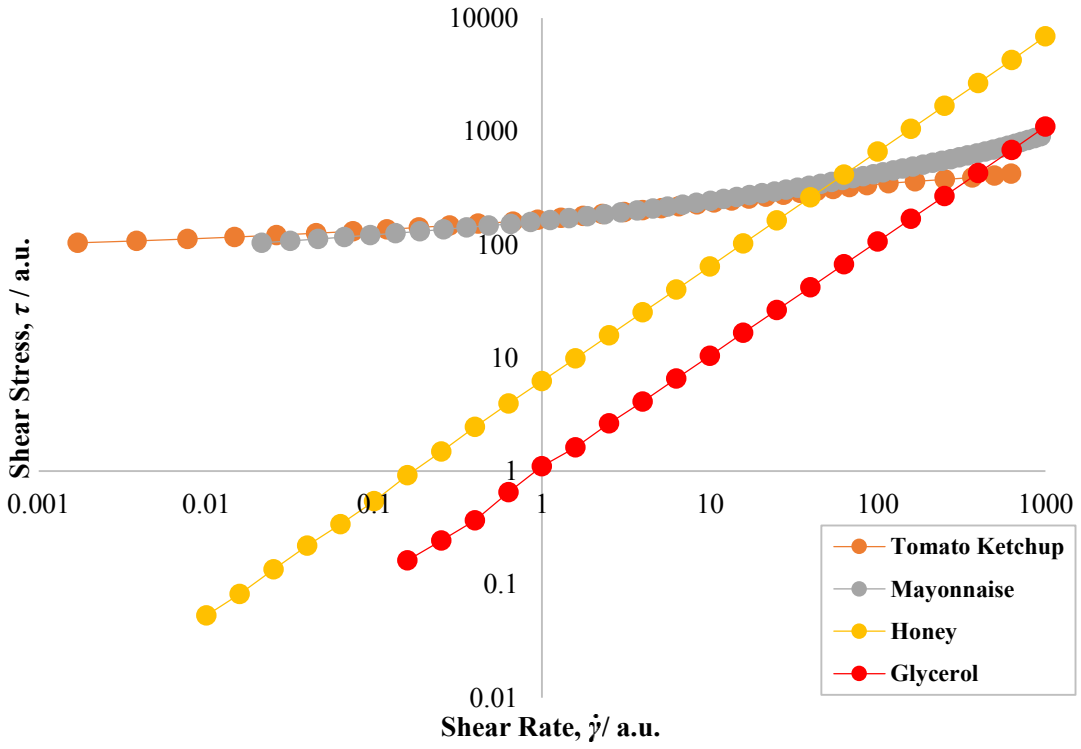

Figure 2.50. Raw rheological flow curves, using 6-bladed vane geometry, for mayonnaise and tomato ketchup samples (acquired through shear stress down sweeps), and for honey and glycerol samples (acquired through shear rate down sweeps).

Table 2.23. Herschel-Bulkley fitted data of the commercial products, along with the associated error quantification of the mathematical fits and the shear rate range over which the fits occurred.

	Herschel-Bulkley rheological properties			**Error quantification and analysis**		
Fluid	**Yield stress, τ_y / a.u.**	**Flow consistency index, K / a.u.**	**Flow behaviour index, n**	**Optimised fit AAD / %**	**Optimised fit R^2 value**	**Shear rate range of fit / a.u.**
Mayonnaise	91.4	66.9	0.35	1.91	0.997	0.0143-942
Tomato ketchup	76.8	95.1	0.21	2.13	0.993	0.00171-626
Honey	0.0	6.0	1.02	2.29	1.000	0.01-1000
Glycerol	0.0	1.0	1.00	3.36	1.000	0.1-1000

2.11 Rheology space

In this section, plots can be seen of the Herschel-Bulkley parameters (Figure 2.51(a)) and the Casson parameters (Figure 2.51(b)) for all fluids that have been rheologically investigated in this work. The idea behind this chapter was to not only find suitable model fluid systems that have the desired viscoplastic rheological properties, but also to try and cover as much of this 'rheological space' or 'viscoplastic space' as possible. All of the fitted data of the fluids are stored in a rheological database, as part of a computational platform, known as the *Model Fluid Selection Tool*, that has the capability to suggest appropriate model fluid systems, based on matched rheological properties with respect to the 'to-be-matched' (or 'real') fluid in question. Further discussion of this computational tool can be found in Chapter 3.

As seen in Figure 2.51(a), the majority of fluids created had τ_y values ranging from 0-200 a.u., and n values ranging 0.20-0.60, whilst K spanned from 0-120 a.u.. It was determined that $n > 0.6$ were generally only attainable when $\tau_y < 50$ a.u. and $K < 30$ a.u.. From Figure 2.51(b), η_{pl} ranged from 0.00-0.35 a.u., however with the odd exception, only values of $\tau_y < 100$ a.u. were associated with this entire range in η_{pl}, with only values of $\eta_{pl} < 0.05$ a.u. being associated with $\tau_y > 100$ a.u.. Therefore, fluids with wide ranging viscoplastic fluids have been examined, with future work looking to push the boundaries further and explore a wider range of this rheological space, if possible.

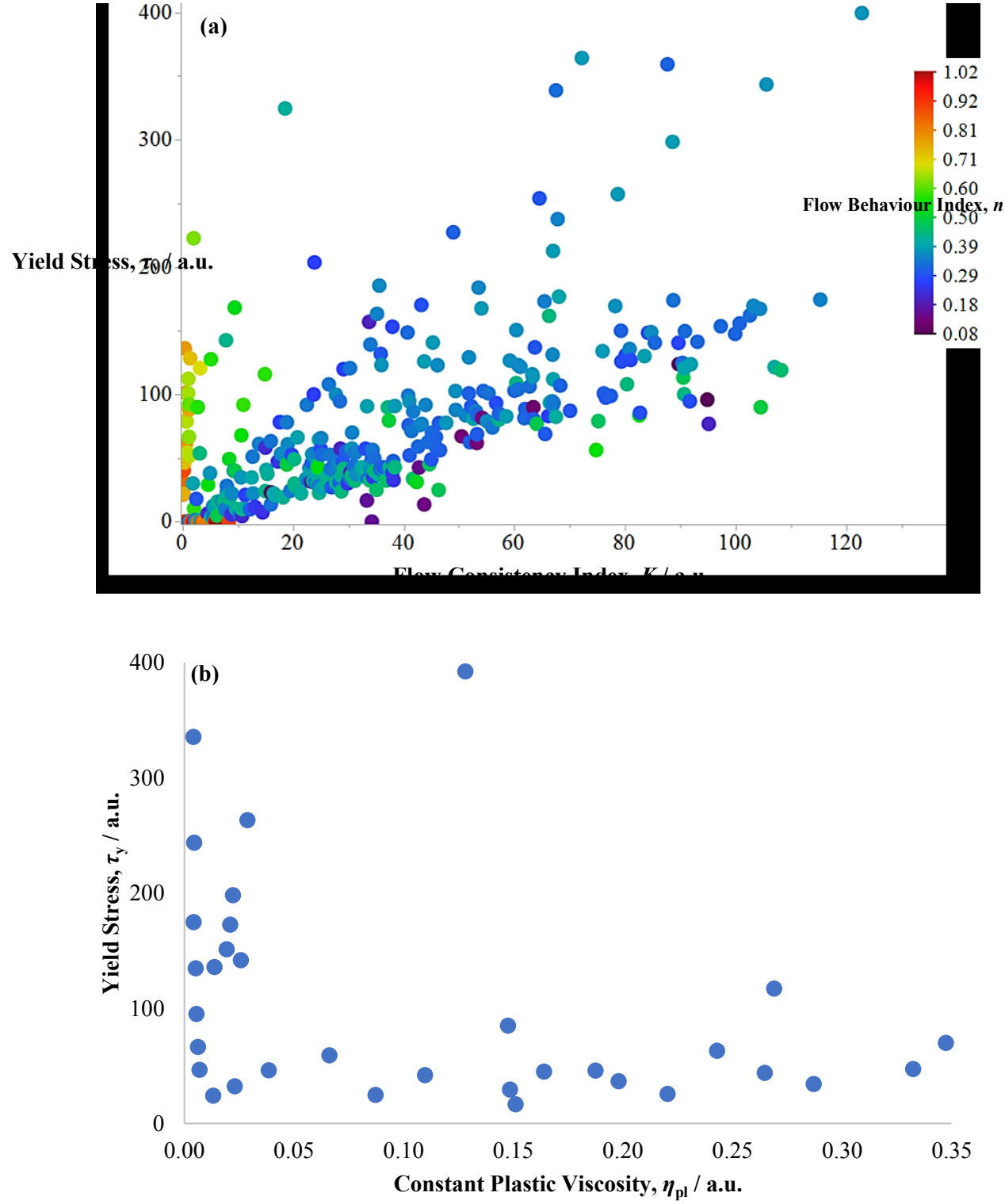

Figure 2.51. Mathematically-fitted rheological data for all fluids formulated and characterised in this work, with (a) being a plot of the fluids described by the Herschel-Bulkley (and Power Law) model and (b) a plot of the Casson fluids.

2.12 Errors associated with fluid formulation and rheological characterisation

In this section, the reproducibility of the rheological properties of fluids will be investigated, using a 7.00 wt% sepiolite as the example fluid. Two 7.00 wt% sepiolite samples were created, using similar methods. For *Sample 1*: A 10.00 wt% sepiolite (Aldrich) stock suspension was formulated (100 g Sepiolite, 900 g deionised water). The sepiolite was added to the deionised water and the stock suspension was stirred via magnetic agitation, then with an overhead stirrer (IKA EUROSTAR 60 motor) for 10 min before being high-shear mixed (Silverson high-shear mixer, maximum speed) for 5 min. A 7.00 wt% Sepiolite sample (pH 8.84) was generated using 56.00 g stock suspension and 24.00 g of additional deionised water. The sample was left to rest ~ 20-30 h before rheological testing. For *Sample 2*: A 10.00 wt% sepiolite stock suspension was also created, using the same quantities of sepiolite and deionised water as before, but the suspension was stirred using a dual-impeller stirring system for 90 min at 700 rpm. The stock suspension was left to rest for ~16 hours before the 7.00 wt% sepiolite sample (pH 8.10) was generated using 56.00 g of the 10.00 wt% sepiolite stock suspension and 24.00 g of additional water. The raw rheological flow curves can be seen in Figure 2.52 and the resulting Herschel-Bulkley fitted data can be found in Table 2.24, along with the shear rate ranges of the fits, the associated errors of the fits and the physical properties of the fluids. As seen from Figure 2.52 and Table 2.24, both raw and fitted rheological data are very similar, with *Sample 2*, having very slightly larger τ_y, K and n values than *Sample 1*. This shows that through good practice, reproducible results can be obtained.

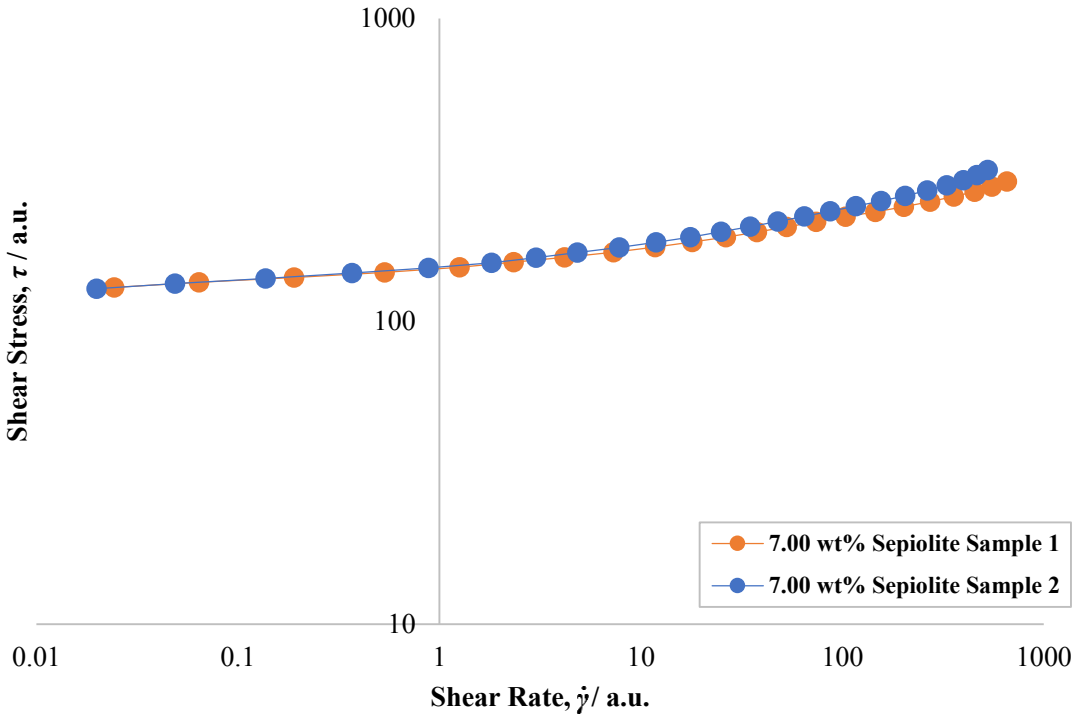

Figure 2.52. Raw rheological flow curves, acquired from shear stress down sweeps using 6-bladed vane geometry, of both 7.00 wt% sepiolite fluids: *Samples 1* and *2*.

Table 2.24. Herschel-Bulkley fitted data and the physical properties of *Samples 1* and *2*, along with the associated error quantification of the mathematical fits and the shear rate range over which the fits occurred.

Physical properties		**Herschel-Bulkley rheological properties**			**Error quantification and analysis**		
7.00 wt% sepiolite fluid	**pH**	**Yield stress, τ_y / a.u.**	**Flow consistency index, *K* / a.u.**	**Flow behaviour index, *n***	**Optimised fit AAD / %**	**Optimised fit R^2 value**	**Shear rate range of fit / a.u.**
Sample 1	8.84	119.9	29.1	0.27	0.44	0.999	0.0243-657
Sample 2	8.10	120.9	29.7	0.29	0.55	0.999	0.0199-528

2.13 Conclusion

In this chapter, a number of different model fluid systems were formulated and rheologically characterised, to find model fluids with rheological properties representative of 'real' or 'industrial' fluids. The target fluids were those that could be described as having viscoplastic behaviour: fluids that exhibited a yield stress, which once exceeded, deformed with shear-thinning characteristics. A wide range of different fluid groups were investigated, including particulate suspensions (with a particular focus on clays), polymer solutions, microgels (focusing on various Carbopol solutions), mixtures and commercial products (for example, tomato ketchup, mayonnaise and honey). The clay suspensions included: Bentopharm, Laponite RD, sepiolite, hectorite and Acti-gel 208 suspensions, whilst the polymer solutions of interest were carboxymethyl cellulose, hydroxypropyl cellulose and Actigum solutions. Five Carbopol grades were investigated, including including Carbopol 980, Carbopol 981, Carbopol Ultrez 10, Carbopol Ultrez 21 and Carbopol Ultrez 30. Numerous mixtures were assessed, with a particular focus on clay-glycerol, clay-CMC(aq), and Carbopol-glycerol systems. The effect of varying mass fraction on rheological properties was evaluated for all fluids, with the effects of pH and salt concentration in the Carbopol solutions also being determined. Every fluid underwent a downward shear stress sweep (with the exception of honey and glycerol), to obtain the steady shear rheological flow curves of the fluids, with the 'good' rheological data being selected and fitted with mathematical models, namely the Herschel-Bulkley model, the Casson model and the Power Law model. The models that most accurately described each fluid were used and the resulting fitted parameters were presented, with the intention of including this data in the *Model Fluid Selection Tool* (Chapter 3). Carbopol- and Laponite-based fluids were selected as being ideal model fluid candidates as they not only displayed the target viscoplastic rheological properties, but also had the characteristics of being highly transparent in nature. As a result, when using these model fluids for a particular application, such as mixing in stirred vessels, facile and inexpensive dye visualisation techniques could be employed.

Chapter 3: Model Fluid Selection Tool

3.1 Introduction

The '*Model Fluid Selection Tool*' (referred to as 'MFST' from here onwards) is a computational platform developed in Microsoft Excel, using Visual Basic for Application programming methods and recorded macros. Its development was inspired by the work of Broekhuijsen (2014), who developed an early-stage computational tool that looked at matching the rheological properties of model fluids systems to those of the 'real' or 'to-be-matched' fluid in question. That work was carried out as a M.Sc. project, as part of a collaboration between Syngenta Ltd and Imperial College London. The current MFST has extended the capability for finding 'best-matched' model fluids, in terms of rheological properties, to the 'real' fluid in question, whilst also acting as an extensive rheological database, containing the physical and rheological properties of approximately 400 different model fluid systems. As discussed in Chapter 2, the fluids of interest to this work display a yield stress, which once exceeded, deform with shear-thinning characteristics, and are known as viscoplastic fluids. The vast majority of the model fluids stored in the MFST have these desired viscoplastic properties (some are shear-thinning fluids, lacking a yield stress), and hence mimic the rheological properties of the 'real' fluids, whilst also being safe, inexpensive and easy-to-handle. The physical and rheological properties of these model fluids are summarised in Chapter 2. Suitable replacement model fluid systems are required so that key industrial mixing-based unit operations can be simulated without needing to use the real, industrial formulation, which are expensive and toxic, with the aim of better understanding and optimising the unit operation in question, through overcoming any potential issues that may arise, in a safe and cost effective environment, either in the laboratory or on the pilot and plant scale. As far as it can be determined, the development of a full-scale computational tool, capable of fitting raw viscoplastic flow curves with different mathematical rheology models, storing the fluids in a rheological database, suggesting suitable model fluid systems that most accurately match the rheological properties of the 'real' fluid in question, and using interpolation methods to propose hypothetical model fluids that may result in superior matching of rheological properties, is a novel concept. The MFST has been developed for the benefit of Syngenta Ltd, however its use could be extended to other industries and companies. The aim of this chapter is to walk the reader through the various functionalities of the MFST, in a step-by-step manner, through the use of numerous different case studies to highlight all of the operational features of the computational platform. As discussed in Chapter 2, all model fluid systems were formulated and characterised using highly specific rheological protocols, with discussion of the importance of similarity of methods presented at the end of this chapter.

3.2 Overview of the '*Model Fluid Selection Tool*'

The MFST is comprised of a number of different Microsoft Excel worksheets and is capable of performing various operations, including: adding rheological data, through fitting the raw data with mathematical models (the '*Adding Data to Library (Data & Fitting Thereof)*' operation) or by adding known fitted data (the '*Adding Data to Library (By Fitted Parameters)*' operation), to a rheological database; finding best matched model fluids with regards to a 'to-be matched' industrial fluid or formulation (which will be referred to as the 'real' fluids from here onwards), through the matching of rheological properties (the '*Finding Best Match*' operation); and interpolating within datasets of fluids from the same family, to propose a hypothetical model fluid system that may be a better match in terms of rheological properties, to the 'real' fluid in question (the '*Perform Interpolation*' operation). In addition, the MFST also has the capability to perform minor operations, such as the automated deletion of a given fluid dataset from the library (the '*Delete Library Entry*' operation) and clearing all previously inputted data, to allow new rheological data to be entered (the '*Clearing Old Data*' operation).

The '*Data Entry*' worksheet (Section 3.3) is the location where raw rheological flow curves of both 'model' and 'real' fluids are inputted, and where appropriate, the shear rate range of interest required for the '*Finding Best Match*' operation is entered. This worksheet is also the site where the majority of the operations are executed from, including the '*Standard Operations*' and the '*Library Additions*' operations. The '*Optimisation Fitting*' worksheet (Section 3.4) is the platform for the mathematical fitting of the raw, inputted rheological data of model fluids with different mathematical rheology models. The '*Library_Fitted*' worksheet (Section 3.5) is where the rheological and physical properties of model fluids are stored and acts as a rheology database, which is called upon when performing all of the operations found in the '*Data Entry*' worksheet (excluding the '*Clearing Old Data*' operation). The '*Top Matches_Graph*' worksheet (Section 3.6) is associated with the '*Finding Best Match*' operation. Upon execution of this operation, the library of fitted rheological data is copied across from the '*Library_Fitted*' worksheet to the '*Top Matches_Graph*' worksheet, and is sorted based on how closely matched the rheological properties of each model fluid is relative to the real fluid. The top 15 'best-matched' fluids are then plotted on a graph, along with the raw and fitted rheological data of the real fluid, to allow the user to visualise the quality of the suggested top matched fluids. This worksheet is also the location of where the '*Perform Interpolation*' operation can be executed from (when prompted). Physical and rheological properties of the top 15 'best-matched' fluids are copied across to the '*Top Matches_Details*' worksheet (Section 3.7), along with fluid formulation details of each fluid. The '*Best Interpolated Fluid*' worksheet (Section 3.8) is activated when the '*Perform Interpolation*' operation is executed. In this worksheet, all the rheological datasets of a given family of fluids are copied across from the library and the interpolation occurs by attempting to minimise the average absolute deviation when matching the rheological properties of model fluids to the real fluid. Finally, the '*MFST Instructions*' worksheet (Section 3.9) contains step-by-step instructions to aid the user with how to execute and

perform each of the operational features of the MFST. In the following selections, an in-depth discussion of each worksheet will take place (with relevant screengrabs from the MFST), including the description of a number of case studies to demonstrate the functionality of all of the MFST operations.

3.3 '*Data Entry*' worksheet

A screen-grab of the '*Data Entry*' worksheet can be seen in Figure 3.1, and is the location within the MFST where all operations, excluding the '*Perform Interpolation*' operation, can be executed from. Within this worksheet, there are five main sections: '*(1) Rheology Input*', '*(2) Shear Rate Range*', '*(3) Standard Operations*', '*(4) Library Additions*' and a shear stress vs. shear rate plot highlighting the rheological flow curve of the inputted fluid, along with various mathematical fits of the raw rheological data of the inputted fluid (where appropriate). The '*(1) Rheology Input*' section is the site within the worksheet whereby the user can enter in the raw rheological data of their inputted fluid, in the form of shear stress and associated shear rate values. This can be carried out with the intention of either performing mathematical fits on the data and adding fitted rheological data into the library through execution of the '*Adding Data to Library (Data & Fitting Thereof)*' operation, or finding the most appropriate model fluids in terms of matched rheological properties, through the use of the *'Finding Best Match*' operation. As stated in Figure 3.1, the user can input a maximum of 200 shear stress and shear rate values into this section. The inputted raw data is then plotted in the graph titled '*Rheological Flow Curve of Inputted Fluid*', in semi-log format, with shear rate on the *x*-axis (logarithmic format), and shear stress on the *y*-axis (linear format). It should be noted that the fits with the three mathematical models: the Herschel-Bulkley model, the Power Law model and the Casson model, will only be plotted once the '*Adding Data to Library (Data & Fitting Thereof)*' or the *'Finding Best Match*' operations are executed. The '*(2) Shear Rate Range*' section relates only to the '*Finding Best Match*' operation and therefore the cells relating to the upper and lower shear rate limit will be empty, unless this operation is executed, as discussed in Section 3.6.1. These values define the shear rate range over which the rheological matching process occurs, with shear stress and shear rate values of the inputted fluid outside of this range being overlooked. Inputting the upper and lower shear rate limits occurs through the use of a userform, which is incorporated into the '*Finding Best Match*' macro, and therefore if the user were to manually enter values into the two relevant cells, they would be disregarded when the operation is executed. The two sections: '*(3) Standard Operations*' and '*(4) Library Additions*' are where all of the individual operations, excluding the '*Perform Interpolation*' operation, are executed from. The operations have been separated into these two sections, depending on function. The two methods for adding rheological data into the '*Library_Fitted*' worksheet being grouped together in the '*(4) Library Additions*' section, whilst all other operations can be found in the '*(3) Standard Operations*' section.

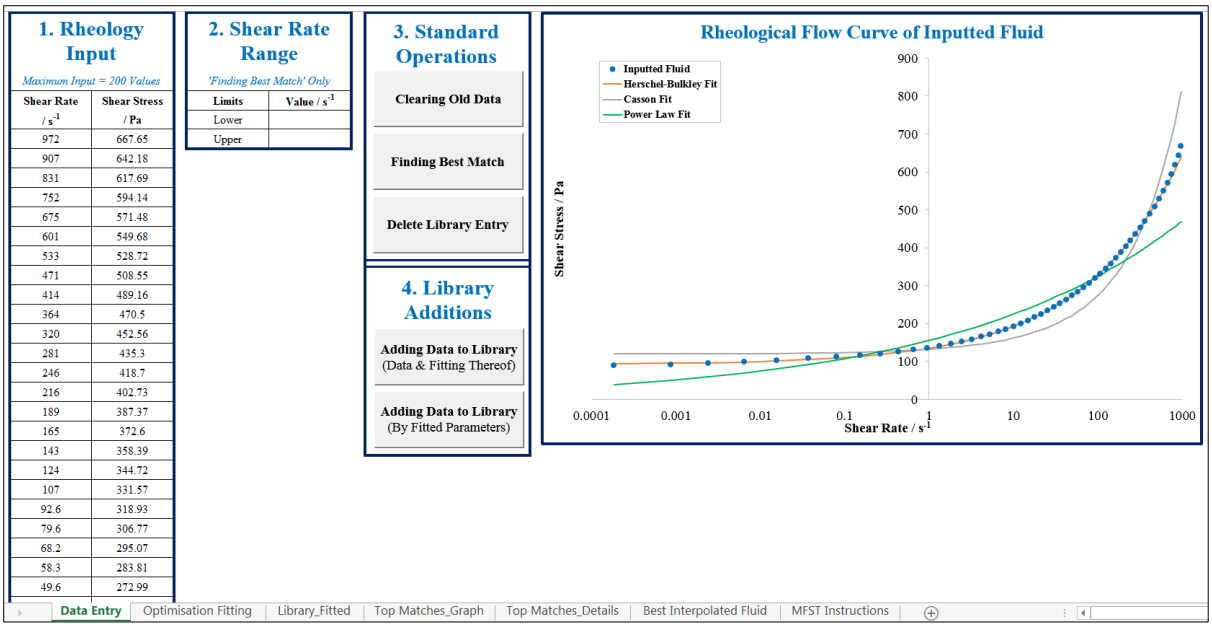

Figure 3.1. Screen-grab from the MFST showing the '*Data Entry*' worksheet. This is the location for the entry of raw rheological datasets, whilst all operations, excluding '*Perform Interpolation*', can also be executed from this worksheet.

3.3.1 Case Study 1: '*Clearing Old Data*' operation

The '*Clearing Old Data*' operation acts by deleting all old data from the '*Data Entry*', '*Optimisation Fitting*', '*Top Matches_Graph*', '*Top Matches_Details*' and '*Best Interpolated Fluid*' worksheets, allowing new rheological data to be entered into the '*(1) Rheology Input*' section of the '*Data Entry*' worksheet. When this operation is executed, the message box in Figure 3.2(a) is displayed, at which stage the user can abort the operation by activating the '*No*' button, or proceed with the operation as intended, resulting in all relevant data from the aforementioned worksheets being deleted. A message box is then displayed, informing the user that new data can now be entered into the '*(1) Rheology Input*' section (Figure 3.2(b)). The '*Adding Data to Library (Data & Fitting Thereof)*' and '*Finding Best Match*' operations are also programmed to delete any previous data that may affect the functionality of the operation in question.

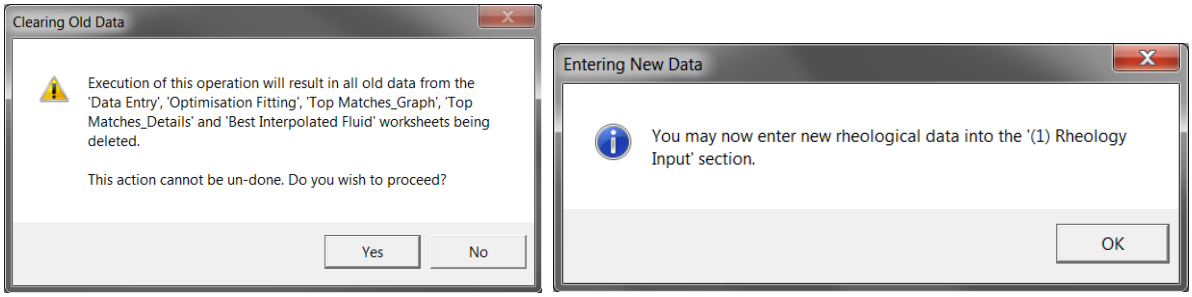

(a) **(b)**

Figure 3.2. (a) Through executing the '*Clearing Old Data*' operation, this warning message box is displayed to the user. (b) After the operation has run, this message box is displayed, informing the user that new data can now be entered into the '*(1) Rheology*' section of the worksheet.

3.4 '*Optimisation Fitting*' worksheet

Figure 3.3 shows screen-grabs from the MFST of the '*Optimisation Fitting*' worksheet, which is the site for the mathematical fitting of the raw rheological data. As mentioned in Section 3.3, mathematical fitting of the data is carried out with three mathematical models: the Power Law model (Eq. 1.8), the Herschel-Bulkley model (Eq. 1.11) and the Casson model (Eq. 1.13), with the equation for each model seen at the top of the screen-grab in Figure 3.3(a). Using each of these mathematical models, the nonlinear regression fitting process occurs using the Microsoft Excel Solver add-in function, whereby the Solver iteratively optimises the relevant fit of the raw data by minimising a particular value relating to the error, or difference, between the outputted fitted data and the raw data, by changing the various parameters relating to each model. In this case, at each given shear rate value, the difference between the associated raw and fitted shear stress values is calculated as a squared normalised error. The sum of squared normalised error value is then calculated using Eq. 3.1, and it is this value that is minimised by the Solver function as a means of optimising the various fits.

$$Sum\ Error = \sum \left(\frac{\tau_R - \tau_F}{\tau_R} \right)^2 \tag{3.1}$$

where τ_R is a given raw shear stress value and τ_F is the associated fitted shear stress value. The parameters that are varied as part of the optimisation process for the Herschel-Bulkley model are the yield stress, τ_y, the flow consistency index, K and the flow behaviour index, n; for the Power Law model are K and n; and for the Casson model are τ_y and constant plastic viscosity, η_{pl}. The 'average absolute deviation' (AAD) is another method for quantifying the deviation between the raw and fitted datasets, and is also calculated over the range of investigated values as part of the optimisation fitting process. As before, at every shear rate value, the absolute deviation of the raw and fitted shear stress values is calculated with respect to the raw shear stress value, and this is multiplied by 100 to convert the value into a percentage. Over the entire shear rate range investigated, the AAD value is then calculated, using Equation 3.2.

$$AAD = \left(\frac{\sum \left| \frac{(\tau_R - \tau_F)}{\tau_R} \right|}{s} \right) \times 100 \tag{3.2}$$

where s is the number of analysed data points, with all other terms having been previously defined. The AAD values for the resulting fits with each of the three mathematical models are calculated so the user is able to quantify the quality of the fits. Along with the visualisation of the fits presented in the shear stress-shear rate plots in both the '*Data Entry*' (as seen in Figure 3.1) and the '*Optimisation Fitting*' (Figure 3.3(b)) worksheets, when the '*Adding Data to Library (Data & Fitting Thereof)*' operation is executed, the user will be quoted the AAD values, along with the resulting R^2 values, of the three fits and will be prompted to add the data to the '*Library_Fitted*' worksheet via the mathematical fit that resulted in the lowest AAD value. Further discussion of this can be found in Section 3.5.1.

(a)

Mathematical Modelling of Data:

Herschel-Bulkley Model: $\tau = \tau_y + K\dot{\gamma}^n$

Casson Model: $(\tau)^{0.5} = (\tau_y)^{0.5} + (\eta_{pl}\dot{\gamma})^{0.5}$

Power Law Model: $\tau = K\dot{\gamma}^n$

(1) Herschel-Bulkley:

τ_y / Pa	91.81
K / Pa s^n	43.19
n	0.369
Sum Error	0.01168
AAD / %	0.9874
R^2	0.999

(2) Casson:

τ_y / Pa	119.92
η / Pa s	0.316
Sum Error	1.24048
AAD / %	13.3864
R^2	0.953

(3) Power Law:

K / Pa s^n	155.59
n	0.160
Sum Error	1.85349
AAD / %	15.3157
R^2	0.919

Raw Data:

Shear Rate / s^{-1}	Shear Stress / Pa
0.000185	88.394
0.000873	91.898
0.00242	95.542
0.00642	99.33
0.0158	103.27
0.0372	107.36
0.0806	111.62
0.154	116.05
0.268	120.65
0.436	125.43
0.651	130.4
0.962	135.57
1.34	140.95
1.83	146.54
2.44	152.35
3.23	158.39
4.13	164.67
5.24	171.2
6.62	177.99
8.17	185.04
10	192.38
12.2	200.01
14.8	207.94
17.8	216.18
21.3	224.76
25.4	233.67
30.2	242.93
35.7	252.56

(1) Herschel-Bulkley Fitted Data:

Shear Stress / Pa	Normalised Error^2	Deviation / %
93.62	0.0035	5.91
95.02	0.0012	3.39
96.48	0.0001	0.99
98.51	0.0001	0.83
101.15	0.0004	2.05
104.62	0.0006	2.55
108.86	0.0006	2.47
113.46	0.0005	2.23
118.37	0.0004	1.89
123.60	0.0002	1.46
128.67	0.0002	1.33
134.38	0.0001	0.87
139.92	0.0001	0.73
145.79	0.0000	0.51
151.84	0.0000	0.34
158.39	0.0000	0.00
164.71	0.0000	0.02
171.40	0.0000	0.12
178.58	0.0000	0.33
185.58	0.0000	0.29
192.84	0.0000	0.24
200.54	0.0000	0.26
208.58	0.0000	0.31
216.81	0.0000	0.29
225.37	0.0000	0.27
234.34	0.0000	0.29
243.74	0.0000	0.33
253.42	0.0000	0.34

(2) Casson Fitted Data:

Shear Stress / Pa	Normalised Error^2	Deviation / %
120.09	0.1286	35.86
120.28	0.0954	30.89
120.53	0.0684	26.15
120.91	0.0472	21.73
121.47	0.0311	17.63
122.31	0.0194	13.92
123.44	0.0112	10.59
124.80	0.0057	7.54
126.38	0.0023	4.75
128.19	0.0005	2.20
130.07	0.0000	0.26
132.31	0.0006	2.41
134.61	0.0020	4.50
137.17	0.0041	6.40
139.94	0.0066	8.15
143.09	0.0093	9.66
146.27	0.0125	11.18
149.78	0.0157	12.51
153.72	0.0186	13.64
157.72	0.0218	14.76
162.05	0.0249	15.77
166.82	0.0275	16.60
172.00	0.0299	17.28
177.53	0.0320	17.88
183.52	0.0337	18.35
190.05	0.0348	18.67
197.19	0.0355	18.83
204.83	0.0357	18.90

(3) Power Law Fitted Data:

Shear Stress / Pa	Normalised Error^2	Deviation / %
39.31	0.3084	55.53
50.39	0.2040	45.17
59.32	0.1437	37.91
69.35	0.0911	30.19
80.10	0.0503	22.44
91.87	0.0208	14.43
103.97	0.0047	6.85
115.32	0.0000	0.63
126.02	0.0020	4.45
136.23	0.0074	8.61
145.26	0.0130	11.39
154.63	0.0198	14.06
163.05	0.0246	15.68
171.39	0.0288	16.96
179.47	0.0317	17.80
187.71	0.0343	18.51
195.24	0.0345	18.57
202.83	0.0341	18.47
210.56	0.0335	18.30
217.77	0.0313	17.69
224.93	0.0286	16.92
232.21	0.0259	16.10
239.50	0.0230	15.18
246.68	0.0199	14.11
253.87	0.0168	12.95
261.13	0.0138	11.75
268.47	0.0110	10.51
275.75	0.0084	9.18

Data Entry | Optimisation Fitting | Library_Fitted | Top Matches_Graph | Top Matches_Details | Best Interpolated Fluid | MFST Instructions

(b)

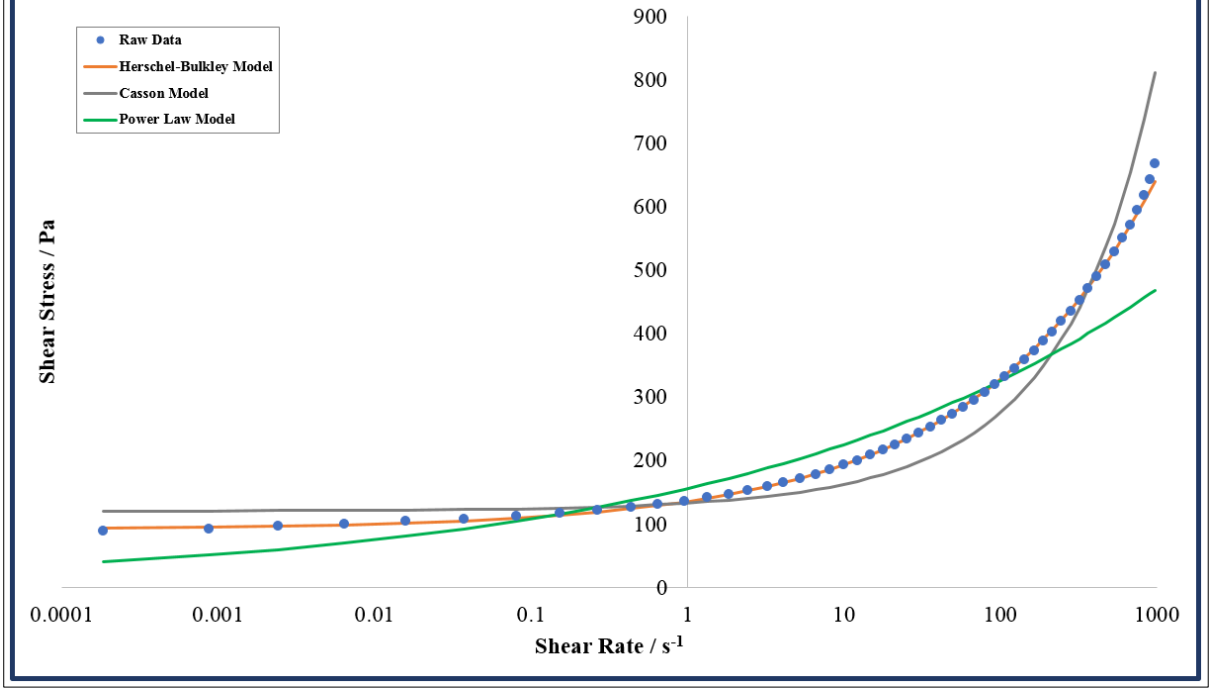

Figure 3.3. Screen-grabs from the MFST showing the '*Optimisation Fitting*' worksheet: (a) is the location in the MFST where the mathematical fitting process occurs through the use of the Microsoft Excel Solver function, whilst (b) is a plot of the resulting fitted data, along with the original raw rheological flow curve, also located in the '*Optimisation Fitting*' worksheet.

3.5 '*Library_Fitted*' worksheet

The '*Library_Fitted*' worksheet, seen in Figure 3.4, is a model fluid database, where the physical and rheological properties for almost 400 fluid systems are stored, with this data being presented in Chapter 2 and the Appendix. Figure 3.4(a) highlights the physical properties of each model fluid system (where model fluids can be either one- or two-compound systems, and the continuous phase, such as water, does not count as a compound), including details relating to how each fluid was formulated, whilst Figure 3.4(b) shows the fitted rheological data of the model fluids, including the type of mathematical model that was chosen for the fitting procedure, the errors associated with the optimised fit, namely the AAD and R^2 values, and the shear rate range over which the fitting process occurred. Ratings and rankings, where 1 is the lowest and 5 is the highest, for '*Health & Safety*', '*Expense*' and '*Opacity*' can also be seen in Figure 3.4(b), which gives the user an indication of the suitability of their chosen model fluid for the end application in question. As discussed in Chapters 1 and 2, it is important that model fluids are inexpensive, limited in reactivity and toxicity, and are easy to handle. The column titled '*Constant pH Fluid Set?*' refers to whether or not the fluid is part of a family of fluids in which the natural pH of the solutions were used, or if the pH of the solutions were manipulated through the addition of an external substance, such as a dilute NaOH (aq) solution.

(a)

Library of Fitted Rheological Data:

Compound 1 Name	Compound 2 Name	Compound 1 Mass Fraction / wt%	Compound 2 Mass Fraction / wt%	Fluid pH	Fluid Formulation Comments
Carbopol Ultrez 10	-	6.00	-	2.20	A bulk 6.00 wt% Carbopol Ultrez 10 (CU10, Lubrizol) solution was formulated (42 g CU10, 658 g deionised water). Solution was stirred with an overhead stirrer for 1.5 h. A 6.00 wt% CU10 sample was generated by taking 80 g of the bulk solution and adding 0 g of additional deionised water. Sample was then rheologically tested (vane) via a downward shear rate (SR) sweep and downward shear stress (SS) sweep, having undergone a pre-shear at 1200 /s for 15 seconds. Data here is from SS sweep.
Carbopol Ultrez 10	-	5.50	-	2.27	A bulk 6.00 wt% Carbopol Ultrez 10 (CU10, Lubrizol) solution was formulated (42 g CU10, 658 g deionised water). Solution was stirred with an overhead stirrer for 1.5 h. A 3.25 wt% CU10 sample was generated by taking 43.33 g of the bulk solution and adding 36.67 g of additional deionised water. Sample was then rheologically tested (vane) via a downward shear rate (SR) sweep and downward shear stress (SS) sweep, having undergone a pre-shear at 1200 /s for 15 seconds. Data here is from SS sweep.
Carbopol Ultrez 10	-	5.00	-	2.29	A bulk 6.00 wt% Carbopol Ultrez 10 (CU10, Lubrizol) solution was formulated (42 g CU10, 658 g deionised water). Solution was stirred with an overhead stirrer for 1.5 h. A 6.00 wt% CU10 sample was generated by taking 80 g of the bulk solution and adding 0 g of additional deionised water. Sample was then rheologically tested (vane) via a downward shear rate (SR) sweep and downward shear stress (SS) sweep, having undergone a pre-shear at 1200 /s for 15 seconds. Data here is from SS sweep.
Carbopol Ultrez 10	-	4.50	-	2.35	A bulk 6.00 wt% Carbopol Ultrez 10 (CU10, Lubrizol) solution was formulated (42 g CU10, 658 g deionised water). Solution was stirred with an overhead stirrer for 1.5 h. A 3.25 wt% CU10 sample was generated by taking 43.33 g of the bulk solution and adding 36.67 g of additional deionised water. Sample was then rheologically tested (vane) via a downward shear rate (SR) sweep and downward shear stress (SS) sweep, having undergone a pre-shear at 1200 /s for 15 seconds. Data here is from SS sweep.
Carbopol Ultrez 10	-	4.00	-	2.39	A bulk 6.00 wt% Carbopol Ultrez 10 (CU10, Lubrizol) solution was formulated (42 g CU10, 658 g deionised water). Solution was stirred with an overhead stirrer for 1.5 h. A 6.00 wt% CU10 sample was generated by taking 80 g of the bulk solution and adding 0 g of additional deionised water. Sample was then rheologically tested (vane) via a downward shear rate (SR) sweep and downward shear stress (SS) sweep, having undergone a pre-shear at 1200 /s for 15 seconds. Data here is from SS sweep.
Carbopol Ultrez 10	-	3.75	-	2.44	A bulk 6.00 wt% Carbopol Ultrez 10 (CU10, Lubrizol) solution was formulated (42 g CU10, 658 g deionised water). Solution was stirred with an overhead stirrer for 1.5 h. A 3.25 wt% CU10 sample was generated by taking 43.33 g of the bulk solution and adding 36.67 g of additional deionised water. Sample was then rheologically tested (vane) via a downward shear rate (SR) sweep and downward shear stress (SS) sweep, having undergone a pre-shear at 1200 /s for 15 seconds. Data here is from SS sweep.
Carbopol Ultrez 10	-	3.50	-	2.42	A bulk 6.00 wt% Carbopol Ultrez 10 (CU10, Lubrizol) solution was formulated (42 g CU10, 658 g deionised water). Solution was stirred with an overhead stirrer for 1.5 h. A 6.00 wt% CU10 sample was generated by taking 80 g of the bulk solution and adding 0 g of additional deionised water. Sample was then rheologically tested (vane) via a downward shear rate (SR) sweep and downward shear stress (SS) sweep, having undergone a pre-shear at 1200 /s for 15 seconds. Data here is from SS sweep.
Carbopol Ultrez 10	-	3.25	-	2.49	A bulk 6.00 wt% Carbopol Ultrez 10 (CU10, Lubrizol) solution was formulated (42 g CU10, 658 g deionised water). Solution was stirred with an overhead stirrer for 1.5 h. A 3.25 wt% CU10 sample was generated by taking 43.33 g of the bulk solution and adding 36.67 g of additional deionised water. Sample was then rheologically tested (vane) via a downward shear rate (SR) sweep and downward shear stress (SS) sweep,

Data Entry | Optimisation Fitting | Library_Fitted | Top Matches_Graph | Top Matches_Details | Best Interpolated Fluid | MFST Instructions

(b)

Data From Experiment or Literature?	Health & Safety Rating	Expense Ranking	Opacity Ranking	Type of Fit	Herschel-Bulkley Yield Stress, τ_y / Pa	Flow Consistency Index, K / Pa s^n	Flow Behaviour Index, n	Infinite Viscosity Plateau / Pa s	Casson Yield Stress, τ_y / Pa	Optimised Fit Average Absolute Deviation / %	Optimised Fit R^2 Value	Shear Rate Range of Optimised Fit / s^{-1}	Constant pH Fluid Set?
Experiment	1	1	4	Herschel-Bulkley	364.23	72.16	0.39	-	-	0.72	0.999	0.0184-971	Yes
Experiment	1	1	4	Herschel-Bulkley	237.68	67.80	0.36	-	-	1.06	0.998	0.0181-743	Yes
Experiment	1	1	4	Herschel-Bulkley	183.87	53.52	0.36	-	-	0.86	0.999	0.00997-876	Yes
Experiment	1	1	4	Herschel-Bulkley	123.06	35.96	0.38	-	-	0.88	0.999	0.0181-866	Yes
Experiment	1	1	4	Herschel-Bulkley	66.28	20.80	0.40	-	-	1.15	0.998	0.0122-843	Yes
Experiment	1	1	4	Herschel-Bulkley	40.72	15.19	0.41	-	-	1.07	0.999	0.0126-740	Yes
Experiment	1	1	3	Herschel-Bulkley	34.72	12.53	0.41	-	-	0.96	0.999	0.0206-659	Yes
Experiment	1	1	3	Herschel-Bulkley	20.03	8.10	0.43	-	-	1.57	0.997	0.0132-507	Yes

y | Optimisation Fitting | Library_Fitted | Top Matches_Graph | Top Matches_Details | Best Interpolated Fluid | MFST Instructions

Figure 3.4. Screen-grabs from the MFST showing the '*Library_Fitted*' worksheet: (a) shows information relating to the physical properties of the fluids that have been entered into the library (including fluid formulation details), whilst (b) highlights the details of the mathematical fitting of the fluids and the associated deviations (or errors) of the fits.

3.5.1 Case Study 2: '*Adding Data to Library (Data & Fitting Thereof)*' operation

When the user inputs rheological data into the '*(1) Rheology Input*' section in the '*Data Entry*' worksheet (Figure 3.1) and executes the '*Adding Data to Library (Data & Fitting Thereof)*', an initial warning message informing the user to be wary of 'good' vs 'bad' rheological data and the necessity for the data to have been acquired using vane rheometrical geometry, is displayed (discussion relating to why the vane geometry must be used for the rheological characterisation of both 'real' and model fluids can be found in Section 2.4). A userform (Figure 3.5) is then shown, prompting the user to enter in details relating to the fluid's physical properties (including the ratings and rankings of important factors relating to the fluid type) and the experimental procedure used in the formulation of the fluid. If the user wishes to abort the operation at the stage, the '*Cancel*' button can be used. In the example in Figure 3.5, an aqueous 'Carbopol Ultrez 21 (CU21, 5.00 wt%, pH 2.51)' solution was used as the test fluid, with the fitting process occurring over the shear rate range, $\dot{\gamma}$ = 0.000185-972 s^{-1}. In this example, due to the test fluid being a one-compound system, the entry boxes relating to the '*Compound 2*' name and mass fraction have been left blank. Having entered in the fluid details, the macro finds the next empty row in the '*Library_Fitted*' worksheet (Figure 3.4) and inputs the data into the relevant columns. After this, the raw rheological data then undergo the optimised fitting procedure with the three mathematical models, as outlined in Section 3.4.

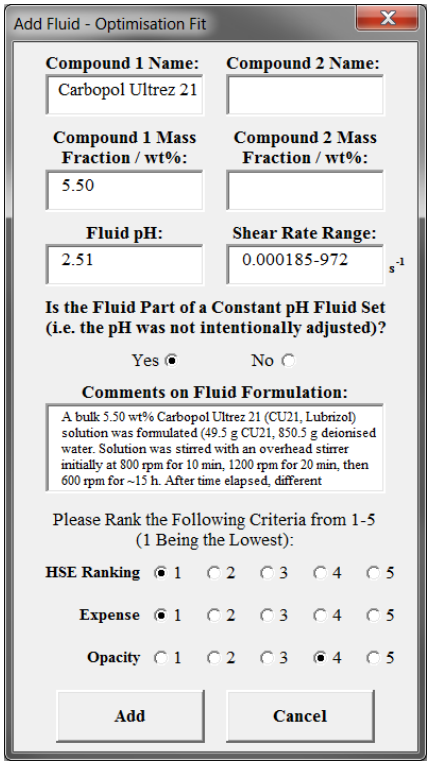

Figure 3.5. When the user adds the raw rheological data of a fluid to the '*Library_Fitted*' worksheet via the '*Adding Data to Library (Data & Fitting Thereof)*' operation, this userform is displayed, allowing the identity and physical properties of the fluid, along with the shear rate range over which the fit is occurring, various rankings and details of how the fluid was formulated, to be entered.

As mentioned in Section 3.4, after the optimised fitting process is complete, the operation will output a message box to the user, quoting the AAD and R^2 values associated with each of the mathematical fits. The user will then be prompted to add the fitted data to the '*Library Fitted*' worksheet via the mathematical fit that resulted in the lowest AAD value, with all three fitted shear stress-shear rate curves, along with the raw flow curve, being displayed in the plots in the '*Data Entry*' (Figure 3.1) and '*Optimisation Fitting*' (Figure 3.3(a)) worksheets. The message box in Figure 3.6(a) shows an example of this, whereby the Herschel-Bulkley model produced the best fit (AAD = 0.99%, R^2 = 0.999), followed by the Casson model (AAD = 13.39%, R^2 = 0.953), with the Power Law model resulting in the worst fit (AAD = 15.32%, R^2 = 0.919). In this example, the user is therefore prompted to add the data to the library via the Herschel-Bulkley model. If the user accepts the recommended mathematical fit, the fitted parameters, along with the type of fit, shear rate range of fit and associated AAD and R^2 values will be automatically inputted into the relevant sections within the '*Library_Fitted*' worksheet and the choice of mathematical fit will be confirmed to the user via the message box interface. However, the user can decide not to accept the recommended fit and opt to add the data into the '*Library_Fitted*' worksheet via a model that produced a worse fit. The model that produces a fit with the second lowest AAD value will be suggested next, and if this option is rejected by the user, adding data into the '*Library_Fitted*' worksheet via the model with the poorest fit will then be an option. If the user chooses not into add the data to the '*Library_Fitted*' worksheet via any of the mathematical models,

a message box (as seen in Figure 3.6(b)) is displayed asking the user to confirm that they do not want to add the fluid to the '*Library_Fitted*' worksheet via any of the mathematical models and therefore the process will be terminated. If the user decides that they would like to add their fluid to the library, a message box notifying the user to re-execute the '*Adding Data to Library (Data & Fitting Thereof)*' operation is displayed, otherwise, a message box confirming the termination of the process will be seen.

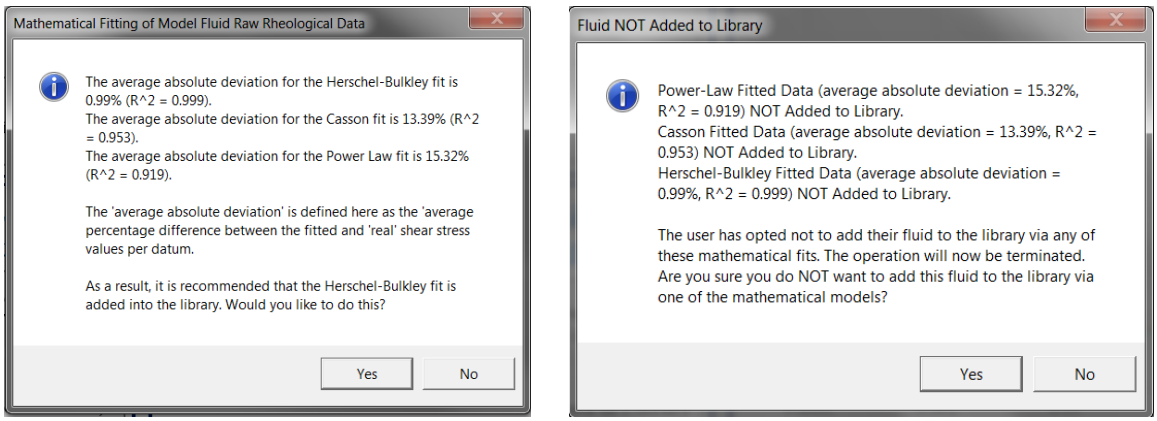

(a) **(b)**

Figure 3.6. (a) Message box quantifying the deviations (AAD and R^2) between the raw and fitted data for each mathematical model, and prompting the user to add the user to add the data to the '*Library_Fitted*' worksheet via the mathematical model that produces the best fit (in terms of lowest AAD), which in this example is the Herschel-Bulkley model. (b) Message box that is displayed if the user has opted not to add their data to the library via any of the mathematical fits.

In the example shown previously, the Herschel-Bulkley model provided a good fit of the raw rheological data, whilst the Casson and Power Law models produced relatively poor fits. If all three of the mathematical models result in poor fits, to the extent whereby AAD $\geq$ 7% and $R^2 < 0.95$, the message box seen in Figure 3.7 is displayed, informing the user that it is not recommended that any of the fitted data are added to the '*Library_Fitted*' worksheet. The user is given the option of proceeding with the addition if they choose to do so, which would then result in a similar message box to the one seen in Figure 3.6(a) being displayed. However, if the user opts to follow the suggestion of not adding the data to the '*Library_Fitted*' worksheet, the operation will be terminated and a message box confirming this will be displayed. The values of AAD = 7% and $R^2 = 0.95$ were selected based on numerous independent trials and were deemed as an appropriate threshold for what is classed as being 'acceptable' and 'unacceptable' fits. It was imperative to include both AAD and R^2 in this threshold definition, because in some circumstances, a given fit may produce a decent AAD value and a poor R^2 value, and vice versa. For example, in the case where a small sample of data points are being fitted, the resulting fit can produce an acceptable AAD value but a very poor R^2 value. Taking the case of a very weakly shear-thinning fluid as an example, the AAD value of the fits may be distorted by the noticeable deviations between the raw and fitted data in the low shear rate range, hence resulting in large AAD values. However, the R^2 definition

may produce values > 0.99 for the same fit. Therefore, including AAD and R^2 into the threshold definition allows for differentiation between potentially biased results and actual poor fits to be deduced.

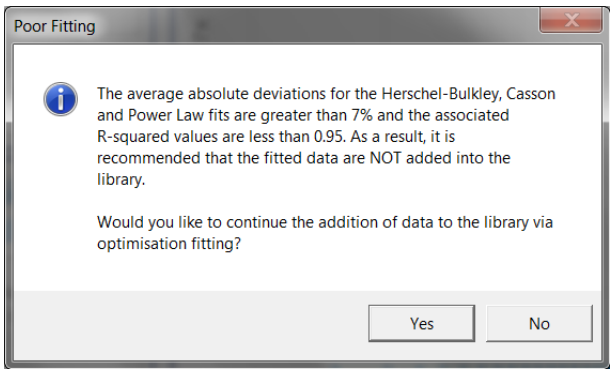

Figure 3.7. Message box displayed to the user when the fits of the data using from each mathematical model are particularly poor. In this work, the threshold defining the boundary between an acceptable and unacceptable fit is AAD ≥ 7% and $R^2 < 0.95$.

3.5.2 Case Study 3: '*Adding Data to Library (By Fitted Parameters)*' operation

Data can also be added into the '*Library_Fitted*' worksheet using the '*Adding Data to Library (By Fitted Parameters)*' operation. This operation should be used if the fitted parameters of the model fluid system are already known, for example if data have been acquired from a literature source. It is recommended that instead of solely relying on data from the literature, the user follows the formulation protocol from the literature to formulate the fluid of interest, and then uses the same rheological measurement procedure to attain the rheological properties of the fluid directly. When the operation is executed, a message box stating this is displayed, asking the user if they wish to continue with their library addition. If the user chooses to proceed, a message box is displayed warning the user to enter in either Herschel-Bulkley or Casson parameters, but not both, because doing so will result in the operation being aborted. After this, the userform shown in Figure 3.8 is presented, where the physical properties and the rheological parameters of the fluid can be entered, including details of how the fluid was formulated or the literature source for where the fluid formulation details can be found (for example, a DOI or title of the article could be entered). If the user wishes to enter in Power Law parameters, then the flow consistency index, K and flow behaviour index, n values should be entered in the '*Herschel-Bulkley Parameters*' section. The '*Yield Stress'* entry box can either remain blank, or "-" or "0" can be entered. As with the userform associated with the '*Adding Data to Library (Data & Fitting Thereof)*' operation, the user can abort the operation through activating the '*Cancel*' button. From the example in Figure 3.8, a 'Carbopol Ultrez 10 (0.10 wt%)/glycerol (15.00 wt%) (pH 6.63)' solution was used as the test fluid. As seen in the userform, the fitted data were acquired using the Herschel-Bulkley model, over the shear-rate range of 0.178-934 s^{-1}, therefore the entry boxes relating to the Casson model were left blank. When entry into the userform is complete, the data are added into the '*Library Fitted*' worksheet in a similar manner as the '*Adding Data to Library (Data & Fitting Thereof)*'

operation, however, the relevant cells relating to errors of the fit are denoted with "-". Addition of the data to the '*Library Fitted*' worksheet is then confirmed via a message box. Under the column '*Data From Experiment or Literature*', when fluids are added using the '*Adding Data to Library (Data & Fitting Thereof)*' operation, the relevant cell will show '*Experiment*', whereas '*Literature*' will be entered into this cell if the '*Adding Data to Library (By Fitted Parameters)*' was executed.

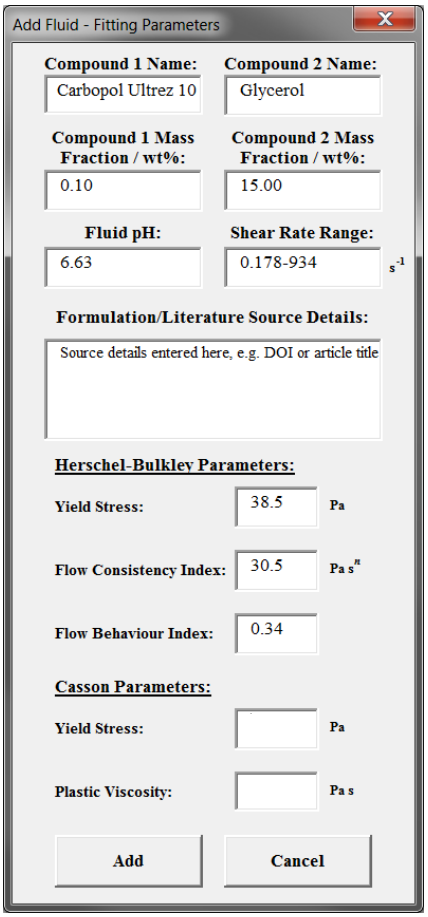

Figure 3.8. Userform displayed to the user when the '*Adding Data to Library (By Fitting Parameters)*' operation has been executed. This userform allows the user to enter in the identity of the fluid, along with the physical and rheological properties of the fluid, the shear rate range over which the fit is valid, and details of how the fluid was formulated or the literature source where fluid formulation comments can be ascertained.

3.5.3 Case Study 4: '*Delete Library Entry*' operation

Data can be deleted from the '*Library_Fitted*' worksheet through the use of the '*Delete Library Entry*' operation. Due to the methods used in the programming process, it is imperative that if the user wishes to delete an entry from the '*Library_Fitted*' worksheet, they do so using this operation and not by manually deleting the data. Through execution of the '*Delete Library Entry*' operation, the userform in Figure 3.9 can be seen and the physical properties of the 'to-be-deleted' fluid system can be entered. In

this example, the fluid from '*Case Study 3*' will be deleted from the library and therefore details relating to the 'Carbopol Ultrez 10 (0.10 wt%)/glycerol (15.00 wt%) (pH 6.63)' solution have been entered. If the fluid is a one-compound system, the entry boxes relating to '*Compound 2*' can be left blank, with the user being notified of this through a message box before the userform in Figure 3.9 is displayed. As before, the operation can be terminated at this stage through operating the '*Cancel*' button. By activating the '*Delete*' button, the entry is found within the '*Library_Fitted*' worksheet and the user is asked to confirm the deletion of the entry, after which the worksheet is formatted back to the original presentation (alternating blue and white rows), as seen Figure 3.4. If the entry is not found within the '*Library_Fitted*' worksheet, the user will be notified of this using a message box and the operation is then terminated.

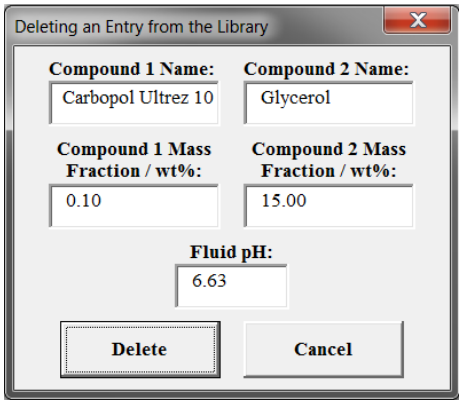

Figure 3.9. When the '*Delete Library Entry*' operation is executed, this userform is displayed, allowing the user to enter in the identity and physical properties of fluid entry they wish to be deleted from the '*Library_Fitted*' worksheet.

3.6 '*Top Matches_Graph*' worksheet

The '*Top Matches_Graph*' worksheet can be seen in Figure 3.10, and is the worksheet within the MFST associated with the '*Finding Best Match*' operation, whereby the rheological properties all of the model fluids stored in the '*Library_Fitted*' worksheet are compared to raw rheological flow curve of the 'real' fluid, with the 'best-matched' model fluid system, in the sense of rheological similitude to the 'real' fluid being determined, and this information being outputted through a message box to the user. This worksheet, in conjunction with the '*Finding Best Match*' operation, is the most important feature of the MFST. Figure 3.10(a) shows the plot that would result after the '*Finding Best Match*' operation has occurred, with the 15 top 'best-matched' fluids being plotted on the some graph, along with the raw and fitted rheological data of the 'real' fluid. As before, fitting occurred using the Herschel-Bulkley, Casson and Power Law models, with the model producing the most accurate fit being plotted. The checkboxes, under the column heading '*Include in Plot?*' relate to each of the top 15 'best-matched' fluids, with checkbox '1' referring to the 'best-matched' model fluid, checkbox '2' referring to the 'second best-matched' model fluid, and so on. If these checkboxes become unmarked, the fitted flow curve of the associated model fluid system

will be hidden from the plot, whilst marking the box will result in the flow curve reappearing on the plot, allowing the user to be selective with which of the top 15 'best-matched' fluids feature in the plot. In tabular format, Figure 3.10(b) shows the physical properties of the top 15 'best-matched' model fluids, the type of fit for each model fluid system, the AAD of the fitted flow curve from the 'real' flow curve for each model fluid and the resulting fitted shear rate-shear stress rheological data for each system. The R^2 value from the comparison of the 'best-matched' model fluid flow curve to that of the 'real' fluid can also be seen. Figure 3.10(c) and (d) show the location within the worksheet where the details (both physical and rheological) of all model fluids are copied across from the '*Library_Fitted*' worksheet and where the process behind the '*Finding Best Match*' operation occurs (see Section 3.6.1 for a more in-depth discussion of this operation and its functions). Along with the physical details of the model fluids, Figure 3.10(c) highlights the location of the '*Perform Interpolation*' operation in the worksheet, which should only be executed when prompted by the MFST during the '*Finding Best Match*' operation (further discussion of this can be found in Section 3.8.1). Figure 3.10(d) shows the rheological properties of the model fluid systems, and the associated fitted shear rate-shear stress rheological data over the pre-defined shear rate range required for the matching process. The fitted parameters (Herschel-Bulkley parameters in this example) and resulting AAD and R^2 values for the 'real' fluid can also be seen in Figure 3.10(d), along with the associated fitted shear rate-shear stress rheological data.

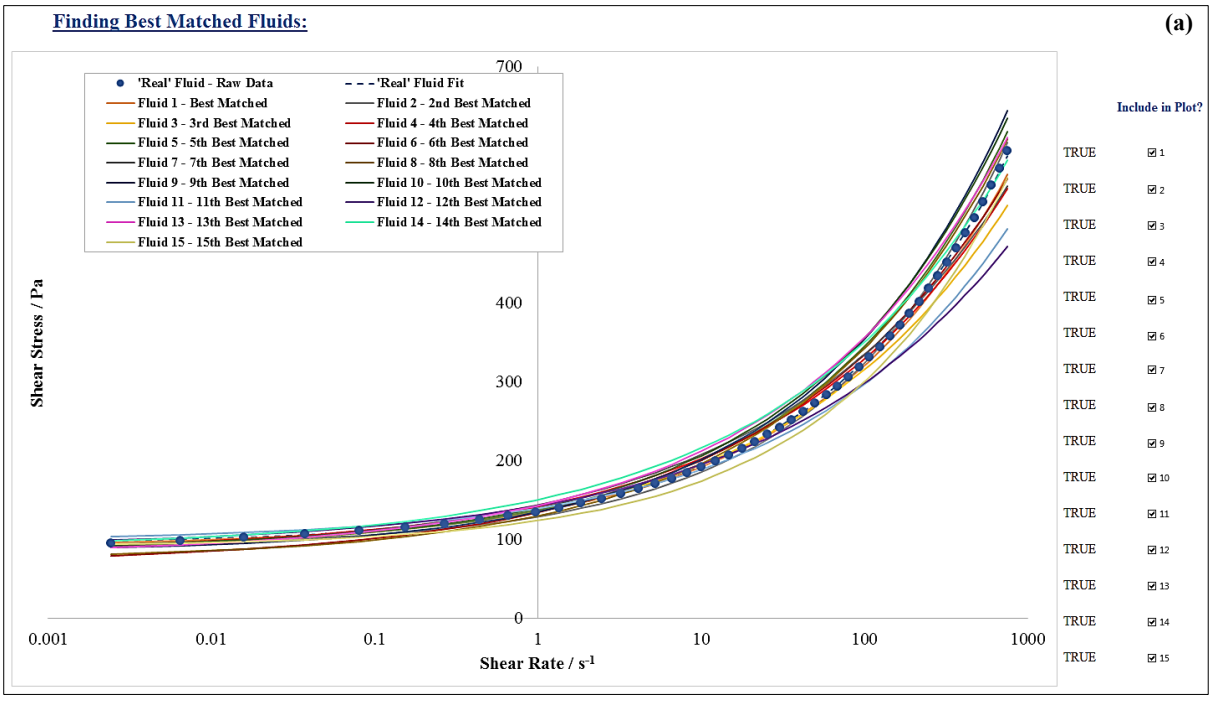

(b)

Best-Matched Fluid and 'Real' Fluid - R^2 value: 1.000

Top 15 'Best-Matched' Fluids - Fitted Data:

Best-Matched Ranking	Compound 1 Name	Compound 2 Name	Compound 1 Mass Fraction / wt%	Compound 2 Mass Fraction / wt%	Fluid pH	Type of Fit	Average Absolute Deviation of Match / %	Shear Rate / s^{-1}	0.00242	0.00642
1	Carbopol Ultrez 30	-	0.10	-	8.04	Herschel-Bulkley	1.50	Shear Stress / Pa	96.800	98.923
2	Carbopol 980	Glycerol	0.15	45.00	7.78	Herschel-Bulkley	2.76	Shear Stress / Pa	94.530	96.218
3	Carbopol Ultrez 10	-	0.15	-	6.68	Herschel-Bulkley	3.58	Shear Stress / Pa	91.790	94.634
4	Carbopol Ultrez 10	-	0.15	-	8.58	Herschel-Bulkley	3.59	Shear Stress / Pa	93.408	96.494
5	Carbopol Ultrez 30	1 wt% NaCl (aq)	0.15	1.63	7.36	Herschel-Bulkley	4.30	Shear Stress / Pa	93.505	95.892
6	Carbopol Ultrez 21	Glycerol	0.13	10.00	6.66	Herschel-Bulkley	4.38	Shear Stress / Pa	79.435	83.065
7	Carbopol Ultrez 10	-	0.15	-	8.94	Herschel-Bulkley	4.73	Shear Stress / Pa	90.720	94.232
8	Carbopol Ultrez 21	Glycerol	0.13	23.75	6.76	Herschel-Bulkley	5.18	Shear Stress / Pa	81.255	84.093
9	Carbopol Ultrez 30	Glycerol	0.08	15.00	7.26	Herschel-Bulkley	6.56	Shear Stress / Pa	89.439	91.891
10	Carbopol Ultrez 30	1 wt% NaCl (aq)	0.15	1.25	7.37	Herschel-Bulkley	6.74	Shear Stress / Pa	93.110	95.712
11	Carbopol Ultrez 10	-	0.20	-	4.92	Herschel-Bulkley	6.93	Shear Stress / Pa	104.218	106.272
12	Carbopol 980	1 wt% NaCl (aq)	0.20	1.25	7.41	Herschel-Bulkley	7.16	Shear Stress / Pa	99.119	102.029
13	Carbopol Ultrez 10	Glycerol	0.15	15.00	6.30	Herschel-Bulkley	7.31	Shear Stress / Pa	90.202	93.463
14	Carbopol Ultrez 10	-	0.15	-	7.45	Herschel-Bulkley	7.40	Shear Stress / Pa	98.014	101.373
15	Carbopol Ultrez 30	-	2.00	-	2.91	Herschel-Bulkley	7.78	Shear Stress / Pa	93.711	95.147

ntry | Optimisation Fitting | Library_Fitted | **Top Matches_Graph** | Top Matches_Details | Best Interpolated Fluid | MFST Instructions

(c)

Perform Interpolation

ONLY PRESS THIS BUTTON WHEN PROMPTED!!

Perform Interpolation

Fluids From Library:

Constant pH Fluid Set?	Compound 1 Name	Compound 2 Name	Compound 1 Mass Fraction / wt%	Compound 2 Mass Fraction / wt%	Fluid pH	Data From Experiment or Literature?	Health & Safety Rating	Expense Rating	Opacity Rating
No	Carbopol Ultrez 30	-	0.10	-	8.04	Experiment	1	1	1
Yes	Carbopol 980	Glycerol	0.15	45.00	7.78	Experiment	1	1	1
No	Carbopol Ultrez 10	-	0.15	-	6.68	Experiment	1	1	1
No	Carbopol Ultrez 10	-	0.15	-	8.58	Experiment	1	1	1
Yes	Carbopol Ultrez 30	1 wt% NaCl (aq)	0.15	1.63	7.36	Experiment	1	1	1
Yes	Carbopol Ultrez 21	Glycerol	0.125	10.00	6.66	Experiment	1	1	1
No	Carbopol Ultrez 10	-	0.15	-	8.94	Experiment	1	1	1
Yes	Carbopol Ultrez 21	Glycerol	0.125	23.75	6.76	Experiment	1	1	1
Yes	Carbopol Ultrez 30	Glycerol	0.075	15.00	7.26	Experiment	1	1	1
Yes	Carbopol Ultrez 30	1 wt% NaCl (aq)	0.15	1.25	7.37	Experiment	1	1	1
No	Carbopol Ultrez 10	-	0.20	-	4.92	Experiment	1	1	1
Yes	Carbopol 980	1 wt% NaCl (aq)	0.20	1.25	7.41	Experiment	1	1	1
Yes	Carbopol Ultrez 10	Glycerol	0.15	15.00	6.30	Experiment	1	1	1
No	Carbopol Ultrez 10	-	0.15	-	7.45	Experiment	1	1	1
Yes	Carbopol Ultrez 30	-	2.00	-	2.91	Experiment	1	1	2
Yes	Carbopol 980	1 wt% NaCl (aq)	0.20	0.63	7.46	Experiment	1	1	1
Yes	Carbopol 980	Glycerol	0.15	30.00	7.67	Experiment	1	1	1
No	Carbopol 980	-	0.20	-	11.01	Experiment	1	1	1
No	Carbopol 980	-	0.20	-	5.37	Experiment	1	1	1
Yes	Carbopol Ultrez 30	Glycerol	0.075	30.00	7.30	Experiment	1	1	1
Yes	Carbopol Ultrez 10	-	4.50	-	2.35	Experiment	1	1	4

Data Entry | Optimisation Fitting | Library_Fitted | **Top Matches_Graph** | Top Matches_Details | Best Interpolated Fluid | MFST Instructions

(d)

Mathematically Fitted Data of 'To-Be-Matched' Fluid:

τ_y / Pa	93.93	AAD / %	0.3756
K / Pa s^n	41.88	R^2	0.9999
n	0.372		

Raw Data of 'To-Be-Matched' Fluid:

Shear Rate / s^{-1}	0.00242	0.00642	0.0158	0.0372
Shear Stress / Pa	95.542	99.33	103.27	107.36

Type of Fit	H-B Yield Stress, τ_y / Pa	Flow Consistency Index, K / Pa s^n	Flow Behaviour Index, n	Constant Plastic Viscosity / Pa s	Casson Yield Stress, τ_y / Pa	Average Absolute Deviation of Match / %	Shear Rate / s^{-1}	0.00242	0.00642	0.0158	0.0372
Herschel-Bulkley	91.73	43.94	0.36	-	-	1.503	**Shear Stress / Pa**	96.800	98.923	101.663	105.232
Herschel-Bulkley	90.90	38.39	0.39	-	-	2.760	**Shear Stress / Pa**	94.530	96.218	98.467	101.481
Herschel-Bulkley	84.00	53.22	0.32	-	-	3.583	**Shear Stress / Pa**	91.790	94.634	98.173	102.624
Herschel-Bulkley	84.82	57.21	0.32	-	-	3.589	**Shear Stress / Pa**	93.398	96.484	100.310	105.106
Herschel-Bulkley	87.80	49.39	0.36	-	-	4.303	**Shear Stress / Pa**	93.505	95.892	98.974	102.987
Herschel-Bulkley	68.90	65.55	0.30	-	-	4.375	**Shear Stress / Pa**	79.435	83.065	87.517	93.042
Herschel-Bulkley	80.45	63.46	0.30	-	-	4.717	**Shear Stress / Pa**	90.765	94.294	98.614	103.966
Herschel-Bulkley	74.05	56.01	0.34	-	-	5.183	**Shear Stress / Pa**	81.255	84.093	87.697	92.315
Herschel-Bulkley	83.64	51.18	0.36	-	-	6.561	**Shear Stress / Pa**	89.439	91.891	95.066	99.212
Herschel-Bulkley	86.78	53.03	0.35	-	-	6.743	**Shear Stress / Pa**	93.110	95.712	99.053	103.383
Herschel-Bulkley	99.05	40.80	0.34	-	-	6.927	**Shear Stress / Pa**	104.218	106.272	108.886	112.243
Herschel-Bulkley	90.58	52.19	0.30	-	-	7.160	**Shear Stress / Pa**	99.119	102.029	105.588	109.992
Herschel-Bulkley	81.44	61.78	0.32	-	-	7.314	**Shear Stress / Pa**	90.202	93.463	97.541	102.693
Herschel-Bulkley	88.61	61.97	0.31	-	-	7.399	**Shear Stress / Pa**	98.014	101.373	105.528	110.729
Herschel-Bulkley	90.69	33.37	0.40	-	-	7.776	**Shear Stress / Pa**	93.711	95.147	97.072	99.670

Data Entry | Optimisation Fitting | Library_Fitted | **Top Matches_Graph** | Top Matches_Details | Best Interpolated Fluid | MFST Instructions

Figure 3.10. Screen-grabs from the '*Top Matches*' worksheet, demonstrating: (a) the shear rate-shear stress plot of the 'real' fluid and the top 15 'best-matched' model fluids; (b) the table of physical and rheological properties of the top 15 'best-matched' model fluids; (c) and (d) the physical properties of all model fluids from the library, along with the calculated rheological properties over the pre-defined shear rate range of interest used in the '*Finding Best Match*' process.

3.6.1 Case Study 5: '*Finding Best Match*' operation

As with the majority of the operations in the MFST, the '*Finding Best Match*' operation is located in and executed from the '*Data Entry*' worksheet. Before performing the operation, the user enters the rheological properties of the 'real' fluid into the '*(1) Rheology Input*' section within the worksheet, making sure that the data were acquired using the vane geometry and that only data deemed as being 'good' are included. A description of what constitutes as 'good' and 'bad' rheological data can be found in the '*MFST Instructions*' worksheet. After successfully inputting the rheological data, the '*Finding Best Match*' operation is executed. The message box seen in Figure 3.11(a) is displayed, informing the user of the shear rate range of the inputted fluid, before the userform in Figure 3.11(b) is presented, allowing the user to enter the shear rate range over which they would like to find a 'best-matched' model fluid. The shear rate range of interest may vary depending on the application, however, the selected range must be within the original shear rate range of the inputted 'real' fluid. If values outside of this range are chosen, the operation will be terminated and the user will have to start the process again. Having entered an appropriate shear rate range for the '*Finding Best Match*' process into the userform, the selected values are displayed in the relevant cells in the '*(2) Shear Rate Range*' section of the '*Data Entry*' worksheet and a message box is displayed, informing the user of their chosen shear rate range for the '*Finding Best Match*' process, as seen in Figure 3.11(c).

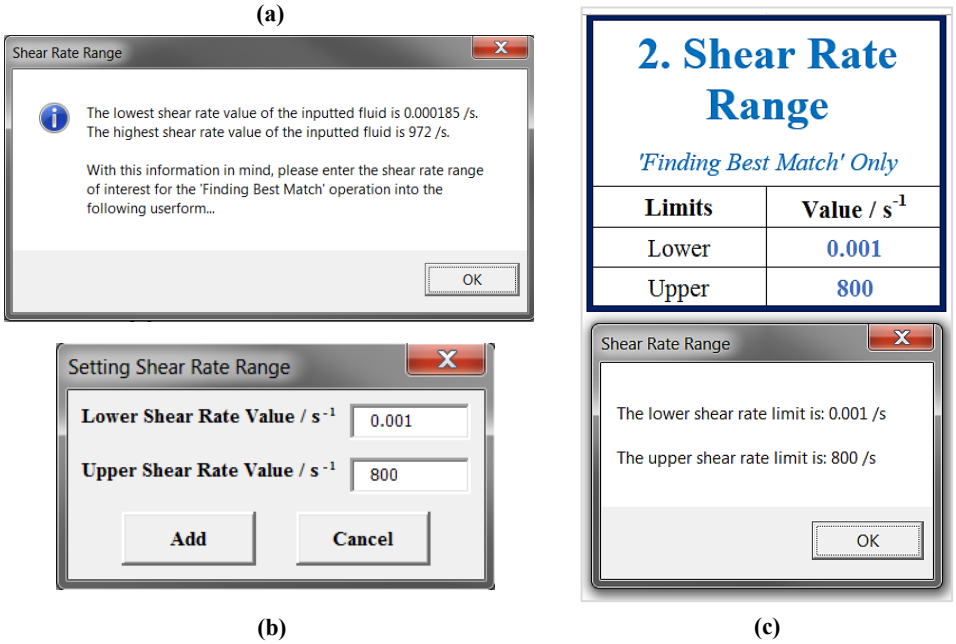

Figure 3.11. (a) Message box informing the user of the shear rate range of the inputted 'real' fluid. (b) Userform allowing the user to define the shear rate range over which the '*Finding Best Match*' process will occur. (c) The resulting message box informing the user of their chosen shear rate range, which is also displayed in the '*(2) Shear Rate Range*' section of the '*Data Entry*' worksheet.

After the shear rate range has been set, the '*Finding Best Match*' operation proceeds, with the physical and rheological properties of every fluid from the '*Library_Fitted*' worksheet being copied across into the '*Top Matches_Graph*' worksheet (as seen in Figure 3.10(c) and (d)). Using the rheological parameters of each fluid (either Herschel-Bulkley, Casson or Power Law parameters), fitted shear stress-shear rate datasets are then calculated for each model fluid, over the pre-defined shear rate range of interest. The AAD method (Equation 3.2) for deviation quantification is then utilised to determine how closely matched the fitted flow curve of each model fluid is to that of the 'real' fluid's raw flow curve, with the models fluids being ranked in terms of smallest to largest value of AAD. Using the three models, the raw rheological dataset of the 'real' fluid is mathematically fitted in the '*Optimisation Fitting*' worksheet, with the resulting rheological parameters of the model that produces the most accurate fit of the raw data being copied across into the relevant cells of the '*Top Matches_Graph*' worksheet (Figure 3.10(d)). The details of the top 15 'best-matched' model fluid systems are then copied into a table (Figure 3.10(b)) and the fitted flow curves, along with the raw and fitted flow curve of the 'real' fluid can be visualised in a shear rate-shear stress plot (Figure 3.10(a)), as previously discussed (Section 3.6). The message box in Figure 3.12(a) is then displayed, informing the user of the 'best-matched' fitted model fluid system, including information relating to the AAD and R^2 values of the original mathematical fit of the model fluid, and the AAD and R^2 values for the matching process between the flow curves of the model and 'real' fluid (in this example, AAD = 1.50% and R^2 = 1.000).

The user is also instructed to view the '*Top Matches_Details*' worksheet (Figure 3.13) for fluid formulation details of the 'best-matched' model fluid, and the other fluids from the top 15 'best-matched' model fluids. In this example, the 'best-matched' fluid is 'Carbopol Ultrez 30 (CU30, 0.10 wt%, pH 8.04)' solution, which is a single-compound fluid, part of the CU30 fluid family, whereby the mass fraction of CU30 in the solution remains constant, but the pH is varied. As a result, the '*Perform Interpolation*' operation (Section 3.8) should not be executed because the fluid is not part of a 'constant pH, varying mass fraction' fluid family, and the interpolation process can only occur with respect to mass fraction. If the 'best-matched' fluid was part of a 'constant pH, varying mass fraction' fluid family, then the macro would go through the top 2-15 'best-matched' fluids looking for fluids from the same fluid family. If fluids from the same family are found, the user would then be informed that the '*Perform Interpolation*' operation is possible and can be executed. However, if no other fluids from the same family as the 'best-matched' fluids are found within the top 2-15 'best-matched' fluids, then the message box in Figure 3.12(b) is displayed, notifying the user that the '*Perform Interpolation*' operation should not be executed. Detailed discussion concerning the '*Perform Interpolation*' operation can be found in Section 3.8.

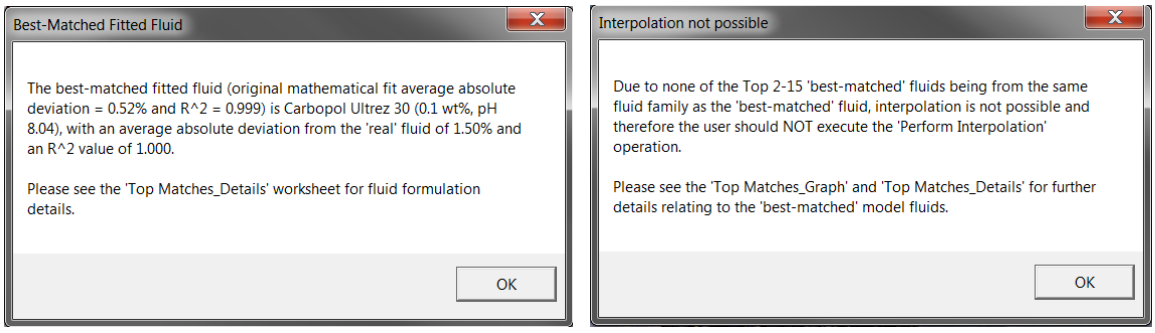

(a) **(b)**

Figure 3.12. (a) Message box informing the user of the 'best-matched' model fluid, in terms of rheological properties, to the 'real' fluid in question, along with information relating to the AAD and R^2 value of the match and the AAD and R^2 value of the original mathematical fit of the model fluid. (b) Message box notifying the user that none of the top 2-15 'best-matched' fluids are part of the same 'constant mass fraction' fluid family as the 'best-matched' model fluid and hence the '*Perform Interpolation*' should not be executed. Both message boxes report information relating to the location of the fluid formulation and other details of the 'best-matched' model fluids.

3.7 '*Top Matches_Details*' worksheet

As discussed in Section 3.6.1, the '*Top Matches_Details*' worksheet is the location within the MFST workbook where information concerning the physical and rheological properties of the top 15 'best-matched' fluids can be easily accessed, including details of how the fluids were formulated and rheologically characterised. The '*Top Matches_Details*' worksheet can be seen in Figure 3.13, with Figure 3.13(a) displaying the identity and physical properties of each fluid, along with which rheology model was used to mathematically fit the fluid, and Figure 3.13(b) providing the rheological

properties and the fluid formulation details of each fluid, the AAD values from the matching process, and the AAD and R^2 values from the original mathematical fitting process.

Top 15 'Best-Matched' Model Fluids:

(a)

Best-Matched Ranking	Compound 1 Name	Compound 2 Name	Compound 1 Mass Fraction / wt%	Compound 2 Mass Fraction / wt%	Fluid pH	Data From Experiment or Literature?	Health & Safety Rating	Expense Rating	Opacity Rating
1	Carbopol Ultrez 30	-	0.10	-	8.04	Experiment	1	1	1
2	Carbopol 980	Glycerol	0.15	45.00	7.78	Experiment	1	1	1
3	Carbopol Ultrez 10	-	0.15	-	6.68	Experiment	1	1	1
4	Carbopol Ultrez 10	-	0.15	-	8.58	Experiment	1	1	1
5	Carbopol Ultrez 30	1 wt% NaCl (aq)	0.15	1.625	7.36	Experiment	1	1	1
6	Carbopol Ultrez 21	Glycerol	0.13	10.00	6.66	Experiment	1	1	1

Data Entry | Optimisation Fitting | Library_Fitted | Top Matches_Graph | **Top Matches_Details** | Best Interpolated Fluid | MFST Instructions

(b)

H-B Yield Stress, τ_y / Pa	Flow Consistency Index, K / Pa s^n	Flow Behaviour Index, n	Constant Plastic Viscosity / Pa s	Casson Yield Stress, τ_y / Pa	Average Absolute Deviation of Match / %	Fluid Formulation Comments	Average Deviation of Original Mathematical Fit / %	R-Squared Value of Original Mathematical Fit	Constant pH Fluid Set?
91.73	43.94	0.36	-	-	1.503	A bulk 0.5 wt% Carbopol Ultrez 30 (CU30, Lubrizol) solution was formulated (2 g CU30, 398 g deionised water. Solution was magnetically stirred for ~16 h. After time elapsed, different quantities of a 2 wt% NaOH (aq) solution (5.92 g NaOH, 294.01 g deionised water) (1.75 g) and additional deionised water (62.25 g) were added to 16 g samples of the CU30 bulk solution, to formulate 0.1 wt% CU30 solutions of varying pH. Sample was then rheologically tested (vane) via a downward shear stress (SS) sweep, having undergone a pre-shear at 1200 /s for 15 seconds.	0.52	0.999	No
90.90	38.39	0.39	-	-	2.760	A bulk Carbopol 980 (C980, Lubrizol) solution was formulated (10 g C980, 990 g deionised water. Solution was stirred with an overhead stirrer at 650 rpm for ~ 16 h. After time elapsed, 200.67 g of a 2 wt% NaOH (aq) (5.92 g NaOH (Sigma Aldrich), 294.01 g deionised water) solution and 466 g of deionised water were added to the bulk C980 solution to form a 0.6 wt% bulk C980 solution at pH 6.85. Different quantities of additional deionised water (24 g) and glycerol (36 g, glycerol bidistilled 99.5%, VWR Chemicals) were added to 20 g of the C980 bulk solution, to formulate a 0.15 wt% C980 solution (45 wt% glycerol). Sample was then rheologically tested (vane) via a downward shear stress (SS) sweep, having undergone a pre-shear at 1200 /s for 15 seconds.	1.04	0.999	Yes
84.00	53.22	0.32	-	-	3.583	A bulk 0.3 wt% Carbopol Ultrez 10 (CU10, Lubrizol) solution was formulated (1.5g CU10, 498.5 g deionised water. Solution was magnetically stirred for ~15 h. After time elapsed, different quantities of a 2 wt% NaOH (aq) solution (4.01 g NaOH, 196g deionised water) (1.5 g) and additional deionised water (38.5 g) were added to 40 g samples of the CU10 bulk solution, to formulate 0.15 wt% CU10 solutions of varying pH. Sample was then rheologically tested (vane) via a downward shear rate (SR) sweep and downward shear stress (SS) sweep, having undergone a pre-shear at 1200 s-1 for 15 seconds. Data here is from SS sweep.	0.64	0.999	No
84.82	57.21	0.32	-	-	3.589	A bulk 0.3 wt% Carbopol Ultrez 10 (CU10, Lubrizol) solution was formulated (1.5g CU10, 498.5 g deionised water. Solution was magnetically stirred for ~15 h. After time elapsed, different quantities of a 2 wt% NaOH (aq) solution (4.01 g NaOH, 196g deionised water) (2.5 g) and additional deionised water (37.5 g) were added to 40 g samples of the CU10 bulk solution, to formulate 0.15 wt% CU10 solutions of varying pH. Sample was then rheologically tested (vane) via a downward shear rate (SR) sweep and downward shear stress (SS) sweep, having undergone a pre-shear at 1200 s-1 for 15 seconds. Data here is from SS sweep.	0.86	0.999	No
87.80	49.39	0.36	-	-	4.303	A bulk 0.3 wt% Carbopol Ultrez 30 (CU30, Lubrizol) solution was formulated (1.2 g CU30, 318.8 g deionised water. Solution was magnetically stirred for ~24 h. After time elapsed, 23 g of a 2 wt% NaOH (aq) solution (3.935 g NaOH, 196 g deionised water) solution and 57 g of deionised water were added to the bulk CU30 solution to form a solution at pH 7.23. Different quantities of additional deionised water (38.7 g) and 1 wt% NaCl (aq) (3 g NaCl, (Sigma Aldrich), 297 g deionised water) (1.3 g) were added to 40 g of the CU30 bulk solution, to formulate a 0.15 wt% CU30 solution. Sample was then rheologically tested (vane) via a downward shear stress (SS) sweep, having undergone a pre-shear at 1200 /s for 15 seconds.	0.70	0.999	Yes
68.90	65.55	0.30	-	-	4.375	A bulk Carbopol Ultrez 21 (CU21, Lubrizol) solution was formulated (2.4 g CU21, 317.6 g deionised water. Solution was magnetically stirred for ~ 16 h. After time elapsed, 29.58 g of a 2 wt% NaOH (aq) (6.045 g NaOH (Sigma Aldrich), 294.01 g deionised water) solution and 50.42 g of deionised water were added to the bulk CU21 solutions to form a 0.6 wt% bulk CU21 solution at pH 6.23. Different quantities of additional deionised water (55.33 g) and glycerol (8 g, glycerol bidistilled 99.5%, VWR Chemicals) were added to 16.67 g of the CU21 bulk solution, to formulate a 0.125 wt% CU21 solution (10 wt% glycerol). Sample was then rheologically tested (vane) via a downward shear stress (SS) sweep, having undergone a pre-shear at 1200 /s for 15 seconds.	1.07	0.998	Yes

Data Entry | Optimisation Fitting | Library_Fitted | Top Matches_Graph | **Top Matches_Details** | Best Interpolated Fluid | MFST Instructions

Figure 3.13. Screen-grabs of the '*Top Matches_Details*' worksheet, with: (a) displaying information relating to the physical properties of each fluid, along with various rankings and details concerning how the data was originally acquired (experiment vs literature); and (b) showing the rheological properties of the fluids, the AAD values of the matching process, fluid formulation comments for each fluid, and the AAD and R^2 values for the original mathematical fitting of each fluid.

3.8 '*Best Interpolated Fluid*' worksheet

The final of the key worksheets within the MFST is the '*Best Interpolated Fluid*' worksheet, which can be seen in Figure 3.14 and is associated with the '*Perform Interpolation*' operation, located in the '*Top Matches_Graph*' worksheet (seen in Figure 3.10(c)). When this operation is executed, details relating to the identity and physical properties of the 'best-matched' fluid are used to find all other fluids from the same fluid family in the '*Library_Fitted*' worksheet. Every time a fluid is found in the library, the physical and rheological properties of the fluid are then copied-and-pasted into the '*Best Interpolated Fluid'* worksheet. The matching process, relative to the 'real' fluid's raw flow curve then occurs over the shear rate range of interest for each fluid in the fluid family, and the data are sorted from lowest to highest, with respect to the resulting AAD values. The AAD values of the top 4 fluids are then plotted against the associated mass fraction values of the fluids, and the data points are fitted with a third-order polynomial fit to ensure that the curve passes through each point (i.e. $R^2 = 1$). After this has occurred, the user is then able to determine their hypothetical '*best interpolated fluid'* using this plot, by reading off the mass fraction value that results in the minimum in AAD. This '*Perform Interpolation*' process will only occur for single-compound systems and with respect to mass fraction.

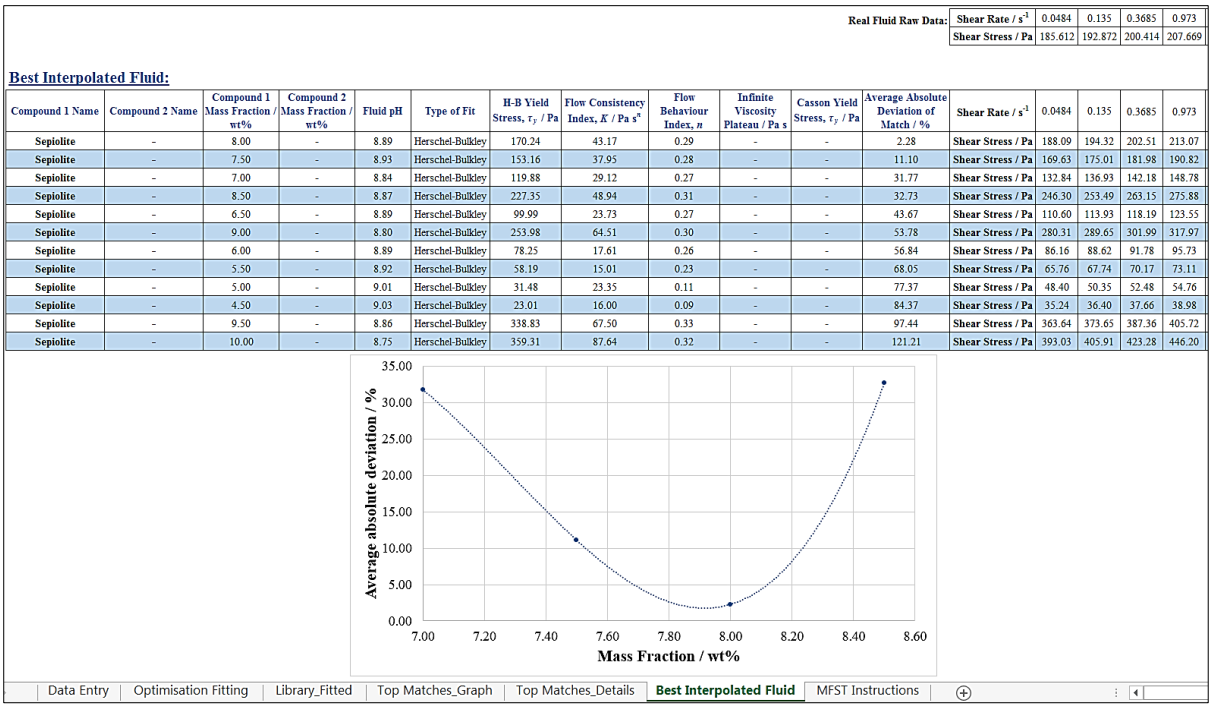

Real Fluid Raw Data:

Shear Rate / s^{-1}	0.0484	0.135	0.3685	0.973
Shear Stress / Pa	185.612	192.872	200.414	207.669

Best Interpolated Fluid:

Compound 1 Name	Compound 2 Name	Compound 1 Mass Fraction / wt%	Compound 2 Mass Fraction / wt%	Fluid pH	Type of Fit	H-B Yield Stress, τ_y / Pa	Flow Consistency Index, K / Pa s^n	Flow Behaviour Index, n	Infinite Viscosity Plateau / Pa s	Casson Yield Stress, τ_y / Pa	Average Absolute Deviation of Match / %	Shear Rate / s^{-1}	0.0484	0.135	0.3685	0.973
Sepiolite	-	8.00	-	8.89	Herschel-Bulkley	170.24	43.17	0.29	-	-	2.28	Shear Stress / Pa	188.09	194.32	202.51	213.07
Sepiolite	-	7.50	-	8.93	Herschel-Bulkley	153.16	37.95	0.28	-	-	11.10	Shear Stress / Pa	169.63	175.01	181.98	190.82
Sepiolite	-	7.00	-	8.84	Herschel-Bulkley	119.88	29.12	0.27	-	-	31.77	Shear Stress / Pa	132.84	136.93	142.18	148.78
Sepiolite	-	8.50	-	8.87	Herschel-Bulkley	227.35	48.94	0.31	-	-	32.73	Shear Stress / Pa	246.30	253.49	263.15	275.88
Sepiolite	-	6.50	-	8.89	Herschel-Bulkley	99.99	23.73	0.27	-	-	43.67	Shear Stress / Pa	110.60	113.93	118.19	123.55
Sepiolite	-	9.00	-	8.80	Herschel-Bulkley	253.98	64.51	0.30	-	-	53.78	Shear Stress / Pa	280.31	289.65	301.99	317.97
Sepiolite	-	6.00	-	8.89	Herschel-Bulkley	78.25	17.61	0.26	-	-	56.84	Shear Stress / Pa	86.16	88.62	91.78	95.73
Sepiolite	-	5.50	-	8.92	Herschel-Bulkley	58.19	15.01	0.23	-	-	68.05	Shear Stress / Pa	65.76	67.74	70.17	73.11
Sepiolite	-	5.00	-	9.01	Herschel-Bulkley	31.48	23.35	0.11	-	-	77.37	Shear Stress / Pa	48.40	50.35	52.48	54.76
Sepiolite	-	4.50	-	9.03	Herschel-Bulkley	23.01	16.00	0.09	-	-	84.37	Shear Stress / Pa	35.24	36.40	37.66	38.98
Sepiolite	-	9.50	-	8.86	Herschel-Bulkley	338.83	67.50	0.33	-	-	97.44	Shear Stress / Pa	363.64	373.65	387.36	405.72
Sepiolite	-	10.00	-	8.75	Herschel-Bulkley	359.31	87.64	0.32	-	-	121.21	Shear Stress / Pa	393.03	405.91	423.28	446.20

Figure 3.14. Screen-grab of the '*Best Interpolated Fluid*' worksheet, highlighting the physical and rheological properties of fluids from the same fluid family, the resulting AAD values of the match compared to the raw rheological properties of the 'real' fluid, and the plot of mass fraction against AAD, whereby the mass fraction that produces the minimum in AAD is the hypothetical '*best interpolated fluid*'.

3.8.1 Case Study 6: '*Perform Interpolation*' operation

As briefly mentioned in Section 3.8, in order for the '*Perform Interpolation*' operation to be executed, the '*Finding Best Match*' operation must be run first, with the '*Perform Interpolation*' operation only being run when prompted by the MFST. In the following example, a fictitious rheological dataset was generated using a combination of the rheological flow curves of 'sepiolite (8.00 wt%, pH 8.89)' and 'sepiolite (7.50 wt%, pH 8.93)' fluids. The shear rate-shear stress data were entered into the '*(1) Rheology Input*' section of the '*Data Entry*' worksheet, the '*Finding Best Match*' operation was executed and the shear rate range was set to 0.04-700 s^{-1}. The resulting plot of the 'real' fluid's raw and fitted flow curves, along with the fitted flow curves of the top 15 'best-matched' fluids can be visualised in Figure 3.15(a). As seen in the message box in Figure 3.15(b) the 'best-matched' fluid is the single-compound system of 'sepiolite (8.00 wt%, pH 8.89)', with AAD and R^2 values of 0.40 wt% and 0.999, respectively for the original mathematical fit, and AAD and R^2 values of 2.28% and 1.000, respectively for the matching process. Due to the 6th 'best-matched' fluid being 'sepiolite (7.50 wt%, pH 8.93)', the message box in Figure 3.15(c) is then displayed to the user, because 2 of the top 15 'best-matched' fluids are from the same fluid family as the 'best-matched' fluid and it is now possible for the interpolation process to occur. As a result, the user is then prompted to activate the '*Perform Interpolation*' operation, if they so desire.

Upon activation of the '*Perform Interpolation*' operation, the physical and rheological properties of other fluids in the sepiolite 'varied mass fraction, constant pH' family are copied across from the '*Library_Fitted*' worksheet, mathematically fitted over the pre-defined shear rate range and the AAD values from the matching process compared to the 'real' fluid raw dataset are calculated for each fluid. The AAD values are then sorted from lowest to highest and the mass fractions of the four fluids that produce the lowest AAD values (8.00 wt%, 7.50 wt%, 7.00 wt% and 8.50 wt%) are plotted against AAD and the data points are fitted with a third-order polynomial fit (as seen in Figure 3.14). The mass fraction of the hypothetical '*best interpolated fluid*' is then determined by reading off the mass fraction value that produces a minimum in AAD. The message box in Figure 3.16 is displayed to the user, informing them that the interpolation process has been run and how to determine the '*best interpolated fluid*'. In this example a mass fraction of 7.90 wt% produces the minimum in AAD. This would be expected because the weighting of the fictitious fluid was 80% 'sepiolite (8.00 wt%, pH 8.89)' and 20% 'sepiolite (7.50 wt%, pH 8.93)'. As stated in Figure 3.16, it is recommended that the user then formulates and rheologically characterises the suggested '*best interpolated fluid*' for themselves, using a similar protocol to one outlined for the 'best-matched' fluid, to confirm that suggested fluid is indeed the best model fluid for the system in question.

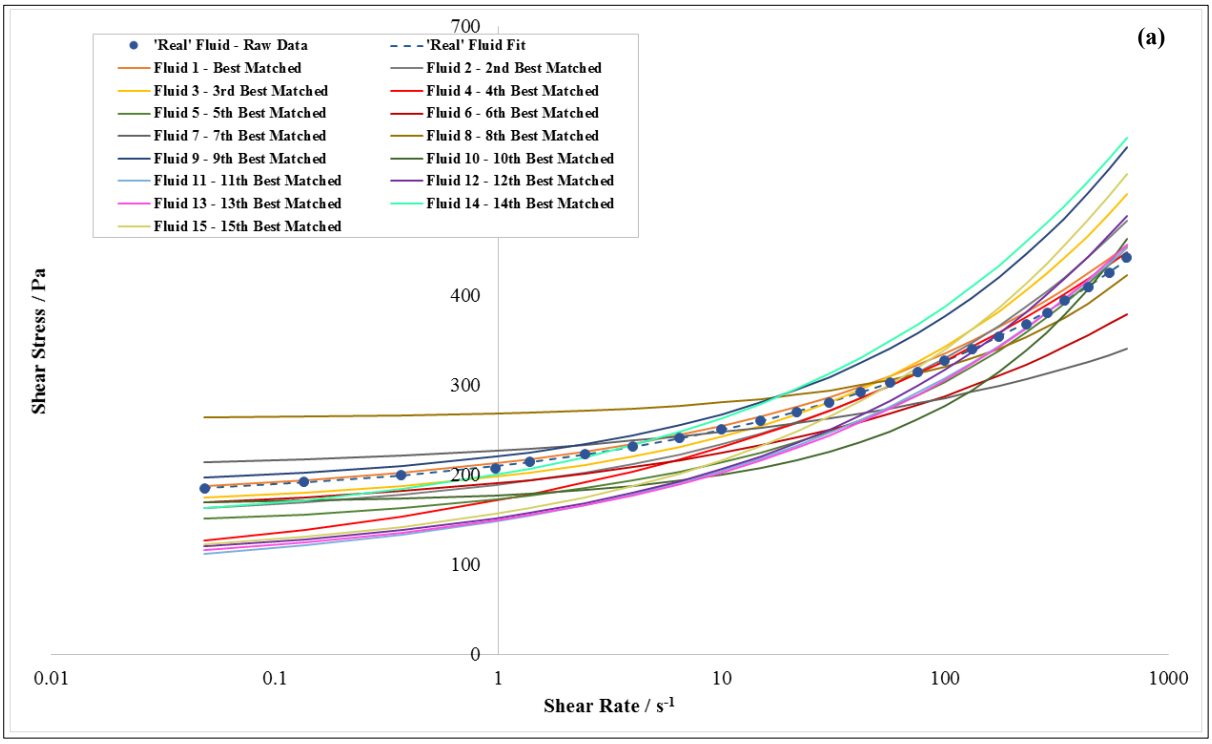

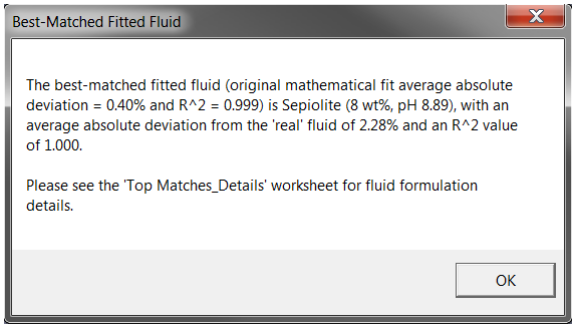

(b)

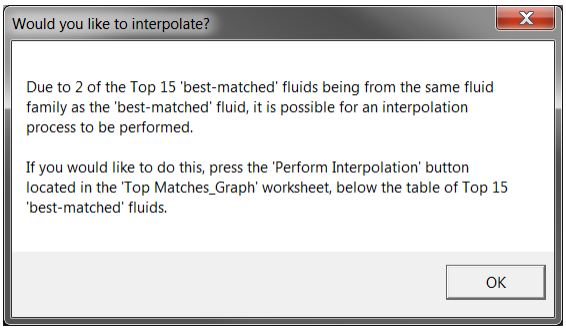

(c)

Figure 3.15. Having executed the '*Finding Best Match*' operation for the fictitious rheological dataset acquired through a combination of the raw rheological datasets of the 'sepiolite (8wt%, pH 8.89)' and 'sepiolite (7.50 wt%, pH 8.93)' fluids, over the shear rate range of 0.04-700 s^{-1}, (a) is the resulting plot of the raw and fitted flow curves for the 'real' fluid and the fitted flow curves of the top 15 'best-matched' fluids; (b) is the message box informing the user of the 'best-matched' fluid and the details of the match, whilst (c) is the message box notifying the user that 2 of the top 15 'best-matched' fluids are from the same fluid family as the 'best-matched' fluid and therefore interpolation using the '*Perform Interpolation*' operation is possible.

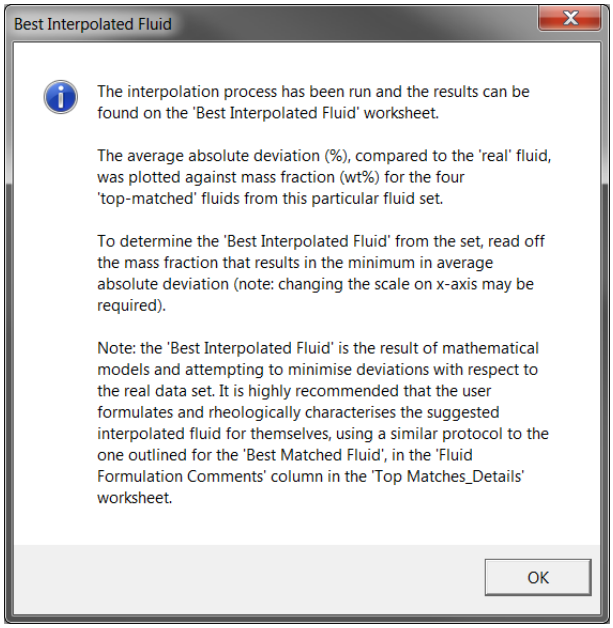

Figure 3.16. Message box informing the user the interpolation has run to completion and how to determine the hypothetical '*best interpolated fluid*' from the set, by reading off the mass fraction that produces the minimum in AAD.

3.9 '*MFST Instructions*' worksheet

This worksheet contains step-by-step instructions for how to run each of the aforementioned operations, as well as examples of what constitutes as 'good' and 'bad' rheology and a detailed description of the generic rheological protocol used in the characterisation of each model fluid system found in the library. These instructions can be found in the Appendix (Section A.2).

3.10 Issues relating to rheometrical geometry and mixing

All model fluid systems stored in the '*Library_Fitted*' worksheet were rheologically characterised using a 6-bladed vane (Anton Paar ST20-6V-20/112.5 stirrer) and cup geometry (vane diameter = 20.00 mm, blade height = 20.00 mm, cup diameter = 28.92 mm). As stated in Chapter 2, each fluid underwent an initial pre-shear test for 15 s at 1200 a.u., before undergoing a downward shear stress sweep, with shear stress upper and lower limits chosen to cover as many shear rate decades as possible, often ranging from approximately 1000 a.u., down to the lowest possible shear rate values for the fluid in question, to get the best possible description of the yield stress. The constant pH Carbopol Ultrez 10 fluid family also underwent downward shear rate sweeps, whilst the constant pH Bentopharm and Sepiolite fluid families underwent upward and downward shear stress sweeps, as well as upward and downward shear rate sweeps, however, on all occasions, the downward shear stress sweep data were fitted with the mathematical models upon addition to the '*Library_Fitted*' worksheet of the MFST. The vane geometry was used for the rheological characterisation of model fluids in this work to match both the geometry and

the protocol previously used at Syngenta in the rheological characterisation of their industrial fluids and formulations (a detailed discussion of why it is important to match rheological measurement protocols in this work can be found in Section 2.4). As a result, the same methods should be used when attempting to characterise the rheological properties of all 'real' fluids in the future, to allow the '*Finding Best Match*' process to be as accurate as possible. However, the true novelty of this section of work is the process behind finding the 'best-matched' fluids and therefore the MFST could be adapted and altered to accommodate for the rheological properties of fluids acquired via different geometries and measurement protocols, by creating a new database of fluids obtained using this new procedure. Another approach would include retrofitting the current vane-based data with the correct conversion factors so that the data were comparable to data that would be acquired when using other types of geometries, namely the cone-and-plate geometry.

Numerous experimental (and numerical) studies in the literature have looked at the mixing of viscoplastic fluids in vessel systems, equipped with either small, central impellers, close-clearance impellers or multi-impeller systems, as discussed in Section 1.4. When performing such experimental studies, the rheological properties of the test fluids are commonly acquired using cone-and-plate geometry (Elson *et al.* (1986); Amanullah *et al.* (1997); Arratia et al. (2006); Adams and Barigou (2007); Pakzad *et al.* (2008a, 2013a)). As a result, to be consistent with the literature, but also to ensure that the rheological parameters of the fluids being mixed are as accurate as possible (and to negate the need for retrofitting vane-based data), all rheological measurements in Chapters 4-6 have been performed using a roughened cone-and-plate geometry (0.998° cone angle, 12.6 μm roughness, cone and plate diameter = 50 mm, CP50-1-41592). The computational tool, known as the '*Matching and Predictive Mixing Tool*' (MPMT), presented in Chapter 5 was developed so that only rheological data obtained with cone-and-plate rheometrical geometry can be used. Further discussion of the MPMT can be found in Chapter 5.

3.11 Conclusion

A computational platform, known as the '*Model Fluid Selection Tool*' (MFST) has been developed and is capable of fitting raw rheological flow curves with a number of mathematical models, including the Herschel-Bulkley model, Power Law model and the Casson model, storing these fitted data in a rheological database and finding 'best-matched' model fluids from the database that most closely match the rheological properties of 'to-be-matched' (or 'real') fluid. The MFST was developed in Microsoft Excel, using Visual Basic for Application programming methods and recorded macros, and is comprised of a number of different worksheets, including the '*Data Entry*', '*Optimisation Fitting*', '*Library_Fitted*', '*Top Matches_Graph*', '*Top Matches_Details*', '*Best Interpolated Fluid*' and '*MFST Instructions*' worksheets. The '*Data Entry*' worksheet is home to the majority of the key operations within the MFST, with these operations are sub-divided into '*Standard Operations*' and '*Library Additions*'. The '*Standard Operations*' include: '*Clearing Old Data*' which deletes all old data from all worksheets, excluding the

'*Library_Fitted*' and '*MFST Instructions*' worksheets; '*Finding Best Match*' which finds the 'best-matched' model fluids stored in the '*Library_Fitted*' worksheets, in terms of rheological properties over a pre-defined shear rate range, compared to the 'real' fluid in question; and '*Delete Library Entry*' which allows the user to enter in the identity and physical properties of the model fluid system they wish to delete, which is then found within the '*Library_Fitted*' worksheet and deleted. The '*Library Additions*' operations include: '*Adding Data to Library (Data & Fitting Thereof)*' whereby the raw rheological shear rate-shear stress data of potential model fluid system is entered into the '*(1) Rheology Input*' section in the worksheet, and undergoes fitting with the aforementioned mathematical models before the user is then prompted to add the data into the '*Library_Fitted*' worksheet via the model that produces the best mathematical fit; and '*Adding Data to Library (By Fitted Parameters)*' where the rheological parameters of a model fluid system can be directly stored in the '*Library_Fitted*' worksheet through a userform interface. The '*Optimisation Fitting*' worksheet is the location where the fitting of raw rheological data with the three mathematical models occurs, by the using the Microsoft Excel Solver add-in function, whereby the Solver iteratively optimises the relevant fit of the raw data by changing the various parameters relating to each model to minimise a particular value relating to the 'error' between the outputted fitted data and the raw data. The '*Library_Fitted*' worksheet is a model fluids database, storing the identity, physical and rheological properties of each model fluid system that has been added to the MFST, as well as information relating to fluid formulation and rheological protocol, various fluid rankings and details of where the data was acquired from (experiment or literature). This worksheet is called upon during most of the key operations, excluding '*Clearing Old Data*'. The '*Top Matches_Graph*' worksheet is the site in the MFST where the '*Finding Best Match*' operation takes place, as well as hosting the '*Perform Interpolation*' operation, which can be utilised by the user if one or more of the top 2-15 outputted 'best-matched' fluids are part of the same fluid family as the 'best-matched' fluid. If executed, the operation will attempt to determine a hypothetical '*best interpolated fluid'* in terms of suggesting a mass fraction of the fluid which has not been formulated, rheologically characterised and stored in the '*Library_Fitted*' worksheet, but may minimise the average absolute deviation (AAD) of the matching process, compared to the suggested 'best-matched' fluid. The '*Top Matches_Details*' worksheet stores the more important information concerning the top 15 'best-matched' model fluids for a given '*Finding Best Match*' process, including comments relating to fluid formulation. The '*Best Interpolated Fluid* worksheet is the location within the MFST where the '*Perform Interpolation*' occurs, with the suggested mass fraction of the hypothetical '*best interpolated fluid*' being associated with the mass fraction from a fluid family that minimises the AAD in the '*Finding Best Match*' process. Finally, the '*MFST Instructions*' worksheet contains step-by-step instructions for how to run each of the operations, as well as providing information and examples of what constitutes as 'good' or 'bad' rheological data. The importance of being consistent with the choice of rheometrical geometry and measurement procedure was highlighted, with it being concluded that 6-bladed vane geometry and downward shear stress sweeps should be used when rheologically characterising a fluid for use in the MFST.

Chapter 4: Mixing Viscoplastic Fluids in Stirred Vessels

Publication: Russell, A.W., Kahouadji, L., Mirpuri, K., Quarmby, A., Piccione, P.M., Matar, O.K., Luckham, P.F., Markides, C.N., 2019. Mixing Viscoplastic Fluids in Stirred Vessels Over Multiple Scales: A Combined Experimental and CFD Approach. Chem. Eng. Sci. 208, 115129-1–16

4.1 Introduction

The focus of this chapter is to characterise the flow of viscoplastic fluids in stirred vessels, through the use of dye visualisation techniques and CFD, with the aim of matching dimensionless cavern sizes and achieving flow similarity over multiple scales. Carbopol^{TM} solutions are used as the test fluids, due to their viscoplastic character and highly transparent nature. Centrally-mounted, geometrically-similar Rushton turbine (RT) impellers are used to agitate various Carbopol 980 (C980) fluids in vessels over a range of volumes, specifically 2 L (Scale 1), 5 L (Scale 2) and 20 L (Scale 3), whilst geometrically-similar pitched-blade turbine (PBT) impellers are used to agitate C980 fluids on Scales 1 and 2. The effects of impeller rotational speed (N), fluid rheology, mixing system scale and impeller type, on cavern shape and size were investigated. The experimental and numerical dimensionless cavern diameters, D_c/D of the resulting caverns are initially scaled with respect to N, which results in unmatched flows. As a result, all D_c/D data are then scaled against a combination of dimensionless parameters: $Re_m^{-0.3}Re_y^{0.6}n^{-0.1}k_s^{-1}$, where Re_m, Re_y, n and k_s are the modified power-law Reynolds number, yield stress Reynolds number, flow behaviour index and impeller geometry constant, respectively. Scaling in this fashion results in flow similarity being achieved for datasets acquired with the same impeller type. Comparisons are made between the cavern morphologies and sizes that result from agitation with both the RT and the PBT impellers (using the Scale 1 system) and the same scaling method results in cavern size similarity being achieved. CFD provides information relating to velocity field distributions and flow patterns within the caverns produced by RT and PBT agitation, helping to explain the observed ‘horn’ torus and ‘apple’ torus cavern morphologies, respectively, obtained from experiment. The results from this chapter are important in the context of scale-up/scale-down mixing processes in stirred vessels containing fluids with complex rheological properties and can be used to show that flow similarity can be achieved in these systems if the processes are scaled appropriately.

4.2 Experimental methods

4.2.1 Carbopol

In this work, various solutions of Carbopol 980 (C980, Lubrizol Corporation) were used as the test viscoplastic fluids for the experimental mixing studies. When Carbopol is dispersed in aqueous media, a non-thixotropic, swollen microgel forms. Carbopol gels have been described as being formed of polydisperse, elastic “sponges”, which have the capacity to swell in aqueous media (Piau, 2007). This

swelling is heightened in basic media (natural pH ~3 of Carbopol in water), through the ionisation of carboxylic acid groups to carboxylate groups on the polymer chains, resulting in strong electrostatic repulsions between neighbouring chains. The microgel sponges then become jammed together, resulting in the formation of disordered, glass-like suspension and leading to enhanced viscoplastic properties and optical clarity (Barry and Meyer (1979); Kim *et al.* (2003); Bonacucina *et al.* (2004); Islam *et al.* (2004); Oppong *et al.* (2006); Piau (2007)). A full description of the properties of Carbopol can be found in Section 1.2.3.1.

4.2.2 Formulation and rheological characterisation of Carbopol 980 fluids

A number of C980 fluids were prepared for this section of the work. In each case, the C980 powder was dissolved in deionised water via mechanical or magnetic agitation, and on complete dissolution (approximately 12-24 h), small quantities of 2-3 wt% aqueous NaOH (Sigma Aldrich) solution were added to the C980 solution, until the fluid had a pH 6–7.5. The rheological properties of all fluids were measured using a shear-stress controlled Anton Paar Modular Compact Rheometer 302 rheometer, fitted with a roughened cone-and-plate geometry (12.6 μm roughness, 0.998° cone angle, cone and plate diameter = 50 mm, CP50-1-41592). All fluids underwent shear stress down-sweep measurements (60 pt dec^{-1}, 5 s pt^{-1}) and the resulting flow curves were mathematically fitted to the Herschel-Bulkley model (Herschel and Bulkley, 1926) (Eq. 1.11, Section 1.1.3.3). Note: for each of the rheological measurements performed in this study, the range of shear rate values (~0.001-1000 s^{-1}) investigated ensured that the resulting full range of shear rates (and shear stresses) in the mixing vessel systems were accounted for. The viscoelastic properties of C980 solutions have been investigated, with and the storage modulus, *G'* typically ~400 Pa and the loss modulus, *G"* typically ~30 Pa, depending on pH, however are not relevant to this current section of the project.

These Herschel-Bulkley fitted data, along with other physical properties of the fluids used in the fourteen main cases from this section of the project, are presented in Table 4.1 and Table 4.2, respectively. *Mixing Study A*, *Mixing Study B* and *Mixing Study C* correspond to the three main studies where mixing occurred with various geometrically-similar 6-bladed Rushton turbine (RT) impellers, whilst *Mixing Study D*, *Mixing Study E* and *Mixing Study F* describe the three main studies where mixing was carried out with a set of geometrically-similar 4-bladed 45° pitched-blade turbine (PBT) impellers. From Table 4.1 and Table 4.2: comparison of *Cases 1-3* enables *Mixing Study A*, which relates to mixing fluids with different rheological properties on the same scale; comparison of *Cases 1, 4* and *5* enables *Mixing Study B*, which relates to mixing the same fluid over different scales; and comparison of *Cases 2, 3* and *5* enables *Mixing Study C*, which relates to mixing fluids with different rheological properties over different scales. *Cases 6-8* are details relating to the repeat study in *Mixing Study B*, where a different (but similar) fluid was mixed over the three scales. Comparison of RT and PBT agitation of fluids with similar rheology occurred using the Scale 1 (2 L) system, where *Case 2* related to the RT system, whilst *Case 11* relates

to the PBT system. Similar to *Mixing Study A*, *Mixing Study D* corresponds to mixing of different fluids on the same scale, but now with a PBT impeller and was enabled by comparison of *Cases 9-13*; *Mixing Study E* is analogous to *Mixing Study B* and corresponds to the mixing of two very similar fluids over different scales with geometrically-similar PBT impellers, enabled by comparison of *Cases 10* and *14*; whilst the comparison of *Cases 9*, *12*, *13* and *14* enables *Mixing Study F*, which is the mixing of different fluids over different scales (again, with PBT impellers), respectively.

Table 4.1. Herschel-Bulkley rheological properties of the main fluids and systems used in this work. Agitation with RT impellers occurred in *Cases 1-8*, whilst PBT agitation was used in *Cases 9-14*. See Section 4.2.5 for details relating fluid and systems used for the error analyses, not shown here.

Mixing System			**Herschel-Bulkley rheological properties**			**Error analysis**		
Case	**Vessel volume / L**	**Impeller Type**	**Yield stress, τ_y / Pa**	**Flow consistency index, K / Pa s^n**	**Flow behaviour index, n**	**Shear rate range of optimised fit / s^{-1}**	**Average absolute deviation per datum / %**	**R^2**
1	2	RT	42.8	11.6	0.41	0.00209-986	1.34	0.999
2	2	RT	21.5	5.0	0.46	0.0148-979	1.59	0.999
3	2	RT	9.3	2.4	0.48	0.00417-962	2.08	0.998
4	5	RT	42.8	11.6	0.41	0.00209-986	1.34	0.999
5	20	RT	41.6	11.8	0.41	0.00126-957	1.50	0.999
6	2	RT	44.2	11.7	0.41	0.0109-845	0.95	0.999
7	5	RT	44.2	11.7	0.41	0.0109-845	0.95	0.999
8	20	RT	42.9	11.7	0.41	0.00749-865	1.10	0.999
9	2	PBT	50.8	13.0	0.42	0.000568-959	1.63	0.999
10	2	PBT	27.7	6.9	0.44	0.000473-933	1.85	0.999
11	2	PBT	20.7	4.8	0.46	0.00253-933	1.82	0.998
12	2	PBT	16.5	5.2	0.44	0.000156-999	2.71	0.997
13	2	PBT	8.9	2.4	0.48	0.000572-984	2.25	0.998
14	5	PBT	26.2	6.7	0.45	0.000489-954	1.99	0.998

Table 4.2. Physical properties of the main fluids and systems used in this work. Agitation with RT impellers occurred in *Cases 1-8*, whilst PBT agitation was used in *Cases 9-14*. See Section 4.2.5 for details relating fluid and systems used for the error analyses, not shown here.

	Mixing system			Fluid composition and physical properties		
Case	**Vessel volume / L**	**Impeller Type**	**Impeller Diameter, *D* / m**	**C980 mass fraction / wt%**	**Fluid pH**	**Fluid temperature / °C**
1	2	RT	0.041	0.20	6.1	23.6
2	2	RT	0.041	0.15	6.1	23.1
3	2	RT	0.041	0.12	6.5	26.8
4	5	RT	0.059	0.20	6.1	23.6
5	20	RT	0.084	0.20	6.1	20.8
6	2	RT	0.041	0.20	6.2	24.8
7	5	RT	0.059	0.20	6.2	24.8
8	20	RT	0.084	0.20	6.2	23.1
9	2	PBT	0.041	0.20	6.4	27.2
10	2	PBT	0.041	0.15	6.3	25.5
11	2	PBT	0.041	0.15	6.0	26.8
12	2	PBT	0.041	0.12	6.7	24.3
13	2	PBT	0.041	0.10	6.7	24.3
14	5	PBT	0.059	0.15	6.7	26.2

4.2.3 Stirred vessel system and experimental procedures

Three unbaffled, cylindrical vessel systems were used, with quoted vessel volumes of 2 L (Scale 1), 5 L (Scale 2) and 20 L (Scale 3) and tank diameters (T) of 0.148 m, 0.201 m and 0.300 m, respectively. For the mixing studies performed using the jacketed Scale 3 vessel, a water-filled, flat-faced container was placed around the vessel. However, water-filled containers were not placed around Scale 1 and 2 unjacketed vessels. The reason for this was because the jacket around the Scale 3 vessel could potentially lead to three-dimensional optical distortions and hence refractive index matching the medium (water) inside the jacket with the water in the container helped to minimise these distortions. The lack of a jacket around the Scale 1 and 2 vessels meant the need to minimise optical distortions was not required. A verification test was performed through the insertion of a ruler into the vessel, and it was shown that the lack of the container gave similar information compared to when the container was used. A set of geometrically-similar 6-bladed Rushton turbine (RT) impellers, with impeller diameters of D = 0.041 m, D = 0.059 m and D = 0.084 m were used for agitation on Scale 1 (2 L), Scale 2 (5 L), and Scale 3 (20 L), respectively. D = 0.041 m and D = 0.059 m 4-bladed 45° pitched-blade turbine (PBT) impellers were used for mixing on Scale 1 (2 L) and 2 (5 L), respectively. The RT impellers had a disc diameter-to-impeller diameter, D_d/D = 0.70; a blade width-to-impeller diameter, W_b/D = 0.24; and a blade height-to-impeller diameter, H_b/D = 0.20. The PBT impellers had a blade width-to-impeller diameter, W_b/D = 0.30; and an angled blade height-to-impeller diameter, H_{ab}/D = 0.28. All impellers

had an impeller diameter-to-tank diameter ratio (D/T) ≈ 0.285, for each respective vessel. For all systems, the impeller clearance (the distance from the centre of the impeller to the bottom of the tank) and the fluid fill height are $C \approx 1.42D$ and $H \approx 3.30D$, respectively, with the exception of *Case 14*, where $H \approx 3.00D$. In each experimental mixing study, the relevant impeller (either RT or PBT) was fitted to a shaft, with shaft diameter-to-impeller diameter (S/D) ≈ 0.24 and was centrally-mounted onto an IKA EUROSTAR 60 motor. An image of the two sets of three geometrically-similar RT and PBT impellers can be seen in Figure 4.1.

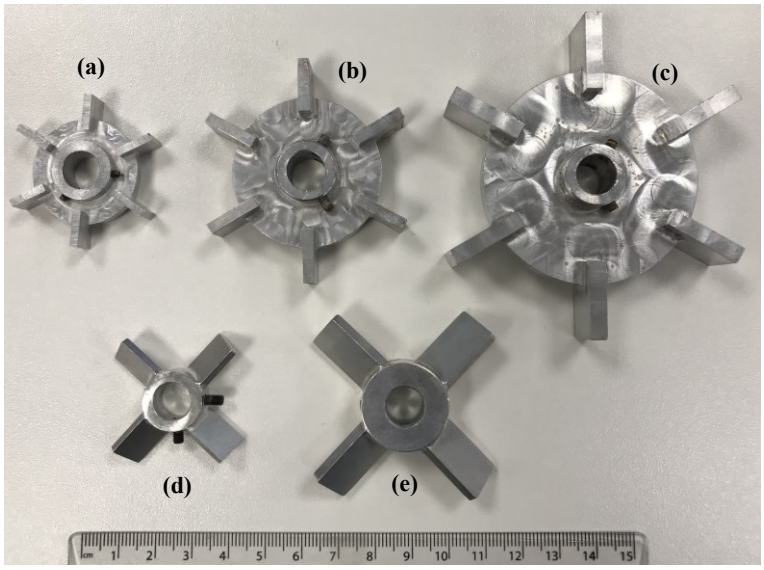

Figure 4.1. Images of the 6-bladed Rushton turbine impellers used for the experimental mixing studies on: (a) Scale 1, (b) Scale 2, and (c) Scale 3; and the 4-bladed 45° pitched-blade turbine impellers used on (d) Scale 1 and (e) Scale 2.

For Scale 1 and Scale 2 systems, caverns were visualised using food dyes, whilst UV fluorescent dyes and techniques were employed in the Scale 3 system (*Cases 5* and *8*). The reason for this difference in dye system was because, unlike the food dyes, the UV dyes do not stain the fluid too strongly (in the absence of a UV source), hence allowing the material from the Scale 3 system to be reused for the scaled down studies. For the Scale 1 and Scale 2 RT and PBT mixing studies, having loaded the fluid into the vessel, the impeller was set to a low rotational speed (150-250 rpm) and ~1-2 mL of the green/blue food dye (Sainsbury's Supermarkets Ltd) was injected at the impeller tip. The impeller rotational speed, N was then incrementally increased, with images taken (Panasonic HDC-SD90 camera or iPhone 7 camera) at each N value after approximately 30 seconds, to allow the cavern to reach an equilibrium size and shape. N values were increased until the cavern reached the tank wall. For the Scale 3 system, a similar method to Scale 1 and Scale 2 was implemented, however UV fluorescent dyes were used. 2-3 mL of dilute Fluorescein (Sigma Aldrich) injected at the impeller tip and was mixed so that homogeneity was achieved

throughout the vessel. This was used to create a background fluorescence within the vessel. 1-2 mL of Rhodamine B (Sigma Aldrich) was then injected at the impeller tip at a low speed (~120 rpm) and fluorescence was induced through the use of a UV lamp (UVP Blak-Ray B100AP). As before, N was then incrementally increased, with images (Canon EOS 700D) of the cavern being taken at each N value.

In each of the experiments, the cavern boundary was defined by the sharp transition from dyed to non-dyed material. Before the start of every experiment, a calibration image was taken of the experimental setup, and using the measurement tools in Microsoft Paint, the impeller diameter, D was measured (in pixels). Images of the flows were then taken at each selected N value, for a given system, from the same location used for the calibration image. Using the same measurement techniques, cavern diameter, D_c and heights, H_c were both measured (in pixels), and D was used to non-dimensionalise the D_c values.

4.2.4 Dimensionless parameters

A dimensional analysis study was carried out by the author using Buckingham Pi theorem to determine the key dimensionless groups that describe the agitation of viscoplastic fluids in stirred vessel systems. The process involved the grouping of dimensional variables that define the mixing system, including rheological and length scale parameters, into key dimensionless groups, with the following groups being outputted: the Power number, Po (Eq. 4.1), a modified power-law Reynolds number, Re_m (Eq. 4.2), a Froude number, Fr (Eq. 4.3), the yield stress Reynolds number, Re_y (Eq. 4.4), a dimensionless shear rate $\bar{\dot{\gamma}}/N$, the flow behaviour index, n and key geometrical ratios. An example of this dimensional analysis process can be found in Section A.3 in the Appendix.

$$Po = \frac{P}{\rho N^3 D^5} \tag{4.1}$$

$$Re_m = \frac{\rho N^{2-n} D^2}{K} \tag{4.2}$$

$$Fr = \frac{N^2 D}{g} \tag{4.3}$$

$$Re_y = \frac{\rho N^2 D^2}{\tau_y} \tag{4.4}$$

$$\bar{\dot{\gamma}} = k_s N \tag{4.5}$$

where P, D, N, K, n, τ_y, g and k_s are the power input, impeller diameter, impeller rotational speed, flow consistency index, flow behaviour index, yield stress, gravitational acceleration and impeller geometry constant, respectively. When in the laminar flow regime (which was the case for all mixing studies in this work), the Metzner-Otto correlation (Eq. 4.5) can be utilised to show that the dimensionless mean shear rate is equal to the impeller geometry constant, k_s (Metzner and Otto (1957)).

In this work, the Herschel-Bulkley model (Eq. 1.11), in conjunction with Newtonian's law of viscosity (Eq. 1.2) and the Metzner Otto correlation (Eq. 4.5) could have been inputted into a generic Reynolds number definition ($Re = \rho ND^2/\mu$) to produce the Herschel-Bulkley Reynolds number (Re_{HB}), as seen in Eq. 4.6. Re_{HB} combines contributions to the total stress from two terms: the yield stress term and the power law term. However, this definition was not used here and a dimensional analysis approach was used instead, because a specific attempt was made to describe independently the regions in the vessel that flow (the power law component), and regions that resist flow (the yield stress component), through splitting the Reynolds number into two terms: Re_m and Re_y.

$$Re_{HB} = \frac{\rho N^2 D^2}{\tau_y + K(k_s N)^n} k_s \tag{4.6}$$

When performing scale-up/scale-down studies, it is usually recommended that all key geometrical ratios are maintained over scales. In this case, all details and length scale ratios relating to the impeller geometry, the impeller clearance-to-impeller diameter ratio (C/D), the liquid fill height-to-impeller diameter ratio (H/D) and the shaft diameter-to-impeller diameter ratio (S/D) were maintained over the three scales investigated. For these types of stirred vessel systems and viscoplastic flows, the Froude number is seen as having a negligible impact on the mixing process, because over all conditions investigated in this chapter, the impeller is sufficiently far enough away from the air-material interface for the interface to be considered as being undisturbed and permanently flat (Edwards (1985); Cortada-Garcia *et al.* (2017)). As a result, Po can be seen to be dependent on the four dimensionless parameters: Re_m, Re_y, k_s and n; Re_m is the ratio of inertial to viscous forces and provides an indication of the flow regime in the cavern, whilst Re_y is a dimensionless fluid yield stress term, which will have a bearing on cavern size. As previously mentioned, k_s is the impeller geometry, which has a weak dependence on impeller type and size. For the RT and PBT impellers used in this work, assigned k_s values of 11.5 and 13, respectively, are deemed as appropriate for these systems (Metzner *et al.* (1961)). Typical ranges of N, Re_m and Re_y for the fourteen main cases in this study can be seen in Table 4.3 (with their rheological and physical properties found in Table 4.1 and Table 4.2, respectively). Due to the dependence of Po on the four aforementioned parameters, it can be determined that the dimensionless cavern diameter (D_c/D) is also a function of Re_m, Re_y, k_s and n:

$$\frac{D_c}{D} \sim f(Re_m, Re_y, k_s, n) \tag{4.7}$$

When attempting to match the flow of viscoplastic fluids in stirred vessels over different scales, the functional relationship in Eq. 4.7 must be determined and adhered to in all cases. In this work, the previously discussed cavern models presented in Chapter 1 (Section 1.4) will not be used as methods for predicting cavern sizes. This is due to the difficulties associated with accurately measuring torque values and hence calculating Po values (Solomon *et al.* (1981); Elson *et al.* (1986); Amanullah *et al.*

(1998); Wilkens *et al.* (2005); Hui *et al.* (2009); Xiao *et al.* (2014)), the dependence of *Po* on Re_m, Re_y, k_s and n (as previously discussed), the toroidal (rather than spherical or cylindrical) morphology of the caverns formed in this study (Solomon *et al*. (1981); Elson *et al.* (1986)), difficulties in measuring the axial force component of flows (Amanullah *et al.* (1998); Hui *et al.* (2009); Xiao *et al.* (2014)) and the vertical, rather than side-entering setup of the impeller (Hui *et al.* (2009)).

Table 4.3. Typical ranges of impeller rotational speed, N, modified power-law Reynolds number, Re_m and yield stress Reynolds number, Re_y for the fourteen main cases in this study (see Table 4.1 and Table 4.2 for the resulting rheological and physical properties, respectively).

		Dimensional variable		Dimensionless parameters	
Case	**Impeller Type**	**Impeller Diameter, D / m**	**Impeller rotational speed range, N / s^{-1}**	**Modified power-law Reynolds number range, Re_m**	**Yield stress Reynolds number, Re_y**
1	RT	0.041	10.0-26.3	5.6-26.0	3.9-27.2
2	RT	0.041	8.3-19.3	8.8-32.0	5.4-29.2
3	RT	0.041	5.0-13.7	8.1-37.4	4.5-33.9
4	RT	0.059	8.2-18.2	8.4-29.9	5.4-26.8
5	RT	0.084	5.6-14.0	9.2-39.6	5.2-33.3
6	RT	0.041	11.7-26.3	7.1-25.8	5.2-26.4
7	RT	0.059	7.7-18.0	7.5-29.2	4.6-25.6
8	RT	0.084	5.8-13.3	9.9-40.5	5.6-33.0
9	PBT	0.041	11.7-33.3	6.3-33.3	4.5-36.8
10	PBT	0.041	10.0-26.7	8.8-40.7	6.1-34.2
11	PBT	0.041	8.3-24.0	9.2-46.7	5.6-46.7
12	PBT	0.041	6.5-20.8	6.1-37.6	4.3-44.1
13	PBT	0.041	5.8-15.7	10.2-45.5	6.4-46.3
14	PBT	0.059	7.3-19.2	11.5-51.2	7.1-48.8

4.2.5 Error analysis

4.2.5.1 Errors associated with fluid formulation and rheological characterisation

The main sources of error in this work are likely to be associated with the fluid formulation and rheological characterisation procedure, and the mixing process itself. To quantify the errors associated with the fluid formulation and rheological characterisation, two C980 fluids (*Fluid A* and *Fluid B*) were formulated via identical experimental protocols. Both fluids were made up to 0.15 wt% C980, with a total solution weight of 100 g and a NaOH concentration of 1.33×10^{-2} mol dm^{-3}. The resulting pH values of the solutions were 6.43 and 6.46 for *Fluid A* and *Fluid B*, respectively. Each solution then underwent a shear stress down-sweep (280-28 Pa, 30 pt dec^{-1}, 5 s pt^{-1}) rheological measurement using an Anton Paar Modular Compact Rheometer 302 rheometer, equipped with roughened cone-and-plate (12.6 μm roughness, 0.998° cone angle, cone and plate diameter = 50 mm, CP50-1-41592) geometry. The curves

were empirically fitted to the Herschel-Bulkley model; the resulting Herschel-Bulkley fitted parameters for each fluid, along with uncertainties, can be seen in Table 4.4. The model fits for each fluid were then plotted over the $\dot{\gamma}$ range = 0.00189-944 s^{-1} and the resulting curves can be seen in Figure 4.2.

Table 4.4. Herschel-Bulkley properties of *Fluids A* and *B*, used to highlight the errors associated with the fluid formulation and characterisation procedures.

	Herschel-Bulkley rheological properties		
Fluid name	**Yield stress, τ_y / Pa**	**Flow consistency index, K / Pa s^n**	**Flow behaviour index, n**
Fluid A	40.5 ± 2.0	14.2 ± 3.6	0.39 ± 0.03
Fluid B	37.4 ± 1.4	19.0 ± 0.8	0.36 ± 0.01

Fluid A and *Fluid B* experienced the same formulation and rheological characterisation procedures, resulting in the fluids having the same composition. However, despite this, there were slight differences in τ_y, K and n values between the two fluids, as seen in Table 4.4. There were also uncertainties relating to each parameter, which resulted from multiple flow curves being mathematically fitted for each fluid and mean values being taken for each parameter. In Figure 4.2, the average absolute deviation (AAD) per datum between the two fitted flow curves over the $\dot{\gamma}$ range of 0.00189-944 s^{-1} was 4.2% ($R^2 = 0.999$). The results from Table 4.4 and Figure 4.2 highlight that there are errors associated with the reproducibility of the formulation procedure, the rheological characterisation and Herschel-Bulkley fitting methods, which therefore could be a source of error for this work.

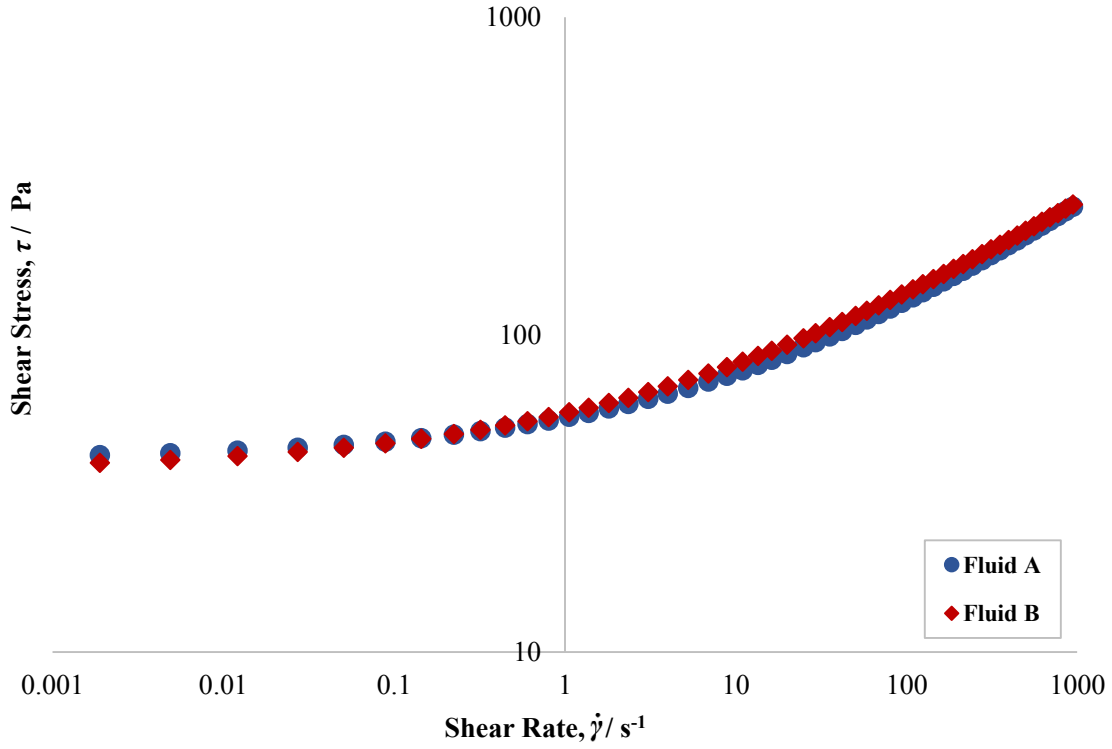

Figure 4.2. Curves for the Herschel-Bulkley fits (over the $\dot{\gamma}$ range of 0.00189-944 s^{-1}, to 3 significant figures) for *Fluid A* and *Fluid B* using the parameters in Table 4.4.

4.2.5.2 Errors associated with the mixing procedure in the stirred vessel system

To determine the extent of error associated with the mixing procedure and cavern measurement process, a bulk C980 fluid was formulated and rheologically characterised via the methods previously described. A portion of the bulk fluid then underwent mixing with the D = 0.041 m Rushton turbine (RT) in the Scale 1 mixing system ($C \approx 1.42\,D$, $H \approx 3.30\,D$, $S \approx 0.24D$). The cavern was visualised with food dyes, and as previously discussed, N was incrementally increased, with images capturing the cavern size at each N value. The procedure was repeated under the same conditions with the remaining material from the bulk fluid, and the results were compared. Figure 4.3 is a plot of dimensionless cavern diameter, D_c/D against N and it can be seen that there is good agreement between the two sets of data (*Fluid C* and *Fluid D*, respectively), with an average difference in D_c/D at a given N value of 0.67% (R^2 = 1.000). Average H_c/D_c values of 0.50 and 0.51 for *Fluid C* and *Fluid D*, respectively, were obtained.

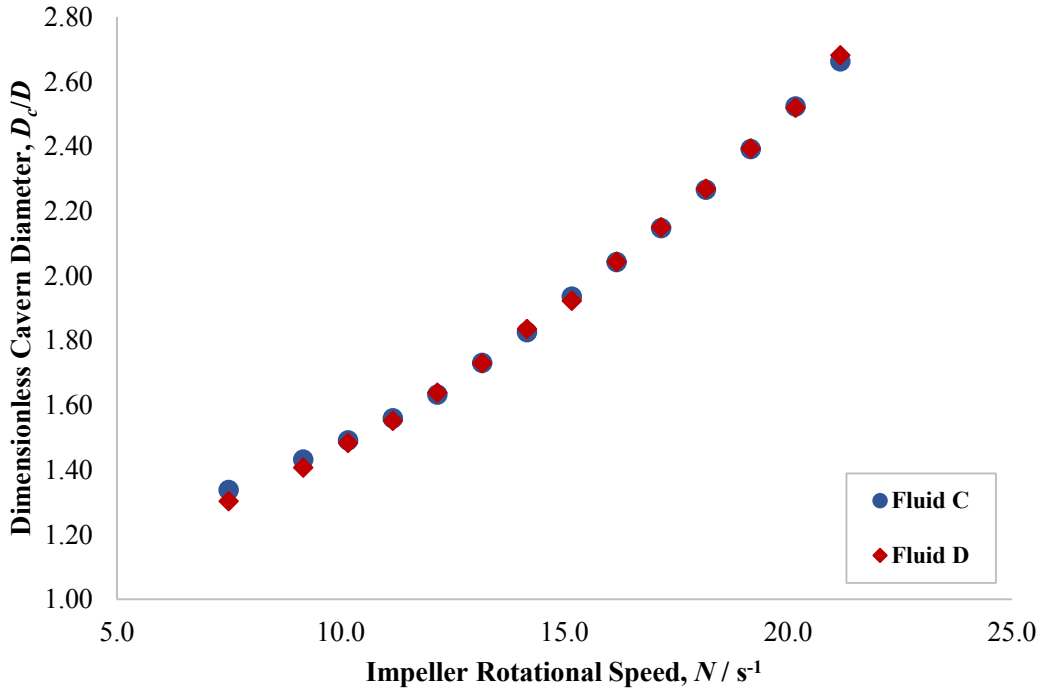

Figure 4.3. D_c/D versus N datasets for *Fluid C* and *Fluid D*, respectively. There is good agreement between the two sets of data, with an average difference in D_c/D values at a given N of 0.67% (R^2 = 1.000).

The C980 formulation and rheological characterisation processes were then repeated and the fluid was mixed twice with the D = 0.041 m pitched-blade turbine (PBT) in the Scale 1 mixing system ($C \approx 1.42\,D$, $H \approx 3.30\,D$, $S \approx 0.24D$). Figure 4.4 is a plot of D_c/D against N and it can be seen that there is good agreement between the two sets of data (*Fluid E* and *Fluid F*, respectively), with an average difference in D_c/D at a given N value of 0.93% (R^2 = 0.999). Average H_c/D_c values of 0.45 and 0.47 for *Fluid E* and *Fluid F*, respectively, were obtained.

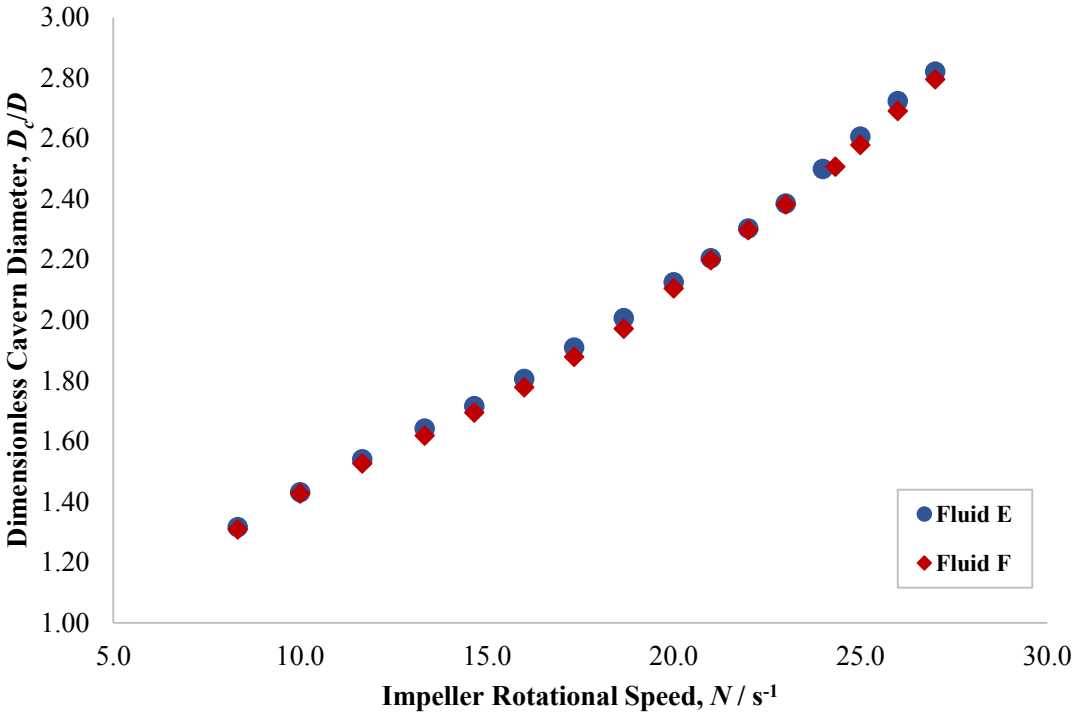

Figure 4.4. D_c/D versus N datasets for *Fluid E* and *Fluid F*, respectively. There is good agreement between the two sets of data, with an average difference in D_c/D values at a given N of 0.93% ($R^2 = 0.999$).

From Section 4.2.5.1, the AAD associated with the fluid formulation and rheological characterisation procedure was 4.2% ($R^2 = 0.997$), whilst the errors associated with the mixing procedure (Section 4.2.5.2), in terms of the average difference in D_c/D values at a given N, for the RT was AAD = 0.67% ($R^2 = 0.100$) and the pitched-blade turbine was AAD = 0.93% ($R^2 = 0.999$). Based on these findings, it can be determined that the main sources of error stem from the formulation and rheological characterisation of fluids. Potential reasons for these errors may include the limited control of the entrainment of air within the sample of material being rheologically characterised, and errors associated with weighing out the various quantities of each of the materials used in the fluid formulation process. Unless otherwise stated, the errors and associated error bars fall within the size of the data points, or their mutual overlap, on all plots in this work.

4.3 Numerical methods

Throughout the entirety of this PhD project, all numerical simulations were carried out by Dr Lyes Kahouadji, as part of a collaboration with Dr Lyes Kahouadji, Prof Omar Matar and the Matar Fluids Group. Dr Lyes Kahouadji has given permission for the numerical results to be presented in full in this thesis. Details relating to the numerical construction of the mixing system, the governing equations, numerical methods and the numerical validation can found in Section A.4 of the Appendix. Figure 4.5 shows the numerical structure of the mixing vessel system, equipped with a RT impeller.

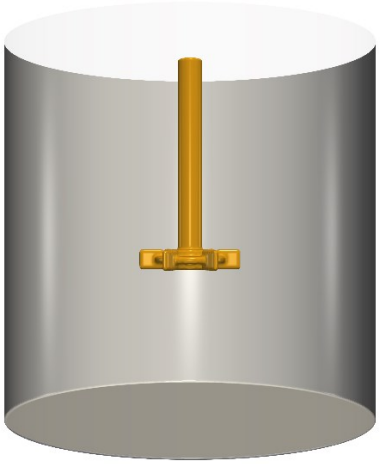

Figure 4.5. Numerical construction of all parts of the mixing system. In this case, the mixing vessel is equipped with a RT impeller.

4.4 Results and discussion

4.4.1 *Preliminary study:* Increasing impeller rotational speed, *N*

As an initial study, the effect of impeller rotational speed, N on cavern size was investigated. Taking the experimental Scale 3 (20 L) system equipped with a Rushton turbine (RT) impeller (D = 0.084 m) as an example (see '*Case 5*' in Table 4.1 and Table 4.2 for the rheological and physical properties, respectively), Figure 4.6 shows that as N increased, the cavern size increased. The three selected N values were (a) 9.3 s^{-1}, (b) 11.7 s^{-1} and (c) 14.0 s^{-1}, and resulted in dimensionless cavern diameters, D_c/D of (a) 1.74, (b) 2.17, and (c) 2.59, respectively. As N increases, the shear stress imparted on the material by the impeller increases, and therefore more of the material experiences shear stress values greater than that of the yield stress, resulting in a greater extent of fluid flow and increased cavern sizes. Increased N producing larger cavern sizes is a common finding in the literature (Solomon *et al.* (1981); Elson *et al.* (1986)). With increased N and cavern sizes, there was also an expected increase in the modified power-law Reynolds number, Re_m: (a) 20.5, (b) 29.5 and (c) 39.6 and the yield stress Reynolds number, Re_y: (a) 14.5, (b) 23.0 and (c) 33.3. Similar behaviour was displayed by fluids at the other scales and when using different impeller types (PBT), namely as N increased, the cavern became larger.

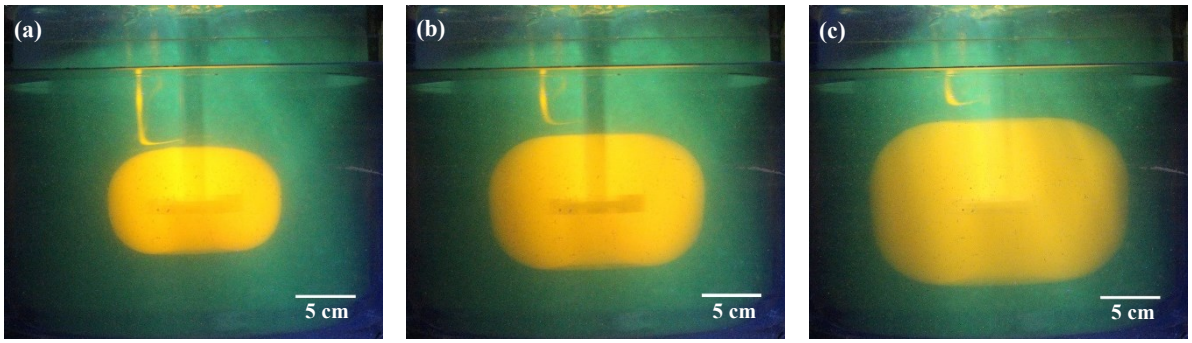

Figure 4.6. Experimental images from the Scale 3 setup equipped with 6-bladed RT impeller (D = 0.084 m), when the fluid (*Case 5*) was agitated at (a) N = 9.3 s^{-1} (Re_m = 20.5, Re_y = 14.5), (b) N = 11.7 s^{-1} (Re_m = 29.5, Re_y = 23.0), and (c) N = 14.0 s^{-1} (Re_m = 39.6, Re_y = 33.3), leading to caverns with D_c/D of (a) 1.74, (b) 2.17 and (c) 2.59, respectively.

4.4.2 Possible factors impacting flows

4.4.2.1 Varying tank diameter, *T*

To investigate the impact of tank diameter on the flows, a fluid was mixed in the Scale 1 (2 L) and Scale 2 (5 L) tanks, both with the D = 0.041 m RT impeller. Various geometrical ratios were maintained between the two studies, including $H/D \approx 3.30$, $C/D \approx 1.42$ and $S/D \approx 0.24$. The Scale 1 tank had a T_1 = 0.201 m, whilst the Scale 2 tank had a T_2 = 0.147 m, leading to $T_1/D \approx 3.59$ and $T_2/D \approx 4.90$. The C980 fluid had Herschel-Bulkley parameters: τ_y = 20.1 Pa, K = 5.2 and n = 0.44 ($\dot{\gamma}$ range = 0.00247-962 s^{-1}, AAD = 1.96%, R^2 = 0.998). The fluid was mixed over the range of N = 6.7-19.2 s^{-1} (Re_m = 6.1-31.8, Re_y = 3.7-30.8) for both studies, with D_c/D being measured at each incremental N value. As seen by the plot of D_c/D against N in Figure 4.7, there was good agreement between both D_c/D datasets, over the range of N investigated, with an AAD in D_c/D at a given N of 0.45% and an R^2 = 1.000. The average cavern aspect ratio, H_c/D_c for each fluid over the range of N investigated was H_c/D_c = 0.50 for the $T_1/D \approx 3.59$ system, and H_c/D_c = 0.51 for the $T_2/D \approx 4.90$ system. The upper limit in N value was dictated by the cavern reaching the tank wall ($D_c \approx T_1$) in the 2 L vessel, hence showing that the size of the tank had no impact on the development of caverns up until $D_c \geq T$, as would be expected because the material outside of the cavern wall is stagnant.

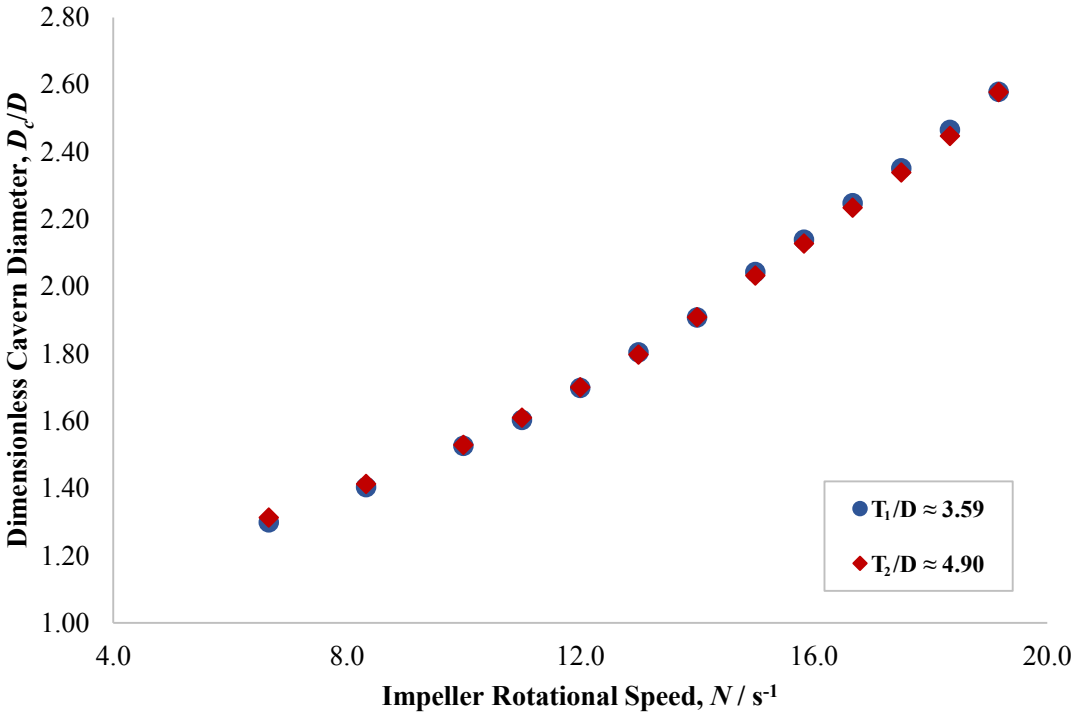

Figure 4.7. D_c/D versus N datasets, resulting from RT (D = 0.041 m) agitation, for the $T_1/D \approx 3.59$ (Scale 1) and the $T_2/D \approx 4.90$ (Scale 2) systems, respectively. There is good agreement between the two sets of data, with an AAD in D_c/D values at a given N of 0.45% (R^2 = 1.000).

The process was repeated using both the Scale 1 (2 L) and Scale 2 (5 L) tanks, and a C980 fluid with Herschel-Bulkley parameters: τ_y = 27.7 Pa, K = 6.9 and n = 0.44 ($\dot{\gamma}$ range = 0.000473-933 s^{-1}, AAD = 1.85%, R^2 = 0.999), but now using the PBT impeller (D = 0.041 m) for agitation. The fluid was mixed over the range of N = 10.0-26.7 s^{-1} (Re_m = 8.8-40.7, Re_y = 6.1-43.2) for both studies, leading to an AAD in D_c/D at a given N of 1.31% and an R^2 = 0.998 (Figure 4.8). The average H_c/D_c for the $T_1/D \approx 3.59$ and the $T_2/D \approx 4.90$ systems were both 0.47. These results are in good agreement with the RT study, helping to validate the conclusion that when $D_c < T$, the size of the vessel has no impact on the cavern size or shape.

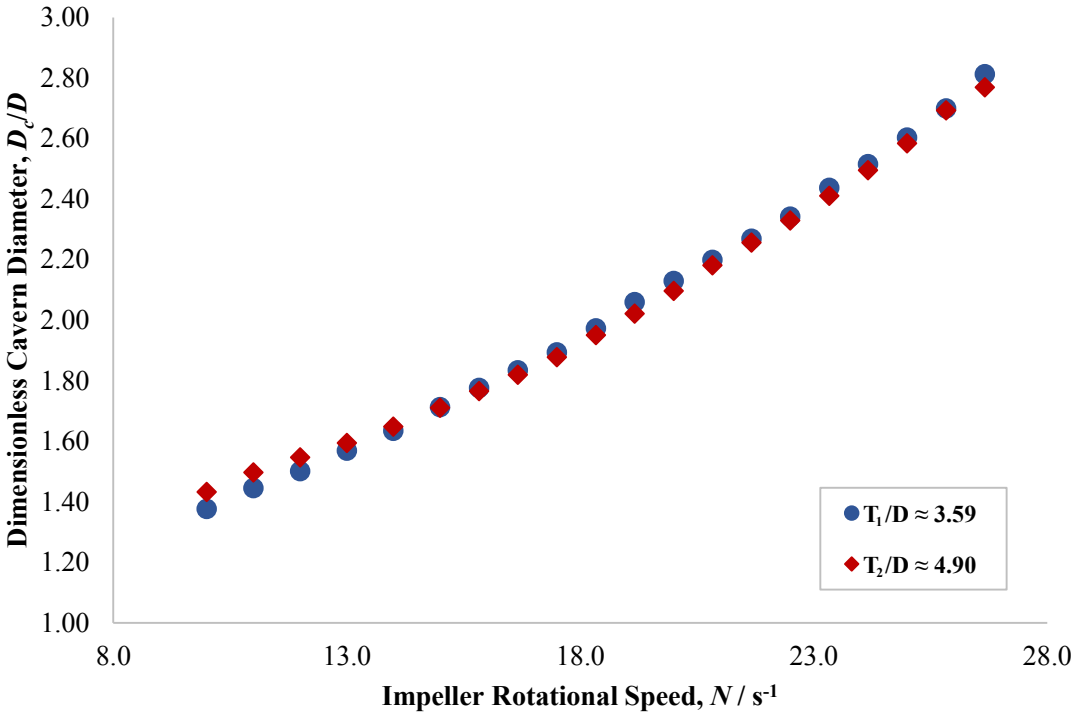

Figure 4.8. D_c/D versus N datasets, resulting from PBT (D = 0.041 m) agitation, for the $T_1/D \approx 3.59$ (Scale 1) and the $T_2/D \approx 4.90$ (Scale 2) systems, respectively. There is good agreement between the two sets of data, with an AAD in D_c/D values at a given N of 1.31% (R^2 = 0.998).

4.4.2.2 Varying liquid fill height, *H*

To study the impact of liquid fill height, H on the flow properties of viscoplastic fluids in agitated systems, the Scale 1 (2 L) tank was equipped with an RT impeller (D = 0.041 m) and a C980 fluid, with Herschel-Bulkley parameters: τ_y = 20.1 Pa, K = 5.2 and n = 0.44 ($\dot{\gamma}$ range = 0.00247-962 s^{-1}, AAD = 1.96%, R^2 = 0.998), was loaded into the vessel at two H values: H_1 = 0.135 m and H_2 = 0.100 m, leading to $H_1/D \approx 3.30$ and $H_2/D \approx 2.44$, respectively. As before, various geometrical length scales were maintained over both studies, including: C = 0.058 m ($C/D \approx 1.42$), T = 0.147 m ($T/D \approx 3.59$) and S = 0.01 m ($S/D \approx 0.24$). The range of investigated N was: N = 6.7-19.2 s^{-1} (Re_m = 6.1-31.8, Re_y = 3.7-30.8) for the $H_1/D \approx 3.30$ system, and N = 6.7-16.7 s^{-1} (Re_m = 6.1-25.6, Re_y = 3.7-23.2) for the $H_2/D \approx 2.44$ system, with the upper limit of N being dictated by when the cavern reached the interface in the $H_2/D \approx 2.44$ system. Over the range of N = 6.7-16.7 s^{-1} (Re_m = 6.1-25.6, Re_y = 3.7-23.2), there was an AAD in D_c/D at a given N of 1.65% and an R^2 = 0.998, with the two datasets of D_c/D versus N being seen in Figure 4.9, whereby the values of D_c/D for the $H_1/D \approx 3.30$ system are slightly greater at a given N than the D_c/D values for the $H_2/D \approx 2.44$ system, with the exception of the D_c/D values at N = 6.7 s^{-1} (Re_m = 6.1, Re_y = 3.7). Again, over the range of N = 6.7-16.7 s^{-1} (Re_m = 6.1-25.6, Re_y = 3.7-23.2), the average H_c/D_c for the $H_1/D \approx 3.30$ and $H_2/D \approx 2.44$ systems were 0.49 and 0.50, respectively. These results highlight that the cavern shape

and size in these viscoplastic fluids were only very slightly affected by the liquid fill height, before the cavern reached the interface (which often became deflected if the impeller was situated near the interface).

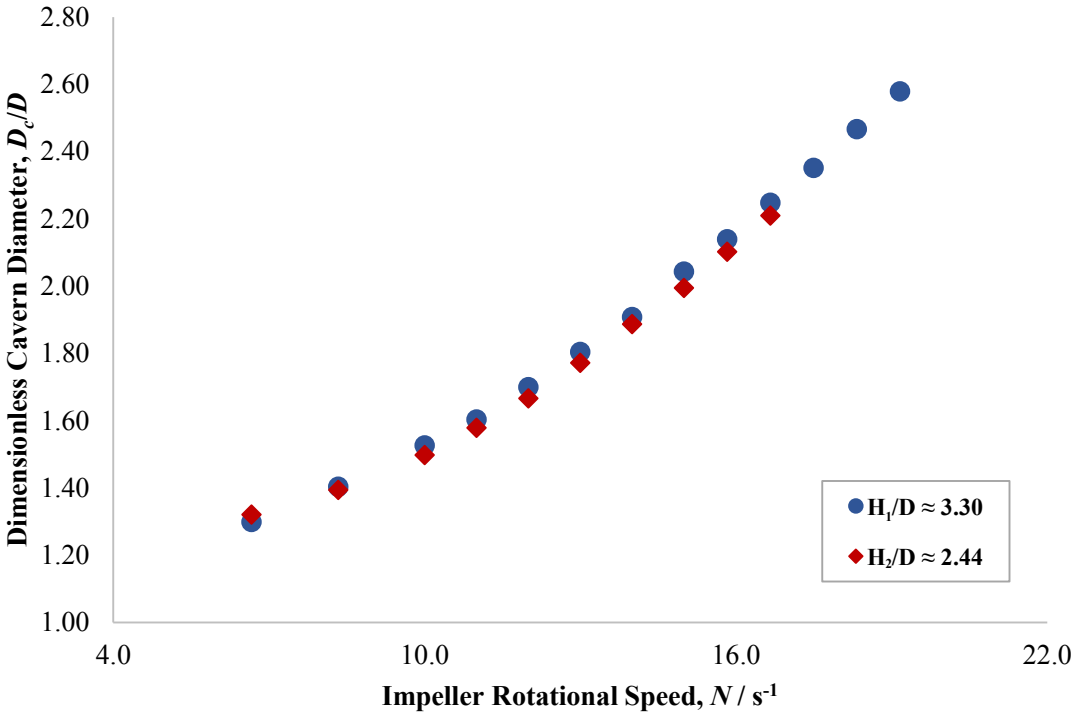

Figure 4.9. D_c/D versus N datasets, resulting from RT (D = 0.041 m) agitation, for the $H_1/D \approx 3.30$ and the $H_2/D \approx 2.44$ systems, respectively. There is good agreement between the two sets of data, with an AAD in D_c/D values at a given N of 1.65% (R^2 = 0.998) over the range of N = 6.7-16.7 s^{-1} (Re_m = 6.1-25.6, Re_y = 3.7-23.2).

As before, the procedure was repeated, using the same vessel, C/D, T/D and S/D, but now using a PBT (D = 0.041 m) impeller. In this case, the C980 fluid had Herschel-Bulkley parameters: τ_y = 27.7 Pa, K = 6.9 and n = 0.44 ($\dot{\gamma}$ range = 0.000473-933 s^{-1}, AAD = 1.85%, R^2 = 0.999) and the H values were again: H_1 = 0.135 m and H_2 = 0.100 m, leading to $H_1/D \approx 3.30$ and $H_2/D \approx 2.44$, respectively. D_c/D values were measured over the range of N = 10.0-26.7 s^{-1} (Re_m = 8.8-40.7, Re_y = 6.1-43.2) (although only data up to N = 24.2 s^{-1} (Re_m = 34.9, Re_y = 35.4) shown in Figure 4.10) for the $H_1/D \approx 3.30$ system, and N = 10.0-21.7 s^{-1} (Re_m = 8.8-29.5, Re_y = 6.1-28.5) for the $H_2/D \approx 2.44$ system. At N > 21.7 s^{-1} (Re_m = 29.5, Re_y = 28.5), the cavern reached the interface in the $H_2/D \approx 2.44$ system. Figure 4.10 shows that in this example, there was a bigger deviation in the D_c/D datasets over the range of N = 10.0-21.7 s^{-1} (Re_m = 8.8-29.5, Re_y = 6.1-28.5) compared to the RT case, with an AAD in D_c/D at a given N of 4.41% and an R^2 = 0.993. Similar to the RT case, the $H_1/D \approx 3.30$ system produced larger D_c/D values at every value of N, whilst the average H_c/D_c value over the range of N = 10.0-21.7 s^{-1} (Re_m = 8.8-29.5, Re_y = 6.1-28.5) was 0.46 and 0.45 for $H_1/D \approx 3.30$ and $H_2/D \approx 2.44$, respectively. These results highlight that H does have an impact on the cavern size and morphology, before the cavern reaches the interface, likely to be caused by the effects of

interface deflection seen in the $H_2/D \approx 2.44$ system, but not in the $H_2/D \approx 3.30$ system. As a result, if mixing studies were performed over different scales, efforts should be made to maintain H/D, if possible.

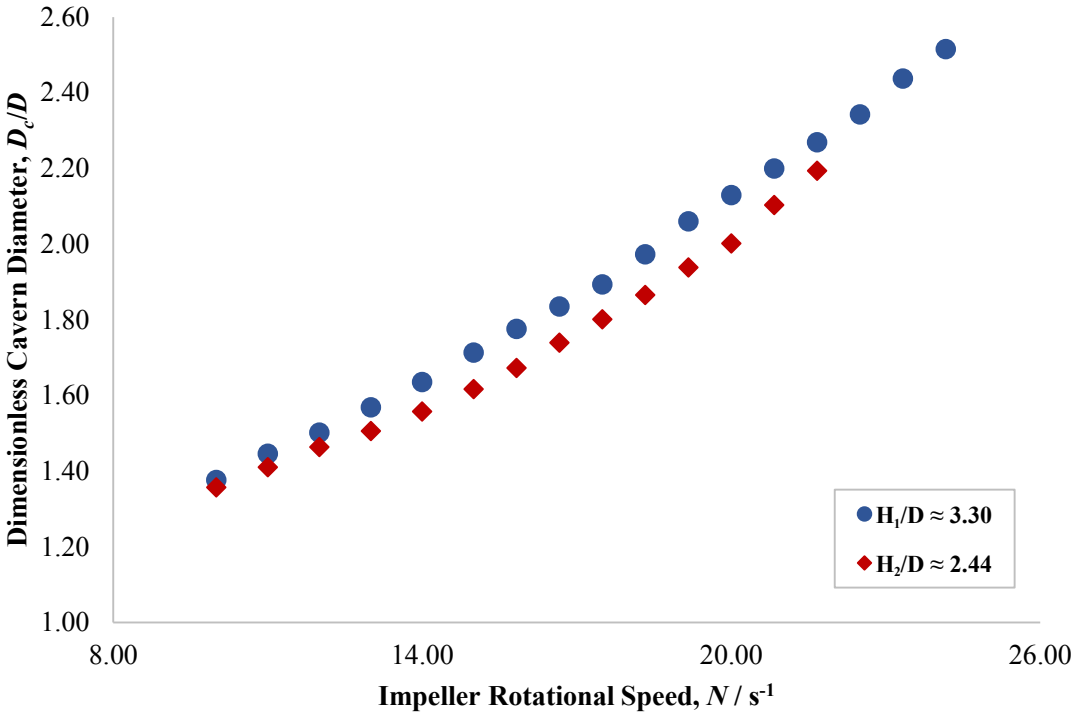

Figure 4.10. D_c/D versus N datasets, resulting from PBT (D = 0.041 m) agitation, for the $H_1/D \approx 3.30$ and the $H_2/D \approx 2.44$ systems, respectively. There is relatively good agreement between the two sets of data, with an AAD in D_c/D values at a given N of 4.41% (R^2 = 0.993) over the range of N = 10-21.7 s^{-1} (Re_m = 8.8-29.5, Re_y = 6.1-28.5), however, the $H_1/D \approx 3.30$ system seemed to produce slightly larger D_c/D values at every investigated N.

4.4.2.3 Varying shaft diameter, *S*

Another variable thought to have a possible effect on the flow properties of viscoplastic materials was shaft diameter, with three different shafts being used in the agitation setup, each in conjunction with the RT (D = 0.059 m) impeller. The Scale 2 (5 L) vessel was utilised for each study and the C980 fluid had Herschel-Bulkley parameters: τ_y = 43.4 Pa, K = 12.6 and n = 0.40 ($\dot{\gamma}$ range = 0.000208-741 s^{-1}, AAD = 1.93%, R^2 = 0.998). Over the three studies, various geometrical length scales were maintained, including: C = 0.084 m ($C/D \approx 1.42$), T = 0.201 m ($T/D \approx 3.41$) and H = 0.177 m ($H/D \approx 3.00$), and the three shafts used had S values of: S_1 = 0.010 m ($S_1/D \approx 0.17$), S_2 = 0.014 m ($S_2/D \approx 0.24$) and S_3 = 0.20 m (S_3/D = 0.35).

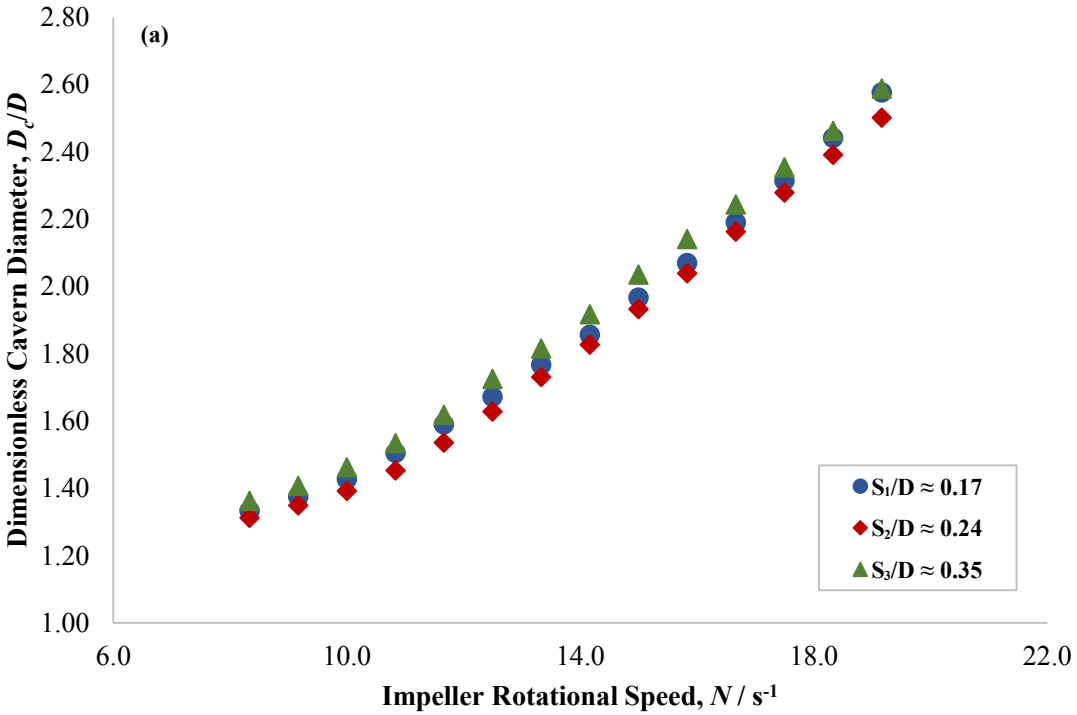

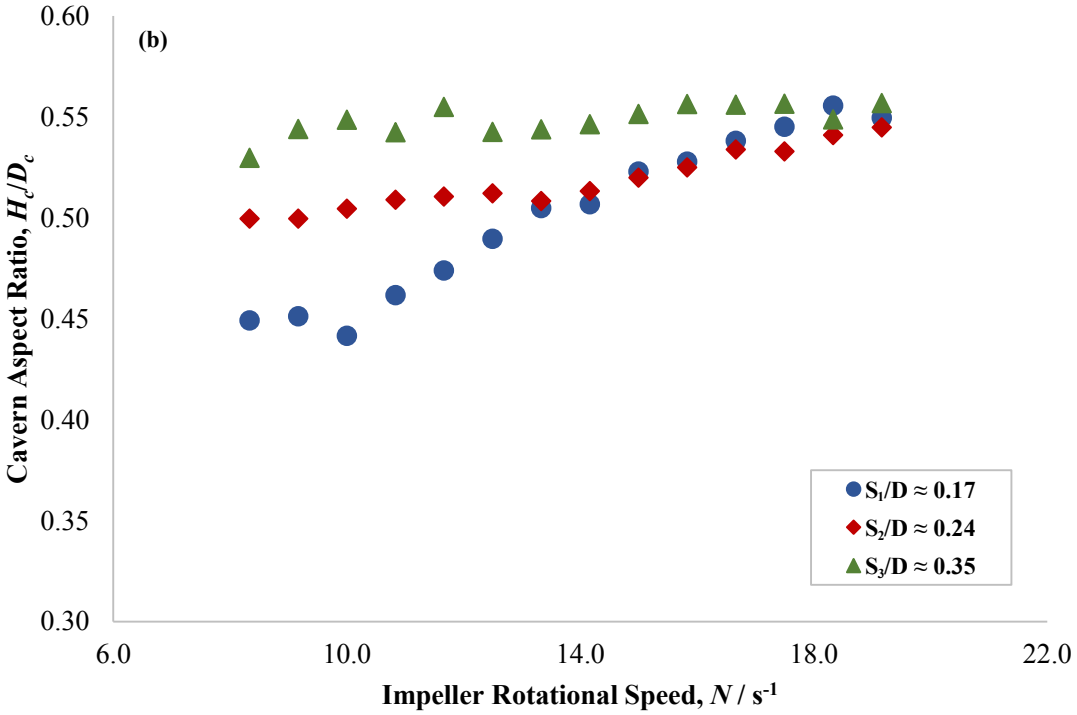

Figure 4.11. (a) D_c/D versus N datasets, resulting from RT (D = 0.041 m) agitation, for $S_1/D \approx 0.17$, $S_2/D \approx 0.24$ and $S_3/D \approx 0.35$ systems, respectively. There was good agreement between the datasets, showing that S had limited effect on D_c. (b) H_c/D_c versus N dataset for the three systems, showing that S had a significant impact on cavern size, particularly at low N.

For the three studies, the range of investigated $N = 8.3\text{-}19.2\ s^{-1}$ ($Re_m = 8.2\text{-}31.2$, $Re_y = 5.6\text{-}29.5$), with Figure 4.11(a) showing D_c/D datasets for each system. As can been seen from the figure, there is good agreement between the three datasets, suggesting that shaft diameter has a limited impact on D_c. The average H_c/D_c for the $S_1/D \approx 0.17$ system was 0.50, for the $S_2/D \approx 0.24$ system was 0.52 and for the $S_3/D \approx 0.35$ was 0.55. Inspection of Figure 4.11(b), which is a plot of H_c/D_c against N for the three systems, explains why the average H_c/D_c increases with increasing S, because at low N values, S has a significant impact on the flow, with the largest shaft system producing caverns with greater H_c/D_c than the smallest shaft systems. For example, at $N = 9.2\ s^{-1}$ ($Re_m = 9.6$, $Re_y = 6.7$), the $S_1/D \approx 0.17$ system had an H_c/D_c 0.45, for the $S_2/D \approx 0.24$ system had an H_c/D_c 0.50 and for the $S_3/D \approx 0.35$ had an H_c/D_c 0.54. As N increased, H_c/D_c for the three systems approximately converged. As a result, if mixing studies were to be performed over different scales, with the intention of maintaining geometric similarity, S has a significant impact on the cavern properties of viscoplastic materials, namely H_c/D_c and hence S/D should be preserved.

As with the previous investigations, the process was repeated using the same vessel (5 L), C/D, T/D and H/D, but now using a PBT ($D = 0.059$ m) impeller. In this case, the C980 fluid used had noticeably different rheology, with Herschel-Bulkley parameters: $\tau_y = 22.9$ Pa, $K = 5.8$ and $n = 0.45$ ($\dot{\gamma}$ range = 0.000254-992 s^{-1}, AAD = 2.12%, $R^2 = 0.998$). The same S values were used as with the RT case: $S_1 = 0.010$ m ($S_1/D \approx 0.17$), $S_2 = 0.014$ m ($S_2/D \approx 0.24$) and $S_3 = 0.20$ m ($S_3/D = 0.35$), and range of $N = 7.3\text{-}18.3\ s^{-1}$ ($Re_m = 13.2$, $Re_y = 8.2$) was investigated for each system. Figure 4.12(a) shows there is good agreement between the three D_c/D datasets over the range of $N = 7.3\text{-}18.3\ s^{-1}$ ($Re_m = 13.2$, $Re_y = 8.2$), however, as before the H_c/D_c datasets (Figure 4.12(b)) show that at low N, as S increases, H_c/D_c increases, with H_c/D_c approximately converging to a similar value at higher N, for the three systems. The average H_c/D_c for the $S_1/D \approx 0.17$ system was 0.46, for the $S_2/D \approx 0.24$ system was 0.48 and for the $S_3/D \approx 0.35$ was 0.51. These results further highlight the need to uphold S/D when performing mixing studies over different scales.

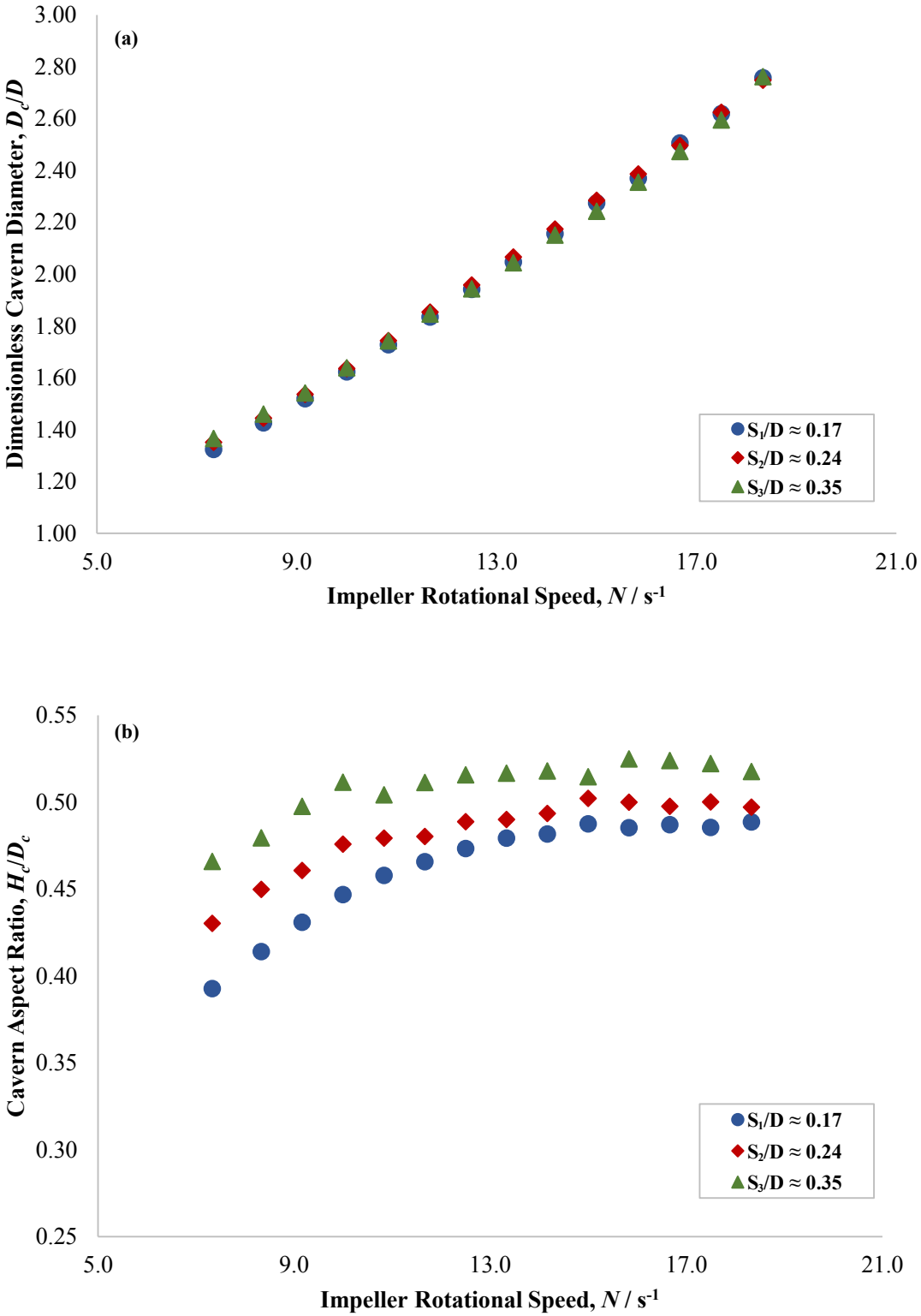

Figure 4.12. (a) D_c/D versus N datasets, resulting from PBT (D = 0.041 m) agitation, for $S_1/D \approx 0.17$, $S_2/D \approx 0.24$ and $S_3/D \approx 0.35$ systems, respectively. There was good agreement between the datasets, showing that S had limited effect on D_c. (b) H_c/D_c versus N dataset for the three systems, showing that S had a significant impact on cavern size, particularly at low N.

4.4.2.4 Varying impeller clearance, *C*

This parameter was not directly investigated, as it was assumed that the effects of C from the bottom of the vessel, are similar to the effects of T, with cavern sizes and morphologies not being impacted by C, until the cavern reaches the bottom of the tank.

4.4.2.5 Factors impacting flow properties in viscoplastic mixing processes

Based on the findings of the previous four sections, when mixing viscoplastic fluids in stirred vessel system, S appears to have a significant influence on the flow properties of the fluid, in particular H_c/D_c, whilst H has a minor impact on cavern development, likely to be caused by the effects of interface deflection if the impeller is situated near the interface. T appears to have a negligible impact on the flows, when $D_c < T$, and it is hypothesised that C has a limited effect on cavern properties, until the cavern reaches the bottom of the tank. As a result, when performing mixing processes of viscoplastic fluids over different scales, it is important to maintain S/D, with less significance being placed on preserving H/D, T/D and C/D. However, for the remaining work presented in this chapter, efforts have been made to uphold S/D, H/D, T/D and C/D (where possible) when performing mixing processes over all scales investigated, as a means of good practice.

4.4.3 *Mixing Study A*: Changing fluid rheology (RT agitation)

In the first of the main mixing studies in this work, the same mixing system and scale was used throughout, however the rheological properties of the fluids being mixed were varied, with the aim of matching dimensionless cavern sizes within each of the fluids. More specifically, the Scale 1 (2 L) vessel was utilised, equipped with an RT impeller (D = 0.041 m), and three different fluids were mixed. For each process: C = 0.058 m ($C/D \approx 1.42$), T = 0.147 m ($T/D \approx 3.59$), S = 0.01 m ($S/D \approx 0.24$) and H = 0.135 m ($H/D \approx 3.30$). The comparison of *Case 1*, *Case 2* and *Case 3* enabled *Mixing Study A*, with the Herschel-Bulkley fitted data and the physical properties for these three cases being found in Table 4.1 and Table 4.2, respectively (Section 4.2.2). The rheological flow curves of the three fluids used in *Mixing Study A* can be seen in Figure 4.13.

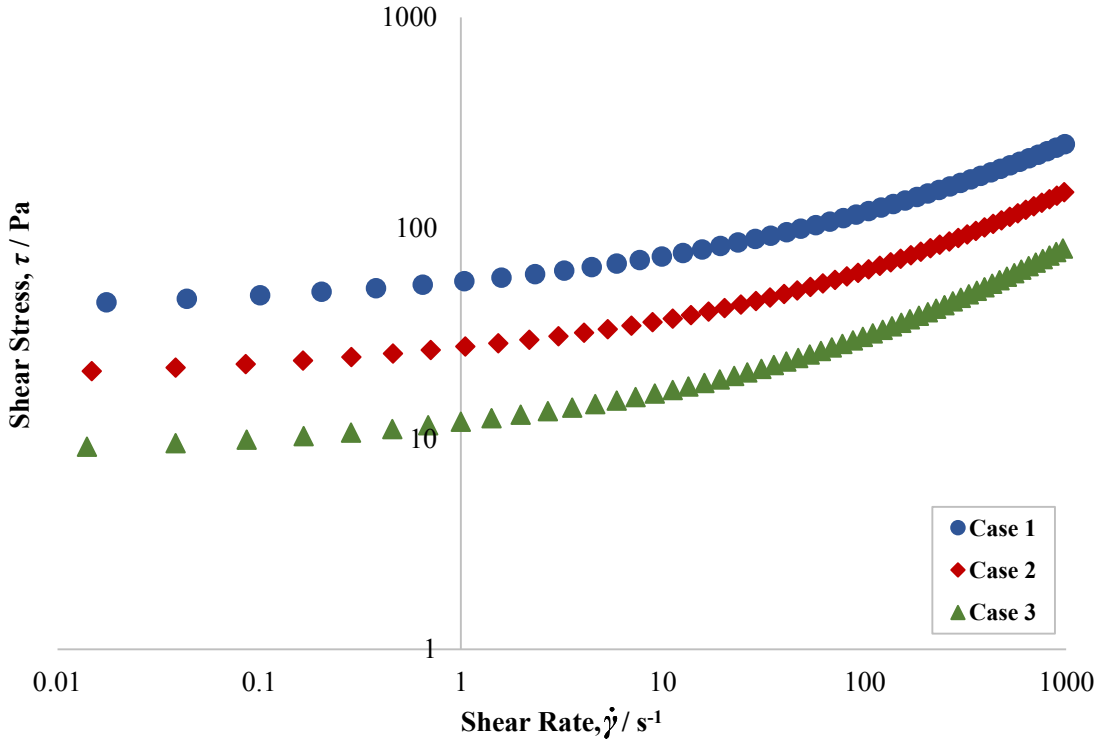

Figure 4.13. Raw rheological flow curves for the fluids from *Case 1*, *Case 2* and *Case 3*, acquired through shear-stress down sweeps using the shear-stress controlled Anton Paar Modular Compact Rheometer 302 rheometer, fitted with a roughened cone-and-plate geometry (12.6 μm roughness, 0.998° cone angle, cone and plate diameter = 50 mm, CP50-1-41592).

Each of the three fluids underwent agitation with the RT impeller, with N being incrementally increased until each of the caverns reached the tank wall ($D_c \approx T$). Cavern sizes increased with increasing N, however the N value required to generate caverns of given size varied from fluid to fluid due to the differences in rheological properties. As the τ_y and K values of a fluid decreased, the N value required to generate a cavern of a particular size decreased. The stress (and therefore the force) being imparted on the material is controlled by the N, if the impeller size and shape remains constant. In Figure 4.14, (a)-(c) are images of caverns formed in the *Case 1* (largest τ_y and K), *Case 2* and *Case 3* (smallest τ_y and K) systems, respectively. For (a) *Case 1* and (b) *Case 2*, the caverns have been distinguished with a green food dye, whereas a blue food dye was used for (c) *Case 3*. These images highlight caverns of approximately constant size, with $D_c/D \approx 1.92$. The N required to generate these caverns decreased from (a) 19.3 s^{-1} (Re_m = 15.9, Re_y = 14.7) to (b) 14.0 s^{-1} (Re_m = 19.5, Re_y = 15.3) and down to (c) 9.7 s^{-1} (Re_m = 22.1, Re_y = 17.0). Figure 4.15 is a plot of the experimentally-derived D_c/D against a range of N for *Cases 1-3*, along with the numerical results for selected N values. Over these ranges, the average cavern aspect ratios, H_c/D_c were 0.51, 0.53 and 0.49 for *Case 1*, *Case 2* and *Case 3*, respectively. There is good agreement between the experimentally- and numerically-derived D_c/D at each of the selected N values. In the numerical study, the cavern boundary was defined as having a velocity magnitude of 0.01 m s^{-1}. The AAD between experimental and numerical results for *Case 1*, *Case 2* and *Case 3* were 2.7%, 2.7%

and 5.1%, respectively. These results further justified the validity of the CFD model. The cavern boundary definition of 0.01 m s^{-1} was selected as it was confirmed via independent numerical trials that this gave good agreement with the experimental data. As a result, this value was used in the main mixing studies in this work. Other velocity magnitude values were tested, however 0.01 m s^{-1} gave the best results.

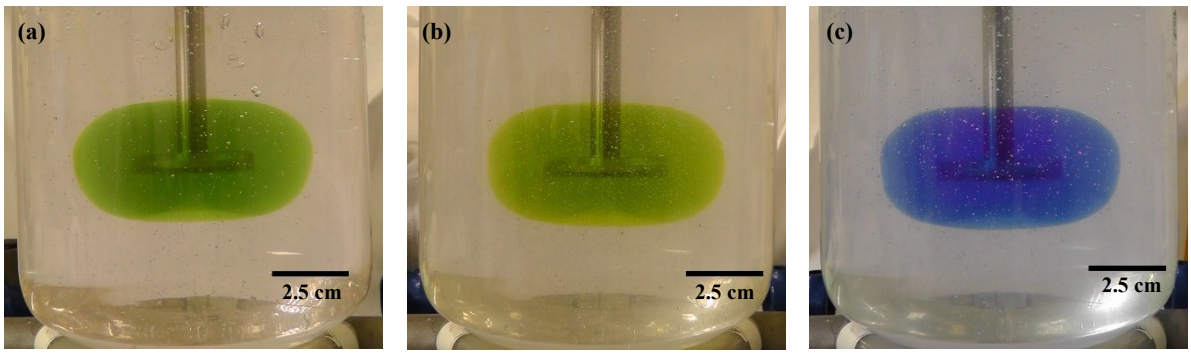

Figure 4.14. Images of caverns with D_c/D ~1.92, formed in: (a) *Case 1*, (b) *Case 2*, and (c) *Case 3*. The τ_y and K values decrease from *Case 1* to *Case 3*, and with that, the necessary N required to generate caverns of this size, decreased: (a) 19.3 s^{-1} (Re_m = 15.9, Re_y = 14.7), (b) 14.0 s^{-1} (Re_m = 19.5, Re_y = 15.3), and (c) 9.7 s^{-1} (Re_m = 22.1, Re_y = 17.0).

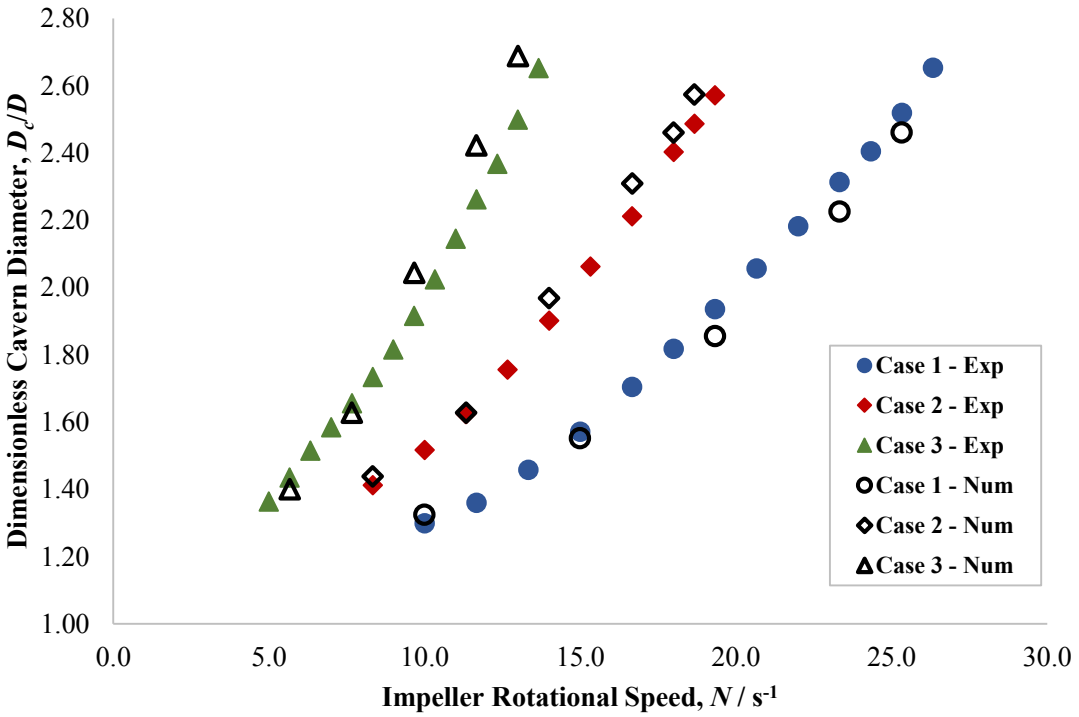

Figure 4.15. Both experimentally- and numerically-derived D_c/D against a range of N for *Case 1*, *Case 2* and *Case 3*. As expected, the experimental curves do not overlap with one another, and there is good agreement between the experimental and numerical data.

As can be seen from each image in Figure 4.14, the section of material directly below the centre of the impeller, at the base of the cavern, appears to be lighter in colour than the rest the cavern. This is due to radial nature of the Rushton turbine impeller, with the impeller blades inducing centrifugal forces and flow of the material towards the tank wall. As the fluid reaches the cavern wall, conservation of mass results in recirculation of the fluid back towards the impeller, with vortices forming above and below the impeller blades. The result is the formation of a 'horn' torus (or 'ringed-donut') cavern morphology, which is apparent in all the fluids mixed with a 6-bladed Rushton turbine impeller in this study, although it is less clear from the Scale 3 images (see Figure 4.6) due to the nature of the UV fluorescent dye system implemented. The formation of vortices above and below the impeller blades was further demonstrated via the CFD simulations using *Case 1* at $N = 19.3$ s^{-1} ($Re_m = 15.9$, $Re_y = 14.7$) as an example (Figure 4.16). Figure 4.16(a) and (c) show the velocity magnitude distribution within the cavern from both a (a) side-view and (c) top-view perspective, whilst Figure 4.16(b) shows the flow patterns, along with the overall cavern size. As seen in Figure 4.16(a) and (c), the velocity magnitude is greatest at the tip of each blade, with a sharp drop off in velocity going from the blade tips to the cavern wall. Figure 4.16(a) highlights the radial character of the flow, whilst Figure 4.16(c) highlights the anticlockwise nature of the rotation, as seen by the relatively high velocity magnitude values behind each blade. Further discussion can be found in Section 4.4.4. The vortices that result through Rushton turbine agitation of viscoplastic fluids have previously been observed by Arratia *et al.* (2006).

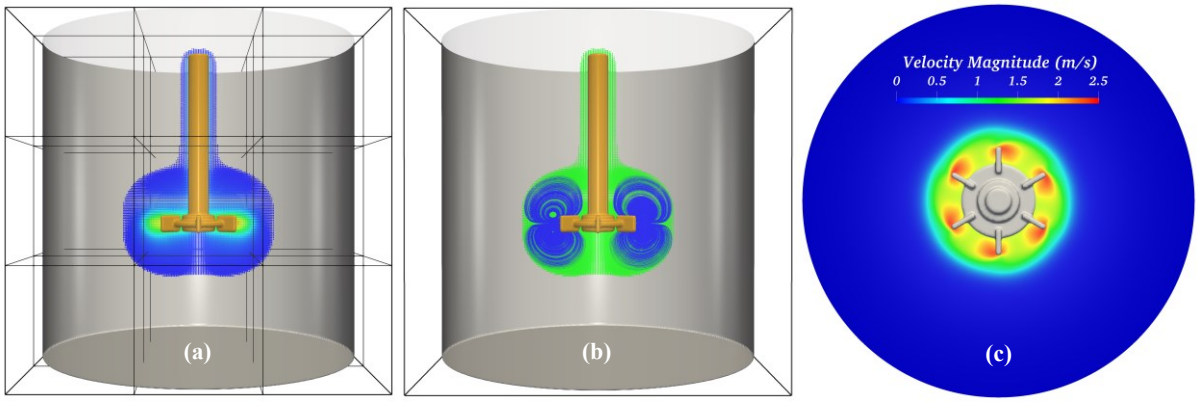

Figure 4.16. Velocity magnitude distribution formed in *Case 1* at $N = 19.33$ s^{-1} ($Re_m = 15.9$, $Re_y = 14.7$) from a side-view (a) and top-view (c) perspective, with the cavern boundary definition having a velocity magnitude of 0.01 m s^{-1}. Formation of vortices above and below the impeller blades, along with the overall cavern size can be seen in (b). (a) Highlights the subdomain decomposition for Scale 1. The calculation domain is divided into 3 × 3 × 3 = 27 subdomains, where each subdomain holds a regular grid mesh of 64 × 64 × 64 cells. The global resolution in the entire domain is then 192 × 192 × 192.

The results presented in Figures 4.14 and 4.15 show that when the rotational speed, N (a dimensional variable) was kept constant, dimensionless cavern sizes were not able to be matched and flow similarity was not achieved between fluids of varying rheological properties. From Section 4.2.4, the

dimensional analysis study suggested that scaling with respect to dimensionless parameters: Re_m, Re_y, n and k_s, may be more appropriate when attempting to achieve matched flows and dimensionless cavern sizes for these systems. Scaling with Re_m and Re_y instead of N resulted in slightly improved agreement between the curves of the three fluids, as seen in Figure 4.17(a) and (b), however the datasets still do not collapse upon one another, suggesting unmatched flows.

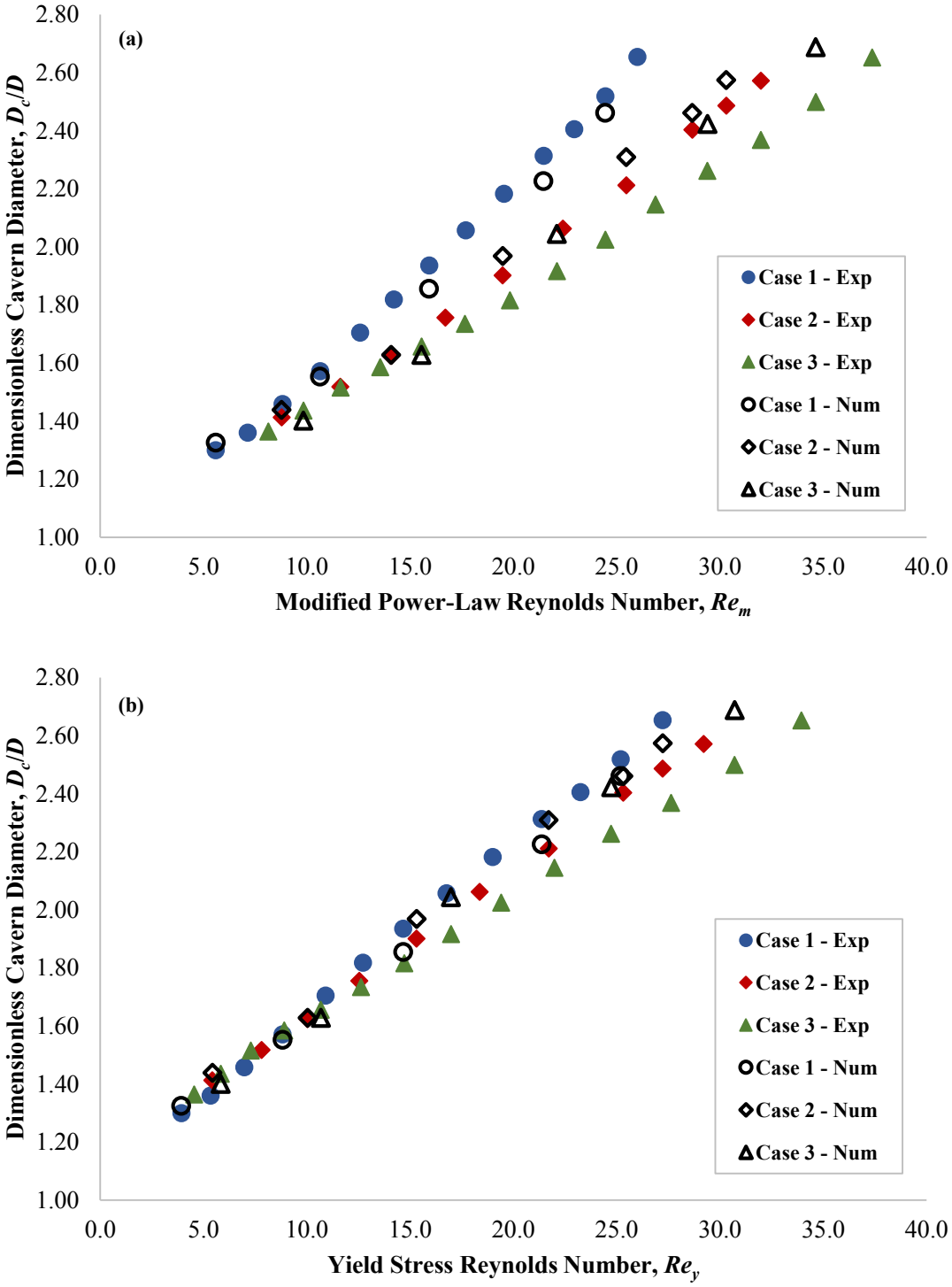

Figure 4.17. Both experimentally- and numerically-derived D_c/D against a range of (a) Re_m and (b) Re_y for *Case 1*, *Case 2* and *Case 3*. As expected, the experimental curves do not overlap with one another, in particular when scaling with respect to Re_y.

Due to this relatively poor collapse when scaling with Re_m (in particular) and Re_y, the D_c/D datasets were then scaled with respect to a combination of all of the outputted dimensionless parameters (Re_m, Re_y, n and k_s). Through the use of the Microsoft Excel Solver function, it was determined that both the experimental and numerical D_c/D datasets appear to collapse relatively well when scaling with $Re_m^{-0.3} Re_y^{0.6} n^{-0.1} k_s^{-1}$ (Figure 4.18), with a maximum absolute deviation in experimental and numerical D_c/D at a given $Re_m^{-0.3} Re_y^{0.6} n^{-0.1} k_s^{-1}$ of approximately 8% and 9%, respectively. As a result, this scaling method resulted in the best non-dimensional matching of cavern sizes when mixing fluids of varying rheological properties, on the same scale.

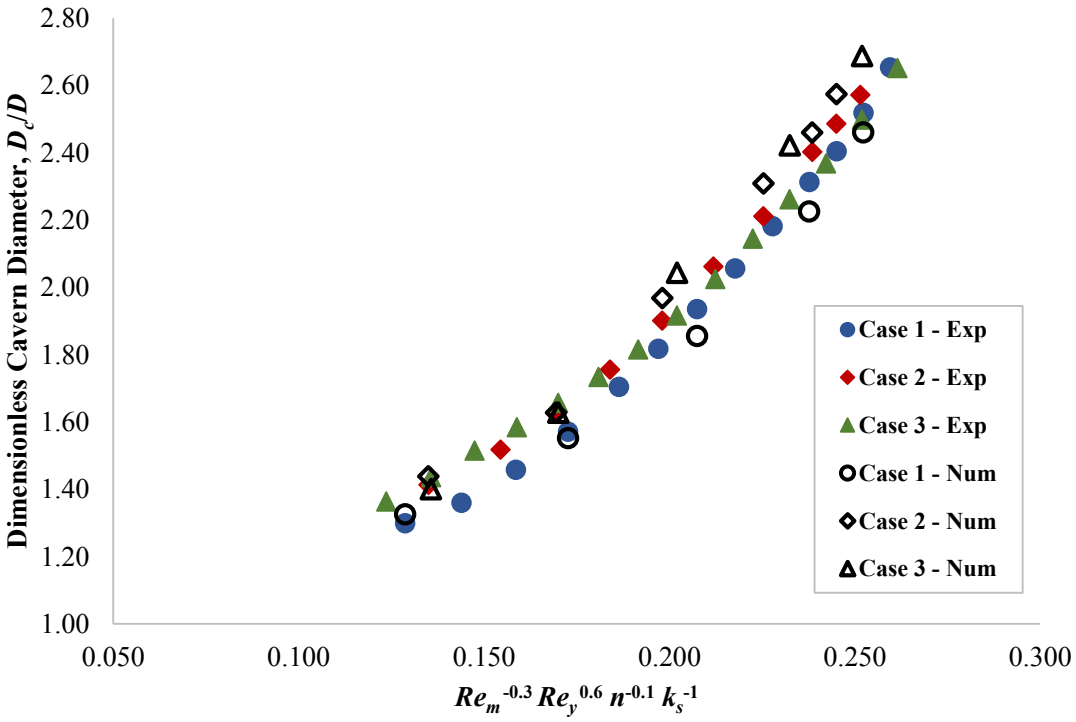

Figure 4.18. Experimentally- and numerically-derived dimensionless cavern diameters, D_c/D for *Case 1*, *Case 2* and *Case 3*, plotted against a combination of Re_m, Re_y, n and k_s. Through empirical fitting, the exponent terms which led to the best non-dimensional flow matching were -0.3, 0.6, -0.1 and -1 for Re_m, Re_y, n and k_s respectively.

4.4.4 *Mixing Study B*: Changing tank and impeller scale (RT agitation)

In this section, a C980 fluid was selected and mixed with geometrically-similar RT impellers over three different scales, with quoted vessel volumes of 2 L (Scale 1), 5 L (Scale 2) and 20 L (Scale 3). For the Scale 1, Scale 2 and Scale 3 systems, the diameters of the RT impellers used were D = 0.041 m, D = 0.059 m and D = 0.084 m, respectively. The comparison of *Case 1*, *Case 4* and *Case 5* enabled *Mixing Study B*, with the Herschel-Bulkley data and the physical properties for these three systems being found in Table 4.1 and Table 4.2 (Section 4.2.2). *Case 1* involved use of the smallest scale

system (Scale 1), *Case 4* involved mixing on the middle scale (Scale 2), whilst mixing in *Case 5* was performed on the largest scale (Scale 3) system. For each process, various important length scale ratios relating to the vessels were maintained, including: $C/D \approx 1.42$, $S/D \approx 0.24$, and $H/D \approx 3.30$. There was a slight discrepancy in T/D, with: $T_1/D_1 \approx 3.59$, $T_2/D_2 \approx 3.41$ and $T_3/D_3 \approx 3.57$, where, in this context, the subscripts '1', '2' and '3' denote Scale 1, Scale 2 and Scale 3, respectively, however as discussed in Section 4.4.2.1, this should have a negligible effect on the results. The same fluid was mixed over the three scales, however the rheological properties of the fluid varied slightly between *Cases 1* and *4*, compared with *Case 5*. This slight discrepancy was due to the variance in temperature of the fluid when the mixing studies were carried out and the accuracy of the Herschel-Bulkley fitting procedure. Hence, despite this discrepancy, the rheological properties were seen as being sufficiently similar to be within the errors associated with the rheological formulation and measurement procedure (outlined in Section 4.2.5) and thus had a limited effect on the results.

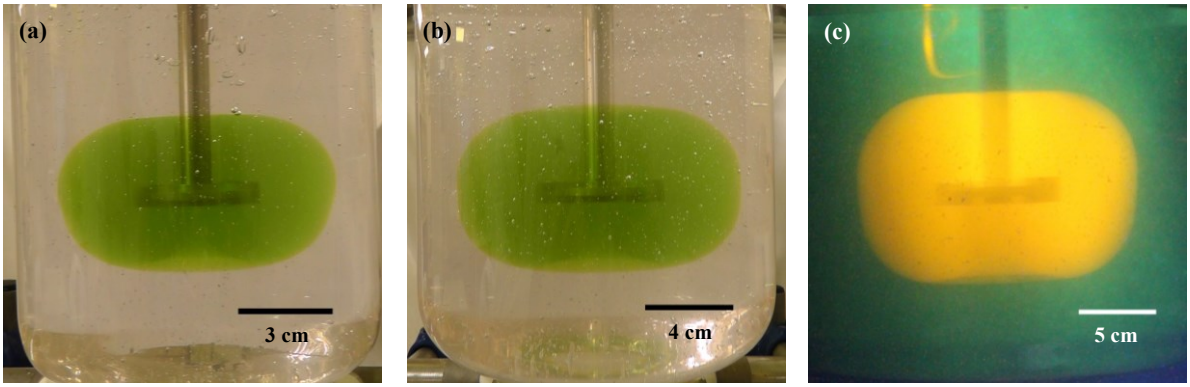

Figure 4.19. Experimental images of caverns with $D_c/D \sim 2.20$, formed in the: (a) *Case 1*, (b) *Case 4*, and (c) *Case 5* systems. With increasing scale (and hence impeller diameter, D), the necessary N required to generate caverns of this size, decreased: (a) 22.0 s^{-1} ($Re_m = 19.6$, $Re_y = 19.0$), (b) 15.5 s^{-1} ($Re_m = 23.2$, $Re_y = 19.5$) and (c) 11.7 s^{-1} ($Re_m = 29.5$, $Re_y = 23.0$).

Using similar methods to *Mixing Study A*, N was incrementally increased until the cavern reached the tank wall ($D_c \approx T$), with cavern sizes being captured at each selected N. Figure 4.19 shows images for caverns of $D_c/D \approx 2.20$ for (a) *Case 1*, (b) *Case 4* and (c) *Case 4*, respectively. Whilst mixing the same fluid, as the impeller diameter, D increased in size, less force from the impeller was required to obtain a cavern of a defined dimensionless size. This was reflected in the decrease in N required to generate caverns of $D_c/D \sim 2.20$, from 22.0 s^{-1} ($Re_m = 19.6$, $Re_y = 19.0$) to 15.5 s^{-1} ($Re_m = 23.2$, $Re_y = 19.5$) and down to 11.7 s^{-1} ($Re_m = 29.5$, $Re_y = 23.0$) for *Case 1*, *Case 4* and *Case 5*, respectively. As previously discussed, caverns with a 'horn' torus morphology were produced in each case, due to the radial nature of the RT impeller producing vortices above and below the impeller blades. This was further highlighted in the CFD snapshots in Figure 4.20(a)-(c), with the three caverns having a $D_c/D = 1.55$, 1.54 and 1.68, for *Case 1* (Figure 4.20(a)), *Case 4* (Figure 4.20(b)) and *Case 5* (Figure 4.20(c)), respectively. Due to

the qualitative nature of the experimental visualisation techniques employed in this study, CFD allows for independent confirmation of the experimentally observed cavern sizes, as well as information relating to velocity field distributions and flow patterns within the caverns to be attained, that would otherwise be unobtainable from experiment. The top row of images in Figure 4.20 display the velocity magnitude distributions that result when mixing the material with $N = 15.0$ s^{-1} (*Case 1*; $Re_m = 10.6$, $Re_y = 8.8$), N = 10.8 s^{-1} (*Case 4*; $Re_m = 13.2$, $Re_y = 9.5$) and $N = 8.6$ s^{-1} (*Case 5*; $Re_m = 18.3$, $Re_y = 12.6$). As would be expected, the velocity magnitude quickly decreases away from the blade region in the radial direction to the cavern wall. This sharp drop off in velocity away from the impeller blades is caused by decreased stresses being exerted on the material. As the stresses being imparted on the material by the impeller blades decrease, the fluid is able to re-build its structures within the material, resulting in the fluid becoming less liquid-like and more gel-like as distance from the blades increases, owing to the decreased velocity values of the fluid. This occurs until the stresses being imparted on the material are not great enough to overcome the material's yield stress and the material can no longer flow. This happens at the cavern wall, which is associated with very low velocity magnitude values (in this case 0.01 m s^{-1}), outside of which, the material is stagnant. The middle row of Figure 4.20 highlights the overall cavern size (indicated via the green colour) on each scale, defined by material flowing with a velocity magnitude of 0.01 m s^{-1} or greater. The vortices above and below the impeller blades are indicated via the blue flow lines and give reason to the observed 'horn' torus cavern morphology from the experimental studies. The high degree of symmetry between the sets of vortices highlights to the exclusively radial nature of the RT impeller. The bottom row from Figure 4.20 are CFD snapshots from a top-view perspective. These images show the velocity magnitude distributions within the caverns and highlight a maxima in velocity magnitude values within the direct vicinity of each of the impeller blades, and in particular behind the blades (impeller rotation in an anti-clockwise direction), as was observed in the top row images. From this top-view perspective, the result is the cavern adopting a morphology with slight hexagonal character at small D_c/D, developing into a circular shape at larger D_c/D. As was the case in the side-view snapshots, there is a sharp drop-off in velocity from the blade regions to the cavern wall, resulting in stagnant material outside of the cavern. The side-view CFD images from Figure 4.20 show that the cavern tracks up the shaft, as would be expected because the rotating shaft is able to agitate the material and induce fluid flow. Whilst performing the experimental mixing studies, fluid flow up the shaft was visualised, however, the dye system was unable to induce coloration in this section of the cavern.

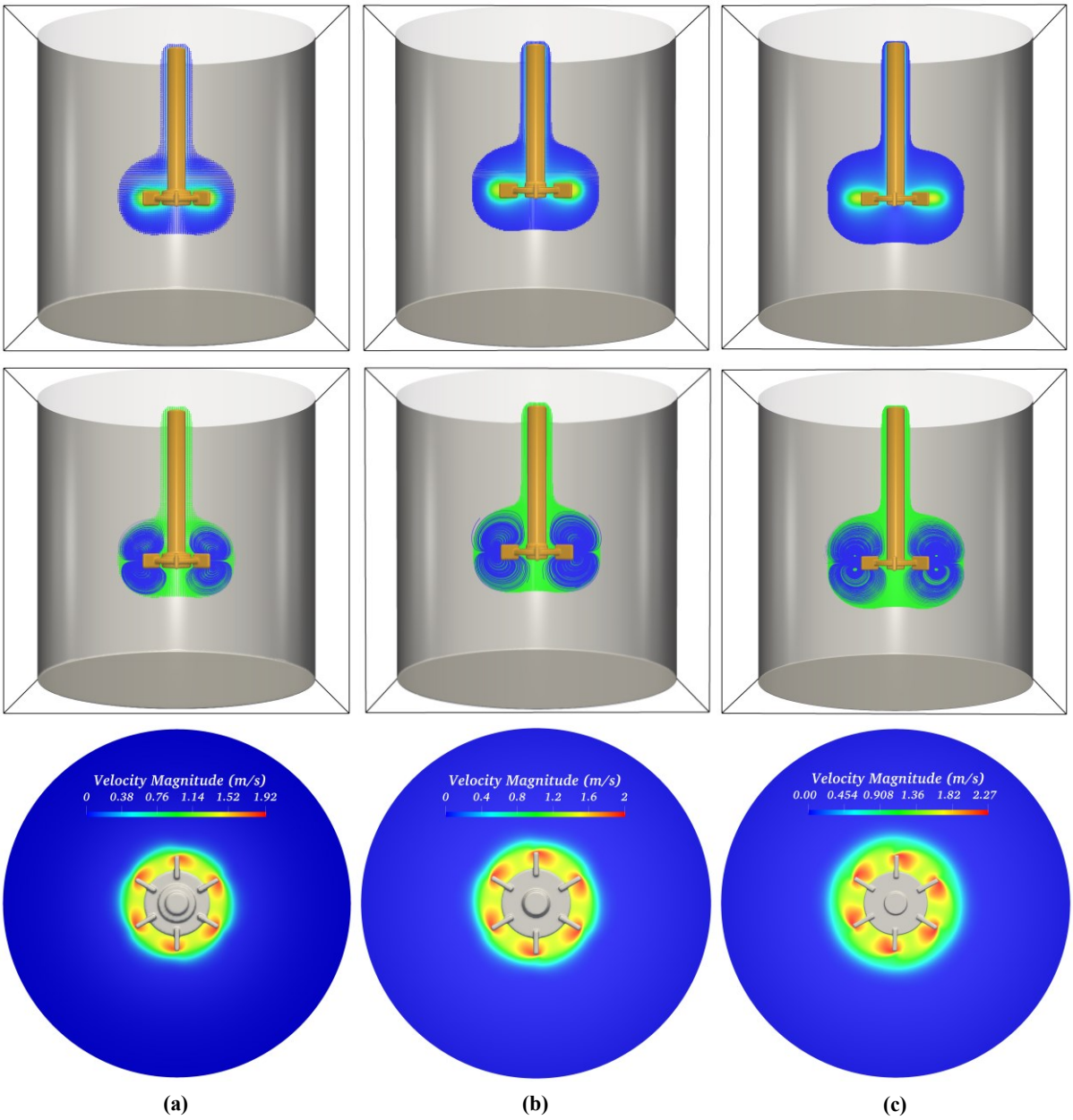

Figure 4.20. Side-view and top-view snapshots taken from CFD simulations of caverns with D_c/D = 1.55, 1.54 and 1.68, formed in the : (a) *Case 1*, (b) *Case 4*, and (c) *Case 5* systems. The necessary N required to generate caverns of this size were 15.0 s^{-1} (*Case 1*; Re_m = 10.6, Re_y = 8.8), 10.8 s^{-1} (*Case 4*; Re_m = 13.2, Re_y = 9.5) and 8.6 s^{-1} (*Case 5*; Re_m = 18.3, Re_y = 12.6). Velocity magnitude distributions can be seen in the top and bottom row of images, whilst vortices above and below the impeller blades, along with the overall cavern sizes, can be seen in the middle row images.

Figure 4.21 shows both the experimentally- and numerically-derived D_c/D plotted against the full range of N used on each scale. As before, the curves for the three scales did not collapse upon one another and flow similarity was not achieved scaling in this manner. Figure 4.21 shows good agreement between the numerical and experimental results, again with the cavern boundary defined by a velocity magnitude = 0.01 m s^{-1}. The AAD between experimental and numerical results for *Case 1*, *Case 4* and *Case 5* were 2.7%, 1.9% and 2.3%, respectively. Over this range of N, the average H_c/D_c were 0.51, 0.53 and 0.63

for *Case 1*, *Case 4* and *Case 5*, respectively. The reason for this discrepancy in H_c/D_c is not known, but thought to be the result of either some physical phenomenon not considered in this work, or slight optical distortion effects in the vertical direction.

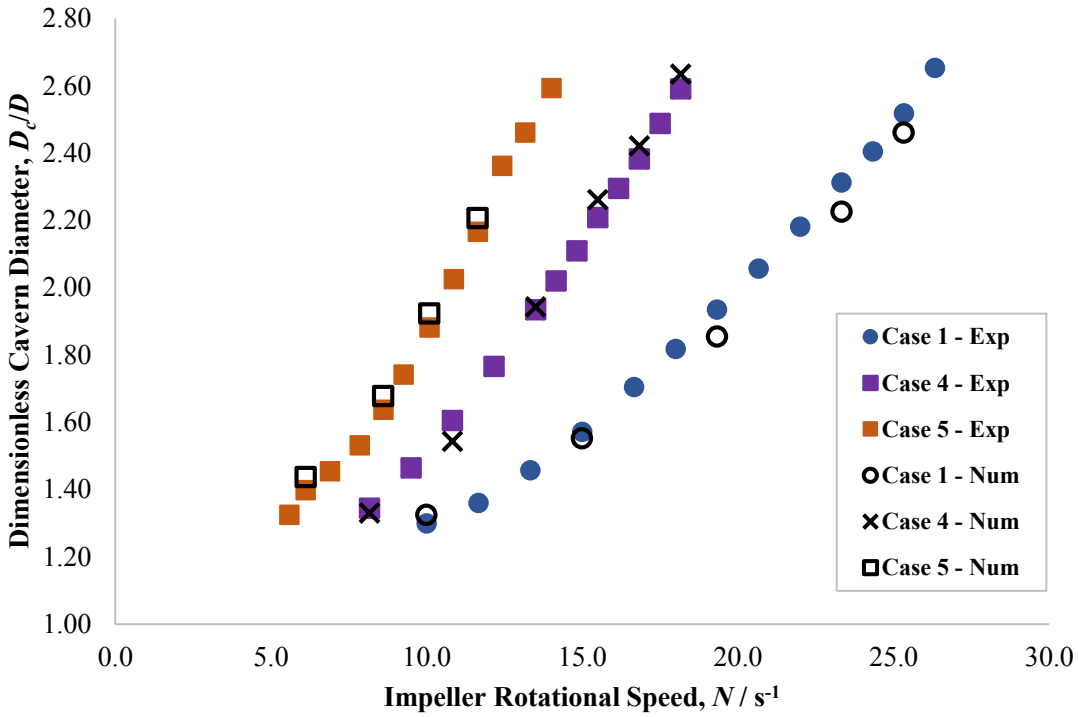

Figure 4.21. Both experimentally- and numerically-derived D_c/D against a range of N for mixing the fluid in the *Case 1*, *Case 4* and *Case 5* systems. As would be expected, the experimental curves do not overlap with one another, but there is good agreement between the experimental and numerical data.

Figure 4.22 shows good agreement between the D_c/D datasets for the *Case 1*, *Case 4* and *Case 5* when scaling with respect to $Re_m^{-0.3} Re_y^{0.6} n^{-0.1} k_s^{-1}$, with a maximum absolute deviation in experimental and numerical D_c/D at a given $Re_m^{-0.3} Re_y^{0.6} n^{-0.1} k_s^{-1}$ of 8% and 9%, respectively. To further validate this choice of scaling method, another fluid of similar rheology underwent the same mixing process over the three scales (with, S/D = 0.24, C/D = 1.42, H/D = 3.00) and the resulting D_c/D data against $Re_m^{-0.3} Re_y^{0.6} n^{-0.1} k_s^{-1}$ were compared to the *Case 1*, *Case 4* and *Case 5* data (Figure 4.22). The rheological and physical properties for *Case 6* (Scale 1), *Case 7* (Scale 2) and *Case 8* (Scale 3) can be found in Table 4.1 and Table 4.2 (Section 4.2.2), respectively. As before, there was a slight difference in Herschel-Bulkley parameters for *Case 6* and *7*, compared to *Case 8*, which again fall within the errors associated with the rheological formulation and measurement procedures, and the Herschel-Bulkley fitting process, hence having a negligible effect on the results. Figure 4.22 shows that each dataset from both experimental studies scale well with $Re_m^{-0.3} Re_y^{0.6} n^{-0.1} k_s^{-1}$, with a maximum absolute deviation in experimental D_c/D at a given $Re_m^{-0.3} Re_y^{0.6} n^{-0.1} k_s^{-1}$ of approximately 8%.

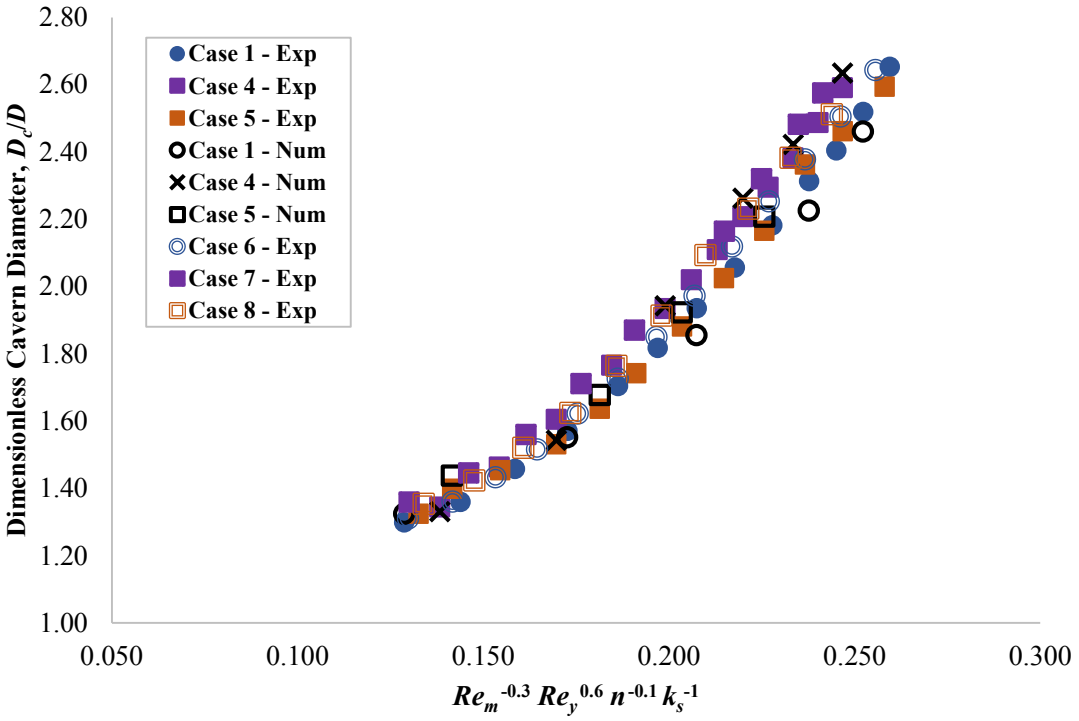

Figure 4.22. Experimentally- and numerically-derived dimensionless cavern diameters, D_c/D for *Case 1*, *Case 4* and *Case 5*, and experimentally-derived D_c/D for the repeat study, *Cases 6-8*, plotted against a combination of Re_m, Re_y, n and k_s. As before, the exponent terms which led to the best non-dimensional flow matching were -0.3, 0.6, -0.1 and -1 for Re_m, Re_y, n and k_s respectively.

4.4.5 *Mixing study C*: Changing scale and fluid rheology (RT agitation)

Here, the effects of changing both fluid rheology and scale simultaneously are investigated, with the focus of achieving flow similarity over scales with different fluids, enabled by comparison of *Case 2*, *Case 3* and *Case 5*. *Mixing Study A* highlighted that as the τ_y and K of a fluid decreased on a given scale, the N required to induce a cavern with a specific D_c/D decreased. However, *Mixing Study B* showed that as D (and hence scale) decreased when mixing a given fluid, the N needed to induce cavern of a defined dimensionless size increased. In this section, fluids with varying rheological properties were mixed with RT impellers over two different scales (Scale 1 and Scale 3), and the resulting dimensionless cavern sizes were again scaled with respect to $Re_m^{-0.3} Re_y^{0.6} n^{-0.1} k_s^{-1}$, for each fluid. *Case 5* had the largest τ_y and K values and was mixed in the Scale 3 (20 L) system, whilst *Case 2* and *Case 3* were mixed in Scale 1 (2 L) system, with *Case 3* having the lowest values of τ_y and K. The rheological and physical properties for *Case 2*, *Case 3* and *Case 5* can be found in Table 4.1 and Table 4.2 (Section 4.2.2). The rheological flow curves of the three fluids used for *Mixing Study C* can be seen in Figure 4.23.

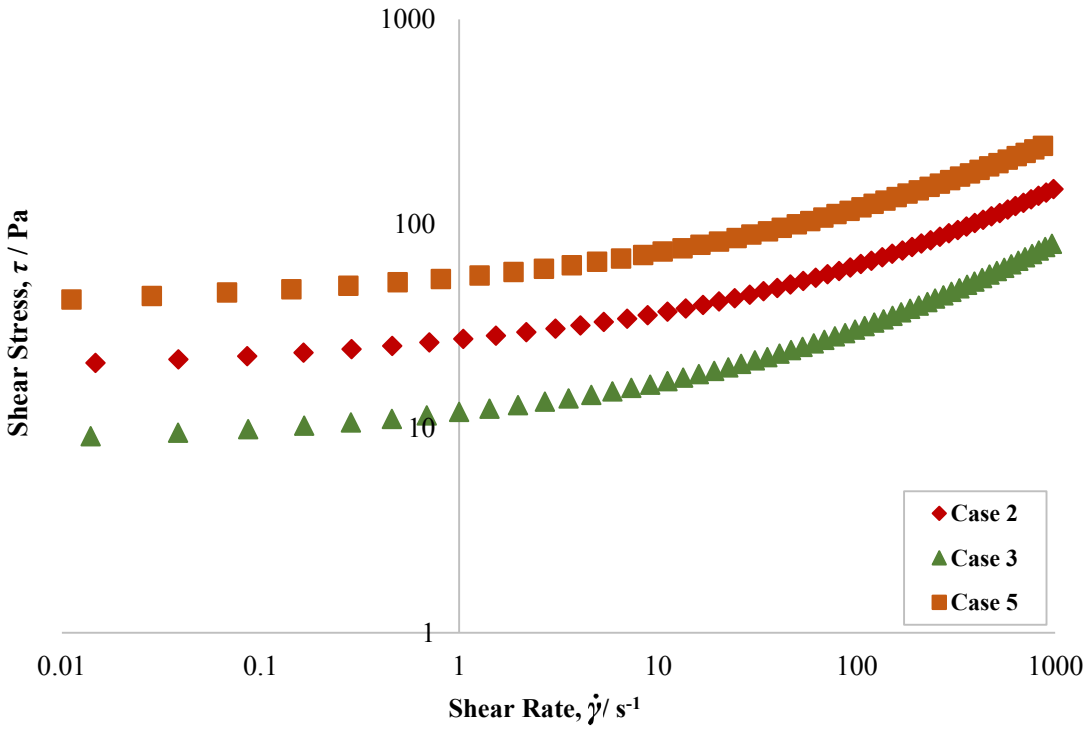

Figure 4.23. Raw rheological flow curves for fluids used in *Case 2, Case 3* and *Case 5* of *Mixing Study C*. The data was acquired through shear-stress down sweeps using the shear-stress controlled Anton Paar Modular Compact Rheometer 302 rheometer, fitted with a roughened cone-and-plate geometry (12.6 µm roughness, 0.998° cone angle, cone and plate diameter = 50 mm, CP50-1-41592).

As before, for each case, N was incrementally increased with cavern sizes being measured at each selected N value, until $D_c \approx T$. In Figure 4.24, experimental images of caverns with $D_c/D \approx 1.75$ for (a) *Case 5*, (b) *Case 2* and (c) *Case 3* can be seen. The N values required to induce caverns of this dimensionless size for the three systems were (a) 9.3 s^{-1} ($Re_m = 20.5$, $Re_y = 14.5$), (b) 12.7 s^{-1} ($Re_m = 16.7$, $Re_y = 12.5$) and (c) 8.3 s^{-1} ($Re_m = 17.6$, $Re_y = 12.6$), respectively. Similar N were required for *Case 3* and *Case 5*, because the effects of increased D and increased τ_y and K values for the *Case 5* system were approximately counteracted by the effects of decreased D and decreased τ_y and K values for *Case 3*, as discussed above. However, for the *Case 2* system, the effects of decreased D outweighed the small reduction of τ_y and K, and hence greater N was required to induce a cavern of $D_c/D \approx 1.75$ in this system. As before, Figure 4.24 also shows that all three fluids produced caverns with toroidal character, highlighted by less intense colour in the central, lower region of each cavern, characteristic of vortices. The complete D_c/D datasets scaled against N for each of the three cases can be seen in Figure 4.25, and for the same reasons as above, the *Case 3* and *Case 5* datasets are in relatively good agreement over the entire range of N, whilst the *Case 2* results did not coincide with the other two datasets. As with *Mixing Study B*, there was an unknown discrepancy in the average H_c/D_c for the Scale 1 (2 L) systems (*Case 2* and *Case 3*) compared to the Scale 3 (20 L) system (*Case 5*), which was thought to be caused by either some physical phenomenon not

considered in this work, or slight optical distortion effects in the vertical direction. The average H_c/D_c for *Case 5* was 0.63 compared to 0.53 and 0.49 for the *Case 2* and *Case 3* systems, respectively.

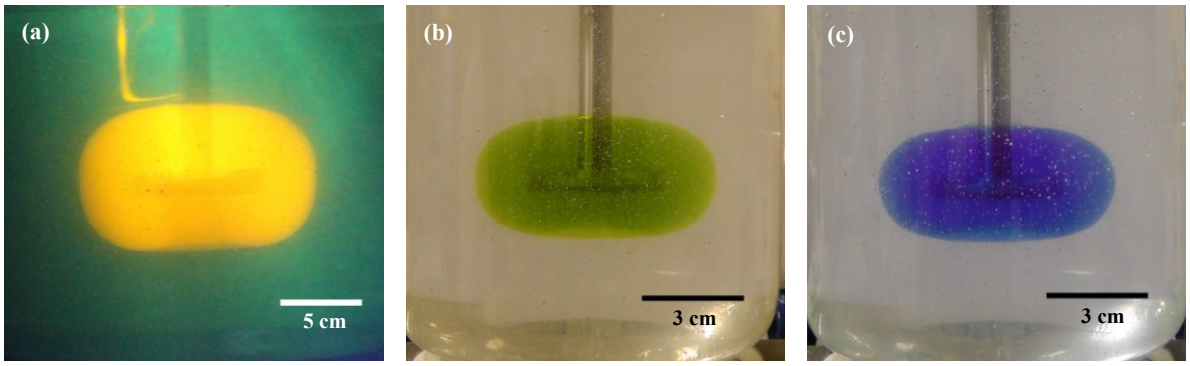

Figure 4.24. Images from the experimental study of caverns with $D_c/D \sim 1.75$ for (a) *Case 5*, (b) *Case 2* and (c) *Case 3*. For each of the three fluids, the N values required to induce caverns of this dimensionless size were: (a) 9.3 s^{-1} (Re_m = 20.5, Re_y = 14.5), (b) 12.7 s^{-1} (Re_m = 16.7, Re_y = 12.5) and (c) 8.3 s^{-1} (Re_m = 17.6, Re_y = 12.6), respectively.

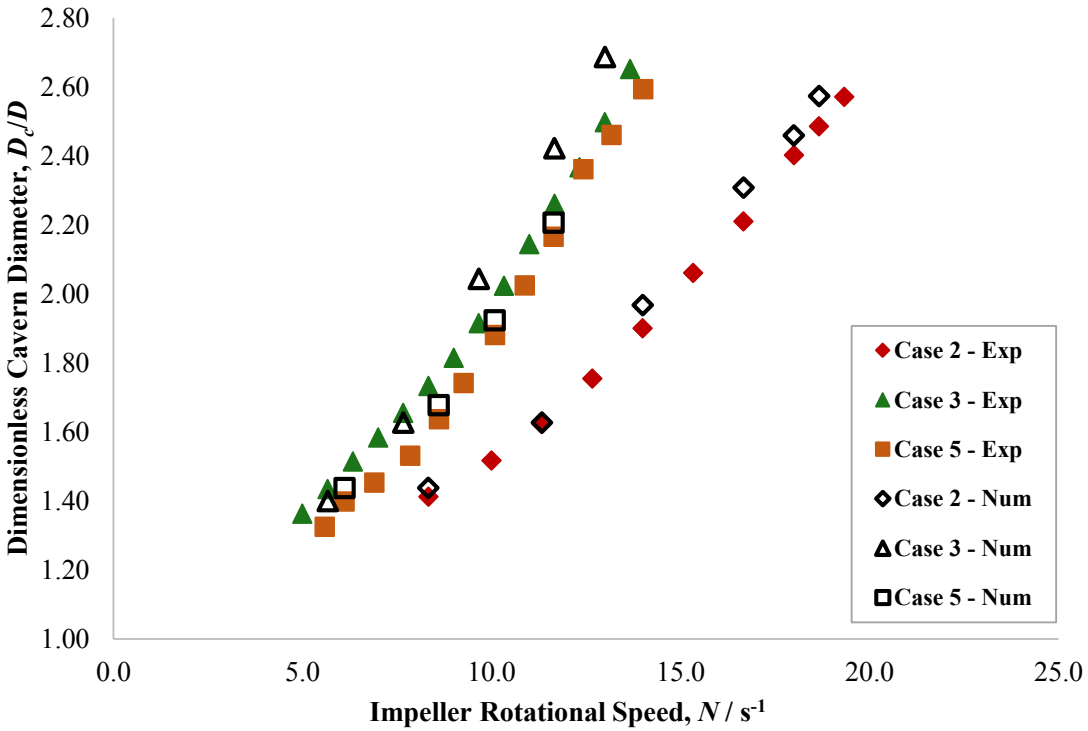

Figure 4.25. Experimentally- and numerically-derived D_c/D scaled with respect to N for *Case 2*, *Case 3* and *Case 5*. There is relatively good agreement between the *Case 3* and *Case 5* datasets when scaling with N, but a lack of agreement when comparing these datasets to the dataset of *Case 2*. However, there is good agreement between the experimental and numerical data for each case.

Again, scaling with respect to $Re_m^{-0.3}Re_y^{0.6}n^{-0.1}k_s^{-1}$ results in good agreement between the three cases, with a maximum absolute deviation in experimental and numerical D_c/D at a given $Re_m^{-0.3}Re_y^{0.6}n^{-0.1}k_s^{-1}$

of approximately 8% and 6%, respectively (Figure 4.26). These data assist in validating the choice of the dimensionless parameters and their associated exponent terms, as a method for scaling processes of this nature. It also showed that flow similarity can be achieved with respect to D_c/D for different fluids over different scales, however for true flow similarity to be achieved, dimensionless cavern sizes must be matched in all directions, including H_c/D_c. Figure 4.27 is a plot of both the experimentally- and numerically-derived D_c/D for all the fluids characterised with a Rushton turbine in this work (including the repeat of the three-scale mixing study). It shows that for all the fluids, the maximum absolute deviation in experimental and numerical D_c/D when scaling with $Re_m^{-0.3}Re_y^{0.6}n^{-0.1}k_s^{-1}$ was approximately 11% and 9%, respectively. This scaling approach should be applied to industrially relevant scales and fluids, to determine the applicability of this method, however over the scales and selected rheological properties from this study, D_c/D versus $Re_m^{-0.3}Re_y^{0.6}n^{-0.1}k_s^{-1}$ appeared to be a good approach for attempting to match flows of viscoplastic fluids in vessels equipped with RT impellers.

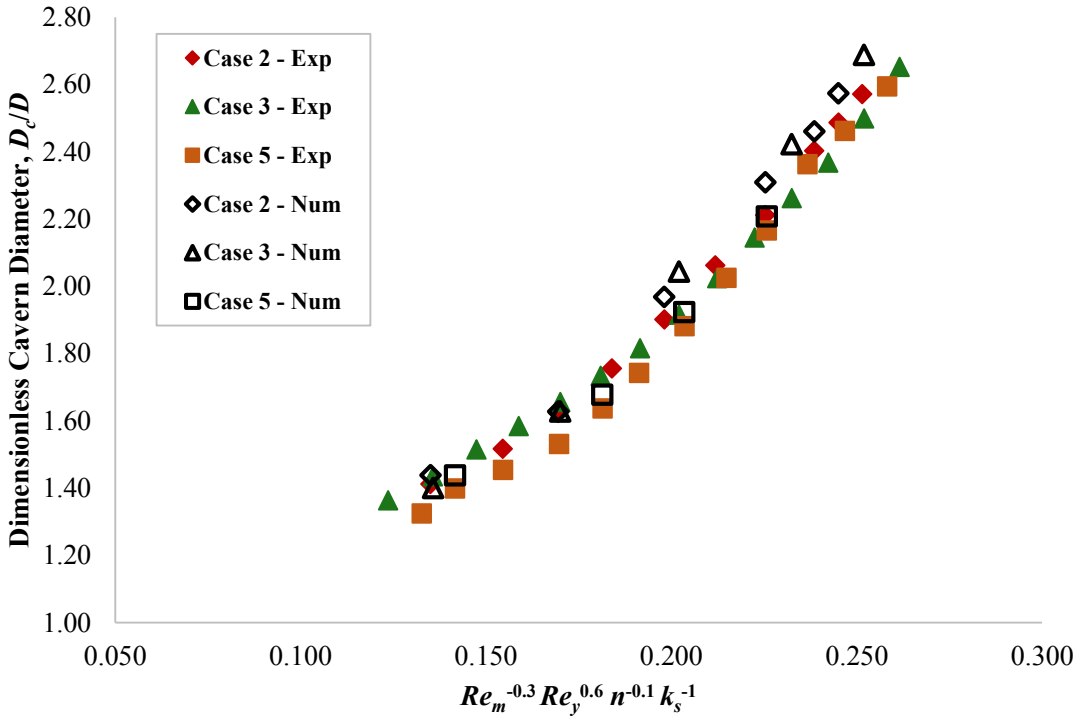

Figure 4.26. Experimentally- and numerically-derived dimensionless cavern diameters, D_c/D for the *Case 2*, *Case 3 Case 5* systems have been scaled with respect $Re_m^{-0.3}Re_y^{0.6}n^{-0.1}k_s^{-1}$. Scaling in this manner led to good agreement of dimensionless cavern diameters between each of the three datasets.

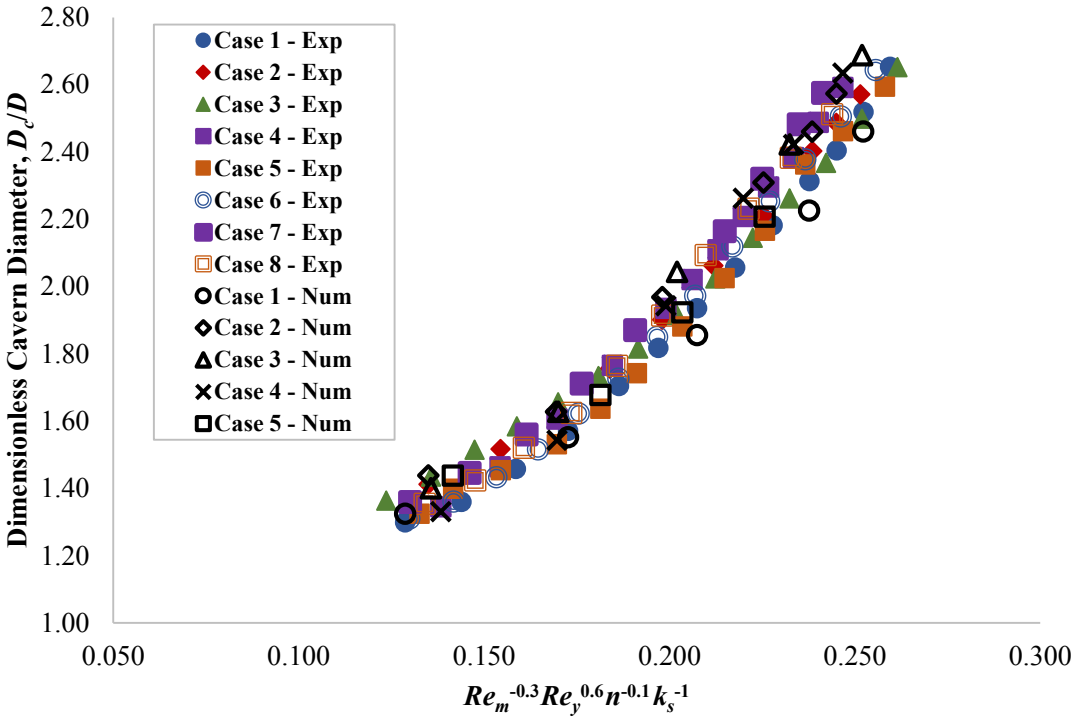

Figure 4.27. Experimentally- and numerically- derived dimensionless cavern diameters, D_c/D for all the fluids mixed with a RT impeller during this section of the study (*Mixing Studies A-C*), scaled with respect to $Re_m^{-0.3} Re_y^{0.6} n^{-0.1} k_s^{-1}$.

4.4.6 Comparison between RT and PBT agitation

Next, the mixing of fluids with two different types of impellers is considered. The scale (Scale 1, 2 L) over which the fluids were mixed and the diameter of both impellers was kept constant (D = 0.041 m); however the geometry of the impellers was changed, with *Case 11* being agitated with a 4-bladed 45° pitched-blade turbine (PBT) and *Case 2* being agitated with a 6-bladed Rushton turbine (RT). There was a slight variation in the rheological properties of the two fluids used, with the Herschel-Bulkley parameters of the fluid in *Case 11* having: τ_y = 20.7 Pa, K = 4.8 Pa s^n and n = 0.46 and the fluid in *Case 2* having: τ_y = 21.5 Pa, K = 5.0 Pa s^n and n = 0.46 (see Table 4.1 and 4.2, Section 4.2.2 for a summary of the rheological and physical properties of each system, respectively). Figure 4.28 shows experimental images for (a) *Case 11* and (b) *Case 2*, and numerical snapshots for (c) *Case 11* and (d) *Case 2*, of caverns with $D_c/D \approx 2.43$, where the corresponding N required to induce caverns of this size were 22.0 s^{-1} (Re_m = 40.9, Re_y = 39.3) for *Case 11,* and 18.0 s^{-1} (Re_m = 28.7, Re_y = 25.3) for *Case 2*. This highlighted that to generate a cavern with this dimensionless diameter, a greater N value was required when mixing with the PBT. This would be expected as the PBT has both radial and axial character, compared to the fully radial nature of the RT, and as a result, a greater power input would be required by the PBT to generate comparable D_c/D values to the RT. Due to this difference in flow characteristics of the two impeller types, different cavern morphologies may be expected. Xiao *et al*. (2014) numerically studied the mixing of viscoplastic fluids with PBT impellers and found that as the cavern sizes grow, the cavern develops an 'apple' torus shape, rather than the 'horn' torus

shape produced by the RT. In the current study, CFD was used to obtain information relating to the velocity field distributions and flow patterns within the caverns produced by both the RT and PBT impellers, to explain the observed cavern morphologies from the experimental study. Detailed discussion on the flow dynamics resulting from RT agitation can be found in Section 4.4.3 and 4.4.4, however Figure 4.28(d) clearly highlights the exclusively radial nature of the flow, resulting in highly symmetrical vortices above and below the blades, owing to the observed 'horn' torus morphology. In the case of the PBT, due to the direction of rotation, the impeller is downward pumping in nature. The CFD results in Figure 4.28(c) clearly highlight this, with a maxima in velocity magnitude (and hence force being exerted on the material) at a 45° angle to the radial direction at the blade tips. This results in two sets of vortices being produced, with material being pushed away from the blades at this 45° angle, towards the cavern wall, with material recirculating around the cavern, above and below the impeller and back towards the blades, leading to the observed 'apple' torus morphology. These differences in flow dynamics within each of the caverns (Figure 4.28(c) and (d)) clearly explain the varying toroidal morphologies associated with RT and PBT agitation that were observed from experiment. As with RT agitation, there was a sharp drop off in velocity away from the blades of the PBT impeller, with the cavern boundary having a velocity magnitude = 0.01 m s^{-1}.

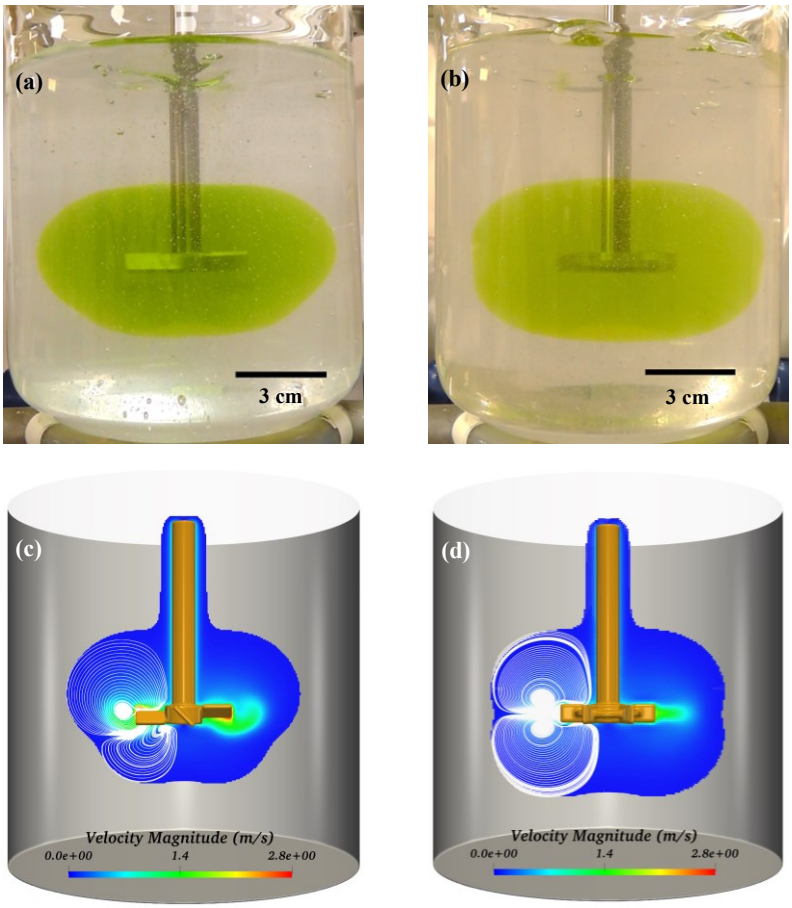

Figure 4.28. Images from experiment for (a) *Case 11* and (b) *Case 2*, and numerical snapshots of (c) *Case 11* and (d) *Case 2*, of caverns with $D_c/D \sim 2.43$. N values required to generate caverns of this dimensionless size were for *Case 11* were 22.0 s^{-1} ($Re_m = 40.9$, $Re_y = 39.3$), and and *Case 2* were 18.0 s^{-1} ($Re_m = 28.7$, $Re_y = 25.3$), respectively.

Figure 4.29 shows the experimental and numerical D_c/D versus N datasets for both cases. For every given D_c/D, greater N values were required by the PBT, compared to the RT. There was good agreement between the experimental and numerical D_c/D data, with an AAD in D_c/D per N value of 2.7% and 3.9% for *Case 2* and *Case 11*, respectively. The average cavern aspect ratios for these two systems were 0.53 and 0.50, for *Case 2* and *Case 11*, respectively. This suggested that despite the mixed flow character of the PBT, the RT produced caverns with greater dimensionless heights and combined with the D_c/D data, this suggested the RT is a more effective impeller for mixing viscoplastic fluids than the PBT.

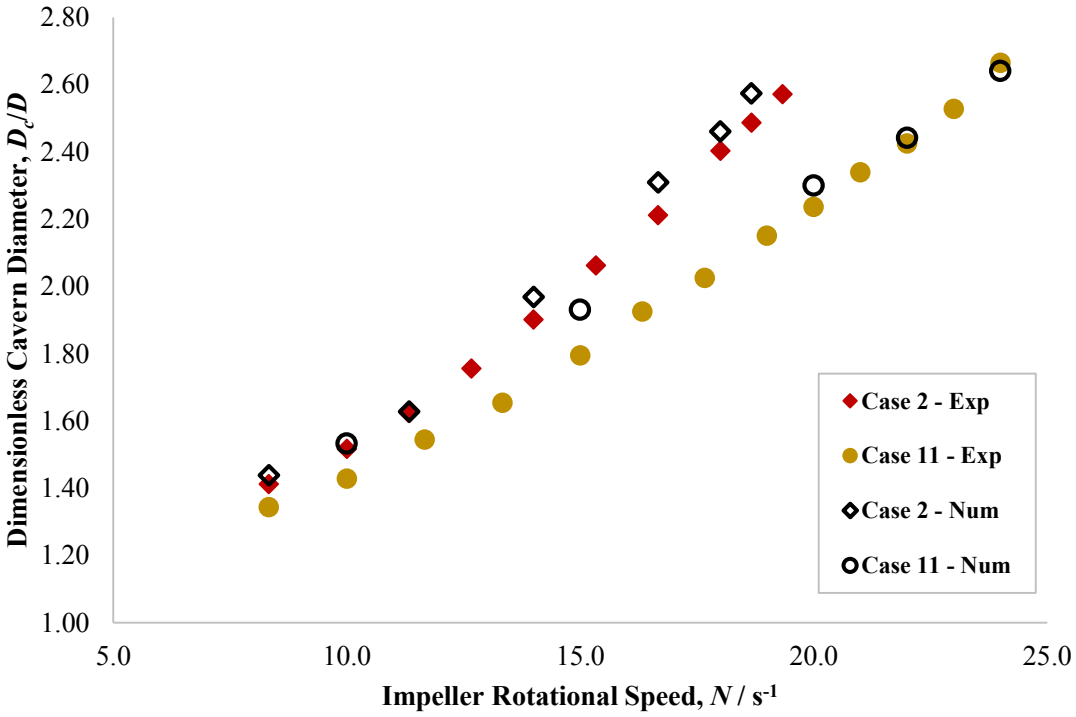

Figure 4.29. Experimentally- and numerically-derived D_c/D scaled with respect to N for *Case 11*, mixed with a 4-bladed 45° PBT (D = 0.041 m) and *Case 2*, mixed with a 6-bladed RT (D = 0.041 m).

As before, both D_c/D datasets were scaled with respect to $Re_m^{-0.3} Re_y^{0.6} n^{-0.1} k_s^{-1}$ (Figure 4.30), which led to cavern size similarity between the two systems, with a maximum absolute deviation in D_c/D at a given $Re_m^{-0.3} Re_y^{0.6} n^{-0.1} k_s^{-1}$ value of approximately 3%. When mixing viscoplastic fluids with different types of centrally-mounted, small impellers, the resulting flow patterns and cavern morphologies cannot necessarily be matched when comparing impellers with varying degrees of axial and radial character (for example, PBT vs RT), however these results show that it is possible to achieve cavern size similarity when mixing with different types of impellers. Due to these findings, Section 4.47-4.49 will look at the mixing of viscoplastic fluids over different scales, but now with PBT impellers, as a means of further validating the scaling method presented here.

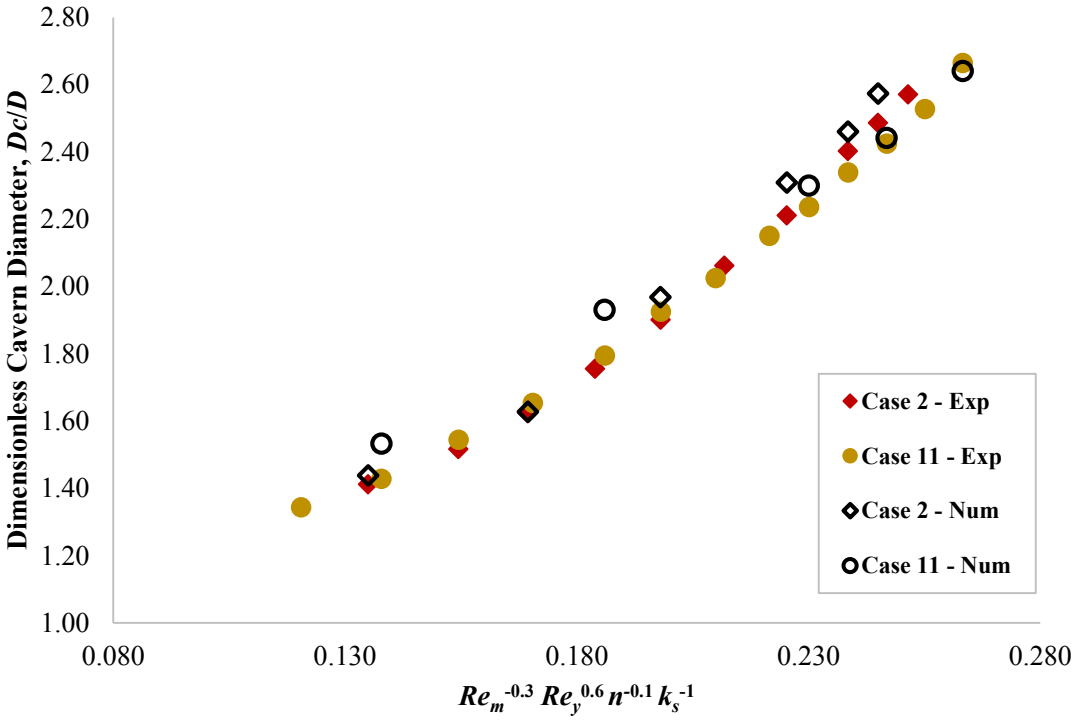

Figure 4.30. Experimentally- and numerically-derived D_c/D scaled with respect to $Re_m^{-0.3}Re_y^{0.6}n^{-0.1}k_s^{-1}$ for *Case 11*, mixed with a 4-bladed 45° PBT (D = 0.041 m) and *Case 2*, mixed with a 6-bladed RT (D = 0.041 m). k_s for the PBT = 13 and for the RT = 11.5.

4.4.7 *Mixing Study D*: Changing fluid rheology (PBT agitation)

In this section, a similar approach to *Mixing Study A* was taken. A number of C980 fluids of varying rheological properties were agitated using the same mixing system (Scale 1), but now with the 4-bladed 45° PBT impeller (D = 0.041 m), rather than the comparable 6-bladed RT impeller. As before, the aim was to match the dimensionless cavern sizes within each of the fluids, by implementing the previously proposed $Re_m^{-0.3}Re_y^{0.6}n^{-0.1}k_s^{-1}$ scaling method. *Mixing Study D* was enabled by comparison of *Cases 9-13*, with the rheological and physical properties of the fluids used in each case found in Table 4.1 and Table 4.2 (Section 4.2.2), respectively. From these systems, the fluid in *Case 9* had the greatest values of τ_y and K, whilst *Case 13* had the smallest τ_y and K values. The raw rheological flow curves of the five fluids can be seen in Figure 4.31.

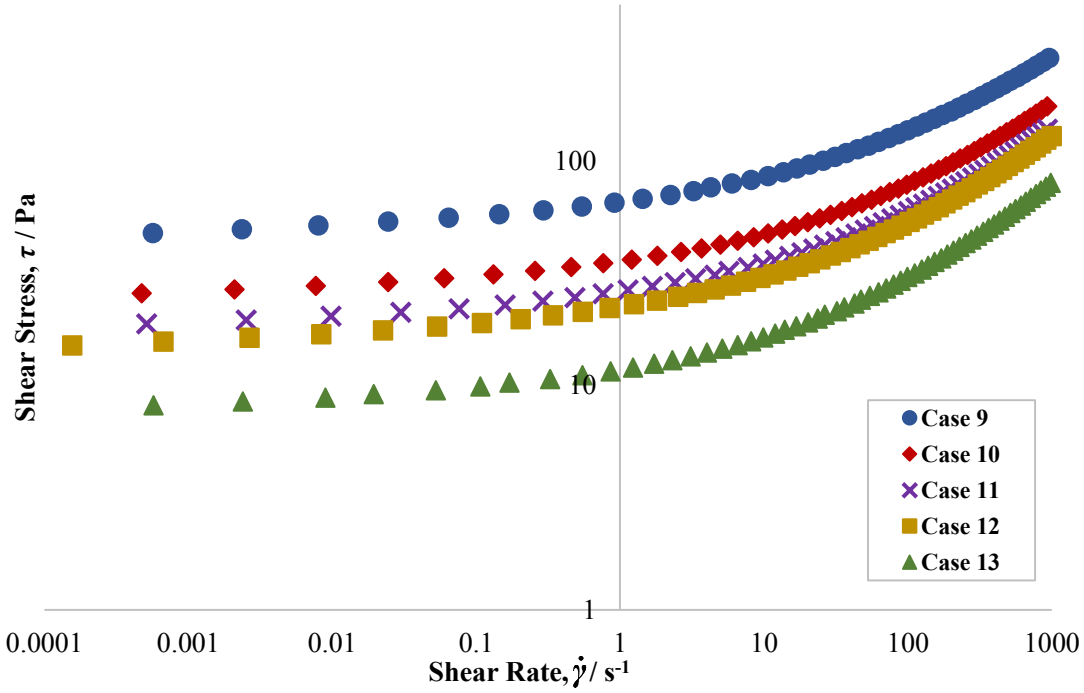

Figure 4.31. Raw rheological flow curves for the fluids from *Cases 9-13*, acquired through shear-stress down sweeps using the shear-stress controlled Anton Paar Modular Compact Rheometer 302 rheometer, fitted with a roughened cone-and-plate geometry (12.6 µm roughness, 0.998° cone angle, cone and plate diameter = 50 mm, CP50-1-41592).

For each process: $C = 0.058$ m ($C/D \approx 1.42$), $T = 0.147$ m ($T/D \approx 3.59$), $S = 0.01$ m ($S/D \approx 0.24$) and $H = 0.135$ m ($H/D \approx 3.30$), and the same approach was taken as previously described, in terms of the incremental increase in N, with cavern sizes being measured at each selected N value. Figure 4.32 highlights experimental images of caverns with $D_c/D \approx 2.52$, for (a) *Case 9*, (b) *Case 10*, (c) *Case 11*, (d) *Case 12* and (e) *Case 13*. The N values required to generate caverns with these dimensionless sizes were: (a) 31.0 s^{-1} ($Re_m = 29.7$, $Re_y = 31.8$), (b) 24.2 s^{-1} ($Re_m = 34.9$, $Re_y = 35.4$), (c) 23.0 s^{-1} ($Re_m = 43.8$, $Re_y = 42.9$), (d) 19.2 s^{-1} ($Re_m = 33.0$, $Re_y = 37.4$), and (e) 14.3 s^{-1} ($Re_m = 39.7$, $Re_y = 38.7$). The caverns were highlighted with blue food dye in *Cases 9* and *13*, and green food dye in *Cases 10-12*. As was the case in *Mixing Study A*, when the τ_y and K values of a fluid decreased, the N value required to generate a cavern of a particular size decreased. This is caused by the fact that, when impeller size and shape remains constant, the stress (and therefore the force) being imparted on the material is controlled by N, and when τ_y and K decrease, the stress (or force) necessary to induce a cavern of a given size decreases, which is reflected by decrease in N value when going from *Case 9* to *Case 13*.

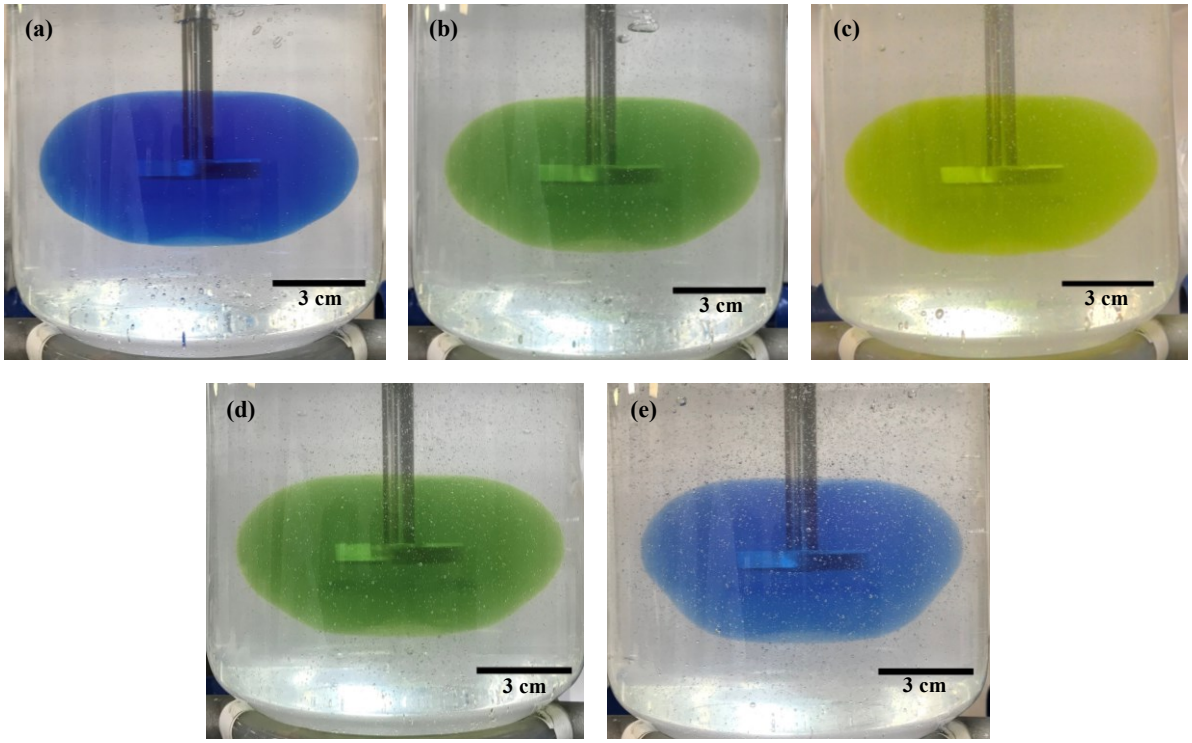

Figure 4.32. Images of caverns with D_c/D ~2.52, formed in: (a) *Case 9*, (b) *Case 10*, (c) *Case 11*, (d) *Case 12* and (e) *Case 13*. The τ_y and K values decrease from *Case 9* to *Case 13*, and with that, the necessary N required to generate caverns of this size, decreased: (a) 31.0 s^{-1} (Re_m = 29.7, Re_y = 31.8), (b) 24.2 s^{-1} (Re_m = 34.9, Re_y = 35.4), (c) 23.0 s^{-1} (Re_m = 43.8, Re_y = 42.9), (d) 19.2 s^{-1} (Re_m = 33.0, Re_y = 37.4), and (e) 14.3 s^{-1} (Re_m = 39.7, Re_y = 38.7).

This is further highlighted in Figure 4.33, which is a plot of experimentally-derived D_c/D datasets against various ranges of N for *Cases 9-13*. This figure shows that, as would be expected, the D_c/D datasets do not collapse onto the same curve when scaling with N, due to the differences in rheological properties between each of the fluids. Over the ranges of investigated N for each case, the average H_c/D_c of the caverns were: (a) 0.46 for *Case 9*; (b) 0.47 for *Case 10*; (c) 0.50 for *Case 11*; (d) 0.44 for *Case 12*; and (e) 0.48 for *Case 13*. In each of the images from Figure 4.32, the 'apple' torus morphology of the cavern can be seen, highlighted by the lack of symmetry about the radial (horizontal) plane.

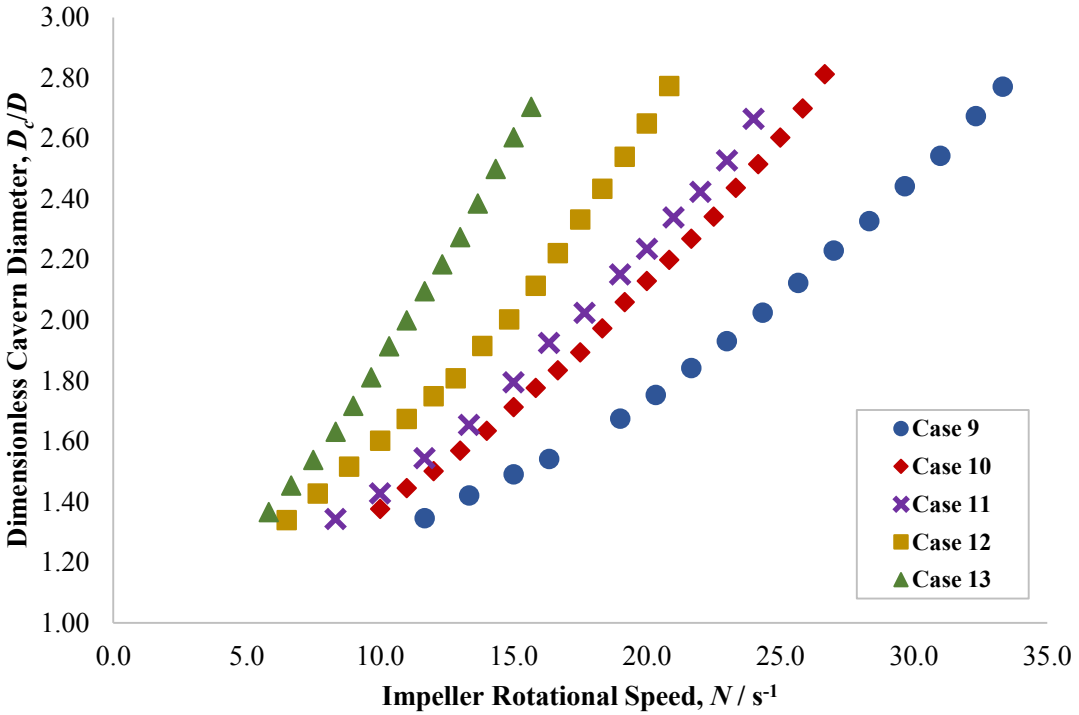

Figure 4.33. Experimentally-derived D_c/D datasets against a range of N for *Cases 9-13*. As expected, the curves do not overlap with one another, due to the differences in rheological properties between each fluid.

When scaling the five cases with respect to $Re_m^{-0.3}Re_y^{0.6}n^{-0.1}k_s^{-1}$ (Figure 4.34) there was better agreement between the datasets, with a maximum absolute deviation in D_c/D at a given $Re_m^{-0.3}Re_y^{0.6}n^{-0.1}k_s^{-1}$ of approximately 9%. These results highlight that this scaling method is not only appropriate for RT agitation of these C980 viscoplastic fluids, but also for PBT agitation, further validating the choice of scaling method for the comparison between RT and PBT agitation from Section 4.4.6. It should be emphasised that when using this scaling method for different impeller types, the aim is to achieve cavern size similarity. It would be unreasonable to also assume that flow similarity has been achieved, because the degree of axial and radial flow may vary from one impeller type to the next. However, in the case of the five fluids agitated with the PBT (D = 0.041 m) in this section, when combining the results from Figure 4.34 with the H_c/D_c data, it can be concluded that flow similarity has been achieved in these systems.

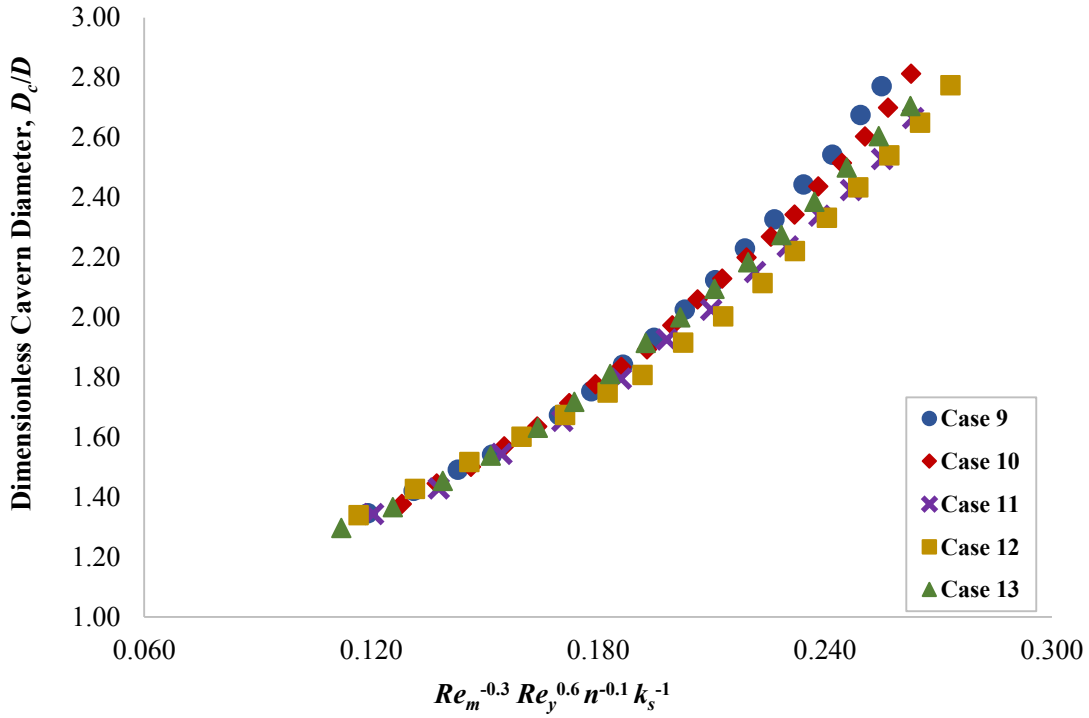

Figure 4.34. Experimentally-derived dimensionless cavern diameters, D_c/D, for the *Cases 9-13* systems, scaled with respect $Re_m^{-0.3}Re_y^{0.6}n^{-0.1}k_s^{-1}$. Scaling in this manner led to good agreement of D_c/D between each of the five datasets.

4.4.8 *Mixing Study E*: Changing tank and impeller scale (PBT agitation)

Here, the mixing of very similar fluids over two different scales is investigated. The scales selected were Scale 1 (2 L) and Scale 2 (5 L), and the PBT impellers used for agitation had D = 0.041 m and D = 0.059 m, respectively. Over both scales, various geometrical length scale ratios were maintained, including $C/D \approx 1.42$ and $S/D \approx 0.24$. There was a slight variance in H/D, with $H/D \approx 3.30$ in the Scale 1 system and $H/D \approx 3.00$, however, as stated in Section 4.4.2.2, this should have a relatively limited effect on the results, because the impeller positioned at $H/D \approx 3.00$ does not result in interface deflection. There was a slight discrepancy in T/D, with: $T/D \approx 3.59$ in the Scale 1 system and $T/D \approx 3.41$ in the Scale 2 system. As discussed in Section 4.4.2.1, this difference should have a negligible effect on the results. *Mixing Study E* was enabled by the comparison of *Case 10* and *Case 14*, with details relating to the rheological and physical properties of these cases being found in Table 4.1 and Table 4.2 (Section 4.2.2), respectively. There was a very small difference in rheological properties between the two fluids used in this section, however, they were seen as being sufficiently similar to be within the errors associated with the rheological formulation and measurement procedure (outlined in Section 4.2.5) and had a limited effect on the results. Figure 4.35 shows two caverns with $D_c/D \approx 2.27$ for (a) *Case 10* (2 L vessel) and (b) *Case 14* (5 L vessel), respectively. As discussed in *Mixing Study B*, when mixing the same fluid, as the impeller diameter, D increases in size, less force from the impeller is required to obtain a cavern of a defined

dimensionless size. The result is lower N values being required as D increases, with $N = 21.7\ s^{-1}$ ($Re_m = 29.5$, $Re_y = 28.5$) and $N = 15.8\ s^{-1}$ ($Re_m = 38.1$, $Re_y = 33.3$) required in *Case 10* and *Case 14*, respectively. This is further reflected in Figure 4.36, which is a plot of both D_c/D datasets against a range of N. Over the entire range of investigated D_c/D values, at a given D_c/D, a lower N value is required in the *Case 14* system, compared with the *Case 10* system, leading to poor scaling with N. Over the investigated range of N, the average H_c/D_c values for *Case 10* and *Case 14* were 0.47 and 0.47, respectively.

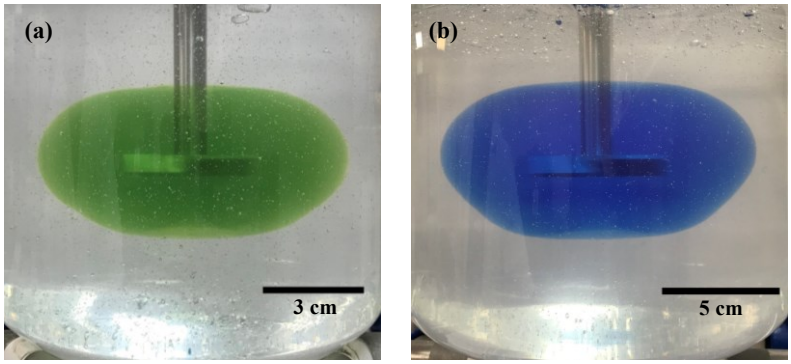

Figure 4.35. Images of caverns with $D_c/D \sim 2.27$ in (a) *Case 10* and (b) *Case 14*. The N values required to induce caverns of this size were (a) $21.7\ s^{-1}$ ($Re_m = 29.5$, $Re_y = 28.5$) and (b) $15.8\ s^{-1}$ ($Re_m = 38.1$, $Re_y = 33.3$).

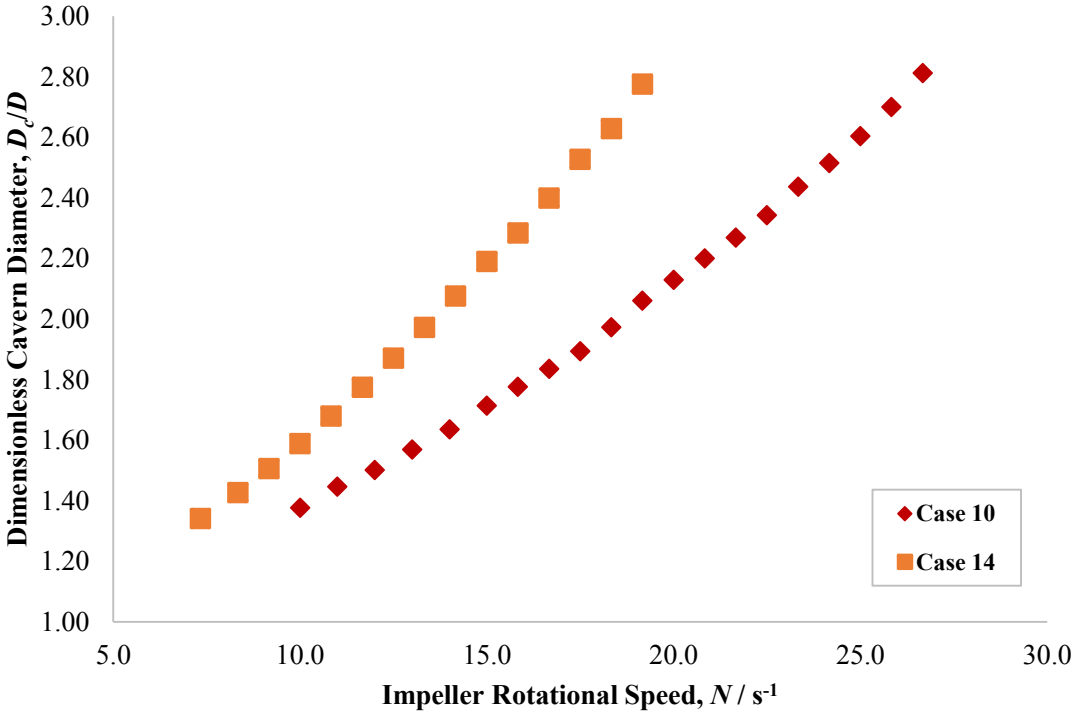

Figure 4.36. Experimentally-derived D_c/D datasets against a range of N for *Cases 10* and *14*. As expected, the curves do not overlap with one another, due to the differences in rheological properties between each fluid.

As with all the other mixing studies investigated in this work, scaling with $Re_m^{-0.3}Re_y^{0.6}n^{-0.1}k_s^{-1}$ (Figure 4.37) resulted in a much better agreement between the two sets of D_c/D, with a maximum absolute deviation in D_c/D at a given $Re_m^{-0.3}Re_y^{0.6}n^{-0.1}k_s^{-1}$ of approximately 2%, between *Case 10* and *Case 14*. In combination with the H_c/D_c data, it can be concluded that flow similarity was achieved between these two systems.

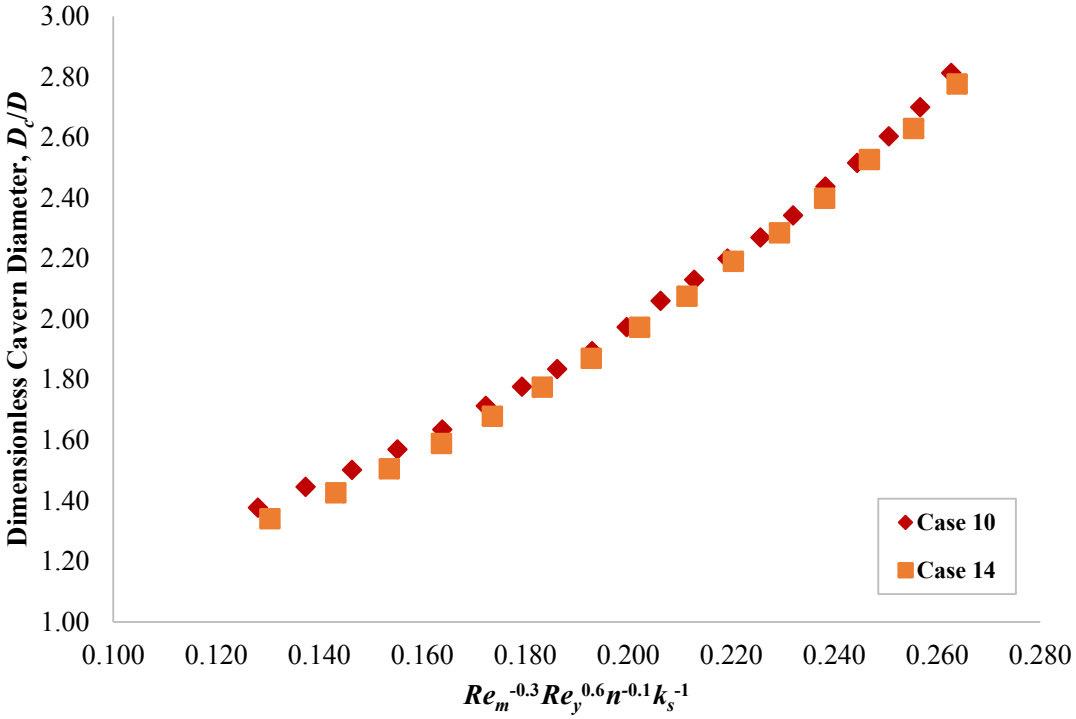

Figure 4.37. Experimentally-derived dimensionless cavern diameters, D_c/D, for the *Cases 10* and *14* systems, scaled with respect $Re_m^{-0.3}Re_y^{0.6}n^{-0.1}k_s^{-1}$. Scaling in this manner led to good agreement of D_c/D between the two systems.

4.4.9 *Mixing Study F*: Changing scale and fluid rheology (PBT agitation)

In this final mixing study, the effects of changing both tank and impeller scale, and the fluid rheology of the C980 viscoplastic fluids were investigated. Agitation with geometrically-similar PBT impellers occurred over two scales: Scale 1 (2 L) and Scale 2 (5 L), with the PBT impellers having D = 0.041 m and D = 0.059 m, respectively. As with *Mixing Study E*, $C/D \approx 1.42$ and $S/D \approx 0.24$ were upheld over the two scales, whilst H/D (Scale 1: $H/D \approx 3.30$ vs Scale 2: $H/D \approx 3.00$) and T/D (Scale 1: $T/D \approx 3.59$ vs Scale 2: $T/D \approx 3.41$) varied slightly, however, these differences are unlikely to have an impact on the results (see Section 4.4.2.1 and Section 4.4.2.2). *Mixing Study F* was enabled by the comparison of *Cases 9*, *13* and *14*, where fluids of *Case 9* and *Case 13* were mixed in the Scale 1 system, and the *Case 14* fluid was mixed in the Scale 2 system. The *Case 9* fluid had the greatest τ_y and K values, whilst the fluid of *Case 13* had the lowest τ_y and K values. The rheological and physical properties of *Case 9*, *Case*

13 and *Case 14* can be found in Table 4.1 and Table 4.2 (Section 4.2.2), respectively. The raw rheological flows curves of the three fluids can be seen in Figure 4.38.

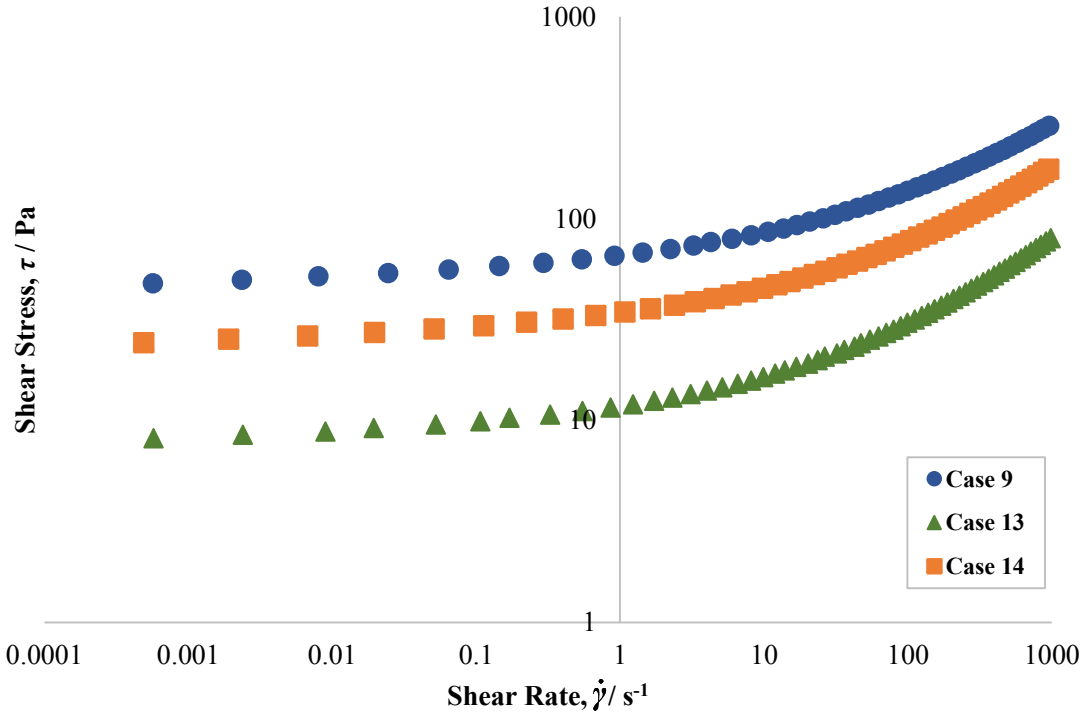

Figure 4.38. Raw rheological flow curves for the fluids from *Cases 9, 13* and *14*, acquired through shear-stress down sweeps using the shear-stress controlled Anton Paar Modular Compact Rheometer 302 rheometer, fitted with a roughened cone-and-plate geometry (12.6 µm roughness, 0.998° cone angle, cone and plate diameter = 50 mm, CP50-1-41592).

It was shown previously that as the τ_y and K of a fluid decreased on a given scale, the N required to induce a cavern with a specific D_c/D decreased. However, when the fluid rheology was kept constant and D increased, the N necessary to produce a cavern with a specific D_c/D decreased. Figure 4.39 shows images of caverns of $D_c/D \approx 2.10$ for (a) *Case 9*, (b) *Case 13* and (c) *Case 14*. The N values required to induce caverns of this size were: (a) $N = 25.7$ s^{-1} ($Re_m = 22.0$, $Re_y = 21.8$), (b) $N = 11.7$ s^{-1} ($Re_m = 29.1$, $Re_y = 25.7$) and (c) $N = 14.2$ s^{-1} ($Re_m = 32.0$, $Re_y = 26.7$).

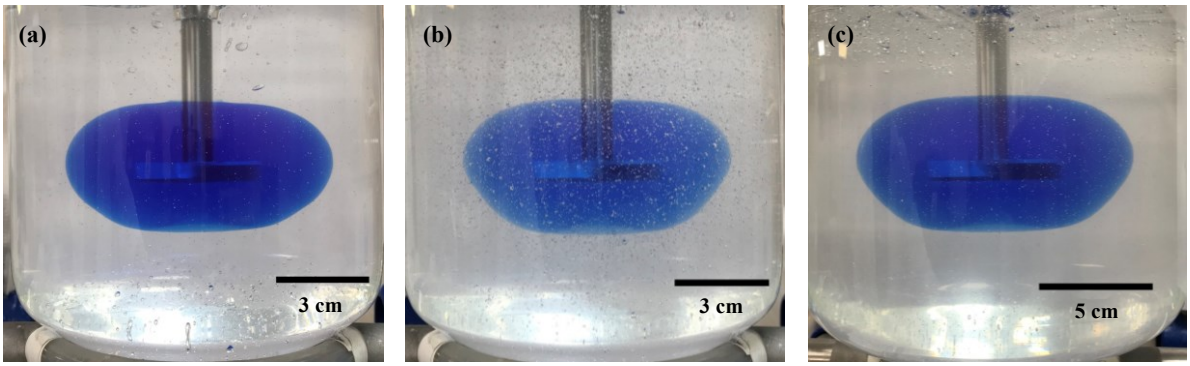

Figure 4.39. Images of caverns with $D_c/D \sim 2.10$ in (a) *Case 9*, (b) *Case 13* and (c) *Case 14*. The N values required to induce caverns of this size were: (a) $N = 25.7$ s^{-1} ($Re_m = 22.0$, $Re_y = 21.8$), (b) $N = 11.7$ s^{-1} ($Re_m = 29.1$, $Re_y = 25.7$) and (c) $N = 14.2$ s^{-1} ($Re_m = 32.0$, $Re_y = 26.7$).

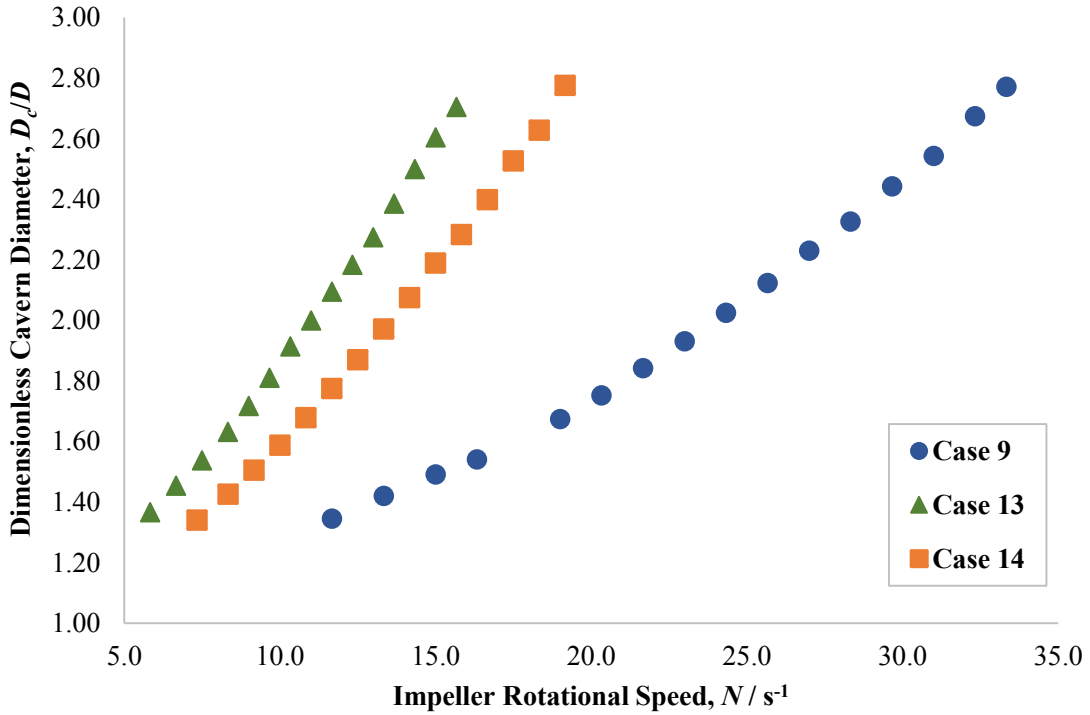

Figure 4.40. Experimentally-derived D_c/D datasets against a range of N for *Cases 9*, *13* and *14*. The curves do not overlap with one another, despite there being both changes in scale and fluid rheology.

Figure 4.40 is a plot of the complete D_c/D datasets for *Cases 9*, *13* and *14*, scaled against N. Combined with the results presented in Figure 4.39, it can be seen that *Case 9* scales very differently with N compared with the other two cases. Over the entire range of investigated D_c/D, the N values required to induce a cavern of a specific size were much greater in *Case 9*, compared to *Case 13* and *Case 14*,

because, as discussed above, *Case 9* occurred using the Scale 1 system (D = 0.041 m), and also the fluid used in *Case 9* had the greatest τ_y and K values, compared to the fluids used in the other two cases. The D_c/D datasets for *Case 13* and *Case 14* were more comparable because the effects of decreased τ_y and K values in *Case 13* were partially counteracted by the increased D used in *Case 14*. Over the various ranges of N investigated in these three cases, the average H_c/D_c values of the caverns in *Case 9*, *Case 13* and *Case 14* were 0.46, 0.48 and 0.48, respectively.

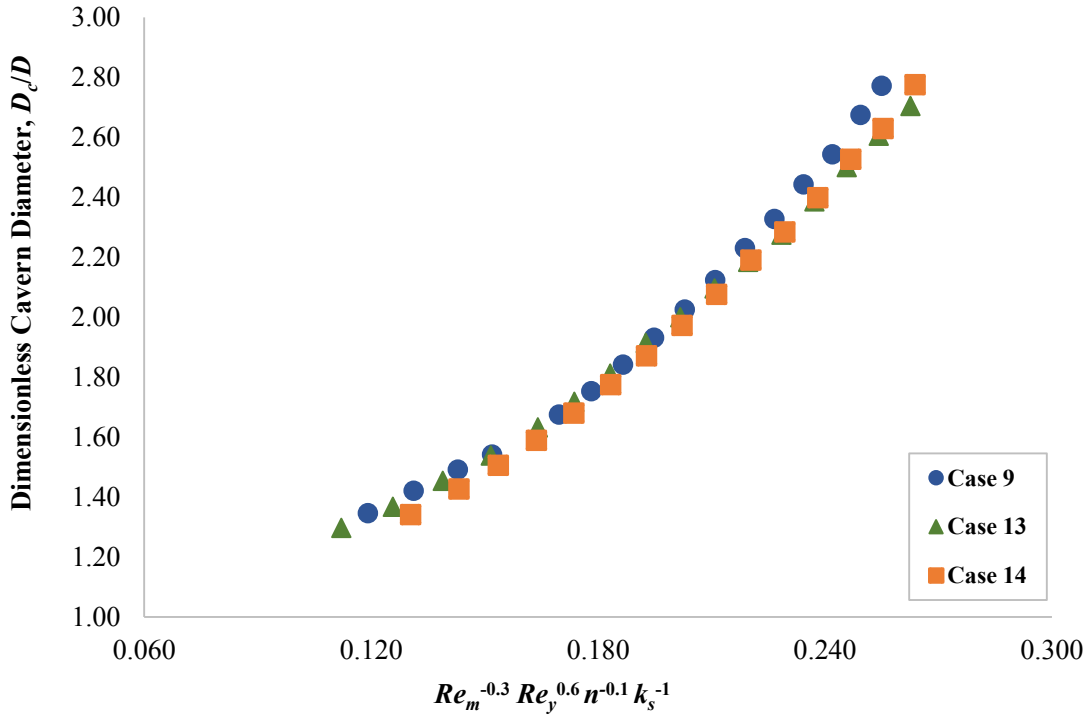

Figure 4.41. Experimentally-derived dimensionless cavern diameters, D_c/D, for the *Cases 9*, *13* and *14* systems, scaled with respect $Re_m^{-0.3}Re_y^{0.6}n^{-0.1}k_s^{-1}$. Scaling in this manner led to good agreement of D_c/D between each of the three datasets.

As with the other cases in this work, scaling with $Re_m^{-0.3}Re_y^{0.6}\ n^{-0.1}\ k_s^{-1}$ led to much better agreement between the datasets of *Cases 9*, *13* and *14*, with a maximum absolute deviation in D_c/D at a given value of $Re_m^{-0.3}Re_y^{0.6}\ n^{-0.1}\ k_s^{-1}$ of 5%, as seen in Figure 4.41. Combined with the average H_c/D_c data, it shows that flow similarity was achieved over scales through PBT agitation of fluids with varying viscoplastic properties. A plot of D_c/D against $Re_m^{-0.3}Re_y^{0.6}\ n^{-0.1}\ k_s^{-1}$ for all the fluids agitated with a PBT in this section of the work (*Cases 9-14*) can be seen in Figure 4.42. The maximum absolute deviation in D_c/D at a given value of $Re_m^{-0.3}Re_y^{0.6}\ n^{-0.1}\ k_s^{-1}$ for all the fluids and systems investigated in *Cases 9-14* was 9%. Again, by analysing the average H_c/D_c data from the previous three mixing studies (*Mixing Studies D-F*) and combining with the data in Figure 4.42, it can be deduced that scaling method of $Re_m^{-0.3}Re_y^{0.6}\ n^{-0.1}\ k_s^{-1}$ is an appropriate means of matching flows and achieving flow similarity when performing PBT agitation of viscoplastic fluids, over the range of fluids and scales investigated in this work. It should be noted that

three scales (Scale 1-3, 2-20 L) were investigated for the RT agitation studies (*Mixing Studies A-C*), whereas only the Scales 1 (2 L) and 2 (5 L) systems were implemented for the PBT agitation studies (*Mixing Studies D-F*). Although flow similarity was achieved in various fluids over these two scales, further work using the Scale 3 system would be priority, to ensure that use of the scaling method also extends to this scale, for PBT agitation as well as RT agitation, and to deduce whether the slight discrepancies in H_c/D_c values from going from Scales 1 and 2, to Scale 3 was a feature of PBT agitation, as well as RT agitation.

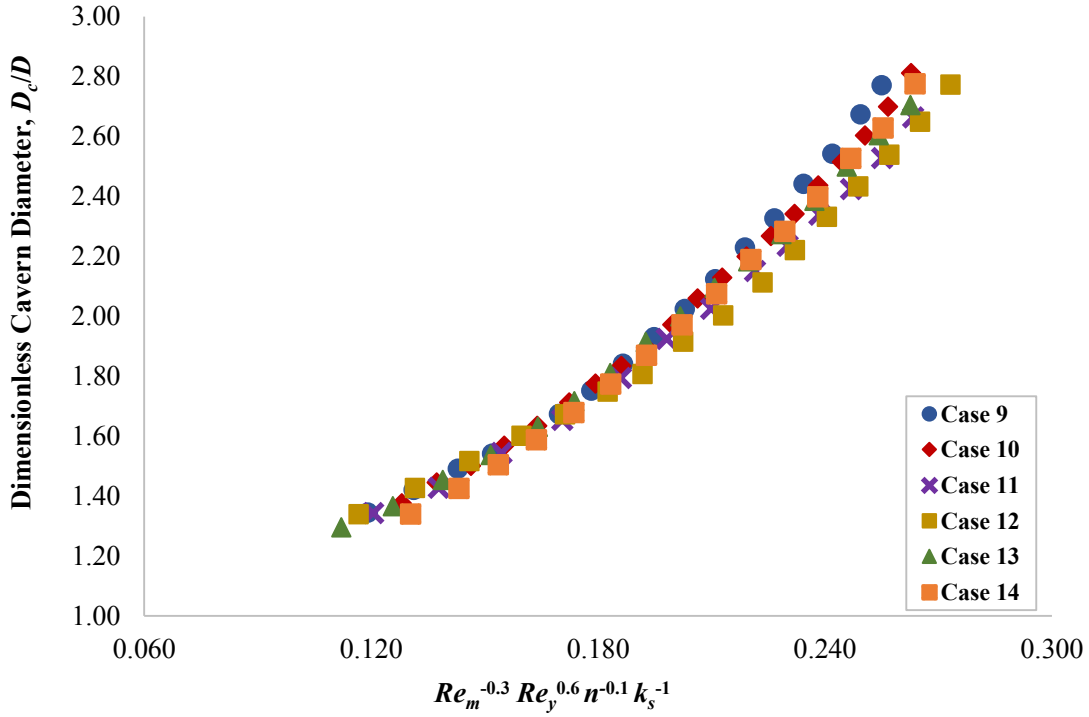

Figure 4.42. Experimentally-derived dimensionless cavern diameters, D_c/D for all the fluids mixed with a PBT impeller during this section of the study (*Mixing Studies D-F*), scaled with respect to $Re_m^{-0.3}Re_y^{0.6}n^{-0.1}k_s^{-1}$.

4.4.10 Comparison of all mixing study data

It was shown over the previous sections that flow similarity can be achieved over multiple scales with different fluids when agitating with either an RT or a PBT impeller, when scaling D_c/D with $Re_m^{-0.3}Re_y^{0.6}$ $n^{-0.1}$ k_s^{-1}. When comparing the two different impeller types, flow similarity cannot be achieved due to the varying extent of axial and radial character of the impellers, leading to difference flow dynamics within the resulting caverns. However, cavern size similarity was achieved when scaling via the same methods. A plot of the experimental D_c/D datasets against $Re_m^{-0.3}Re_y^{0.6}\,n^{-0.1}\,k_s^{-1}$ for all fluids from this chapter can be seen Figure 4.43. By determining the relationship between D_c/D and $Re_m^{-0.3}Re_y^{0.6}\,n^{-0.1}\,k_s^{-1}$, D_c/D can be approximately predicted on a given scale for these types of C980 viscoplastic fluids, if the rheology and scale is known, at a given value of N. By knowing at what value of $Re_m^{-0.3}Re_y^{0.6}\,n^{-0.1}\,k_s^{-1}$ will give a value of D_c/D (±10%), the prediction process can be extended further to allow for predictive mixing over scales

with the same fluid or over scales with different fluids, with the aim of matching dimensionless cavern sizes between the two systems in question. From Figure 4.43, a second order polynomial fit has been applied to the data, with the intercept being set to 1, as $D_c/D \neq$ less than 1, because the cavern diameter physically cannot be smaller than the diameter. From this fit, the relationship of $y = 29.19x^2 - 1.14x + 1$ was determined, with $y = D_c/D$ and $x = Re_m^{-0.3} Re_y^{0.6} n^{-0.1} k_s^{-1}$, with an $R^2 = 0.982$ for the fit. Further discussion how this relationship for the prediction of dimensionless cavern diameters in C980 viscoplastic fluids over scales can be utilised, through a computational platform called the '*Matching and Predictive Mixing Tool*' (MPMT), can be found in Chapter 5. It should be noted that to be able to predict dimensionless cavern sizes, knowledge of H_c/D_c is required. From all the fluids investigated in this work, the average H_c/D_c resulting from RT agitation was 0.55 (±15%), whilst for PBT agitation is was 0.51 (±15%). From Chapter 5, these are the values used for average H_c/D_c when performing predictive mixing with RT impellers and PBT impellers, respectively.

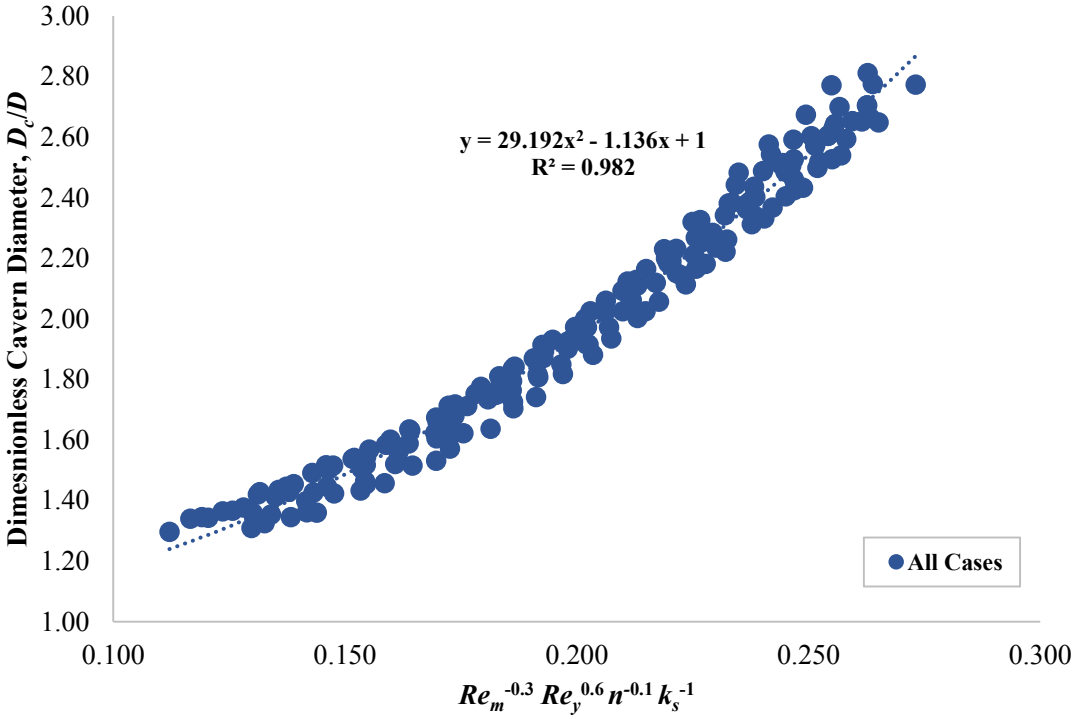

Figure 4.43. Experimentally-derived dimensionless cavern diameters, D_c/D for all the fluids from this chapter (*Mixing Studies A-F*) scaled with respect to $Re_m^{-0.3} Re_y^{0.6} n^{-0.1} k_s^{-1}$, where ····· = 2nd order polynomial fit of the data. Knowledge of this relationship between D_c/D and $Re_m^{-0.3} Re_y^{0.6} n^{-0.1} k_s^{-1}$ can allow for the cavern sizes to be predicted over the range of investigated fluids and scales from this work.

4.5 Conclusion

In this chapter, simple experimental techniques in conjunction with a validated CFD model were used to characterise the flow of Carbopol 980 (C980) solutions in stirred vessels. C980 solutions have

viscoplastic rheological properties and were agitated with 6-bladed Rushton turbine (RT) impellers and 4-bladed 45° pitched-blade turbine (PBT) impellers. The effects of impeller rotational speed (N), fluid rheology, mixing system scale and impeller type on cavern shape and size were investigated. It was determined that caverns of increased size form when the C980 solutions were agitated at increased N. When focusing on one scale, greater N were required to produce caverns of a given size when the rheological properties, τ_y and K, of the solutions increased. However, when the scale increased (where geometric similarity of the RT impellers was conserved), but the rheological properties of the fluid were maintained, lower N were required to induce a cavern of a given dimensionless size. To be able to match the dimensionless cavern diameter, D_c/D, regardless of fluid rheology or mixing system scale, it was necessary to scale the process with respect to a combination of dimensionless parameters (obtained from dimensional analysis), namely: Re_m, Re_y, n and k_s. Specifically, for the fluids and flows considered in this chapter, scaling D_c/D with respect to $Re_m^{-0.3}Re_y^{0.6}n^{-0.1}k_s^{-1}$, resulted in data collapse onto the same curve with good agreement, i.e., maximum absolute deviaitons in experimental and numerical D_c/D at a given $Re_m^{-0.3}Re_y^{0.6}n^{-0.1}k_s^{-1}$ of approximately 11% and 9%, for systems agitated with RT impellers. For the fluids and systems agitated with PBT impellers in this section, the maximum absolute deviation in experimental D_c/D at a given $Re_m^{-0.3}Re_y^{0.6}n^{-0.1}k_s^{-1}$ was approximately 9%. Comparison of RT and PBT impeller types (both D = 0.041 m) on the flow dynamics, the cavern morphology and size that result from the mixing of C980 solutions was performed. Both impellers created toroidal-shaped caverns, however the RT resulted in a 'horn' torus shape whilst the PBT produced a cavern with 'apple' torus shape, due to angled nature of the PBT blades. The CFD data allowed for a direct comparison of the flow patterns and velocity field distributions that result from agitation with the RT and PBT impellers, helping to explain the differences in cavern morphologies observed via experiment. When scaling D_c/D against $Re_m^{-0.3}Re_y^{0.6}n^{-0.1}k_s^{-1}$, there was cavern size similarity between the datasets that resulted from agitation with RT and PBT impellers, when mixing fluids with varying rheological properties over different scales, with a maximum absolute deviation of D_c/D at a given $Re_m^{-0.3}Re_y^{0.6}n^{-0.1}k_s^{-1}$ of approximately 10%. It can be concluded that over the scales and selected rheological properties used in this work, $Re_m^{-0.3}Re_y^{0.6}n^{-0.1}k_s^{-1}$ was deemed to be an appropriate scaling method for matching flows. Knowledge of this relationship between D_c/D and $Re_m^{-0.3}Re_y^{0.6}n^{-0.1}k_s^{-1}$ can then be used for predicting caverns sizes in C980 viscoplastic flows over scales using a computational platform known as the '*Matching and Predictive Mixing Tool*' (further discussion in Chapter 5). Due to the good agreement between the numerical and experimental results throughout the study, the CFD model has potential, in future studies, to also be used as method for predicting cavern sizes in viscoplastic fluids, over the range of scales used in this work. Future work would involve looking at a wider range of rheological properties and centrally-mounted, small impeller types, with the aim of producing a scaling system for all centrally-mounted, small impellers.

Chapter 5: Matching and Predictive Mixing Tool

5.1 Introduction

The '*Matching and Predictive Mixing Tool*' (referred to as the MPMT from here onwards) is a computational platform developed in Microsoft Excel, using Visual Basic for Application programming methods and recorded macros. Whilst having many of the same features of the *Model Fluid Selection Tool* (MFST) presented in Chapter 3, it has operational features capable of predicting cavern sizes in pre-defined stirred vessel systems containing a viscoplastic fluid with known rheology, whilst also being able to suggest the operating conditions required for matching dimensionless cavern sizes in a second system when the scale of the geometry and/or the fluid rheology has been changed. Both the prediction and matching processes occur using the functional relationship between dimensionless cavern diameter, D_c/D and the combination of dimensionless parameters acquired from dimensional analysis (as outlined in Section 4.2.4) of a stirred vessel system mixing a viscoplastic fluid: $Re_m^{-0.3} Re_y^{0.6} n^{-0.1} k_s^{-1}$. Having scaled D_c/D against $Re_m^{-0.3} Re_y^{0.6} n^{-0.1} k_s^{-1}$ for all systems and cases discussed in Chapter 4, the functional relationship for these Carbopol 980 fluids, agitated with 6-bladed Rushton turbines and 4-bladed 45° pitched-blade turbines in vessels ranging from quoted volumes of 2 L to 20 L, was a second-order polynomial, of the form: $y = 29.19x^2 - 1.14x + 1$, with $y = D_c/D$ and $x = Re_m^{-0.3} Re_y^{0.6} n^{-0.1} k_s^{-1}$, and an $R^2 = 0.982$ for the fit. The proposed dimensionless cavern size matching and prediction processes are only applicable to the systems and fluids investigated, however similar approaches could be used when looking at a wider range of rheological properties and mixing systems, including looking at other types of centrally-mounted, small impeller types, with the aim of producing a MPMT capable of predicting and matching dimensionless cavern sizes for all viscoplastic fluids and all types of centrally-mounted, small impellers, over a wider range of scales. If this was possible, then the MPMT could be applied to industrially-relevant scales and mixing systems, (which are generally made of opaque materials) and 'real' fluids (which are also often opaque) with the aim of understanding the mixing behaviour within the vessels and how to achieve homogeneity throughout the fluid, without having to perform appropriate scale down studies when potential issues arise.

5.2 Overview of the 'Matching and Predictive Mixing' tool

The MPMT is comprised of a number of the same worksheets as the MFST from Chapter 3, including the '*Data Entry*', '*Optimisation Fitting*', '*Library_Fitted*', '*Top Matches_Graph*' and '*Top Matches_Details*' worksheets. However, in addition to the '*MPMT Instructions*' worksheet, which is a step-by-step guide for how to run all of the operations within the MPMT (presented in Section A.5 in the Appendix), there is another new worksheet, called the '*Mixing In Stirred Vessels*' worksheet. The '*Data Entry*' worksheet in the MPMT is very similar to the '*Data Entry*' worksheet in the MFST, however, the one key difference

is the addition of the '*Mixing In Stirred Vessels*' operation, located in the '*(3) Standard Operations*' section. Further discussion of both the '*Mixing In Stirred Vessels*' worksheet and '*Mixing In Stirred Vessels*' operation can be found in Section 5.3. For a full description (along with example case studies) of the other operations found in the '*(3) Standard Operations*' and '*(4) Library Additions*' sections of this computational tool, namely the '*Clearing Old Data*', '*Finding Best Match*', '*Delete Library Entry*', '*Adding Data to Library (Data & Fitting Thereof)*' and '*Adding Data to Library (By Fitted Parameters)*' operations, the reader is directed to Chapter 3, as the functional features of each of these operations in the MPMT are the same as those in the MFST. As with the MFST, the '*Optimisation Fitting*' worksheet is the platform used for fitting raw rheological data with mathematical models, including the Herschel-Bulkley model, the Casson model and the Power Law model. The '*Library_Fitted*' worksheet is a viscoplastic fluids database, where the identity, physical and rheological properties of model fluids are stored. The key difference between the MFST and MPMT is that rheological data was acquired using vane geometry in the MFST, whilst roughened cone-and-plate geometry was used for data acquisition in the MPMT. Discussion concerning the reasons for the use of different geometries can be found in Section 3.10. Both the '*Top Matches_Graph*' and '*Top Matches_Details*' are associated with the '*Finding Best Match*' operation and visually are very similar to the analogous worksheets in the MFST, with the key difference being that the '*Perform Interpolation*' operation is not necessary in the MPMT and hence cannot be found in the '*Top Matches_Graph*' worksheet, as was the case for the MFST. The '*Mixing In Stirred Vessels*' worksheet is associated with the '*Mixing In Stirred Vessels*' operation. By executing this operation, the user can either predict cavern sizes at a given impeller rotational speed, N in systems where the dimensions and setup of the tank and impeller are known, as are the rheological properties of the fluid in question, or the user can determine the necessary operating conditions in a second system, where the scale and/or fluid rheology has changed from the first system, that would be required for matching the dimensionless cavern sizes over both systems. Finally, as discussed the '*MPMT Instructions*' worksheet contains operational step-by-step instructions relating to each of the MPMT operations, with particular focus on the '*Mixing In Stirred Vessels*' operation. In the following sections, an in-depth discussion of the '*Mixing In Stirred Vessels*' worksheet will take place, including the description of a number of case studies to demonstrate the various features of the '*Mixing In Stirred Vessels*' operation.

5.3 '*Mixing In Stirred Vessels*' worksheet

The '*Mixing In Stirred Vessels*' worksheet can be seen in Figure 5.1, and is associated with the '*Mixing In Stirred Vessels*' operation, which can be executed from the '*Data Entry*' worksheet. The worksheet is constructed of two parts: a section titled '*Predicting Cavern Sizes in Viscoplastic Fluids*' (Figure 5.1(a)) and a second section titled '*Matching Viscoplastic Fluids*' (Figure 5.1(b)). The '*Predicting Cavern Sizes in Viscoplastic Fluids*' section relates to the prediction of dimensionless cavern sizes in tank and impeller

systems of a given size, containing a fluid with a known rheology. The user will input an initial N value into a userform, and the predicted dimensionless cavern diameter, D_c/D will be outputted. Through the use of the System 1: '*Change Impeller Speed*' operation, the user can investigate the predicted D_c/D values at different N values. When looking to match the dimensionless cavern sizes of a known system to a system that has been scaled up or down, or when changing the fluid rheology (or both), both the '*Predicting Cavern Sizes in Viscoplastic Fluids*' and the '*Matching Viscoplastic Flows*' sections are utilised. In this case, the details of the known system (System 1) are inputted into the '*Predicting Cavern Sizes in Viscoplastic Fluids*' section, via a userform platform, including the upper and lower limits in N that were used to induce the largest and smallest cavern sizes in that system. The user is then able to decide whether they wish to change the scale and/or the rheology of the system, with the details of the new system (System 2), and the required N values for producing the maximum and minimum dimensionless cavern sizes being inputted into the '*Matching Viscoplastic Flows*' section. The user will be asked to input a given N value and resulting D_c/D value from their experimental study on System 1, and the operation will output the required N value to produce a cavern with the same D_c/D value for System 2. Using the System 2: '*Change System 1 Impeller Speed and* D_c/D' operation the user is able to change the known N value and resulting D_c/D from System 1, and in turn the N value required to produce a cavern with the same D_c/D value on System 2 will be outputted via a message box. If the System 2: '*Change System 2 Scale/Fluid*' operation is activated, the user then has the option to change the details of System 2. If changes are made to the System 2 scale and/or fluid rheology, new N values required for producing the same maximum and minimum dimensionless cavern sizes as System 1 will be outputted to the user, and again, the user will be asked to input a specific N value and associated D_c/D from System 1, with the N value required to produce this specific D_c/D value on System 2 being outputted to the user in the form of a message box. For both System 1 and System 2, schematic visualisations of the resulting cavern sizes for a given system can be seen (green and purple caverns for System 1 and 2, respectively), with the cavern sizes and relative tank sizes changing depending on the tank geometry, impeller geometry, fluid rheology and N values inputted into the various userforms. Case study examples for the prediction process and the matching process can be found in Sections 5.3.1 and 5.3.2, respectively.

(a)

Predicting Cavern Sizes in Viscoplastic Flows:

System 1:

Change Impeller Speed

Inputted Data - *System 1*:

(1) Fluid Rheology & Density:

Yield Stress, τ_y / Pa	42.8
Flow Consistency Index, K / Pa s^n	11.6
Flow Behaviour Index, n	0.41
Fluid Density, ρ / kg m^{-3}	1000

(2) Tank & Impeller Geometrical Setup:

Tank Shape	Cylindrical
Tank Diameter, T_1 / m	0.147
Tank Height / m	0.147
Tank Volume, V_1 / L	2.49
Impeller Type	Rushton turbine
Impeller Blade Number	6
Impeller Diameter, D_1 / m	0.041
Impeller Clearance, C_1 / m	0.058
Liquid Fill Height, H_1 / m	0.135
Impeller Geometry Constant, k_s	11.5

(3) Impeller Speed Range (*MATCHING ONLY*!):

Lowest Impeller Speed, N_L / rpm	600
Lowest Impeller Speed, N_L / s^{-1}	10.00
Smallest D_c/D	1.30
Highest Impeller Speed, N_H / rpm	1580
Highest Impeller Speed, N_H / s^{-1}	26.33
Largest D_c/D	2.65

Prediction Process - *System 1:*

Impeller Speed, N / rpm	1400
Impeller Speed, N / s^{-1}	23.33
Power law Reynolds Number, Re_m	21.69
Yield stress Reynolds Number, Re_y	21.38
$Re_m^{-0.3} Re_y^{0.6} n^{-0.1} k_s^{-1}$	0.24
D_c/D (±10%)	2.31
Estimated Average H_c/D_c (±15%)	0.55

System 1:

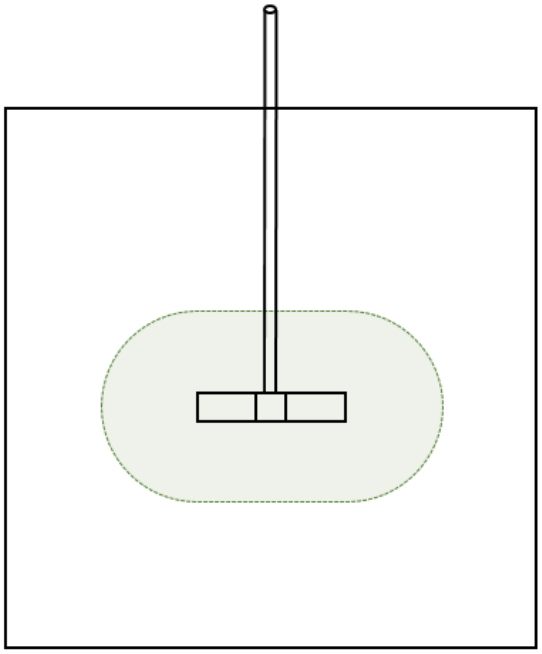

(b)

Matching Viscoplastic Flows:

System 2:

Change System 1 Impeller Speed and D_c/D	Change System 2 Scale/Fluid

Outputted Data - *System 2*:

Process Details:

If $D_1 > D_2$, then the process is being scaled DOWN
If $D_1 < D_2$, then the process is being scaled UP

Same Fluid?	No
Larger or Smaller Yield Stress?	Larger

Same Scale?	No
Larger or Smaller Impeller Diameter?	Larger (Scale-Up)
Approx. How Many Times Larger/Smaller?	2.00

(1) Fluid Rheology & Density:

Suggested Fluid	Carbopol 980
Fluid Mass Fraction / wt%	0.26
Fluid pH	7.48
Yield Stress, τ_y / Pa	68.6
Flow Consistency Index, K / Pa s^n	19.7
Flow Behaviour Index, n	0.40
Fluid Density, ρ / kg m^{-3}	1000

(2) Tank & Impeller Geometrical Setup:

Scale	Larger (Scale-Up)
Tank Shape	Cylindrical
Tank Diameter, T_2 / m	0.294
Tank Height / m	0.294
Tank Volume, V_2 / m^3	19.96
Impeller Type	Rushton turbine
Impeller Blade Number	6
Impeller Diameter, D_2 / m	0.082
Impeller Clearance, C_2 / m	0.116
Liquid Fill Height, H_2 / m	0.270
Impeller Geometry Constant, k_s	11.5

(3) Impeller Speed Range (*MATCHING ONLY*!):

Lowest Impeller Speed, N_L / rpm	376
Lowest Impeller Speed, N_L / s^{-1}	6.27
Smallest D_c/D	1.30
Highest Impeller Speed, N_H / rpm	1064
Highest Impeller Speed, N_H / s^{-1}	17.73
Largest D_c/D	2.65

Matching Process - *System 2:*

Impeller Speed, N / rpm	918
Impeller Speed, N / s^{-1}	15.30
Power law Reynolds Number, Re_m	27.00
Yield stress Reynolds Number, Re_y	22.86
$Re_m^{-0.3} Re_y^{0.6} n^{-0.1} k_s^{-1}$	0.23
Matched D_c/D (±10%)	2.31
Estimated Average H_c/D_c (±15%)	0.55

System 2:

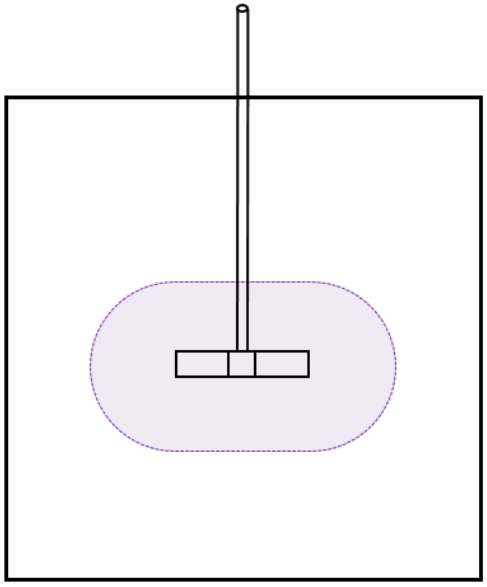

Figure 5.1. Screen-grabs from the '*Mixing In Stirred Vessels*' worksheet from the MPMT, with (a) showing the '*Predicting Cavern Sizes in Viscoplastic Fluids*' section of the worksheet and (b) showing the '*Matching Viscoplastic Flows*' section of the worksheet.

5.3.1 Case Study 1: Predicting cavern sizes in viscoplastic flows

Performing both the dimensionless cavern size prediction and matching processes occurs through execution of the '*Mixing In Stirred Vessels*' operation located within the '*Data Entry*' worksheet. When this operation is activated, the userform in Figure 5.2(a) is presented to the user. In this case, the

'*Prediction on known system*' option is selected and the message box in Figure 5.2(b) is displayed, confirming the choice and informing the user to input in the details of the known system into the following userform. It is also vital that the rheological properties of the fluid were characterised using the 'cone-and-plate' rheometrical geometry (preferably roughened, to avoid wall slip). If the '*Cancel*' button is activated in either the initial userform (Figure 5.2(a)), the message box (Figure 5.2(b)) or any further userforms and message boxes in this process, the operation will be terminated.

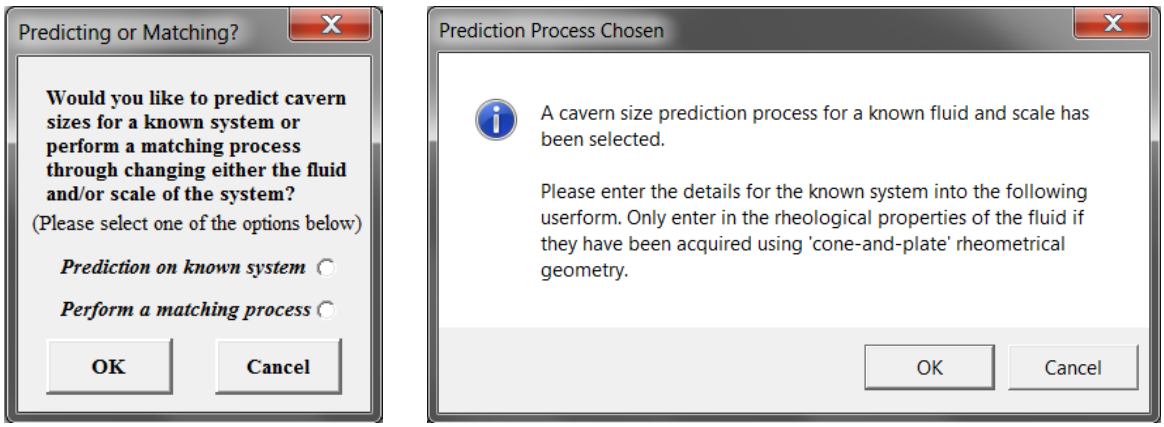

(a) **(b)**

Figure 5.2. (a) Userform that is displayed upon execution of the '*Mixing In Stirred Vessels*' operation, allowing the user to either perform a cavern size prediction for a given system, or a dimensionless cavern size matching process when either the scale of the setup or the fluid rheology (or both) is changed. (b) The message box that is shown when the '*Prediction on known system*' is selected.

Upon execution of the '*OK*' button in the '*Prediction Process Chosen*' message box in (Figure 5.2(b)), the userform in Figure 5.3 is displayed. As seen in the figure, the userform allows the user to enter in the details of their system of interest, including rheological (Herschel-Bulkley parameters only, as this is the preferred model for describing the viscoplastic fluids of interest to this section) and physical properties relating to the fluid, and details relating to the tank and impeller setup, including: type of tank and impeller, number of impeller blades and numerous details concerning the dimensions of both the impeller and tank. From the userform, there are some options involving drop-down lists, including '*Tank Shape*', where either '*Cylindrical*' or '*Rectangular*' (which affect the automated tank volume calculation) can be selected, and '*Impeller Type*', where either '*Rushton turbine*' or '*Pitched-blade turbine*' can be selected. Through activating the '*OK*' button, these details are inputted into the relevant sections of the '*Predicting Cavern Sizes in Viscoplastic Fluids*' section of the '*Mixing In Stirred Vessels*' worksheet (see Figure 5.1(a) to visualise the layout of the worksheet). During the prediction process, the sub-section titled '*(3) Impeller Speed Range (MATCHING ONLY!)*' would remain blank because this section is only utilised when performing the 'matching' process.

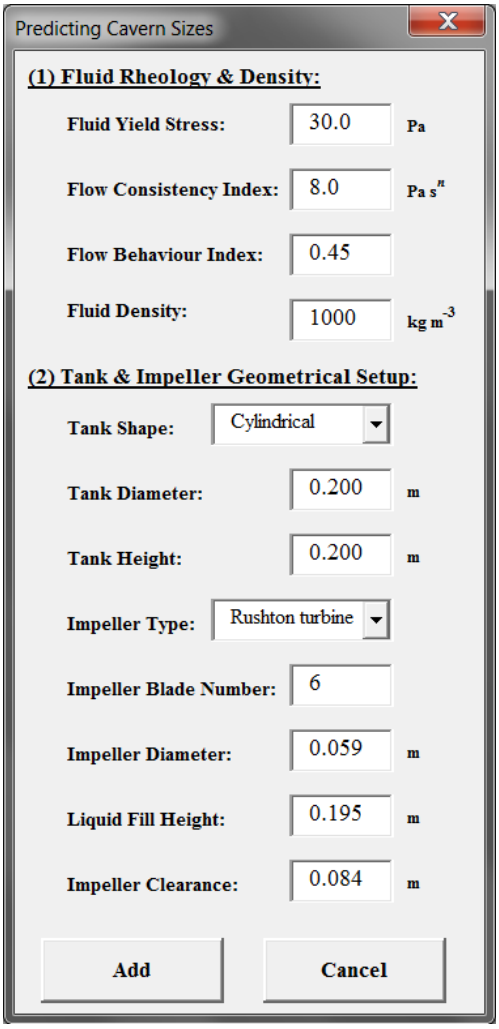

Figure 5.3. Displayed userform allowing the user to input details relating to the tank and impeller setup, and the rheological and physical properties of the fluid, for the system they would like to perform the cavern size prediction process on.

Having inputted the relevant details into the worksheet via the userform interface, the '*Selected Impeller Speed*' userform, seen in Figure 5.4(a) is presented to the user, allowing the desired N value to be entered, with the MPMT in turn determining the predicted D_c/D value (±10%) for that given N value, as well the average cavern aspect ratio, H_c/D_c for fluids of this type, that have been experimentally agitated with 6-bladed RT impellers over all investigated scales, which has a value of 0.55 (±15%). If the PBT impeller was originally selected in the userform in Figure 5.3, an average $H_c/D_c = 0.51$ (±15%) is outputted, due to this being the average value for all fluids experimentally agitated with 4-bladed 45° PBT impellers over all investigated scales, in this work (Chapter 4). Having recorded this N value, which in this case is 900 rpm, the resulting D_c/D and H_c/D_c values of 2.45 and 0.55, respectively are outputted via a message box, as seen in Figure 5.4(b). The user is also informed that to investigate other N values, the System 1 '*Change Impeller Speed*' operation, located within the '*Predicting Cavern Sizes*

in Viscoplastic Fluids' section of the '*Mixing In Stirred Vessels*' worksheet (see Figure 5.1(a)) must be executed, with the userform in Figure 5.4(a) again being presented to the user.

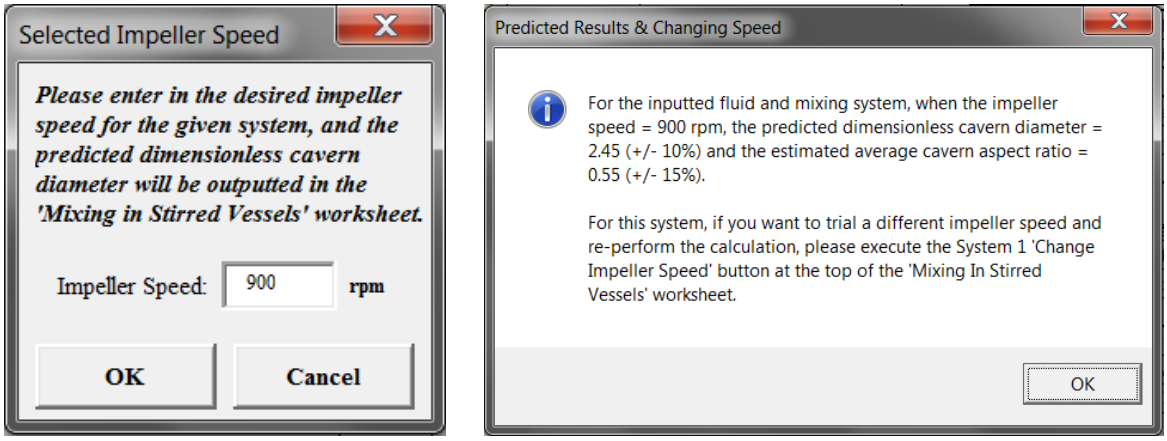

(a) **(b)**

Figure 5.4. (a) Userform allowing the user to input the target impeller speed, N value into the worksheet. The prediction is then performed, with the message box in (b) being displayed to the user, showing the predicted D_c/D and H_c/D_c values for the given system and N value in question. The user is also informed that they are able to trial a different N value through execution of the System 1 '*Change Impeller Speed*' operation.

In addition to the message box informing the user of the predicted D_c/D and H_c/D_c values at their given N value, schematic visualisations of the predicted cavern sizes for a given system can be seen in the worksheet, as highlighted in Figure 5.5. In Figure 5.5(a), the cavern (highlighted green) has a $D_c/D = 2.45$ and corresponds to $N = 900$ rpm for the system in question. When the System 1 '*Change Impeller Speed*' operation is then utilised, a cavern with D_c/D values of 1.37 (Figure 5.5(b)) and 3.28 (Figure 5.5(c)) were achieved at N values of 400 rpm and 1150 rpm, respectively. In these two cases, D_c is of similar size to the impeller diameter, D (Figure 5.5(b)) and the tank diameter, T (Figure 5.5(c)), respectively, with the MPMT able to predict cavern sizes when $D \leq D_c \leq T$. If $D_c \leq D$, the message box in Figure 5.6(a) is displayed notifying the user that the inputted N value results in a cavern with a predicted D_c value either smaller than or equal to D, and if $D_c \geq T$, the message box in Figure 5.6(b) is displayed to inform the user that the inputted N value would produce a cavern with a predicted D_c value larger than, or equal to, T. It is not realistic for the cavern to have a diameter smaller than the impeller, and if a scenario is reached in which a chosen N value results in the cavern reaching the tank wall, D_c is unable to increase in size (but the cavern height, H_c will continue to grow). In these situations, along with the appropriate message boxes in Figure 5.6 being displayed, the schematic of cavern and the tank from the worksheet will be hidden from the user, leaving

only the impeller being visualised. As seen in Figure 5.6, the user is then prompted to trial a different N value using the System 1 '*Change Impeller Speed*' operation.

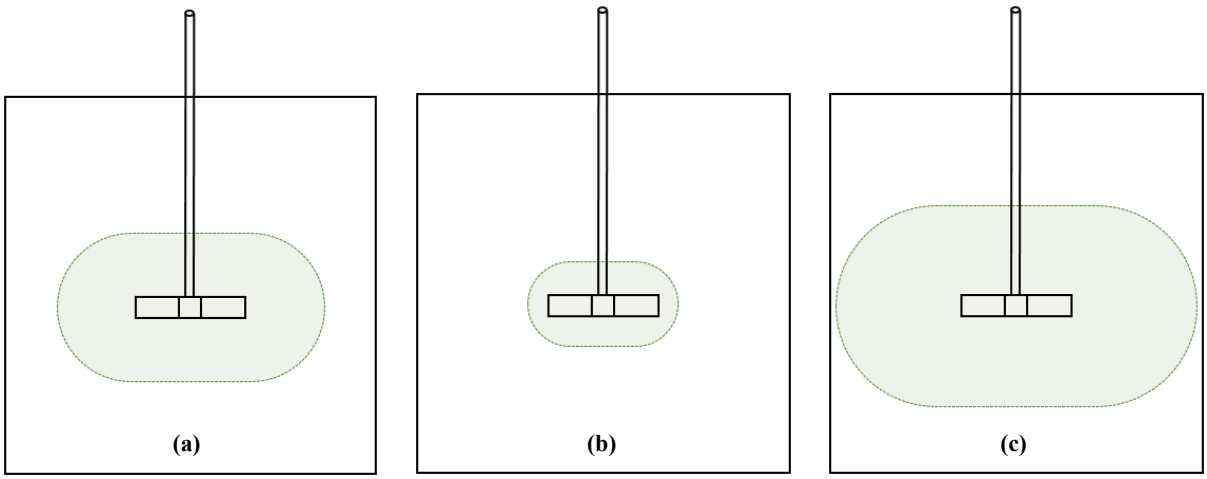

Figure 5.5. Schematic visualisations of the predicted cavern sizes for the example tank and impeller setup, containing the test fluid, at: (a) 900 rpm (D_c/D = 2.45), (b) 400 rpm (D_c/D = 1.37) and (c) 1150 rpm (D_c/D = 3.28).

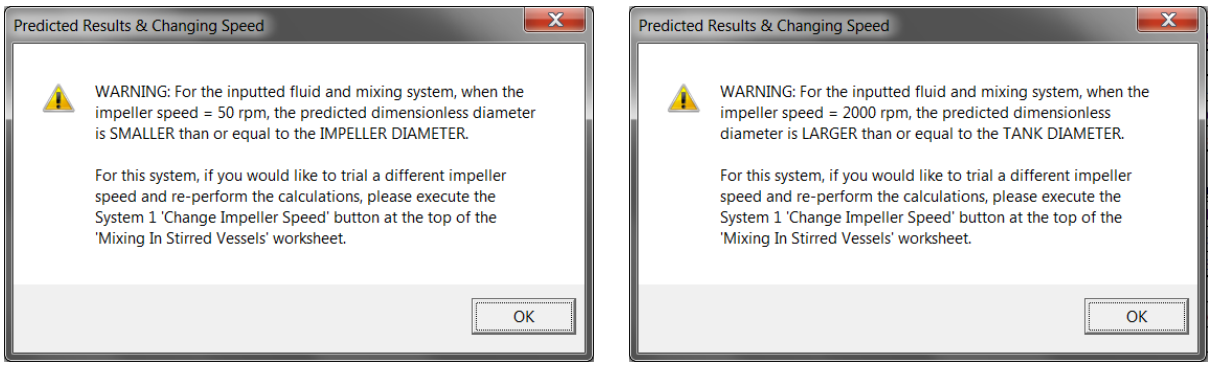

Figure 5.6. Message boxes warning the user that the value of N that has been entered would result in: (a) the predicted D_c/D being smaller than or equal to D, or (b) the predicted D_c/D being greater than or equal to T.

5.3.2 Case Study 2: Matching cavern sizes in viscoplastic flows

As stated in Section 5.3.1, to perform the dimensionless cavern size matching process, the '*Mixing In Stirred Vessels*' operation is executed from the '*Data Entry*' worksheet, and when the userform in Figure 5.2(a) is presented to the user, the '*Perform a matching process*' option should be selected. Having implemented this, a very similar message box to the one seen in Figure 5.2(b) is displayed, however this time notifying the user that "a matching cavern size process through changing the fluid/scale has been selected", and again reminding the user to only run the process if the rheological data for the fluid has been acquired using the 'cone-and-plate' geometry. A userform is then displayed (Figure 5.7), allowing

the user to enter in the details of the 'to-be-matched' system (System 1), including: the rheological and physical properties of the fluid, details of the tank and impeller setup and the N values required to produce the minimum and maximum investigated D_c/D values from the experimental mixing study of System 1.

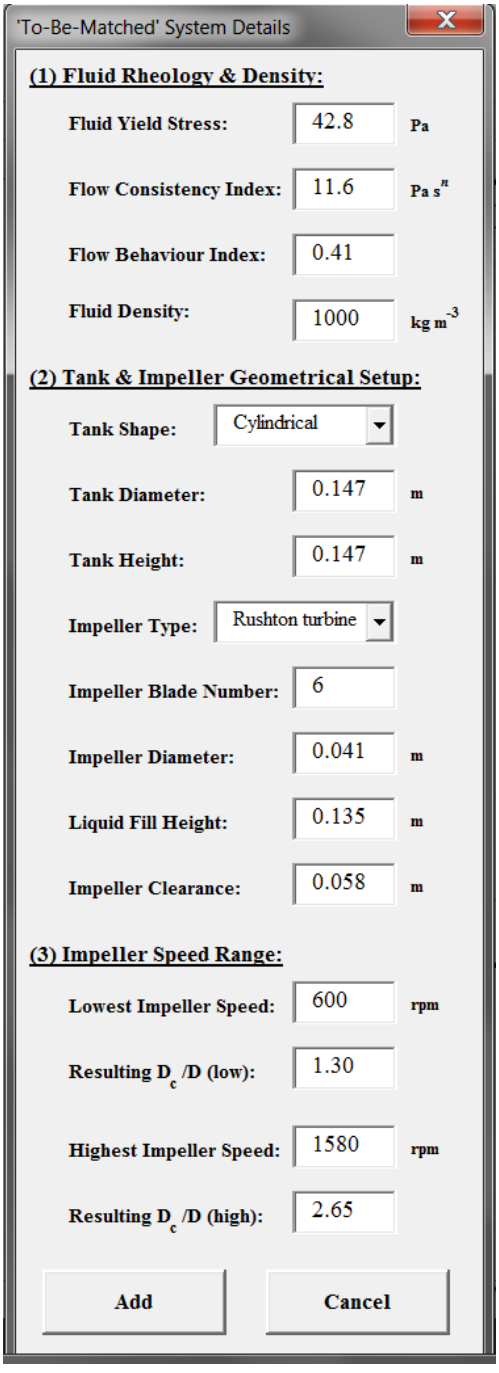

Figure 5.7. Userform allowing the details relating to the tank and impeller setup, the rheological and physical properties of the fluid, and the N values required to produce the maximum and minimum D_c/D values for the 'to-be-matched' System 1 to be inputted.

The System 1 details are inputted into the relevant sections of the '*Predicting Cavern Sizes in Viscoplastic Fluids*' section of the '*Mixing In Stirred Vessels*' worksheet (see Figure 5.1(a) to visualise the worksheet layout). Unlike the prediction process, during the matching process the sub-section titled '*(3) Impeller Speed Range (MATCHING ONLY!)*' will contain information relating to the maximum and minimum D_c/D and associated N values for System 1, as seen in Figure 5.8.

(3) Impeller Speed Range (*MATCHING ONLY*!):	
Lowest Impeller Speed, N_L / rpm	600
Lowest Impeller Speed, N_L / s^{-1}	10.00
Smallest D_c/D	1.30
Highest Impeller Speed, N_H / rpm	1580
Highest Impeller Speed, N_H / s^{-1}	26.33
Largest D_c/D	2.65

Figure 5.8. Sub-section within the '*Predicting Cavern Sizes in Viscoplastic Fluids*' section of the '*Mixing In Stirred Vessels*' worksheet, titled '*Impeller Speed Range (MATCHING ONLY!)*', where the experimental N values corresponding to the minimum and maximum D_c/D for System 1 can be seen.

The userform in Figure 5.9 is then displayed, allowing the user to input in information relating to the scale and fluid rheology of System 2. If the user wishes to use either the same fluid or perform the matching process on the same scale, then the questions: '*Would you like to perform the matching process using the same fluid?*' and '*Would you like to perform the matching process using the same scale?*', would be answered '*Yes*' using the associated drop-down boxes, with all other questions remaining unanswered. This information is then fed into the relevant cells in the '*Process Details*' sub-section in the '*Matching Viscoplastic Flows*' part of the worksheet. In this scenario, if the same fluid is selected, the rheological and physical properties of the System 1 details are copied into the associated cells of the '*(1) Fluid Rheology & Density*' sub-section in the '*Matching Viscoplastic Flows*' part of the worksheet. If the same scale is selected, the System 1 tank and impeller setup is inputted into relevant cells of the System 2 '*(2) Tank and Impeller Geometrical Setup*' sub-section. In the example shown in Figure 5.9, both a different fluid and different scale have been selected for System 2, with a fluid with a larger yield stress being selected, and an impeller with a diameter twice that of the System 1 impeller being chosen. From the drop-down boxes relating to changing the fluid, the user could select to use a fluid in System 2 with either a larger or smaller yield stress than System 1. In terms of the changing the scale, the user can select to either scale-up or scale-down the process, by choosing a larger or smaller impeller diameter for System 2, respectively. Once this has been selected, the extent of how much smaller or larger the System 2 impeller is can be chosen by selecting one of the designated values from the associated drop-down box. From the example in Figure 5.9, an impeller with a diameter 2x larger

than the System 1 impeller was selected for the System 2 setup, however the user is able to choose values ranging from 1.25 to 2.50, in increments of 0.25.

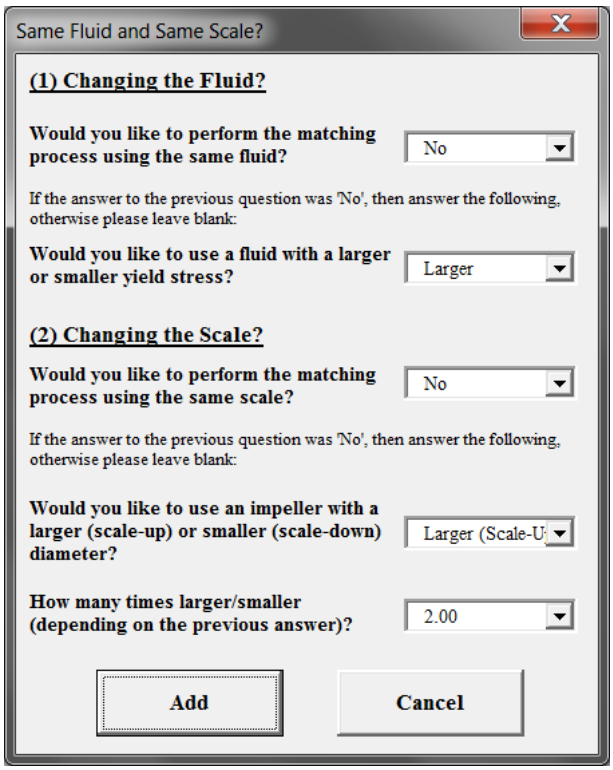

Figure 5.9. Userform presented to the user, allowing the details relating to the scale and fluid rheology of System 2 to be entered into the '*Process Details*' sub-section of the '*Matching Viscoplastic Flows*' part of the worksheet.

Having decided to use a different fluid in System 2, the operation proceeds by finding a suitable potential fluid system stored in the '*Library_Fitted*' worksheet. In this example, the yield stress value of the System 1 fluid is 42.8 Pa, and the option of using a fluid with a larger yield stress on System 2 has been chosen. A suitable fluid is chosen by multiplying the System 1 yield stress value of 42.8 Pa by 1.5, giving a value of 64.2 Pa, and then searching through the '*Library_Fitted*' worksheet until a fluid is found that has a yield stress $\geq$ 64.2 Pa. When an appropriate fluid is found, the message box in Figure 5.10(a) is displayed to the user, asking them whether the yield stress of the new fluid (in this case, τ_y = 68.6 Pa) is enough of an increase compared to the yield stress of the System 1 fluid. If the '*Yes*' button is selected, the message box in Figure 5.10(b) is presented, informing the user of the chosen fluid and the identity, physical and rheology properties of the fluid is copied into the System 2 '*(1) Fluid Rheology & Density*' sub-section of the worksheet from the '*Library_Fitted*' worksheet (as seen in Figure 5.1(b)). If the user opts for '*No*' in the Figure 5.10(a) message box, the operation will then search the '*Library_Fitted*' worksheet for a fluid with an even larger yield stress. If found, the details of this fluid will then be presented to the user and inputted into the System 2 '*(1) Fluid Rheology & Density*' sub-section, however if there are no fluids in

the '*Library_Fitted*' worksheet with a yield stress value greater than that of the proposed System 2 fluid (τ_y = 68.6 Pa), then this fluid will then be selected for the matching process. In this example, if the System 1 fluid has a larger yield stress than any of the fluids in the library, then the user will be notified of this and the matching process will proceed using the System 1 fluid. If the user originally opted to find a fluid for System 2 with a smaller yield stress than the System 1 fluid, then a similar process occurs, however now the yield stress value of the System 1 fluid will be divided by 1.5 and the '*Library_Fitted*' being searched until a fluid is found with a yield stress smaller than or equal to this value.

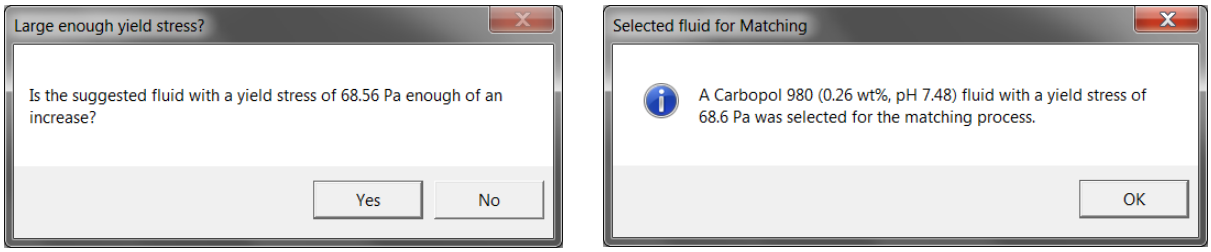

Figure 5.10. (a) Message box asking the user whether the yield stress of the potential System 2 fluid is enough of an increase compared to the yield stress of the System 1 fluid. If '*Yes*' is selected, the message box in (b) will be displayed, informing the user of the identity of physical properties of the chosen System 2 fluid.

In this example, the decision to scale-up the mixing system geometry was selected, with the chosen impeller diameter for System 2 being twice that of the diameter of the impeller used in the System 1 mixing system. As a result, the same tank shape (cylindrical) and impeller type (Rushton turbine, 6 blades) are copied across into the System 2 '*(2) Tank & Impeller Geometrical Setup*' sub-section, and every length is multiplied by two, to maintain geometrical similarity over System 1 and System 2. As seen in Figure 5.1(b), both the tank diameter and tank height are now equal to 0.294 m, resulting in the System 2 tank having a tank volume of approximately 20 L, compared to the System 1 tank volume of approximately 2.5 L. The System 2 impeller diameter, impeller clearance and liquid fill height is now 0.082 m, 0.116 m and 0.270 m, respectively. With all of these details being stored in the System 2 '*(2) Tank & Impeller Geometrical Setup*' sub-section, the matching process is now able to occur. Using the aforementioned functional relation between D_c/D and $Re_m^{-0.3} Re_y^{0.6} n^{-0.1} k_s^{-1}$ (Section 5.1), the N values required to produce the minimum and maximum D_c/D values from System 1 (D_c/D = 1.30 and D_c/D = 2.65, respectively), are calculated and inputted into the relevant cells in the System 2 '*(3) Impeller Speed Range (MATCHING ONLY!)*' sub-section. For this given system, the range of N values required to fulfil the range of D_c/D values for System 2 are 376-1064 rpm, and a screen-grab of the System 2 '*(3) Impeller Speed Range (MATCHING ONLY!)*' sub-section can be seen in Figure 5.11.

(3) Impeller Speed Range (*MATCHING ONLY!*):	
Lowest Impeller Speed, N_L / rpm	376
Lowest Impeller Speed, N_L / s^{-1}	6.27
Smallest D_c/D	1.30
Highest Impeller Speed, N_H / rpm	1064
Highest Impeller Speed, N_H / s^{-1}	17.73
Largest D_c/D	2.65

Figure 5.11. Sub-section of the '*Matching Viscoplastic Flows*' part of the worksheet, titled '*(3) Impeller Speed Range (MATCHING ONLY!)*', where the range of N values that would be required in System 2 to match the range of D_c/D values from System 1 are stored, along with the target range of D_c/D values.

Having determined the range of N values that would be required in System 2 to match the range of D_c/D values from System 1, a userform (Figure 5.12(a)) is presented, permitting the user to input in a specific D_c/D value (and associated N value) from System 1 that they would like to match in System 2. In this example, the specific D_c/D value from System 1 is 2.31, with the $N = 1400$ rpm being used to generate a cavern of this size in System 1. The operation then outputs a message box (Figure 5.12(b)) informing the user of the range of calculated N values that would be required in System 2 to match the range of D_c/D values from System 1, as well as the specific N value that would be required in System 2 to achieve the target D_c/D value from System 1. In this case, to attain $D_c/D = 2.31$ in System 2, $N = 918$ rpm would be needed. The user is then able to change the target D_c/D by implementing the System 2 '*Change System 1 Impeller Speed and* D_c/D' operation, with the same userform from Figure 5.12(a) being displayed. Again, having entered in the System 1 N and D_c/D values, a very similar message box to Figure 5.12(b) is outputted, however now just informing the user of the specific N value required to produce a cavern with the desired D_c/D value.

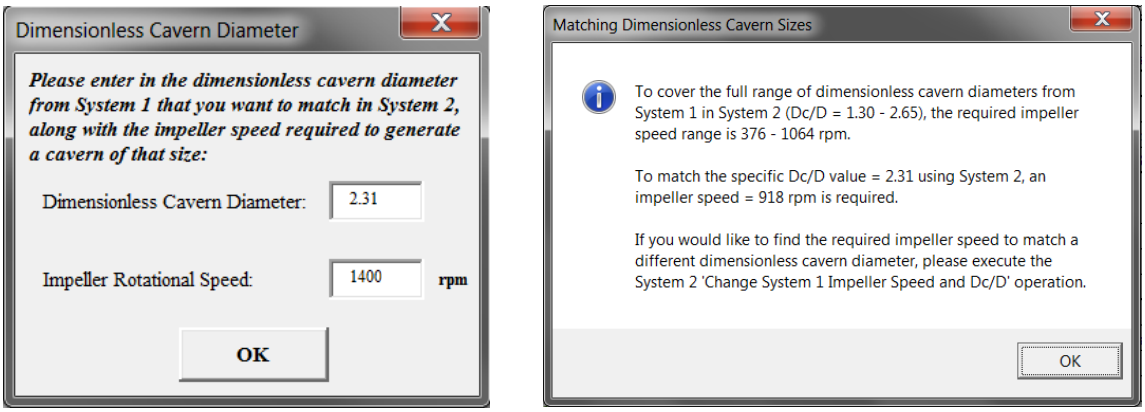

Figure 5.12. (a) Userform allowing the user to input in a specific D_c/D value from System 1 (along with the associated N value) that they want to match in System 2. (b) The resulting message box that is outputted, notifying the range of N values required in System 2 to achieve the range of D_c/D from System 1, as well as the specific N value that would be needed in System 2 to attain the desired D_c/D value from System 1.

As with the prediction process outlined in Section 5.3.1, schematic visualisations of the resulting caverns within each vessel can be seen in the worksheet. As before, the System 1 cavern is green in colour, whilst the System 2 cavern is purple. Figure 5.13 shows the caverns for System 1 and System 2 when the D_c/D for both systems is: (a) 1.46, (b) 1.94 and (c) 2.31. From experiment, to achieve caverns of these sizes in System 1, N values of (a) 900 rpm, (b) 1160 rpm and (c) 1400 rpm, were required. Using the previously discussed correlation, the resulting calculated N values for System 2 were: (a) 482 rpm, (b) 746 rpm and (c) 918 rpm.

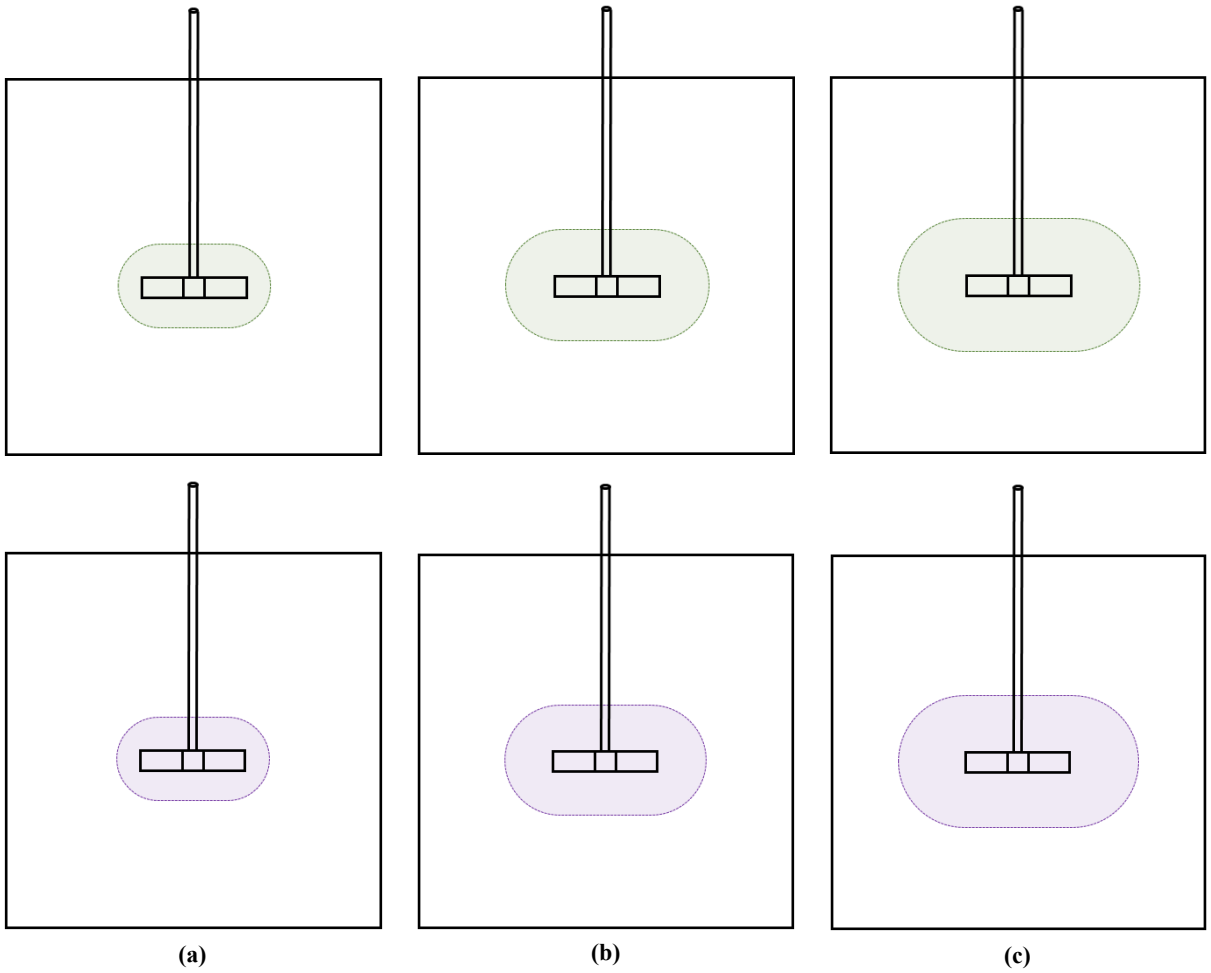

Figure 5.13. Schematic visualisations of the caverns in System 1 (top row) and System 2 (bottom row), with D_c/D values of: (a) 1.46, (b) 1.94 and (c) 2.31. In System 1, caverns of this size were achieved experimentally using N values of (a) 900 rpm, (b) 1160 rpm and (c) 1400 rpm. In System 2, the calculated D_c/D values were matched using N values of (a) 482 rpm, (b) 746 rpm and (c) 918 rpm.

Having investigated a given system, the user is able to change the details of the scale and fluid rheology in System 2, whilst maintaining the same System 1 details, by executing the System 2 '*Change System 2 Scale/Fluid*' operation, located within the '*Matching Viscoplastic Flows*' section of the '*Mixing In Stirred Vessels*' worksheet. Upon activation of this operation, the userform from Figure 5.9 is then presented to the user, and after the new details of System 2 have been chosen, the matching process then proceeds in the same manner as previously described.

5.4 Applicability of the MPMT

The MPMT was constructed based on the results and findings of the mixing studies described in Chapter 4, whereby numerous viscoplastic Carbopol 980 fluids were agitated with either 6-bladed RT impellers or 4-bladed 45° PBT impellers, in vessels with quoted volumes of 2-20 L. In each system, cavern sizes were monitored and a functional relationship between D_c/D and $Re_m^{-0.3}Re_y^{0.6}n^{-0.1}k_s^{-1}$ was attained: $y = 29.19x^2 - 1.14x + 1$, with $y = D_c/D$ and $x = Re_m^{-0.3}Re_y^{0.6}n^{-0.1}k_s^{-1}$. As a result, this functional relationship was used in both the prediction and matching processes of the MPMT's '*Mixing In Stirred Vessels*' operation. Although fluids with wide ranging rheological properties were used in the various mixing studies, all of the fluids had a ratio of yield stress, τ_y-to-flow consistency index, K ranging from approximately 3.1 to 4.4, with flow behaviour index, n values ranging from approximately 0.39-0.49. Therefore, the functional relationship between D_c/D and $Re_m^{-0.3}Re_y^{0.6}n^{-0.1}k_s^{-1}$ is applicable to fluids that fall within these ranges, and if rheological properties of fluids are inputted into the relevant userforms that fall outside of this range, the '*Mixing In Stirred Vessels*' operation will not run and the user will be asked to start the operation again, entering in different rheological properties. It is likely that the functional relationship between D_c/D and $Re_m^{-0.3}Re_y^{0.6}n^{-0.1}k_s^{-1}$ used in the MPMT would be appropriate for fluids with rheological properties that fall outside of this range, however such fluids have not yet been investigated and therefore this claim cannot be made without experimental or CFD validation. Upon further experimental and numerical work, if different functional relationships between D_c/D and $Re_m^{-0.3}Re_y^{0.6}n^{-0.1}k_s^{-1}$ arise, these can be easily included within the code, resulting in the MPMT then being applicable to a wider range of systems and fluids.

Other 'fail-safe' measures, based on logic and practicality, have also been implemented within the code, to ensure that only matching or predictions on 'real' systems can occur. For example, the inputted impeller diameter, D-to-tank diameter, T ratios must be within 0.2-0.8; the liquid fill height, H-to-tank height must be within 0.5-1; the impeller clearance, C-to-liquid fill height, H must be within 0.25-0.75; and the tank height-to-tank diameter, T must be within 0.5-2.5.

5.5 Conclusion

Using Microsoft Excel, a computational platform, known as the '*Matching and Predictive Mixing Tool*' (MPMT) was developed. As well as having many of the same capabilities as those seen in the MFST (Chapter 3), the MPMT also has an additional feature: the '*Mixing in Stirred Vessels*' operation. This operation has the capability of both predicting dimensionless cavern sizes in viscoplastic fluids in a known stirred vessel system, and suggesting the operating conditions required for matching dimensionless cavern sizes in a second system. When performing the prediction process, known details relating to the geometrical setup and the fluid's rheological properties are inputted into the operation, and in turn the predicted D_c/D value, at a given N value, is outputted to the user. The user is then able to change the desired N value by executing the System 1 '*Change Impeller Speed*' operation, located

within the '*Predicting Cavern Sizes in Viscoplastic Fluids*' section of the '*Mixing In Stirred Vessels*' worksheet, resulting in the new D_c/D value being outputted. Upon execution of the matching process, the user inputs into the operation the properties relating to the System 1's fluid rheological properties and tank and impeller setup, and then chooses whether the scale of the geometry and/or the fluid rheology in their second system (System 2) is to be changed. The minimum and maximum D_c/D values from System 1 (acquired from experiment), and the associated N values, are inputted into the operation, along with a specific 'to-be-matched' D_c/D value (and the N value used to produce a cavern of this size). In turn, the operation outputs the range of N values required in System 2 to achieve the range of D_c/D from System 1, along with the N value needed in System 2 to attain the specific D_c/D value from System 1. If the user wishes to use a fluid in System 2 with a different rheology to the System 1 fluid, a fluid with either an increased or decreased yield stress, τ_y, will be selected from the '*Library_Fitted*' worksheet and suggested to the user as being an appropriate fluid for System 2. The System 2 scale and/or fluid rheology can be altered by activating the System 2 '*Change System 2 Scale/Fluid*' operation, whilst the desired System 1 D_c/D value (and N value) can be changed through the use of the '*Change System 1 Impeller Speed and D_c/D*' operation. Both of these operations are located within the '*Matching Viscoplastic Flows*' section of the '*Mixing In Stirred Vessels*' worksheet. The '*Mixing In Stirred Vessels*' operation was constructed based on the findings of the mixing systems and fluids investigated in Chapter 4. However through further experimental and CFD validation of different systems and fluids, the capabilities of the MPMT could be extended to a wider range of viscoplastic flows, central impeller types and tank scales, with the aim of producing a MPMT that could be applied to industrially-relevant mixing systems and 'real' fluids, to better understand the mixing behaviour within the vessels without having to perform appropriate scale down studies when potential issues arise.

Chapter 6: Assessing the Mixing Effectiveness of Dual-Impeller Systems

6.1 Introduction

The focus of this chapter is to use dye visualisation techniques, in conjunction with CFD to evaluate the mixing effectiveness and performance of various centrally-mounted, dual-impeller systems in the agitation of viscoplastic fluids in mixing vessels. In practice, to avoid poor mixing caused by cavern formation, as seen in Chapter 4, dual- or multi-impeller systems are often utilised. The viscoplastic fluids that will be used as the test fluids in this section are Carbopol™ 980 solutions, due to their highly transparent nature, aiding the selected visualisation techniques. A 2 L mixing vessel system will be utilised throughout this chapter, equipped with different combinations of 6-bladed Rushton turbine (RT) and 4-bladed 45° pitched-blade turbine (PBT) impellers (all D = 0.041 m). The effects of various operating conditions on the flows will be investigated, including impeller rotational speed, N, impeller separations, G and impeller configurations. Comparisons will be made between the experimental and numerical results, with CFD providing information about the flow patterns and velocity field distributions that result from agitation with the various impeller configurations, helping to explain the observed phenomena, including cavern-cavern mixing, cavern-cavern segregation and flow compartmentalisation. The impeller configuration that is able to most effectively minimise stagnant zones, flow segregations and arrive at a state of homogeneity throughout the vessel, whilst minimising mixing times, will be suggested. The results from this chapter are important in the context of achieving flow homogeneity in fluids with complex rheological properties in stirred vessels equipped with dual-impeller systems, and can be used to show that these flows are sensitive to impeller geometrical setup and other important operating conditions, such as impeller rotational speed, modified power-law Reynolds number, yield stress Reynolds number and mixing times.

6.2 Experimental methods

6.2.1 Formulation and rheological characterisation of C980 fluids

In this section, C980 fluids were formulated and characterised via similar methods to those outlined in Chapter 4. C980 powder (0.15 wt%) was dispersed in deionised water via mechanical agitation, and on complete dissolution, small quantities of 2 wt% NaOH(aq) solution were added, so that each fluid was between pH 6.40-7.40. The fluids were rheologically characterised using a shear-stress controlled Anton Paar MCR 302 rheometer, equipped with a roughened cone-and-plate geometry (12.6 μm roughness, 0.998° cone angle, cone and plate diameter = 50 mm, CP50-1-41592). All fluids underwent shear stress down-sweep measurements (60 pt dec^{-1}, ramp logarithmic profile 5 s pt^{-1}) and the resulting flow cures were mathematically fitted to the Herschel-Bulkley model (Herschel and Bulkley (1926))

(Eq. 1.11). Note: for each of the rheological measurements performed in this study, the range of shear rate values (~0.001-1000 s^{-1}) investigated ensured that the resulting full range of shear rates (and shear stresses) in the mixing vessel systems were accounted for. The viscoelastic properties of C980 solutions have been investigated, however are not relevant to this current section of the project. The Herschel-Bulkley rheological data and physical properties of three fluids used (called *Case 15*, *Case 16* and *Case 17*) from this section of the study can be seen in Table 6.1 and Table 6.2, respectively. From Table 6.1 and Table 6.2: *Case 15* was used in *Mixing Study G*, where the fluid was agitated with dual-Rushton turbine (dual-RT) systems; *Case 16* was used in *Mixing Study H*, where the fluid was agitated with dual-pitched blade turbine (dual-PBT) systems, and *Case 17* was used in *Mixing Study I*, where the fluid was mixed with systems comprising of one Rushton turbine and one pitched-blade turbine (RT-PBT).

Table 6.1. Herschel-Bulkley properties of the three fluids (*Cases 15-17*) used in this section of the study, along with the errors associated with each fit and the shear rate range over which the fit occurred.

Mixing System		**Herschel-Bulkley rheological properties**			**Error analysis**		
Case	**Agitation system**	**Yield stress, τ_y / Pa**	**Flow consistency index, K / Pa s^n**	**Flow behaviour index, n**	**Shear rate range of fit, $\dot{\gamma}$ / s^{-1}**	**AAD of optimised fit / %**	**R^2 value for optimised fit**
15	Dual-RT	28.1	5.7	0.46	0.0216-932	1.12	0.999
16	Dual-PBT	27.7	6.2	0.46	0.0078-962	1.37	0.999
17	RT-PBT	32.6	8.6	0.43	0.00176-945	1.80	0.999

Table 6.2. Physical properties of the three fluids (*Cases 15-17*) used in this section of the study.

Mixing system		**Fluid composition and physical properties**		
Case	**Agitation system**	**C980 mass fraction / wt%**	**Fluid pH**	**Fluid temperature / °C**
15	Dual-RT	0.15	6.4	25.6
16	Dual-PBT	0.15	6.6	24.6
17	RT-PBT	0.15	7.4	23.4

6.2.2 Stirred vessel system and experimental procedures

An unbaffled, cylindrical vessel system, with a quoted tank volume of 2 L and tank diameter, $T = 0.148$ m was used throughout this study. The two impeller types were 6-bladed RTs and 4-bladed 45° PBTs, each with diameters, $D = 0.041$ m and hence, an impeller diameter-to-tank diameter ratio, $D/T = 0.28$. The impellers were fitted to a shaft, with shaft diameter-to-impeller diameter, $S/D = 0.24$ and shaft-impeller system was centrally mounted onto an IKA EUROSTAR 60 motor. For each mixing study, the fluid was filled to a height, $H = 0.135$ m ($H/D = 3.29$) and the clearance for lower of the two impellers, $C_2 = 0.045$ m

(C_2/D = 1.10). The clearance for the upper of the two impellers, C_1 = 0.095 m (C_1/D = 2.32) or 0.075 m (C_1/D = 1.83), depending on the system in question, resulting in an impeller separation, G = 0.05 m (G/D = 1.22) or 0.03 m (G/D = 0.73), respectively. A schematic of the mixing system and details relating to each of the mixing studies can be found in Figure 6.1 and Table 6.3, respectively. The impeller separations and impeller clearances were measured from the centre of each of the impellers, as illustrated in Figure 6.1.

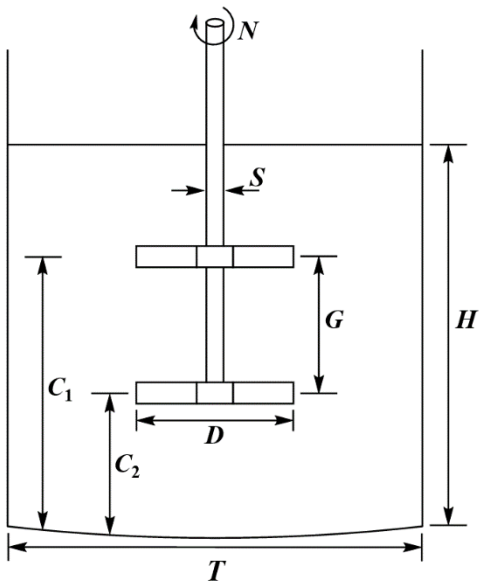

Property	Symbol
Impeller rotational speed, N	N = 0.0–33.3 s^{-1}
Tank volume, V	V = 2 L
Tank diameter, T	T = 0.148 m
Impeller diameter, D	D = 0.041 m
Shaft diameter, S	S = 0.24D
Liquid fill height, H	H = 3.29D
Upper impeller clearance, C_1	See Table 2
Lower impeller clearance, C_2	C_2 = 1.10D
Impeller separation, G	See Table 2

Figure 6.1. Details and schematic of the experimental and numerical dual-impeller tank setup used throughout this work. The impeller gap and impeller clearances were measured from the centre of each impeller.

Table 6.3. Details of the experimental and numerical dual-impeller tank setups used in the various mixing studies in this section of the work.

Mixing Study	Upper Impeller	Lower Impeller	Upper Impeller Clearance, C_1 / m	Lower Impeller Clearance, C_2 / m	Impeller Separation, G / m
G(1)	RT	RT	0.095	0.045	0.05
G(2)	RT	RT	0.075	0.045	0.03
H(1)	PBT	PBT	0.095	0.045	0.05
H(2)	PBT	PBT	0.075	0.045	0.03
I(1)	RT	PBT	0.095	0.045	0.05
I(2)	PBT	RT	0.095	0.045	0.05

For each mixing study, the fluid was loaded into the vessel, the impeller was set to a rotational speed, N = 4.2 s^{-1} and 2-3 mL of food dye (Sainsbury's Supermarkets Ltd) was injected at the tip of each impeller. For each mixing study where G = 0.05 m (G/D = 1.22, *Mixing Studies G(1), H(1), I(1) and I(2)*), blue food dye was injected at the tip of the lower impeller and green food dye was injected at the upper impeller tip. For the studies where G = 0.03 m (G/D = 0.73, *Mixing Studies G(2) and H(2)*), this was

reversed. N was then incrementally increased up to 2000 rpm (33.3 s^{-1}), with images taken (Panasonic HDC-SD90/Apple iPhone 7 camera (12 megapixel resolution)) at each speed after 30 s, to capture the caverns at their equilibrium shape and size. In each mixing study, the cavern boundary was defined by the distinct transition from dyed to non-dyed material, which showed a clear demarcation on the images generated over the course of these experiments. The dimensions of the RT and PBT impellers used in this work can be seen in Figure 6.2 and Table 6.4.

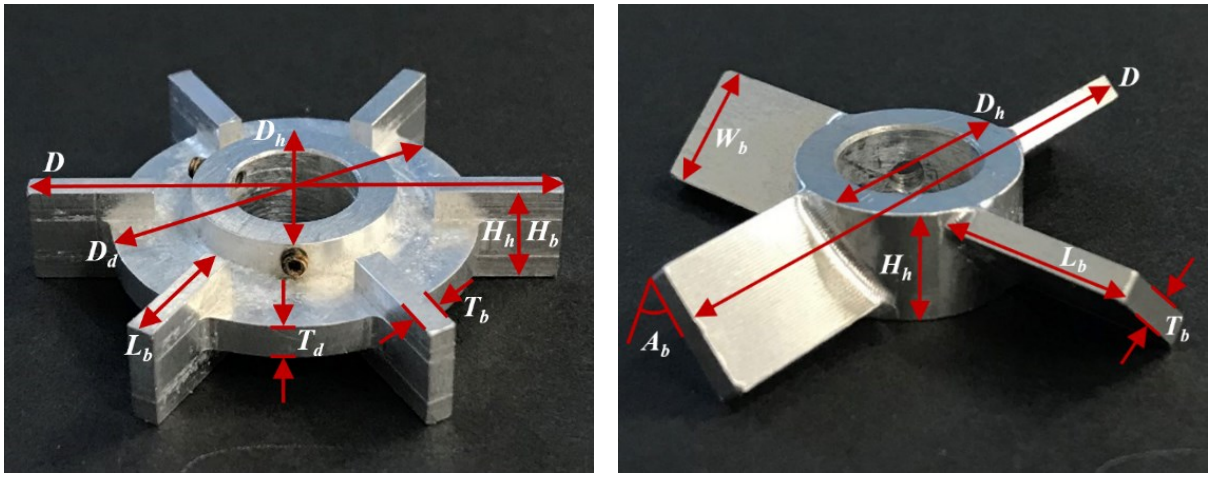

Figure 6.2. (a) 6-bladed RT impeller and (b) 4-bladed 45° PBT used in this section of the study. The impeller dimensions, in conjunction with the tank setup in Figure 6.1, were replicated in the CFD model (see Section A.4 in the Appendix for more details of the numerical methods used in this work). The various impeller properties and relationships, for both impeller types, have been defined and quantified in Table 6.4.

Table 6.4. Impeller properties and relationships for both the RT and PBT used in this section of the study. The properties relating to the tank setup can be found in Figure 6.1.

Impeller Property	**Relationship**	
	Rushton turbine (RT)	**Pitched-blade turbine (PBT)**
Impeller diameter, D	D = 0.041 m	D = 0.041 m
Disc diameter, D_d	$D_d = 0.70D$	N/A
Disc thickness, T_d	$T_d = 0.07D$	N/A
Blade length, L_b	$L_b = 0.24D$	$L_b = 0.30D$
Blade height, H_b	$H_b = 0.20D$	N/A
Blade width, W_b	N/A	$W_b = 0.28D$
Blade thickness, T_b	$T_b = 0.05D$	$T_b = 0.05D$
Hub height, H_h	$H_h = 0.20D$	$H_h = 0.20D$
Hub diameter, D_h	$D_h = 0.39D$	$D_h = 0.39D$
Blade number, N_b	$N_b = 6$	$N_b = 4$
Blade angle, A_b	$A_b = 0°$	$A_b = 45°$

6.2.3 Dimensionless parameters

As discussed in Section 4.2.4, dimensional analysis can be used to determine the key dimensionless parameters that describe the agitation of viscoplastic fluids in stirred vessel systems. These include: the Power number, Po (Eq. 4.1), a modified power-law Reynolds number, Re_m (Eq. 4.2), the Froude number, Fr (Eq. 4.3), the yield stress Reynolds number, Re_y (Eq. 4.4), a dimensionless mean shear rate, $\bar{\dot{\gamma}}/N$, the flow behaviour index, n and key geometrical ratios. An example of the dimensional analysis process can be seen in the Appendix, Section A.3. It was shown in Chapter 4, that scaling the dimensionless cavern diameters, D_c/D of caverns produced upon agitation with centrally-mounted RT and PBT impellers in given viscoplastic fluids on given scales, with $Re_m^{-0.3}Re_y^{0.6}n^{-0.1}k_s^{-1}$ led to cavern size similarity. In this section of the work, Re_m and Re_y values will be quoted, however the proposed scaling method will not be used, because cavern-cavern interactions resulting from dual-impeller mixing will impact the shape and size of the caverns, compared to the caverns that are produced by single-impeller mixing.

6.2.4 Error analysis

A full error analysis, relating to the errors associated with fluid formulation and rheological characterisation, and those relating to the mixing procedure in the stirred vessel system, can be found in Section 4.2.5. The methods and procedures used in this chapter were the same as those used in Chapter 4.

6.3 Numerical methods

The mixing system configuration considered in this section of the work is very similar to the description outlined in Section A.4 in the Appendix. The key difference here is that two impellers are being utilised for mixing, rather than one. Figure 6.3 shows the numerical structure of the mixing vessel system, equipped with a dual-impeller system consisting of the PBT and the RT as the upper and lower impellers, respectively. See Section A.4 for a full description of the numerical construction of the mixing system, the governing equations and numerical methods used, and the numerical validation of the CFD model.

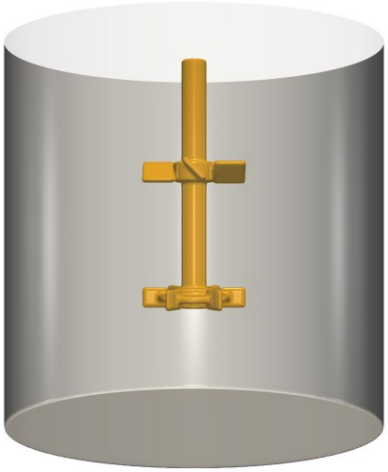

Figure 6.3. Numerical construction of all parts of the mixing system. In this case, the mixing vessel is equipped with a dual-impeller system consisting of the PBT as the upper impeller and the RT as the lower impeller.

6.4 Results and discussion

6.4.1 *Mixing Study G*: Combination of Rushton turbine and Rushton turbine (dual-RT)

Here, the mixing of a viscoplastic fluid with dual-RT system at different impeller separations, G was assessed. As stated in Table 6.3 (Section 6.2.2), G = 0.05 m (G/D = 1.22, *Mixing Study G(1)*) and G = 0.03 m (G/D = 0.73, *Mixing Study G(2)*), at a fixed lower impeller clearance, C_2 = 1.10D, were investigated. For the experimental studies, N was set to a low speed (N = 4.2 s^{-1}, Re_m = 2.7, Re_y = 1.0) and food dye was injected at the impeller tips. N was then incrementally increased and the resulting caverns and flows were monitored. The experimental and numerical flows at five selected impeller speeds: N = 11.7 s^{-1} (Re_m = 13.0, Re_y = 8.1), N = 14.9 s^{-1} (Re_m = 18.9, Re_y = 13.3), N = 18.2 s^{-1} (Re_m = 25.6, Re_y = 19.7), N = 20.3 s^{-1} (Re_m = 30.5, Re_y = 24.7) and N = 33.3 s^{-1} (Re_m = 65.4, Re_y = 66.5), for each the impeller system can be visualised in Figure 6.4, with Rows (a) and (b) associated with *Mixing Study G(1)* and Rows (c) and (d) related to *Mixing Study G(2)*. When viscoplastic fluids are agitated with RT impellers, caverns with 'horn' torus morphology are formed. This morphology stems from the strongly radial nature of the RT impeller, as discussed in Section 4.4.3. Details relating to the Herschel-Bulkley rheological properties and the physical properties of the fluid (*Case 15*) used in *Mixing Study G* can be found in Table 6.1 and Table 6.2 (Section 6.2.1), respectively.

In *Mixing Study G(1)* (dual-RT, G = 0.05 m, G/D = 1.22), there was strong compartmentalisation between the two caverns and flows over the range of N investigated. At lower N values, the stresses being applied to the fluid were not large enough to induce interaction between the two caverns (see Figure 6.4(a)(i)), resulting in the formation of two independent caverns. Interestingly, the upper of the two caverns had a greater cavern aspect ratio than the lower one, with experimental cavern height-to-cavern diameter ratios, H_c/D_c = 0.53 and 0.44, respectively at N = 11.7 s^{-1} (Re_m = 13.0, Re_y = 8.1). The increased

H_c in the upper cavern resulted in a decreased D_c, with respect to the lower cavern, with an experimental dimensionless cavern diameter, D_c/D = 1.44 and 1.49 for the upper and lower caverns, respectively. It is hypothesised that this variation is caused by fluid agitation induced by the shaft both above and below the upper impeller, compared to shaft agitation solely above the lower impeller. As a result, the vortices above and below the upper impeller, and above the lower impeller were stretched in the z-direction, but the vortex below the lower impeller remained more compressed, as highlighted by the streamlines in the numerical result (Figure 6.4(b)(i)), leading to a slightly increased H_c/D_c and reduced D_c/D in the upper cavern. By further inspection of the numerical result at N = 11.7 s^{-1} (Re_m = 13.0, Re_y = 8.1), cavern interaction was observed. However, when the velocity was resolved into its component parts, focusing on the axial and azimuthal velocity profiles in the region between the impellers (Figure 6.5), cavern-cavern interaction and transfer of material between the impellers was seen to be unlikely. Figure 6.5(a) is the velocity field distribution within the vessel at N = 11.7 s^{-1} (Re_m = 13.0, Re_m = 8.1), with only flow at a velocity magnitude $\geq$ 0.01 m s^{-1} highlighted. The velocity profiles for the axial (u_z) and azimuthal (u_θ) components were taken along the vertical line (black line in Figure 6.5(a)), which extends from the top to the bottom of the vessel and passes the tips of both impellers, as seen in Figure 6.5(b) and (c). In the region between the impellers ($z \approx$ 0.066-0.082 m), which remains uncoloured in the experimental results, $u_\theta >$ 0.01 m s^{-1}, whereas u_z, the component responsible for cavern-cavern interaction and cross-impeller fluid flow, is negligible by comparison, hence u_θ dominates the flow in this region, accounting for the observed discrepancy between the experimental and numerical results at N = 11.7 s^{-1} (Re_m = 13.0, Re_y = 8.1).

As N was increased in *Mixing Study G(1)*, the two caverns grew in size, interacting with one another to produce distinct compartmentalisation between the two flows and pronounced cavern-cavern segregation. When N reached 33.3 s^{-1} (Re_m = 65.4, Re_y = 66.5), the entire vessel contents was in motion, though clear segregation between the flows still existed despite the prominent deflection of the interface (Figure 6.4(a)(v)). The observed interface deflection was caused by the upper impeller being positioned close enough to the interface, so that when N was increased to a great enough extent, the resulting upper cavern (or flow) was able to interact the interface, and hence fluid displacement within the cavern led interface deflection close to the shaft. As impeller speed continued to increase, more material at the interface was drawn into the flow patterns of the upper cavern, leading to a greater degree of interface deflection, until the entirety of the vessel was in motion at N = 33.3 s^{-1}. It is hypothesised that slip effects at the vessel wall may have also slightly contributed to the observed interface deflection, under conditions where the upper flow had not reached the vessel wall. The numerical results (Figure 6.4(b)(ii-v)) show that the vortices produced by both impellers are very similar in shape and size, leading to high levels of symmetry in the radial direction about the centre point between impellers. This symmetry results in the vortical behaviour below the upper RT blades counteracting the vortices above the lower RT blades leading to the observed flow segregation. The formation of distinct cavern-cavern segregation in viscoplastic fluids agitated with

sets of RT impellers is in agreement with the observed results of Arratia *et al.* (2006), who examined the agitation of Carbopol fluids with a 3-RT configuration (all $D = 0.075$ m, $G = 0.09$ m, $G/D = 1.20$).

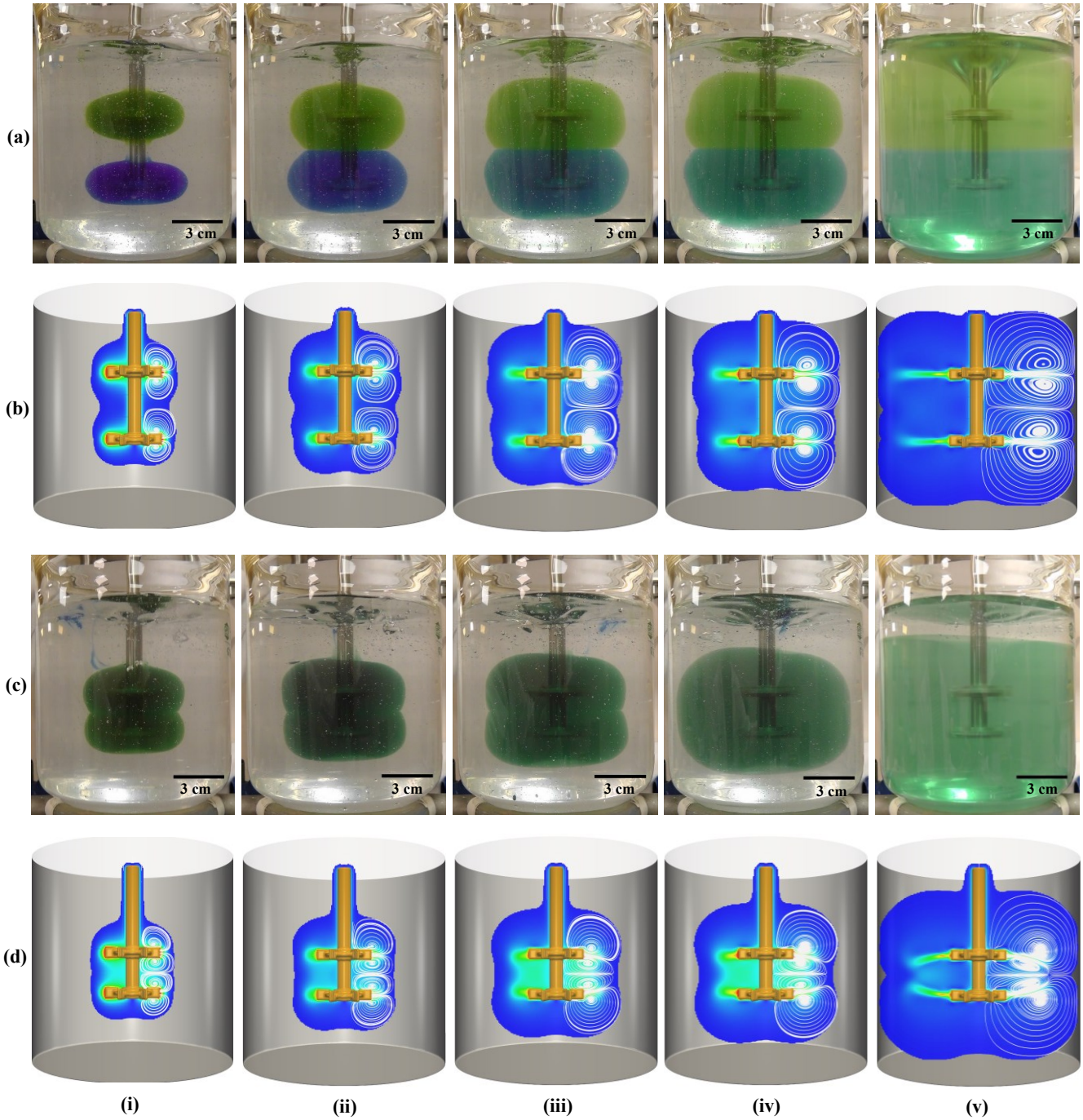

Figure 6.4. Experimental images and CFD snapshots for *Mixing Study G(1)* (Rows (a) and (b)) and *Mixing Study G(2)* (Rows (c) and (d), respectively). For both *Mixing Study G(1)* and *G(2)*, the following impeller rotational speeds, N were used in the images and snapshots: (i) 11.7 s^{-1} ($Re_m = 13.0$, $Re_y = 8.1$), (ii) 14.9 s^{-1} ($Re_m = 18.9$, $Re_y = 13.3$), (iii) 18.2 s^{-1} ($Re_m = 25.6$, $Re_y = 19.7$), (iv) 20.3 s^{-1} ($Re_m = 30.5$, $Re_y = 24.7$) and (v) 33.3 s^{-1} ($Re_m = 65.4$, $Re_y = 66.5$).

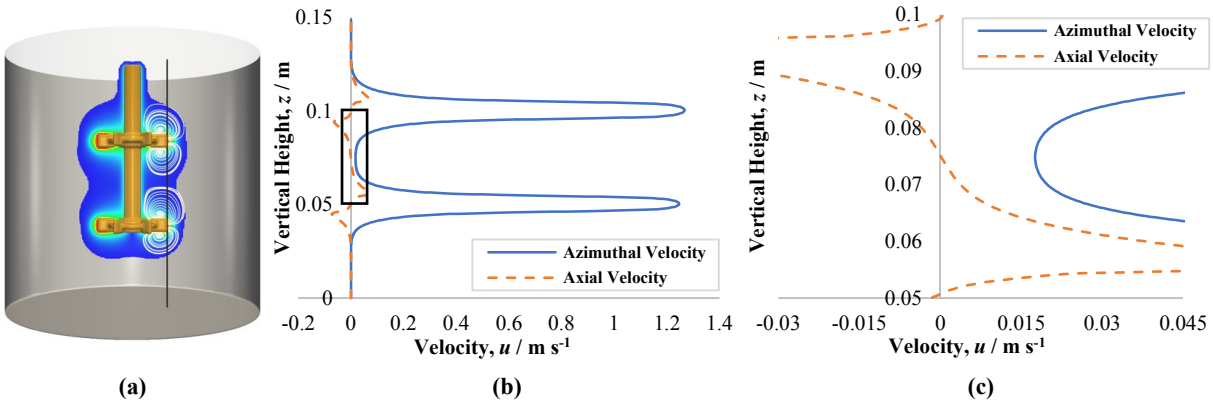

Figure 6.5. (a) The velocity field distribution within the vessel at $N = 11.7$ s^{-1} ($Re_m = 13.0$, $Re_y = 8.1$) in *Mixing Study G(1)*, with only flow at a velocity magnitude ≥ 0.01 m s^{-1} highlighted. The vertical black line at the impeller tips, which extends from the top to the bottom of the vessel, denotes where in the vessel the azimuthal, u_θ and axial, u_z velocity profiles in (b) were taken from. (c) Zoomed-in plot of the u_θ and u_z profiles for the region in the vessel between the centre of the two impellers (non-coloured in the experimental results), shown by the black box in (b).

The *Mixing Study G(1)* setup (dual-RT, $G = 0.05$ m, $G/D = 1.22$) was then utilised to investigate the effect of time on flow compartmentalisation, at $N = 33.3$ s^{-1} ($Re_m = 61.5$, $Re_y = 70.7$). The test C980 fluid had the rheological properties: $\tau_y = 26.4$ Pa, $K = 6.2$ Pa s^n and $n = 0.45$ ($\dot{\gamma}$ range = 0.00059-963 s^{-1}, AAD = 1.97%, $R^2 = 0.998$), and green and blue food dye was injected into the top and bottom halves of the vessel contents, respectively at $N = 3.33$ s^{-1} ($Re_m = 1.7$, $Re_y = 0.7$). N was ramped up to 33.3 s^{-1} ($Re_m = 61.5$, $Re_y = 70.7$) to spread the dyes throughout the vessel. The motor was switched off, then back on, with images (Figure 6.6) taken at: (a) $t = 0$ s (immediately after the motor was switched on), (b) $t = 148$ s, (c) $t = 267$ s and (d) $t = 368$ s. At $t = 0$ s, there was limited transfer of material between the impellers, resulting in distinct compartmentalisation. Mixing between compartments increased with time until a homogenous state was reached at $t = 368$ s. It is hypothesised that this slow mass transfer resulted from the diffusion of dyed material from one compartment to the other, being swept into the flow patterns of the neighbouring compartment. This diffusion process was relatively slow compared to the rate of recirculation caused by agitation within each compartment, explaining why initially flow compartmentalisation was observed, before homogeneity was eventually achieved.

(a) (b) (c) (d)

Figure 6.6. Mixing with the dual-RT system (G = 0.05 m, G/D = 1.22) at constant N = 33.3 s^{-1} (Re_m = 61.5, Re_y = 70.7). Going from (a) to (d) time, t is increasing: (a) t = 0 s, (b) t = 148 s, (c) t = 267 s, and (d) t = 368 s. t = 0 s indicates when N first reached 33.3 s^{-1}.

In *Mixing Study G(2)*, G was reduced to 0.03 m (G/D = 0.73) and over the entire range of N investigated, mixing between the two caverns was observed. In the experimental study, this was highlighted by the homogeneous green/blue colour that formed in the regions of flow. In Figure 6.4(c)(i-iii), despite the homogeneous colour, distinctions between the two caverns were observed, as seen by the 'indentations' at the edges of the flows. It is hypothesised that this is likely to be caused by the u_z values being large enough to induce cross-impeller flow in the central part of the caverns; at the peripheries, u_θ greatly dominates over u_z and hence recirculation of material within the separate caverns is favoured over vertical mixing. The numerical results for the first three selected N values (Figure 6.4(d)(i-iii)) show that the velocity magnitudes are greater at the impeller region and between the impellers, than at the cavern periphery, aiding the observed mixing between impellers and the flow compartmentalisation at the cavern edges from experiment. At N = 18.2 s^{-1} (Re_m = 25.6, Re_y = 19.7) in Figure 6.4(d)(iii), the lower vortex of the upper RT and the upper vortex of the lower RT are distinctly more compacted compared to the upper and lower vortices of the upper and lower RTs, respectively. This compaction becomes more pronounced with increasing N, until at N = 33.3 s^{-1} (Re_m = 65.4, Re_y = 66.5) in Figure 6.4(d)(v), where the upper and lower vortices of the upper and lower RT, respectively, encroach on the two central vortices and interact with one another. At N = 20.3 s^{-1} (Re_m = 30.5, Re_y = 24.7) in the experimental study (Figure 6.4(c)(iv)), it was hypothesised that the forces being applied to the material were large enough to induce sufficient cross-impeller flow for one continuous cavern to form and for the impellers to function as a single entity effectively. The result was the formation of a single cavern with approximately spherical morphology. This, however, was not predicted by the CFD model, where a cavern was produced (Figure 6.4(d)(iv)) that still had some segregation characteristics at the periphery. At N = 33.3 s^{-1} (Re_m = 65.4, Re_y = 66.5), the flowing material reached the tank wall (Figure 6.4(d and c)(v)), but the segregation characteristics still partially remained in the numerical results. Nevertheless, the CFD model predicted the observed stagnant zone near the top of

the vessel well. It was surmised that the upper RT was too far from the interface to cause perturbation, resulting in a stagnant layer of material forming. Despite a substantial fraction of the material being well-mixed, complete homogeneity was not achieved throughout the vessel in *Mixing Study G(2)*. Stagnancy in a vessel could lead to production losses in an industrial setting.

Arriving at homogeneity in a dual-RT agitation system is evidently a time dependent process and although flow compartmentalisation was observed using simple techniques (dye visualisation, transparent fluid and vessel) in this study, the visualisation of this phenomenon would be problematic on the industrial scale whilst formulating a 'real' fluid. If the material-air interface deflection, as seen in *Mixing Study G(1)* and Figure 6.6, was observed in an industrial setting, it could misleadingly suggest the material was well-mixed throughout the vessel. However, unless the necessary precautions are taken, such as appropriate mixing times and impeller separations, a homogeneous state may not be reached, potentially leading to limited production formation and precursor losses. As a result, mixing with a dual-RT system would not be the recommended method for efficiently achieving homogeneity during the agitation of viscoplastic fluids.

6.4.2 *Mixing Study H*: Combination of pitched-blade turbine and pitched-blade turbine (dual-PBT)

Here, the mixing of a C980 fluid with a dual-PBT system (both $D = 0.041$ m) was evaluated at $G = 0.05$ m ($G/D = 1.22$, *Mixing Study H(1)*) and $G = 0.03$ m ($G/D = 0.73$, *Mixing Study H(2)*). Further details relating to the tank and impeller setup can be found in Figure 6.1 and Table 6.3 (Section 6.2.2). Unlike the exclusively radial nature of RT impellers, PBT impellers produce flows with some axial character. Due to the rotational direction, the PBT impellers in this study were downward pumping, and there is a maxima in the velocity magnitude (and hence force being exerted on the material) at a 45° angle to the radial direction at the blade tips. As a result, when a viscoplastic fluid is agitated by a PBT, the resulting cavern adopts an 'apple-shaped' torus, in contrast to the axisymmetic 'horn' torus shape produced by RT agitation (Xiao *et al.* (2014)). This is particularly evident at larger N values, when D_c is comparable to the tank diameter, T. Further discussion of this can be found in Section 4.4.6. Details relating to the Herschel-Bulkley rheological properties and the physical properties of the fluid (*Case 16*) used in *Mixing Study H* can be found in Table 6.1 and Table 6.2 (Section 6.2.1), respectively.

For both experimental studies in *Mixing Study H*, the impeller was set to $N = 4.2$ s^{-1} ($Re_m = 2.5$, $Re_y = 1.1$) and dye was injected at the tip of both impellers. N was then incrementally increased, with images capturing the flow at each N value. The experimental and numerical results at five selected speeds of $N = 11.7$ s^{-1} ($Re_m = 12.2$, $Re_y = 8.3$), 16.0 s^{-1} ($Re_m = 19.8$, $Re_y = 15.5$), 18.2 s^{-1} ($Re_m = 24.1$, $Re_y = 20.0$), 20.3 s^{-1} ($Re_m = 28.7$, $Re_y = 25.1$) and 33.3 s^{-1} ($Re_m = 61.6$, $Re_y = 67.4$), for both studies are presented in Figure 6.7, where Figure 6.7(a) and (b) relate to *Mixing Study H(1)*, and Figure 6.7(c) and (d) relate to *Mixing Study H(2)*.

In *Mixing Study H(1)*, two distinct caverns form at $N = 11.7$ s^{-1} ($Re_m = 12.2$, $Re_y = 8.3$), because the force being imparted on the material by the impellers was not great enough to induce cavern-cavern interaction (Figure 6.7(a)(i)). As with the dual-RT, $G = 0.05$ m system, the upper of the two caverns had a larger H_c/D_c and a smaller D_c due to the effects of shaft agitation. More specifically, H_c/D_c = 0.52 and 0.41, and D_c/D = 1.34 and 1.52, for the upper and lower cavern, respectively. The analogous numerical result (Figure 6.7(b)(i)) suggested cavern-cavern interaction occurred, however, as with *Mixing Study G(1)*, the u_θ component dominated flow in the region between the impellers which remained uncoloured in the experiment, with u_z, the velocity component responsible for cavern-cavern interaction and cross-impeller fluid flow, being negligible by comparison.

In Figure 6.7(a), as N increased from (ii) 16.0 s^{-1} ($Re_m = 19.8$, $Re_y = 15.5$) to (iv) 20.3 s^{-1} ($Re_m = 28.7$, Re_y = 25.1), there was interaction between the two caverns and noticeable cavern-cavern segregation. Both PBTs are downward-pumping, resulting in a lack of symmetry of the flows about the *x*-*y* plane at the centre point between the impellers (if *z* is the vertical direction). This is in contrast to the dual-RT impeller system of *Mixing Study G(1)*, where the flows are axisymmetric about this central plane. As a result, the nature of flow compartmentalisation between the two studies was different. With increasing N from (ii) to (iv) in Figure 6.7(a), the rate of cavern growth of the lower cavern is faster than the upper cavern, with the upper cavern becoming increasingly faint in colour, whilst the lower cavern became progressively more green-blue in colour. It is hypothesised that despite the cavern-cavern segregation, small amounts of vertical mixing from upper to the lower cavern is occurring, due to the downward-pumping nature of the PBT. This material is then recirculated around the lower cavern but is unable to transfer back to the upper cavern. Conservation of mass results in the new material from just outside the upper cavern being drawn into its flow patterns, compensating for the material 'lost' from the upper to the lower cavern. Both the one-way vertical mixing and the new material being drawn in elucidate the aforementioned colour changes associated with both caverns. The observed cavern-cavern segregation is due to recirculation rates in the upper cavern being vastly superior to the vertical mixing rates from the upper to lower cavern, combined with the lower cavern being unable to transfer material back to the upper cavern. If the agitation system was symmetric about the aforementioned central *x*-*y* plane, the observed compartmentalisation would be stronger, with the comparable cavern growth rates, similar to *Mixing Study G(1)*. For this to occur for a dual-PBT system, the pumping direction for the two PBT would have to be opposing, i.e. upward-downward or downward-upward for the upper and lower PBTs, respectively.

The analogous numerical results in Figure 6.7(b)(ii-iv) show that the observed experimental vertical mixing was not predicted by CFD, with stringent cavern-cavern segregation highlighted by the compartmentalisation of the sets of streamlines within the caverns. The result is a disparity between the predicted and observed cavern sizes and morphologies, with the predicted segregation resulting in the caverns growing at similar rates, with the lower cavern maintaining its 'apple' torus morphology, which was not seen in the experimental study. However, the CFD model accurately predicted the upper cavern

morphology over these N values. As was the case in *Mixing Study G(1)*, deflection of the material-air interface close to the shaft (also known as 'Newton's bucket') was observed in *Mixing Study H(1)*, as highlighted in Figure 6.7(a)(iii-v) and Figure 6.8. As before, this was caused by the upper PBT being situated close to the interface. However, due to its downward-pumping nature, the PBT was more effective at drawing material from the interface into the flow patterns of the upper cavern than the radial-flow RT impellers, resulting in interface deflection at lower impeller speeds. However, the corresponding simulations were run for a single-phase system, and hence the stress-free assumption imposed on the upper boundary, applied to the corresponding simulations was no longer valid, leading to the observed deflection not being accounted for. As a result, this was the likely cause of the discrepancies between the observed and simulated cavern morphologies and sizes.

From the experimental study, when $N = 33.3$ s^{-1} ($Re_m = 61.6$, $Re_y = 67.4$), the entirety of the vessel contents was in motion and well-mixed, owing to the observed homogeneous green-blue colour (Figure 6.7(a)(v)). As N increased from (iv) $N = 20.3$ s^{-1} ($Re_m = 28.7$, $Re_y = 25.1$) to (v) $N = 3.33$ s^{-1} ($Re_m = 61.6$, $Re_y = 67.4$), the lower cavern reached the tank wall, encroached upon and then engulfed the upper cavern to form one continuous, well-mixed cavern. This can be seen in Figure 6.8, which are two experimental images from *Mixing Study H(1)*, taken at $N = 25.0$ s^{-1} ($Re_m = 39.5$, $Re_y = 37.9$), (a) just after N was ramped to 25.0 s^{-1} and (b) when the cavern required its equilibrium state. With increasing N, the volume of well-mixed fluid increased, until the full tank was in motion at (v) $N = 33.3$ s^{-1} ($Re_m = 61.6$, $Re_y = 67.4$). This engulfment process was well predicted by the CFD model, as seen by the streamlines connecting the lower and upper PBT in Figure 6.7(b)(v).

In *Mixing Study H(2)*, with $G = 0.03$ m ($G/D = 0.73$) (Figure 6.7(c)), the upper PBT was positioned further away from the fluid/air interface compared to *Mixing Study H(1)*. With this, over the investigated range of N, the force being exerted on the material by the upper PBT was not great enough to induce interface deflection, resulting in the stress-free assumption applied to the simulations being valid. However, there was still an inconsistency in cavern morphologies between the experimental (Figure 6.7(c)) and numerical (Figure 6.7(d)) results. In the experimental section, there was marked mixing between the two flows over the range of N investigated. From the initial dye injections, there were cavern-cavern interactions and dyed material flowed between the two impellers to form a continuous green-blue cavern. However, when N increased to (ii) 16.0 s^{-1} ($Re_m = 19.8$, $Re_y = 15.5$), similar behaviour to *Mixing Study H(1)* was displayed. The downward-pumping characteristics of the upper PBT resulted in material flowing from the upper to the lower cavern, resulting in faster growth of the lower cavern, and faded coloration of the upper cavern. As N further increased to (iv) $N = 20.3$ s^{-1} ($Re_m = 28.7$, $Re_y = 25.1$), vertical mixing was able to occur in both directions, to form one continuous cavern of homogeneous green-blue colour. When (v) $N = 33.3$ s^{-1} ($Re_m = 61.6$, $Re_y = 67.4$), the singular cavern reached the tank wall. However, due to the distance of the upper PBT from the interface, a stagnant zone of material was observed near the interface, so although the fluid was well-mixed within the cavern, only 80-90% of the vessel contents was in motion. When

comparing to the respective numerical results (Figure 6.7(d)), there were noticeable differences in the cavern morphologies. At (i) $N = 11.7$ s^{-1} ($Re_m = 12.2$, $Re_y = 8.3$), the resulting flow was well predicted by the CFD model, with the streamlines showing vertical mixing from upper to the lower PBT, and recirculation back from the lower to the upper PBT. At (ii) $N = 16.0$ s^{-1} ($Re_m = 19.8$, $Re_y = 15.5$), experiment showed that the rate of material transfer from the upper to the lower PBT outweighed the recirculation back to the upper PBT from the lower. However, the numerical result suggests this rate of material transfer and the rate of recirculation were comparable and therefore the increased growth of the lower cavern, along with the loss of 'apple' torus character were not predicted by CFD. As a result, at (iii) $N = 18.2$ s^{-1} ($Re_m = 24.1$, $Re_y = 20.0$) and (iv) $N = 20.3$ s^{-1} ($Re_m = 28.7$, $Re_y = 25.1$), despite both experiment and CFD suggesting cross-impeller fluid flow in both directions and the formation of a singular, continuous cavern, the morphology of lower PBT flow remained toroidal due to the previous overestimation of the material recirculation from the lower to the upper PBT. By (v) $N = 33.3$ s^{-1} ($Re_m = 61.6$, $Re_y = 67.4$), the degree of both vertical mixing and circulation is large enough for only two sets of streamlines to be generated. The model accurately predicted the fact that the cavern reached the tank wall and the development of a stagnant region at top of the vessel.

When a pair of vortices rotate in the same direction, but lack axisymmetric characteristics, they will merge to form a single vortex (Tóth and Házi (2010)). However, if they rotate in the opposing direction, or in an axisymmetric fashion (as was the case in *Mixing Study G*), they will remain as a vortex dipole (Delbende and Rossi (2009)). In the case of *Mixing Study H(2)*, due to the downward pumping nature of the PBT impellers, the vortices above both impellers were rotating with the same characteristics, in an anti-clockwise direction. The impellers were close enough to result in the merging of these two vortices, to produce a single, large vortex. Consequently, the vortex below the upper impeller, which was rotating in a clockwise direction, was confined to the region near the rotating shaft, and resembled the vortex breakdown generated by rotating discs (Daube (1991); Spohn *et al.* (1993, 1998); Lopez *et al.* (1995, 2004); Piva and Meiburg (2005); Kahouadji and Martin Witkowski (2014)). As N increases, the size of this clockwise-rotating vortex decreases.

Comparing the results from both studies in *Mixing Study H*, there was better mixing between the two flows over a wider range of N in *Mixing Study H(2)*, however full-tank homogeneity was not achieved in this system. At sufficiently high N values in *Mixing Study H(1)*, cavern-cavern segregation was eliminated, resulting in the entire vessel contents being well-mixed. By comparison of the results from *Mixing Study G(1)* and *Mixing Study H(1)*, full-tank homogeneity was achievable using the dual-RT system if an appropriate amount of time was given for the diffusion process to occur. However, at comparable N, Re_m and Re_y values, this homogeneous state was attained almost instantaneously with the dual-PBT setup. Therefore, to achieve full tank homogeneity in viscoplastic mixing processes using the lowest possible N, Re_m, Re_y and mixing times, agitation with the dual-PBT setup in *Mixing Study H(1)* appeared to be the superior method when comparing to the analogous dual-RT system of *Mixing Study G(1)*.

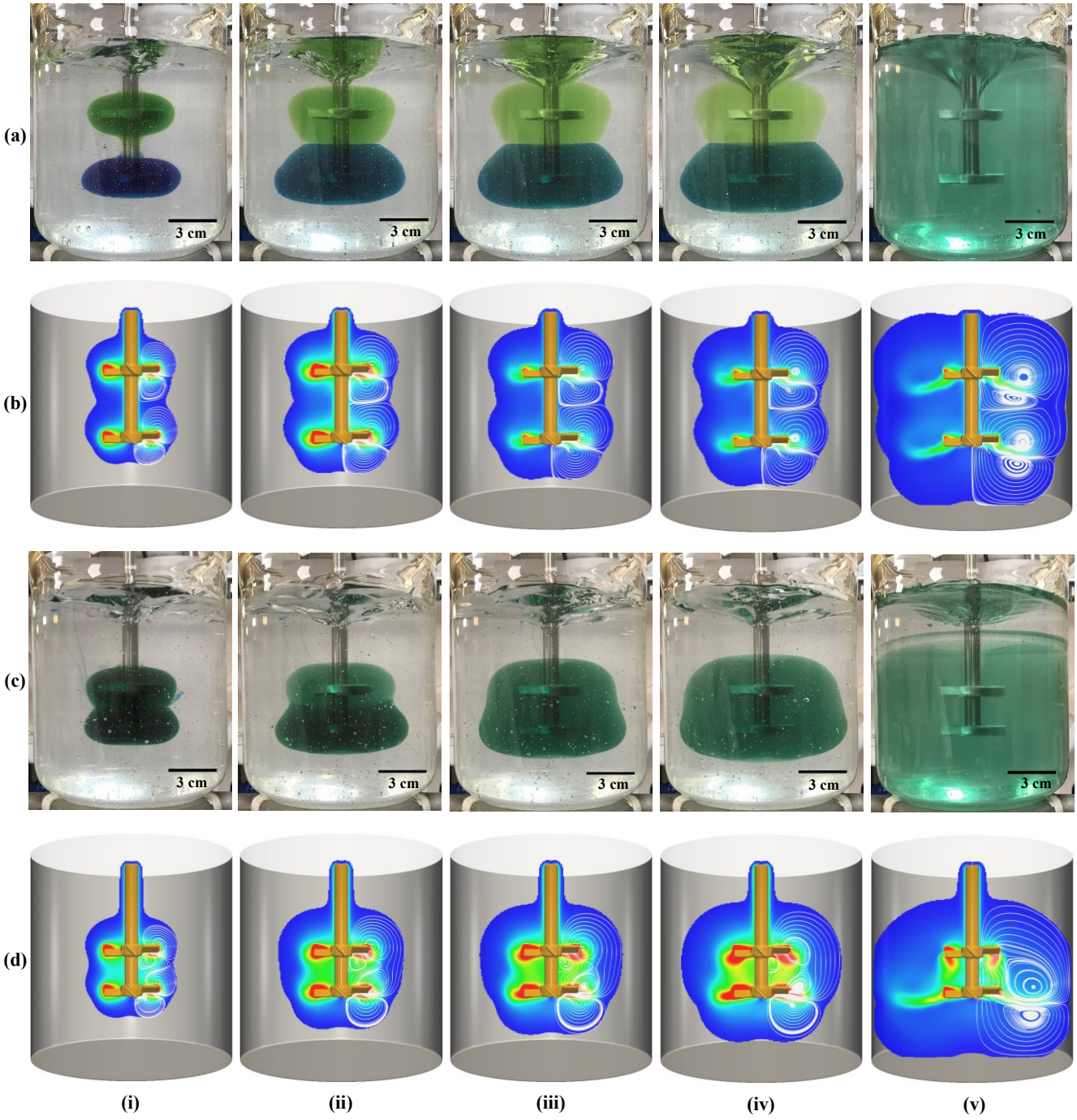

Figure 6.7. Experimental images and CFD snapshots for *Mixing Study H(1)* ((a) and (b), respectively) and *Mixing Study H(2)* ((c) and (d), respectively). For both *Mixing Study H(1)* and *H(2)*, the following impeller rotational speeds, *N* were used in the images and snapshots: (i) 11.7 s^{-1} (Re_m = 12.2, Re_y = 8.3), (ii) 16.0 s^{-1} (Re_m = 19.8, Re_y = 15.5), (iii) 18.2 s^{-1} (Re_m = 24.1, Re_y = 20.0), (iv) 20.3 s^{-1} (Re_m = 28.7, Re_y = 25.1) and (v) 33.3 s^{-1} (Re_m = 61.6, Re_y = 67.4).

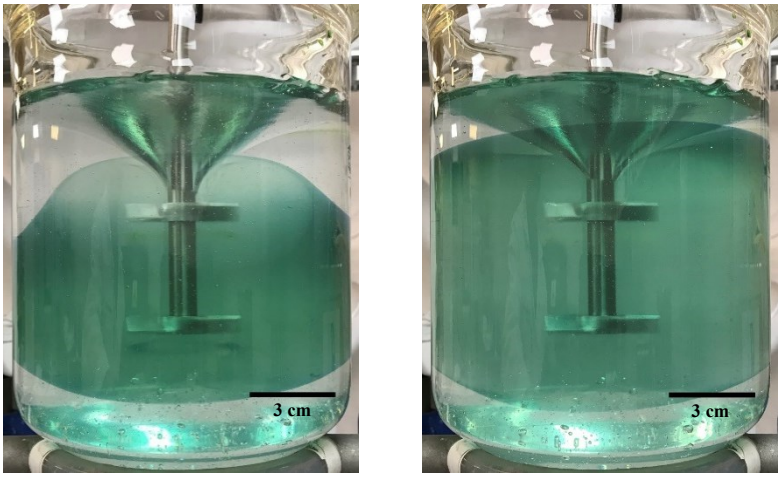

(a) (b)

Figure 6.8. Experimental images from *Mixing Study H(1)*, taken at an impeller speed of N = 25.0 s^{-1} (Re_m = 39.5, Re_y = 37.9), at (a) just after N was ramped to 25.0 s^{-1} and (b) when the cavern required its equilibrium state. (a) The dynamic engulfment of the upper cavern by the lower cavern, and (b) the resulting single, homogeneous flow.

6.4.3 *Mixing Study I*: Combination of Rushton Turbine and pitched-blade turbine (RT-PBT)

Finally, the mixing of a C980 fluid with an impeller system comprising of one RT and one PBT was evaluated. In *Mixing Study I(1)*, the upper impeller was the RT and the lower impeller was the PBT, with G = 0.05 m (G/D = 1.22). In *Mixing Study I(2)*, the setup was reversed with the upper and lower impellers being the PBT and RT, respectively, whilst G = 0.05 m (G/D = 1.22) was retained. Further details relating to the tank and impeller setup can be found in Figure 6.1 and Table 6.3 (Section 6.2.2). The *Case 17* fluid was agitated in both systems, with the Herschel-Bulkley rheological properties and the physical properties of *Case 17* summarised in Table 6.1 and Table 6.2 (Section 6.2.1), respectively. For both experimental studies, dye injection occurred at N = 4.2 s^{-1} (Re_m = 1.8, Re_y = 0.9). The experimental and numerical flows at five selected impeller speeds: N = 11.7 s^{-1} (Re_m = 9.3, Re_y = 7.0), 16.0 s^{-1} (Re_m = 15.2, Re_y = 13.2), 18.2 s^{-1} (Re_m = 18.6, Re_y = 17.0), 20.3 s^{-1} (Re_m = 22.2, Re_y = 19.1) and 33.3 s^{-1} (Re_m = 48.2, Re_y = 57.3), for *Mixing Study I(1)* and *Mixing Study I(2)*, can be seen in Figure 6.9(a) and (b), and Figure 6.9(c) and (d), respectively.

From the experimental results of *Mixing Study I(1)* (Figure 6.9(a)), distinct cavern-cavern segregation was observed over the range of investigated N. As with all G = 0.05 m mixing studies in this work, at (i) N = 11.7 s^{-1} (Re_m = 9.3, Re_y = 7.0), cavern-cavern interaction was unable to occur, resulting in two independent caverns forming. The upper RT produced a larger cavern than the lower PBT, with a D_c/D = 1.51 and an H_c/D_c = 0.48 for the RT-agitated cavern, compared to a cavern of D_c/D = 1.39 and H_c/D_c = 0.41 produced by the PBT. It was shown in Section 4.4.6 that for a given fluid agitated at a specific N, the RT produced a cavern with greater D_c than the PBT. It was suggested earlier in this work, that due to the effects of shaft rotation, the upper cavern often has a larger H_c/D_c but smaller D_c than the

lower cavern. However, in this case, the fact that the RT is able to create larger caverns at a given N than the PBT outweighs the effects of shaft rotation, resulting in the upper cavern having both a greater H_c/D_c and D_c than the lower cavern at $N = 11.7$ s^{-1} ($Re_m = 9.3$, $Re_y = 7.0$). In Figure 6.9(b)(i), cavern-cavern interaction was predicted numerically for the reasons previously discussed.

As previously discussed, RT impellers have solely radial character, with a maximum in the velocity magnitude at the tip of the impeller blades. In contrast, the PBT also has axial character, with a maximum in velocity magnitude at the impeller tips in a 45° downward direction. Therefore, through PBT agitation, similar vortices are produced to those seen through RT agitation, however now at this 45° angle. For both the RT and PBT, due to the shear-thinning nature of the material, the fluid recirculating around the edges of the caverns will have relatively low, but comparable velocity values. As a result, when these flows meet at the cavern-cavern boundary in the *Mixing Study I(1)* setup, there is not enough force exerted by either impeller to induce significant transfer of material from one cavern to the other, leading to flow compartmentalisation and cavern-cavern segregation. When N was increased to (v) 33.3 s^{-1} ($Re_m = 48.2$, $Re_y = 57.3$), both caverns reached the tank wall and the majority of the vessel was in motion, but the flow compartmentalisation remained. These findings were relatively well predicted by the CFD simulations, as seen by the distinction between the sets of streamlines in Figure 6.9(b), over all N investigated. The simulations also correctly predicted that as N increased, the cavern produced by RT agitation grew slightly faster than the PBT cavern and that at (v) $N = 33.3$ s^{-1} ($Re_m = 48.2$, $Re_y = 57.3$), there were some stagnant zones near the tank wall, in particular at the bottom of the tank. As seen previously, interface deflection (Newton's bucket) was observed in Figure 6.9(a)(iii-v). This behaviour was not accommodated for numerically and probably accounts for the discrepancies in cavern morphology and size when comparing the experimental and numerical results. In a similar manner to *Mixing Study G(1)*, if the flow was agitated at $N = 33.3$ s^{-1} ($Re_m = 48.2$, $Re_y = 57.3$) for a sufficient time, mixing between the caverns through diffusion would occur. However, as was the case in *Mixing Study G(1)*, if the aim of the viscoplastic mixing process is to produce homogeneity throughout the vessel at reduced mixing times, then the dual-RT(upper)-PBT(lower) system presented here would not be the recommended setup.

From the experimental findings in *Mixing Study I(2)* (Figure 6.9(c)), at (i) $N = 11.7$ s^{-1} ($Re_m = 9.3$, $Re_y = 7.0$), the expected lack of interaction between the two caverns was observed. The lower cavern, agitated with the RT, had a $D_c/D = 1.66$ and an $H_c/D_c = 0.39$, whilst the PBT-induced upper cavern had a $D_c/D = 1.37$ and an $H_c/D_c = 0.45$. These results agreed with the previous findings that the RT produces larger D_c values at a given N and fluid rheology than the PBT (dominant effect), in conjunction with the lower cavern often having a greater D_c, but a smaller H_c/D_c, due to shaft agitation effects. The numerical result in Figure 6.9(d)(i) suggested cavern-cavern interaction for the same reasons as previously discussed. As N increased to (v) $N = 33.3$ s^{-1} ($Re_m = 48.2$, $Re_y = 57.3$) in the experimental study, similar behaviour was observed to that seen in the dual-PBT system from *Mixing Study G(1)*. At (ii) $N = 16.0$ s^{-1} ($Re_m = 15.2$, $Re_y = 13.2$) and (iii) $N = 18.17$ s^{-1} ($Re_m = 18.6$, $Re_y = 17.0$), vertical mixing of material from the downward-pumping axial flow

of the PBT to the lower cavern occurred, with the RT unable to transfer material back to upper cavern. The result was faster growth rates of the lower cavern than the upper cavern, the increased green-blue colour of the lower cavern and the green colour of the upper cavern becoming increasingly faint as new, uncoloured material was drawn into the flow patterns of the upper cavern. Cavern-cavern segregation was seen due to recirculation rates in the upper cavern dominating over the rate of material transfer to the lower cavern, in conjunction with the inability of the RT to transfer material back to the upper cavern. As N increased, the dynamic engulfment process of the upper cavern by the lower cavern was again observed, until full-tank homogeneity occurred at (v) $N = 33.3\ s^{-1}$ ($Re_m = 48.2$, $Re_y = 57.3$). Comparing the numerical and experimental results in *Mixing Study I(2)*, vertical mixing from the upper cavern to the lower cavern was not predicted via CFD, and therefore faster growth rates of lower cavern in experiment were not accounted for in the simulations, leading to the similar growth rates of both caverns. However, at (v) $N = 33.3\ s^{-1}$ ($Re_m = 48.2$, $Re_y = 57.3$), the vertical mixing in the upward and downward directions was correctly predicted by CFD, leading to the near-full tank homogeneity being seen in both the numerical and experimental results. As before, interface deflection (Newton's bucket) was not accounted for in the CFD model, which could be an explanation for the discrepancies between the experimental and numerical results.

Comparison of the results of *Mixing Study I(2)* to those of *Mixing Study H(1)*, very similar flow behaviour was exhibited. The fluid used in *Mixing Study I(2)*, had a larger τ_y and K, and had a slightly more shear-thinning nature than the fluid used in *Mixing Study H(1)*. Because of this, it was expected that the encroachment and engulfment process would start (i.e. when the lower cavern has $D_c \approx T$) at a lower N and therefore a lower Re_m and Re_y in *Mixing Study H(1)*, than in *Mixing Study I(2)*. However the reverse is true, with $N \approx 19.0\ s^{-1}$ ($Re_m \approx 19.9$, $Re_y \approx 18.6$) for *Mixing Study I(2)*, compared to $N \approx 22.0\ s^{-1}$ ($Re_m \approx 32.4$, $Re_y \approx 29.4$) for *Mixing Study H(1)*. This may be because the RT produces larger caverns than the PBT, for a given N and fluid rheology. As a result, at a fixed G and fluid rheology, lower N, Re_m and Re_y values are required to achieve full-tank homogeneity in the PBT(upper)-RT(lower) system of *Mixing Study I(2)*, compared to the dual-PBT system of *Mixing Study H(1)*. Therefore, and comparing to the results from all mixing studies in this work, the PBT(upper)-RT(lower), $G = 0.05$ m ($G/D = 1.22$) system of *Mixing Study I(2)* produced the best mixing in terms of achieving full vessel homogeneity at the lowest N, Re_m, Re_y and mixing times.

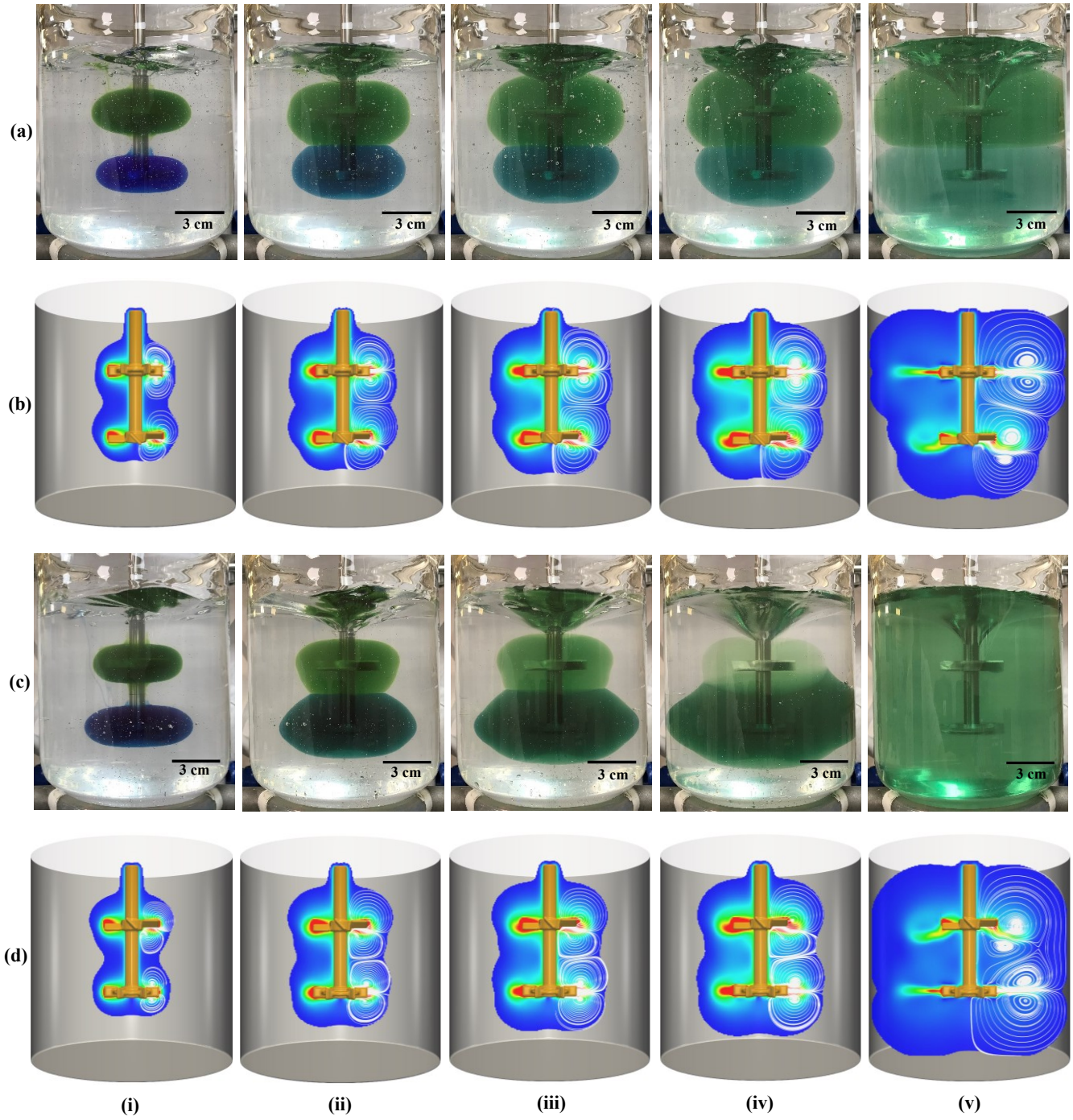

Figure 6.9. Experimental images and CFD snapshots for *Mixing Study I(1)* ((a) and (b), respectively) and *Mixing Study I(2)* ((c) and (d), respectively). For both *Mixing Study I(1)* and *I(2)*, the following *N* values were used in the images and snapshots: (i) 11.7 s^{-1} (Re_m = 9.3, Re_y = 7.0), (ii) 16.0 s^{-1} (Re_m = 15.2, Re_y = 13.2), (iii) 18.2 s^{-1} (Re_m = 18.6, Re_y = 17.0), (iv) 20.3 s^{-1} (Re_m = 22.2, Re_y = 19.1) and (v) 33.3 s^{-1} (Re_m = 48.2, Re_y = 57.3).

6.5 Conclusion

In this section of the study, dye visualisation techniques in conjunction with a validated CFD model were used to characterise the flow of Carbopol 980 (C980) fluids (*Cases 15-17*) in a 2 L vessel equipped with various dual-impeller systems. The C980 solutions exhibited viscoplastic rheological properties, and were agitated with different combinations of 6-bladed Rushton turbine (RT) impellers and 4-bladed 45° pitched-blade turbine (PBT) impellers (D = 0.041 m), with the lower impeller positioned at C_2/D = 1.10, in all cases. In *Mixing Study G*, a dual-RT impeller system was used, at impeller separations, G = 0.05 m (G/D = 1.22) and G = 0.03 m (G/D = 0.73), whilst *Mixing Study H* focused on dual-PBT impeller systems with the same G values. *Mixing Study I* looked at a combination of the RT and the PBT, with the RT as the upper impeller in *Mixing Study I(1)* and the PBT as the upper impeller in *Mixing Study I(2)*, with G = 0.05 m (G/D = 1.22) in both cases. In *Mixing Study G*, mixing with the dual-RT, G = 0.05 m (G/D = 1.22) system led to distinct cavern-cavern segregation and flow compartmentalisation over the range of impeller speeds, N investigated, which was well predicted by the CFD model. A similar C980 fluid was then agitated with the same impeller setup, at a constant N = 33.3 s^{-1} (Re_m = 61.5, Re_y = 70.7) and the cavern-cavern segregation was found to be a time dependent process, with a state of full-vessel homogeneity being reached after ~6 min. In the dual-RT, G = 0.03 m (G/D = 0.73) system, mixing between the caverns occurred over the range of N investigated, with a stagnant layer forming near the interface at 33.3 s^{-1} (Re_m = 65.4, Re_y = 66.5), which was well predicted by CFD. In *Mixing Study H*, due to the downward pumping nature of the PBT, although noticeable cavern-cavern segregation remained in the G = 0.05 m (G/D = 1.22) system, vertical mixing from the upper to the lower cavern occurred, resulting in faster cavern growth rates of the lower flow. At higher N values, the lower cavern encroached upon and engulfed the upper cavern, to form a continuous, homogeneous flow. The vertical mixing was not predicted by CFD, resulting in the increased rate of growth of the lower cavern not being projected. However, at higher N, mixing between the two caverns was forecast by CFD. For the dual-PBT, G = 0.03 m system, at a relatively low N value, slight cavern-cavern segregation was witnessed, before a continuous, homogeneous flow was seen at higher N values. As with the dual-RT, G = 0.03 m (G/D = 1.22), a stagnant zone of material formed at the top of the vessel, due to the distance of the upper PBT from the interface. The analogous numerical results over-predicted the degree of recirculation of material from the lower to the upper PBT at low N values, resulting in the faster growth of the lower cavern not being accounted for and hence there were differences in cavern morphology between the experimental and numerical results. The stagnant zone at the top of the vessel was well predicted. In *Mixing Study I*, the RT(upper)-PBT(lower) system produced similar cavern-cavern segregation to *Mixing Study G(1)* dual-RT, G = 0.05 m (G/D = 1.22) system over the range of investigated, which was forecasted by the CFD model. The PBT(upper)-RT(lower) system displayed very similar behaviour to the dual-PBT, G = 0.05 m system, resulting in full tank homogeneity at higher N values. The CFD did not predict the vertical mixing between caverns at lower N values, and hence the faster growth of the lower cavern compared to the upper cavern. However, full tank homogeneity at higher N values was projected well numerically.

Throughout the study, the effects of interface deflection on cavern size and morphology were not accounted for by the CFD model, due to the stress-free assumption imposed on the upper boundary. It was concluded that for dual-impeller, viscoplastic mixing, the PBT(upper)-RT(lower), $G = 0.05$ m setup from *Mixing Study I(2)* resulted in the best mixing, in terms of full-tank homogeneity being achieved with the lowest mixing times, N, Re_m and Re_y values. Future work would involve the inclusion of a fluid-air interface into the CFD model, to try and capture the interface deflection observed from experiment and to therefore minimise the discrepancies between the experimental and numerical results.

Chapter 7: Conclusion and Future Work

7.1 Conclusion

Mixing-based unit operations are often utilised in the chemical sector to influence the transport phenomena governing a particular engineering system. The materials used in these processes are often associated with complex rheological properties, along with high levels of reactivity, handling difficulty and expense. As a result, replacement 'model' fluid systems are often employed when attempting to better understand and optimise these processes, through the use of scaled-down, physically-similar laboratory-based experiments. These model fluids must simulate the rheological properties of the 'real' fluids, whilst also being safe, easy-to-handle and inexpensive. In this case, Syngenta's fluids and formulations display viscoplastic rheological properties, whereby the fluids exhibit a yield stress, which once exceeded, flow with shear-thinning characteristics, and are commonly described by mathematical models, such as the Herschel-Bulkley model and the Casson model.

Based on the literature findings of Chapter 1, a wide range of different model fluid systems were investigated and formulated, with the steady shear rheological properties of the fluids being attained through shear stress down sweeps using an Anton Paar Modular Compact Rheometer 302 rheometer, equipped with roughened 6-bladed vane and cup geometry, with all measurements being performed at 25°C. The fluid groups that were studied included: particulate, clay suspensions (Bentopharm, Laponite RD, sepiolite, hectorite and Acti-Gel 208 suspensions), polymer solutions (carboxymethyl cellulose (CMC), hydroxypropyl cellulose and Actigum solutions), microgels (Carbopol 980, Carbopol 981, Carbopol Ultrez 10, Carbopol Ultrez 21 and Carbopol Ultrez 30 solutions), clay-glycerol, clay-CMC(aq), and Carbopol-glycerol mixtures, and commercial products (for example, tomato ketchup and mayonnaise). Carbopol- and Laponite-based fluids were deemed as being ideal model fluid candidates, because they displayed the desired viscoplastic properties, whilst being associated with high levels of optical clarity and transparency, which is a useful property for mixing-based applications.

The flow curves of the model fluids were fitted with mathematical rheology models and the fitted rheological data were added into a computational platform, known as the '*Model Fluid Selection Tool*' (MFST). The MFST acted as a database of viscoplastic fluids, and was capable of performing various operations. Rheological data could be added into the database via two methods, either through the fitting of raw data (the '*Adding Data to Library (Data & Fitting Thereof)*' operation), or through the addition of known fitted data (the '*Adding Data to Library (By Fitted Parameters)*' operation). Using the '*Finding Best Match*' operation, best-matched model fluids were found from the database that most closely resembled the rheological properties of an inputted, 'real' fluid. Hypothetical replacement model fluids were proposed, through the use of the '*Perform Interpolation*' operation, as a means of potentially optimising the match of rheological properties, with the 'real' fluid in question. The MFST

is a novel method for storing the physical and rheological properties of viscoplastic model fluids and suggesting suitable replacement fluids to model 'real' fluids in a given application.

When viscoplastic materials are mixed in stirred vessel systems equipped with centrally-mounted, small impellers, a '*cavern*' can form; which is a region of flow surrounding the impeller, in which the impeller-induced stress exceeds the yield stress of the material. Outside of this region, the material is stagnant and exhibits solid-like behaviour. Carbopol 980 solutions were used as the model viscoplastic fluids in this work due to these systems having high levels of transparency. The fluids were agitated with 6-bladed Rushton turbine impellers and 4-bladed 45° pitched-blade turbine impellers, in vessels ranging in volume from 2-20 L. Over these scales, key geometrical length scales were maintained, and the effects of impeller rotational speed, fluid rheology, mixing system scale and impeller type, on cavern shape and size were investigated. Cavern size similarity (in terms of a dimensionless cavern diameter, D_c/D) was achieved for all investigated fluids and flows, using a scaling method involving a combination of dimensionless parameters: $Re_m^{-0.3}Re_y^{0.6}n^{-0.1}k_s^{-1}$, where: Re_m is the modified power-law Reynolds number, Re_y is the yield stress Reynolds number, n is the flow behaviour index and k_s is the impeller geometry constant. There were slight discrepancies in cavern height between the fluids mixed on the two smaller scales, compared to the larger scale, with the reasons for this being unknown.

Knowledge of the functional relationship between D_c/D and $Re_m^{-0.3}Re_y^{0.6}n^{-0.1}k_s^{-1}$ was then used in the development of a computational platform, known as the '*Matching and Predictive Mixing Tool*' (MPMT). The MPMT was used for predicting cavern sizes in pre-defined stirred vessel systems containing a viscoplastic fluid of known rheology, and for obtaining the operating conditions for matching dimensionless cavern sizes in a second system, when the scale of the geometry and/or fluid rheology has been changed. The MPMT was developed for the prediction/matching processes (which form the '*Mixing in Stirred Vessels*' operation) to occur for the geometrical systems and fluid flows investigated in Chapter 4, however the aim for the MPMT would be to extend its capabilities to investigate flows with wider ranging rheological properties, mixed in systems over a larger range of scales, with all types of centrally-mounted small impellers. As well as the '*Mixing in Stirred Vessels*' operation, the MPMT has all the operational features of the MFST, with the exception of the '*Perform Interpolation*' operation.

Finally, the mixing of viscoplastic Carbopol 980 fluids in stirred vessels equipped with dual-impeller systems were investigated using dye visualisation techniques and CFD. Combinations of 6-bladed Rushton turbine impellers and 4-bladed 45° pitched-blade turbine impellers were used for agitation, with the effects of impeller configuration, impeller separations, impeller rotational speeds and mixing times on the characteristics of the flow being investigated. CFD provided information on the flow patterns and velocity field distributions within the vessel, helping to explain the observed phenomena, such as cavern-cavern interaction and flow compartmentalisation. The impeller configuration that most

effectively minimised stagnant zones, flow segregation and arrived at a state of homogeneity throughout the vessel at reduced mixing times was deduced.

7.2 Future work

7.2.1 Model fluid systems

A large number of potential model fluid systems were investigated, formulated and rheologically characterised throughout this work, with approximately 400 fluids being stored in the MFST. Continued efforts will be made to find suitable model fluid systems, with the aim of extending the 'rheological space' presented in Section 2.10, to ensure that all future Syngenta fluids and formulations can be suitably modelled with replacement systems. A focus should be placed on fluids which display high levels of transparency, as these fluids exhibit the greatest extent of versatility in terms of using these fluids to model mixing-based unit operations. An example of a potential model fluid system that could be investigated are suspensions of cellulose nanofibers, which have been shown to display viscoplastic behaviour and are transparent in nature (Nazari *et al.* (2016); Isobe *et al.* (2018); Kasuga *et al.* (2018); Noguchi *et al.* (2018)). From the perspective of Syngenta, continued use of the 6-bladed vane rheometrical geometry would be vital, however, increasing the diameter of the associated cup geometry could be trialled in an attempt to completely eliminate slip effects (Section 2.2).

Further work could also involve the characterisation of model fluid systems with rheometrical geometries other than the 6-bladed vane. For the purpose of the current work, the use of the 6-bladed vane for rheological characterisation of model fluids was essential in terms of matching the protocol used at Syngenta (as discussed in Section 3.10). However, as was shown in Chapter 4, using geometries such as the cone-and-plate, which are often roughened to avoid slip effects, results in the true rheological characteristics of the viscoplastic fluids being obtained (as long as sedimentation and particle-jamming effects are not seen), and therefore developing a MFST with a rheological database of fluids characterised with cone-and-plate geometry would result in the computational platform being more applicable to a wider audience.

7.2.2 Mixing viscoplastic fluids in stirred vessels

As shown in Chapter 4, a number of different fluids and flows, over multiple scales and using different impeller types, were investigated and a scaling method was developed which resulted in cavern size similarity being achieved for all systems that were studied. Despite the successes of the proposed scaling method, further work would involve the mixing of fluids with more varied rheological properties, with the aim of matching flows over a wider range of scales. Although there was a factor of 10 difference between the smallest (2 L) and largest scale (20 L), it would be valuable to increase the scale further, to see if flows could eventually be matched between the laboratory scale and the pilot/plant scale. In the

current study, two impeller types were studied, namely the 6-bladed Rushton turbine and the 4-bladed 45° pitched-blade turbine. Extending the investigations (both experimentally and numerically) to study the mixing of viscoplastic fluids with a variety of different centrally-mounted impeller types, including close-clearance impellers such as the anchor or helical ribbon, could lead to a universal scaling method being developed. In turn, having performed more investigations, the resulting relationships between dimensionless cavern sizes and the numerous dimensionless parameters (as discussed in Section 4.2.4) could be programmed into the MPMT, allowing for the cavern size prediction and matching processes to be extended to a broader range of fluids and systems, and hence allowing the computational platform to have a wider applicability. If a universal method was developed for scaling viscoplastic fluids, the need for scaling-down processes, which require both time and cost, could be eliminated and replaced by the cavern size prediction and matching features of the MPMT.

As seen in Figure 7.1, very different mixing systems are starting to be investigated numerically. In this example, a common, single-mixer kitchen appliance has been used for the mixing of a viscoplastic fluid (τ_y = 42.8 Pa, K = 11.6 Pa s^n, n = 0.41). The CFD images in Figure 7.1 show that the mixer system has a rotational speed of 5 s^{-1} and translational speed of 1 s^{-1}, resulting in the cavern 'moving' in the mixing bowl (T = 0.45 m). The top-view snapshots are shown approximately every quarter translation. Efforts are being made to investigate this type of mixing experimentally, using an experimental system replicating the numerical setup.

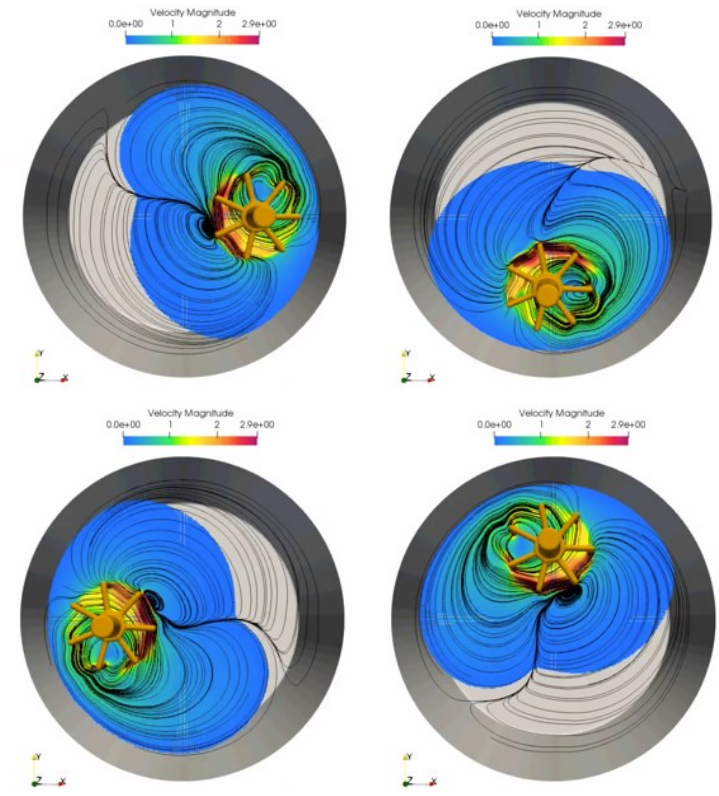

Figure 7.1 Numerical simulations of the mixing of a viscoplastic fluid with a single-mixer kitchen appliance.

7.2.3 Assessing the mixing effectiveness in dual-impeller systems

In Chapter 6, mixing of viscoplastic fluids with dual-impeller systems were performed, using combinations of the 6-bladed Rushton turbine and the 4-bladed 45° pitched-blade turbine impellers, in an attempt to determine an impeller configuration that resulted in full-tank homogeneity being achieved at reduced mixing times, impeller rotational speeds, modified power-law Reynolds numbers and yield stress Reynolds numbers. In the current work, the rheological properties of the fluids remained relatively constant, with three different impeller configurations and two different impeller separations being investigated. Future work would involve mixing fluids with varying rheological properties, investigating different impeller types and configurations, whilst possibly extending the system to other scales and studying impeller systems consisting of more than two impellers. A fluid-air interface would also be included into the CFD model, to try and capture the interface deflection observed from experiment and minimise the discrepancies between the experimental and numerical results seen in Chapter 6. Efforts could also be placed into attempting to develop a similar scaling method to those discussed in Chapter 4, but now for dual-/multi-impeller systems.

References

Abramoff, B., Covino, J., 1992. Transmittance and Mechanical Properties of PMMA-Fumed Silica Composites. J. Appl. Polym. Sci. 46, 1785–1791.

Abu-Jdayil, B., 2011. Rheology of sodium and calcium bentonite-water dispersions: Effect of electrolytes and aging time. Int. J. Miner. Process. 98, 208–213.

Adamčíková, L., Pavlíková, K., Ševčík, P., 1999. The Methylene Blue-D- Oxidation of D-Glucose by Methylene Blue in the Presence and the Absence. Intern. J. Chem. Kinet. 31, 463–468.

Adams, L.W., Barigou, M., 2007. CFD analysis of caverns and pseudo-caverns developed during mixing of non-Newtonian fluids. Chem. Eng. Res. Des. 85, 598–604.

Alvarez, A., Santarén, J., Esteban-Cubillo, A., Aparicio, P., 2011. Current Industrial Applications of Palygorskite and Sepiolite, in: Galan, E., Singer, A. (Eds.), Developments in Palygorskite-Sepiolite Research: A New Outlook on These Nanomaterials. Elsevier, Oxford, pp. 279–297.

Alvarez, M.M., Zalc, J.M., Shinbrot, T., Arratia, P.E., Muzzio, F.J., 2002. Mechanisms of mixing and creation of structure in laminar stirred tanks. AIChE J. 48, 2135–2148.

Amanullah, A., Hjorth, S.A., Nienow, A.W., 1998a. A new mathematical model to predict cavern diameters in highly shear thinning, power-law liquids using axial-flow impellers. Chem. Eng. Sci. 53, 455–469.

Amanullah, A., Hjorth, S.A., Nienow, A.W., 1997. Cavern sizes generated in highly shear thinning viscous fluids by SCABA 3SHP1 impellers. Food Bioprod. Process. 75, 232–238.

Amanullah, A., Serrano-Carreon, L., Castro, B., Galindo, E., Nienow, A.W., 1998b. The influence of impeller type in pilot scale Xanthan fermentations. Biotechnol. Bioeng. 57, 95–108.

Ameur, H., 2015. Energy efficiency of different impellers in stirred tank reactors. Energy 93, 1980–1988.

Ameur, H., Bouzit, M., Ghenaim, A., 2015. Numerical study of the performance of multistage Scaba 6SRGT impellers for the agitation of yield stress fluids in cylindrical tanks. J. Hydrodyn. 27, 436–442.

Amorim, L.V., Barbosa, M.I.R., Lira, H. de L., Ferreira, H.C., 2007. Influence of ionic strength on the viscosities and water loss of bentonite suspensions containing polymers. Mater. Res. 10, 53–56.

Anderson, L., Wittkopp, S.M., Painter, C.J., Liegel, J.J., Schreiner, R., Bell, J.A., Shakhashiri, B.Z., 2012. What Is Happening When the Blue Bottle Bleaches: An Investigation of the Methylene Blue-Catalyzed Air Oxidation of Glucose. J. Chem. Educ. 89, 1425–1431.

Araki, J., 2013. Electrostatic or steric? - preparations and characterizations of well-dispersed systems containing rod-like nanowhiskers of crystalline polysaccharides. Soft Matter 9, 4125–4141.

Ardakani, H.A., Mitsoulis, E., Hatzikiriakos, S.G., 2011. Thixotropic flow of toothpaste through extrusion dies. J. Nonnewton. Fluid Mech. 166, 1262–1271.

Arratia, P.E., Kukura, J., Lacombe, J., Muzzio, F.J., 2006. Mixing of shear-thinning fluids with yield stress in stirred tanks. AIChE J. 52, 2310–2322.

Aubin, J., Naude, I., Bertrand, J., Xuereb, C., 2000. Blending of Newtonian and Shear-Thinning Fluids in a Tank Stirred with a Helical Screw Agitator. Chem. Eng. Res. Des. 78, 1105–1114.

Aubin, J., Xuereb, C., 2006. Design of Multiple Impeller Stirred Tanks for the Mixing of Highly Viscous Fluids Using CFD. Chem. Eng. Res. Des. 61, 2913–2920.

Avery, R.G., Ramsay, J.D.F., 1986. Colloidal properties of synthetic hectorite clay dispersions. II. Light and small angle neutron scattering. J. Colloid Interface Sci. 109, 448–454.

Balci, S., 1999. Effect of heating and acid pre-treatment on pore size distribution of sepiolite. Clay Miner. 34, 647–655.

Balmforth, N.J., Frigaard, I.A., Ovarlez, G., 2014. Yielding to Stress: Recent Developments in Viscoplastic Fluid Mechanics. Annu. Rev. Fluid Mech. 46, 121–146.

Barnes, H.A., 1999. The yield stress - a review or "παντα ρει" - everything flows? J. Nonnewton. Fluid Mech. 81, 133–178.

Barnes, H.A., 1997. Thixotropy - A review. J. Nonnewton. Fluid Mech. 70, 1–33.

Barnes, H.A., 1995. A review of the slip (wall depletion) of polymer solutions, emulsions and particle suspensions in viscometers: its cause, character, and cure. J. Nonnewton. Fluid Mech. 56, 221–251.

Barnes, H.A., Hutton, J.F., Walters, K., 1989. An Introduction to Rheology. Elsevier, Amsterdam.

Barnes, H.A., Nguyen, Q.D., 2001. Rotating vane rheometry — a review. J. Nonnewton. Fluid Mech. 98, 1–14.

Barnes, H.A., Walters, K., 1985. The yield stress myth? Rheol. Acta 24, 323–326.

Barry, B.W., Meyer, M.C., 1979. The Rheological Properties of Carbopol Gels I. Continuous Shear and Creep Properties of Carbopol Gels. Int. J. Pharm. 2, 1–25.

Baskurt, O.K., Meiselman, H.J., 2003. Blood rheology and hemodynamics. Semin. Thromb. Hemost. 29, 435–450.

Baudou, C., Xuereb, C., Bertrand, J., 1997. 3-D Hydrodynamics Generated in a Stirred Vessel by a Multiple-propeller system. Can. J. Chem. Eng. 75, 653–663.

Ben Azouz, K., Bekkour, K., Dupuis, D., 2016. Influence of the temperature on the rheological properties of bentonite suspensions in aqueous polymer solutions. Appl. Clay Sci. 123, 92–98.

Benchabane, A., Bekkour, K., 2008. Rheological properties of carboxymethyl cellulose (CMC) solutions. Colloid Polym. Sci. 286, 1173–1180.

Bender, J.W., Wagner, N.J., 1995. Optical measurement of the contributions of colloidal forces to the rheology of concentrated suspensions. J. Colloid Interface Sci. 172, 171–184.

Benna-Zayani, M., Kbir-Ariguib, N., Magnin, A., Bergaya, F., 1999. Effect of pH on rheological properties of purified sodium bentonite suspensions. J. Colloid Interface Sci. 218, 442–455.

Benyounes, K., Mellak, A., Benchabane, A., 2010. The effect of carboxymethylcellulose and xanthan on the rheology of bentonite suspensions. Energy Sources, Part A Recover. Util. Environ. Eff. 32, 1634–1643.

Bertrand, F., Tanguy, P.A., Brito-De La Fuente, E., 1996. A New Perspective for the Mixing of Yield Stress Fluids with Anchor Impellers. J. Chem. Eng. Japan 29, 51–58.

Bilotti, E., 2009. Polymer/Sepiolite Clay Nanocomposites. Queen Mary, University of London.

Bilotti, E., Fischer, H.R., Peijs, T., 2008. Polymer nanocomposites based on needle-like sepiolite clays: effect of functionalized polymers on dispersion of nanofiller, crystallinity, and mechanical properties. J. Appl. Polym. Sci. 107, 1116–1123.

Bingham, E.C., 1922. Fluidity and Plasticity, 1st ed. McGraw-Hill Book Company Inc., New York.

Björn, A., Seguar de La Monja, P., Karlsson, A., Ejlertsson, J., Svensson, B.H., 2012. Rheological Characterisation, in: Kumar, S. (Ed.), Biogas. InTechOpen, Rijeka, pp. 63–76.

Boersma, W.H., Laven, J., Stein, H.N., 1995. Computer simulations of shear thickening of concentrated dispersions. J. Rheol. 39, 841–860.

Bonacucina, G., Martelli, S., Palmieri, G.F., 2004. Rheological, mucoadhesive and release properties of Carbopol gels in hydrophilic cosolvents. Int. J. Pharm. 282, 115–130.

Bonham, J.A., Faers, M.A., van Duijneveldt, J.S., 2014. Non-aqueous microgel particles: synthesis, properties and applications. Soft Matter 10, 9384–9398.

Bonn, D., Kellay, H., Tanaka, H., Wegdam, G., Meunier, J., 1999. Laponite: What is the difference between a Gel and a Glass? Langmuir 15, 7534–7536.

Bonn, D., Tanaka, H., Wegdam, G., Kellay, H., Meunier, J., 1998. Aging of a colloidal "Wigner" glass. Europhys. Lett. 45, 52–57.

Bonn, D., Tanase, S., Abou, B., Tanaka, H., Meunier, J., 2002. Laponite: Aging and shear rejuvenation of a colloidal glass. Phys. Rev. Lett. 89, 157011–157014.

Bottiglieri, P., De Sio, F., Fasanaro, G., Mojoli, G., Impembo, M., Castaldo, D., 1991. Rheological Characterization of Ketchup. J. Food Qual. 14, 497–512.

Brandenburg, U., Lagaly, G., 1988. Rheological properties of sodium montmorillonite dispersions. Appl. Clay Sci. 3, 263–279.

Braun, D.D., Rosen, M.R., 1999. Rheology Modifiers Handbook: Practical Use and Application. William Andrew Publishing, New York.

Broekhuijsen, D.M., 2014. Bringing plant potential to life through intelligent model fluid selection. Imperial College London.

Brown, D.A.R., Jones, P.N., Middleton, J.C., 2004. Part A: Measuring Tools an Techniques for Mixing and Flow Visualization Studies, in: Atiemo-Obeng, V.A., Kresta, S.M. (Eds.), Handbook of Industrial Mixing: Science and Practice. John Wiley & Sons Inc., Hoboken, pp. 145–167.

Brownawell, B.J., Chen, H., Collier, J.M., Westall, J.C., 1990. Adsorption of Organic Cations to Natural Materials. Environ. Sci. Technol. 24, 1234–1241.

Bujalski, W., Jaworski, Z., Nienow, A.W., 2002. CFD Study of Homogenisation with Dual Rushton Turbines - Comparison with Experimental Results Part II: The Multiple Reference Frame. Chem. Eng. Res. Des. 80, 97–104.

Buscall, R., 2010. Letter to the Editor: Wall slip in dispersion rheometry. J. Rheol. 54, 1177–1183.

Buscall, R., Mcgowan, J.I., Morton-Jones, A.J., 1993. The rheology of concentrated dispersions of weakly attracting colloidal particles with and without wall slip. J. Rheol. 37, 621–641.

Caillère, S., Hénin, S., 1961. Palygorskite, in: Brown, G. (Ed.), The X-Ray Identification and Crystal Structures of Clay Minerals. Jarrold and Sons Ltd, Norwich, pp. 325–343.

Campbell, J.A., 1963. Kinetics - Early and Often. J. Chem. Educ. 40, 578–583.

Cao, E., Bryant, R., Williams, D.J.A., 1996. Electrochemical Properties of Na-Attapulgite. J. Colloid Interface Sci. 179, 143–150.

Carmona, J.A., Ramírez, P., Trujillo-Cayado, L.A., Caro, A., Muñoz, J., 2018. Rheological and microstructural properties of sepiolite gels. Influence of the addition of ionic surfactants. J. Ind. Eng. Chem. 59, 1–7.

Casal, B., Merino, J., Serratosa, J.M., Ruiz-Hitzky, E., 2001. Sepiolite-based materials for the photo- and thermal-stabilization of pesticides. Appl. Clay Sci. 18, 245–254.

Casson, N., 1959. Rheology of disperse systems. Pergamon Press, Oxford.

Chen, J.S., Cushman, J.H., Low, P.F., 1990. Rheological behavior of Na-montmorillonite suspensions at low electrolyte concentration. Clays Clay Miner. 38, 57–62.

Cheng, D.C.H., 1986. Yield stress: A time-dependent property and how to measure it. Rheol. Acta 25, 542–554.

Choppe, E., Puaud, F., Nicolai, T., Benyahia, L., 2010. Rheology of xanthan solutions as a function of temperature, concentration and ionic strength. Carbohydr. Polym. 82, 1228–1235.

Chorin, A.J., 1968. Numerical Solution of the Navier-Stokes Equations. Math. Comput. 22, 745–762.

Çinar, M., Can, M.F., Sabah, E., Karagüzel, C., Çelik, M.S., 2009. Rheological properties of sepiolite

ground in acid and alkaline media. Appl. Clay Sci. 42, 422–426.

Collini, H., Mohr, M., Luckham, P., Shan, J., Russell, A.W., 2018. The effects of polymer concentration, shear rate and temperature on the gelation time of aqueous Silica-Poly(ethylene-oxide) "Shake-gels." J. Colloid Interface Sci. 517, 1–8.

Cook, A.G., Tolliver, R.M., Williams, J.E., 1994. The Blue Bottle Experiment Revisited. J. Chem. Educ. 71, 160–161.

Cortada-Garcia, M., Dore, V., Mazzei, L., Angeli, P., 2017. Experimental and CFD studies of power consumption in the agitation of highly viscous shear thinning fluids. Chem. Eng. Res. Des. 119, 171–182.

Cortada-Garcia, M., Weheliye, W.H., Dore, V., Mazzei, L., Angeli, P., 2018. Computational fluid dynamic studies of mixers for highly viscous shear thinning fluids and PIV validation. Chem. Eng. Sci. 179, 133–149.

Coussot, P., 2014. Yield stress fluid flows: A review of experimental data. J. Nonnewton. Fluid Mech. 211, 31–49.

Coussot, P., Nguyen, Q.D., Huynh, H.T., Bonn, D., 2002. Avalanche behavior in yield stress fluids. Phys. Rev. Lett. 88, 175501-1–4.

Coussot, P., Piau, J.M., 1994. On the behavior of fine mud suspensions. Rheol. Acta 33, 175–184.

Coussot, P., Proust, S., Ancey, C., 1996. Rheological interpretation of deposits of yield stress fluids. J. Nonnewton. Fluid Mech. 66, 55–70.

Coussot, P., Tocquer, L., Lanos, C., Ovarlez, G., 2009. Macroscopic vs. local rheology of yield stress fluids. J. Nonnewton. Fluid Mech. 158, 85–90.

Crawford, N.C., Popp, L.B., Johns, K.E., Caire, L.M., Peterson, B.N., Liberatore, M.W., 2013. Shear thickening of corn starch suspensions: Does concentration matter? J. Colloid Interface Sci. 396, 83–89.

Cui, Y., Pizzey, C.L., Van Duijneveldt, J.S., 2013. Modifying the structure and flow behaviour of aqueous montmorillonite suspensions with surfactant. Philos. Trans. R. Soc. A Math. Phys. Eng. Sci. 371, 20120262-1–13.

Cummins, H.Z., 2007. Liquid, glass, gel: The phases of colloidal Laponite. J. Non. Cryst. Solids 353, 3891–3905.

Curran, S.J., Hayes, R.E., Afacan, A., Williams, M.C., Tanguy, P.A., 2000. Experimental Mixing Study of a Yield Stress Fluid in a Laminar Stirred Tank. Ind. Eng. Chem. Res. 39, 195–202.

Cyr, M., Legrand, C., Mouret, M., 2000. Study of the shear thickening effect of superplasticizers on the rheological behaviour of cement pastes containing or not mineral additives. Cem. Concr. Res. 30, 1477–1483.

Daube, O., 1991. Numerical simulation of axisymmetric vortex breakdown in a closed cylinder, in: Anderson, C.R., Greengard, C. (Eds.), Lectures in Applied Mathematics Vol. 28. American Chemical Society, pp. 131–152.

Dealy, J.M., Vu, T.K.P., 1977. The Weissenberg effect in molten polymers. J. Nonnewton. Fluid Mech. 3, 127–140.

Delbende, I., Rossi, M., 2009. The dynamics of a viscous vortex dipole. Phys. Fluids 21, 073605-1–15.

Denkov, N.D., Subramanian, V., Gurovich, D., Lips, A., 2005. Wall slip and viscous dissipation in sheared foams: Effect of surface mobility. Colloids Surfaces A Physicochem. Eng. Asp. 263, 129–145.

Derjaguin, B. V, 1940. On the repulsive forces between charged colloid particles and on the theory of slow coagulation and stability of lyophobe sols. Trans. Faraday Soc. 35, 203–215.

Derjaguin, B. V, Landau, L., 1941. Theory of the stability of strongly charged lyophobic sols and of te adhesion of strongly charged particles in solutions of electrolytes. Acta Physicochem URSS 14.

Dinkgreve, M., Fazilati, M., Denn, M.M., Bonn, D., 2018. Carbopol: From a simple to a thixotropic yield stress fluid. J. Rheol. 62, 773–780.

Dinkgreve, M., Paredes, Denn, M.M., Bonn, D., 2016. On different ways of measuring "the" yield stress. J. Nonnewton. Fluid Mech. 238, 233–241.

Eastman, J., 2005. Stability of Charge-stabilised Colloids, in: Cosgrove, T. (Ed.), Colloid Science: Principles, Methods and Applications. Blackwell Publishing Ltd, Oxford, pp. 36–49.

Edwards, M.F., 1985. Mixing of Low Viscosity Liquids in Stirred Tanks, in: Harnby, N., Edwards, M.F., Nienow, A.W. (Eds.), Mixing in the Process Industries. Butterworth & Co (Publishers) Ltd, London, pp. 131–144.

Ein-Mozaffari, F., Upreti, S.R., 2009. Using ultrasonic Doppler velocimetry and CFD modeling to investigate the mixing of non-Newtonian fluids possessing yield stress. Chem. Eng. Res. Des. 87, 515–523.

Elson, T.P., 1990a. X-Ray flow visualisation of flow patterns during the mixing of yield stress, newtonian and dilatant fluids. Chem. Eng. Commun. 94, 143–158.

Elson, T.P., 1990b. The growth of caverns formed around rotating impellers during the mixing of a yield stress fluid. Chem. Eng. Commun. 96, 303–319.

Elson, T.P., 1988. Mixing of Fluids Possessing a Yield Stress, in: 6th European Conference on Mixing. Pavia, pp. 485–492.

Elson, T.P., Cheesman, D.J., Nienow, A.W., 1986. X-Ray Studies of Cavern Sizes and Mixing Performance with Fluids Possessing a Yield Stress. Chem. Eng. Sci. 41, 2555–2562.

Everett, D.H., 1999. Basic Principles of Colloid Science. RSC Publishing, Cambridge.

Fadlun, E.A., Verzicco, R., Orlandi, P., Mohd-Yusof, J., 2000. Combined Immersed-Boundary Finite-Difference Methods for Three-Dimensional Complex Flow Simulations. J. Comput. Phys. 161, 35–60.

Fernanda, P., 2018. Methods Used in the Study of the Physical Properties of Fats, in: Maragoni, A.G. (Ed.), Structure-Function Analysis of Edible Fats. Academic Press, London, pp. 313–385.

Franchini, E., Galy, J., Gérard, J.F., 2009. Sepiolite-based epoxy nanocomposites: Relation between processing, rheology, and morphology. J. Colloid Interface Sci. 329, 38–47.

Galan, E., 1996. Properties and applications of palygorskite-sepiolite clays. Clay Miner. 31, 443–453.

Galindo, E., Argüello, M.A., Velasco, D., Albiter, V., Martínez, A., 1996. A comparison of cavern development in mixing a yield stress fluid by Rushton and Intermig impellers. Chem. Eng. Technol. 19, 315–323.

Galindo, E., Nienow, A.W., 1993. Performance of the scaba 6SRGT agitator in mixing of simulated xanthan gum broths. Chem. Eng. Technol. 16, 102–108.

Galindo, E., Nienow, A.W., 1992. Mixing of Highly Viscous Simulated Xanthan Fermentation Broths with the Lightnin A-315 Impeller. Biotechnol. Prog. 8, 233–239.

García-Romero, E., Suárez, M., 2010. On the chemical composition of sepiolite and palygorskite. Clays Clay Miner. 58, 1–20.

Ghannam, M.T., Esmail, M.N., 1997. Rheological properties of carboxymethyl cellulose. J. Appl. Polym. Sci. 64, 289–301.

Goda, K., 1979. A Multistep Technique with implicit Difference Schemes for Calculating Two- or Three-Dimensional Cavity Flows. J. Comput. Phys. 30, 79–95.

Goodwin, J.W., 2004. Colloids and Interfaces with Surfactant and Polymer: An Introduction. John

Wiley & Sons Inc., Hoboken.

Goodwin, J.W., Hughes, R.W., 2008. Rheology for Chemists: An Introduction, 2nd ed. RSC Publishing, Cambridge.

Grassi, M., Lapasin, R., Pricl, S., 1996. A study of the rheological behavior of scleroglucan weak gel systems. Carbohydr. Polym. 29, 169–181.

Grim, R.E., 1968. Clay Mineralogy, 2nd ed. The McGraw-Hill Companies Inc, New York.

Gupta, V., Hampton, M.A., Stokes, J.R., Nguyen, A. V., Miller, J.D., 2011. Particle interactions in kaolinite suspensions and corresponding aggregate structures. J. Colloid Interface Sci. 359, 95–103.

Gupta, V., Miller, J.D., 2010. Surface force measurements at the basal planes of ordered kaolinite particles. J. Colloid Interface Sci. 344, 362–371.

Hamley, I.W., 2000. Introduction of Soft Matter: Polymers, Colloids, Amphiphiles and Liquid Crystals. John Wiley & Sons Inc., Chichester.

Harlow, F.H., Welch, J.E., 1965. Numerical Calculation of Time-Dependent Viscous Incompressible Flow of Fluid with Free Surface. Phys. Fluids 8, 2182–2189.

Hasanzadeh, M., Mottaghitalab, V., Rezaei, M., 2015. Rheological and viscoelastic behavior of concentrated colloidal suspensions of silica nanoparticles: A response surface methodology approach. Adv. Powder Technol. 26, 1570–1577.

Heller, H., Keren, R., 2001. Rheology of Na-rich montmorillonite suspensions as affected by electrolyte concentration and shear rate. Clays Clay Miner. 49, 286–291.

Herschel, W.H., Bulkley, R., 1926. Konsistenzmessungen von gummi-benzollösungen. Colloid Polym. Sci. 39, 291–300.

Hirata, Y., Nienow, A.W., Moore, I.P.T., 1994. Estimation of Cavern Sizes in a Shear-thinning Plastic Fluid Agitated by a Rushton Turbine Based on LDA Measurements. J. Chem. Eng. Japan 27, 235–237.

Hoffman, R.L., 1998. Explanations for the cause of shear thickening in concentrated colloidal suspensions. J. Rheol. 42, 111–123.

Hoffman, R.L., 1972. Discontinuous and Dilatant Viscosity Behavior in Concentrated Suspensions. I. Observation of a Flow Instability. Trans Soc Rheol 16, 155–173.

Hogg, R., Healy, T.W., Fuerstenau, D.W., 1966. Mutual coagulation of colloidal dispersions. Trans. Faraday Soc. 62, 1638–1651.

Hooton, J.C., Kibbe, A.H., Crehan, E.C., Hapgood, K.P., Fulzele, S.S., Fulzele, S., Shah, H.C., Singh, K.K., 2017. Handbook of Pharmaceutical Excipients, 8th ed. Pharmaceutical Press, London.

Huang, A.Y., Berg, J.C., 2006. High-salt stabilization of Laponite clay particles. J. Colloid Interface Sci. 296, 159–164.

Hui, L.K., Bennington, C.P.J., Dumont, G.A., 2009. Cavern formation in pulp suspensions using side-entering axial-flow impellers. Chem. Eng. Sci. 64, 509–519.

Hunter, R.J., 1987. Foundations of Colloid Science: Volume I, 1st ed. Oxford University Press Inc., Oxford.

Ihejirika, I., Ein-Mozaffari, F., 2007. Using CFD and ultrasonic velocimetry to study the mixing of pseudoplastic fluids with a helical ribbon impeller. Chem. Eng. Technol. 30, 606–614.

Iranshahi, A., Heniche, M., Bertrand, F., Tanguy, P.A., 2006. Numerical investigation of the mixing efficiency of the Ekato Paravisc impeller. Chem. Eng. Sci. 61, 2609–2617.

Islam, M.T., Rodríguez-Hornedo, N., Ciotti, S., Ackermann, C., 2004. Rheological characterization of topical carbomer gels neutralized to different pH. Pharm. Res. 21, 1192–1199.

Isobe, N., Kasuga, T., Nogi, M., 2018. Clear transparent cellulose nanopaper prepared from a concentrated dispersion by high-humidity drying. RSC Adv. 8, 1833–1837.

Jatav, S., Joshi, Y.M., 2014. Chemical stability of Laponite in aqueous media. Appl. Clay Sci. 97–98, 72–77.

Jaworski, Z., Bujalski, W., Otomo, N., Fellow, A.W.N., 2000. CFD Study of Homogenization with Dual Rushton Turbines - Comparison with Experimental Results Part I: Initial Studies. Chem. Eng. Res. Des. 78, 327–333.

Jaworski, Z., Pacek, A.W., Nienow, A.W., 1994. On Flow Close to Cavern Boundaries in Yield Stress Fluids. Chem. Eng. Sci. 49, 3321–3324.

Jenkins, P., Snowden, M., 1996. Depletion flocculation in colloidal dispersions. Adv. Colloid Interface Sci. 68, 57–96.

Jindal, N., Khattar, J.S., 2018. Microbial Polysaccharides in Food Industry, in: Grumezescu, A.M., Holban, A.M. (Eds.), Biopolymers for Food Design. Academic Press, London, pp. 95–123.

Kahouadji, L., Batcharov, A., Constante Amores, R., Shin, S., Chergui, J., Juric, D., Craster, R. V, Matar, O.K., 2019. The Transition to Aeration in Two-Phase Mixing. Phys. Rev. Fluids (Submitted).

Kahouadji, L., Martin Witkowski, L., 2014. Free surface due to a flow driven by a rotating disk inside a vertical cylindrical tank: Axisymmetric configuration. Phys. Fluids 26, 072105-1–17.

Kahouadji, L., Nowak, E., Kovalchuk, N., Chergui, J., Juric, D., Shin, S., Simmons, M.J.H., Craster, R. V, Matar, O.K., 2018. Simulation of immiscible liquid – liquid flows in complex microchannel geometries using a front‐tracking scheme. Microfluid. Nanofluidics 22, 1–12.

Kasuga, T., Isobe, N., Yagyu, H., Koga, H., Nogi, M., 2018. Clearly transparent nanopaper from highly concentrated cellulose nanofiber dispersion using dilution and sonication. Nanomaterials 8, 104-1–10.

Kawashima, S., Chaouche, M., Corr, D.J., Shah, S.P., 2013. Rate of thixotropic rebuilding of cement pastes modified with highly purified attapulgite clays. Cem. Concr. Res. 53, 112–118.

Kazemzadeh, A., Ein-Mozaffari, F., Lohi, A., Pakzad, L., 2017. Intensification of Mixing of Shear-Thinning Fluids Possessing Yield Stress with the Coaxial Mixer Composed of Two Different Central Impellers and an Anchor. Chem. Eng. Process. Process Intensif. 111, 101–114.

Kazemzadeh, A., Ein-Mozaffari, F., Lohi, A., Pakzad, L., 2016a. -Effect of the rheological properties on the mixing of Herschel-Bulkley fluids with coaxial mixers: Applications of tomography, CFD, and response surface methodology. Can. J. Chem. Eng. 94, 2394–2406.

Kazemzadeh, A., Ein-Mozaffari, F., Lohi, A., Pakzad, L., 2016b. A new perspective in the evaluation of the mixing of biopolymer solutions with different coaxial mixers comprising of two dispersing impellers and a wall scraping anchor. Chem. Eng. Res. Des. 114, 202–219.

Kelessidis, V.C., Maglione, R., 2008. Yield stress of water-bentonite dispersions. Colloids Surfaces A Physicochem. Eng. Asp. 318, 217–226.

Kelessidis, V.C., Poulakakis, E., Chatzistamou, V., 2011. Use of Carbopol 980 and carboxymethyl cellulose polymers as rheology modifiers of sodium-bentonite water dispersions. Appl. Clay Sci. 54, 63–69.

Kelly, W.J., Humphrey, A.E., 1998. Computational Fluid Dynamics Model for Predicting Flow of Viscous Fluids in a Large Fermentor with Hydrofoil Flow Impellers and Internal Cooling Coils. Biotechnol. Prog. 14, 248–258.

Khandavalli, S., Rothstein, J.P., 2014. Extensional rheology of shear-thickening fumed silica nanoparticles dispersed in an aqueous polyethylene oxide solution. J. Rheol. (N. Y. N. Y). 58, 411–431.

Kim, J.-Y., Song, J.-Y., Lee, E.-J., Park, S.-K., 2003. Rheological properties and microstructures of Carbopol gel network system. Colloid Polym. Sci. 281, 614–623.

King, R.J., 2009. Kaolinite. Geol. Today 25, 232–237.

Kiser, P.F., Wilson, G., Needham, D., 1998. A synthetic mimic of the secretory granule for drug delivery. Nature 394, 459–462.

Kuang, W., Facey, G.A., Detellier, C., Casal, B., Serratosa, J.M., Ruiz-Hitzky, E., 2003. Nanostructured Hybrid Materials Formed by Sequestration of Pyridine Molecules in the Tunnels of Sepiolite. Chem. Mater. 15, 4956–4967.

Labanda, J., Llorens, J., 2005. Influence of sodium polyacrylate on the rheology of aqueous Laponite dispersions. J. Colloid Interface Sci. 289, 86–93.

Labanda, J., Sabaté, J., Llorens, J., 2007. Rheology changes of Laponite aqueous dispersions due to the addition of sodium polyacrylates of different molecular weights. Colloids Surfaces A Physicochem. Eng. Asp. 301, 8–15.

Laudelout, H., 1987. Cation Exchange Equilibria In Clays, in: Newman, A.C.D. (Ed.), Chemistry of Clays and Clay Minerals. Longman Scientific & Technical, Harlow, pp. 225–236.

Leach, E.S.H., Hopkinson, A., Franklin, K., Van Duijneveldt, J.S., 2005. Nonaqueous suspensions of laponite and montmorillonite. Langmuir 21, 3821–3830.

Lee, S., Kim, D.H., Huh, C., Pope, G.A., 2009. Development of a comprehensive rheological property database for EOR polymers, in: SPE Annual Technical Conference and Exhibition. Society of Petroleum Engineers, New Orleans.

Lemić, J., Tomašević-Čanović, M., Djuričić, M., Stanić, T., 2005. Surface modification of sepiolite with quaternary amines. J. Colloid Interface Sci. 292, 11–19.

Letellier, B., Xuereb, C., Swaels, P., Hobbes, P., Bertrand, J., 2002. Scale-up in laminar and transient regimes of a multi-stage stirrer, a CFD approach. Chem. Eng. Sci. 57, 4617–4632.

Li, Z., Bowman, R.S., 1998. Sorption of chromate and PCE by surfactant-modified clay minerals. Environ. Eng. Sci. 15, 237–245.

Liu, H., Xu, X.M., Guo, S.D., 2007. Rheological, texture and sensory properties of low-fat mayonnaise with different fat mimetics. LWT. 40, 946–954.

Liu, P., Zhang, L., 2007. Adsorption of dyes from aqueous solutions or suspensions with clay nano-adsorbents. Sep. Purif. Technol. 58, 32–39.

Liu, Q., Chen, D., 2008. Viscoelastic behaviors of poly(ε-caprolactone)/attapulgite nanocomposites. Eur. Polym. J. 44, 2046–2050.

López-Galindo, A., Viseras, C., Aguzzi, C., Cerezo, P., 2011. Pharmaceutical and Cosmetic Use of Fibrous Clays, in: Developments in Palygorskite-Sepiolite Research: A New Outlook on These Nanomaterials. Elsevier, Oxford, pp. 299–316.

Lopez, J.M., 1995. Unsteady swirling flow in an enclosed cylinder with reflectional symmetry. Phys. Fluids 7, 2700–2714.

Lopez, J.M., Marques, F., Hirsa, A.H., Miraghaie, R., 2004. Symmetry breaking in free-surface cylinder flows. J. Fluid Mech. 502, 99–126.

Luckham, P.F., Rossi, S., 1999. Colloidal and rheological properties of bentonite suspensions. Adv. Colloid Interface Sci. 82, 43–92.

Lundén, M., 1995. Simulation of three-dimensional Flow in Stirred Vessels. Influence of the impeller modeling and scale-up. Chem. Eng. Commun. 139, 79–114.

Ma, C., Eggleton, R.A., 1999. Cation Exchange Capacity of Kaolinite. Clays Clay Miner. 47, 174–180.

MacEwan, D.M.C., 1961. Montmorillonite Minerals, in: Brown, G. (Ed.), The X-Ray Identification and

Crystal Structures of Clay Minerals. Jarrold and Sons Ltd, Norwich, pp. 143–208.

Maestro, A., González, C., Gutiérrez, J.M., 2002. Shear thinning and thixotropy of HMHEC and HEC water solutions. J. Rheol. 46, 1445–1457.

Malkin, A., Kulichikhin, V., Ilyin, S., 2017. A modern look on yield stress fluids. Rheol. Acta 56, 177–188.

Martin, C., Pignon, F., Piau, J.M., Magnin, A., Lindner, P., Cabane, B., 2002. Dissociation of thixotropic clay gels. Phys. Rev. E 66, 021401-1–11.

Mavros, P., 2001. Flow Visualization in Stirred Vessels - A Review of Experimental Techniques. Chem. Eng. Res. Des. 79, 113–127.

Metzner, A.B., Feehs, R.H., Ramos, H.L., Otto, R.E., Tuthill, J.D., 1961. Agitation of viscous Newtonian and non-Newtonian fluids. AIChE J. 7, 3–9.

Metzner, A.B., Otto, R.E., 1957. Agitation of non-Newtonian fluids. AIChE J. 3, 3–10.

Mewis, J., 1979. Thixotropy - a general review. J. Nonnewton. Fluid Mech. 6, 1–20.

Mewis, J., Wagner, N.J., 2012. Colloidal Suspension Rheology. Cambridge University Press, Cambridge.

Mitsoulis, E., 2007. Flows of viscoplastic materials: models and computations. Rheol. Rev. 135–178.

Møller, P.C.F., Fall, A., Bonn, D., 2009a. Origin of apparent viscosity in yield stress fluids below yielding. Europhys. Lett. 87, 38004-1–6.

Møller, P.C.F., Fall, A., Chikkadi, V., Derks, D., Bonn, D., 2009b. An attempt to categorize yield stress fluid behaviour. Philos. Trans. R. Soc. A 367, 5139–5155.

Møller, P.C.F., Mewis, J., Bonn, D., 2006. Yield stress and thixotropy: On the difficulty of measuring yield stresses in practice. Soft Matter 2, 274–283.

Mongondry, P., Tassin, J.F., Nicolai, T., 2005. Revised state diagram of Laponite dispersions. J. Colloid Interface Sci. 283, 397–405.

Montante, G., Magelli, F., 2004. Liquid homogenization characteristics in vessels stirred with multiple Rushton turbines mounted at different spacings: CFD study and comparison with experimental data. Chem. Eng. Res. Des. 82, 1179–1187.

Mooney, R.W., Keenan, A.G., Wood, L.A., 1952. Adsorption of Water Vapor by Montmorillonite. II. Effect of Exchangeable Ions and Lattice Swelling as Measured by X-Ray Diffraction. J. Am. Chem. Soc. 74, 1371–1374.

Moore, I.P.T., Cossor, G., Baker, M.R., 1995. Velocity distributions in a stirred tank containing a yield stress fluid.

Morvan, M., Espinat, D., Lambard, J., Zemb, T., 1994. Ultrasmall- and small-angle X-ray scattering of smectite clay suspensions. Colloids Surfaces A Physicochem. Eng. Asp. 82, 193–203.

Mourchid, A., Delville, A., Lambard, J., Lécolier, E., Levitz, P., 1995. Phase Diagram of Colloidal Dispersions of Anisotropic Charged Particles: Equilibrium Properties, Structure, and Rheology of Laponite Suspensions. Langmuir 11, 1942–1950.

Mpofu, P., Addai-Mensah, J., Ralston, J., 2003. Investigation of the effect of polymer structure type on flocculation, rheology and dewatering behaviour of kaolinite dispersions. Int. J. Miner. Process. 71, 247–268.

Nazari, B., Kumar, V., Bousfield, D.W., Toivakka, M., 2016. Rheology of cellulose nanofibers suspensions: Boundary driven flow. J. Rheol. 60, 1151–1159.

Neumann, B.S., Sansom, K., 1970. Laponite clay-a synthetic inorganic gelling agent for aqueous solutions of polar organic compounds. J. Soc. Cosmet. Chem. 21, 237–258.

Newman, A.C.D., Brown, G., 1987. The Chemical Constitution of Clays, in: Newman, A.C.D. (Ed.),

Chemistry of Clays and Clay Minerals. Longman Scientific & Technical, Harlow, pp. 1–129.

Nguyen, Q.D., Boger, D. V, 1992. Measuring the flow properties of yield stress fluids. Annu. Rev. Fluid Mech. 24, 47–88.

Nguyen, Q.D., Boger, D. V, 1985. Direct Yield Stress Measurement with the Vane Method. J. Rheol. 29, 335–347.

Nguyen, Q.D., Boger, D. V, 1983. Yield Stress Measurement for Concentrated Suspensions. J. Rheol. 27, 321–349.

Nienow, A.W., Wisdom, D.J., Solomon, J., Machon, V., Vlcek, J., 1983. The effect of rheological complexities on power consumption in an aerated, agitated vessel. Chem. Eng. Commun. 19, 273–293.

Noguchi, Y., Homma, I., Matsubara, Y., Fushimi, H., Banzashi, G., 2018. Preparation and utilization of highly transparent and viscous dispersion of phosphorylated cellulose nanofibers, in: Batchelor, W., Söderberg, D. (Eds.), Advances in Pulp and Paper Research, Oxford 2017. FRC, Manchester, pp. 813–821.

Norrish, K., 1954. Manner of Swelling of Montmorillonite. Discuss. Faraday Soc. 18, 120–134.

Olphen, H. van, 1964. Internal mutual flocculation in clay suspensions. J. Colloid Sci. 19, 313–322.

Oppong, F.K., Rubatat, L., Frisken, B.J., Bailey, A.E., De Bruyn, J.R., 2006. Microrheology and structure of a yield-stress polymer gel. Phys. Rev. E 73, 041405-1–9.

Osipov, V.I., Nikolaeva, S.K., Sokolov, V.N., 1984. Microstructural changes associated with thixotropic phenomena in clay soils. Geotechnique 34, 293–303.

Ostwald, W., 1926. Ueber die Viskosität kolloider Lösungen im Struktur-, Laminar- und Turbulenzgebiet. Kolloid. Z. 38, 261–280.

Ovarlez, G., Bertrand, F., Coussot, P., Chateau, X., 2012. Shear-induced sedimentation in yield stress fluids. J. Nonnewton. Fluid Mech. 177–178, 19–28.

Ovarlez, G., Cohen-Addad, S., Krishan, K., Goyon, J., Coussot, P., 2013. On the existence of a simple yield stress fluid behavior. J. Nonnewton. Fluid Mech. 193, 68–79.

Overbeek, J.T.G., 1977. Recent developments in the understanding of colloid stability. J. Colloid Interface Sci. 58, 408–422.

Pakzad, L., Ein-Mozaffari, F., Chan, P., 2008a. Using electrical resistance tomography and computational fluid dynamics modeling to study the formation of cavern in the mixing of pseudoplastic fluids possessing yield stress. Chem. Eng. Sci. 63, 2508–2522.

Pakzad, L., Ein-Mozaffari, F., Chan, P., 2008b. Using computational fluid dynamics modeling to study the mixing of pseudoplastic fluids with a Scaba 6SRGT impeller. Chem. Eng. Process. Process Intensif. 47, 2218–2227.

Pakzad, L., Ein-Mozaffari, F., Chan, P., 2008c. Measuring mixing time in the agitation of non-Newtonian fluids through electrical resistance tomography. Chem. Eng. Technol. 31, 1838–1845.

Pakzad, L., Ein-Mozaffari, F., Upreti, S.R., Lohi, A., 2013a. Agitation of Herschel–Bulkley fluids with the Scaba–anchor coaxial mixers. Chem. Eng. Res. Des. 91, 761–777.

Pakzad, L., Ein-Mozaffari, F., Upreti, S.R., Lohi, A., 2013b. Experimental and Numerical Studies on Mixing of Yield-Pseudoplastic Fluids with a Coaxial Mixer. Chem. Eng. Commun. 200, 1553–1577.

Pakzad, L., Ein-Mozaffari, F., Upreti, S.R., Lohi, A., 2013c. A novel and energy-efficient coaxial mixer for agitation of non-Newtonian fluids possessing yield stress. Chem. Eng. Sci. 101, 642–654.

Papanastasiou, T.C., 1987. Flows of Materials with Yield. J. Rheol. 31, 385–404.

Park, J.K., Khan, T., 2009. Other microbial polysaccharides: pullulan, scleroglucan, elsinan, levan,

alternant, dextran, in: Phillips, G.O., Williams, P.A. (Eds.), Handbook of Hydrocolloids. Woodhead Publishing Ltd, Cambridge, pp. 592–614.

Patel, D., Ein-Mozaffari, F., Mehrvar, M., 2015. Effect of rheological parameters on non-ideal flows in the continuous-flow mixing of biopolymer solutions. Chem. Eng. Res. Des. 100, 126–134.

Patel, D., Ein-Mozaffari, F., Mehrvar, M., 2014a. Tomography Images to Analyze the Deformation of the Cavern in the Continuous-Flow Mixing of Non-Newtonian Fluids. AIChE J. 60, 315–331.

Patel, D., Ein-Mozaffari, F., Mehrvar, M., 2014b. Using tomography to visualize the continuous-flow mixing of biopolymer solutions inside a stirred tank reactor. Chem. Eng. J. 239, 257–273.

Patel, D., Ein-Mozaffari, F., Mehrvar, M., 2013a. Characterization of the continuous-flow mixing of non-Newtonian fluids using the ratio of residence time to batch mixing time. Chem. Eng. Res. Des. 91, 1223–1234.

Patel, D., Ein-Mozaffari, F., Mehrvar, M., 2013b. Using Tomography to Characterize the Mixing of Non-Newtonian Fluids with a Maxblend Impeller. Chem. Eng. Technol. 36, 687–695.

Patel, D., Ein-Mozaffari, F., Mehrvar, M., 2012a. Improving the dynamic performance of continuous-flow mixing of pseudoplastic fluids possessing yield stress using Maxblend impeller. Chem. Eng. Res. Des. 90, 514–523.

Patel, D., Ein-Mozaffari, F., Mehrvar, M., 2012b. Effect of Impeller Type on Continuous-Flow Mixing of Non-Newtonian Fluids in Stirred. Can. J. Chem. Eng. 90, 290–298.

Patel, D., Ein-Mozaffari, F., Mehrvar, M., 2011. Dynamic Performance of Continuous-Flow Mixing of Pseudoplastic Fluids Exhibiting Yield Stress in Stirred Reactors. Ind. Eng. Chem. Res. 50, 9377–9389.

Patruyo, L.G., Müller, A.J., Sáez, A.E., 2002. Shear and extensional rheology of solutions of modified hydroxyethyl celluloses and sodium dodecyl sulfate. Polymer 43, 6481–6493.

Perkins, R., Brace, R., Matijević, E., 1974. Colloid and surface properties of clay suspensions. I. Laponite CP. J. Colloid Interface Sci. 48, 417–426.

Pevere, A., Guibaud, G., van Hullebusch, E., Lens, P., 2007. Identification of rheological parameters describing the physico-chemical properties of anaerobic sulphidogenic sludge suspensions. Enzyme Microb. Technol. 40, 547–554.

Piau, J.M., 2007. Carbopol gels: Elastoviscoplastic and slippery glasses made of individual swollen sponges. Meso- and macro-scopic properties, constitutive equations and scaling laws. J. Nonnewton. Fluid Mech. 144, 1–29.

Piccione, P.M., Rasheed, A.A., Quarmby, A., Dionisi, D., 2017. Direct Visualization of Scale-Up Effects on the Mass Transfer Coefficient through the “Blue Bottle” Reaction. J. Chem. Educ. 94, 726–729.

Pignon, F., Magnin, A., Piau, J.-M., 1998. Thixotropic behavior of clay dispersions: Combinations of scattering and rheometric techniques. J. Rheol. 42, 1349–1373.

Pignon, F., Magnin, A., Piau, J., 1996. Thixotropic colloidal suspensions and flow curves with minimum: Identification of flow regimes and rheometric consequences. J. Rheol. 40, 573–587.

Pignon, F., Magnin, A., Piau, J.M., Belina, G., Panine, P., 2009. Structure and orientation dynamics of sepiolite fibers-poly(ethylene oxide) aqueous suspensions under extensional and shear flow, probed by in situ SAXS. Rheol. Acta 48, 563–578.

Piva, M., Meiburg, E., 2005. Steady axisymmetric flow in an open cylindrical container with a partially rotating bottom wall. Phys. Fluids 17, 063603-1–12.

Prajapati, P., Ein-Mozaffari, F., 2009. CFD investigation of the mixing of yield-pseudoplastic fluids with anchor impellers. Chem. Eng. Technol. 32, 1211–1218.

Preisinger, A., 1957. X-Ray Study of the Structure of Sepiolite. Clays Clay Miner. 6, 61–67.

Rabideau, B.D., Moucheront, P., Bertrand, F., Rodts, S., Mélinge, Y., Lanos, C., Coussot, P., 2012. Internal flow characteristics of a plastic kaolin suspension during extrusion. J. Am. Ceram. Soc. 95, 494–501.

Raghavan, S.R., Khan, S.A., 1997. Shear-Thickening Response of Fumed Silica Suspensions under Steady and Oscillatory Shear. J. Colloid Interface Sci. 185, 57–67.

Raghavan, S.R., Khan, S.A., 1995. Shear-induced microstructural changes in flocculated suspensions of fumed silica. J. Rheol. 39, 1311–1325.

Raghavan, S.R., Riley, M.W., Fedkiw, P.S., Khan, S.A., 1998. Composite Polymer Electrolytes Based on Poly(ethylene glycol) and Hydrophobic Fumed Silica: Dynamic Rheology and Microstructure. Chem. Mater. 10, 244–251.

Raghavan, S.R., Walls, H.J., Khan, S.A., 2000. Rheology of Silica Dispersions in Organic Liquids: New Evidence for Solvation Forces Dictated by Hydrogen Bonding. Langmuir 16, 7920–7930.

Ramachandran, S., Chen, S., Etzler, F., 1999. Rheological characterization of hydroxypropylcellulose gels. Drug Dev. Ind. Pharm. 25, 153–161.

Ramos-Tejada, M.M., Luckham, P.F., 2015. Shaken but not stirred: The formation of reversible particle - polymer gels under shear. Colloids Surfaces A Physicochem. Eng. Asp. 471, 164–169.

Ramsay, J.D.F., 1986. Colloidal properties of synthetic hectorite clay dispersions. I. Rheology. J. Colloid Interface Sci. 109, 441–447.

Rand, B., Pekenć, E., Goodwin, J.W., Smith, R.W., 1980. Investigation into the existence of edge-face coagulated structures in Na-montmorillonite suspensions. J. Chem. Soc. Faraday Trans. I. 76, 225–235.

Richardson, S.M., 1989. Fluid Mechanics. Hemisphere Publishing Corporation, New York.

Rossi, S., 1997. Polymer adsorption and rheology of clay suspensions. Imperial College London.

Rossi, S., Luckham, P.F., Tadros, T.F., 2003. Influence of non-ionic polymers on the rheological behaviour of Na^+-montmorillonite clay suspensions. Part II. Homopolymer ethyleneoxide and polypropylene oxide-polyethylene oxide ABA copolymers. Colloids Surfaces A Physicochem. Eng. Asp. 215, 1–10.

Rossi, S., Luckham, P.F., Tadros, T.F., 2002. Influence of non-ionic polymers on the rheological behaviour of Na^+-montmorillonite clay suspensions - I Nonylphenol-polypropylene oxide-polyethylene oxide copolymers. Colloids Surfaces A Physicochem. Eng. Asp. 201, 85–100.

Ruiz-Hitzky, E., 2001. Molecular access to intracrystalline tunnels of sepiolite. J. Mater. Chem. 11, 86–91.

Ruiz-Hitzky, E., Aranda, P., Alvarez, A., Santaren, J., Esteban-Cubillo, A., 2011. Advanced Materials and New Applications of Sepiolite and Palygorskite, in: Galan, E., Singer, A. (Eds.), Developments in Palygorskite-Sepiolite Research: A New Outlook on These Nanomaterials. Elsevier, Oxford, pp. 393–441.

Russel, W.B., Grant, M.C., 2000. Distinguishing between dynamic yielding and wall slip in a weakly flocculated colloidal dispersion. Colloid Sci. Princ. Methods Appl. 161, 271–282.

Russell, A.W., 2015. The Visualisation of Fluorescently Dyed Sepiolite Rods Within a Polyurethane Foam Matrix. University of Bristol.

Russell, A.W., Kahouadji, L., Mirpuri, K., Quarmby, A., Piccione, P.M., Matar, O.K., Luckham, P.F., Markides, C.N., 2019. Mixing Viscoplastic Fluids in Stirred Vessels Over Multiple Scales: A Combined Experimental and CFD Approach. Chem. Eng. Sci. 208, 115129-1–16.

Sabzi, M., Jiang, L., Atai, M., Ghasemi, I., 2013. PLA/sepiolite and PLA/calcium carbonate nanocomposites: A comparison study. J. Appl. Polym. Sci. 129, 1734–1744.

Saeed, S., Ein-Mozaffari, F., 2008. Using dynamic tests to study the continuous mixing of xanthan gum

solutions. J. Chem. Technol. Biotechnol. 83, 559–568.

Saeed, S., Ein-Mozaffari, F., Upreti, S.R., 2008. Using computational fluid dynamics to study the dynamic behavior of the continuous mixing of Herschel-Bulkley fluids. Ind. Eng. Chem. Res. 47, 7465–7475.

Saeed, S., Ein-Mozaffari, F., Upreti, S.R., 2007. Using computational fluid dynamics modeling and ultrasonic doppler velocimetry to study-pulp suspension mixing. Ind. Eng. Chem. Res. 46, 2172–2179.

Sakthivelu, S., Manisha Vidyavathy, S., Manohar, P., 2012. Effect of Polyvinyl Alcohol on Stability and Rheology of Nano Kaolinite Suspensions. Trans. Indian Ceram. Soc. 71, 175–180.

Schaefer, D.W., Hurd, A.J., 1990. Growth and Structure of Combustion Aerosols: Fumed Silica. Aerosol Sci. Technol. 12, 876–890.

Schramm, G., 2000. A Practical Approach to Rheology and Rheometry, 2nd ed. Gebrueder Haake, Karlsruhe.

Seth, J.R., Cloitre, M., Bonnecaze, R.T., 2008. Influence of short-range forces on wall-slip in microgel pastes. J. Rheol. 52, 1241–1268.

Shalkevich, A., Stradner, A., Bhat, S.K., Mulle, F., Schurtenberger, P., 2007. Cluster, glass, and gel formation and viscoelastic phase separation in aqueous clay suspensions. Langmuir 23, 3570–3580.

Shekhar, S.M., Jayanti, S., 2003. Mixing of Power-Law Fluids Using Anchors : Metzner-Otto Concept Revisited. AIChE J. 49, 30–40.

Shen, L., Lin, Y., Du, Q., Zhong, W., Yang, Y., 2005. Preparation and rheology of polyamide-6/attapulgite nanocomposites and studies on their percolated structure. Polymer 46, 5758–5766.

Shu, C.-W., Osher, S., 1989. Efficient Implementation of Essentially Non-oscillatory Shock-Capturing Schemes, II. J. Comput. Phys. 83, 32–78.

Shuali, U., Nir, S., Rytwo, G., 2011. Adsorption of Surfactants, Dyes and Cationic Herbicides on Sepiolite and Palygorskite: Modifications, Applications and Modelling, in: Galan, E., Singer, A. (Eds.), Developments in Palygorskite- Sepiolite Research: A New Outlook on These Nanomaterials. Elsevier, Oxford, pp. 351–369.

Sjöberg, M., Bergström, L., Larsson, A., Sjöström, E., 1999. The effect of polymer and surfactant adsorption on the colloidal stability and rheology of kaolin dispersions. Colloids Surfaces A Physicochem. Eng. Asp. 159, 197–208.

Skelland, A.H.P., 1967. Non-Newtonian Flow and Heat Transfer. John Wiley & Sons Inc., New York.

Solomon, J., Elson, T.P., Nienow, A.W., Pace, G.W., 1981. Cavern sizes in agitated fluids with a yield stress. Chem. Eng. Commun. 11, 143–164.

Sossa-Echeverria, J., Taghipour, F., 2015. Computational simulation of mixing flow of shear thinning non-newtonian fluids with various impellers in a stirred tank. Chem. Eng. Process. 93, 66–78.

Sossa-Echeverria, J., Taghipour, F., 2014. Effect of Mixer Geometry and Operating Conditions on Flow Mixing of Shear Thinning Fluids with Yield Stress. AIChE J. 60, 1156–1167.

Spohn, A., Mory, M., Hopfinger, E.J., 1998. Experiments on vortex breakdown in a confined flow generated by a rotating disc. J. Fluid Mech. 370, 73–99.

Spohn, A., Mory, M., Hopfinger, E.J., 1993. Observations of vortex breakdown in an open cylindrical container with a rotating bottom. Exp. Fluids 14, 70–77.

Stefanescu, E.A., Schexnailder, P.J., Dundigalla, A., Negulescu, I.I., Schmidt, G., 2006. Structure and thermal properties of multilayered Laponite/PEO nanocomposite films. Polymer 47, 7339-7348

Stevens, M.P., 1990. Polymer Chemistry: An Introduction, 2nd ed. Oxford University Press Inc., New

York.

Streeter, V.L., Wylie, E.B., Bedford, K.W., 1998. Fluid Mechanics, 9th ed. The McGraw-Hill Companies Inc., New York.

Suárez, M., García-Romero, E., 2011. Advances in the Crystal Chemistry of Sepiolite and Playgorskite, in: Galan, E., Singer, A. (Eds.), Developments in Palygorskite-Sepiolite Research: A New Outlook on These Nanomaterials. Elsevier, Oxford, pp. 33–55.

Sun, A., Gunasekaran, S., 2009. Yield stress in foods: Measurements and applications. Int. J. Food Prop. 12, 70–101.

Sun, J.Z., Erickson, M.C.E., Parr, J.W., 2005. Refractive index matching and clear emulsions. J. Cosmet. Sci. 56, 253–265.

Sussman, M., Fatemi, E., Smereka, P., Osher, S., 1998. An improved level set method for incompressible two-phase flow. Comput. Fluids 27, 663–680.

Swartzen-Allen, S.L., Matijević, E., 1974. Surface and colloid chemistry of clays. Chem. Rev. 74, 385–400.

Temam, R., 1968. An Approximation Method for Solving Navier-Stokes Equations. B Soc Math Fr 96, 115.

Thompson, D.W., Butterworth, J.T., 1992. The nature of laponite and its aqueous dispersions. J. Colloid Interface Sci. 151, 236–243.

Todica, M., Pop, C. V., Udrescu, L., Pop, M., 2010. Rheological behavior of some aqueous gels of carbopol with pharmaceutical applications. Chinese Phys. Lett. 27, 018301-1–4.

Tornberg, E., 2016. Influence of Fibers and Particle Size Distribution on Food Rheology, in: Ahmed, J. (Ed.), Advances in Food Rheology and Its Applications. Woodhead Publishing Ltd, Cambridge, pp. 177–208.

Torres, M.D., Hallmark, B., Wilson, D.I., 2014. Effect of concentration on shear and extensional rheology of guar gum solutions. Food Hydrocoll. 40, 85–95.

Tóth, G., Házi, G., 2010. Merging of shielded Gaussian vortices and formation of a tripole at low Reynolds numbers. Phys. Fluids 22, 053101-1–7.

van Duijneveldt, J.S., 2001. Colloids, in: Moore, J.H., Spencer, N.D. (Eds.), Encyclopedia of Chemical Physics and Physical Chemistry. Institute of Physics Publishing Ltd, Bristol, pp. 2367–2393.

Velde, B., 1992. Introduction to Clay Minerals: Chemistry, Origins, Uses and Environmental Significance, 1st ed. Chapman & Hall, London.

Verwey, E.J.W., Overbeek, J.T.G., 1948. Theory of the Stability of Lyophobic Colloids. Elsevier, Amsterdam.

Viseras, C., Meeten, G.H., Lopez-Galindo, A., 1999. Pharmaceutical grade phyllosilicate dispersions: The influence of shear history on floc structure. Int. J. Pharm. 182, 7–20.

Vrabel, P., van der Lans, R.G.J.M., Luyben, K.C.A.M., Boon, L., Nienow, A.W., 2000. Mixing in large-scale vessels stirred with multiple radial or radial and axial up-pumping impellers : modelling and measurements. Chem. Eng. Sci. 55, 5881–5896.

Walls, H.J., Caines, S.B., Sanchez, A.M., Khan, S.A., 2003. Yield stress and wall slip phenomena in colloidal silica gels. J. Rheol. 47, 847–868.

Walters, K., 1975. Rheometry. Chapman & Hall, London.

Walton, D., Lorimer, P., 2000. Polymers. Oxford University Press Inc., Oxford.

Wichterle, K., Wein, O., 1981. Threshold of mixing of non-Newtonian liquids. Int. Chem. Eng. 21, 116–120.

Wichterle, K., Wein, O., 1975. Agitation of Concentrated Suspensions, in: CHISA 75. Prague, p. B4.6.

Wiese, G.R., Healy, 1970. Effect of particle size on colloid stability. Trans. Faraday Soc. 66, 490–499.

Wilkens, R.J., Miller, J.D., Plummer, J.R., Dietz, D.C., Myers, K.J., 2005. New techniques for measuring and modeling cavern dimensions in a Bingham plastic fluid. Chem. Eng. Sci. 60, 5269–5275.

Wilkinson, W.L., 1960. Non-Newtonian Fluids: Fluids Mechanics, Mixing and Heat Transfer. Pergamon Press, London.

Wu, Q., Ruan, J., Huang, B., Zhou, Z., Zou, J., 2006. Rheological behavior of fumed silica suspension in polyethylene glycol. J. Cent. South Univ. Technol. 13, 1–5.

Xiao, Q., Yang, N., Zhu, J., Guo, L., 2014. Modeling of Cavern Formation in Yield Stress Fluids in Stirred Tanks. AIChE J. 60, 3057–3070.

Xue, S., Reinholdt, M., Pinnavaia, T.J., 2006. Palygorskite as an epoxy polymer reinforcement agent. Polymer 47, 3344–3350.

Yan, J., Adams, J.E., 1997. The yield surface of viscoelastic and plastic fluids in a vane viscometer. J. Nonnewton. Fluid Mech. 70, 237–253.

Yin, H., Mo, D., Chen, D., 2009. Orientation behavior of attapulgite nanoparticles in poly(acrylonitrile)/attapulgite solutions by rheology analysis. J. Polym. Sci. 27, 945–954.

Yoshimura, A., Prud'homme, R.K., 1988. Wall Slip Corrections for Couette and Parallel Disk Viscometers. J. Rheol. 32, 53–67.

Yoshimura, A.S., Prud'homme, R.K., Princen, H.M., Kiss, A.D., 1987. A Comparison of Techniques for Measuring Yield Stresses. J. Rheol. 31, 699–710.

Yu, Y., Qi, S., Zhan, J., Wu, Z., Yang, X., Wu, D., 2011. Polyimide/sepiolite nanocomposite films: Preparation, morphology and properties. Mater. Res. Bull. 46, 1593–1599.

Zhang, Z.X., Van Duijneveldt, J.S., 2006. Isotropic-nematic phase transition of nonaqueous suspensions of natural clay rods. J. Chem. Phys. 124, 154910-1–7.

Zhao, G.Q., Chen, S.B., 2007. Nonlinear rheology of aqueous solutions of hydrophobically modified hydroxyethyl cellulose with nonionic surfactant. J. Colloid Interface Sci. 316, 858–866.

Appendix

A.1 Model fluid systems

Carbopol Fluids

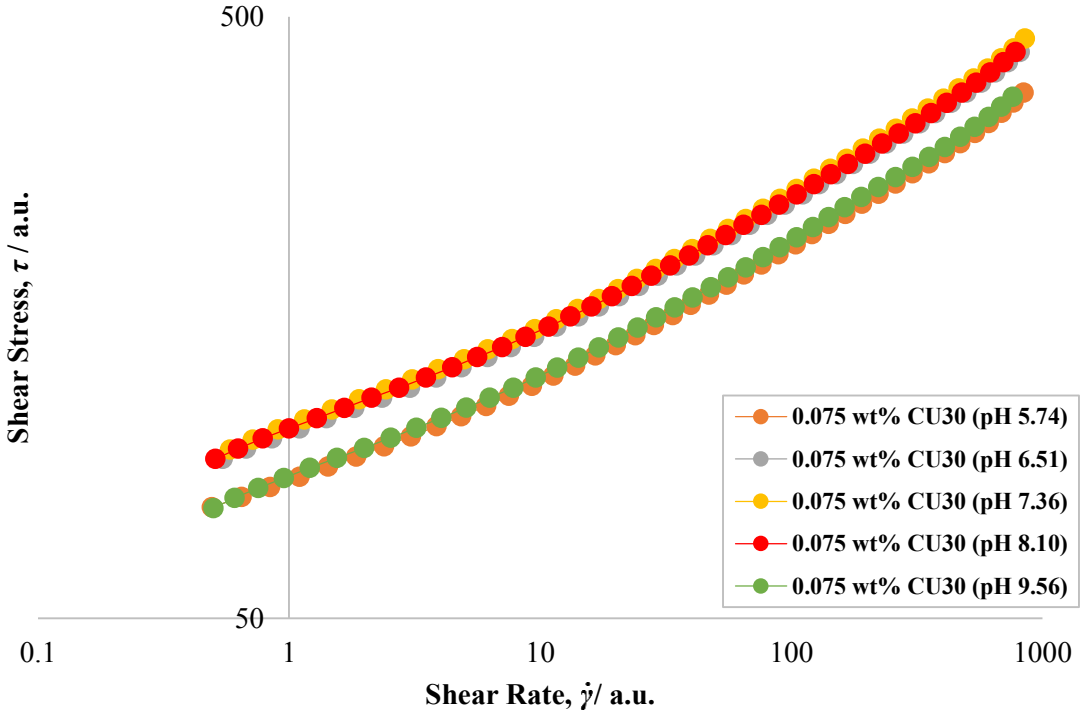

Figure A.1. Raw rheological flow curves, acquired from shear stress down sweeps using 6-bladed vane geometry, of CU30 solutions at constant mass fraction of 0.075 wt%, but varying pH values through additions of different quantities of a 2 wt% NaOH (aq) solution, ranging from pH: 5.49-10.44.

Table A.1. Herschel-Bulkley fitted data and the physical properties of the 0.075 wt% CU30 fluids, along with the associated error quantification of the mathematical fits and the shear rate range over which the fits occurred.

Physical properties			**Herschel-Bulkley rheological properties**			**Error quantification and analysis**		
CU30 mass fraction / wt%	**NaOH mass fraction / wt%**	**pH**	**Yield stress, τ_y / a.u.**	**Flow consistency index, K / a.u.**	**Flow behaviour index, n**	**Optimised fit AAD / %**	**Optimised fit R^2 value**	**Shear rate range of optimised fit / a.u.**
0.075	0.008	5.74	49.9	34.7	0.33	0.37	1.000	0.492-843
0.075	0.014	6.51	59.0	42.6	0.32	0.39	1.000	0.544-812
0.075	0.020	7.36	57.9	45.9	0.32	0.53	1.000	0.582-853
0.075	0.025	8.10	56.2	46.5	0.31	0.58	1.000	0.509-782
0.075	0.030	9.56	47.6	38.1	0.32	0.49	1.000	0.500-762

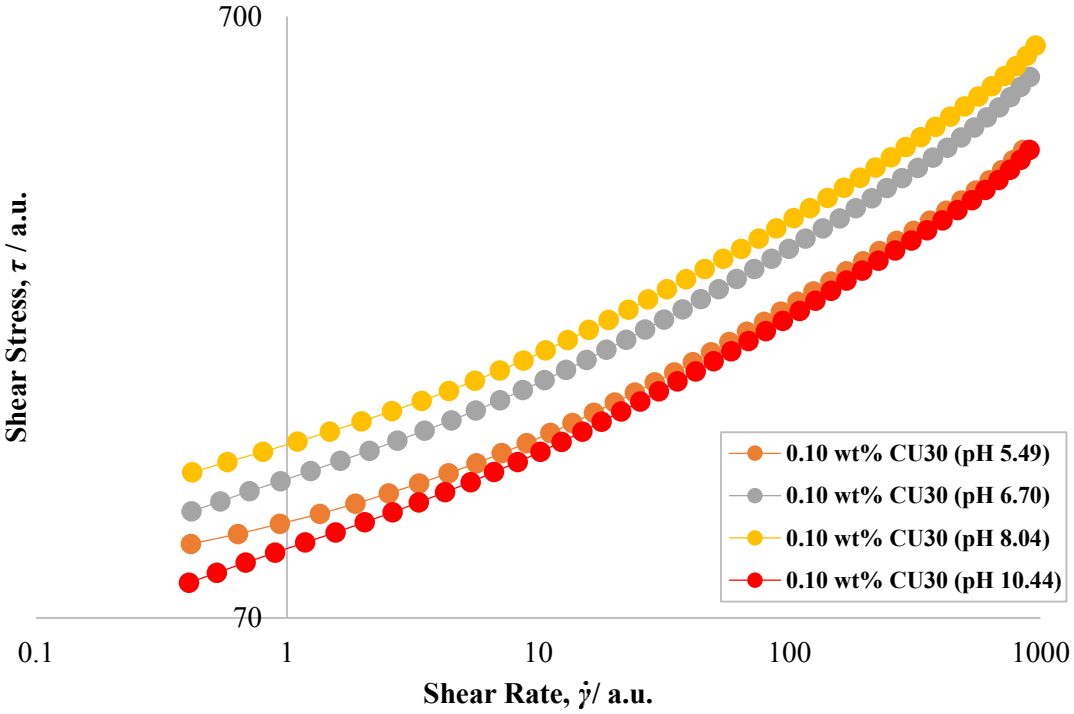

Figure A.2. Raw rheological flow curves, acquired from shear stress down sweeps using 6-bladed vane geometry, of CU30 solutions at constant mass fraction of 0.10 wt%, but varying pH values through additions of different quantities of a 2 wt% NaOH (aq) solution, ranging from pH: 5.49-10.44.

Table A.2. Herschel-Bulkley fitted data and the physical properties of the 0.10 wt% CU30 fluids, along with the associated error quantification of the mathematical fits and the shear rate range over which the fits occurred.

Physical properties			**Herschel-Bulkley rheological properties**			**Error quantification and analysis**		
CU30 mass fraction / wt%	**NaOH mass fraction / wt%**	**pH**	**Yield stress, τ_y / a.u.**	**Flow consistency index, *K* / a.u.**	**Flow behaviour index, *n***	**Optimised fit AAD / %**	**Optimised fit R^2 value**	**Shear rate range of optimised fit / a.u.**
0.10	0.010	5.49	70.0	30.7	0.36	0.45	1.000	0.414-855
0.10	0.020	6.70	75.9	42.9	0.35	0.72	0.999	0.416-910
0.10	0.035	8.04	91.7	43.9	0.36	0.52	0.999	0.419-958
0.10	0.040	10.44	56.4	34.4	0.34	0.47	0.999	0.407-905

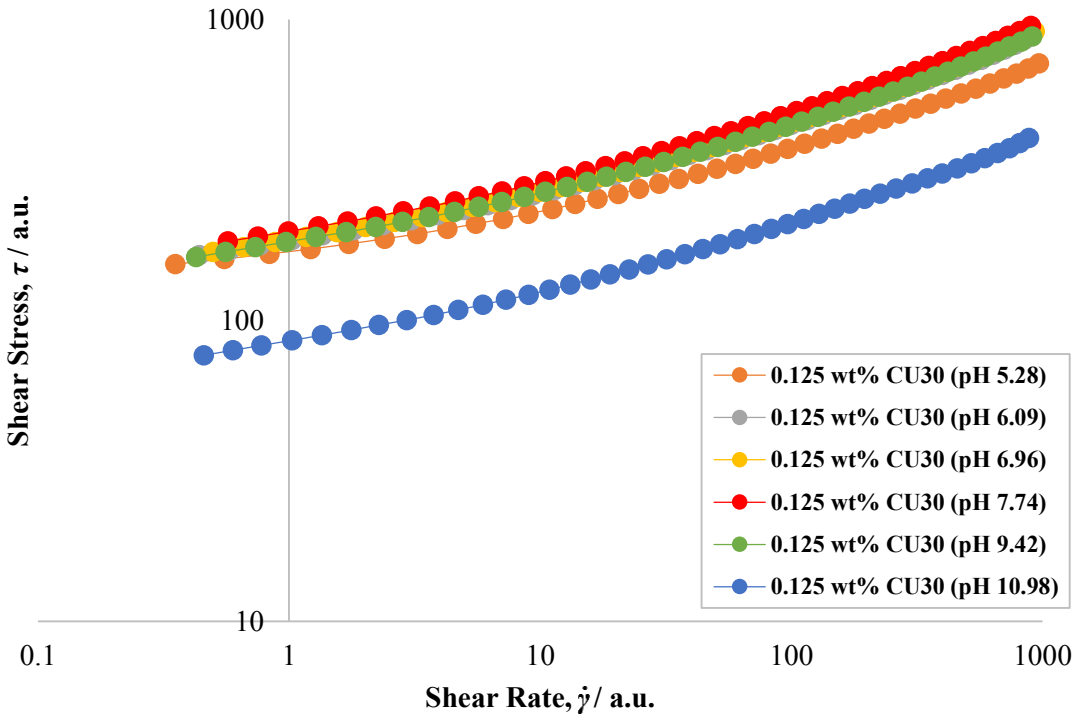

Figure A.3. Raw rheological flow curves, acquired from shear stress down sweeps using 6-bladed vane geometry, of CU30 solutions at constant mass fraction of 0.125 wt%, but varying pH values through additions of different quantities of a 2 wt% NaOH (aq) solution, ranging from pH: 5.28-10.98.

Table A.3. Herschel-Bulkley fitted data and the physical properties of the 0.125 wt% CU30 fluids, along with the associated error quantification of the mathematical fits and the shear rate range over which the fits occurred.

Physical properties			**Herschel-Bulkley rheological properties**			**Error quantification and analysis**		
CU30 mass fraction / wt%	**NaOH mass fraction / wt%**	**pH**	**Yield stress, τ_y / a.u.**	**Flow consistency index, *K* / a.u.**	**Flow behaviour index, *n***	**Optimised fit AAD / %**	**Optimised fit R^2 value**	**Shear rate range of optimised fit / a.u.**
0.125	0.010	5.28	122.9	46.1	0.37	0.19	1.000	0.352-969
0.125	0.020	6.09	123.0	60.7	0.36	0.62	0.999	0.439-849
0.125	0.030	6.96	126.6	59.2	0.37	0.79	0.999	0.498-933
0.125	0.040	7.74	131.2	66.9	0.37	0.38	1.000	0.571-902
0.125	0.050	9.42	121.6	61.1	0.36	0.76	0.999	0.426-911
0.125	0.055	10.98	54.1	31.3	0.35	0.41	1.000	0.457-885

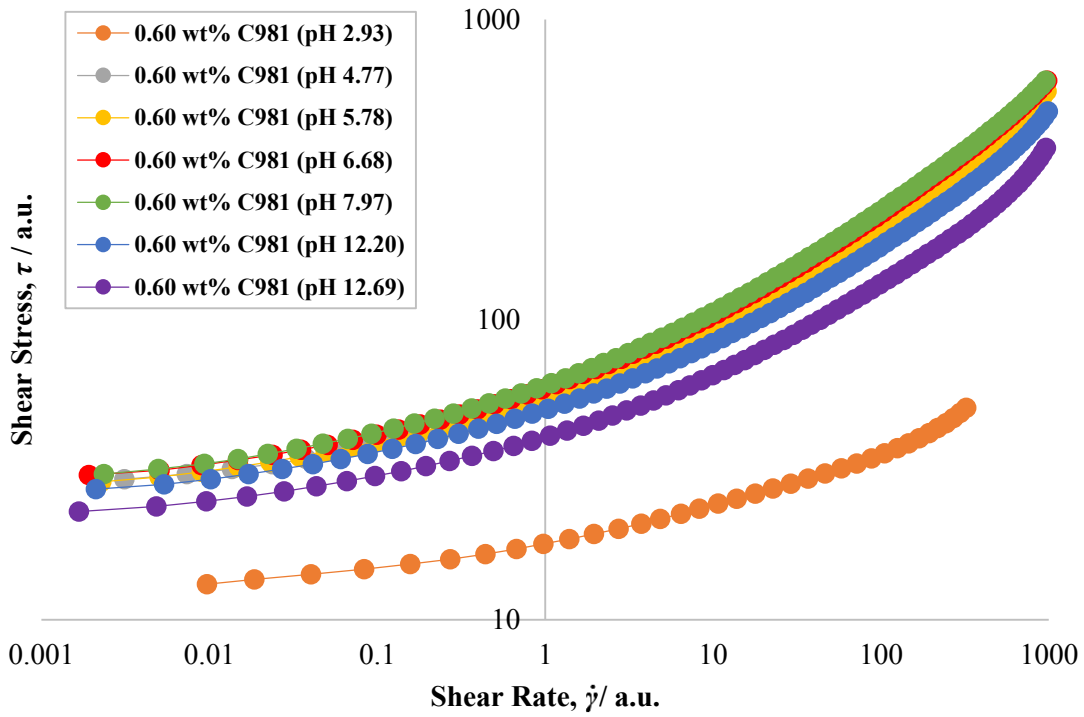

Figure A.4. Raw rheological flow curves, acquired from shear stress down sweeps using 6-bladed vane geometry, of C981 solutions at constant mass fraction of 0.60 wt%, but varying pH values through additions of different quantities of a 3 wt% NaOH (aq) solution, ranging from pH: 2.93-12.69.

Table A.4. Herschel-Bulkley fitted data and the physical properties of the 0.60 wt% C981 fluids, along with the associated error quantification of the mathematical fits and the shear rate range over which the fits occurred.

Physical properties			**Herschel-Bulkley rheological properties**			**Error quantification and analysis**		
C981 mass fraction / wt%	**NaOH mass fraction / wt%**	**pH**	**Yield stress, τ_y / a.u.**	**Flow consistency index, *K* / a.u.**	**Flow behaviour index, *n***	**Optimised fit AAD / %**	**Optimised fit R^2 value**	**Shear rate range of optimised fit / a.u.**
0.60	0.000	2.93	12.2	5.6	0.32	1.48	0.995	0.00967-322
0.60	0.060	4.77	29.9	20.3	0.44	2.20	0.996	0.00311-967
0.60	0.120	5.78	29.4	24.5	0.44	2.27	0.997	0.00227-970
0.60	0.180	6.68	30.9	26.6	0.44	2.21	0.997	0.00191-979
0.60	0.240	7.97	30.9	27.8	0.43	2.14	0.998	0.00235-954
0.60	0.300	12.20	28.1	20.4	0.44	2.57	0.995	0.00211-986
0.60	0.360	12.69	24.1	15.0	0.44	3.10	0.991	0.00167-960

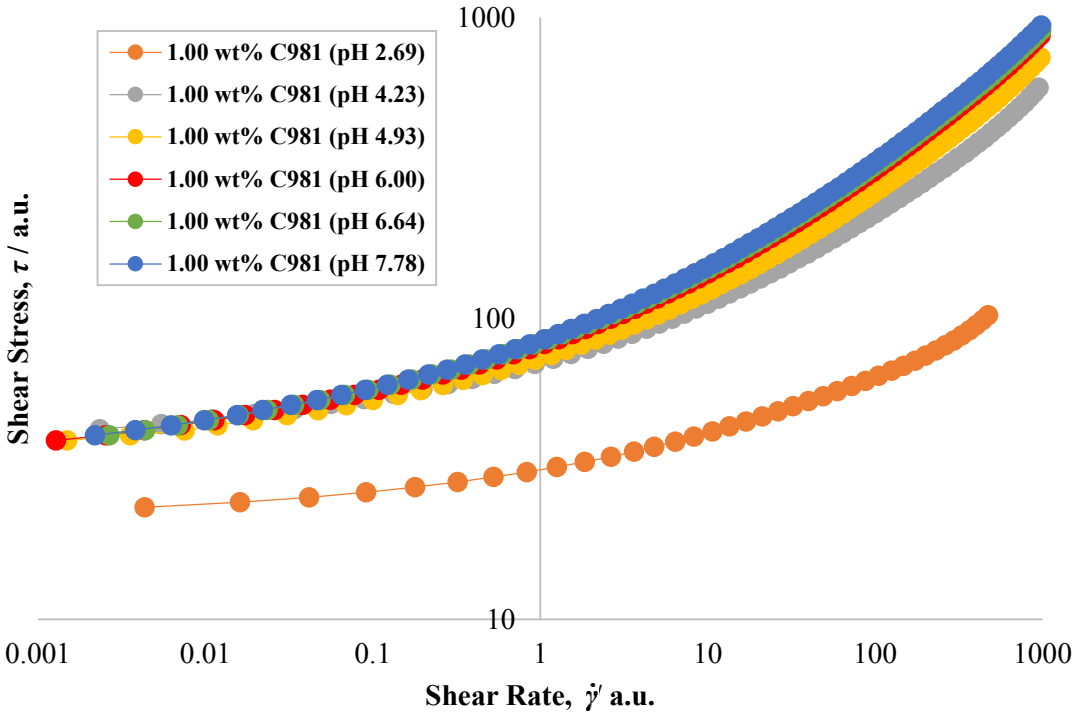

Figure A.5. Raw rheological flow curves, acquired from shear stress down sweeps using 6-bladed vane geometry, of C981 solutions at constant mass fraction of 1.00 wt%, but varying pH values through additions of different quantities of a 3 wt% NaOH (aq) solution, ranging from pH: 2.69-7.78.

Table A.5. Herschel-Bulkley fitted data and the physical properties of the 1.00 wt% C981 fluids, along with the associated error quantification of the mathematical fits and the shear rate range over which the fits occurred.

Physical properties			**Herschel-Bulkley rheological properties**			**Error quantification and analysis**		
C981 mass fraction / wt%	**NaOH mass fraction / wt%**	**pH**	**Yield stress, τ_y / a.u.**	**Flow consistency index, *K* / a.u.**	**Flow behaviour index, *n***	**Optimised fit AAD / %**	**Optimised fit R^2 value**	**Shear rate range of optimised fit / a.u.**
1.00	0.000	2.69	23.0	8.0	0.36	1.34	0.996	0.00433-475
1.00	0.060	4.23	44.7	24.4	0.44	2.24	0.997	0.00234-952
1.00	0.120	4.93	41.6	29.2	0.45	2.65	0.997	0.00149-974
1.00	0.240	6.00	41.9	36.2	0.44	2.87	0.997	0.00128-975
1.00	0.315	6.64	42.7	37.5	0.44	2.75	0.997	0.00267-986
1.00	0.400	7.78	42.8	38.4	0.45	2.81	0.997	0.00219-984

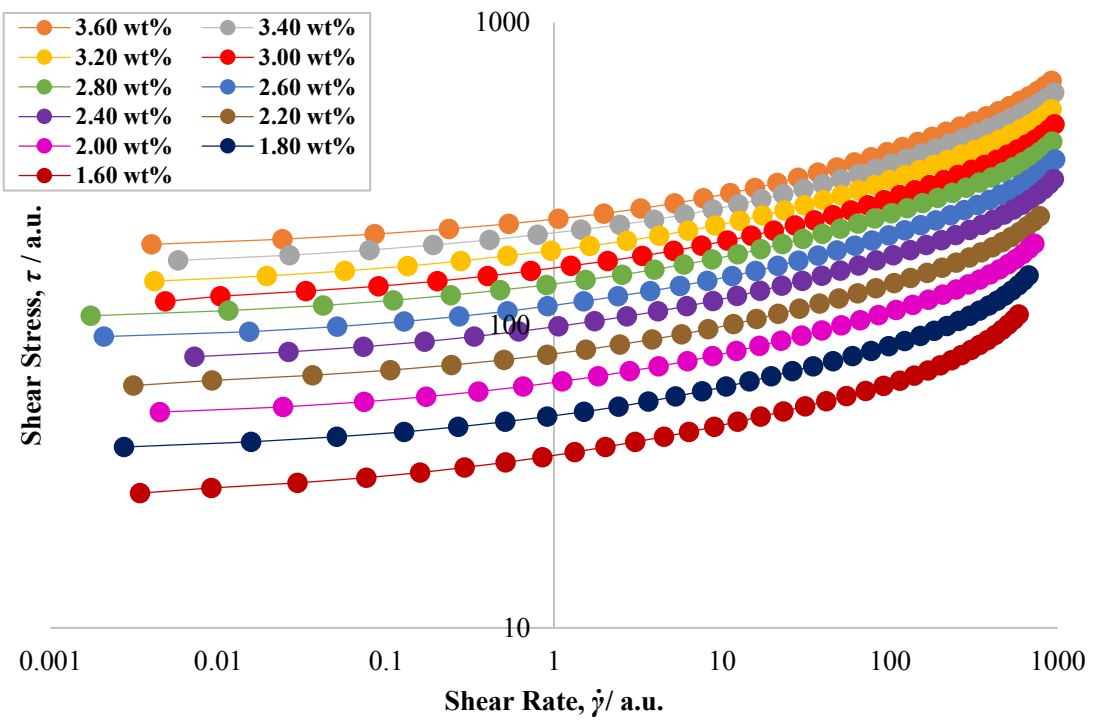

Figure A.6. Raw rheological flow curves, acquired from shear stress down sweeps using 6-bladed vane geometry, of C980 solutions at various mass fractions, ranging from 1.60-3.60 wt%, with all solutions at an approximately constant pH: 2.38-2.55.

Table A.6. Herschel-Bulkley fitted data and the physical properties of the C980 fluids, along with the associated error quantification of the mathematical fits and the shear rate range over which the fits occurred.

Physical properties		**Herschel-Bulkley rheological properties**			**Error quantification and analysis**		
C980 mass fraction / wt%	**pH**	**Yield stress, τ_y / a.u.**	**Flow consistency index, *K* / a.u.**	**Flow behaviour index, *n***	**Optimised fit AAD / %**	**Optimised fit R^2 value**	**Shear rate range of optimised fit / a.u.**
3.60	2.38	185.4	35.6	0.37	0.95	0.998	0.00400-921
3.40	2.38	163.3	35.2	0.35	1.13	0.998	0.00577-952
3.20	2.44	139.2	34.0	0.34	1.24	0.997	0.00416-920
3.00	2.41	120.7	30.3	0.34	1.61	0.996	0.00483-958
2.80	2.43	107.9	26.5	0.34	1.40	0.996	0.00174-931
2.60	2.46	78.1	18.9	0.35	2.02	0.992	0.00721-950
2.40	2.45	91.8	22.5	0.34	1.72	0.994	0.00208-965
2.20	2.50	63.3	16.0	0.34	1.67	0.994	0.00311-782
2.00	2.50	51.1	12.7	0.34	1.88	0.993	0.00449-728
1.80	2.53	40.0	9.3	0.36	2.32	0.990	0.00274-672
1.60	2.55	28.2	8.0	0.34	2.87	0.987	0.00342-586

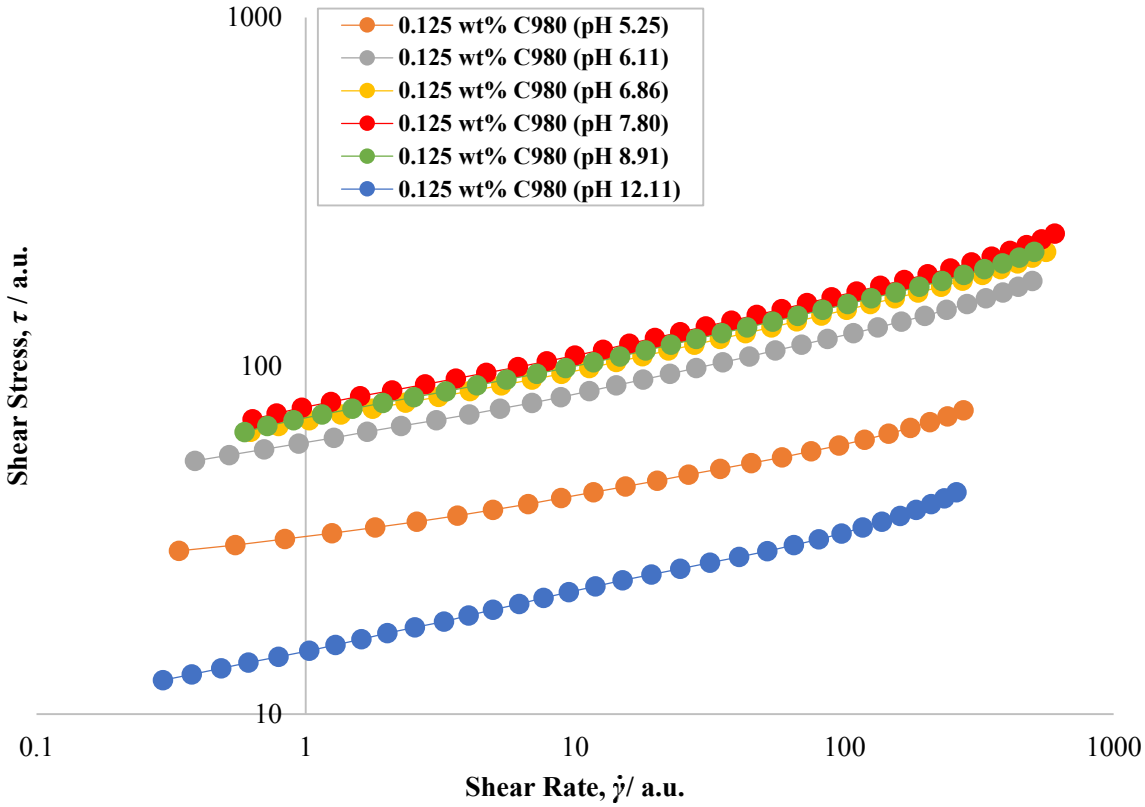

Figure A.7. Raw rheological flow curves, acquired from shear stress down sweeps using 6-bladed vane geometry, of C980 solutions at constant mass fraction of 0.125 wt%, but varying pH values through additions of different quantities of a 2 wt% NaOH (aq) solution, ranging from pH: 5.25-12.10.

Table A.7. Herschel-Bulkley fitted data and the physical properties of the 0.125 wt% C980 fluids, along with the associated error quantification of the mathematical fits and the shear rate range over which the fits occurred.

Physical properties			**Herschel-Bulkley rheological properties**			**Error quantification and analysis**		
C980 mass fraction / wt%	**NaOH mass fraction / wt%**	**pH**	**Yield stress, τ_y / a.u.**	**Flow consistency index, K / a.u.**	**Flow behaviour index, n**	**Optimised fit AAD / %**	**Optimised fit R^2 value**	**Shear rate range of optimised fit / a.u.**
0.125	0.010	5.25	21.0	11.4	0.27	0.58	0.999	0.338-277
0.125	0.020	6.11	30.2	29.9	0.25	0.61	0.998	0.387-499
0.125	0.030	6.86	35.0	34.5	0.25	0.65	0.999	0.624-562
0.125	0.040	7.80	38.5	37.9	0.25	0.81	0.999	0.635-605
0.125	0.050	8.91	32.7	38.2	0.24	0.63	0.999	0.593-508
0.125	0.060	12.10	4.4	10.8	0.22	1.29	0.995	0.295-261

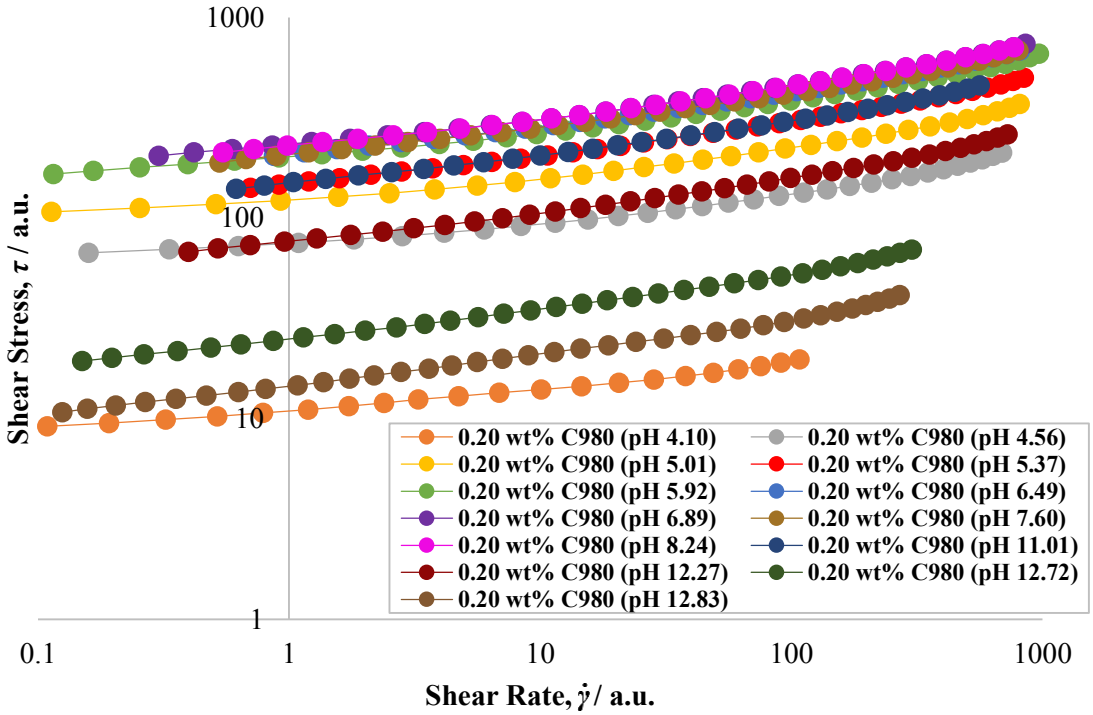

Figure A.8. Raw rheological flow curves, acquired from shear stress down sweeps using 6-bladed vane geometry, of C980 solutions at constant mass fraction of 0.20 wt%, but varying pH values through additions of different quantities of a 2 wt% NaOH (aq) solution, ranging from pH: 4.10-12.83.

Table A.8. Herschel-Bulkley fitted data and the physical properties of the 0.20 wt% C980 fluids, along with the associated error quantification of the mathematical fits and the shear rate range over which the fits occurred.

Physical properties			**Herschel-Bulkley rheological properties**			**Error quantification and analysis**		
C980 mass fraction / wt%	**NaOH mass fraction / wt%**	**pH**	**Yield stress, τ_y / a.u.**	**Flow consistency index, K / a.u.**	**Flow behaviour index, n**	**Optimised fit AAD / %**	**Optimised fit R^2 value**	**Shear rate range of optimised fit / a.u.**
0.20	0.005	4.10	6.4	4.6	0.22	0.77	0.997	0.109-108
0.20	0.010	4.56	61.0	13.9	0.36	1.14	0.996	0.159-692
0.20	0.015	5.01	94.7	28.5	0.33	0.87	0.997	0.113-813
0.20	0.020	5.37	93.2	56.7	0.29	0.72	0.999	0.702-845
0.20	0.030	5.92	137.0	63.7	0.30	0.88	0.998	0.115-970
0.20	0.040	6.49	130.9	80.1	0.28	0.60	0.999	0.869-816
0.20	0.050	6.89	148.4	84.1	0.28	0.51	0.999	0.302-857
0.20	0.060	7.60	127.0	81.0	0.28	1.09	0.998	0.528-804
0.20	0.070	8.24	140.5	89.6	0.28	0.44	1.000	0.546-770
0.20	0.080	11.01	83.1	66.1	0.27	0.78	0.998	0.616-564
0.20	0.085	12.27	47.7	29.0	0.29	1.06	0.997	0.397-728
0.20	0.094	12.72	11.6	13.1	0.25	1.09	0.997	0.150-302
0.20	0.100	12.83	5.6	8.9	0.24	1.58	0.994	0.125-270

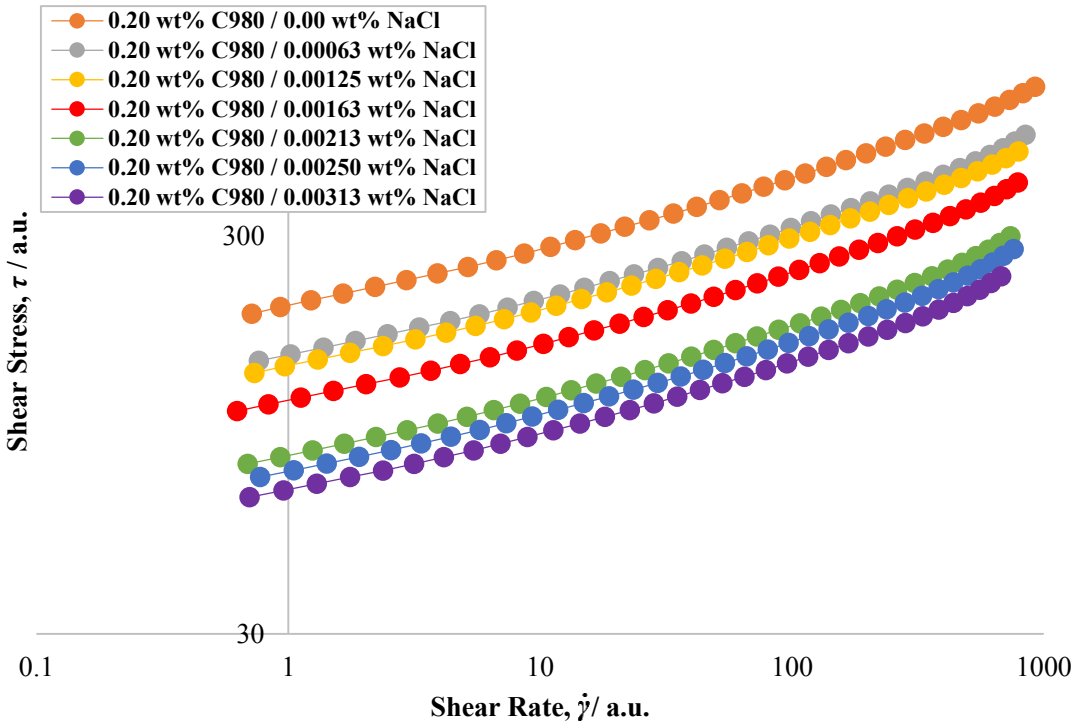

Figure A.9 Raw rheological flow curves, acquired from shear stress down sweeps using 6-bladed vane geometry, of C980 solutions at constant mass fraction of 0.20 wt%, but containing varying quantities of 1 wt% NaCl (aq) solution, ranging from 0.00-3.13 wt%, with all solutions at an approximately constant pH: 7.27-7.62.

Table A.9. Herschel-Bulkley fitted data and the physical properties of the 0.20 wt% C980 fluids, along with the associated error quantification of the mathematical fits and the shear rate range over which the fits occurred.

Physical properties			**Herschel-Bulkley rheological properties**			**Error quantification and analysis**		
C980 mass fraction / wt%	**NaCl mass fraction ($\times 10^{-3}$) / wt%**	**pH**	**Yield stress, τ_y / a.u.**	**Flow consistency index, K / a.u.**	**Flow behaviour index, n**	**Optimised fit AAD / %**	**Optimised fit R^2 value**	**Shear rate range of optimised fit / a.u.**
0.20	0.00	7.62	112.4	88.1	0.27	0.62	0.999	0.717-924
0.20	0.63	7.46	100.8	51.8	0.31	0.78	0.999	0.764-848
0.20	1.25	7.41	90.6	52.2	0.30	0.57	0.999	0.734-794
0.20	1.63	7.36	75.8	40.9	0.31	0.79	0.999	0.626-789
0.20	2.13	7.31	55.5	26.6	0.31	0.99	0.998	0.689-738
0.20	2.50	7.30	52.8	25.1	0.32	1.04	0.998	0.774-759
0.20	3.13	7.27	46.4	23.4	0.31	0.95	0.998	0.702-679

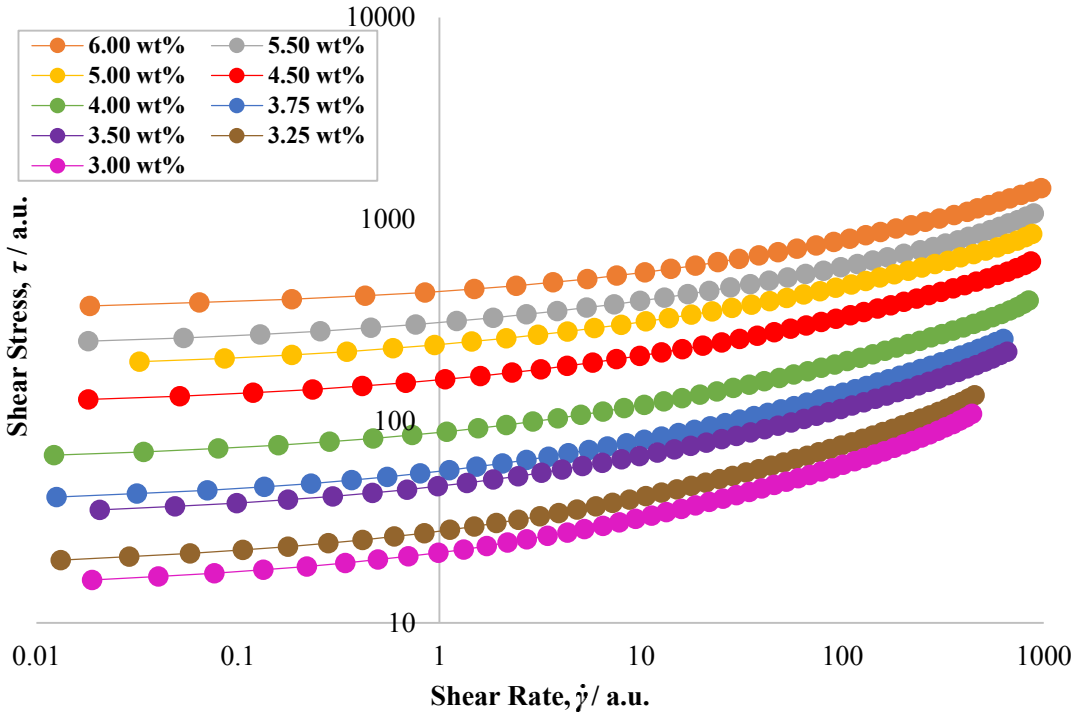

Figure A.10. Raw rheological flow curves, acquired from shear stress down sweeps using 6-bladed vane geometry, of CU10 solutions at various mass fractions, ranging from 3.00-6.00 wt%, with all solutions at an approximately constant pH: 2.20-2.50.

Table A.10. Herschel-Bulkley fitted data and the physical properties of the CU10 fluids, along with the associated error quantification of the mathematical fits and the shear rate range over which the fits occurred.

Physical Properties		**Herschel-Bulkley rheological properties**			**Error quantification and analysis**		
CU10 mass fraction / wt%	**pH**	**Yield stress, τ_y / a.u.**	**Flow consistency index, *K* / a.u.**	**Flow behaviour index, *n***	**Optimised fit AAD / %**	**Optimised fit R^2 value**	**Shear rate range of optimised fit / a.u.**
6.00	2.20	364.2	72.2	0.39	0.72	0.999	0.0184-971
5.50	2.27	237.7	67.8	0.36	1.06	0.998	0.0181-743
5.00	2.29	183.9	53.5	0.36	0.86	0.999	0.00997-876
4.50	2.35	123.1	36.0	0.38	0.88	0.999	0.0181-866
4.00	2.39	66.3	20.8	0.40	1.15	0.998	0.0122-843
3.75	2.44	40.7	15.2	0.41	1.07	0.999	0.0126-740
3.50	2.42	34.7	12.5	0.41	0.96	0.999	0.0206-659
3.25	2.49	20.0	8.1	0.43	1.57	0.997	0.0132-507
3.00	2.50	15.8	6.3	0.43	1.50	0.997	0.0189-467

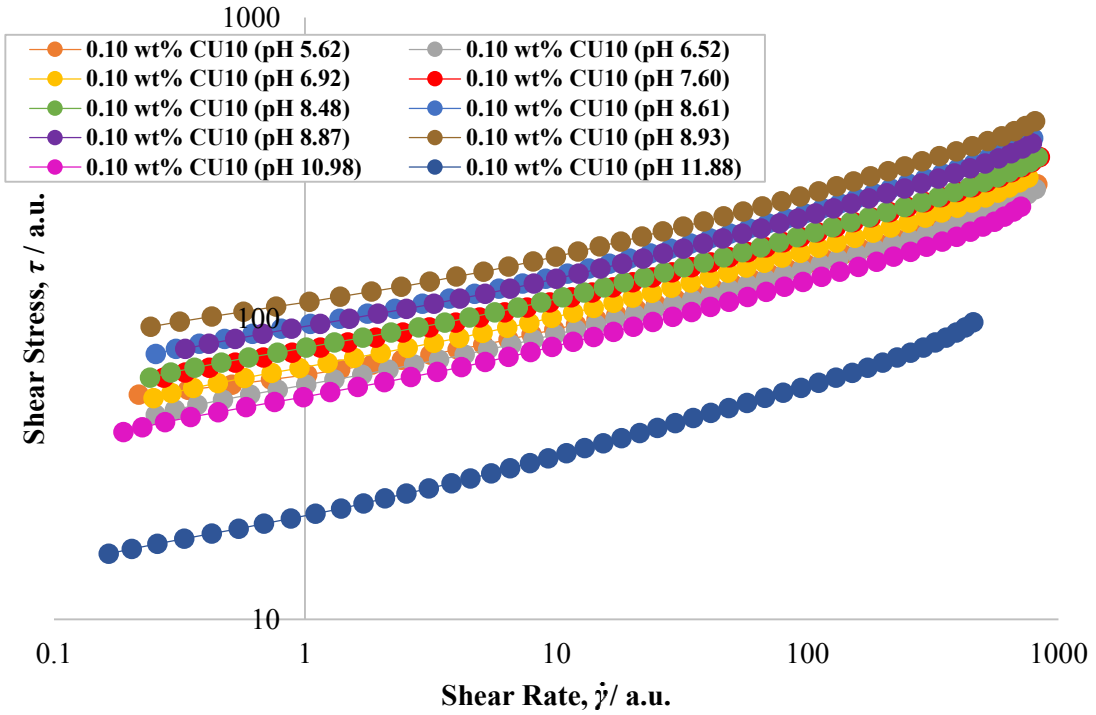

Figure A.11. Raw rheological flow curves, acquired from shear stress down sweeps using 6-bladed vane geometry, of CU10 solutions at constant mass fraction of 0.10 wt%, but varying pH values through additions of different quantities of a 2 wt% NaOH (aq) solution, ranging from pH 5.62-11.88.

Table A.11. Herschel-Bulkley fitted data and the physical properties of the 0.10 wt% CU10 fluids, along with the associated error quantification of the mathematical fits and the shear rate range over which the fits occurred.

Physical properties			**Herschel-Bulkley rheological properties**			**Error quantification and analysis**		
CU10 mass fraction / wt%	**NaOH mass fraction / wt%**	**pH**	**Yield stress, τ_y / a.u.**	**Flow consistency index, *K* / a.u.**	**Flow behaviour index, *n***	**Optimised fit AAD / %**	**Optimised fit R^2 value**	**Shear rate range of optimised fit / a.u.**
0.10	0.010	5.62	42.1	22.9	0.34	0.87	0.998	0.218-826
0.10	0.016	6.52	30.9	28.4	0.31	1.04	0.997	0.254-813
0.10	0.020	6.92	34.4	33.8	0.30	0.81	0.998	0.294-759
0.10	0.026	7.60	41.6	35.8	0.31	0.85	0.998	0.274-845
0.10	0.034	8.48	42.9	36.3	0.31	0.81	0.998	0.292-829
0.10	0.035	8.61	49.0	45.0	0.30	0.84	0.999	0.254-793
0.10	0.036	8.87	52.1	41.0	0.31	0.74	0.999	0.333-785
0.10	0.039	8.93	66.5	45.8	0.31	0.58	0.999	0.243-809
0.10	0.040	10.98	27.1	27.0	0.30	1.13	0.997	0.189-711
0.10	0.048	11.88	9.8	12.3	0.31	0.82	0.998	0.165-426

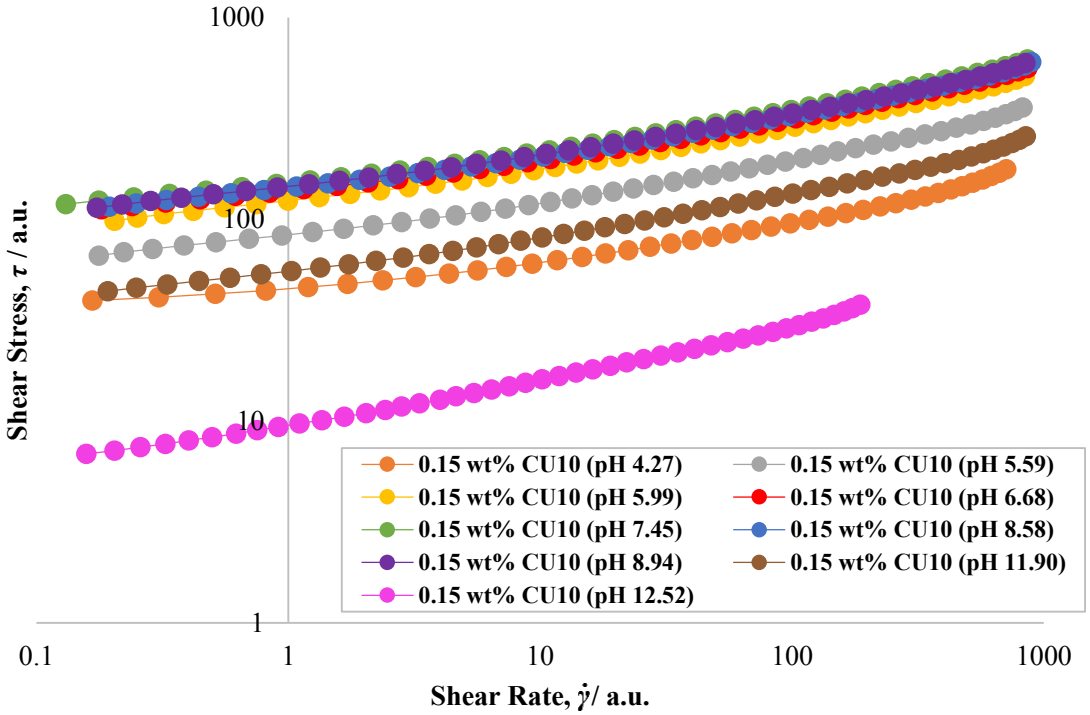

Figure A.12. Raw rheological flow curves, acquired from shear stress down sweeps using 6-bladed vane geometry, of CU10 solutions at constant mass fraction of 0.15 wt%, but varying pH values through additions of different quantities of a 2 wt% NaOH (aq) solution, ranging from pH 4.27-12.52.

Table A.12. Herschel-Bulkley fitted data and the physical properties of the 0.15 wt% CU10 fluids, along with the associated error quantification of the mathematical fits and the shear rate range over which the fits occurred.

Physical properties			**Herschel-Bulkley rheological properties**			**Error quantification and analysis**		
CU10 mass fraction / wt%	**NaOH mass fraction / wt%**	**pH**	**Yield stress, τ_y / a.u.**	**Flow consistency index, K / a.u.**	**Flow behaviour index, n**	**Optimised fit AAD / %**	**Optimised fit R^2 value**	**Shear rate range of optimised fit / a.u.**
0.15	0.005	4.27	34.8	10.6	0.38	1.38	0.996	0.167-711
0.15	0.014	5.59	48.6	34.2	0.32	0.88	0.998	0.177-824
0.15	0.020	5.99	68.7	53.2	0.31	0.69	0.999	0.204-843
0.15	0.030	6.68	84.0	53.2	0.32	0.64	0.999	0.181-861
0.15	0.041	7.45	88.6	62.0	0.31	0.49	0.999	0.131-861
0.15	0.050	8.58	84.8	57.2	0.32	0.86	0.999	0.195-894
0.15	0.055	8.94	80.5	63.5	0.30	0.85	0.999	0.174-848
0.15	0.060	11.90	32.0	22.8	0.33	1.35	0.996	0.192-849
0.15	0.070	12.52	3.9	5.5	0.33	0.93	0.998	0.158-187

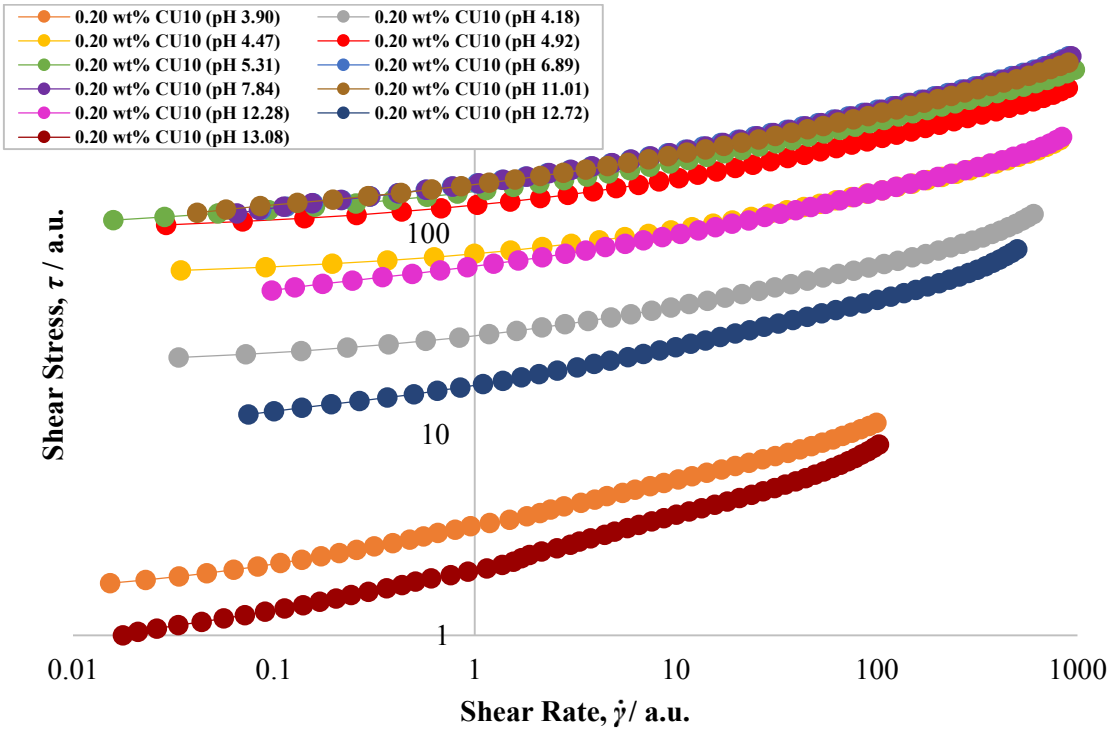

Figure A.13. Raw rheological flow curves, acquired from shear stress down sweeps using 6-bladed vane geometry, of CU10 solutions at constant mass fraction of 0.20 wt%, but varying pH values through additions of different quantities of a 2 wt% NaOH (aq) solution, ranging from pH 3.90-13.08.

Table A.13. Herschel-Bulkley fitted data and the physical properties of the 0.20 wt% CU10 fluids, along with the associated error quantification of the mathematical fits and the shear rate range over which the fits occurred.

Physical properties			**Herschel-Bulkley rheological properties**			**Error quantification and analysis**		
CU10 mass fraction / wt%	**NaOH mass fraction / wt%**	**pH**	**Yield stress, τ_y / a.u.**	**Flow consistency index, K / a.u.**	**Flow behaviour index, n**	**Optimised fit AAD / %**	**Optimised fit R^2 value**	**Shear rate range of optimised fit / a.u.**
0.20	0.004	3.90	1.2	2.3	0.32	1.01	0.998	0.0153-100
0.20	0.006	4.18	22.1	9.0	0.37	1.58	0.995	0.0336-605
0.20	0.008	4.47	60.8	19.0	0.37	0.73	0.998	0.0345-822
0.20	0.014	4.92	99.1	40.8	0.34	0.49	0.999	0.0291-898
0.20	0.020	5.31	103.0	60.0	0.32	0.32	1.000	0.0159-973
0.20	0.050	6.89	100.8	76.1	0.31	0.97	0.998	0.0866-905
0.20	0.065	7.84	98.8	77.4	0.31	1.14	0.998	0.0654-935
0.20	0.080	11.01	106.9	68.3	0.32	0.71	0.999	0.0415-903
0.20	0.090	12.28	41.6	26.8	0.33	1.05	0.998	0.0977-840
0.20	0.100	12.72	9.8	7.8	0.35	1.66	0.994	0.0746-502
0.20	0.120	13.08	0.7	1.4	0.36	1.64	0.996	0.0177-103

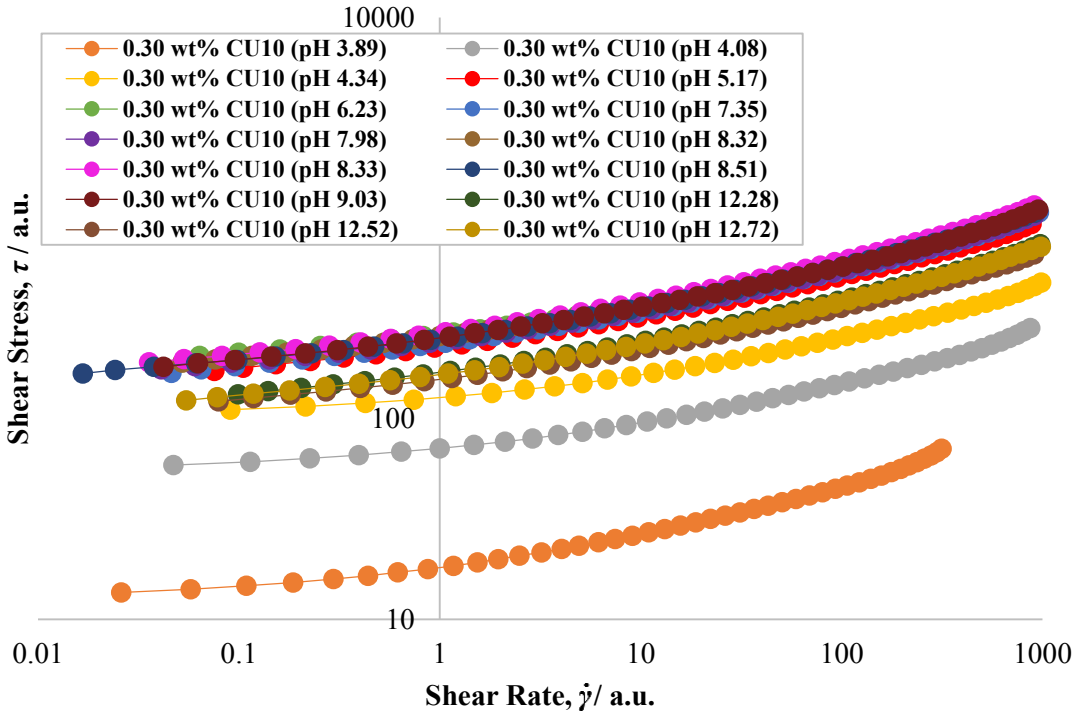

Figure A.14. Raw rheological flow curves, acquired from shear stress down sweeps using 6-bladed vane geometry, of CU10 solutions at constant mass fraction of 0.30 wt%, but varying pH values through additions of different quantities of a 3 wt% NaOH (aq) solution, ranging from pH 3.89-12.72.

Table A.14. Herschel-Bulkley fitted data and the physical properties of the 0.30 wt% CU10 fluids, along with the associated error quantification of the mathematical fits and the shear rate range over which the fits occurred.

Physical properties			**Herschel-Bulkley rheological properties**			**Error quantification and analysis**		
CU10 mass fraction / wt%	**NaOH mass fraction / wt%**	**pH**	**Yield stress, τ_y / a.u.**	**Flow consistency index, *K* / a.u.**	**Flow behaviour index, *n***	**Optimised fit AAD / %**	**Optimised fit R^2 value**	**Shear rate range of optimised fit / a.u.**
0.30	0.006	3.89	12.4	5.7	0.39	1.29	0.996	0.026-315
0.30	0.009	4.08	53.4	17.8	0.37	0.93	0.997	0.0473-870
0.30	0.012	4.34	99.7	27.7	0.37	0.53	0.999	0.0906-986
0.30	0.030	5.17	140.6	85.4	0.32	0.84	0.999	0.0755-883
0.30	0.060	6.23	174.0	88.7	0.34	0.48	1.000	0.0637-899
0.30	0.090	7.35	141.4	93.1	0.32	1.47	0.997	0.0462-961
0.30	0.099	7.98	149.7	90.8	0.33	1.06	0.998	0.041-909
0.30	0.105	8.32	155.7	100.7	0.32	0.67	0.999	0.0523-875
0.30	0.113	8.33	162.1	102.5	0.33	1.05	0.999	0.0357-910
0.30	0.116	8.51	147.5	99.9	0.32	0.97	0.999	0.0167-916
0.30	0.118	9.03	153.5	97.3	0.32	1.22	0.998	0.0627-869
0.30	0.120	12.28	106.2	62.7	0.33	0.76	0.999	0.099-977
0.30	0.129	12.52	100.9	55.3	0.34	0.53	1.000	0.0792-911
0.30	0.138	12.72	103.9	60.6	0.33	0.69	0.999	0.0547-984

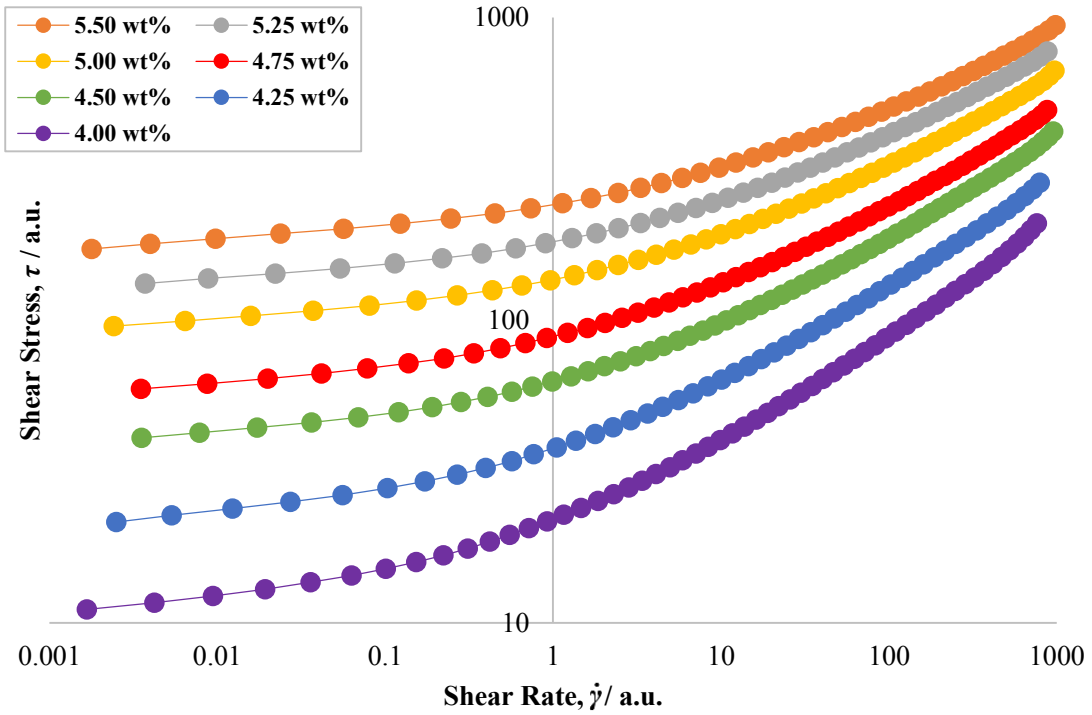

Figure A.15. Raw rheological flow curves, acquired from shear stress down sweeps using 6-bladed vane geometry, of CU21 solutions at various mass fractions, ranging from 4.00-5.50 wt%, with all solutions at an approximately constant pH: 2.43-2.61.

Table A.15. Herschel-Bulkley fitted data and the physical properties of the CU21 fluids, along with the associated error quantification of the mathematical fits and the shear rate range over which the fits occurred.

Physical Properties		**Herschel-Bulkley rheological properties**			**Error quantification and analysis**		
CU21 mass fraction / wt%	**pH**	**Yield stress, τ_y / a.u.**	**Flow consistency index, *K* / a.u.**	**Flow behaviour index, *n***	**Optimised fit AAD / %**	**Optimised fit R^2 value**	**Shear rate range of optimised fit / a.u.**
5.50	2.43	173.0	65.4	0.35	0.85	0.999	0.00178-983
5.25	2.46	129.1	51.8	0.37	0.41	1.000	0.00372-880
5.00	2.51	94.5	41.0	0.38	0.59	0.999	0.00242-972
4.75	2.51	57.4	30.7	0.39	0.53	1.000	0.0035-879
4.50	2.54	39.6	23.1	0.40	0.43	1.000	0.00354-953
4.25	2.61	20.9	16.7	0.41	0.53	1.000	0.0025-793
4.00	2.57	10.8	11.1	0.42	0.87	0.999	0.00167-762

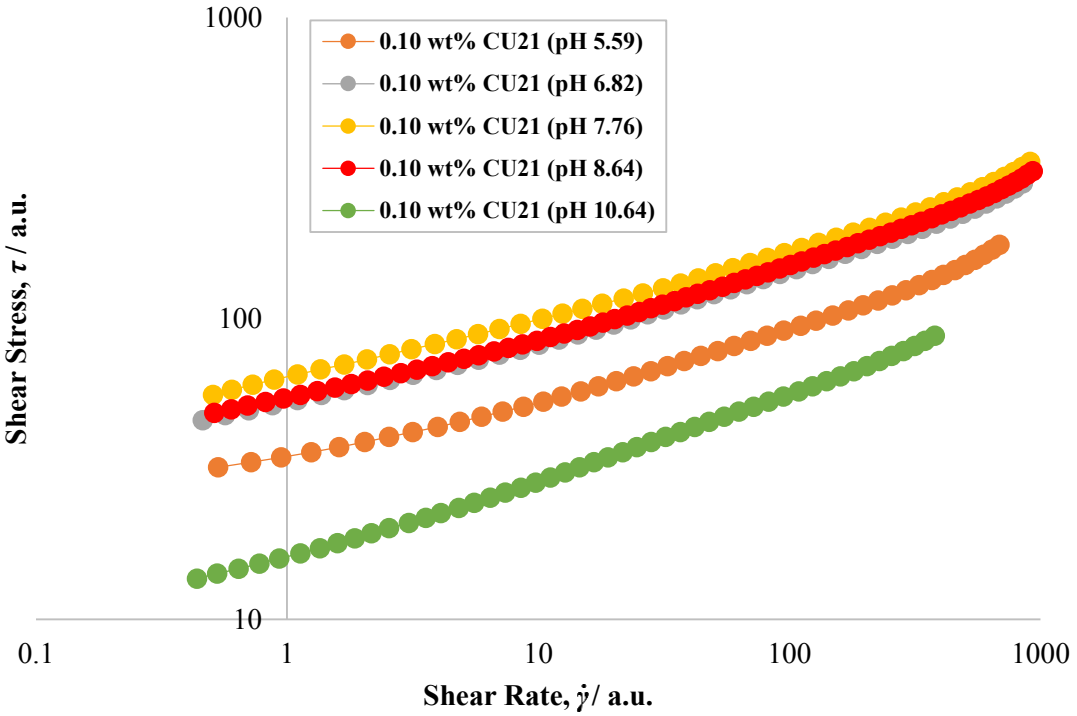

Figure A.16. Raw rheological flow curves, acquired from shear stress down sweeps using 6-bladed vane geometry, of CU21 solutions at constant mass fraction of 0.10 wt%, but varying pH values through additions of different quantities of a 2 wt% NaOH (aq) solution, ranging from pH 5.59-10.64.

Table A.16. Herschel-Bulkley fitted data and the physical properties of the 0.10 wt% CU21 fluids, along with the associated error quantification of the mathematical fits and the shear rate range over which the fits occurred.

Physical properties			**Herschel-Bulkley rheological properties**			**Error quantification and analysis**		
CU21 mass fraction / wt%	**NaOH mass fraction / wt%**	**pH**	**Yield stress, τ_y / a.u.**	**Flow consistency index, *K* / a.u.**	**Flow behaviour index, *n***	**Optimised fit AAD / %**	**Optimised fit R^2 value**	**Shear rate range of optimised fit / a.u.**
0.10	0.010	5.59	22.2	12.8	0.37	1.07	0.997	0.532-687
0.10	0.020	6.82	27.9	24.7	0.34	0.94	0.998	0.461-851
0.10	0.030	7.76	33.7	30.3	0.32	1.55	0.997	0.507-912
0.10	0.034	8.64	30.7	24.0	0.35	0.94	0.998	0.513-932
0.10	0.040	10.64	5.7	10.4	0.34	0.59	1.000	0.438-380

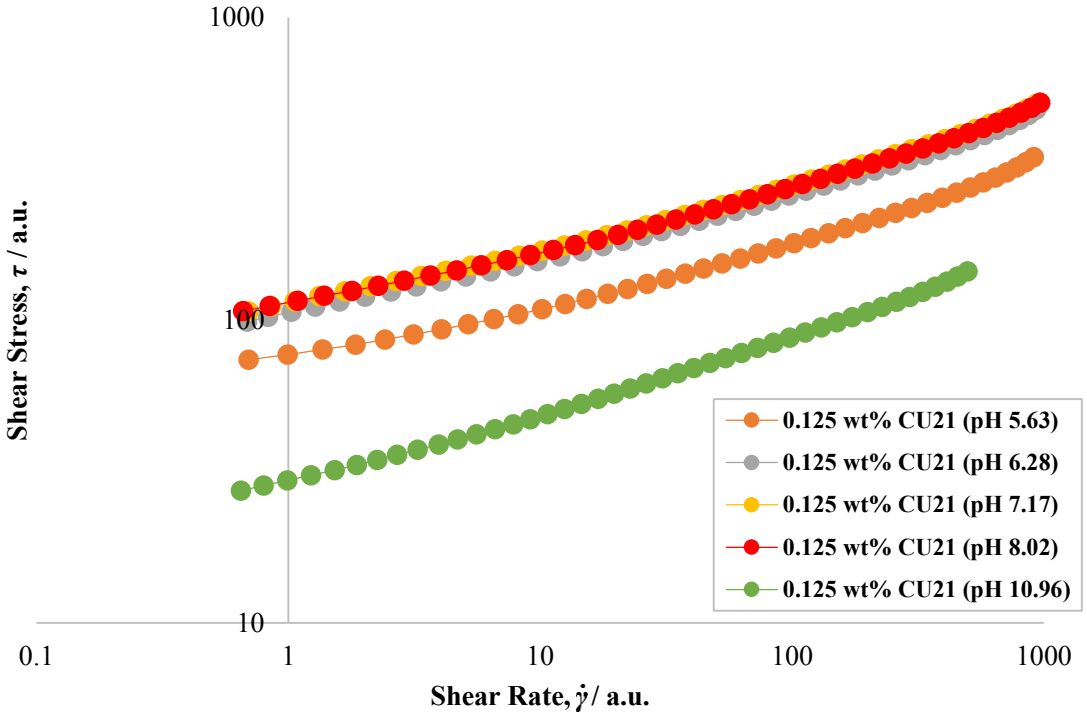

Figure A.17. Raw rheological flow curves, acquired from shear stress down sweeps using 6-bladed vane geometry, of CU21 solutions at constant mass fraction of 0.125 wt%, but varying pH values through additions of different quantities of a 2 wt% NaOH (aq) solution, ranging from pH 5.63-10.96.

Table A.17. Herschel-Bulkley fitted data and the physical properties of the 0.125 wt% CU21 fluids, along with the associated error quantification of the mathematical fits and the shear rate range over which the fits occurred.

Physical properties			**Herschel-Bulkley rheological properties**			**Error quantification and analysis**		
CU21 mass fraction / wt%	**NaOH mass fraction / wt%**	**pH**	**Yield stress, τ_y / a.u.**	**Flow consistency index, K / a.u.**	**Flow behaviour index, n**	**Optimised fit AAD / %**	**Optimised fit R^2 value**	**Shear rate range of optimised fit / a.u.**
0.125	0.012	5.63	53.5	23.9	0.36	0.78	0.998	0.696-914
0.125	0.020	6.28	62.7	44.4	0.32	0.94	0.998	0.686-932
0.125	0.030	7.17	62.5	52.0	0.31	0.64	0.999	0.696-939
0.125	0.040	8.02	70.0	45.1	0.33	0.68	0.999	0.662-968
0.125	0.050	10.96	13.6	16.0	0.33	0.51	0.999	0.649-498

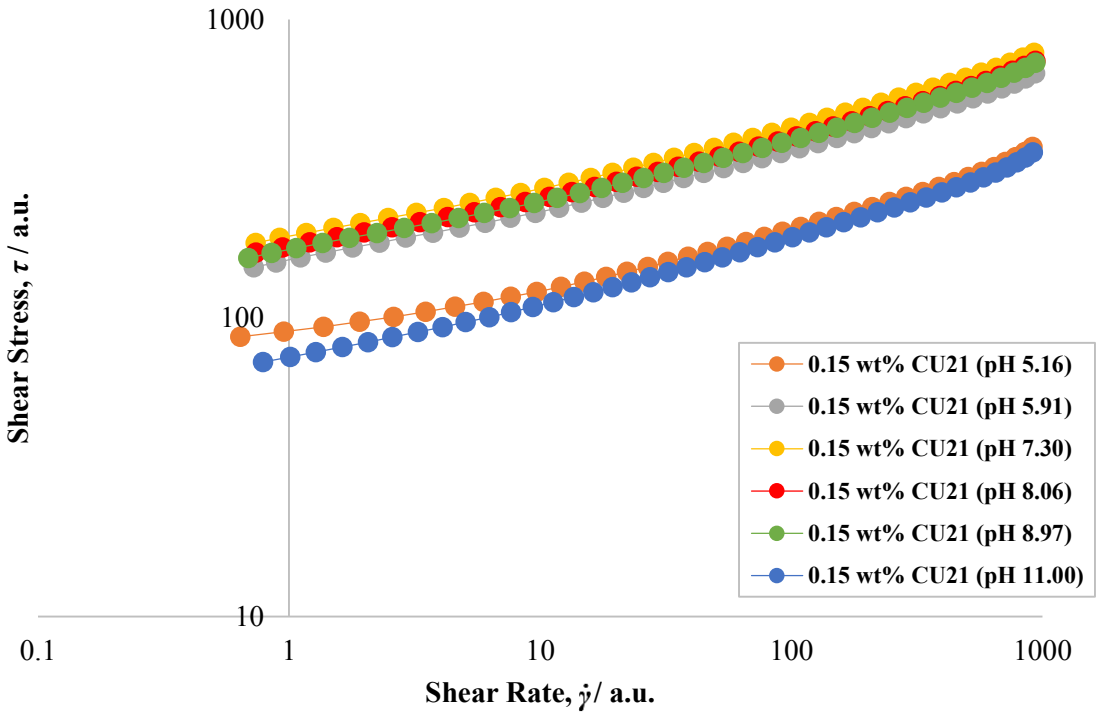

Figure A.18. Raw rheological flow curves, acquired from shear stress down sweeps using 6-bladed vane geometry, of CU21 solutions at constant mass fraction of 0.15 wt%, but varying pH values through additions of different quantities of a 2 wt% NaOH (aq) solution, ranging from pH 5.16-11.00.

Table A.18. Herschel-Bulkley fitted data and the physical properties of the 0.15 wt% CU21 fluids, along with the associated error quantification of the mathematical fits and the shear rate range over which the fits occurred.

Physical properties			**Herschel-Bulkley rheological properties**			**Error quantification and analysis**		
CU21 mass fraction / wt%	**NaOH mass fraction / wt%**	**pH**	**Yield stress, τ_y / a.u.**	**Flow consistency index, *K* / a.u.**	**Flow behaviour index, *n***	**Optimised fit AAD / %**	**Optimised fit R^2 value**	**Shear rate range of optimised fit / a.u.**
0.15	0.010	5.16	65.7	25.1	0.36	0.73	0.998	0.640-914
0.15	0.020	5.91	87.1	70.0	0.30	0.65	0.999	0.723-936
0.15	0.040	7.30	94.6	91.7	0.29	0.87	0.999	0.737-928
0.15	0.050	8.06	97.5	76.5	0.30	0.64	0.999	0.739-939
0.15	0.054	8.97	85.6	82.7	0.29	0.99	0.998	0.688-938
0.15	0.060	11.00	43.6	31.0	0.33	0.84	0.998	0.788-918

Clay/CMC mixtures

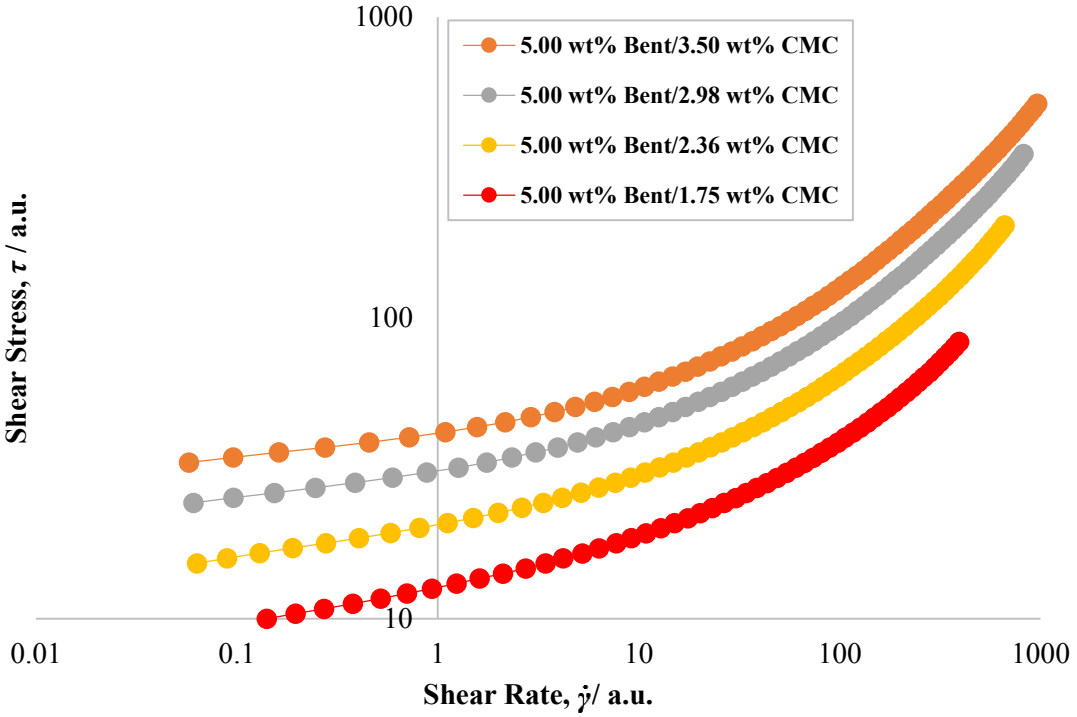

Figure A.19. Raw rheological flow curves, acquired from shear stress down sweeps using 6-bladed vane geometry, of Bentopharm/CMC mixtures at a Bentopharm mass fraction of 5.00 wt%, and varying CMC mass fractions: 1.75-3.50 wt%, with all solutions at an approximately constant pH: 8.87-9.06. In the legend, Bentopharm has been abbreviated to 'Bent'.

Table A.19. Herschel-Bulkley and Casson fitted data, and the physical properties of the 5.00 wt% Bentopharm/CMC mixtures, along with the associated error quantification of the mathematical fits and the shear rate range over which the fits occurred.

Physical properties			**Herschel-Bulkley rheological properties**			**Casson rheological properties**		**Error quantification and analysis**		
Bentopharm mass fraction / wt%	**CMC mass fraction / wt%**	**pH**	**Yield stress, τ_y / a.u.**	**Flow consistency index, K / a.u.**	**Flow behaviour index, n**	**Yield stress, τ_y / a.u.**	**Constant plastic viscosity, η_{pl} / a.u.**	**Optimised fit AAD / %**	**Optimised fit R^2 value**	**Shear rate range of optimised fit / a.u.**
5.00	1.75	9.06	10.29	2.11	0.58	-	-	3.11	0.995	0.141-394
5.00	2.36	8.87	-	-	-	16.91	0.151	2.87	0.999	0.0633-664
5.00	2.98	8.90	-	-	-	25.78	0.220	1.57	1.000	0.0608-826
5.00	3.50	9.05	-	-	-	34.39	0.287	1.00	1.000	0.0578-964

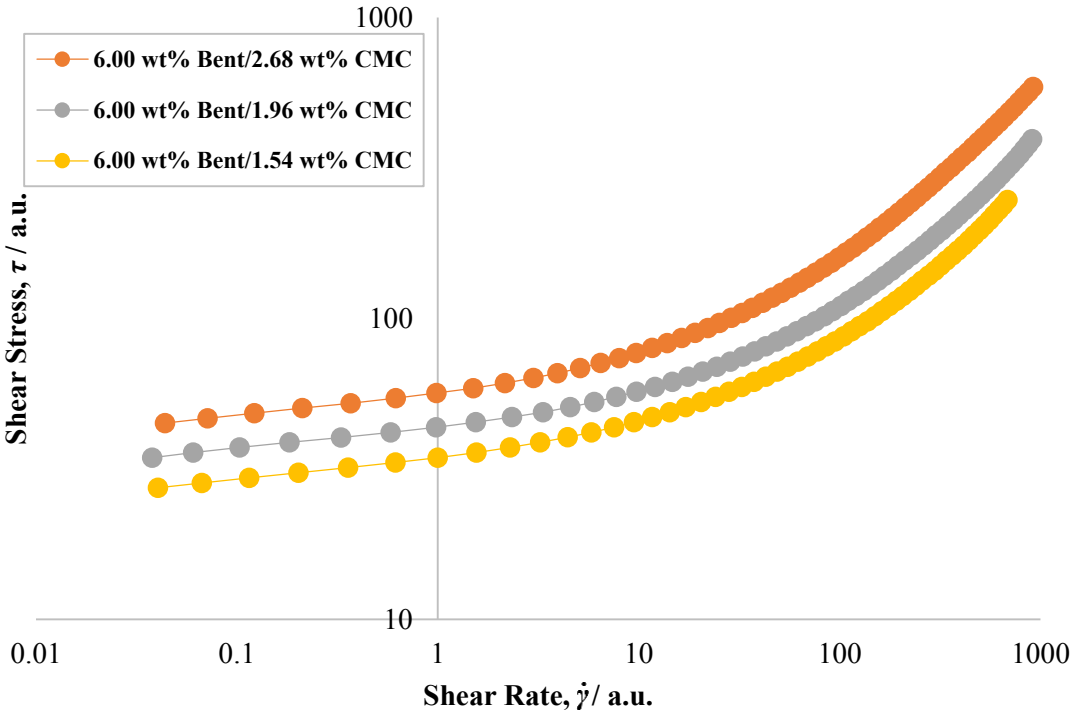

Figure A.20. Raw rheological flow curves, acquired from shear stress down sweeps using 6-bladed vane geometry, of Bentopharm/CMC mixtures at a Bentopharm mass fraction of 6.00 wt%, and varying CMC mass fractions: 1.93-3.35 wt%, with all solutions at an approximately constant pH: 8.64-8.97. In the legend, Bentopharm has been abbreviated to 'Bent'.

Table A.20. Casson fitted data and the physical properties of the 6.00 wt% Bentopharm/CMC mixtures, along with the associated error quantification of the mathematical fits and the shear rate range over which the fits occurred.

Physical properties			**Casson rheological properties**		**Error quantification and analysis**		
Bentopharm mass fraction / wt%	**CMC mass fraction / wt%**	**pH**	**Yield stress, τ_y / a.u.**	**Constant plastic viscosity, η_{pl} / a.u.**	**Optimised fit AAD / %**	**Optimised fit R^2 value**	**Shear rate range of optimised fit / a.u.**
6.00	1.93	8.97	29.46	0.149	1.78	0.999	0.0405-687
6.00	2.45	8.64	36.73	0.198	1.50	0.999	0.0379-912
6.00	3.35	8.70	47.35	0.332	0.95	1.000	0.0439-920

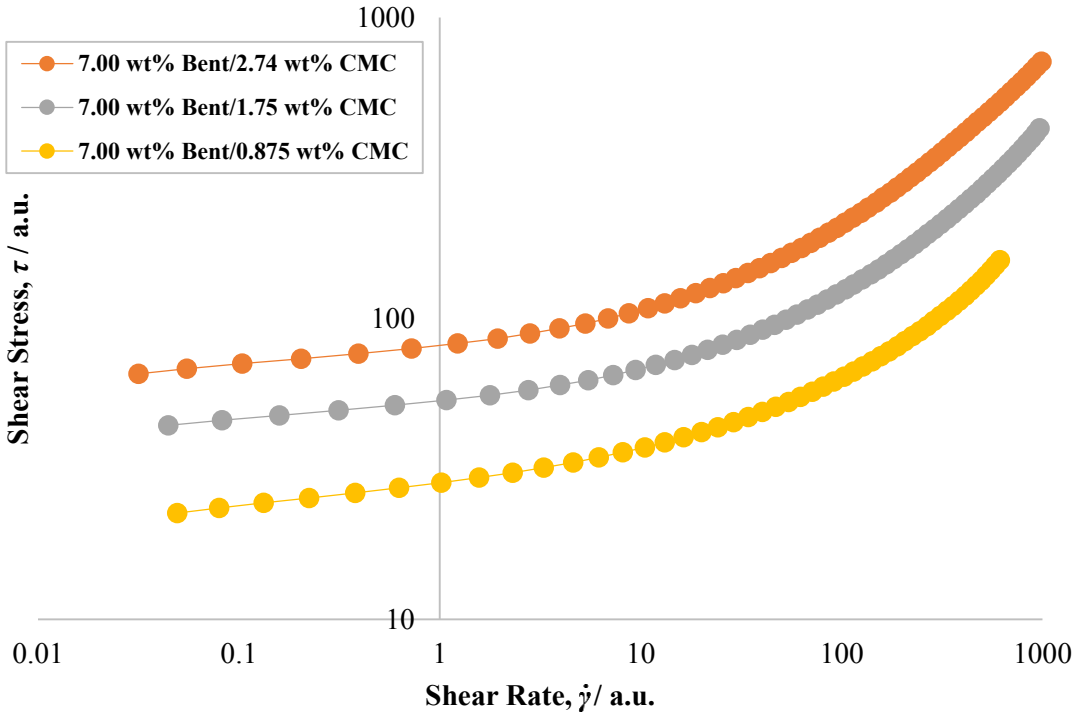

Figure A.21. Raw rheological flow curves, acquired from shear stress down sweeps using 6-bladed vane geometry, of Bentopharm/CMC mixtures at a Bentopharm mass fraction of 7.00 wt%, and varying CMC mass fractions: 0.875-2.74 wt%, with all solutions at an approximately constant pH: 8.56-8.92. In the legend, Bentopharm has been abbreviated to 'Bent'.

Table A.21. Casson fitted data and the physical properties of the 7.00 wt% Bentopharm/CMC mixtures, along with the associated error quantification of the mathematical fits and the shear rate range over which the fits occurred.

Physical properties			**Casson rheological properties**		**Error quantification and analysis**		
Bentopharm mass fraction / wt%	**CMC mass fraction / wt%**	**pH**	**Yield stress, τ_y / a.u.**	**Constant plastic viscosity, η_{pl} / a.u.**	**Optimised fit AAD / %**	**Optimised fit R^2 value**	**Shear rate range of optimised fit / a.u.**
7.00	0.875	8.92	24.99	0.087	2.79	0.998	0.0493-614
7.00	1.75	8.56	46.12	0.188	1.40	0.999	0.0445-970
7.00	2.74	8.72	70.07	0.347	1.16	1.000	0.0317-989

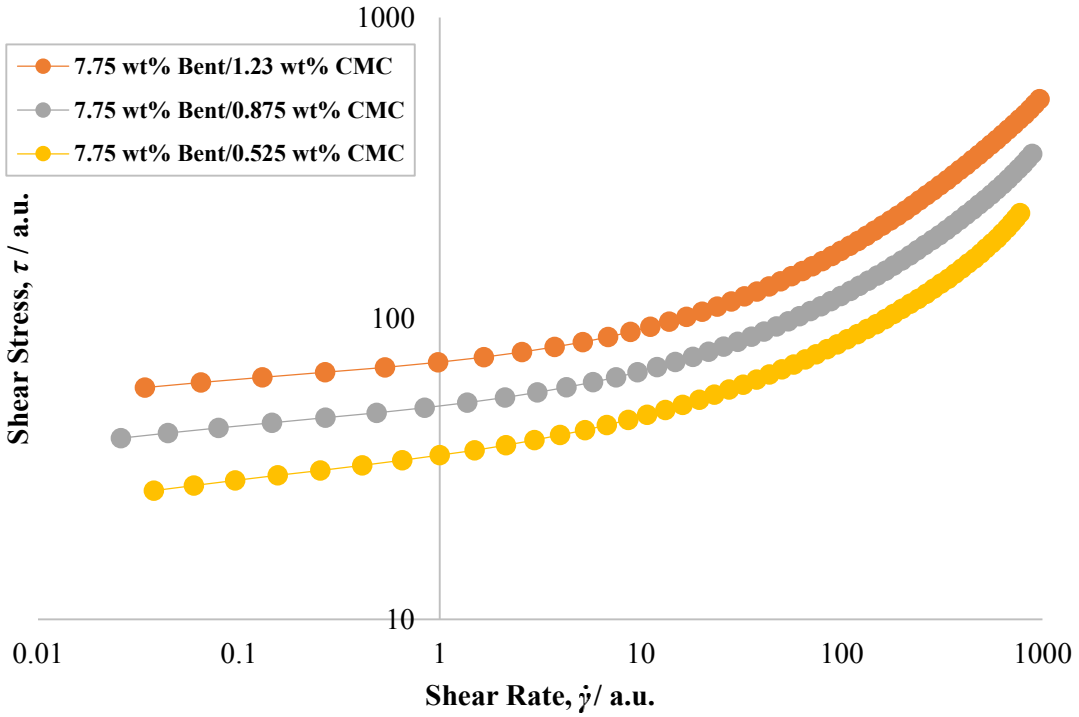

Figure A.22. Raw rheological flow curves, acquired from shear stress down sweeps using 6-bladed vane geometry, of Bentopharm/CMC mixtures at a Bentopharm mass fraction of 7.75 wt%, and varying CMC mass fractions: 0.525-1.23 wt%, with all solutions at an approximately constant pH: 8.89-8.98. In the legend, Bentopharm has been abbreviated to 'Bent'.

Table A.22. Herschel-Bulkley and Casson fitted data, and the physical properties of the 7.75 wt% Bentopharm/CMC mixtures, along with the associated error quantification of the mathematical fits and the shear rate range over which the fits occurred.

Physical properties			**Herschel-Bulkley rheological properties**			**Casson rheological properties**		**Error quantification and analysis**		
Bentopharm mass fraction / wt%	**CMC mass fraction / wt%**	**pH**	**Yield stress, τ_y / a.u.**	**Flow consistency index, K / a.u.**	**Flow behaviour index, n**	**Yield stress, τ_y / a.u.**	**Constant plastic viscosity, η_{pl} / a.u.**	**Optimised fit AAD / %**	**Optimised fit R^2 value**	**Shear rate range of optimised fit / a.u.**
7.75	0.525	8.98	29.05	4.64	0.54	-	-	3.41	0.993	0.0377-776
7.75	0.875	8.97	-	-	-	45.19	0.164	2.86	0.999	0.0259-890
7.75	1.23	8.89	-	-	-	63.23	0.243	1.48	1.000	0.0341-969

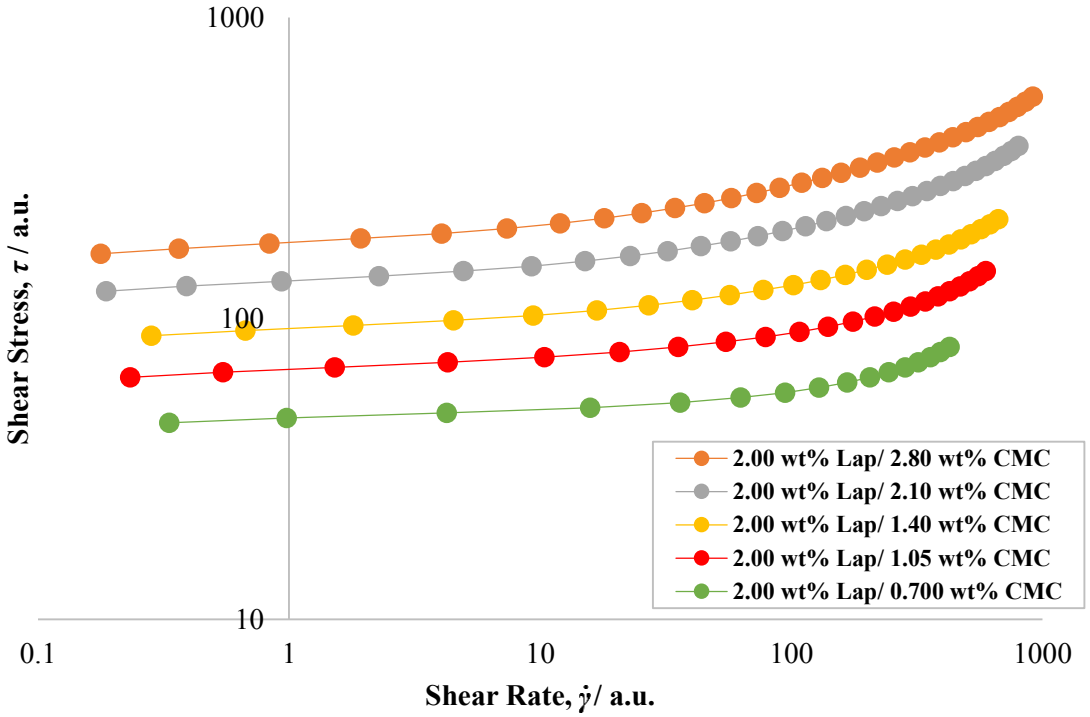

Figure A.23. Raw rheological flow curves, acquired from shear stress down sweeps using 6-bladed vane geometry, of Laponite/CMC mixtures at a Laponite mass fraction of 2.00 wt%, and varying CMC mass fractions: 0.700-2.80 wt%, with all solutions at an approximately constant pH: 9.72-10.17. In the legend, Laponite has been abbreviated to 'Lap'.

Table A.23. Herschel-Bulkley fitted data and the physical properties of the 2.00 wt% Laponite/CMC mixtures, along with the associated error quantification of the mathematical fits and the shear rate range over which the fits occurred.

Physical properties			**Herschel-Bulkley rheological properties**			**Error quantification and analysis**		
Laponite mass fraction / wt%	**CMC mass fraction / wt%**	**pH**	**Yield stress, τ_y / a.u.**	**Flow consistency index, *K* / a.u.**	**Flow behaviour index, *n***	**Optimised fit AAD / %**	**Optimised fit R^2 value**	**Shear rate range of optimised fit / a.u.**
2.00	0.700	10.17	46.5	0.36	0.74	1.52	0.990	0.333-427
2.00	1.05	10.10	66.7	1.2	0.64	2.06	0.990	0.233-595
2.00	1.40	10.07	89.9	2.8	0.57	1.75	0.993	0.283-668
2.00	2.10	9.91	127.6	5.2	0.57	1.64	0.996	0.187-804
2.00	2.80	9.72	168.2	9.5	0.53	1.45	0.997	0.178-917

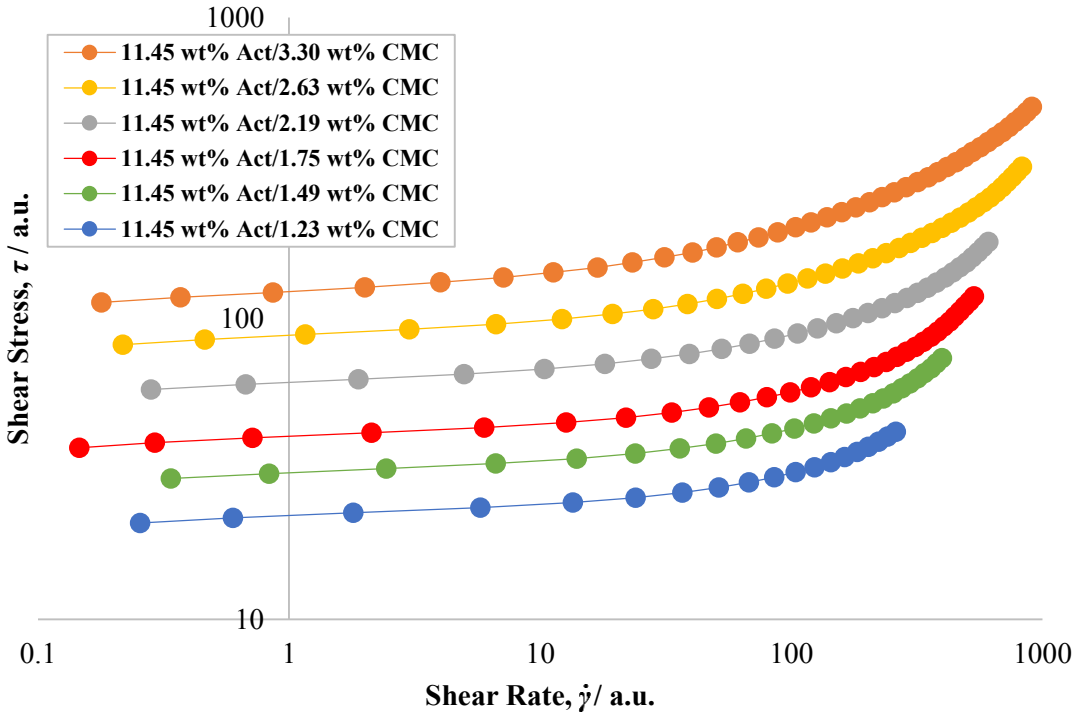

Figure A.24. Raw rheological flow curves, acquired from shear stress down sweeps using 6-bladed vane geometry, of Actigel/CMC mixtures at a Actigel mass fraction of 11.45 wt%, and varying CMC mass fractions: 1.23-3.30 wt%, with all solutions at an approximately constant pH: 8.54-9.00. In the legend, Actigel has been abbreviated to 'Act'.

Table A.24. Herschel-Bulkley fitted data and the physical properties of the 11.45 wt% Actigel/CMC mixtures, along with the associated error quantification of the mathematical fits and the shear rate range over which the fits occurred.

Physical properties			**Herschel-Bulkley rheological properties**			**Error quantification and analysis**		
Actigel mass fraction / wt%	**CMC mass fraction / wt%**	**pH**	**Yield stress, τ_y / a.u.**	**Flow consistency index, *K* / a.u.**	**Flow behaviour index, *n***	**Optimised fit AAD / %**	**Optimised fit R^2 value**	**Shear rate range of optimised fit / a.u.**
11.45	1.23	9.00	21.8	0.29	0.75	1.60	0.993	0.255-261
11.45	1.49	8.96	30.9	0.24	0.85	2.16	0.991	0.338-398
11.45	1.75	8.83	40.5	0.26	0.89	3.29	0.987	0.146-535
11.45	2.19	8.74	61.7	0.67	0.79	2.46	0.991	0.282-610
11.45	2.63	8.85	88.1	1.2	0.77	2.71	0.992	0.218-830
11.45	3.30	8.54	120.6	3.2	0.69	2.24	0.995	0.179-909

Carbopol/glycerol mixtures

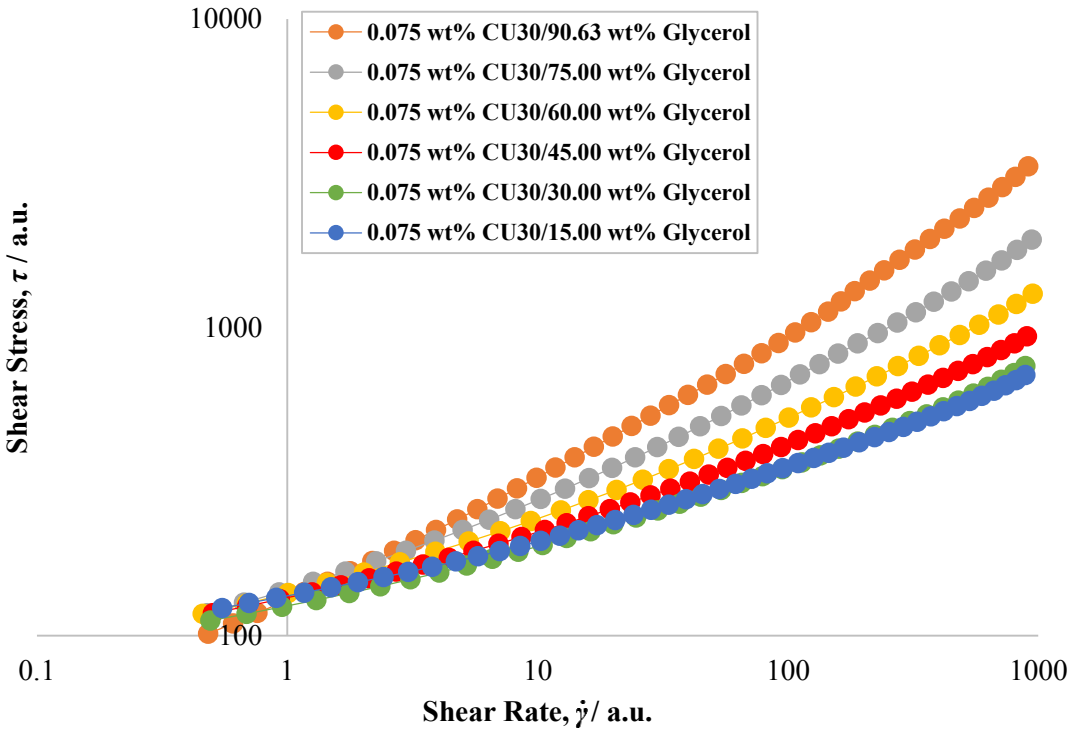

Figure A.25. Raw rheological flow curves, acquired from shear stress down sweeps using 6-bladed vane geometry, of CU30/glycerol mixtures at a constant CU30 mass fraction of 0.075 wt%, and glycerol mass fractions, ranging from 15.00-90.63 wt%, with all solutions at an approximately constant pH 7.26-7.90.

Table A.25. Herschel-Bulkley fitted data and the physical properties of the 0.075 wt% CU30/glycerol mixtures, along with the associated error quantification of the mathematical fits and the shear rate range over which the fits occurred.

Physical properties			**Herschel-Bulkley rheological properties**			**Error quantification and analysis**		
CU30 mass fraction / wt%	**Glycerol mass fraction / wt%**	**pH**	**Yield stress, τ_y / a.u.**	**Flow consistency index, *K* / a.u.**	**Flow behaviour index, *n***	**Optimised fit AAD / %**	**Optimised fit R^2 value**	**Shear rate range of optimised fit / a.u.**
0.075	15.00	7.26	83.6	51.2	0.36	0.54	0.999	0.55-890
0.075	30.00	7.30	77.7	47.7	0.38	0.99	0.999	0.494-891
0.075	45.00	7.44	80.8	52.6	0.41	0.76	1.000	0.506-903
0.075	60.00	7.48	80.2	57.2	0.44	0.96	0.999	0.46-953
0.075	75.00	7.79	76.9	64.0	0.48	1.02	0.999	0.481-944
0.075	90.63	7.90	56.3	74.8	0.54	2.43	0.998	0.484-913

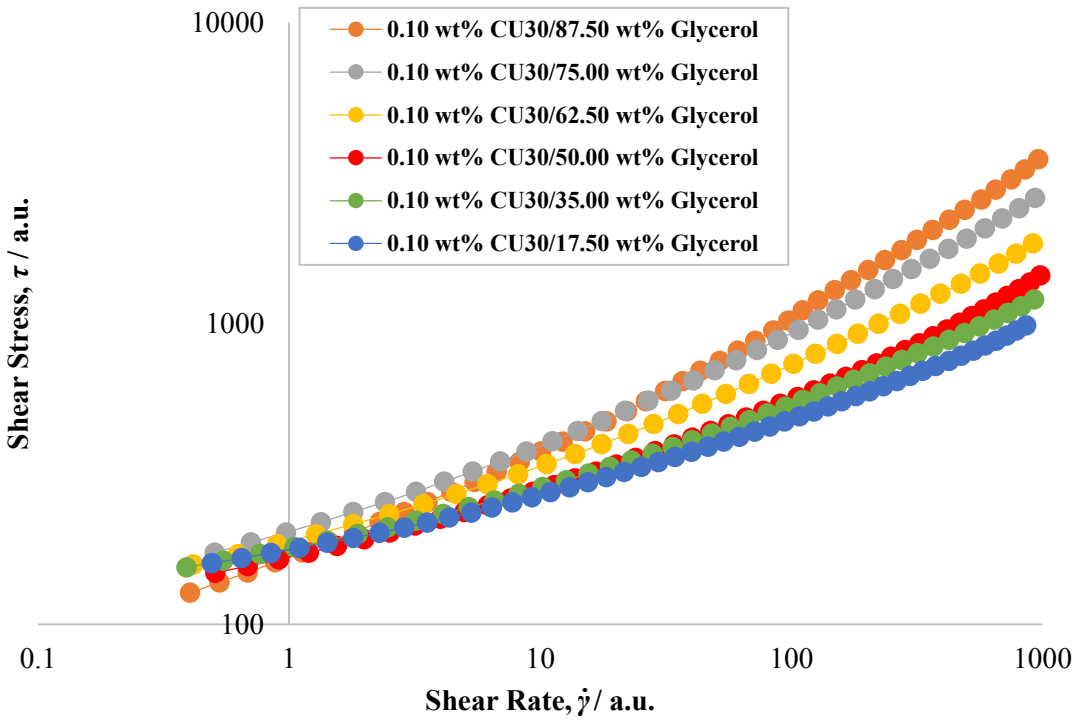

Figure A.26. Raw rheological flow curves, acquired from shear stress down sweeps using 6-bladed vane geometry, of CU30/glycerol mixtures at a constant CU30 mass fraction of 0.10 wt%, and glycerol mass fractions, ranging from 17.50-87.50 wt%, with all solutions at an approximately constant pH 7.20-7.88.

Table A.26. Herschel-Bulkley fitted data and the physical properties of the 0.10 wt% CU30/glycerol mixtures, along with the associated error quantification of the mathematical fits and the shear rate range over which the fits occurred.

Physical properties			**Herschel-Bulkley rheological properties**			**Error quantification and analysis**		
CU30 mass fraction / wt%	**Glycerol mass fraction / wt%**	**pH**	**Yield stress, τ_y / a.u.**	**Flow consistency index, *K* / a.u.**	**Flow behaviour index, *n***	**Optimised fit AAD / %**	**Optimised fit R^2 value**	**Shear rate range of optimised fit / a.u.**
0.10	17.50	7.20	113.9	63.3	0.38	0.62	0.999	0.492-861
0.10	35.00	7.40	111.8	67.0	0.40	0.71	1.000	0.391-927
0.10	50.00	7.41	108.9	60.3	0.44	1.71	0.998	0.509-981
0.10	62.50	7.49	108.0	80.3	0.45	0.85	1.000	0.415-918
0.10	75.00	7.59	113.2	90.5	0.48	1.00	1.000	0.505-935
0.10	87.50	7.88	83.5	82.6	0.54	1.73	0.999	0.403-965

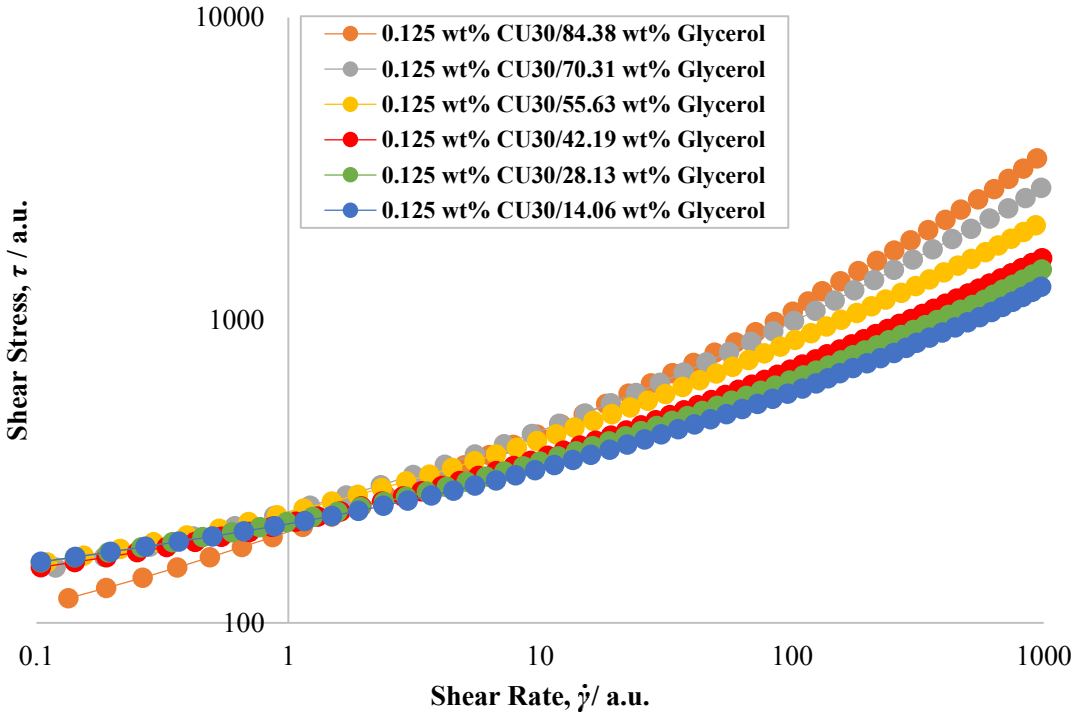

Figure A.27. Raw rheological flow curves, acquired from shear stress down sweeps using 6-bladed vane geometry, of CU30/glycerol mixtures at a constant CU30 mass fraction of 0.125 wt%, and glycerol mass fractions, ranging from 14.06-84.38 wt%, with all solutions at an approximately constant pH 6.98-7.54.

Table A.27. Herschel-Bulkley fitted data and the physical properties of the 0.125 wt% CU30/glycerol mixtures, along with the associated error quantification of the mathematical fits and the shear rate range over which the fits occurred.

Physical properties			**Herschel-Bulkley rheological properties**			**Error quantification and analysis**		
CU30 mass fraction / wt%	**Glycerol mass fraction / wt%**	**pH**	**Yield stress, τ_y / a.u.**	**Flow consistency index, *K* / a.u.**	**Flow behaviour index, *n***	**Optimised fit AAD / %**	**Optimised fit R^2 value**	**Shear rate range of optimised fit / a.u.**
0.125	14.06	6.98	134.0	75.9	0.39	1.10	0.999	0.104-977
0.125	28.13	7.07	130.1	83.5	0.40	1.14	0.999	0.104-984
0.125	42.19	7.25	120.6	90.7	0.40	0.84	1.000	0.104-985
0.125	55.63	7.39	121.5	107.0	0.42	0.90	1.000	0.11-929
0.125	70.31	7.56	119.0	108.2	0.46	1.51	0.999	0.119-978
0.125	84.38	7.54	89.9	104.5	0.50	2.57	0.998	0.134-940

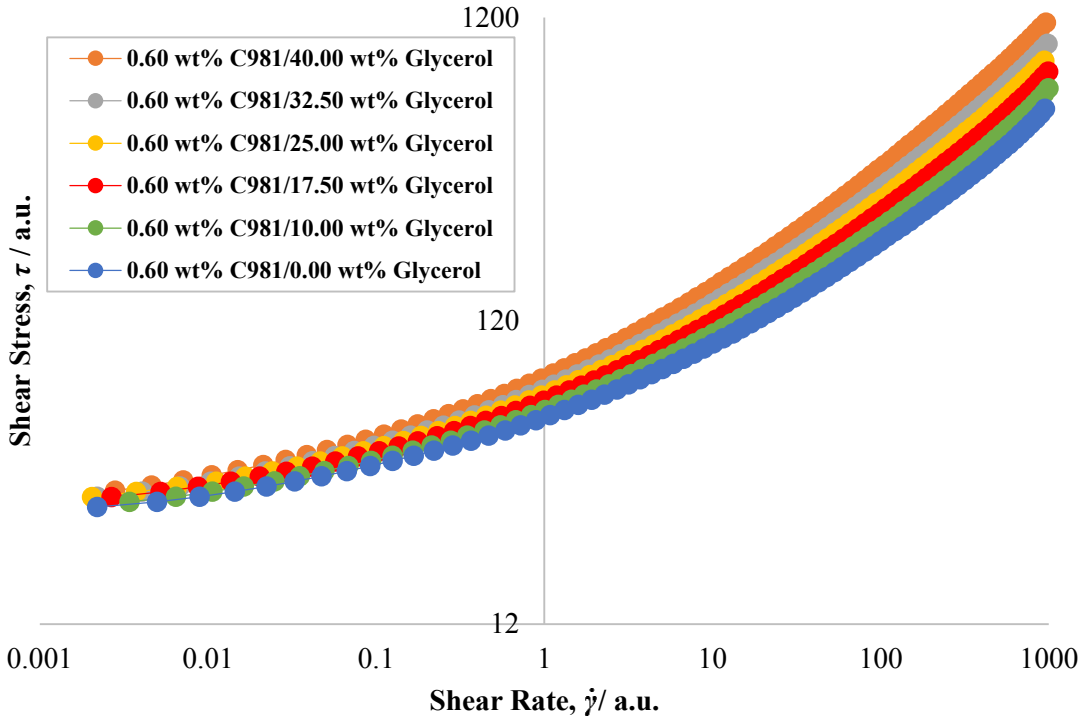

Figure A.28. Raw rheological flow curves, acquired from shear stress down sweeps using 6-bladed vane geometry, of C981/glycerol mixtures at a constant C981 mass fraction of 0.60 wt%, and glycerol mass fractions, ranging from 0.00-40.00 wt%, with all solutions at an approximately constant pH 6.41-6.56.

Table A.28. Herschel-Bulkley fitted data and the physical properties of the 0.60 wt% C981/glycerol mixtures, along with the associated error quantification of the mathematical fits and the shear rate range over which the fits occurred.

Physical properties			**Herschel-Bulkley rheological properties**			**Error quantification and analysis**		
C981 mass fraction / wt%	**Glycerol mass fraction / wt%**	**pH**	**Yield stress, τ_y / a.u.**	**Flow consistency index, *K* / a.u.**	**Flow behaviour index, *n***	**Optimised fit AAD / %**	**Optimised fit R^2 value**	**Shear rate range of optimised fit / a.u.**
0.60	0.00	6.41	29.7	26.1	0.44	2.31	0.997	0.00219-950
0.60	10.00	6.46	30.7	28.2	0.45	2.41	0.997	0.00341-996
0.60	17.50	6.43	32.1	31.2	0.45	2.44	0.998	0.00267-990
0.60	25.00	6.49	32.4	33.9	0.46	2.50	0.998	0.00204-940
0.60	32.50	6.56	32.3	36.8	0.46	2.54	0.998	0.00219-985
0.60	40.00	6.53	33.8	41.7	0.47	2.66	0.998	0.00280-961

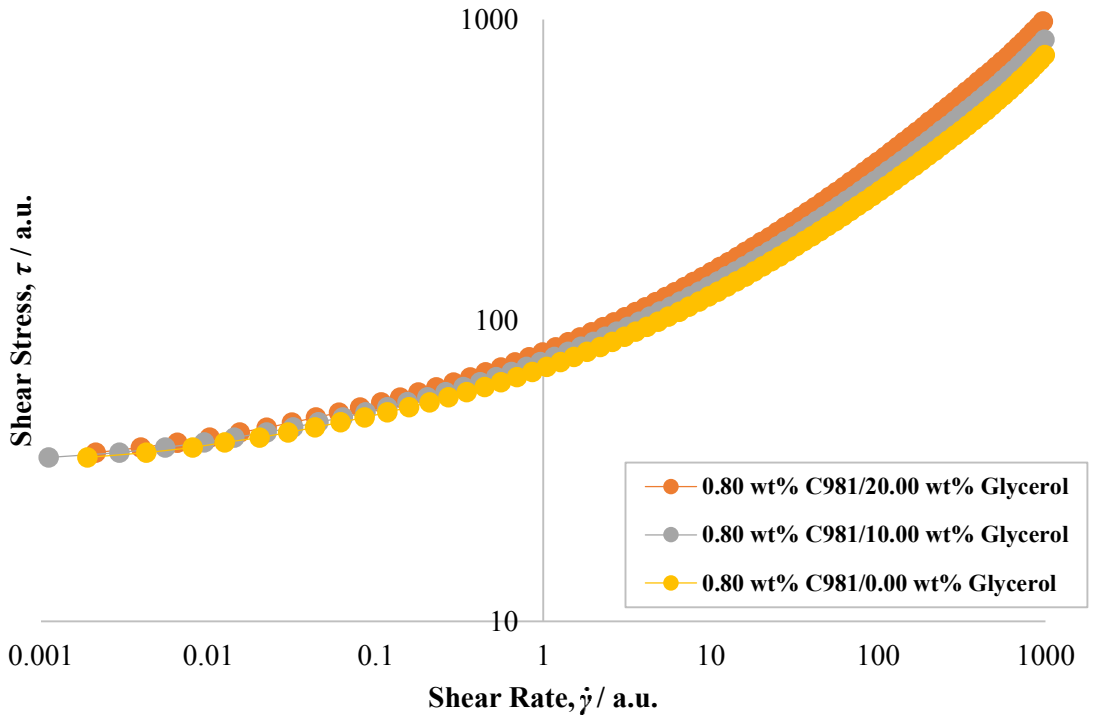

Figure A.29. Raw rheological flow curves, acquired from shear stress down sweeps using 6-bladed vane geometry, of C981/glycerol mixtures at a constant C981 mass fraction of 0.80 wt%, and glycerol mass fractions, ranging from 0.00-20.00 wt%, with all solutions at an approximately constant pH 6.23-6.37.

Table A.29. Herschel-Bulkley fitted data and the physical properties of the 0.80 wt% C981/glycerol mixtures, along with the associated error quantification of the mathematical fits and the shear rate range over which the fits occurred.

Physical properties			**Herschel-Bulkley rheological properties**			**Error quantification and analysis**		
C981 mass fraction / wt%	**Glycerol mass fraction / wt%**	**pH**	**Yield stress, τ_y / a.u.**	**Flow consistency index, *K* / a.u.**	**Flow behaviour index, *n***	**Optimised fit AAD / %**	**Optimised fit R^2 value**	**Shear rate range of optimised fit / a.u.**
0.80	0.00	6.23	36.3	30.57	0.45	2.55	0.997	0.00189-993
0.80	10.00	6.38	36.8	33.72	0.45	2.69	0.997	0.00111-989
0.80	20.00	6.34	37.8	37.67	0.46	2.71	0.998	0.00212-969

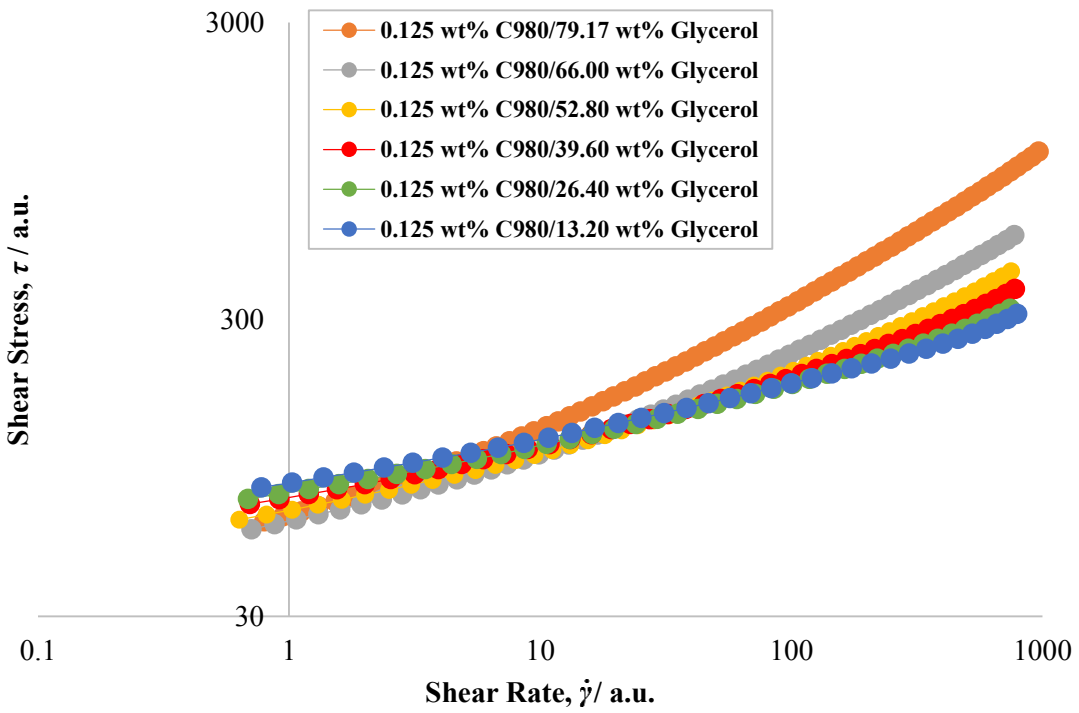

Figure A.30. Raw rheological flow curves, acquired from shear stress down sweeps using 6-bladed vane geometry, of C980/glycerol mixtures at a constant C980 mass fraction of 0.125 wt%, and glycerol mass fractions, ranging from 13.20-79.17 wt%, with all solutions at an approximately constant pH: 7.57-8.49.

Table A.30. Herschel-Bulkley fitted data and the physical properties of the 0.125 wt% C980/glycerol mixtures, along with the associated error quantification of the mathematical fits and the shear rate range over which the fits occurred.

Physical properties			**Herschel-Bulkley rheological properties**			**Error quantification and analysis**		
C980 mass fraction / wt%	**Glycerol mass fraction / wt%**	**pH**	**Yield stress, τ_y / a.u.**	**Flow consistency index, *K* / a.u.**	**Flow behaviour index, *n***	**Optimised fit AAD / %**	**Optimised fit R^2 value**	**Shear rate range of optimised fit / a.u.**
0.125	13.20	7.57	54.1	31.1	0.31	0.94	0.998	0.776-795
0.125	26.40	7.64	52.5	26.7	0.35	0.93	0.999	0.686-744
0.125	39.60	7.98	53.0	23.4	0.39	1.14	0.998	0.698-778
0.125	52.80	8.03	49.0	20.2	0.44	1.03	0.999	0.633-750
0.125	66.00	8.33	44.9	18.9	0.50	0.85	1.000	0.709-774
0.125	79.17	8.49	42.5	24.5	0.54	0.59	1.000	0.796-566

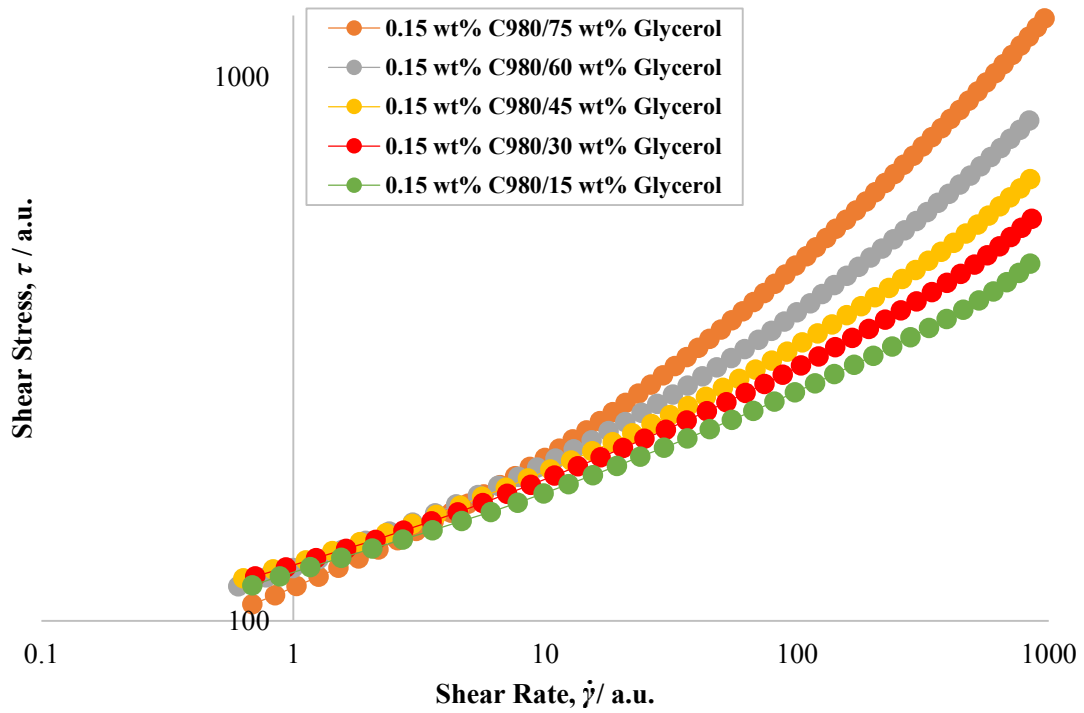

Figure A.31. Raw rheological flow curves, acquired from shear stress down sweeps using 6-bladed vane geometry, of C980/glycerol mixtures at a constant C980 mass fraction of 0.15 wt%, and glycerol mass fractions, ranging from 15-75 wt%, with all solutions at an approximately constant pH: 7.67-8.18.

Table A.31. Herschel-Bulkley fitted data and the physical properties of the 0.15 wt% C980/glycerol mixtures, along with the associated error quantification of the mathematical fits and the shear rate range over which the fits occurred.

Physical properties			**Herschel-Bulkley rheological properties**			**Error quantification and analysis**		
C980 mass fraction / wt%	**Glycerol mass fraction / wt%**	**pH**	**Yield stress, τ_y / a.u.**	**Flow consistency index, *K* / a.u.**	**Flow behaviour index, *n***	**Optimised fit AAD / %**	**Optimised fit R^2 value**	**Shear rate range of optimised fit / a.u.**
0.15	15.00	7.67	77.4	46.4	0.30	0.80	0.999	0.687-844
0.15	30.00	7.67	86.6	41.7	0.35	1.01	0.999	0.707-857
0.15	45.00	7.78	90.9	38.4	0.39	1.04	0.999	0.634-844
0.15	60.00	7.93	89.7	37.1	0.44	0.93	1.000	0.604-836
0.15	75.00	8.18	79.5	37.3	0.50	0.72	1.000	0.687-963

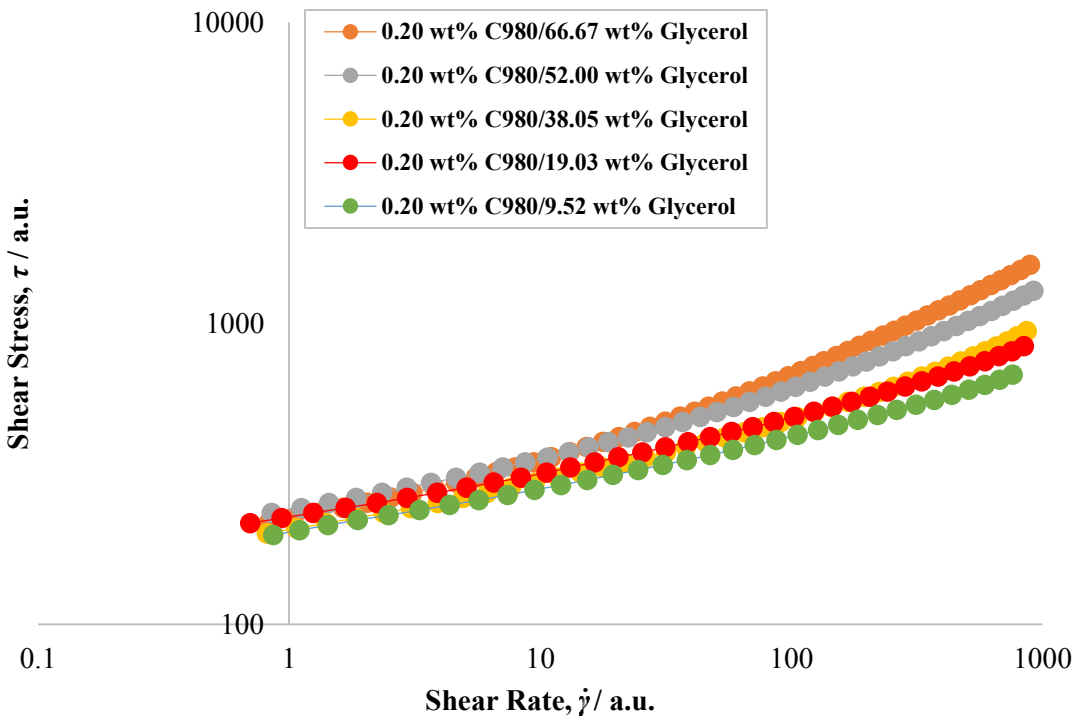

Figure A.32. Raw rheological flow curves, acquired from shear stress down sweeps using 6-bladed vane geometry, of C980/glycerol mixtures at a constant C980 mass fraction of 0.20 wt%, and glycerol mass fractions, ranging from 9.52-66.67 wt%, with all solutions at an approximately constant pH: 7.45-7.87.

Table A.32. Herschel-Bulkley fitted data and the physical properties of the 0.20 wt% C980/glycerol mixtures, along with the associated error quantification of the mathematical fits and the shear rate range over which the fits occurred.

Physical properties			**Herschel-Bulkley rheological properties**			**Error quantification and analysis**		
C980 mass fraction / wt%	**Glycerol mass fraction / wt%**	**pH**	**Yield stress, τ_y / a.u.**	**Flow consistency index, *K* / a.u.**	**Flow behaviour index, *n***	**Optimised fit AAD / %**	**Optimised fit R^2 value**	**Shear rate range of optimised fit / a.u.**
0.20	9.52	7.47	125.8	79.3	0.29	0.64	0.999	0.864-763
0.20	19.03	7.45	150.0	79.2	0.32	0.75	0.999	0.701-844
0.20	38.05	7.67	150.5	60.3	0.37	1.31	0.998	0.815-866
0.20	52.00	7.70	176.8	68.0	0.40	0.90	0.999	0.853-922
0.20	66.67	7.87	161.7	66.3	0.45	0.66	1.000	0.829-893

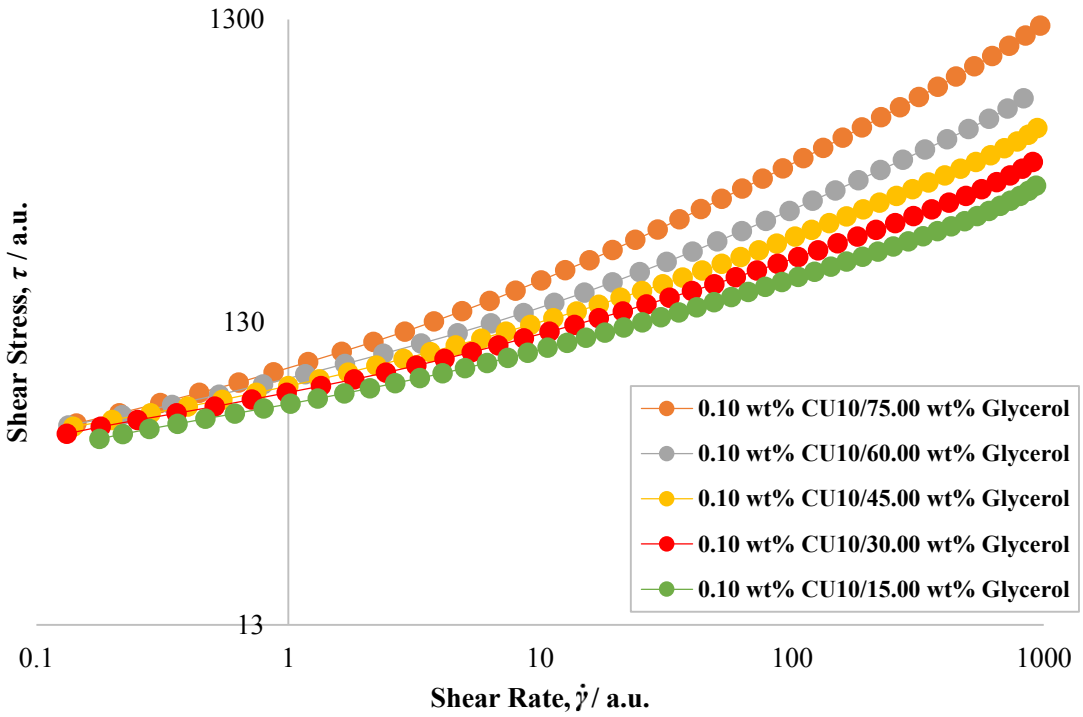

Figure A.33. Raw rheological flow curves, acquired from shear stress down sweeps using 6-bladed vane geometry, of CU10/glycerol mixtures at a constant CU10 mass fraction of 0.10 wt%, and glycerol mass fractions, ranging from 15.00-75.00 wt%, with all solutions at an approximately constant pH: 6.63-7.36.

Table A.33. Herschel-Bulkley fitted data and the physical properties of the 0.10 wt% CU10/glycerol mixtures, along with the associated error quantification of the mathematical fits and the shear rate range over which the fits occurred.

Physical properties			**Herschel-Bulkley rheological properties**			**Error quantification and analysis**		
CU10 mass fraction / wt%	**Glycerol mass fraction / wt%**	**pH**	**Yield stress, τ_y / a.u.**	**Flow consistency index, *K* / a.u.**	**Flow behaviour index, *n***	**Optimised fit AAD / %**	**Optimised fit R^2 value**	**Shear rate range of optimised fit / a.u.**
0.10	15.00	6.63	38.5	30.5	0.34	1.23	0.998	0.178-934
0.10	30.00	6.67	41.1	34.0	0.35	1.29	0.998	0.132-906
0.10	45.00	6.65	44.7	34.4	0.39	1.29	0.999	0.140-945
0.10	60.00	6.91	45.1	38.1	0.42	1.11	0.999	0.134-832
0.10	75.00	7.36	45.2	44.6	0.47	1.18	0.999	0.144-968

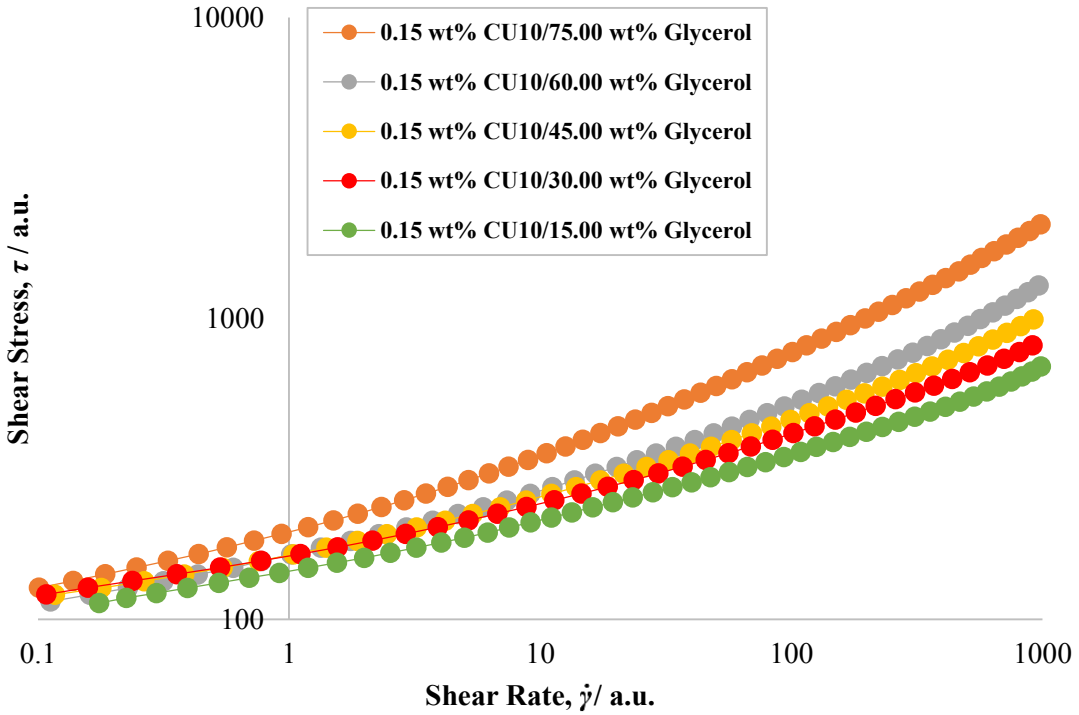

Figure A.34. Raw rheological flow curves, acquired from shear stress down sweeps using 6-bladed vane geometry, of CU10/glycerol mixtures at a constant CU10 mass fraction of 0.15 wt%, and glycerol mass fractions, ranging from 15.00-75.00 wt%, with all solutions at an approximately constant pH: 6.30-6.91.

Table A.34. Herschel-Bulkley fitted data and the physical properties of the 0.15 wt% CU10/glycerol mixtures, along with the associated error quantification of the mathematical fits and the shear rate range over which the fits occurred.

Physical properties			**Herschel-Bulkley rheological properties**			**Error quantification and analysis**		
CU10 mass fraction / wt%	**Glycerol mass fraction / wt%**	**pH**	**Yield stress, τ_y / a.u.**	**Flow consistency index, *K* / a.u.**	**Flow behaviour index, *n***	**Optimised fit AAD / %**	**Optimised fit R^2 value**	**Shear rate range of optimised fit / a.u.**
0.15	15.00	6.30	81.4	61.8	0.32	1.04	0.998	0.175-987
0.15	30.00	6.41	93.3	67.1	0.34	0.93	0.999	0.108-914
0.15	45.00	6.56	94.6	66.8	0.37	1.36	0.999	0.117-923
0.15	60.00	6.91	93.5	66.4	0.41	1.97	0.997	0.112-967
0.15	75.00	6.82	100.1	90.7	0.44	1.47	0.999	0.101-984

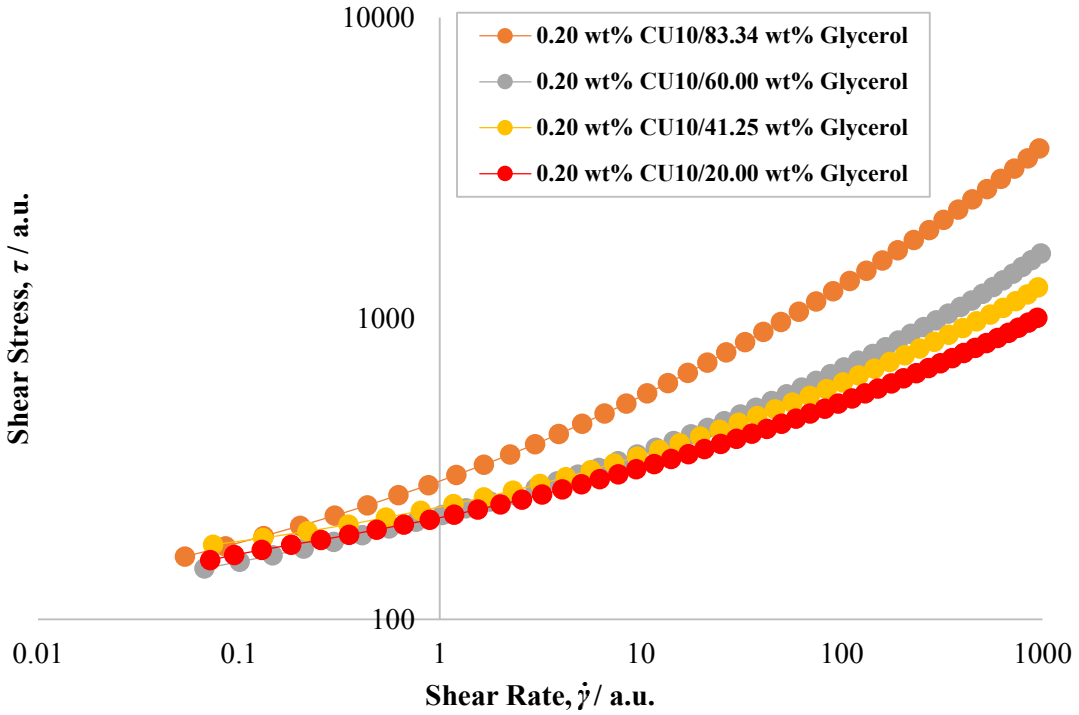

Figure A.35. Raw rheological flow curves, acquired from shear stress down sweeps using 6-bladed vane geometry, of CU10/glycerol mixtures at a constant CU10 mass fraction of 0.20 wt%, and glycerol mass fractions, ranging from 20.00-83.34 wt%, with all solutions at an approximately constant pH: 6.28-7.00.

Table A.35. Herschel-Bulkley fitted data and the physical properties of the 0.20 wt% CU10/glycerol mixtures, along with the associated error quantification of the mathematical fits and the shear rate range over which the fits occurred.

Physical properties			**Herschel-Bulkley rheological properties**			**Error quantification and analysis**		
CU10 mass fraction / wt%	**Glycerol mass fraction / wt%**	**pH**	**Yield stress, τ_y / a.u.**	**Flow consistency index, *K* / a.u.**	**Flow behaviour index, *n***	**Optimised fit AAD / %**	**Optimised fit R^2 value**	**Shear rate range of optimised fit / a.u.**
0.20	20.00	6.28	124.8	90.4	0.33	0.93	0.999	0.0721-945
0.20	41.25	6.57	148.8	84.7	0.37	0.84	0.999	0.0743-953
0.20	60.00	6.63	123.7	91.9	0.40	1.98	0.997	0.0645-983
0.20	83.34	7.00	132.7	146.3	0.45	2.14	0.998	0.0583-967

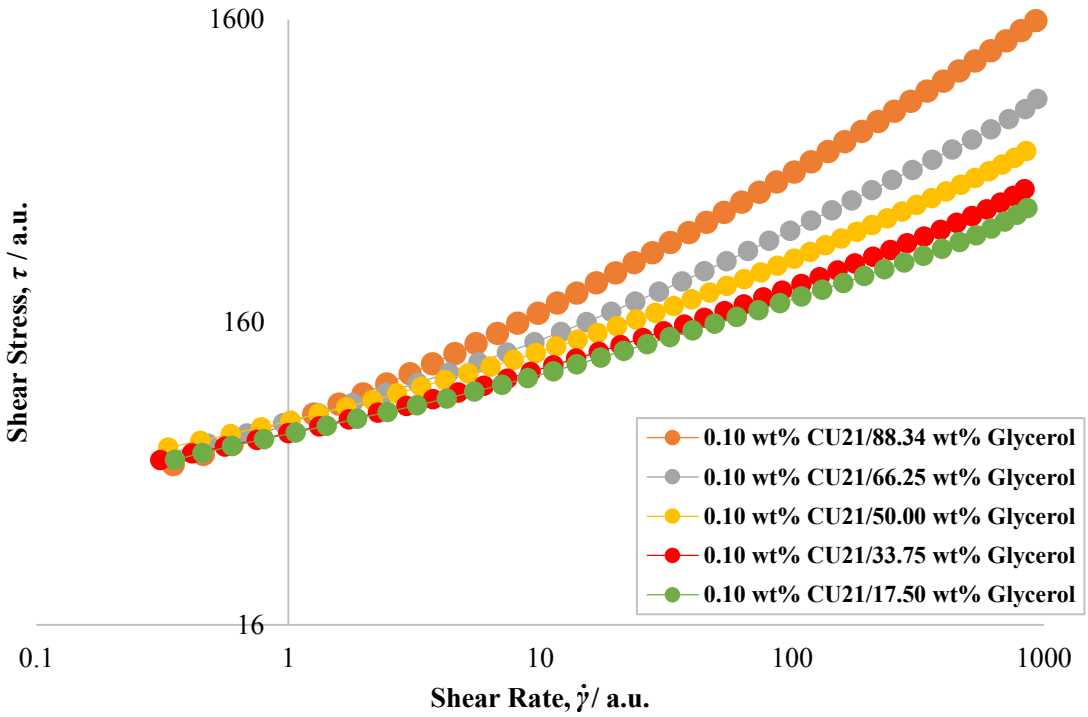

Figure A.36. Raw rheological flow curves, acquired from shear stress down sweeps using 6-bladed vane geometry, of CU21/glycerol mixtures at a constant CU21 mass fraction of 0.10 wt%, and glycerol mass fractions, ranging from 17.50-88.34 wt%, with all solutions at an approximately constant pH 6.82-7.76.

Table A.36. Herschel-Bulkley fitted data and the physical properties of the 0.10 wt% CU21/glycerol mixtures, along with the associated error quantification of the mathematical fits and the shear rate range over which the fits occurred.

Physical properties			**Herschel-Bulkley rheological properties**			**Error quantification and analysis**		
CU21 mass fraction / wt%	**Glycerol mass fraction / wt%**	**pH**	**Yield stress, τ_y / a.u.**	**Flow consistency index, *K* / a.u.**	**Flow behaviour index, *n***	**Optimised fit AAD / %**	**Optimised fit R^2 value**	**Shear rate range of optimised fit / a.u.**
0.10	17.50	6.82	34.4	33.5	0.34	1.12	0.998	0.355-861
0.10	33.75	7.00	37.1	31.4	0.37	0.94	0.999	0.310-840
0.10	50.00	7.15	42.8	32.5	0.41	0.89	1.000	0.334-852
0.10	66.25	7.36	39.6	34.8	0.46	0.89	0.999	0.332-945
0.10	88.34	7.76	31.2	42.3	0.52	0.79	1.000	0.349-929

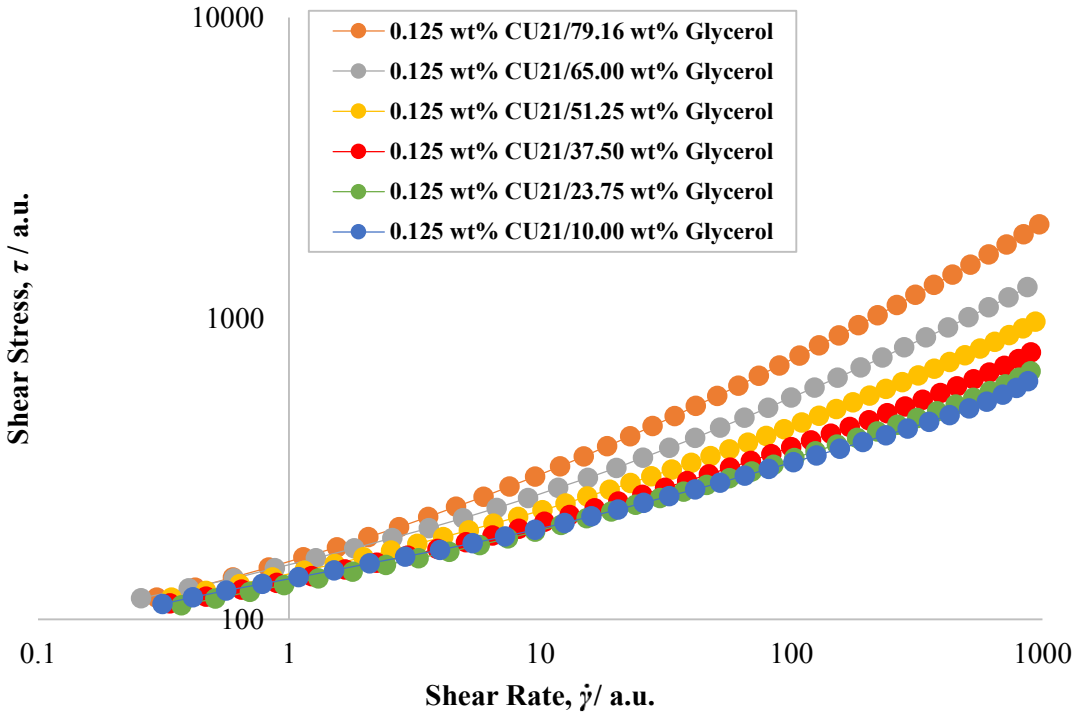

Figure A.37. Raw rheological flow curves, acquired from shear stress down sweeps using 6-bladed vane geometry, of CU21/glycerol mixtures at a constant CU21 mass fraction of 0.125 wt%, and glycerol mass fractions, ranging from 10.00-79.16 wt%, with all solutions at an approximately constant pH 6.66-7.50.

Table A.37. Herschel-Bulkley fitted data and the physical properties of the 0.125 wt% CU21/glycerol mixtures, along with the associated error quantification of the mathematical fits and the shear rate range over which the fits occurred.

Physical properties			**Herschel-Bulkley rheological properties**			**Error quantification and analysis**		
CU21 mass fraction / wt%	**Glycerol mass fraction / wt%**	**pH**	**Yield stress, τ_y / a.u.**	**Flow consistency index, *K* / a.u.**	**Flow behaviour index, *n***	**Optimised fit AAD / %**	**Optimised fit R^2 value**	**Shear rate range of optimised fit / a.u.**
0.125	10.00	6.66	68.9	65.5	0.30	1.07	0.998	0.313-877
0.125	23.75	6.76	74.0	56.0	0.34	0.83	0.999	0.372-898
0.125	37.50	6.86	78.9	55.0	0.37	0.91	0.999	0.335-900
0.125	51.25	7.05	82.8	58.5	0.39	0.87	1.000	0.340-939
0.125	65.00	7.24	82.4	67.5	0.42	0.90	1.000	0.257-872
0.125	79.16	7.50	79.1	75.2	0.47	0.85	1.000	0.297-972

A.2 MFST instructions

'*Clearing Old Data*' operation

1. In the '*Data Entry*' worksheet, select the '*Clearing Old Data*' operation.
2. To clear old data, select the '*Yes*' button. If '*No*' is selected, the operation is terminated (having then selected '*OK*' button in the next message box).
3. If '*Yes*' was selected, old data is deleted and by selecting '*OK*' in the next message box, new data can now be deleted.

'*Deleting Library Entry*' operation

1. In the '*Data Entry*' worksheet, select the '*Delete Library Entry*' operation.
2. When it asks if the user wishes to proceed, select the '*Yes*' button. If '*No*' is selected, the operation is terminated (having then selected '*OK*' button in the next message box).
3. A warning message then pops up informing the user to enter in details relating to the fluid they wish to delete. Select the '*Yes*' button.
4. In the resulting userform, input in the fluid details that are to be deleted from the library. If it is a one-compound system, then leave the '*Compound 2 Name*' and *Compound 2 Mass Fraction*' entry boxes empty.
5. Then press the '*Delete*' button to continue with the operation. If '*Cancel*' is selected, the operation is terminated (having then selected '*OK*' button in the next message box).
6. When the entry has been found, confirm the deletion from the library by selecting the '*Yes*' button. If '*No*' is selected, the operation is terminated (having then selected '*OK*' button in the next message box).
7. Press '*OK*' on the message box notifying the user that the entry has been deleted, and the operation will run to completion.
8. If after Step 5 the entry is not found in the library, press '*OK*' is the resulting message box and the operation will be terminated.

'*Finding Best Match*' operation

1. Enter in the shear rate-shear stress rheological data of the 'to-be-matched' or 'real' fluid into the '*(1) Rheology Input*' section of the '*Data Entry*' worksheet. Make sure the data that is inputted was acquired with the vane rheometrical geometry and only 'good' data is included.
2. In the '*Data Entry*' worksheet, select the '*Finding Best Match*' operation.

3. To confirm that the data was acquired with the vane geometry, select '*Yes*' in the resulting message box. If '*Cancel*' is selected, the operation is terminated (having then selected '*OK*' button in the next message box).
4. Select '*Yes*' in the message box relating to the upper and lower limits of the shear rate range of the inputted fluid.
5. In the '*Setting Shear Rate Range*' userform, input in the lower and upper limits over which '*Finding Best Match*' process should occur and press the '*Add*' button. If '*Cancel*' is selected, the operation is terminated (having then selected '*OK*' button in the next message box).
6. In the resulting message box, press the '*OK*' button to confirm the inputted shear rate range. The '*Finding Best Match*' process will then occur and usually takes 10-15 minutes.
7. The user is then informed of the best-matched fluid and that formulation details can be found in the '*Top Matches_Details*' worksheet. Press the '*OK*' button to continue.
8. If none of the Top 2-15 'best-matched' fluids are from the same fluid family as the 'best-matched' fluid then the user will be informed of this via the '*Interpolation not possible*' message box. They will also be informed that the '*Perform Interpolation*' operation, located within the '*Top Matches_Graph*' worksheet should NOT be executed. If one or more of the Top 2-15 'best-matched' fluids are from the same fluid family as the 'best-matched' fluid then see the section below relating to the '*Perform Interpolation*' operation.
9. The '*Finding Best Match*' process has run to completion. Details relating to the best-matched fluid can be found in the '*Top Matches_Graph*' and '*Top Matches_Details*'. From the shear rate-shear stress plot in the '*Top Matches_Graph*', the various best-matched fluids can be selected and de-selected using the associated checkboxes.

'*Perform Interpolation*' operation

1. Having performed Steps 1-7 of the '*Finding Best Match*' operation, if one or more of the Top 2-15 'best-matched' fluids are from the same 'constant mass fraction' fluid family as the 'best-matched' fluid (see Step 8 in the '*Finding Best Match*' operation), a message box is presented informing the user of this and that the '*Perform Interpolation*' operation can be executed from the '*Top Matches_Graph*' worksheet. Press the '*OK*' button to continue.
2. If the user wishes to undergo the '*Perform Interpolation*' process, the '*Perform Interpolation*' button can then be pressed.
3. The user is then taken to the '*Best Interpolated Fluid*' worksheet and a large message box is displayed, explaining how to determine the mass fraction of the best interpolated fluid (read off the mass fraction in the plots that results in the minimum in average absolute deviation). Press '*OK*' to run the operation to completion.

'*Adding Data to Library (Data & Fitting Thereof)*' operation

1. Enter in the shear rate-shear stress rheological data of the fluid into the '*(1) Rheology Input*' section of the '*Data Entry*' worksheet. Make sure the data that is inputted was acquired with the vane rheometrical geometry and only 'good' data is included.
2. In the '*Data Entry*' worksheet, select the '*Adding Data to Library (Data & Fitting Thereof)*' operation.
3. To confirm that the data was acquired with the vane geometry and that only 'good' data was entered, select '*OK*' in the resulting message box. If '*Cancel*' is selected, the operation is terminated (having then selected '*OK*' button in the next message box).
4. In the resulting '*Add Fluid – Optimisation Fitting*' userform input in all details relating to the fluid, including the shear rate range over which the process is occurring, the formulation details, whether the fluid is part of a 'constant pH fluid set' (i.e. the pH was not intentionally adjusted with an external substance) and the various rankings. To proceed, select the '*Add*' button. If '*Cancel*' is selected, the operation is terminated (having then selected '*OK*' button in the next message box).
5. The user will then be informed of the various deviations associated with fitting the raw data with the three models (Herschel-Bulkley, Casson and Power-Law). The user is advised to add the data to the library via the model that resulting in the lowest average absolute deviation value. Press '*Yes*' to add the fluid to the '*Library_Fitted*' worksheet via the model that gave the most accurate description of the raw data, and then press '*OK*' in the resulting message box confirming the addition. The process will then run to completion.
6. If '*No*' was selected in Step 5, the user will then be asked if they wish to add the fluid to the '*Library_Fitted*' worksheet via the model that gave the second best description of the raw data. At this stage, press '*Yes*' in the message box and then '*OK*' in the resulting message box confirming the addition, and the process will run to completion.
7. If '*No*' was selected in Step 6, the user will then be asked if they wish to add the fluid to the '*Library_Fitted*' worksheet via the model that gave the worst description of the raw data. At this stage, press '*Yes*' in the message box and then '*OK*' in the resulting message box confirming the addition, and the process will run to completion.
8. If '*No*' was selected in Step 7, the user will then be informed that the fluid has not been added to the library via any of the mathematical fits and the operation will be terminated, and if they are sure they do not want to add the fluid to the library via the models. If the '*Yes*' button is pressed, the process will be terminated when the '*OK*' button is pressed in the resulting message box. If '*No*' is pressed, the user will be then be informed that they should re-execute the operation and the current process will be terminated when the '*OK*' button is pressed.

'*Adding Data to Library (By Fitted Parameters)*' operation

1. In the '*Data Entry*' worksheet, select the '*Adding Data to Library (By Fitted Parameters)*' operation.
2. In the resulting message box, press the '*Yes*' button to confirm the addition of fluids to the library via mathematical model parameters. Selecting '*No*' will terminate the operation.
3. A warning message is then displayed asking the user to only enter data from one mathematical model, otherwise the operation will be aborted. Press '*OK*' to continue.
4. In the resulting userform, enter in the identity, physical and rheological properties of the fluid that is going to be added to the '*Library_Fitted*' worksheet. Press '*Add*' to proceed with the operation. If '*Cancel*' is selected, the operation is terminated (having then selected '*OK*' button in the next message box).
5. Having pressed '*Add*' in Step 4, the user will then be notified of the addition of the fluid to the library. Press '*OK*' in the resulting message box to run the operation to completion.

A.3 Dimensional analysis for mixing viscoplastic fluids in vessels

Dimensional analysis and the Buckingham π-theorem were used determine the key dimensionless groups that describe the agitation of viscoplastic fluids in stirred vessel systems. In the following section, the derivation of the yield stress Reynolds number, Re_y is shown as an example:

$$\Pi = \rho^a N^b D^c \tau_y \tag{A.1}$$

$$\Pi = (ML^{-3})^a (T^{-1})^b (L)^c (ML^{-1}T^{-2}) \tag{A.2}$$

$$M: a + 1 = 0 \tag{A.3}$$

$$L: -3a + c - 1 = 0 \tag{A.4}$$

$$T: -b - 2 = 0 \tag{A.5}$$

$$a = -1, b = -2, c = -2 \tag{A.6}$$

$$\Pi = \rho^{-1} N^{-2} D^{-2} \tau_y \tag{A.7}$$

$$Re_y = \frac{\rho N^2 D^2}{\tau_y} \tag{A.8}$$

A.4 Numerical methods for mixing viscoplastic fluids in vessels

Numerical construction of the single-impeller mixing system

The mixing system configuration considered in this study consists of a fixed cylindrical tank and a rotating impeller (a 6-bladed RT and/or a 4-bladed 45° PBT). The construction of both impeller and tank was performed using a similar approach to Kahouadji *et al.* (2018) that circumvents the need for time consuming construction, meshing and re-meshing of any geometrical shape. Instead, a modular manner was used, with the geometry being built from primitive geometrical objects using a state distance function that takes into account the interaction between these objects and the flow for both single (as in the current work) and two-phase flows (Kahouadji *et al.* (2018, 2019)). The final structure in the computational domain, visualised in Figure A.38, consists of the iso-value $(x, y, z) = 0$; the static distance function, $\Psi(x, y, z)$ is positive for the fluid part and negative for the solid part, where (x, y, z) are Cartesian coordinates. Many primitive solid geometries are incorporated into the code, including spheres, planes, cylinders and tori, as are geometrical operations, such as "union" and "intersection" for each primitive object. In this study, only planes, cylinders and a combination of the two are required for the construction of the mixing system. As a first step, the geometrical shape for the system is chosen. For the case of the tank, a vertical cylinder with a radius, $R = 0.074$ m, was selected, where its distance function $\Psi_{cyl}(x, y, z) > 0$ for all Cartesian points that satisfy $(x - x_0)^2 + (y - y_0)^2 < R^2$, with (x_0, y_0) denoting the central axes within the tank. The bottom of the tank is closed off through calling another distance function, $\Psi_{pl}(x, y, z) > 0$ for all Cartesian points that satisfy $z > 0$. The resulting distance function characterising the cylindrical tank is performed by applying the intersection operation $\Psi_{tank} = \Psi_{cyl} \cap \Psi_{pl}$. Finally, the resulting construction of the open-top cylindrical tank is made when the iso-value, $\Psi_{tank} = 0$, as seen in Figure A.38(a). In a similar way, all parts of the impellers (Ψ_{shaft}, Ψ_{hub}, Ψ_{disc} and Ψ_{blades}) were constructed and the union operator was used to produce the resulting distance function characterising each impeller. For the RT impeller: $\Psi_{RT} = \Psi_{shaft} \cup \Psi_{hub} \cup \Psi_{disc} \cup \Psi_{blades}$ and for the PBT impeller: $\Psi_{PBT} = \Psi_{shaft} \cup \Psi_{hub} \cup \Psi_{blades}$. Due to the lack of a disc, the Ψ_{disc} function can be neglected for the PBT. The numerical construction of these two impeller types can be seen in Figure A.38(b), whilst Figure A.38(c) shows the entire mixing system equipped with a PBT impeller.

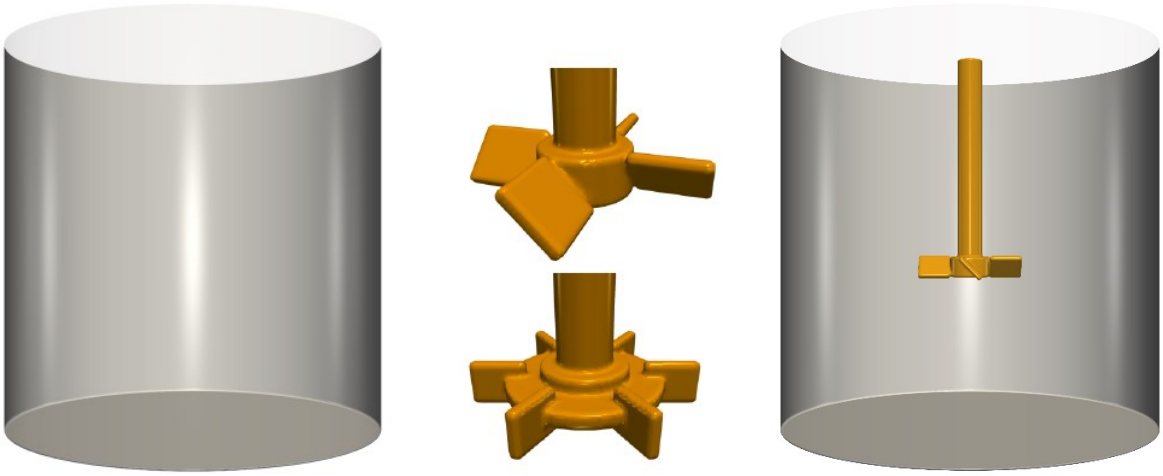

(a) (b) (c)

Figure A.38. Numerical construction of all parts of the mixing system: (a) the cylindrical tank, (b) PBT and RT impellers (both D = 0.041 m) and (c) an example of a single-impeller mixing system, equipped with a PBT impeller.

Governing equations and numerical methods

The mathematical model consists of solving the Navier-Stokes equations for the incompressible viscous fluids in a three-dimensional domain using the Cartesian coordinate $\mathbf{x} = (x, y, z)$:

$$\nabla \cdot \mathbf{u} = 0 \tag{A.9}$$

$$\rho\left(\frac{\partial \mathbf{u}}{\partial t} + \mathbf{u} \cdot \nabla \mathbf{u}\right) = -\nabla p + \nabla \cdot \mu(\nabla \mathbf{u} + \nabla \mathbf{u}^T) + \rho \mathbf{g} + \mathbf{F}_{fsi} \tag{A.10}$$

where ρ is the fluid density, t is the time, μ is the fluid viscosity, $\mathbf{u}$ is the velocity, p is the pressure, $\mathbf{g}$ is the gravitational acceleration and $\mathbf{F}_{fsi}$ is the solid-body force described by Fadlun *et al.* (2000), that has the advantage of keeping the accuracy and efficiency of the solution procedure. This force is defined numerically using the last step of the temporal integration of Eq. A.10:

$$\rho \frac{\mathbf{u}^{n+1} - \mathbf{u}^n}{\Delta t} = \text{local} + \mathbf{F}_{\mathbf{fsi}} \tag{A.11}$$

where "local" stands for the right hand side terms of Eq. A.10, that contains the convective, pressure gradient, viscous, gravitational force terms, and the superscripts denote the timestep. In the solid part of the domain (the impeller), $\mathbf{F}_{fsi}$ enforces the forced rotational motion $\mathbf{V}^{n+1}$:

$$\mathbf{u}^{n+1} = \mathbf{V}^{n+1} = 2\pi N\big((y - y_0) - (x - x_0)\big) \tag{A.12}$$

where (x_0, y_0) give the axis of the impeller and hence $\mathbf{F}_{fsi}$ is:

$$\mathbf{F}_{\mathbf{fsi}} = \rho \frac{\mathbf{V}^{n+1} - \mathbf{u}^n}{\Delta t} - \text{local} \tag{A.13}$$

Therefore, the impeller is considered as a fictive part in the Navier-Stokes solution (Eq. A.10) when a force is applied. From Eq. A.10, $\mu(\mathbf{x}, t)$ refers to the instantaneous local dynamic viscosity implemented explicitly and satisfies the Herschel-Bulkley model (Eq. A.14 and A.15).

$$\text{if } \dot{\gamma} > \dot{\gamma}_c \;\; \rightarrow \;\; \mu = \frac{\tau_y}{\dot{\gamma}} + K\left(\frac{\dot{\gamma}}{\dot{\gamma}_c}\right)^{n-1} \tag{A.14}$$

$$\text{if } \dot{\gamma} < \dot{\gamma}_c \;\; \rightarrow \;\; \mu = \tau_y \frac{\left(2 - \frac{\dot{\gamma}}{\dot{\gamma}_c}\right)}{\dot{\gamma}_c} + K\left((2-n) + (n+1)\frac{\dot{\gamma}}{\dot{\gamma}_c}\right) \tag{A.15}$$

where $\dot{\gamma}_c = 10^{-3}$ s^{-1} is the critical shear rate, or the value of the shear rate that corresponds to the fluid yield stress, and the other variables are as defined earlier. Inclusion of the $\dot{\gamma}_c$ term in Eq. A.14 and A.15 helps to avoid numerical instabilities caused by viscosity values equal to infinity at very low shear rate values when the material displays solid-like behaviour, by acting as a boundary between the solid behaviour and flowing regime. Due to the application of the piecewise equation, a reasonably accurate estimate of the critical shear rate is required for the fluid.

In addition to Eq. A.9-A.15, the boundary conditions applied to our system are as follows: non-slip on all solid objects (rotating impeller and fixed cylindrical tank) and stress-free on the top boundary ($w = 0$ and $\mathrm{d}u/\mathrm{d}z = \mathrm{d}v/\mathrm{d}z = 0$). The code is fully parallelised and can run on various platforms: from laptops to supercomputers. The parallelisation of the code is based on an algebraic domain decomposition technique (subdomains). The code is written in the computing language Fortran 2008 and communication between processors is managed by data exchange across adjacent subdomains via the Messaging Passing Interface (MPI) protocol. The computational domain is cubic and discretized by a uniform fixed three-dimensional mesh using a finite-difference method (Table A.38). This mesh has a standard staggered MAC cell arrangement (Harlow and Welch (1965)), where the u, v and w velocity nodes are located on the corresponding cell faces and scalar variables are located at the cell centres. The Navier-Stokes equations are solved by a projection method (Chorin (1968); Temam (1968)) with incremental pressure correction (Goda (1979)) applied to a finite-difference scheme which has first- and second-order accuracy in time and space, respectively. In addition, a semi-implicit scheme is chosen for the velocities to relax the stability restriction on the time-step due to viscous diffusion. All spatial derivative operators are evaluated using standard centred-differences, except in the nonlinear term where we use a second-order Essentially-Non-Oscillatory (ENO) scheme (Shu and Osher (1989); Sussman *et al.* (1998)).

A mesh dependency test was carried out using the Rushton turbine ($D = 0.041$ m, Scale 1) impeller at $N = 18.0$ s^{-1} ($Re_m = 28.7$, $Re_y = 25.3$), agitating a fluid with rheological properties of: $\tau_y = 21.5$ Pa, $K = 5.0$ Pa s^n and $n = 0.46$. Three different resolutions were trialled: 96^3, 192^3 and 394^3, and the numerical D_c/D values that resulted were: 2.49, 2.46 and 2.36, respectively. The experimental D_c/D value was 2.40, resulting in absolute deviation values of 3.8%, 2.5% and 1.7%, for resolutions of 96^3, 192^3 and

394^3, respectively. Due to these results, the resolution of 192^3 was selected for all simulations in this work. The resolution of 394^3 produced slightly more accurate results, however use of this resolution was extremely time-consuming in terms of computing resources and data post-processing. Therefore, using resolution of 192^3 still produced accurate results, whilst being far less time-consuming.

Table A.38. Summary of the details relating to the computational domain used in the CFD simulations for Scales 1-3.

Scale	Number of subdomains	Regular grid mesh per subdomain / Cells	Global resolution in entire domain
1	3 × 3 × 3 = 27	64 × 64 × 64	192 × 192 × 192
2	4 × 4 × 4 = 64	64 × 64 × 64	256 × 256 × 256
3	6 × 6 × 6 = 216	64 × 64 × 64	384 × 384 × 384

Numerical validation

In this work, the CFD model was validated using the experimental study of Hirata *et al.* (1994), who replicated the geometrical setup presented by Elson *et al.* (1986) proportionally, using a 6-bladed Rushton turbine impeller and a cylindrical tank fitted with four vertical baffles, but utilising a Carbopol fluid rather than a Xanthan gum solution. The geometrical and rheological details of the experimental study from Hirata *et al.* (1994) can be seen in Table A.39.

Table A.39. Tank and impeller geometrical setup and rheological properties used in the experimental study of Hirata *et al.* (1994), which have been replicated in the current work as means of numerical validation.

System	Property	Relationship
Tank geometry	Tank volume, V	$V = 2$ L
	Tank diameter, T	$T = 0.147$ m
	Baffle width, W_B	$W_B = T/10$
	Impeller clearance, C	$C = T/4$
	Liquid fill height, H	$H = T$
Impeller geometry	Impeller diameter, D	$D = T/2$
	Disc diameter, D_d	$D_d = 3D/4$
	Blade width, W_b	$W_b = D/4$
	Blade height, H_b	$H_b = D/5$
Rheology	Fluid yield stress, τ_y	$\tau_y = 18.9$ Pa
	Flow consistency index, K	$K = 4.6$ Pa s^n
	Flow behaviour index, n	$n = 0.46$

Hirata *et al.* (1994) used LDA to measure the azimuthal velocity profiles at a height of approximately z^*= 0.2, where z^*= -0.25 referred to the bottom of the tank and z^*= 0 refers to the centre of the impeller. These were recorded for four N values: 4 s^{-1}, 5 s^{-1}, 7 s^{-1} and 11 s^{-1} in three directions $\theta = \pi/12$, $\pi/4$ and $5\pi/12$ radians, with respect to the baffle in the azimuthal direction the impeller was rotating. The numerical simulations were performed at (a) N = 4 s^{-1} and (b) 7 s^{-1} and using the post-processing software Paraview, azimuthal velocity profiles were taken from the three azimuthal directions and averaged at approximately the same height above the impeller (z^* = 0.15~0.2).

Figure A.39 shows a comparison of the experimental data of Hirata *et al.* (1994) and the CFD predictions for the radial distribution of the azimuthal velocity component normalised by the tip speed, V_{TIP}, at (a) N = 4 s^{-1} and (b) N = 7 s^{-1}. Here, the normalised radial position, r^* = 0 refers to the centre of the shaft, and r^* = 1 corresponds to the location of the tank wall. The CFD data displayed a spike in normalised azimuthal velocity, V_θ/V_{TIP} at $r^* \sim 0.07$ indicating the shaft rotation, which was not seen in the experimental data and have therefore has not been presented in Figure A.39. There was good agreement between the experimental and CFD azimuthal velocity profiles, with the AAD values for the runs at (a) N = 4 s^{-1} and (b) N = 7 s^{-1} of 8.9 % and 13.1%, respectively, and R^2 values of 0.952 and 0.924, respectively. The good agreement between experimental and numerical results validated the CFD model used in this study.

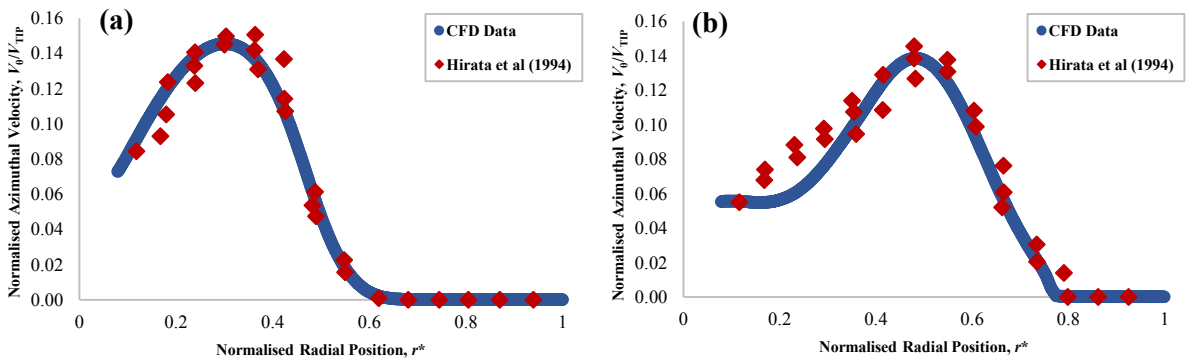

Figure A.39. Azimuthal velocity profile comparison at (a) N = 4 s^{-1} and (b) N = 7 s^{-1} between the CFD data from this work and the experimental data from Hirata *et al.* (1994).

A.5 MPMT instructions

Many of the operational features of this computational tool are the same as those presented in the MFST. For a step-by-step guide relating to the '*Clearing Old Data*', '*Finding Best Match*', '*Delete Library Entry*', '*Adding Data to Library (Data & Fitting Thereof)*' and '*Adding Data to Library (By Fitted Parameters)*' operations, the reader is direction to Section A.3. The key difference between these operations in the MFST and the MPMT is that in the MPMT, only rheological data obtained using the cone-and-plate rheometrical geometry should be inputted into the '*(1) Rheology Input*' section of the

'*Data Entry*' worksheet (whereas only data acquired using the vane should be inputted into the MFST). In this section, a step-by-step guide for using the '*Mixing in Stirred Vessels*' operation is presented.

'*Mixing In Stirred Vessels'* operation – Prediction process

1. In the '*Data Entry*' worksheet, select the '*Mixing In Stirred Vessels*' operation.
2. In the '*Predicting or Matching?*' userform, select the '*Prediction on known system*' option and press the '*OK*' button to proceed. If '*Cancel*' is selected, the operation is terminated (having then selected '*OK*' button in the next message box).
3. Selection of the cavern size prediction process is then confirmed in the resulting message box. Press '*OK*' to continue with the operation. If '*Cancel*' is selected, the operation is terminated (having then selected '*OK*' button in the next message box).
4. In the '*Predicting Cavern Sizes*' userform that is then displayed, input in all details relating to the rheological properties of the fluid and the geometrical setup. Only input in rheological data that has been acquired with the cone-and-plate geometry. Once all details have been filled in, press '*Add*' to proceed with the operation. If '*Cancel*' is selected, the operation is terminated (having then selected '*OK*' button in the next message box).
5. Having pressed '*Add*', the user is taken to the '*Mixing In Stirred Vessels*' worksheet and '*Selected Impeller Speed*' userform is displayed, allowing the user to input in an impeller speed which will be used for the prediction of the dimensionless diameter of the resulting cavern. Once inputted, press '*OK*' to continue. If '*Cancel*' is selected, the operation is terminated (having then selected '*OK*' button in the next message box).
6. Having pressed '*OK*', the prediction calculations are performed and a message box is displayed, informing the user of the dimensionless sizes of the resulting cavern. A schematic of the cavern in the vessel can be visualised in the '*Predicting Cavern Sizes in Viscoplastic Flows*' section of the '*Mixing In Stirred Vessels*' worksheet. Different impeller speeds can then be trialled by selecting the System 1 '*Change Impeller Speed*' operation in the '*Mixing In Stirred Vessels*' worksheet, but first the '*OK*' button in the '*Predicted Results & Changing Speed*' message box must be selected and the current operation will run to completion.

System 1: '*Change Impeller Speed*' operation

1. As discussed in Step 6 in the ''*Mixing in Stirred Vessels*' *operation – Prediction Process*' section above, to change the impeller speed for the prediction process, the System 1 '*Change Impeller Speed*' operation in the '*Mixing In Stirred Vessels*' worksheet is selected.

2. Having selected this operation, the '*Selected Impeller Speed*' userform again appears and the user can input in the desired impeller speed. Once inputted, press '*OK*' to proceed. If '*Cancel*' is selected, the operation is terminated (having then selected '*OK*' button in the next message box).
3. As in Step 6 above, the resulting predicted dimensionless cavern sizes will then be displayed. Press '*OK*' to run the operation to completion. This process can be repeated by re-selecting the System 1 '*Change Impeller Speed*' operation.

'*Mixing In Stirred Vessels'* operation – Matching process

1. In the '*Data Entry*' worksheet, select the '*Mixing In Stirred Vessels*' operation.
2. In the '*Predicting or Matching?*' userform, select the '*Perform a matching process*' option and press the '*OK*' button to proceed. If '*Cancel*' is selected, the operation is terminated (having then selected '*OK*' button in the next message box).
3. Selection of the matching cavern size process is then confirmed in the resulting message box. Press '*OK*' to continue with the operation. If '*Cancel*' is selected, the operation is terminated (having then selected '*OK*' button in the next message box).
4. In the ''*To-Be-Matched' System Details*' userform that is then displayed, input in all details relating to the rheological properties of the fluid and the geometrical setup. Only input in rheological data that has been acquired with the cone-and-plate geometry. Also input in the highest and lowest speeds, and resulting dimensionless cavern diameter range of the known system (System 1), that is to be matched on System 2. Once all details have been filled in, press '*Add*' to proceed with the operation. If '*Cancel*' is selected, the operation is terminated (having then selected '*OK*' button in the next message box).
5. Having pressed '*Add*', the user is taken to the '*Mixing In Stirred Vessels*' worksheet and the '*Same Fluid and Same Scale?*' userform is displayed. In this userform, the user can decide whether they wish to user the same fluid in the matching process or a different fluid, by selecting '*Yes*' or '*No*' respectively, in the appropriate drop-down box in the '*(1) Changing the Fluid?*' section. If '*No*' is selected, the user will then decide if they wish to use a fluid with a '*Larger*' or '*Smaller*' yield stress. The user can then decide whether they wish to user the same scale in the matching process or a different scale, by selecting '*Yes*' or '*No*' respectively, in the appropriate drop-down box in the '*(2) Changing the Scale?*' section. If '*No*' is selected, the user can then decide if they wish to user a fluid with a '*Larger (Scale-Up)*' or '*Smaller (Scale-Down)*' yield stress. The user can then decide by how many times they wish to scale-up or scale-down the impeller using the pre-defined values in the appropriate drop-down box. Once

all details have been included, press '*Add*' to proceed. If '*Cancel*' is selected, the operation is terminated (having then selected '*OK*' button in the next message box).

6. If the same scale and/or same fluid was selected in Step 5, the relevant System 1 details from will be copied across from the '*Predicting Cavern Sizes in Viscoplastic Flows*' section to the appropriate cells in the System 2 '*Matching Viscoplastic Flows*' section of the '*Mixing In Stirred Vessels*' worksheet. If a different scale was selected, appropriate scale-up/-down calculations will be performed, based on the selections from Step 5, which will automatically be inputted into the relevant cells in the '*Matching Viscoplastic Flows*' section. If a different fluid was selected, a fluid with either an increased or decreased yield stress (depending on the selection in Step 5) will be found from the '*Library_Fitted*' worksheet and suggested to the user via a message box. If the increase or decrease of the yield stress of the suggested fluid is great enough, the user should select '*Yes*' in the resulting message box. If not, then '*No*' should be selected and a fluid with a greater increase or decrease in yield stress will be found. If there are no fluids in the '*Library_Fitted*' worksheet with a greater increase or decrease in yield stress at this stage, the first suggested fluid will be used for the matching process.
7. Details of the suggested fluid are then presented to the user and the '*OK*' button should be pressed to proceed with the operation, with these details, along with the rheological properties of the fluid, being inputted into the relevant cells of the '*Matching Viscoplastic Flows*' section.
8. The '*Dimensionless Cavern Diameter*' userform will then be displayed, allowing the user to enter in a specific dimensionless cavern diameter, and associated impeller speed, from the known System 1, that is to be matched on System 2. Press '*OK*' to proceed.
9. The range of impeller speeds required on System 2 to match the dimensionless cavern diameters from System 1 will then be displayed to the user, along with the impeller speed on System 2 required to match the specific dimensionless cavern diameter from System 1. To find the appropriate impeller speed required to match a different specific dimensionless cavern diameter from System 1, the System 2 '*Change System 1 Impeller Speed and D_c/D*' operation can be selected in the '*Matching Viscoplastic Flows*' section, once '*OK*' has been selected in the current message box and the operation has run to completion. The matched dimensionless cavern sizes can be viewed in the schematics in both sections of the '*Mixing In Stirred Vessels*' worksheet.

System 2: '*Change System 1 Impeller Speed and D_c/D*' operation

1. As discussed in Step 9 in the ''*Mixing in Stirred Vessels*' *operation – Mathcing Process*' section above, to change the System 1 impeller speed and dimensionless cavern diameter for the

matching process, the System 2 '*Change System 1 Impeller Speed and D_c/D*' operation in the '*Matching Viscoplastic Flows*' section is selected.

2. Having selected this operation, the '*Dimensionless Cavern Diameter*' userform again appears and the user can input in the desired dimensionless cavern diameter and impeller speed from System 1. Once inputted, press '*OK*' to proceed.
3. As in Step 9 above, the impeller speed on System 2 required to match the specific dimensionless cavern diameter from System 1 is displayed. Press '*OK*' to run the operation to completion. This process can be repeated by re-selecting the System 2 '*Change System 1 Impeller Speed and D_c/D*' operation.

System 2: '*Change System 2 Scale/Fluid*' operation

1. The System 2 scale and/or fluid can be changed by selecting the '*Change System 2 Scale/Fluid*' operation in the '*Matching Viscoplastic Flows*' section.
2. The '*Same Fluid and Same Scale?*' userform is then displayed and the operation proceeds as described from Step 5 onwards in the *''Mixing In Stirred Vessels' operation – Matching process'* section above.